

Øyvind Notland Smogeli

# Control of Marine Propellers

From Normal to Extreme Conditions

Thesis for the degree of philosophiae doctor

Trondheim, September 2006

Norwegian University of  
Science and Technology  
Faculty of Engineering Science & Technology  
Department of Marine Technology



NTNU  
Norwegian University of Science and Technology

Thesis for the degree of philosophiae doctor

Faculty of Engineering Science & Technology  
Department of Marine Technology

©Øyvind Notland Smogeli

ISBN 82-471-8148-7 (printed ver.)  
ISBN 82-471-8147-9 (electronic ver.)  
ISSN 1503-8181

Doctoral Theses at NTNU, 2006:187

Printed by Tapir Uttrykk

# Abstract

This is a thesis about control of marine propellers. All ships and underwater vehicles, as well as an increasing number of offshore exploration and exploitation vessels, are controlled by proper action of their propulsion systems. For safe and cost effective operations, high performance vessel control systems are needed. To achieve this, all parts of the vessel control system, including both plant level and low-level control, must be addressed. However, limited attention has earlier been given to the effects of the propulsion system dynamics. The possible consequences of improper thruster control are:

- Decreased closed-loop vessel performance due to inaccurate thrust production
- Increased vessel down-time and maintenance cost due to unnecessary mechanical wear and tear.
- Increased fuel consumption and risk of blackouts due to unpredictable power consumption.

By focusing explicitly on the propeller operating conditions and the available options for low-level thruster control, this thesis presents several results to remedy these problems.

Two operational regimes are defined: normal, and extreme conditions. In normal operating conditions, the dynamic loading of the propellers is considered to be moderate, and primarily caused by oscillations in the inflow. In extreme conditions, the additional dynamic loads due to ventilation and in-and-out-of-water effects can be severe. In order to improve the understanding of these loads and develop a simulation model suitable for control system design and testing, systematic model tests with a ventilating propeller in a cavitation tunnel and a towing tank have been undertaken.

In conventional propulsion systems with fixed-pitch propellers, the low-level thruster controllers are usually aimed at controlling the shaft speed. Other control options are torque control and power control, as well as combinations of the three. The main scientific contributions of this thesis are:

- A combined torque/power controller and a combined speed/torque/power controller are designed. When compared to conventional shaft speed con-

trol, the proposed controllers give improved thrust production, decreased wear and tear, and reduced power oscillations.

- A propeller load torque observer and a torque loss estimation scheme is developed, enabling on-line monitoring of the propeller performance.
- An anti-spin thruster controller that enables use of torque and power control also in extreme operating conditions is motivated and designed. By applying the load torque observer to detect ventilation incidents, the anti-spin controller takes control of the shaft speed and lowers it until the ventilation incident is terminated.
- A propeller performance measure that can be used to improve thrust allocation in extreme operating conditions is introduced.

The proposed controllers and estimation schemes are validated through theoretical analyses, numerical simulations, and experiments on a model-scale propeller.

# Acknowledgments

This thesis is the main result of my doctoral studies, undertaken in the period August 2002 through September 2006 at the Norwegian University of Technology and Science (NTNU). My funding has been provided by a scholarship from the Research Council of Norway (NFR), and in part also by contributions from the *Centre for Ships and Ocean Structures* (CeSOS) and the project on *Energy Efficient All-Electric Ship* (EEAES), both sponsored by the NFR.

Most of all I would like to thank my supervisor, Professor Asgeir J. Sørensen at the Department of Marine Technology: first of all for taking me in as a MSc student, then for convincing me to do a PhD, and finally for being a great advisor and friend. Special thanks also to my co-advisor, Professor Knut J. Minsaas, for sharing from his immense knowledge of propellers. Additional thanks to Professor Thor I. Fossen for his help on the theoretical parts of this thesis, to Professor Tor Arne Johansen for valuable discussions, and to Dr. Tristan Perez for his support and advice. I would also like to thank my fellow PhD students for a great working environment, and especially Eivind Ruth, Luca Pivano, Jostein Bakkeheim, Damir Radan, and Roger Skjetne for their collaboration on joint publications. Another thanks to the MSc students who have suffered under my supervision, and especially to Leif Aarseth and Eivind Ruth, who have made significant contributions to the results presented in this thesis. Thanks also to Knut Arne Hegstad at the lab for his help with the experimental setups.

I've had many fruitful discussions with industrial partners in the various projects I've been involved in, helping to point my research in the right direction; in particular I will mention Kongsberg Maritime, Rolls-Royce Marine, ABB, Brunvoll Thrusters, Wärtsila Propulsion, and Siemens Energy and Automation. I have also received valuable help from Dr. Alf Kåre Ådnanes and Professor Roy Nilsen on practical issues regarding power systems and motor drives.

Finally, I would like to express my gratitude to all my family and friends for their support and patience, and especially to my parents for their continued support in all my choices.

All the work put into this thesis would not have been possible without someone at home to lean upon. Thank you, Anette, for your love and support, and for putting everything into perspective.

Trondheim, September 29<sup>th</sup> 2006

Øyvind Notland Smogeli



# Contents

<b>Abstract</b>	<b>iii</b>
<b>Acknowledgments</b>	<b>v</b>
<b>Nomenclature</b>	<b>xiii</b>
<b>1 Introduction</b>	<b>1</b>
1.1 Background . . . . .	1
1.2 Problem statement . . . . .	6
1.3 Main contributions . . . . .	6
1.4 List of publications . . . . .	7
1.5 Organization of the thesis . . . . .	9
<b>2 Propeller modelling</b>	<b>11</b>
2.1 Propeller characteristics . . . . .	11
2.1.1 Open-water characteristics . . . . .	13
2.1.2 4-quadrant model . . . . .	16
2.1.3 Simplified 4-quadrant model . . . . .	18
2.1.4 General momentum theory with propeller lift and drag . . . . .	18
2.1.5 Controllable pitch propellers . . . . .	19
2.1.6 Characteristics of various propeller types . . . . .	20
2.1.7 Propeller efficiency . . . . .	20
2.1.8 Thrust and torque relationships . . . . .	22
2.2 Dynamic effects . . . . .	24
2.2.1 Shaft dynamics . . . . .	24
2.2.2 Motor dynamics . . . . .	25
2.2.3 Accounting for gears . . . . .	26
2.2.4 Bollard pull relationships . . . . .	27
2.2.5 Propeller flow dynamics . . . . .	28
2.3 Loss effects . . . . .	29
2.3.1 In-line water inflow . . . . .	30
2.3.2 Ventilation and propeller emergence . . . . .	32
2.4 Ventilation experiments and simulation model . . . . .	36
2.4.1 Cavitation tunnel test results . . . . .	37

2.4.2	Open-water test results . . . . .	39
2.4.3	Scaling of test results . . . . .	41
2.4.4	Ventilation simulation model . . . . .	42
2.4.5	Ventilation simulation model verification . . . . .	45
2.4.6	Blade-frequency loading . . . . .	48
2.5	Propeller simulation model . . . . .	49
<b>3</b>	<b>Propulsion control in normal conditions</b>	<b>51</b>
3.1	Constraints . . . . .	51
3.2	Control objectives . . . . .	52
3.2.1	Thrust production . . . . .	52
3.2.2	Mechanical wear and tear . . . . .	53
3.2.3	Power consumption . . . . .	54
3.2.4	Robustness . . . . .	55
3.2.5	Surface vessels vs. underwater vehicles . . . . .	55
3.3	Thruster controller structure . . . . .	55
3.4	State of the art . . . . .	56
3.5	Control coefficients . . . . .	59
3.5.1	Shaft speed, torque, and power reference . . . . .	59
3.5.2	Choosing $K_{TC}$ and $K_{QC}$ . . . . .	60
3.5.3	Reverse thrust . . . . .	60
3.6	Reference generator . . . . .	61
3.6.1	Rate limiting function . . . . .	62
3.6.2	Shaft speed reference with rate limit . . . . .	63
3.6.3	Shaft speed reference with low-pass filter and rate limit . . . . .	63
3.6.4	Power reference generator . . . . .	64
3.6.5	Reference generator comparison . . . . .	65
3.7	Friction and inertia compensation . . . . .	65
3.7.1	Friction compensation . . . . .	67
3.7.2	Inertia compensation . . . . .	68
3.7.3	Feedforward compensation properties . . . . .	69
3.8	Torque and power limiting . . . . .	69
3.9	Feedback signal filtering . . . . .	70
3.10	Shaft speed feedback control . . . . .	71
3.11	Torque feedforward control . . . . .	71
3.12	Power feedback control . . . . .	72
3.13	Combined torque/power control . . . . .	73
3.13.1	Weighting function . . . . .	74
3.13.2	Controller formulation . . . . .	74
3.14	Modified combined torque/power control . . . . .	75
3.14.1	Additive integral action . . . . .	76
3.14.2	Vanishing integral action . . . . .	77
3.15	Combined speed/torque/power control . . . . .	78
3.16	Thrust control and additional instrumentation . . . . .	79
3.17	Controller summary . . . . .	80

---

3.18	Simulation results . . . . .	80
3.18.1	Controller response . . . . .	81
3.18.2	Fundamental controllers in waves and current . . . . .	83
3.18.3	Fundamental controllers with time-varying thrust reference	84
3.18.4	Combined controllers with time-varying thrust reference .	84
3.19	Discussion . . . . .	92
<b>4</b>	<b>Sensitivity to thrust losses</b>	<b>95</b>
4.1	Thrust, torque, power, and shaft speed relations . . . . .	96
4.2	Thrust sensitivity . . . . .	97
4.2.1	Shaft speed control thrust sensitivity . . . . .	97
4.2.2	Torque control thrust sensitivity . . . . .	97
4.2.3	Power control thrust sensitivity . . . . .	98
4.2.4	Thrust control thrust sensitivity . . . . .	98
4.2.5	Combined torque/power control thrust sensitivity . . . . .	98
4.3	Shaft speed sensitivity . . . . .	99
4.4	Torque sensitivity . . . . .	100
4.5	Power sensitivity . . . . .	100
4.6	Sensitivity function summary . . . . .	101
4.7	Steady-state performance . . . . .	102
4.8	Sensitivity to changes in advance velocity . . . . .	103
4.8.1	Non-dimensional parametrization for $V_a$ and $T_r$ . . . . .	104
4.8.2	Friction compensation errors . . . . .	109
4.9	Sensitivity to large thrust losses . . . . .	109
4.10	Stability properties . . . . .	115
4.10.1	System definition . . . . .	115
4.10.2	Nominal system stability . . . . .	119
4.10.3	Perturbed system stability . . . . .	120
4.10.4	Implications for shaft speed, torque, and power control .	122
<b>5</b>	<b>Propeller observers</b>	<b>125</b>
5.1	Propeller load torque observer . . . . .	126
5.1.1	Observer tuning . . . . .	128
5.1.2	Torque loss estimation . . . . .	128
5.2	$K_Q$ estimation . . . . .	129
5.3	Thrust estimation . . . . .	132
5.4	Performance monitoring . . . . .	132
5.5	Simulation results . . . . .	133
5.5.1	Simulations in waves . . . . .	133
5.5.2	Simulations with ventilation . . . . .	134
<b>6</b>	<b>Propulsion control in extreme conditions</b>	<b>137</b>
6.1	Anti-spin control objectives . . . . .	138
6.2	The anti-spin control concept . . . . .	139
6.3	Ventilation detection . . . . .	140

6.4	Anti-spin control actions . . . . .	141
6.5	Main anti-spin control result: torque scaling . . . . .	142
6.5.1	Primary anti-spin action . . . . .	143
6.5.2	Secondary anti-spin action . . . . .	145
6.5.3	Resulting anti-spin controller . . . . .	147
6.5.4	Steady-state analysis . . . . .	147
6.6	Alternative anti-spin controllers . . . . .	149
6.6.1	Speed bound anti-spin control . . . . .	149
6.6.2	Additive PI anti-spin control . . . . .	150
6.6.3	Shaft speed anti-spin control . . . . .	150
6.7	Controller summary . . . . .	152
6.8	Simulation results . . . . .	153
6.8.1	Controller tuning . . . . .	153
6.8.2	TS AS control vs. API AS control . . . . .	155
6.8.3	Single ventilation incidents . . . . .	156
6.8.4	Time-varying $T_r$ . . . . .	158
6.9	Discussion . . . . .	158
<b>7</b>	<b>Experimental results</b>	<b>165</b>
7.1	Experimental setup . . . . .	165
7.1.1	Measurements, data logging, and filtering . . . . .	167
7.1.2	Propeller characteristics and control coefficients . . . . .	168
7.1.3	Friction and inertia compensation . . . . .	172
7.2	Experiments in normal conditions . . . . .	172
7.2.1	Controller parameters . . . . .	174
7.2.2	Quasi-static tests . . . . .	175
7.2.3	Dynamic tests in waves . . . . .	175
7.2.4	Tracking tests . . . . .	178
7.2.5	Test of the combined SQP controller . . . . .	180
7.3	Experiments in extreme conditions . . . . .	188
7.3.1	Controller parameters . . . . .	188
7.3.2	Controller tuning . . . . .	189
7.3.3	Single ventilation incidents with the ducted propeller . . . . .	190
7.3.4	Single ventilation incidents with the open propeller . . . . .	192
7.3.5	Additional tests . . . . .	196
7.4	Discussion . . . . .	202
<b>8</b>	<b>Extensions to CPP and transit</b>	<b>207</b>
8.1	Extensions to CPP . . . . .	207
8.1.1	Controller modifications for CCP . . . . .	208
8.1.2	Consolidated controller example . . . . .	209
8.1.3	Observer and estimation extensions to CCP . . . . .	212
8.1.4	Anti-spin controller extensions to CCP . . . . .	212
8.1.5	A near optimal controller . . . . .	214
8.2	Extensions to transit . . . . .	214

---

8.2.1	DP vs. transit . . . . .	215
8.2.2	Controller modifications for transit . . . . .	216
8.2.3	Performance evaluation for transit . . . . .	217
8.2.4	Observer and estimation extensions to transit . . . . .	217
8.2.5	Anti-spin controller extensions to transit . . . . .	217
<b>9</b>	<b>Thrust allocation in extreme conditions</b>	<b>219</b>
9.1	Basic principles . . . . .	219
9.1.1	Actuator configuration . . . . .	220
9.1.2	Unconstrained allocation for non-rotatable thrusters . . . . .	220
9.2	Current thrust allocation solutions . . . . .	221
9.3	Motivation . . . . .	221
9.4	Performance monitoring . . . . .	222
9.4.1	Sensitivity estimation . . . . .	222
9.4.2	Ventilation monitoring . . . . .	223
9.4.3	A thruster performance measure . . . . .	223
9.5	Implications for thrust allocation . . . . .	224
<b>10</b>	<b>Conclusions and recommendations</b>	<b>225</b>
10.1	Conclusions . . . . .	225
10.2	Recommendations for future work . . . . .	227
<b>Bibliography</b>		<b>228</b>
<b>A</b>	<b>Propeller simulation data</b>	<b>a-1</b>
A.1	Main propeller parameters . . . . .	a-1
A.2	4-quadrant model parameters . . . . .	a-1
<b>B</b>	<b>Thruster controller tuning issues</b>	<b>a-5</b>
B.1	Shaft speed controller PI tuning . . . . .	a-5
B.2	Torque and power control tuning . . . . .	a-7
B.3	Inertia and friction compensation tuning . . . . .	a-7
B.4	Choice of parameters for the combined controllers . . . . .	a-8
<b>C</b>	<b>Simulation of relative propeller motion</b>	<b>a-9</b>
C.1	Vessel motion . . . . .	a-9
C.2	Transformation tools . . . . .	a-11
C.3	Wave- and current-induced velocities . . . . .	a-12
C.4	Calculation of relative motion . . . . .	a-13
C.5	Simplified calculations . . . . .	a-14
<b>D</b>	<b>Additional ventilation results</b>	<b>a-15</b>
D.1	Experimental set-up . . . . .	a-15
D.2	Scaling laws . . . . .	a-18
D.2.1	The non-ventilated regime . . . . .	a-19
D.2.2	The fully ventilated regime . . . . .	a-20

D.2.3	The partially ventilated regime . . . . .	a-20
D.2.4	Effect of Weber's number . . . . .	a-20
D.3	Additional experimental results . . . . .	a-21
D.3.1	Ducted propeller . . . . .	a-21
D.3.2	Open propeller . . . . .	a-24
<b>E</b>	<b>Additional thruster control results</b>	<b>a-27</b>
E.1	Fault-tolerant control . . . . .	a-27
E.2	Additional instrumentation . . . . .	a-29
E.2.1	Thrust feedback control . . . . .	a-29
E.2.2	Thrust control from torque feedback . . . . .	a-30
E.2.3	Propeller torque feedback control . . . . .	a-30
E.2.4	Propeller power feedback control . . . . .	a-31
E.2.5	Dynamic control coefficients . . . . .	a-31
E.3	Thrust, torque, and power output feedback control . . . . .	a-33
E.3.1	Thrust output feedback . . . . .	a-34
E.3.2	Torque output feedback . . . . .	a-34
E.3.3	Power output feedback . . . . .	a-35
E.4	Shaft speed control with implicit $V_a$ compensation . . . . .	a-35
E.4.1	Controller formulation . . . . .	a-36
E.4.2	Experimental results . . . . .	a-38
<b>F</b>	<b>Additional sensitivity function results</b>	<b>a-41</b>
F.1	Combined controller thrust sensitivity . . . . .	a-41
F.2	Friction compensation sensitivity function errors . . . . .	a-43
F.2.1	Linear friction compensation . . . . .	a-43
F.2.2	Static friction compensation error . . . . .	a-45
F.2.3	Result of errors . . . . .	a-46
F.3	Robustness analysis using Lyapunov theory . . . . .	a-46
F.3.1	Using the comparison method . . . . .	a-46
F.3.2	Determining the damping . . . . .	a-50
F.3.3	Quantifying the trajectory bound . . . . .	a-51
<b>G</b>	<b>Additional observer results</b>	<b>a-53</b>
G.1	Adaptive load torque observer . . . . .	a-53
G.1.1	Observability . . . . .	a-53
G.1.2	$K_\omega$ estimation . . . . .	a-54
G.1.3	Adaptive observer design . . . . .	a-56
G.1.4	Experimental results . . . . .	a-59
G.1.5	Extensions . . . . .	a-60
G.2	Online control parameter estimation . . . . .	a-60
G.2.1	Implementation for normal conditions . . . . .	a-62
G.2.2	Extension to extreme conditions . . . . .	a-62

# Nomenclature

## Abbreviations

API	Additive PI anti-spin (control)
AS	Anti-spin (control)
AUV	Autonomous underwater vehicle
CCP	Consolidated controlled CPP
CPP	Controllable pitch propeller
DOF	Degree of freedom
DP	Dynamic positioning
EMS	Energy management system
FPP	Fixed pitch propeller
GES	Globally exponentially stable
GNC	Guidance, navigation, and control
GPS	Global positioning system
ISS	Input-to-state stable
LP	Low-pass
MQP1	Modified combined torque/power (control) type 1
MQP2	Modified combined torque/power (control) type 2
MTC	Manual thruster control
p	Primary anti-spin action
P	Power (control)
PE	Persistently exciting
PM	Pierson-Moskowitz (wave spectrum) or Position Mooring
PMS	Power management system
Q	Torque (control)
Q <sub>ff</sub>	Friction feedforward (control)
Q <sub>if</sub>	Inertia feedforward (control)
QP	Combined torque/power (control)
ROV	Remotely operated vehicle
rps	revolutions-per-second
s	secondary anti-spin action
S	Speed (control)
SB	Speed bound anti-spin (control)

SQP		Combined speed/torque/power (control)
TS		Torque scaling anti-spin (control)
UGES		Uniformly globally exponentially stable
UGS		Uniformly globally stable
UUB		Uniformly ultimately bounded
UVU		Untethered underwater vehicle

## Lowercase

$a$	[-]	Symmetrical optimum tuning constant
$a_t$	[-]	Propeller constant for a linear $K_T - K_Q$ relationship
$b_t$	[-]	Propeller constant for a linear $K_T - K_Q$ relationship
$d_f$	[kg/m]	Flow dynamics quadratic damping coefficient
$e$	[rps]	Shaft speed error
$e_b$	[rps]	Shaft speed bound error for SB anti-spin controller
$f_Q$	[Nm]	Propeller torque model
$f_T$	[N]	Propeller thrust model
$h$	[m]	Propeller shaft submergence
$h_0$	[m]	Mean propeller shaft submergence
$k$	[-]	Parameter for weighting function $\alpha(z)$
$k_a$	[-]	Load torque observer gain
$k_b$	[-]	Load torque observer gain
$k_g$	[-]	Gear ratio motor:propeller
$k_j$	[m <sup>-1</sup> ]	Wave number for harmonic wave component $j$
$k_m$	[-]	Maximum motor torque/power constant
$k_p$	[-]	Per unit gain for shaft speed control
$k_t$	[-]	PID integral time constant tuning factor
$k_0$	[-]	$K_Q$ estimation scheme gain
$m$	[-]	Thrust/torque loss relation exponent
$m_f$	[kg]	Flow dynamics equivalent mass
$m_V$	[-]	Count of ventilation incidents the last $T_V$ seconds
$m_{V,max}$	[-]	Maximum count of ventilation incidents the last $T_V$ seconds
$n$	[rps]	Propeller shaft speed
$n_{as}$	[rps]	Desired shaft speed during ventilation
$n_b$	[rps]	Shaft speed bound for SB anti-spin control
$n_{bp}$	[rps]	Propeller bollard pull shaft speed
$n_c$	[rps]	Control coefficient switch half width
$n_d$	[rps]	Desired shaft speed, related to $T_d$
$n_f$	[rps]	Friction compensation switch half width
$n_m$	[rps]	Motor speed
$n_{min}$	[rps]	Minimum shaft speed for ventilation detection
$n_N$	[rps]	Rated motor speed
$n_r$	[rps]	Propeller shaft speed reference
$n_{ras}$	[rps]	Shaft speed reference for anti-spin control

$n_s$	[rps]	MQP controller threshold shaft speed
$n_{s1}$	[rps]	SQP controller threshold shaft speed (speed/torque)
$n_{s3}$	[rps]	SQP controller threshold shaft speed (torque/power)
$\dot{n}_{slew}^+$	[ $s^{-2}$ ]	Reference generator increasing speed rate limit
$\dot{n}_{slew}^-$	[ $s^{-2}$ ]	Reference generator decreasing speed rate limit
$\dot{n}_{vent}^+$	[ $s^{-2}$ ]	Rate limit for increasing $n_{ras}$
$\dot{n}_{vent}^-$	[ $s^{-2}$ ]	Rate limit for decreasing $n_{ras}$
$p$	[ $-$ ]	Parameter for weighting function $\alpha(z)$
$r$	[ $-$ ]	Parameter for weighting function $\alpha(z)$
$r_b$	[ $-$ ]	Speed bound factor for SB anti-spin control
$s$	[ $-$ ]	The Laplace operator
$sn_i$	[ $-$ ]	Shaft speed sensitivity function for controller $i$
$sp_i$	[ $-$ ]	Power sensitivity function for controller $i$
$sq_i$	[ $-$ ]	Torque sensitivity function for controller $i$
$st_i$	[ $-$ ]	Thrust sensitivity function for controller $i$
$t$	[s]	Time
$t_d$	[ $-$ ]	Thrust deduction coefficient
$w_h$	[ $-$ ]	Hull wake factor
$\mathbf{x}_p$	[ $-$ ]	Vector of time-varying propeller states

## Uppercase

$A_p$	[ $m^2$ ]	Propeller disc area
$C_Q$	[ $-$ ]	4-quadrant propeller torque coefficient
$C_T$	[ $-$ ]	4-quadrant propeller thrust coefficient
$D$	[m]	Propeller diameter
$H_s$	[m]	Sea state significant wave height
$I_c$	[ $kgm^2$ ]	Inertia compensation rotational inertia
$I_m$	[ $kgm^2$ ]	Rotational inertia seen from the motor
$I_s$	[ $kgm^2$ ]	Rotational inertia seen from the propeller
$J_a$	[ $-$ ]	Advance ratio/advance number
$J_r$	[ $-$ ]	Reference advance ratio
$J_{rn}$	[ $-$ ]	Reference advance ratio for speed control
$J_{rp}$	[ $-$ ]	Reference advance ratio for power control
$J_{rq}$	[ $-$ ]	Reference advance ratio for torque control
$J_{rt}$	[ $-$ ]	Reference advance ratio for thrust control
$K_d$	[ $-$ ]	PID controller derivative gain
$K_i$	[ $-$ ]	PID controller integral gain
$K_p$	[ $-$ ]	PID controller proportional gain
$K_Q$	[ $-$ ]	Actual torque coefficient
$K_{QC}$	[ $-$ ]	Control torque coefficient
$K_{QJ}$	[ $-$ ]	Open-water torque coefficient
$K_{Q0}$	[ $-$ ]	Nominal torque coefficient
$K_{Q0r}$	[ $-$ ]	Reverse nominal torque coefficient

$K_T$	[ $\cdot$ ]	Actual thrust coefficient
$K_{TC}$	[ $\cdot$ ]	Control thrust coefficient
$K_{TJ}$	[ $\cdot$ ]	Open-water thrust coefficient
$K_{T0}$	[ $\cdot$ ]	Nominal thrust coefficient
$K_{T0r}$	[ $\cdot$ ]	Reverse nominal thrust coefficient
$K_y$	[Nm]	Diesel engine torque constant
$K_\omega$	[Nms]	Linear shaft friction coefficient
$N$	[ $\cdot$ ]	Number of harmonic wave components in sea state
$P_a$	[W]	Actual propeller power
$P_{bp}$	[W]	Bollard pull propeller power
$P_m$	[W]	Motor power
$P_{max}$	[W]	Maximum motor power
$P_n$	[W]	Nominal propeller power
$P_N$	[W]	Rated motor power
$P_r$	[W]	Propeller power reference
$P_{rs}$	[W]	Signed propeller power reference
$\dot{P}_{slew}^+$	[W/s]	Reference generator increasing power rate limit
$\dot{P}_{slew}^-$	[W/s]	Reference generator decreasing power rate limit
$P/D$	[ $\cdot$ ]	Propeller pitch ratio
$Q_a$	[Nm]	Actual propeller torque
$Q_b$	[Nm]	Speed bound torque for SB anti-spin controller
$Q_{bp}$	[Nm]	Bollard pull propeller torque
$Q_c$	[Nm]	Saturated commanded torque seen from propeller
$Q_{cas}$	[Nm]	Commanded propeller torque for anti-spin control
$Q_{cc}$	[Nm]	Commanded propeller torque for QP control
$Q_{ccm}$	[Nm]	Commanded propeller torque for MQP control
$Q_{ci}$	[Nm]	Commanded propeller torque, with $i$ the controller index
$Q_{cm}$	[Nm]	Commanded motor torque (related to $Q_c$ )
$Q_{cn}$	[Nm]	Commanded propeller torque for S control
$Q_{cp}$	[Nm]	Commanded propeller torque for P control
$Q_{cq}$	[Nm]	Commanded propeller torque for Q control
$Q_{cs}$	[Nm]	Commanded propeller torque for SQP control
$Q_{c0}$	[Nm]	Unsaturated commanded torque seen from propeller
$Q_f$	[Nm]	Propeller shaft friction torque
$Q_{ff}$	[Nm]	Total friction compensation torque
$Q_{ff0}$	[Nm]	Static friction compensation torque
$Q_{ff1}$	[Nm]	Linear friction compensation torque
$Q_{f0}$	[Nm]	Static friction compensation torque constant
$Q_{f1}$	[Nms]	Linear friction compensation torque constant
$Q_{if}$	[Nm]	Inertia compensation torque
$Q_{if,as}$	[Nm]	Additional inertia compensation torque for anti-spin
$Q_m$	[Nm]	Motor torque
$Q_{max}$	[Nm]	Maximum motor torque
$Q_{mp}$	[Nm]	Motor torque seen from propeller
$Q_n$	[Nm]	Nominal propeller torque

$Q_N$	[Nm]	Rated motor torque
$Q_{PI}$	[Nm]	Additive commanded torque for API anti-spin control
$Q_r$	[Nm]	Propeller torque reference
$Q_s$	[Nm]	Static shaft friction torque constant
$R$	[m]	Propeller radius
$T_a$	[N]	Actual total thrust
$T_{ad}$	[N]	Actual duct thrust
$T_{ap}$	[N]	Actual propeller thrust
$T_{bp}$	[N]	Bollard pull propeller thrust
$T_d$	[N]	Desired thrust from the thrust allocation system
$T_f$	[s]	Shaft speed filter time constant
$T_i$	[s]	PID controller integral time constant
$T_{Is}$	[s]	Mechanical time constant
$T_m$	[s]	Motor time constant
$T_n$	[N]	Nominal propeller thrust
$T_p$	[s]	Sea state peak wave period
$T_r$	[N]	Thrust reference, input to the low-level controller
$T_{ras}$	[N]	Anti-spin thrust reference
$T_{vent}$	[s]	Dwell-time for ventilation detection
$T_V$	[s]	Time interval for thruster performance evaluation
$U$	[m/s]	Vessel surge velocity
$U_a$	[m/s]	Induced velocity in the propeller wake
$V_{0.7}$	[m/s]	Undisturbed incident velocity to the prop. blade at $0.7R$
$V_a$	[m/s]	Propeller advance (inflow) velocity
$V_p$	[m/s]	Flow velocity through the propeller disc
$Y$	[ $\cdot$ ]	Diesel engine fuel index

## Greek

$\alpha_b$	[ $\cdot$ ]	Torque loss calculation weighting function
$\alpha_c$	[ $\cdot$ ]	QP controller weighting function
$\alpha_s$	[ $\cdot$ ]	SQP controller weighting function
$\alpha_\chi$	[ $\cdot$ ]	Performance factor weighting function
$\beta$	[rad]	Propeller blade angle of attack at radius $0.7R$
$\beta_{v,off}$	[ $\cdot$ ]	Threshold torque loss for ventilation termination
$\beta_{v,on}$	[ $\cdot$ ]	Threshold torque loss for ventilation detection
$\beta_Q$	[ $\cdot$ ]	Total torque loss factor
$\beta_{QJ}$	[ $\cdot$ ]	Torque loss factor for inline flow
$\beta_{QV}$	[ $\cdot$ ]	Torque loss factor for ventilation, hysteresis, and disc area
$\beta_T$	[ $\cdot$ ]	Total thrust loss factor
$\beta_{TA}$	[ $\cdot$ ]	Thrust loss factor for loss of propeller disc area
$\beta_{TH}$	[ $\cdot$ ]	Thrust loss factor for lift hysteresis
$\beta_{TJ}$	[ $\cdot$ ]	Thrust loss factor for inline flow
$\beta_{TV}$	[ $\cdot$ ]	Thrust loss factor for ventilation, hysteresis, and disc area

$\beta_{TV0}$	[ $\cdot$ ]	Thrust loss factor for ventilation
$\gamma_Q$	[ $\cdot$ ]	Anti-spin commanded torque scaling factor
$\gamma_T$	[ $\cdot$ ]	Anti-spin thrust reference scaling factor
$\dot{\gamma}_{fall}$	[ $s^{-1}$ ]	Rate limit for decreasing $\gamma_Q$
$\dot{\gamma}_{rise}$	[ $s^{-1}$ ]	Rate limit for increasing $\gamma_Q$
$\epsilon_c$	[ $\cdot$ ]	Control coefficient switch constant
$\epsilon_f$	[ $\cdot$ ]	Friction compensation switch constant
$\epsilon_\phi$	[ $\cdot$ ]	Constant for CCP pitch mapping
$\zeta$	[ $\cdot$ ]	Ventilation detection flag
$\zeta_j$	[m]	Amplitude of harmonic wave component $j$
$\zeta_r$	[ $\cdot$ ]	Reference generator damping ratio
$\zeta_w$	[m]	Surface elevation due to waves
$\eta_a$	[ $\cdot$ ]	Propeller efficiency parameter
$\eta_h$	[ $\cdot$ ]	Hull efficiency
$\eta_m$	[ $\cdot$ ]	Mechanical efficiency
$\eta_p$	[ $\cdot$ ]	Overall propulsion efficiency
$\eta_r$	[ $\cdot$ ]	Relative rotative efficiency
$\eta_0$	[ $\cdot$ ]	Open-water propeller efficiency
$\theta_p$	[ $\cdot$ ]	Vector of fixed propeller parameters
$\lambda_c$	[ $\cdot$ ]	Control coefficient switching function
$\rho$	[kg/m <sup>3</sup> ]	Density of water
$\tau$	[N,Nm]	3DOF total thrust vector acting on the vessel
$\tau_d$	[N,Nm]	3DOF desired thrust vector from thrust allocation
$\tau_n$	[s]	Time constant for $n_{ras}$ filter
$\tau_m$	[s]	Diesel engine time delay
$\tau_r$	[s]	Reference generator time constant
$\tau_\gamma$	[s]	Time constant for $\gamma_Q$ filter
$\phi$	[rad]	Pitch angle
$\phi_{DP}$	[rad]	Maximum pitch angle for DP
$\phi_j$	[rad]	Phase of harmonic wave component $j$
$\phi_r$	[rad]	Reference pitch angle for CPP
$\chi_j$	[ $\cdot$ ]	Performance measure for thruster $j$
$\chi_Q$	[ $\cdot$ ]	Torque performance factor
$\chi_T$	[ $\cdot$ ]	Thrust performance factor
$\chi_V$	[ $\cdot$ ]	Ventilation performance factor
$\chi_{V,min}$	[ $\cdot$ ]	Minimum ventilation performance factor
$\omega$	[rad/s]	Propeller angular velocity ( $\omega = 2\pi n$ )
$\omega_j$	[rad/s]	Circular frequency of harmonic wave component $j$
$\omega_{r0}$	[rad/s]	Reference generator natural frequency

# Chapter 1

## Introduction

Most marine vessels are fitted with propellers and thrusters, and rely on these to conduct station-keeping, manoeuvring, and transit operations. The main focus of this thesis will be on modelling, simulation, and control of propellers on surface vessels with electric propulsion systems. Examples of such vessels are offshore service vessels, shuttle tankers, drilling vessels, pipe-laying vessels, and diving support vessels. The operation of the propellers and thrusters has several important implications:

- The thrust production affects the positioning capability of the vessel.
- The power consumption affects the vessel's fuel consumption, generator wear and tear, and risk of power system blackouts.
- Mechanical wear and tear leads to repairs and vessel down-time.

The operational philosophy of the propulsion system hence affects three important aspects of the operation of a marine vessel: *safety, economy, and performance*.

### 1.1 Background

The real-time control hierarchy of a marine guidance, navigation, and control (GNC) system may be divided into three levels (Balchen *et al.*, 1976, 1980*a,b*; Sørensen *et al.*, 1996; Strand, 1999; Strand and Fossen, 1999; Fossen and Strand, 1999, 2001; Strand and Sørensen, 2000; Lindegaard and Fossen, 2001; Fossen, 2002; Lindegaard, 2003; Bray, 2003; Sørensen, 2005) :

- The guidance and navigation system, including local set-point and path generation.
- The high-level plant control, including thrust allocation and power management.

- The low-level thruster controllers.

The *guidance and navigation system* includes sensors and a vessel observer for filtering and reconstruction of signals. The *local set-point and path generation* may include functions like low-speed tracking, weather-vaning, set-point chasing, and ROV follow. The *high-level controller*, which can be a dynamic positioning (DP) controller, position mooring (PM) controller, or joystick controller, computes the forces in surge and sway and moment in yaw needed to counteract the environmental loads and track the desired path. The *thrust allocation system* calculates the thrust setpoints for each propulsion unit according to a given optimization criterion – e.g. minimization of power consumption – such that the high-level control commands are fulfilled. The *low-level thruster controllers* control the thrusters according to the setpoints from the thrust allocation system. The control hierarchy is illustrated in Figure 1.1, which shows a block diagram of a typical DP operation. In manual thruster control mode (MTC), the setpoints to the thrusters are set by manual operation of the thruster levers.

Various types of propulsion units exist, as well as different types of propellers. The two main types of propellers are fixed pitch propellers (FPP) and controllable pitch propellers (CPP). FPP can only be controlled by the propeller speed, whereas CPP can be controlled by both the propeller speed and the angle of the propeller blades (pitch). Both propeller types can be open or ducted. On a ducted propeller, the propeller is situated inside a duct, or nozzle. This increases the efficiency of the propeller at low vessel speeds (Kort, 1934).

For main propulsion, three common solutions exist: mechanical direct-drive propellers, large azimuth thrusters, and podded propulsion units. Mechanical direct-drive propellers are connected directly to a prime mover (usually a diesel engine), possibly via gears and clutches, and can be either FPP or CPP. Azimuth thrusters can be rotated to produce thrust in any direction. They are driven by an electric motor inside the hull via shafts and gears, and can be either FPP or CPP. The former is the most common solution. Podded propulsion units are usually also rotatable, but the propeller is here normally driven by an electric motor and drive situated in a pod outside the hull. However, also mechanical pods exist. Propellers on pods are usually of the FPP type.

For auxiliary propulsion, to aid in station-keeping and low-speed manoeuvring, the most common solutions are tunnel thrusters and various types of azimuth thrusters. Often, such azimuth thrusters can be stowed inside the hull during transit (retractable or swing-up). Both FPP or CPP are used.

Other propulsion concepts are also in use; examples are the Voith Schneider cycloidal thruster, the Gill jet, and water jets. Some vessels also have rudders and/or stabilizing fins. These topics will not be considered in this thesis.

Strictly speaking, a thruster should be defined as a propeller operated at low vessel speeds. In this work, “thrusters” and “propellers” will be treated as equivalent expressions. More information on various propulsion units and propulsion configurations can be found in e.g. Ådnanes *et al.* (1997), Kallah (1997), Deter (1997), and Bray (2003).

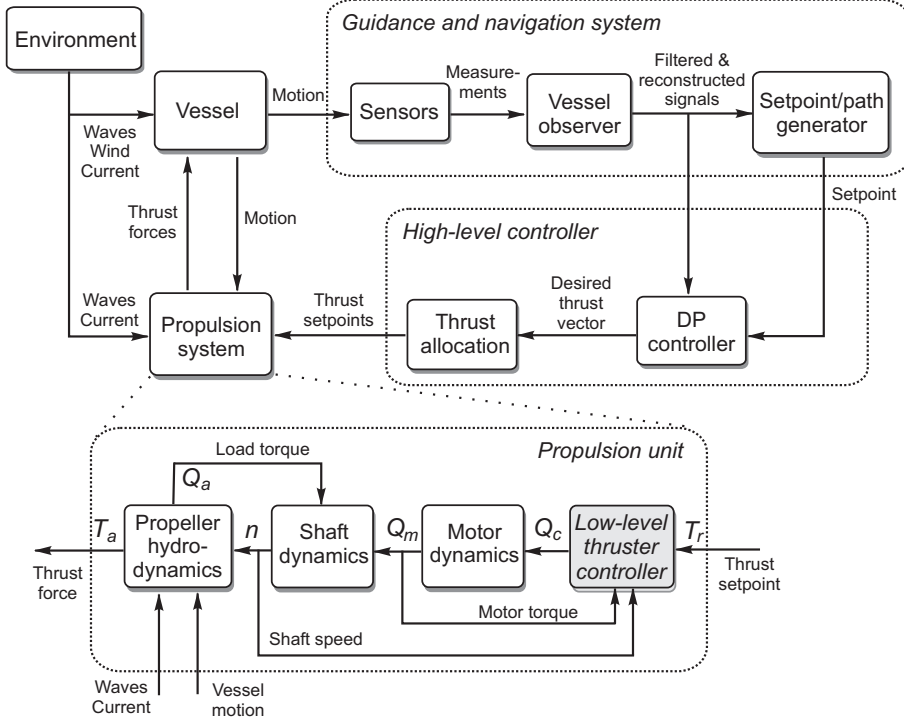


Figure 1.1: Block diagram of a typical DP operation, including environment, vessel, guidance and navigation system, high-level control, and thruster dynamics including low-level thruster control.

Measurements of the actual propeller thrust is normally not available. Hence, the mapping from desired to actual thrust must be considered as an open-loop system, and there is no guarantee of fulfilling the high-level control commands. Therefore, if the low-level controllers have bad performance, the stability and bandwidth of the whole positioning system will be affected. Still, the topic of propulsion control has received relatively little attention in literature, even though the use of electrical thrusters have opened up new possibilities for improved low-level control. It appears that the same has been true for industry; with notable exceptions, most propeller manufacturers have focused on the propeller design, and the control system vendors have focused on the high-level controllers.

More recently, also the issues of low-level thruster dynamics and controller design have received increased attention, and their impact on the overall vessel performance have become more apparent. However, this work has mostly been focused on underwater applications like remotely operated vehicles (ROVs) and autonomous underwater vehicles (AUVs), see Yoerger *et al.* (1991), Healey *et al.*

(1995), Tsukamoto *et al.* (1997), Whitcomb and Yoerger (1999*a,b*), Bachmayer *et al.* (2000), Blanke *et al.* (2000), Fossen and Blanke (2000), Bachmayer and Whitcomb (2001), Guibert *et al.* (2005), and Pivano *et al.* (2006*c*). Control of electrically driven propellers for surface vessels has been treated in Sørensen *et al.* (1997), Strand (1999), Smogeli *et al.* (2003, 2004*a,b*, 2005*a*, 2006), Pivano *et al.* (2006*b,a*), Bakkeheim *et al.* (2006), Ruth *et al.* (2006), Sørensen and Smogeli (2006), and Smogeli and Sørensen (2006*b*). Most of these references form the basis for this thesis. Various governor control schemes for diesel engines with directly driven propellers are presented in Blanke and Busk Nielsen (1987, 1990).

This thesis is focused on DP operations, which includes station-keeping and low-speed tracking, as well as joystick control. A surface vessel in DP will be subject to environmental forces from waves, wind, and current. Depending on the environmental condition and the task the vessel is performing – and hence its velocity and heading relative to the environmental forces – the vessel will be moving in its 6 degrees of freedom (DOF): surge, sway, heave, roll, pitch, and yaw. DP vessels are usually *fully actuated* or *over-actuated* in order to control all three horizontal-plane DOF (surge, sway, and yaw) simultaneously.

The motion of the vessel coupled with the waves and current give dynamic operating conditions for the thrusters, depending on the severity of the environmental condition. In calm conditions, with small waves and little current, the vessel will have no significant motion except its controlled trajectory. The thrusters will then usually be well submerged, and experience small fluctuations in the relative water velocities. This means that the dynamic loading is of small magnitude, and the thruster performance will be close to ideal, which again implies accurate thrust production and small oscillations in shaft speed, motor torque, propeller torque, and motor power. For DP in calm conditions, the thrust demands are usually low compared to the installed thrust capability. Hence, with efficient thrust allocation, it is possible to utilize the thrusters in a near optimal manner. However, some thrust loss effects may still be experienced. These are mainly due to frictional and suction losses caused by the Coanda effect, see e.g. Lehn (1992) and references therein, and thruster-thruster interaction effects if proper forbidden zones are not implemented in the thrust allocation system (Lehn, 1992; Ekstrom and Brown, 2002; Koushan, 2004; Brown and Ekstrom, 2005). These effects cannot be counteracted by the low-level thruster controller, and will therefore not be further treated in this work. The losses can, however, be significant. They must be targeted from the vessel design and thrust allocation system.

For increasing severity of the environmental condition, wind, current, and waves have different influence on the operating condition and utilization of the thrusters. The mean and slowly-varying environmental loads are composed of wind, current, and wave-drift forces, including the dynamic (but low-frequency) loads due to current fluctuations and wind gusts. These forces must be counteracted with the thrusters to make the vessel follow its desired trajectory. The mean loads on the vessel therefore mainly contribute to alter the setpoints sent

to the thrusters from the high-level control system. The first order oscillatory wave forces (Froude-Krylov and diffraction forces) give rise to an oscillatory vessel motion in all six DOF. These wave-frequency motions should not be counteracted in normal to moderate seas, since this would lead to unnecessary wear and tear of the thrusters, as well as increased fuel consumption. This is solved by proper wave-filtering in the DP system (Strand and Fossen, 1999; Lindegaard and Fossen, 2001; Lindegaard, 2003; Fossen, 2002). Dong (2005) and the references therein showed that in high to extreme seas, wave-filtering should not be used, and that hybrid control could be used to switch between a bank of controllers suitable for varying environmental conditions. Even though the thrusters have slowly-varying setpoints, the oscillatory vessel motion combined with the sea elevation and the current- and wave-induced water velocities mean that the thrusters are operating in a dynamic environment. This leads to dynamic loading of the propeller which, depending on the chosen control strategy, leads to oscillations in propeller thrust and torque, shaft speed, motor torque, and motor power. In addition, the mean relative velocity due to current and low-frequency vessel motion alter the operating point of the thrusters. Depending on the performance of the low-level thruster controllers, the result is a deviation of the average produced thrust from the thrust setpoints. This is compensated for by the integral action of the DP system, but at the expense of reduced positioning bandwidth.

In severe to extreme conditions, the large environmental loads often lead to high utilization of the installed thrust capacity. At the same time, the sea elevation and vessel motion means that the thrusters will experience large motions relative to the water. If the thrusters are well submerged, the inflow will be highly disturbed, and the propeller loading affected accordingly. If the submergence becomes too low, the thrusters may suffer severe thrust losses due to ventilation and in-and-out-of-water effects, leading to reduced thrust capability and large power transients. Appropriate operation of the propulsion system is then of high importance for the stability and performance of the power generation and distribution system, since the thrusters often are the main power consumers. This is a critical issue with respect to safe operation of the vessel, which in addition affects the fuel consumption and wear and tear of the generator sets. Recent results also indicate that the unsteady loading during ventilation can give rise to significant mechanical wear and tear of the propulsion unit (Koushan, 2004, 2006). This is believed to be the cause of the widespread mechanical failures of tunnel thrusters and azimuth thrusters, with costly repairs and increased vessel down-time as consequences.

## 1.2 Problem statement

To summarize the previous section, it is clear that a propeller may be subject to a wide range of operating conditions, both in terms of environmental loads and thrust demand. For a DP vessel, the thrust demand will normally increase with the severity of the environmental condition, as will the dynamic loading of the propellers and thrusters. It is then rather contradictory that the thruster controllers today are designed for operation in calm conditions, without considering the effects of the large thrust losses that may occur in harsher conditions.

With the apparent need for high-performance thruster controllers, and the lack of available references on this topic, the motivation for this thesis is to remedy the current situation by focusing explicitly on low-level thruster control. The main problem statement may be formulated as follows:

*“Given a thrust set-point and an unknown environmental condition, how can the propeller be controlled in order to:*

- optimize the thrust production,
- reduce the mechanical wear and tear,
- avoid unnecessary power transients,

*and at the same time have reliable performance?”.*

## 1.3 Main contributions

The following are believed to be the main contributions of this thesis, organized by chapters:

**Chapter 2:** *a)* New experimental results on a propeller subject to ventilation and in-and-out-of-water effects at low advance velocities are presented, both in terms of cavitation tunnel test to capture quasi-static effects, and open-water tests to capture dynamic effects. The test have been performed in cooperation with Aarseth (2003) and Ruth (2005). *b)* An associated ventilation model suitable for time-domain simulation is developed. The results have been partly published in Smogeli *et al.* (2003, 2006).

**Chapter 3:** *a)* The thruster control problem is formalized in terms of control coefficients, friction and inertia compensation, and the three fundamental controllers (speed, torque, and power control). This has earlier been partly published in Smogeli *et al.* (2005a) and Sørensen and Smogeli (2006). The concepts of torque and power control of electrically driven propellers for surface vessels were first published in Sørensen *et al.* (1997) and Strand (1999). *b)* The fundamental controllers are used to construct various combined controllers, as partly published in Smogeli *et al.* (2004a) and Sørensen and Smogeli (2006).

**Chapter 4:** Shaft speed, torque, and power sensitivity functions are introduced, and thrust sensitivity functions, as presented in Sørensen *et al.* (1997) and Strand (1999), are put into an improved framework. An improved steady-state analysis of the controller performance in presence of thrust losses is also presented. The results have been partly published in Sørensen and Smogeli (2006).

**Chapter 5:** The complete chapter on propeller observers, loss estimation, and performance monitoring is believed to be a new contribution. The results have been partly published in Smogeli *et al.* (2004a,b, 2006) and Smogeli and Sørensen (2006b).

**Chapter 6:** The complete chapter on anti-spin thruster control is believed to be a new contribution. The results have been partly published in Smogeli *et al.* (2004b, 2006) and Smogeli and Sørensen (2006b).

**Chapter 7:** *a)* An experimental comparison of the fundamental controllers and the combined controllers, as partly published in Smogeli *et al.* (2005a) and Sørensen and Smogeli (2006), is presented. *b)* An experimental validation of the various anti-spin controllers, and a comparison with the fundamental controllers in extreme conditions, are also presented. The results have been partly published in Smogeli and Sørensen (2006b).

**Chapter 8:** Extensions of the new control concepts to CPP and transit are presented.

**Chapter 9:** *a)* The concept of anti-spin thrust allocation is introduced. *b)* A thruster performance measure that can be utilized to improve thrust allocation is developed.

## 1.4 List of publications

The following authored and coauthored publications are directly connected with the work presented in this thesis, presented in chronological order:

1. Ø. N. Smogeli and A. J. Sørensen (2006b). Anti-Spin Thruster Control for Ships. *Submitted to Automatica*.
2. A. J. Sørensen and Ø. N. Smogeli (2006). Torque and Power Control of Electrically Driven Propellers on Ships. *Accepted for publication in IEEE Journal of Oceanic Engineering*.
3. E. Ruth and Ø. N. Smogeli (2006). Ventilation of Controllable Pitch Thrusters. *SNAME Marine Technology*, 43(4):170-179.
4. Ø. N. Smogeli, A. J. Sørensen and K. J. Minsaas (2006). The Concept of Anti-Spin Thruster Control. *To appear in Control Engineering Practice*.

5. L. Pivano, Ø. N. Smogeli, T. A. Johansen and T. I. Fossen (2006a). Experimental Validation of a Marine Propeller Thrust Estimation Scheme for a Wide Range of Operations. *Proceedings of the 7th IFAC Conference on Manoeuvring and Control of Marine Craft (MCMC'06)*. Lisbon, Portugal, September 20-22.
6. E. Ruth, Ø. N. Smogeli and A. J. Sørensen (2006). Overview of Propulsion Control for Surface Vessels. *Proceedings of the 7th IFAC Conference on Manoeuvring and Control of Marine Craft (MCMC'06)*. Lisbon, Portugal, September 20-22.
7. D. Radan, Ø. N. Smogeli, A. J. Sørensen and A. K. Ådnanes (2006). Operating Criteria for Design of Power Management Systems on Ships. *Proceedings of the 7th IFAC Conference on Manoeuvring and Control of Marine Craft (MCMC'06)*. Lisbon, Portugal, September 20-22.
8. J. Bakkeheim, Ø. N. Smogeli, T. A. Johansen and A. J. Sørensen (2006). Improved Transient Performance by Lyapunov-based Integrator Reset of PI Thruster Control in Extreme Seas. *Proceedings of the 45th IEEE Conference on Decision and Control (CDC'06)*. San Diego, California, December 13-15.
9. L. Pivano, Ø. N. Smogeli, T. A. Johansen and T. I. Fossen (2006b). Marine Propeller Thrust Estimation in Four-Quadrant Operations. *Proceedings of the 45th IEEE Conference on Decision and Control (CDC'06)*. San Diego, California, December 13-15.
10. Ø. N. Smogeli and A. J. Sørensen (2006a). Adaptive Observer Design for a Marine Propeller. *Proceedings of the 14th IFAC Symposium on System Identification (SYSID'06)*. Newcastle, Australia, March 29-31.
11. Ø. N. Smogeli, E. Ruth and A. J. Sørensen (2005a). Experimental Validation of Power and Torque Thruster Control. *Proceedings of the 13th Mediterranean Conference on Control and Automation (MED'05)*. Limassol, Cyprus, June 27-29.
12. Ø. N. Smogeli, J. Hansen, A. J. Sørensen and T. A. Johansen (2004b). Anti-spin control for marine propulsion systems. *Proceedings of the 43rd IEEE Conference on Decision and Control (SYSID'04)*, Paradise Island, Bahamas, December 14-17.
13. Ø. N. Smogeli, A. J. Sørensen and T. I. Fossen (2004a). Design of a hybrid power/torque thruster controller with thrust loss estimation. *Proceedings of the IFAC Conference on Control Applications in Marine Systems (CAMS'04)*. Ancona, Italy, July 7-9.
14. Ø. N. Smogeli, L. Aarseth, E. S. Overå, A. J. Sørensen and K. J. Minnaas (2003). Anti-spin thruster control in extreme seas. *Proceedings of*

*the 6th IFAC Conference on Manoeuvring and Control of Marine Craft (MCMC'03).* Girona, Spain, September 17-19.

Other authored and coauthored publications that have been of supporting importance for this thesis are, in chronological order:

15. T. Perez, Ø. N. Smogeli, T. I. Fossen, and A. J. Sørensen (2005). An Overview of Marine Systems Simulator (MSS): A Simulink Toolbox for Marine Control Systems. *Proceedings of the Scandinavian Conference on Simulation and Modeling (SIMS'05)*. Trondheim, Norway, October 13-14.
16. Ø. N. Smogeli, T. Perez, T. I. Fossen and A. J. Sørensen (2005b). The Marine Systems Simulator State-Space Model Representation for Dynamically Positioned Surface Vessels. *Proceedings of the 11th Congress of the International Maritime Association of the Mediterranean (IMAM'05)*. Lisbon, Portugal, September 26-30.
17. T. I. Fossen and Ø. N. Smogeli (2004). Nonlinear Time-Domain Strip Theory Formulation for Low-Speed Maneuvering and Station-Keeping. *Modeling, Identification and Control (MIC)*, 25(4):201-221.
18. R. Skjetne, Ø. N. Smogeli and T. I. Fossen (2004a). Modeling, Identification, and Adaptive Maneuvering of CyberShip II: A complete design with experiments. *Proceedings of the IFAC Conference on Control Applications in Marine Systems (CAMS'04)*. Ancona, Italy, July 7-9.
19. R. Skjetne, Ø. N. Smogeli and T. I. Fossen (2004b). A non-linear ship maneuvering model: Identification and adaptive control with experiments for a model ship. *Modeling, Identification and Control (MIC)*, 25(1):3-27.
20. A. J. Sørensen, E. Pedersen and Ø. N. Smogeli (2003). Simulation-Based Design and Testing of Dynamically Positioned Marine Vessels. *Proceedings of the International Conference on Marine Simulation And Ship Maneuverability, MARSIM'03*. Kanazawa, Japan, August 25-28.

## 1.5 Organization of the thesis

In order to investigate the importance of proper low-level thruster control, one must start with studying the loads that the propeller is subjected to. This is the topic of Chapter 2, which deals with propeller modelling and simulation. Focus is put on the thrust loss effects that can be counteracted by the low-level thruster controllers, both in normal and extreme conditions. The characteristics of a propeller subject to ventilation and in-and-out-of water effects is investigated, and systematic tests from a cavitation tunnel and a towing tank at NTNU are presented. Based on this, a simplified simulation model that captures the main

characteristics of the losses is proposed. Finally, a complete propeller simulation model suitable for thruster controller design and testing is presented.

Chapter 3 considers thruster control in normal operating conditions. The main control objectives are defined, and the general structure of the proposed thruster controller is shown. Some important aspects regarding choice of control parameters, use of reference generators, and the need for friction and inertia compensation are discussed, before the three *fundamental* control concepts are presented: *shaft speed*, *torque*, and *power control*. It is then shown how the fundamental controllers can be combined in various ways to exploit their best individual properties, followed by a controller comparison by simulations.

The fundamental control concepts are further analyzed in Chapter 4, where *sensitivity functions* are established to investigate the steady-state thrust, torque, shaft speed, and power in the presence of thrust losses. These analysis tools are applied to two cases: losses due to changes in inflow to the propeller, and losses due to ventilation. Further, the transient response of the controllers is discussed with the aid of a Lyapunov analysis of the shaft speed equilibrium.

In Chapter 5 a *propeller load torque observer* is designed, and a *loss estimation* scheme developed. In addition, a scheme for monitoring of the thruster performance is proposed. Simulations are provided to demonstrate the performance of the presented concepts.

Chapter 6 is dedicated to controller design for extreme operating conditions. Motivated by the similar problem of a car wheel losing friction on a slippery surface during braking or acceleration, the concept of *anti-spin thruster control* is introduced. In order to detect the high thrust loss incidents, a *ventilation detection* scheme is designed. An anti-spin thruster controller that is applicable to all the controllers designed for normal operating conditions is then proposed. Finally, some alternative anti-spin control concepts are presented, and the proposed anti-spin controller tested by simulations.

To further validate the proposed control concepts and estimation schemes, extensive model tests in the Marine Cybernetics Laboratory (MCLab) at NTNU have been undertaken. The results from these tests – both in normal and extreme conditions – are presented in Chapter 7, showing that the controllers and observers perform as intended.

Chapter 8 shows how the presented concepts can be extended to CPP and transit. This applies to the controllers for normal conditions, the observers and loss estimation schemes, and the anti-spin thruster controllers.

Finally, *anti-spin thrust allocation* in extreme conditions is discussed in Chapter 9. The main concept is to monitor the performance of all the propulsion units on a vessel, and attempt to utilize the propellers with the best operating conditions. This may both improve the vessel's positioning performance and reduce the mechanical wear and tear of the propulsion units.

The appendices provide additional background material, extensions of the presented concepts, and additional results.

# Chapter 2

## Propeller modelling

The actual propeller thrust  $T_a$  and torque  $Q_a$  are influenced by many parameters.  $T_a$  and  $Q_a$  can in general be formulated as functions of the shaft speed  $n$  in revolutions-per-second (rps), time-varying states  $\mathbf{x}_p$  (e.g. pitch ratio, advance velocity, submergence), and fixed thruster parameters  $\boldsymbol{\theta}_p$  (e.g. propeller diameter, geometry, position):

$$T_a = f_T(n, \mathbf{x}_p, \boldsymbol{\theta}_p), \quad (2.1)$$

$$Q_a = f_Q(n, \mathbf{x}_p, \boldsymbol{\theta}_p). \quad (2.2)$$

In this work, speed controlled FPP are of main concern. The pitch ratio is then a fixed parameter. The functions  $f_T(\cdot)$  and  $f_Q(\cdot)$  may include thrust and torque losses due to e.g. in-line and transverse velocity fluctuations, ventilation, in-and-out-of water effects, thruster-thruster interaction, and dynamic flow effects. In addition, the dynamics of the motor and shaft must be considered. In the following sections, propeller characteristics, some quasi-static loss effects, and dynamic effects due to the water inflow, motor, and shaft are considered.

**Remark 2.1** *Modelling of propellers will in this thesis be treated from a control point of view. This means that the models are required to be accurate enough to capture the main physical effects, and such facilitate control system design and testing. However, details on propeller design and hydrodynamic performance will not be considered.*

### 2.1 Propeller characteristics

Propellers are, with the exception of tunnel thrusters, usually asymmetric and optimized for producing thrust in one direction. The propeller characteristics will therefore depend on both the rotational direction of the propeller and the inflow direction. The four quadrants of operation of a propeller are defined in Table 2.1. The quasi-static relationships between  $T_a$ ,  $Q_a$ ,  $n$ , the diameter  $D$ ,

	1 <sup>st</sup>	2 <sup>nd</sup>	3 <sup>rd</sup>	4 <sup>th</sup>
$n$	$\geq 0$	$< 0$	$< 0$	$\geq 0$
$V_a$	$\geq 0$	$\geq 0$	$< 0$	$< 0$

Table 2.1: The 4 quadrants of operation of a propeller, parameterized by the advance velocity  $V_a$  and the shaft speed  $n$ .

and the density of water  $\rho$  are commonly given by:

$$T_a = f_T(\cdot) = \text{sign}(n)K_T\rho D^4 n^2, \quad (2.3)$$

$$Q_a = f_Q(\cdot) = \text{sign}(n)K_Q\rho D^5 n^2. \quad (2.4)$$

$K_T$  and  $K_Q$  are the *thrust and torque coefficients*, where the effects of thrust and torque losses have been accounted for. For normal operation,  $K_T > 0$  and  $K_Q > 0$ . The propeller power consumption  $P_a$  is written as:

$$P_a = 2\pi n Q_a = \text{sign}(n)2\pi K_Q \rho D^5 n^3. \quad (2.5)$$

In general, the thrust and torque coefficients can be expressed in a similar manner as  $T_a$  and  $Q_a$  in (2.1, 2.2):

$$K_T = K_T(n, \mathbf{x}_p, \boldsymbol{\theta}_p) = \frac{T_a}{\text{sign}(n)\rho D^4 n^2}, \quad (2.6)$$

$$K_Q = K_Q(n, \mathbf{x}_p, \boldsymbol{\theta}_p) = \frac{Q_a}{\text{sign}(n)\rho D^5 n^2}. \quad (2.7)$$

For ease of notation, the arguments of  $K_T$  and  $K_Q$  will mostly be omitted in the remainder of this work. The *nominal* thrust  $T_n$ , torque  $Q_n$ , and power  $P_n$  are the ideal values when no thrust losses are present. They are expressed by the nominal thrust and torque coefficients  $K_{T0}$  and  $K_{Q0}$ :

$$T_n = \text{sign}(n)K_{T0}\rho D^4 n^2, \quad (2.8)$$

$$Q_n = \text{sign}(n)K_{Q0}\rho D^5 n^2, \quad (2.9)$$

$$P_n = 2\pi n Q_n = \text{sign}(n)2\pi K_{Q0} \rho D^5 n^3. \quad (2.10)$$

The nominal thrust, torque, and power of a reversed propeller are expressed as in (2.8, 2.9, 2.10), but with  $K_{T0}$  and  $K_{Q0}$  replaced with their reverse counterparts,  $K_{T0r} > 0$  and  $K_{Q0r} > 0$ . The nominal coefficients are assumed to be constant for a given propeller geometry.

The difference between the nominal and actual thrust and torque may be expressed by the thrust and torque reduction coefficients – or thrust and torque loss factors –  $\beta_T$  and  $\beta_Q$  (Faltinsen *et al.*, 1980; Minsaas *et al.*, 1983, 1987):

$$\beta_T = \beta_T(n, \mathbf{x}_p, \boldsymbol{\theta}_p) = \frac{T_a}{T_n} = \frac{K_T}{K_{T0}}, \quad (2.11)$$

$$\beta_Q = \beta_Q(n, \mathbf{x}_p, \boldsymbol{\theta}_p) = \frac{Q_a}{Q_n} = \frac{K_Q}{K_{Q0}}. \quad (2.12)$$

If the difference between  $K_{T0}$  and  $K_{T0r}$  is included in  $\beta_T$ , and the difference between  $K_{Q0}$  and  $K_{Q0r}$  is included in  $\beta_Q$ , the actual thrust, torque, and power may be written as:

$$T_a = \text{sign}(n)K_{T0}\rho D^4 n^2 \beta_T(n, \mathbf{x}_p, \boldsymbol{\theta}_p), \quad (2.13)$$

$$Q_a = \text{sign}(n)K_{Q0}\rho D^5 n^2 \beta_Q(n, \mathbf{x}_p, \boldsymbol{\theta}_p), \quad (2.14)$$

$$P_a = \text{sign}(n)2\pi K_{Q0}\rho D^5 n^3 \beta_Q(n, \mathbf{x}_p, \boldsymbol{\theta}_p). \quad (2.15)$$

Hence, all disturbances and external states are introduced through  $\beta_T$  and  $\beta_Q$ . The arguments of  $\beta_T$  and  $\beta_Q$  will for notational simplicity mostly be omitted.

### 2.1.1 Open-water characteristics

The thrust and torque coefficients for deeply submerged propellers subject to an in-line inflow will here be termed  $K_{TJ}$  and  $K_{QJ}$ . These coefficients are experimentally determined by so-called open water tests, usually performed in a cavitation tunnel or a towing tank. For a specific propeller geometry,  $K_{TJ}$  and  $K_{QJ}$  are often given as functions of the advance number  $J_a$ :

$$J_a = \frac{V_a}{nD}, \quad (2.16)$$

where  $V_a$  is the propeller advance (inflow) velocity. This relationship is commonly referred to as an open-water propeller characteristics. In general, the coefficients are written as  $K_{TJ} = K_{TJ}(V_a, n)$  and  $K_{QJ} = K_{QJ}(V_a, n)$ . In the following, the arguments  $V_a$  and  $n$  will mostly be omitted. The corresponding open-water efficiency  $\eta_0$  is defined as the ratio of produced to consumed power for the propeller:

$$\eta_0 = \frac{V_a T_a}{2\pi n Q_a} = \frac{V_a K_{TJ}}{2\pi n K_{QJ} D} = \frac{J_a K_{TJ}}{2\pi K_{QJ}}. \quad (2.17)$$

Systematic tests with similar propellers are typically compiled in a propeller series. The perhaps most well-known series is the Wageningen B-series from MARIN in the Netherlands, see van Lammeren *et al.* (1969), Oosterveld and van Oossanen (1975), and the references therein. In the latter reference,  $K_{TJ}$  and  $K_{QJ}$  are given from:

$$K_{TJ} = f_1 \left( J_a, \frac{P}{D}, \frac{A_e}{A_0}, Z \right), \quad (2.18)$$

$$K_{QJ} = f_2 \left( J_a, \frac{P}{D}, \frac{A_e}{A_0}, Z, R_n, \frac{t}{c} \right), \quad (2.19)$$

where  $P/D$  is the pitch ratio,  $A_e/A_0$  is the expanded blade-area ratio,  $Z$  is the number of blades,  $R_n$  is the Reynolds number,  $t$  is the maximum thickness of the blade section, and  $c$  is the chord length of the blade section. Figure 2.1

$Z$	$P/D$	$A_e/A_0$	$K_{T0}$	$K_{Q0}$	$K_{T0r}$	$K_{Q0r}$
4	1.0	0.70	0.445	0.0666	0.347	0.0628

Table 2.2: Wageningen B4-70 example propeller data: Diameter  $D$ , blade number  $Z$ , pitch ratio  $P/D$  at radius  $0.7D/2$ , expanded blade area ratio  $A_e/A_0$ , nominal thrust coefficient  $K_{T0}$ , nominal torque coefficient  $K_{Q0}$ , reverse nominal thrust coefficient  $K_{T0r}$ , and reverse nominal torque coefficient  $K_{Q0r}$ .

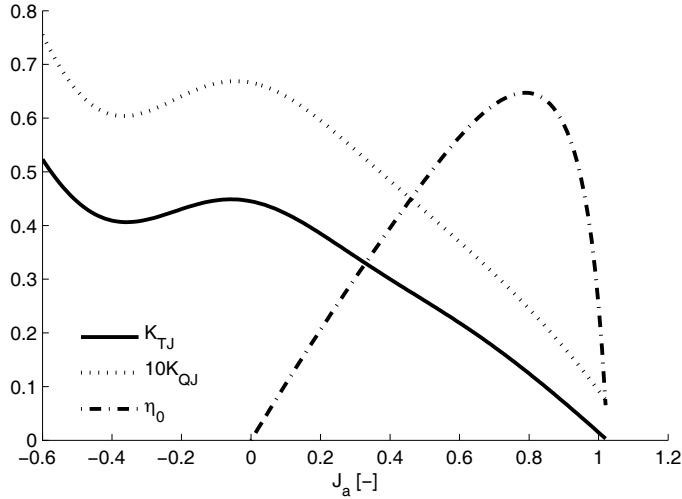


Figure 2.1: Open-water characteristics for the Wageningen B4-70 propeller.

shows an example propeller characteristics for the Wageningen B4-70 propeller with main parameters given in Table 2.2. The Wageningen B4-70 propeller will be used in examples and simulation studies throughout this thesis. The open-water characteristics in Figure 2.1 is extended into the fourth quadrant, i.e. negative  $V_a$ . If the propeller operating direction is reversed, this can be modelled by a similar open-water characteristics for negative shaft speeds. For normal operation,  $K_{TJ}$  and  $K_{QJ}$  are both positive. In off-design conditions, however, this may not be the case. If  $J_a$  is increased slightly beyond the value for which  $K_{TJ}$  is zero (i.e. a high  $V_a$  compared to  $n$ ), the thrust becomes negative while the torque is still positive. For a further increase in  $J_a$ , both the thrust and torque become negative. The propeller is then said to be *windmilling*, and the propeller is in practice producing power instead of absorbing it.

**Remark 2.2** *The open-water characteristics is specific to a certain propeller geometry. However, the general shape, as shown in Figure 2.1, will remain the same, regardless of the propeller. This can be explained by the physics of the propeller; the lift and drag of the propeller blades will give decreasing thrust*

and torque for increasing  $J_a$ , and the unsteady operating conditions for small negative  $J_a$  will lead to a drop in the thrust and torque.

### Model representations

For simulation purposes, various representations of the open-water characteristics may be used. By expressing  $K_{TJ}$  and  $K_{QJ}$  as second order polynomials in  $J_a$ ,  $T_a$  and  $Q_a$  can be written explicitly as functions of  $V_a$  and  $n$ :

$$K_{TJ} = K_{T0} + \alpha_{T1} J_a + \alpha_{T2} J_a |J_a|, \quad (2.20)$$

$$K_{QJ} = K_{Q0} + \alpha_{Q1} J_a + \alpha_{Q2} J_a |J_a|, \quad (2.21)$$

↓

$$T_a = T_{nn} n |n| + T_{nv} |n| V_a + T_{vv} V_a |V_a|, \quad (2.22)$$

$$Q_a = Q_{nn} n |n| + Q_{nv} |n| V_a + Q_{vv} V_a |V_a|, \quad (2.23)$$

where  $\alpha_{T1}$ ,  $\alpha_{T2}$ ,  $\alpha_{Q1}$ , and  $\alpha_{Q2}$  are constants, and:

$$\begin{aligned} T_{nn} &= \rho D^4 K_{T0}, & Q_{nn} &= \rho D^5 K_{Q0}, \\ T_{nv} &= \rho D^3 \alpha_{T1}, & Q_{nv} &= \rho D^4 \alpha_{Q1}, \\ T_{vv} &= \rho D^2 \alpha_{T2}, & Q_{vv} &= \rho D^3 \alpha_{Q2}. \end{aligned} \quad (2.24)$$

With  $\alpha_{T2} = \alpha_{Q2} = 0$ , this reduces to the linear approximation commonly used in the control literature (Blanke, 1981; Fossen, 2002):

$$K_{TJ} = K_{T0} + \alpha_{T1} J_a, \quad (2.25)$$

$$K_{QJ} = K_{Q0} + \alpha_{Q1} J_a, \quad (2.26)$$

↓

$$T_a = T_{nn} n |n| + T_{nv} |n| V_a, \quad (2.27)$$

$$Q_a = Q_{nn} n |n| + Q_{nv} |n| V_a. \quad (2.28)$$

It can be argued that the quadratic polynomial is a physically more reasonable representation than the linear one (Kim and Chung, 2006). (2.22) and (2.23) clearly show the dependence of the thrust and torque on the advance velocity. Figure 2.1 indicates that the linear and quadratic polynomial representations in reality only are applicable in the first quadrant: they clearly cannot capture the drop in  $K_{TJ}$  and  $K_{QJ}$  for small negative  $J_a$ . In addition, as will be discussed in Section 2.1.6, the open-water characteristics of a ducted propeller is usually significantly different, and less linear, than for an open propeller. Hence, these approximations must be used with care both for simulations and controller-observer design, and verified against the open-water characteristics of the actual propeller.

Is it then possible to formulate a better simulation model in terms of  $K_{TJ}$  and  $K_{QJ}$ ? If a higher-order polynomial in  $J_a$  is chosen for  $K_{TJ}$  and  $K_{QJ}$ , the resulting representation is singular for  $n = 0$ . Another option is to tabulate  $K_{TJ}$  and  $K_{QJ}$  as functions of  $J_a$ , and use interpolation and equations (2.3,

2.4) to calculate  $T_a$  and  $Q_a$ . However, since  $n \rightarrow 0$  from (2.16) implies that  $J_a \rightarrow \pm\infty$ , a zero-crossing of  $n$  is not covered by the open-water characteristics unless special precautions are taken. In addition, since  $T_a$  and  $Q_a$  are given as quadratic functions of  $n$ ,  $T_a = Q_a = 0$  for  $n = 0$ , regardless of  $V_a$  (and hence  $J_a$ ). For simulation purposes, the singularity for  $n = 0$  is therefore an inherent weakness in this model representation. The reason is probably that the open-water characteristics originally was developed for propellers on vessels in transit, i.e. for the first quadrant of operation, where only nonzero  $n$  were considered.

In order to capture the correct quasi-static behavior for all 4 quadrants, and also give physically reasonable results for time-varying inflow and shaft speed, it appears necessary to use another parametrization than the open-water characteristics.

### 2.1.2 4-quadrant model

A more accurate propeller characteristics model was apparently first defined by Miniovich (1960), and later used by amongst others van Lammeren *et al.* (1969) for some of the Wageningen B-series propellers. It is based on the angle of attack  $\beta$  of the propeller blade at radius  $0.7R$ :

$$\beta = \arctan\left(\frac{V_a}{0.7\pi n D}\right) = \arctan\left(\frac{V_a}{0.7\omega R}\right), \quad (2.29)$$

where  $R = D/2$  is the propeller radius, and  $\omega = 2\pi n$  is the propeller angular velocity. The four quadrants of operation are now defined as:

$$\begin{aligned} 1^{\text{st}}: \quad & 0^\circ \leq \beta \leq 90^\circ, \quad V_a \geq 0, \quad n \geq 0, \\ 2^{\text{nd}}: \quad & 90^\circ < \beta \leq 180^\circ, \quad V_a \geq 0, \quad n < 0, \\ 3^{\text{rd}}: \quad & -180^\circ < \beta \leq -90^\circ, \quad V_a < 0, \quad n < 0, \\ 4^{\text{th}}: \quad & -90^\circ < \beta \leq 0^\circ, \quad V_a < 0, \quad n \geq 0. \end{aligned} \quad (2.30)$$

This model hence covers also the windmilling regime. The non-dimensional thrust and torque coefficients  $C_T$  and  $C_Q$  are defined as:

$$C_T = \frac{T_a}{\frac{1}{2}\rho(V_a^2 + (0.7\omega R)^2)\frac{\pi}{4}D^2} = \frac{T_a}{\frac{1}{2}\pi R^2 \rho V_{0.7}^2}, \quad (2.31)$$

$$C_Q = \frac{Q_a}{\frac{1}{2}\rho(V_a^2 + (0.7\omega R)^2)\frac{\pi}{4}D^3} = \frac{Q_a}{\pi R^3 \rho V_{0.7}^2}, \quad (2.32)$$

where the undisturbed incident velocity to the propeller blade at radius  $0.7R$  is defined as:

$$V_{0.7} = \sqrt{V_a^2 + (0.7\omega R)^2}. \quad (2.33)$$

For a specific propeller,  $C_T$  is in van Lammeren *et al.* (1969) modelled by a 20<sup>th</sup> order Fourier series in  $\beta$  with coefficients  $A_T(k)$  and  $B_T(k)$ , and  $C_Q$  similarly

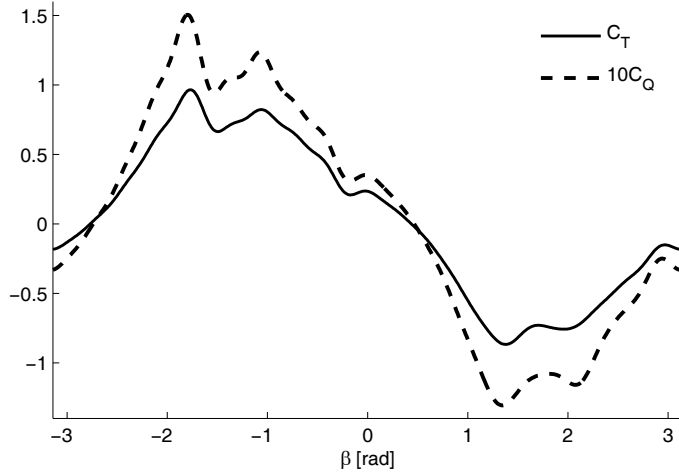


Figure 2.2:  $C_T$  and  $C_Q$  for the 4-quadrant representation of the Wageningen B4-70 propeller.

modelled with coefficients  $A_Q(k)$  and  $B_Q(k)$ :

$$C_T(\beta) = \sum_{k=0}^{20} (A_T(k) \cos \beta k + B_T(k) \sin \beta k), \quad (2.34)$$

$$C_Q(\beta) = \sum_{k=0}^{20} (A_Q(k) \cos \beta k + B_Q(k) \sin \beta k). \quad (2.35)$$

Note that the Fourier series coefficients in (2.34, 2.35) have zero-based indexing. This formulation has many advantages over the open-water characteristics, since it is based on a physically more sound foundation: it is valid for any shaft speed and inflow, and covers all four quadrants of operation. However, it requires significantly more model knowledge than the open-water characteristics, and the necessary data may not be available.

$C_T(\beta)$  and  $C_Q(\beta)$  may be parameterized in other ways than the Fourier series representations in (2.34, 2.35), e.g. by tabulating  $C_T$  and  $C_Q$  as functions of  $\beta$  and using interpolation in this table. Figure 2.2 shows  $C_T(\beta)$  and  $C_Q(\beta)$  for the Wageningen B4-70 propeller with main parameters given in Table 2.2. Numerical values for the Fourier coefficients can be found in van Lammeren *et al.* (1969), and are also reproduced in Appendix A.

Since both the 1-quadrant model in (2.6, 2.7) and the 4-quadrant model in (2.31, 2.32) express  $T_a$  and  $Q_a$  as functions of  $n$  and  $V_a$ , it is possible to establish some relationships between them.  $J_a$  from (2.16) and  $\beta$  from (2.29) are related

by:

$$\beta = \arctan\left(\frac{V_a}{0.7\pi nD}\right) = \arctan\left(\frac{J_a}{0.7\pi}\right). \quad (2.36)$$

By equating (2.6) and (2.31), the relationship between  $K_T$  and  $C_T$  is found to be:

$$K_T = C_T \frac{\pi}{8} (J_a^2 + 0.7^2 \pi^2), \quad (2.37)$$

and similarly between  $K_Q$  and  $C_Q$  from (2.7) and (2.32):

$$K_Q = C_Q \frac{\pi}{8} (J_a^2 + 0.7^2 \pi^2). \quad (2.38)$$

### 2.1.3 Simplified 4-quadrant model

A simplified 4-quadrant model may be derived by using only the first terms in the Fourier series for  $C_T$  and  $C_Q$ :

$$\begin{aligned} C_{TS}(\beta) &= A_T(0) + A_T(1) \cos \beta + B_T(1) \sin \beta \\ &= A_{T0} + A_{T1} \cos \beta + B_{T1} \sin \beta, \end{aligned} \quad (2.39)$$

$$\begin{aligned} C_{QS}(\beta) &= A_Q(0) + A_Q(1) \cos \beta + B_Q(1) \sin \beta \\ &= A_{Q0} + A_{Q1} \cos \beta + B_{Q1} \sin \beta, \end{aligned} \quad (2.40)$$

where  $C_{TS}$  and  $C_{QS}$  are the simplified 4-quadrant coefficients. This model preserves the good properties of the 4-quadrant representation, but gives very coarse approximations of the true propeller characteristics.

### 2.1.4 General momentum theory with propeller lift and drag

An alternative representation of the propeller thrust and torque can be obtained by treating the lift and drag of the individual propeller blades as the source of propeller thrust and torque. This approach is based on the generalized Rankine-Froude momentum theory, and is called the *blade element theory* (Drzewiecki, 1920). It is described in detail in Durand (1963), and can also be found in e.g. Lewis (1989) or Carlton (1994).

While useful for understanding the physics of the propeller, this formulation is less convenient for quasi-static simulation purposes than the representations presented above. The lift and drag based model requires calculation of the axially and rotationally induced velocities in the propeller disc in order to calculate the effective angle of attack of and incident velocity to the propeller blades. Since these velocities depend on the propeller thrust, the representation becomes implicit. However, if the dynamics of the inflow to the propeller is to be accounted for, as done in Healey *et al.* (1995), Whitcomb and Yoerger (1999a), and Bachmayer *et al.* (2000), such a formulation may be necessary. In their model, however, the advance velocity is set to zero, and rotational flow is neglected. Flow dynamics is further treated in Section 2.2.5.

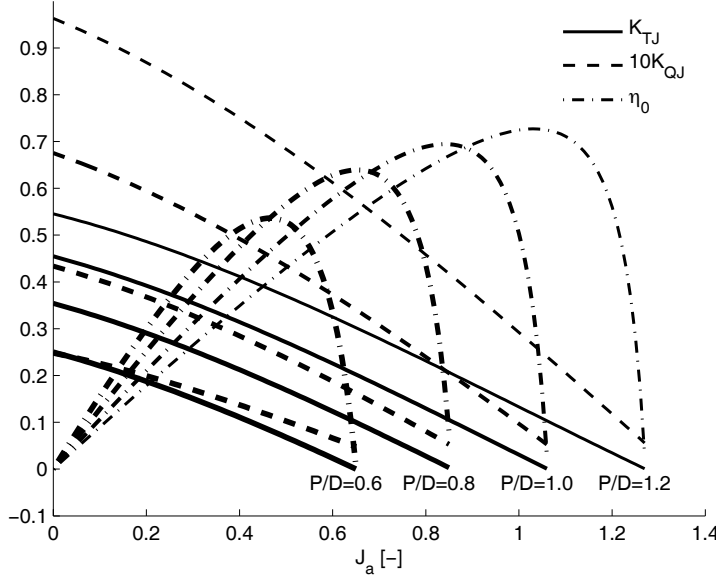


Figure 2.3: Open-water characteristics of the Wageningen B4-70 propeller for varying pitch ratio  $P/D$ .

### 2.1.5 Controllable pitch propellers

On a CPP there are two control parameters: the shaft speed  $n$  and the pitch angle  $\phi$ . Often, the pitch is given in terms of the pitch/diameter ratio  $P/D$ .  $\phi$  is the angle between the propeller blade at 70% of the propeller radius and a line perpendicular to the propeller shaft. The pitch  $P$  is the distance travelled by the propeller in the axial direction after one revolution, if it is assumed to be in an unyielding medium, see e.g. Lewis (1989) or Carlton (1994).  $\phi$  is related to  $P/D$  by:

$$\phi = \arctan\left(\frac{P/D}{\pi}\right). \quad (2.41)$$

The open-water CPP characteristics in terms of  $K_{TJ}$  and  $K_{QJ}$  must be specified with three parameters, i.e.  $K_{TJ} = K_{TJ}(V_a, n, \phi)$  and  $K_{QJ} = K_{QJ}(V_a, n, \phi)$ . This can be viewed as a set of conventional open-water characteristics (in terms of  $J_a$ ) or 4-quadrant characteristics (in terms of  $\beta$ ) for varying  $P/D$ . Figure 2.3 shows the open-water characteristics with varying  $P/D$  for the fixed pitch Wageningen B4-70 propellers, with data taken from Oosterveld and van Oos-senan (1975). For increasing  $P/D$ , the thrust and torque increases for fixed  $V_a$  and  $n$ , and the optimum open-water efficiency  $\eta_0$  is found for a higher  $J_a$ . In order to model a CPP for all 4 quadrants of operation, a large data set is needed. Such data can be found e.g. in Oosterveld (1970), or in Strom-Tejsen

and Porter (1972) based on the work by Gutsche and Schroeder (1963). A 1-quadrant model can be found in Chu *et al.* (1979). Some of these data sets are also reproduced in Carlton (1994).

**Remark 2.3** *It is important to distinguish between a series of FPP with varying P/D, as given in e.g. van Lammeren et al. (1969) and Oosterveld and van Oossanen (1975), and a single CPP with varying P/D, as given in e.g. Chu et al. (1979) and Strom-Tejsen and Porter (1972).*

### 2.1.6 Characteristics of various propeller types

The propeller characteristics presented here are applicable to open and ducted propellers. Tunnel thrusters are a special case where the propeller is not significantly affected by  $V_a$ . This can be explained by the sheltered position of the propeller inside the tunnel, as well as limited sway velocity of the vessel. Tunnel thrusters are therefore usually modelled without any influence from  $V_a$ . For a FPP, this means that  $K_{TJ}(V_a, n) = K_{T0}$  and  $K_{QJ}(V_a, n) = K_{Q0}$ . Note that the effective thrust of a tunnel thruster is strongly affected by the surge velocity of the vessel (Chislett and Björheden, 1966; Brix, 1978; Karlsen *et al.*, 1986). This is regarded as a thrust loss effect, and not included in the propeller characteristics.

From a modelling point of view, the main difference between open and ducted propellers lies in the shape of the thrust and torque coefficients. If the open-water diagrams of an open propeller and a ducted propeller are compared, the total thrust coefficient of the ducted propeller (i.e. including the duct thrust) typically has the steeper slope. The torque coefficient, on the other hand, has a smaller slope. This means that the efficiency of the ducted propeller is higher at low  $J_a$  and lower at high  $J_a$ . Equivalently, the duct increases the efficiency of a *heavily loaded* propeller, whereas it decreases the efficiency of a *lightly loaded* propeller. These relationships are strongly affected by the length of the duct relative to the propeller diameter. More on this can be found in e.g. Lewis (1989), Carlton (1994), and the references therein. A comparison of the open-water characteristics of the Wageningen B4-70 propeller and the Wageningen K<sub>a</sub>4-70 propeller in a 19A nozzle (Oosterveld, 1970) is given in Figure 2.4. The difference in characteristics is the reason for ducted propellers being used on e.g. anchor-handling vessels and tugs, where the bollard pull thrust is of main importance, whereas open propellers are preferred for vessels where the focus is on efficiency in transit.

### 2.1.7 Propeller efficiency

The presence of a hull close to a main propeller affects the propeller efficiency in several ways, see e.g. Lewis (1989). The average advance velocity of the propeller differs from the ship speed  $U$  by the hull wake fraction number  $w_h$ :

$$V_a = U(1 - w_h). \quad (2.42)$$

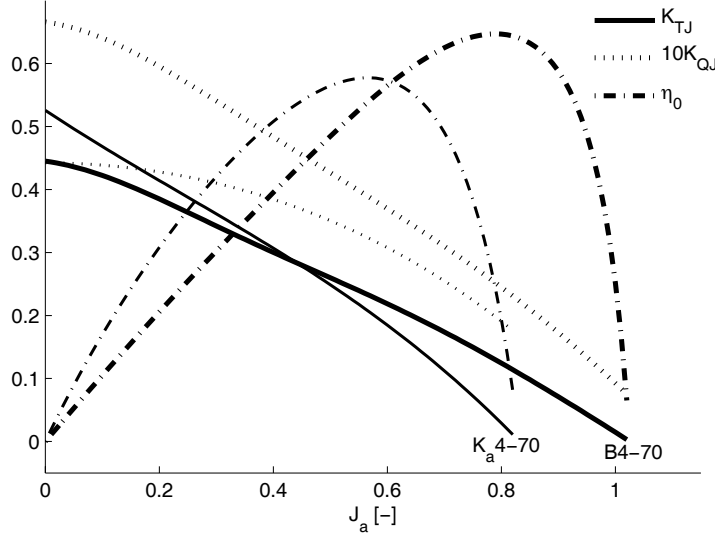


Figure 2.4: Comparison of open-water characteristics for the Wageningen B4-70 propeller (thick lines) and the Wageningen  $K_a$  4-70 propeller in a 19A nozzle (thin lines), both for  $P/D = 1.0$ .

Additionally, the velocity field set up by the propeller changes the pressure distribution on the hull, which leads to an increased resistance  $d_s$ , expressed by the thrust deduction coefficient  $t_d$ :

$$d_s = T_a t_d. \quad (2.43)$$

By the principle of thrust identity, the thrust coefficient behind the hull is normally assumed to be unchanged compared to open water, while the torque coefficient will be affected by the change in inflow at the stern. This is accounted for by the relative rotative efficiency  $\eta_r$ , such that the effective torque coefficient  $K_{QB} = K_Q/\eta_r$ , and hence the effective torque  $Q_B = Q_a/\eta_r$ . The mechanical efficiency representing frictional losses in gears and bearings is termed  $\eta_m$ . The overall propulsion efficiency  $\eta_p$  is found as the ratio between the useful work done by the propeller in overcoming the vessel resistance  $R_v$  at speed  $U$ , divided by the work required to overcome the shaft torque:

$$\begin{aligned} \eta_p &= \frac{R_v U}{(2\pi n Q_B / \eta_m)} = \frac{T_a (1 - t_d) V_a}{(2\pi n Q_a / \eta_r)(1 - w_h)} \eta_m \\ &= \frac{T_a V_a}{2\pi n Q_a} \frac{(1 - t_d)}{(1 - w_h)} \eta_r \eta_m = \eta_0 \eta_h \eta_r \eta_m, \end{aligned} \quad (2.44)$$

where  $\eta_h = (1 - t_d)/(1 - w_h)$  is defined as the hull efficiency, and  $\eta_0$  is defined in (2.17). For station-keeping, where  $U \approx V_a \approx 0$ ,  $\eta_p \approx 0$  since  $\eta_0 \approx 0$ . For

propellers other than main propellers,  $\eta_p$  is not well-defined.

Although  $\eta_0 = 0$  for  $V_a = 0$ , the propeller is still doing work by accelerating water through the propeller disc. By using the momentum theory result for the propeller induced wake velocity, a better indication of the actual propeller hydrodynamic efficiency is given by the efficiency parameter  $\eta_a$ . From momentum theory, see e.g. Durand (1963), the mean water flow velocity  $V_p$  through the propeller disc is given for  $V_a = 0$  by:

$$V_p = \frac{1}{2} \text{sign}(T_n) \sqrt{\frac{2|T_n|}{\rho A_p}}, \quad (2.45)$$

where  $T_n$  is the nominal thrust as given in (2.8), and  $A_p$  is the propeller disc area.  $\eta_a$  is obtained as the ratio of work done in accelerating the water flow to the work done in overcoming the propeller torque:

$$\eta_a = \frac{V_p T_n}{2\pi n Q_n} = \sqrt{\frac{2|T_n|}{\rho A_p}} \frac{|T_n|}{4\pi n Q_n} = \frac{K_{T0}^{3/2}}{\sqrt{2}\pi^{3/2} K_{Q0}}, \quad (2.46)$$

where (2.8) and (2.9) have been inserted for  $T_n$  and  $Q_n$ . The efficiency parameter, which does not take into account the thrust deduction or mechanical efficiency, is obviously a propeller constant. As should be expected, a high thrust coefficient combined with a low torque coefficient will give a high hydrodynamic efficiency, and hence a high  $\eta_a$ . From Table 2.2, the efficiency parameter of the Wageningen B4-70 propeller is  $\eta_a = 0.566$  for  $n > 0$ , and  $\eta_a = 0.413$  for  $n < 0$ . For the Wageningen K<sub>a</sub> 4-70 propeller in a 19A nozzle, as shown in Figure 2.4, the corresponding efficiency parameters are  $\eta_a = 1.094$  for  $n > 0$ , and  $\eta_a = 0.494$  for  $n < 0$ .

### 2.1.8 Thrust and torque relationships

Due to the working principles of the propeller, the thrust and torque are closely coupled. From an investigation of the effect of roughness on open propellers, Lerbs (1952) showed that for a given propeller, a change  $\Delta K_Q$  of  $K_Q$  implies a proportional change  $\Delta K_T$  of  $K_T$ , i.e.:

$$\Delta K_T = c_t \Delta K_Q, \quad (2.47)$$

where  $c_t$  is a constant. This implies that  $K_T$  and  $K_Q$  can be linearly related by:

$$K_T = a_t K_Q + b_t, \quad (2.48)$$

where  $a_t$  and  $b_t$  are constants for an FPP, and functions of the pitch ratio for a CPP. This was applied by Zhinkin (1989), who provided full-scale experimental result to show that this relationship is stable for a large range of propeller operating conditions, including varying advance ratios, in waves, and for oblique inflow. The  $K_T - K_Q$  relationship in (2.48) derived from open-water tests was

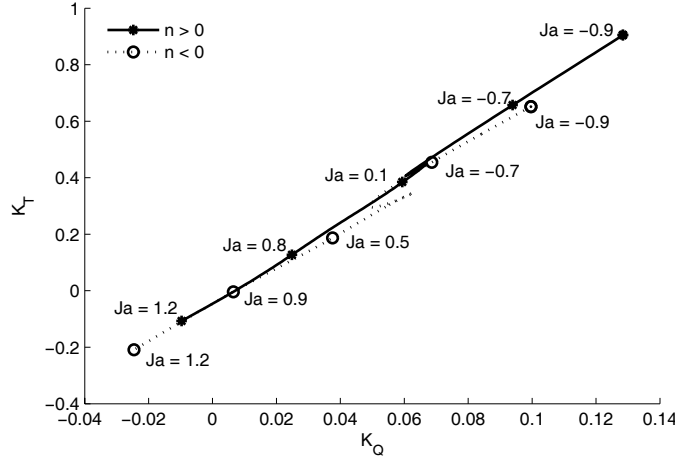


Figure 2.5: Relationship between  $K_T$  and  $K_Q$  for the Wageningen B4-70 propeller in the range  $-0.9 < J_a < 1.2$ .

shown to hold also when the propeller is installed behind a hull. It appears, however, that Zhinkin (1989) only considered the first quadrant of operation. In order to use a relation like (2.48) for all four quadrants, it is hence necessary to investigate its validity in the remaining three quadrants. Figure 2.5 shows the relationship between  $K_T$  and  $K_Q$  for the Wageningen B4-70 propeller in the range  $-0.9 < J_a < 1.2$ , both for positive  $n$  (first and fourth quadrant) and negative  $n$  (second and third quadrant). For  $n > 0$ , the  $K_T - K_Q$  relationship is almost exactly linear. For  $n < 0$ , there are some discrepancies, especially in the second quadrant (negative  $J_a$ ), corresponding to  $K_Q < 0.06$ . The agreement is still found to be acceptable. Although one should not generalize, this indicates that the relationship in (2.48) derived from the first quadrant data is applicable in all four quadrants. For other propellers, it may be that two  $K_T - K_Q$  relationships should be used: one for  $n > 0$  and one for  $n < 0$ . For the Wageningen B4-70 propeller, the  $K_T - K_Q$  relationship is given by the coefficients:

$$a_t = 7.52, \quad b_t = -0.054. \quad (2.49)$$

From the discussion in Section 2.1.6, it can be anticipated that (2.48) will not hold equally well for ducted propellers, since the shapes of the  $K_T$  and  $K_Q$  curves then are inherently different. Figure 2.6 shows the  $K_T - K_Q$  relationship for a Wageningen K<sub>a</sub>4-70 propeller in a 19A nozzle, with data from the first and third quadrant taken from Oosterveld (1970). This indicates that the linear relationship is less applicable to ducted propellers.

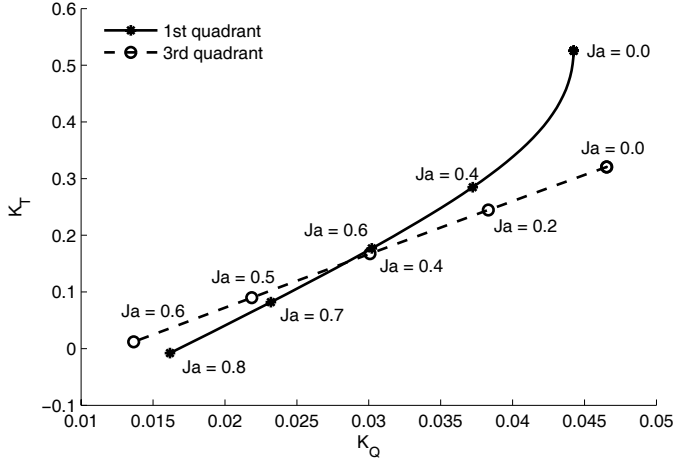


Figure 2.6: Relationship between  $K_T$  and  $K_Q$  for the Wageningen  $K_a$  4-70 propeller with 19A nozzle in the range  $0 \leq J_a < 0.86$ .

## 2.2 Dynamic effects

The propeller models presented in Section 2.1 are all quasi-static. Dynamic effects are introduced by considering the propeller motor and shaft, and also by flow dynamics.

### 2.2.1 Shaft dynamics

The torque balance for the propeller shaft is written:

$$I_s \dot{\omega} = Q_{mp} - Q_a - Q_f(\omega), \quad (2.50)$$

where  $Q_{mp}$  is the motor torque inflicted on the propeller shaft,  $I_s$  is the moment of inertia for the shaft, propeller, and motor,  $\omega$  is the shaft angular velocity, and  $Q_f(\omega)$  is the shaft friction. The friction may for most applications be viewed as a sum of a static friction – or starting torque –  $Q_s$  and a linear component:

$$Q_f(\omega) = \text{sign}(\omega)Q_s + K_\omega\omega, \quad (2.51)$$

where  $K_\omega$  is a linear friction coefficient. If desired, more sophisticated friction models may be used, including e.g. nonlinear elements, Stribeck friction, and other hysteresis effects. This has not been considered in the current work, and the model in (2.51) is considered sufficient for control design purposes.

In general, friction is assumed to be more significant on small thrusters typically used on underwater vehicles and in experimental setups, than on large thrusters used on surface vessels.

**Remark 2.4** The propeller torque  $Q_a$  in (2.50) should in general also include an added mass term due to hydrodynamic forces in phase with  $\dot{\omega}$ . This is discussed in the context of propeller vibrations in e.g. Wereldsma (1965) and Parsons and Vorus (1981). However, the added mass will depend on propeller shaft speed, advance velocity, and propeller submergence, and extensive model knowledge is required in order to include such terms. Neglecting the added mass will give a reduced rotational inertia, and hence faster dynamics. If the necessary model knowledge is available, the added mass could be included in  $I_s$ .

## 2.2.2 Motor dynamics

### Electric motor

The inner torque control loop – or inner current loop – is inherent in the design of most applied control schemes for variable speed drive systems. The torque is controlled by means of motor currents and motor fluxes with high accuracy and bandwidth. By the cascaded control principle, an outer control loop – e.g. a speed controller – sets the commanded torque setpoint of the inner loop. For this principle to work, the inner current loop must have a much higher bandwidth than the outer loop. In the design of the outer control loop, the closed loop of an electric motor and its current controller may be assumed to be equivalent with a first order system (Leonhard, 1996):

$$\dot{Q}_m = \frac{1}{T_m}(Q_{cm} - Q_m), \quad (2.52)$$

where  $Q_m$  is the motor torque,  $T_m$  is the time constant, and  $Q_{cm}$  is the commanded motor torque from the thruster controller. This model is applicable to both AC and DC motors; once the current loop is closed, there is little difference between the two types of machines. From a practical point of view, the current loop is usually embedded in the motor drive, and is not at the disposition of the user. The main importance is therefore to account for its dynamics in the design of the higher-level controllers (Leonhard, 1996). According to Nilsen (2001), the dynamics of the current loop are, in the context of shaft speed controller design, dominated by the filter on the shaft speed measurement. The motor power  $P_m$  is given by:

$$P_m = Q_m 2\pi n_m, \quad (2.53)$$

where  $n_m$  is the motor speed. The rated (nominal) torque and power for continuous operation of the motor are denoted  $Q_N$  and  $P_N$ . The corresponding rated motor shaft speed  $n_N$  is given from:

$$P_N = Q_N 2\pi n_N. \quad (2.54)$$

The maximum torque  $Q_{\max}$  and power  $P_{\max}$  for the motor are usually set to:

$$Q_{\max} = k_m Q_N, \quad P_{\max} = k_m P_N, \quad (2.55)$$

where  $k_m$  typically is in the range of 1.1 – 1.2 (Sørensen *et al.*, 1997).

### Diesel engine

A diesel engine is modelled in a similar way as the electric motor. According to Blanke (1981), the diesel engine dynamics may for control design and propulsion performance evaluation be approximated by a time constant  $T_m$  and a time delay  $\tau_m$ . The diesel engine transfer function becomes:

$$Q_m(s) = e^{-s\tau_m} \frac{K_y}{1 + sT_m} Y(s), \quad (2.56)$$

where  $s$  is the Laplace operator,  $K_y$  is the motor torque constant, and  $Y$  is the fuel index (governor setting). This means that  $Q_{cm}$  in (2.52) is given by  $Q_{cm} = K_y Y$ , where  $Y$  is the control signal from the diesel controller. The diesel engine power is proportional to the fuel flow (Blanke, 1994). From Blanke (1981), the time constant is empirically found to be:

$$T_m \approx \frac{0.9}{2\pi n_m}, \quad (2.57)$$

and the time delay can be approximated by half the period between consecutive cylinder firings. A diesel engine with  $N$  cylinders rotating at speed  $n_m$  rps then has the time delay:

$$\tau_m \approx \frac{1}{2n_m N}. \quad (2.58)$$

### 2.2.3 Accounting for gears

Many electrically driven propulsion units are equipped with a gearbox between the motor and the propeller shaft. In this work,  $Q_m$  is the motor torque as seen from the motor, and  $n$  is the shaft speed as seen from the propeller. The relations between the motor torque  $Q_m$ , the motor shaft speed  $n_m$ , the motor torque  $Q_{mp}$  seen from the propeller, and the propeller shaft speed  $n$ , are given by the gear ratio  $k_g$ :

$$Q_{mp} = k_g Q_m, \quad (2.59)$$

$$n = n_m/k_g. \quad (2.60)$$

For thruster controller design and analysis, all torques and shaft speeds are as seen from the propeller, with the exception of  $Q_m$  and  $Q_{cm}$ . For example, the commanded torque  $Q_c$  from the controller is referred to the propeller, and  $Q_{cm}$  calculated from  $Q_{cm} = Q_c/k_g$ . The various terms are illustrated in Figure 2.7. By the principle of conservation of energy, the rotational inertia  $I_s$  seen by the propeller can be transformed to the rotational inertia  $I_m$  seen by the motor by:

$$\begin{aligned} I_s \dot{\omega} \omega &= I_m k_g \dot{\omega} k_g \omega, \\ &\Downarrow \\ I_m &= I_s / k_g^2. \end{aligned} \quad (2.61)$$

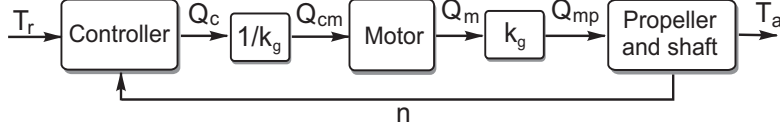


Figure 2.7: Block diagram of the controller, motor, propeller/shaft, and gears.

### 2.2.4 Bollard pull relationships

When the vessel is stationary such that  $V_a = 0$ , and the thruster motor is operated at its max continuous rating, the thruster is said to be in the bollard pull condition. The bollard pull thrust, torque, power, and shaft speed (seen from the propeller) are denoted  $T_{bp}$ ,  $Q_{bp}$ ,  $P_{bp}$ , and  $n_{bp}$ , respectively. From (2.60),  $n_{bp}$  is given from  $n_N$  by:

$$n_{bp} = n_N / k_g, \quad (2.62)$$

and  $T_{bp}$  and  $Q_{bp}$  are given from  $K_{T0}$ ,  $K_{Q0}$ , and  $n_{bp}$  by:

$$T_{bp} = \rho D^4 K_{T0} n_{bp}^2, \quad Q_{bp} = \rho D^5 K_{Q0} n_{bp}^2. \quad (2.63)$$

At the bollard pull condition (with  $Q_m = Q_N$ ), the steady-state rotational dynamics (2.50) must satisfy:

$$k_g Q_N = Q_s + K_\omega 2\pi n_{bp} + Q_{bp}, \quad (2.64)$$

and  $P_N$ ,  $P_{bp}$ , and the mechanical efficiency  $\eta_m$  must satisfy:

$$P_{bp} = Q_{bp} 2\pi n_{bp} = \eta_m P_N. \quad (2.65)$$

That is,  $\eta_m$  is given from the power lost in static and linear friction:

$$\eta_m = \frac{Q_{bp}}{Q_N k_g} = \frac{k_g Q_N - Q_s - K_\omega 2\pi n_{bp}}{Q_N k_g}. \quad (2.66)$$

If higher-order friction terms were to be included, similar relationships would apply.

**Remark 2.5** In industrial applications, a constant mechanical efficiency is usually assumed. This implies that  $P_a = \eta_m P_m$  for any shaft speed, where  $\eta_m$  is found from (2.65). This is equivalent to using a purely quadratic friction model, as opposed to the static plus linear model in (2.51). If the true friction contains significant static and/or linear terms, the assumption of a purely quadratic model will under-estimate the friction losses for  $n < n_{bp}$ .

### 2.2.5 Propeller flow dynamics

Experimental results have shown that overshoots in thrust and torque during transient operation cannot be explained by steady state theory. An investigation into the effects of flow dynamics on the performance of low-level thruster controllers and underwater vehicle positioning was initiated by Yoerger *et al.* (1991). In this work, a lumped parameter one-state model for the shaft dynamics and flow dynamics was proposed:

$$\begin{aligned} I_s \dot{\omega} &= Q_{mp} - K_1 \omega |\omega|, \\ T_a &= K_2 \omega |\omega|, \end{aligned} \quad (2.67)$$

where an instantaneous relationship between the propeller shaft speed and the flow rate is included in the parameters  $K_1$  and  $K_2$ . The shaft friction is neglected.

To describe overshoots in thrust found in experimental data, Healey *et al.* (1995) extended (2.67) to include the flow velocity  $V_p$  through the propeller as a state. From momentum theory, see e.g. Durand (1963),  $V_p$  is connected with the advance velocity  $V_a$  and the induced velocity in the wake  $U_A$  through:

$$V_p = V_a + \frac{1}{2} U_A. \quad (2.68)$$

In the work of Healey *et al.* (1995), a control volume of water around the propeller was modelled as a mass-damper system, leading to the following two-state model:

$$\begin{aligned} I_s \dot{\omega} &= Q_{mp} - K_\omega \omega - Q_a, \\ m_f \dot{V}_p &= T_a - d_f V_p |V_p|, \\ T_a &= T_a(\omega, V_p), \\ Q_a &= Q_a(\omega, V_p), \end{aligned} \quad (2.69)$$

where  $m_f$  can be viewed as the mass of water in the control volume, and  $d_f$  is a quadratic damping coefficient. The mappings  $T(\omega, V_p)$  and  $Q_a(\omega, V_p)$  employ foil theory with sinusoidal lift and drag curves and the local angle of attack at radius  $0.7R$  to model the propeller blade lift and drag. Healey *et al.* (1995) also proposed using a time constant on the thrust and torque for open propellers to model lift and drag build-up. A summary of the theory and assumptions behind these models, as well as experimental verification, can be found in Whitcomb and Yoerger (1999a).

Discrepancies between (2.69) and experimental results were attempted explained by Bachmayer *et al.* (2000). Here it was concluded that the inclusion of rotational flow dynamics did not improve model performance, whereas the use of non-sinusoidal lift and drag curves specific to the tested propeller gave significant performance improvements. Note that these models all assume that  $V_a = 0$ , and hence only are applicable for station-keeping operations with small current.

In Blanke *et al.* (2000) the flow dynamics in (2.69) were extended to be valid for  $V_a \geq 0$  by:

$$m_f \dot{V}_p = T_a - 2d_f |V_p| (V_p - V_a). \quad (2.70)$$

This is useful if the model is needed in the first quadrant of operation, e.g. for an output feedback thrust controller on an AUV, as proposed by Fossen and Blanke (2000).

A flow dynamics model valid for all  $V_a$  is still subject to further research. For surface vessels, which normally have a much slower response than a small underwater vehicle, the flow dynamics of the propeller is probably insignificant (Healey *et al.*, 1995).

## 2.3 Loss effects

In ideal conditions, i.e. deeply submerged and in calm water, a propeller produces thrust and torque according to the nominal models in (2.8) and (2.9). A thrust loss is here defined as any deviation of the thrust and torque from the nominal values. The effect of the thrust losses may be expressed by the thrust and torque reduction coefficients  $\beta_T$  and  $\beta_Q$ , as defined in (2.11) and (2.12). Thrust losses are in this work divided in two groups:

1. Losses that mainly affect the propeller loading,
2. Losses that mainly affect the propeller wake.

For low-level thruster control, loss effects in group 1 are the most interesting, since these to some extent may be compensated for by the thruster controller. The main loss effects to consider in this group are fluctuations in the *in-line* water inflow to the propeller, *ventilation*, and *in-and-out-of-water effects*. These will be studied in more detail in the following sections.

The main loss effects in group 2 are losses due to *transverse* water inflow and *thruster-hull interaction*. Transverse inflow, i.e. water inflow perpendicular to the propeller axis, will introduce a force in the direction of the inflow due to deflection of the propeller race for open and ducted propellers. This may be referred to as *cross-coupling drag* (Lehn, 1992). The transverse flow will to some extent also alter the loading of the propeller. For tunnel thrusters, the transverse inflow will be caused by vessel forward or reverse speed, which gives rise to *speed or suction losses* (Chislett and Björheden, 1966; Brix, 1978; Karlsen *et al.*, 1986).

For azimuthing thrusters, both thrust reduction and change of thrust direction may occur due to thruster-hull interaction caused by frictional losses, and pressure effects when the thruster race sweeps along the hull (Lehn, 1992). The last is referred to as the *Coanda effect*. These effects cannot be significantly affected by the low-level thruster controller, and must be accounted for during design of the propulsion system and hull, as well as in the thrust allocation algorithm. These topics will not be further treated in this thesis.

A loss effect that cannot easily be categorized is *thruster-thruster interaction*, which is caused by influence of the propeller race from one thruster on a neighboring thruster. This may lead to significant thrust losses, if appropriate precautions are not taken in the thrust allocation algorithm (Lehn, 1992; Ekstrom and Brown, 2002; Koushan, 2004; Brown and Ekstrom, 2005). The propeller race may influence the neighboring thruster in several ways, depending on the angle of the propeller race relative to the thrust direction of the affected thruster. In general, both the in-line and the transverse water inflow will be altered. In addition, the level of vorticity in the water is increased, giving rise to unsteady loading.

The hydrodynamics of a propeller affected by thrust losses is highly complex, and each of the mentioned thrust loss effects deserve a detailed study. Additionally, industrial experience shows that a simple superposition of the various loss effects may give too conservative estimates of the total thrust losses. This may be explained by the nonlinear interactions between the loss effects, which are difficult to account for. In order to develop accurate simulation models for propellers on a vessel in a seaway, it will be necessary to undertake comprehensive studies of both the individual loss effects and their interactions. This is considered outside the scope of this work. Instead, simplified models suitable for time-domain simulation and controller design, intended to capture the main characteristics of the loss effects, will be presented.

**Remark 2.6** *The sensitivity to the different thrust losses depends on the type of propeller or thruster, application of skegs and fins, hull design, and operational philosophy. Main propellers are subject to ventilation and in-and-out-of-water effects, as well as in-line and transverse losses. Azimuth thrusters and pods are subject to losses caused by hull friction and interaction with other thrusters, and may also be affected by ventilation. Tunnel thrusters are subject to transverse losses due to current and vessel speed, and ventilation and in-and-out-of water losses in heavy seas.*

### 2.3.1 In-line water inflow

Waves, currents, and vessel motion induce a time-varying velocity field around the propeller. This may be decomposed in an in-line component and a transverse component. This is described in the simplified simulation model presented in Appendix C. The simulation model gives the motion of a thruster on a vessel in a seaway, including the relative submergence with respect to the free surface and the relative water velocities.

The in-line, or axial, component gives rise to changes in the advance velocity  $V_a$ , and hence the advance number  $J_a$  (2.16). With a time-varying  $J_a$ , the propeller operating point is moving on the  $K_{TJ}$  and  $K_{QJ}$  curves, see e.g. Figure 2.1. For a fixed shaft speed  $n$ , this induces fluctuations in thrust, torque, and power. Not many references seem to have discussed these effects explicitly, but some information may be found in Domachowski *et al.* (1997). The

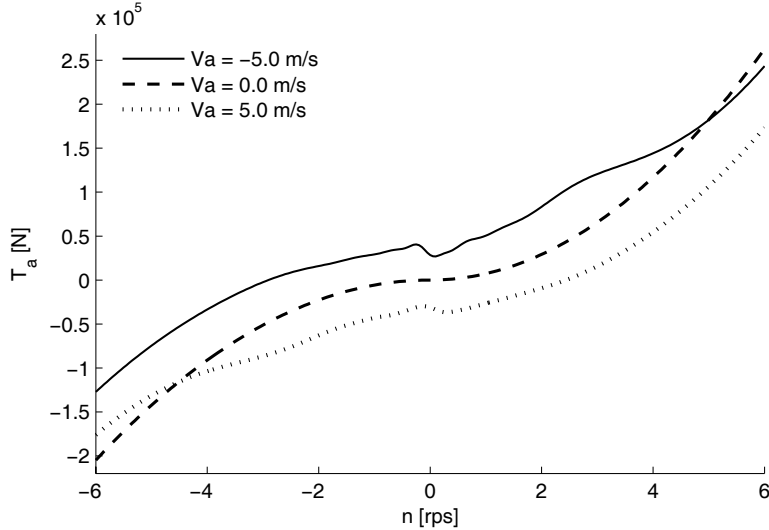


Figure 2.8: Thrust curves as functions of shaft speed  $n$  for varying  $V_a$ , for the Wageningen B4-70 propeller with diameter  $D = 4\text{m}$ .

thrust and torque fluctuations because of non-uniform inflow to the propeller due to the presence of the hull and appendices are more well-documented, see e.g. Ker Wilson (1963), Wereldsma (1965), Carlton (1994), Lewis (1989), and references therein.

The thrust and torque loss factors due to variations in  $V_a$  for a deeply submerged propeller are denoted  $\beta_{TJ}$  and  $\beta_{QJ}$ , and may be written as:

$$\beta_{TJ}(V_a, n) = \frac{K_{TJ}(V_a, n)}{K_{T0}}, \quad (2.71)$$

$$\beta_{QJ}(V_a, n) = \frac{K_{QJ}(V_a, n)}{K_{Q0}}. \quad (2.72)$$

$\beta_{TJ}$  and  $\beta_{QJ}$  can be both larger than and smaller than unity, since the variations in  $V_a$  may lead to both higher and lower propeller loading than the nominal value for  $V_a = 0$ . Figure 2.8 shows example thrust curves as functions of  $n$  for varying  $V_a$ . The 4-quadrant propeller characteristics of the Wageningen B4-70 propeller has been used, and the propeller diameter set to  $D = 4\text{m}$ .

When performing simulations,  $V_a$  and  $n$  will normally be time-varying states, and the in-line thrust losses will be given implicitly from the model of the propeller characteristics. However, it is also interesting to study the in-line losses directly. This will be done more thoroughly in Chapter 4, where the ability to counteract the in-line thrust losses is analyzed for various low-level thruster controllers. Based on the propeller characteristics of the Wageningen

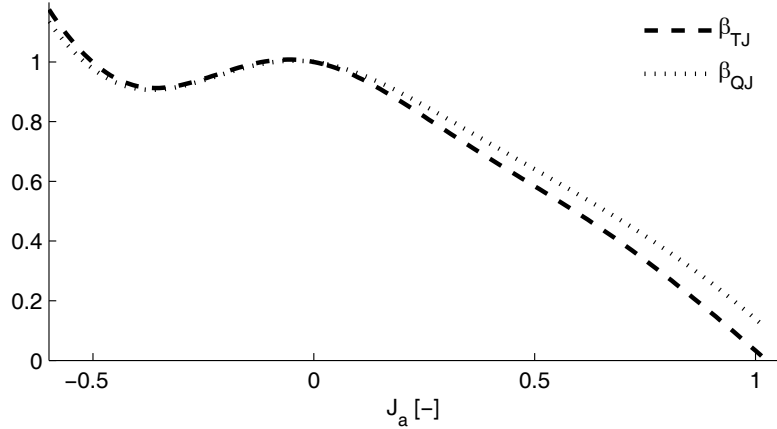


Figure 2.9: Thrust and torque loss factors  $\beta_{TJ}$  and  $\beta_{QJ}$  due to in-line flow as functions of  $J_a$  for the Wageningen B4-70 propeller.

B4-70 propeller in Figure 2.1, Figure 2.9 shows  $\beta_{TJ}$  and  $\beta_{QJ}$  as functions of  $J_a$ . It is clear that vessel speed and/or current will lead to a steady-state offset in thrust and torque, and that oscillations in the inflow caused by waves and vessel motion will give rise to oscillations in thrust and torque.

**Remark 2.7** Stettler et al. (2005) have studied the steady and unsteady forces on open and ducted propellers in oblique inflow. Their findings show that the decoupling in an axial and a transverse flow component, and the use of two decoupled loss models for inline and transverse flow, is inadequate. Especially for open propellers, there exists an effective excess thrust greater than what the decoupled model would suggest. For the research presented here, this simplification is still considered to be adequate, since oblique inflow is not of main concern. However, a further investigation of the low-level controller performance in oblique inflow is an interesting and important topic for future research.

### 2.3.2 Ventilation and propeller emergence

A propeller on a vessel subject to high waves may experience large vertical motions relative to the free surface because of wave elevation and vessel wave-frequency motion. This can result in large and abrupt thrust losses. The losses may be contributed to three effects: *loss of effective propeller disc area*, *ventilation*, and a *lift hysteresis effect*. In this work, *ventilation* will be used as a common term for all these losses. In the literature, sometimes the term *aeration* is also used.

### Loss of effective disc area

If the propeller emerges from the water, a thrust loss due to loss of effective propeller disc area is experienced (Gutsche, 1967; Fleischer, 1973). The corresponding thrust loss factor  $\beta_{TA}$  can be found from a simple geometrical consideration, by assuming that the resulting thrust is proportional to the submerged propeller disc area:

$$\beta_{TA} = \text{real} \left( 1 - \frac{\arccos(h/R)}{\pi} + \frac{h/R}{\pi} \sqrt{1 - (h/R)^2} \right). \quad (2.73)$$

Here,  $h/R$  is the relative submergence, with  $h$  the propeller shaft submergence and  $R$  the propeller radius. An alternative representation, where also the propeller hub diameter is accounted for, is given in Koushan (2004). This loss model is assumed to be valid for any propeller loading. A simplified, piecewise linear representation is given by:

$$\beta_{TA} \approx 0.5 + 0.5(\min(\max(h/R, -1), 1)). \quad (2.74)$$

An alternative representation is given in Minsaas *et al.* (1983) based on the results from Faltinsen *et al.* (1980):

$$\beta_{TA} = \begin{cases} 0, & h/R < -0.48, \\ 1 - 0.675(1 - 0.769h/R)^{1.258}, & -0.48 \leq h/R \leq 1.3, \\ 1, & h > 1.3. \end{cases} \quad (2.75)$$

(2.75) includes contributions from the so-called Wagner effect. This is convenient if the dynamic effects of ventilation can be neglected, and only the average thrust values are needed. In the following, the alternative representation (2.75) will not be used, since the Wagner effect is included as a part of the lift hysteresis effect. The three representations are compared in Figure 2.10.

### Ventilation

Ventilation may occur when a propeller is operating in the proximity of the free surface. If the propeller loading is sufficiently high, the low pressure on the propeller blades may create a funnel through which air is drawn from the free surface. This phenomenon is connected with co-orientation of the energy in the surrounding water. The propeller sets up a rotating flow which causes the free surface to deform, and a vortex starts to develop. Unless the rotating flow is disturbed, this is a self-amplifying process, and the vortex develops into a funnel. Air cavities then spread on the propeller blades, reducing their lift and drag. A fully ventilated propeller may lose as much as 70-80% of its thrust and torque. Several thorough studies of ventilated and partially submerged propellers have been performed, see e.g. Shiba (1953), Gutsche (1967), Kruppa (1972), Brandt (1973), Fleischer (1973), Scherer (1977), Hashimoto *et al.* (1984), Guoqiang *et al.* (1989), and Olofsson (1996). Additional results and further

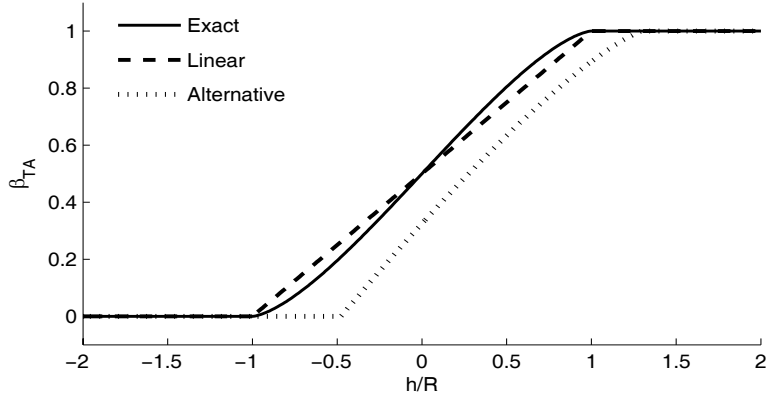


Figure 2.10: Comparison of three different representations for the thrust loss due to loss of effective disc area: exact (2.73), linear (2.74), and alternative (2.75).

studies with respect to vessel operational performance can be found in Faltinsen *et al.* (1980), Minsaas *et al.* (1983, 1986, 1987), Karlsen *et al.* (1986), and Lehn (1992). Ventilation is in the above references typically divided in three regimes: non-ventilated, partially ventilated, and fully ventilated.

*Non-ventilated regime:* The propeller is deeply submerged, or fully submerged and with low propeller loading. No ventilation occurs.

*Partially ventilated regime:* The propeller is partly, but not stationary ventilated. That is, the level of ventilation and the location of the air cavities on the propeller are time-varying. For high  $J_a$ , this regime is persistent. For low  $J_a$ , it is an unstable regime that mainly exists as a transition between the two other regimes.

*Fully ventilated regime:* A single ventilated cavity covers each of the propeller blades, meaning that the pressure on the suction side of the propeller blades is almost atmospheric. This is a relatively stable condition.

The three regimes are sketched as a function of  $J_a$  and  $h/R$  in Figure 2.11, based on a similar figure in Olofsson (1996). The partially ventilated, unstable regime for low  $J_a$  is marked as unstable. The regimes that are relevant for DP are indicated on the  $J_a$ -axis.

The thrust loss factor due to ventilation is termed  $\beta_{TV0}$ , and is in general expected to be a function of shaft speed, advance velocity, and submergence.

### Lift hysteresis

For ventilation to terminate, the supply of air to the cavities on the propeller blades must be stopped. The three most apparent causes for the funnel from

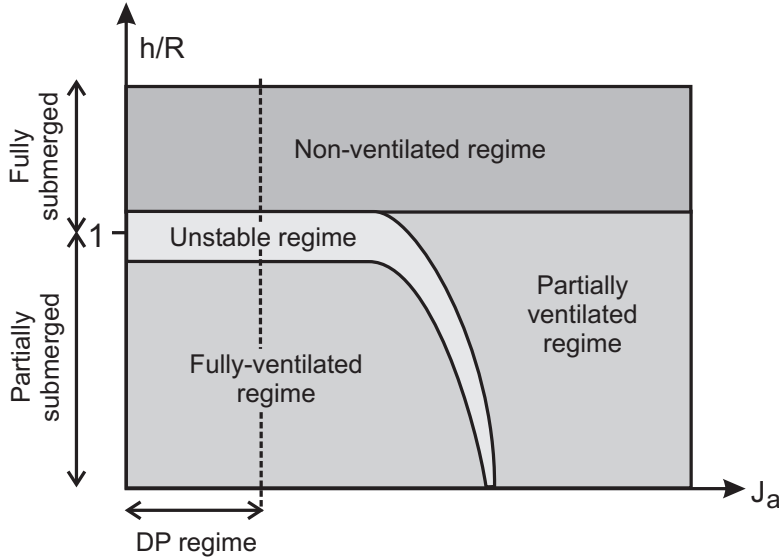


Figure 2.11: Ventilation flow regimes, with the regimes relevant for DP indicated on the  $J_a$  axis. Adopted from Olofsson (1996).

the surface to collapse are increased submergence of the propeller, disturbances in the water, and decreased loading of the propeller. For a propeller in dynamic operating conditions, a combination of the two first causes will lead to termination of the ventilation incident relatively soon after the propeller is fully submerged. When the air supply to the cavities is stopped, two events must take place before the full thrust is restored:

1. The cavities on the propeller blades must vanish in order to restore the suction-side pressure.
2. The produced lift of the propeller blades must build up.

It appears that the first of these two effects has not been explicitly discussed in the literature. However, a lot can be learned by studying the behavior of the air cavities on the propeller blades, as done in Koushan (2006). It seems apparent that the result is a time delay before the lift starts building up.

When the ventilated cavities disappear, there will be a sudden increase in lift on the propeller blades. Wagner (1925) studied a similar problem for a two-dimensional foil, and found that the sudden increase was 50% of the steady-state lift, see also Newman (1977) or Durand (1963). The *Wagner function* gives the ratio between the instantaneous lift and the steady-state lift, and shows that the foil must travel about 20 chord lengths to recover its full lift. A similar behavior is seen for a propeller that is moving in and out of ventilated condition, as first

suggested by Faltinsen *et al.* (1980). According to Koushan (2004), a typical propeller with pitch ratio  $P/D = 1$  must travel about 4 revolutions at full submergence to regain its full thrust.

For a propeller moving in and out of ventilated condition due to e.g. vessel motion and waves, the combination of these two effects means that the thrust build-up when the propeller stops ventilating is slower than the thrust loss when the propeller starts ventilating. This gives a hysteresis in the thrust production, with a corresponding thrust loss factor termed  $\beta_{TH}$ .

### Total thrust and torque loss

With  $\beta_{TA}$  due to loss of disc area from (2.73),  $\beta_{TV0}$  due to ventilation, and  $\beta_{TH}$  due to the lift hysteresis effect, the total thrust loss factor  $\beta_{TV}$  is calculated from:

$$\beta_{TV} = \beta_{TA}\beta_{TV0}\beta_{TH}. \quad (2.76)$$

The corresponding torque loss factor  $\beta_{QV}$  should always be larger than  $\beta_{TV}$ , since otherwise increasing loss would give increasing propeller efficiency. Based on previous results, Faltinsen *et al.* (1980) and Minsaas *et al.* (1983) suggested using the relationship:

$$\beta_{QV} = (\beta_{TV})^m, \quad 0 < m < 1. \quad (2.77)$$

Typical values for  $m$  are 0.8 – 0.85 for an open propeller (Gutsche, 1967), 0.65 for a ducted propeller, and 0.575 for a tunnel thruster (Karlsen *et al.*, 1986). In the following, the lumped parameters  $\beta_{TV}$  and  $\beta_{QV}$  will for simplicity be called *ventilation loss factors*.

The nature of the ventilation loss effects for low-speed applications will be investigated further in the next section, where experimental results with a ventilated propeller are presented, and an associated ventilation simulation model developed.

## 2.4 Ventilation experiments and simulation model

In this work, the main focus is on DP operations, where  $J_a$  is small. Hence, only the left-hand side of Figure 2.11 is relevant. It turns out that little information on ventilation at low  $J_a$  is available in the literature. More specifically, the dependence of the losses on the propeller shaft speed at low advance velocities, i.e.  $V_a \approx 0$ , has not been investigated. This corresponds to  $J_a \approx 0$  in Figure 2.11, which gives only one degree of freedom in the model. Clearly, there must be a dependence on the shaft speed also at  $V_a \approx 0$ . In order to improve the understanding of these loss effects and develop a simulation model for a ventilated propeller at low  $V_a$ , systematic experiments in the cavitation tunnel at NTNU have been performed (Aarseth, 2003; Overå, 2003; Ruth, 2005; Ruth and Smogeli, 2006), as well as open-water experiments in a towing tank.

### 2.4.1 Cavitation tunnel test results

A description of the experimental setup is given in Appendix D. In order to test the propeller performance for normal free surface conditions, the pressure in the cavitation tunnel was kept at atmospheric level. The advance velocity was kept low, and the shaft speed and submergence were systematically varied. Time series of the propeller thrust and torque were recorded, and the mean values for each test run were calculated. Most of the experiments were conducted with a ducted propeller with diameter  $D = 0.25\text{m}$  and pitch ratio  $P/D = 1$ . Some results with an open propeller have also been obtained. Technical specifications of the propeller are given in Section 7.1.

As an example of the obtained results, Figure 2.12 shows the ventilation thrust loss factor  $\beta_{TV}$  as a function of the relative submergence  $h/R$  and propeller shaft speed  $n$  for a ducted propeller at advance ratio  $J_a \approx 0.2$ . Figure 2.13 shows the corresponding relative thrust  $T_a/T_{\max}$ , where  $T_{\max}$  is the maximum thrust obtained in the experiments. The torque loss factor and propeller torque are presented in Appendix D. The results obtained here agree well with previous research, see, e.g. Shiba (1953) or Fleischer (1973), but contain additional information for the case of low  $V_a$ . When deeply submerged, the thruster performs as expected, with thrust proportional to  $n^2$ . For low shaft speeds, and hence low propeller loading, the thrust is constant for  $h/R = 1.5$  to  $h/R = 1$ , and then decreases almost linearly from  $h/R = 1$  to  $h/R = 0$ . This is due to loss of effective propeller disc area. For higher propeller loads, the thrust and torque drop rapidly with decreasing submergence, indicating onset of ventilation. It is evident that for a heavily loaded propeller, proximity to the surface may lead to an abrupt loss of thrust and torque. The results indicate that a reduction of the shaft speed in such a case may increase the thrust, since there is a “ridge” if higher thrust for  $n \approx 9\text{rps}$ . However, further experience with open-water tests in a towing tank shows that once the propeller is ventilated, such an increase in thrust is difficult to obtain. This will be further discussed below. The figure also indicates that it is not possible to increase the thrust significantly by increasing the shaft speed.

For an open propeller, the “ridge” of higher thrust seems to be less apparent, and the thrust during ventilation is slightly increasing for increasing shaft speed. This seems to be the major difference between the two propeller types when considering ventilation; the structure of the losses is otherwise similar. This is further explained in Appendix D, where additional experimental results for an open propeller are presented. More experimental results, where also the propeller pitch ratio is varied, can be found in Ruth and Smogeli (2006).

**Remark 2.8** *It has been assumed that the results obtained at  $J_a \approx 0.2$  are representative for low  $V_a$  in general, and hence also for  $J_a \approx 0$ . From the characteristics of the flow regimes sketched in Figure 2.11, this appears to be a valid assumption.*

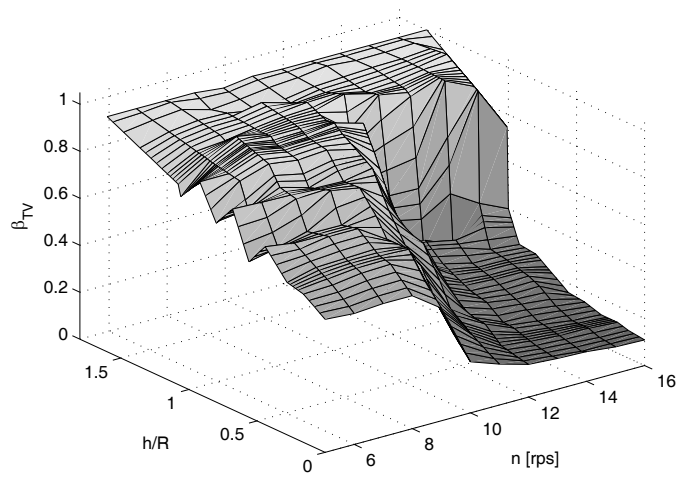


Figure 2.12: Ventilation thrust loss factor  $\beta_{TV}$  vs. relative submergence  $h/R$  and propeller shaft speed  $n$  at  $J_a \approx 0.2$  for a ducted propeller. From experiments.

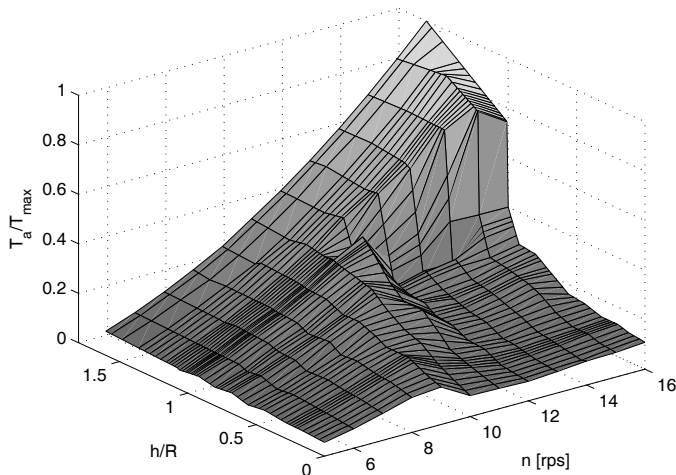


Figure 2.13: Relative thrust  $T_a/T_{\max}$  vs. relative submergence  $h/R$  and propeller shaft speed  $n$  at  $J_a \approx 0.2$  for a ducted propeller. From experiments.

### 2.4.2 Open-water test results

The experimental results from the cavitation tunnel are quasi-static. An actual thruster on a vessel will be operating in more dynamic conditions, where transient effects are important. To investigate this, open water tests in the Marine Cybernetics Laboratory (MCLab) at NTNU were carried out with the same propeller. The experimental setup is described in Section 7.1.

Figure 2.14 shows  $T_a$  for increasing thrust reference  $T_r$  with a ducted propeller in irregular waves. The shaft speed was as given by the shaft speed mapping defined in (3.1), and the waves generated with a wave-maker using the ITTC modified PM wave spectrum in (C.19) with  $H_s = 8\text{cm}$  and  $T_p = 1.2\text{s}$ . The submergence with respect to the calm free surface was  $h_0/R = 1.2$ . The time series show that the thrust corresponds well with its reference for low  $T_r$ , but as  $T_r$  is increased beyond 140N, the thrust drops and becomes highly transient. The propeller here enters a ventilated state, from which it is difficult to exit, even if the shaft speed is reduced significantly: the ventilation persists also for  $t > 270\text{s}$ , even though  $T_r$  is reduced to 100N. Hence, a hysteresis effect appears to be present. This is sketched in Figure 2.15, based on a similar figure in Koushan (2004).

**Remark 2.9** *The hysteresis seen here is different from the hysteresis effect discussed in Section 2.3.2. The latter applies to the time-varying thrust of a propeller moving in and out of ventilated condition, e.g. due to time-varying submergence. The effect sketched in Figure 2.15 applies to the mean ventilation loss as a function of propeller shaft speed for a fixed mean submergence.*

The hysteresis effect discussed in Section 2.3.2 is demonstrated in Figure 2.16, which shows time series of  $T_a$  and  $Q_a$  as functions of  $h/R$  during three ventilation incidents with the open propeller. The ventilation incidents were generated by moving the propeller in a sinusoidal vertical motion with amplitude 20cm and period 20s. The mean submergence was about 22cm, and the thrust reference 240N. For  $h/R > 1.4$ , the propeller is deeply submerged, and  $T_a \approx 240\text{N}$ . As the submergence is reduced, full thrust is maintained until  $h/R \approx 1.2$ , where ventilation starts, and then drops quickly to  $T_a \approx 60\text{N}$  at  $h/R \approx 1.0$  (a loss of about 75% of the thrust). The thrust is then gradually decreased to  $T_a \approx 40\text{N}$  at  $h/R \approx 0.75$ . For  $h/R < 1.0$ , the increasing thrust loss is considered to be mostly due to loss of effective disc area, and there is no significant hysteresis. As the submergence is increased, the thrust builds up slowly until  $h/R \approx 1.2$ , and then starts building significantly up until it reaches the nominal value of  $T_a \approx 240\text{N}$  at  $h/R \approx 1.4$ .

Figure 2.17 shows time series of the propeller thrust for three different thrust references during a ventilation incident for the ducted propeller. The ventilation incidents were generated by moving the propeller in a sinusoidal vertical motion with amplitude 15cm and period 5s. The mean submergence was about 15cm. The ventilation incident starts at time  $t \approx 5.8\text{s}$  and stops at  $t \approx 9\text{s}$ . The resulting thrust during ventilation is practically the same for all the three thrust

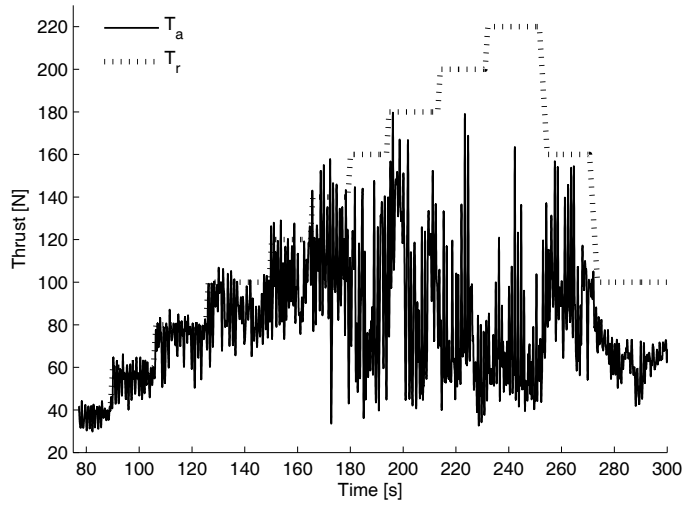


Figure 2.14: Measured thrust  $T_a$  of a ducted propeller for increasing thrust reference  $T_r$  in irregular waves. From experiments.

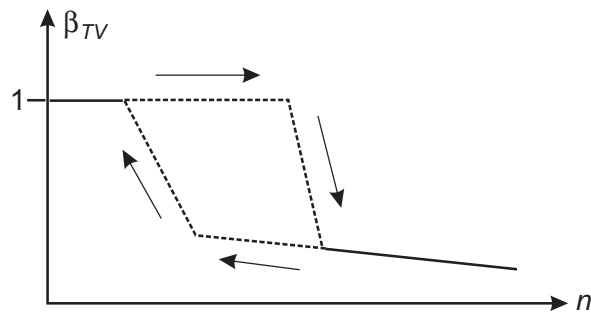


Figure 2.15: Sketch of the hysteresis in the ventilation loss factor  $\beta_{TV}$  as a function of the shaft speed for a fixed propeller submergence.

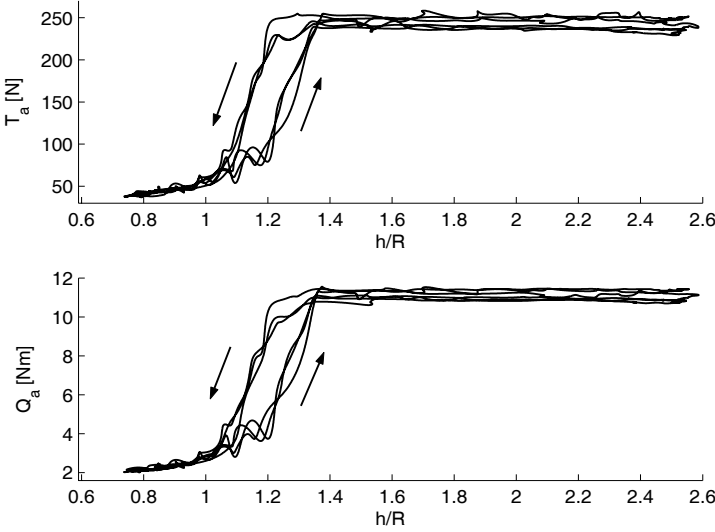


Figure 2.16: Measured thrust  $T_a$  and torque  $Q_a$  vs. relative submergence  $h/R$  during three ventilation incidents with a ducted propeller, illustrating the thrust and torque hysteresis effect. From experiments.

references. For  $T_r = 300\text{N}$ , the loss of thrust is approximately 85%. The deviation of the measured submergence from the imposed motion may be explained by local surface elevation due to disturbances in the water, and possibly also by deviation in the actual from the commanded vertical motion.

#### 2.4.3 Scaling of test results

Care must be taken in order to scale the model tests results to be valid for a large propeller. However, the general behavior of a full-scale propeller subject to ventilation and in-and-out-of water effects is expected to be similar to the results from model scale. A discussion on the scaling laws that must be satisfied in order to transfer the results to full scale is undertaken in Appendix D.

In Section 7, experimental results for a model scale propeller subject to ventilation with various thruster controllers will be presented. These time series cannot easily be transformed to full scale, and must be interpreted as they are – in model scale. Investigation of the performance of various controllers in full scale will instead be done by simulations, where realistic full-scale propeller data can be used. This is believed to be a more appropriate approach, since there are several important structural differences between model scale and full scale: in addition to the problems with scaling of the propeller load, the friction and inertia properties of the propeller and drive system may change significantly.

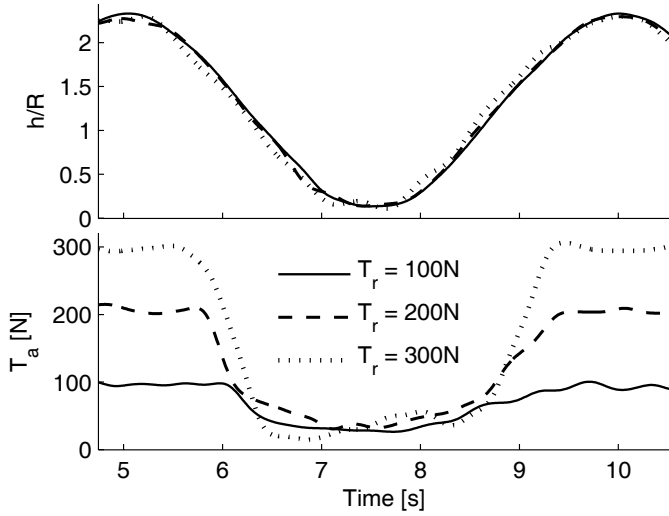


Figure 2.17: Time series of measured thrust during ventilation at three different thrust references for a ducted propeller. From experiments.

#### 2.4.4 Ventilation simulation model

Based on the experimental results presented in the previous sections, simplified ventilation models suitable for time-domain simulation may be developed. The ventilation thrust loss factor  $\beta_{TV}$  can be expressed as a function of the relative immersion  $h/R$  and the relative shaft speed  $n/n_{bp}$ , where  $n_{bp}$  is the bollard pull shaft speed of the propeller, see (2.62). Because of the different characteristics of the thrust during ventilation for open and ducted propellers, two simulation models are proposed.

##### Open propeller

For an open propeller, there is no pronounced “ridge” of higher thrust, and the thrust is slightly increasing for increasing shaft speed during ventilation. The proposed ventilation loss model is shown in Figure 2.18. The loss model is parameterized by two relative shaft speeds, two submergence ratios, and two loss factors, marked as  $n_1$ ,  $n_2$ ,  $h_1$ ,  $h_2$ ,  $b_1$ , and  $b_2$  in the figure. Additionally, the main coordinates defining the loss surface are drawn as circles – the loss factor surface is found by linear interpolation between these points. In the regime with  $h/R > h_2$ , the propeller is deeply submerged, and no losses are experienced ( $\beta_{TV} = 1$ ). For  $h/R < -1$  the propeller exits the water completely, and no thrust is produced ( $\beta_{TV} = 0$ ). The remaining regime is  $-1 < h/R < h_2$ . For  $n/n_{bp} < n_1$  the propeller is lightly loaded, and only losses due to loss of

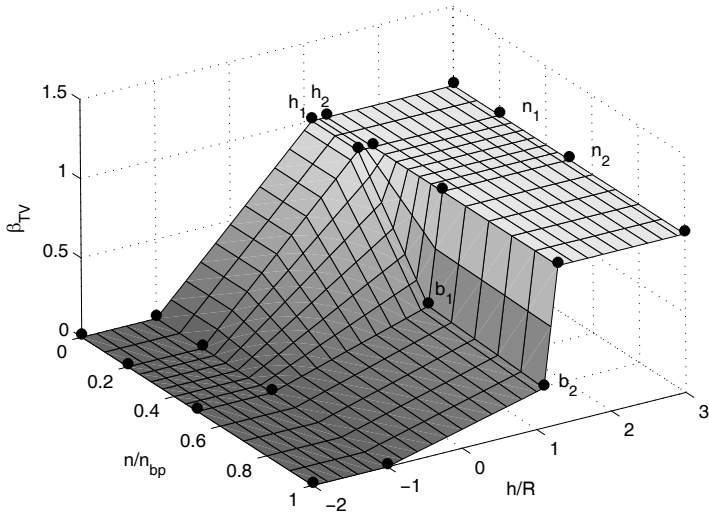


Figure 2.18: Ventilation thrust loss model for an open propeller, as function of relative shaft speed  $n/n_{bp}$  and relative submergence  $h/R$ , with  $n_1 = 0.2$ ,  $n_2 = 0.5$ ,  $h_1 = 1.1$ ,  $h_2 = 1.3$ ,  $b_1 = 0.3$ , and  $b_2 = 0.25$ .

effective disc area are experienced. This is seen as the gradually decreasing  $\beta_{TV}$  for  $-1 < h/R < h_1$ , modelled as in (2.74). For  $n/n_{bp} > n_2$ , the propeller is heavily loaded, and decreasing submergence will lead to an abrupt loss of thrust due to ventilation. The transition to-and-from the ventilated regime happens for  $n_1 < n/n_{bp} < n_2$  and  $h_1 < h/R < h_2$ . For  $h/R < h_1$ , additional thrust losses are experienced due to loss of effective disc area (meaning that  $h_1$  should be close to 1). The thrust loss for a fully submerged and fully ventilated propeller is defined by the two loss factors  $b_1$  and  $b_2$ .  $b_1$  is the loss factor where full ventilation starts ( $h/R = h_1$  and  $n/n_{bp} = n_2$ ), and  $b_2$  is the loss factor at maximum shaft speed ( $h/R = h_1$  and  $n/n_{bp} = 1$ ), with  $b_2$  equal to or slightly lower than  $b_1$ . For  $n > n_{bp}$ , the loss function should be extrapolated. The parameters in Figure 2.18 are chosen as  $n_1 = 0.2$ ,  $n_2 = 0.5$ ,  $h_1 = 1.1$ ,  $h_2 = 1.3$ ,  $b_1 = 0.3$ , and  $b_2 = 0.25$ .

### Ducted propeller

For a ducted propeller, there is a “ridge” of higher thrust, and the thrust is nearly constant for increasing shaft speed during ventilation. The ventilation loss model therefore becomes slightly more complicated, but is still simple to parameterize. The difference from the simulation model for the open propeller is that the loss factor during ventilation, i.e. for  $n/n_{bp} > n_2$  and  $-1 < h/R < h_2$ , is modified to give constant thrust independently of  $n$ . This is done by the

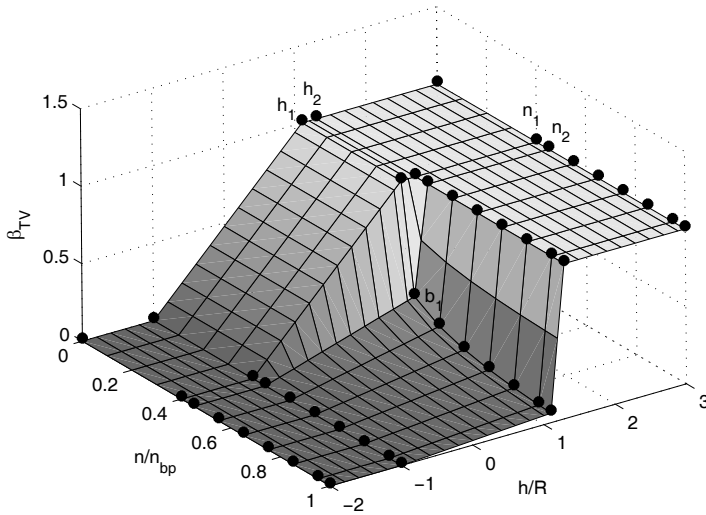


Figure 2.19: Ventilation thrust loss model for a ducted propeller, as function of relative shaft speed  $n/n_{bp}$  and relative submergence  $h/R$ , with  $n_1 = 0.4$ ,  $n_2 = 0.45$ ,  $h_1 = 1.1$ ,  $h_2 = 1.3$ , and  $b_1 = 0.3$ .

following curve for  $h/R = h_1$ :

$$\beta_{TV}|_{h/R=h_1} = b_1 \left( \frac{n_2}{n/n_{bp}} \right)^2, \quad (2.78)$$

and with a linear decrease of  $\beta_{TV}$  as function of  $h/R$ , with  $\beta_{TV} = 0$  for  $h/R = -1$ . Hence, the parameter  $b_2$  is not needed for this model, since the loss factor for high  $n/n_{bp}$  is implicitly given by  $b_1$ . In addition, the change from non-ventilated to ventilated condition is more rapid, which is implemented by a smaller interval between  $n_1$  and  $n_2$ . Figure 2.19 shows an example of the loss model for ducted propellers, with  $n_1 = 0.4$ ,  $n_2 = 0.45$ ,  $h_1 = 1.1$ ,  $h_2 = 1.3$ , and  $b_1 = 0.3$ . The two loss models are further compared with the experimental results in Appendix D.

### Hysteresis effect

The hysteresis in the propeller loading may be modelled by introducing a positive rate limit  $\dot{\beta}_{VH}$  on  $\beta_{TV}$ , such that the load is allowed to drop more quickly than it is allowed to build up, i.e.  $-\infty < \dot{\beta}_{TV} \leq \dot{\beta}_{VH}$ . This approach gives reasonable correspondence with experimental time series. It is of course possible to develop more sophisticated models of the hysteresis effect, but this has not been considered necessary for the present applications. Using as a rule-of-thumb that 4 complete revolutions of the propeller is needed to develop full lift (Koushan,

2004), and choosing the magnitude of the change to be 0.7,  $\dot{\beta}_{VH}$  may be found from:

$$\dot{\beta}_{VH} = \frac{0.7}{4/n} \approx 0.18n. \quad (2.79)$$

A further simplification is to choose the rate limit independent of  $n$ , with e.g. the fixed value  $\dot{\beta}_{VH} \approx 0.18n_{bp}$ .

### Torque loss factor

The torque loss factor  $\beta_{QV}$  is calculated from  $\beta_{TV}$  using (2.77), with  $m = 0.85$  for open propellers, and  $m = 0.65$  for ducted propellers. In terms of simulation variables, the thrust and torque ventilation loss factors for low advance velocities are given as:

$$\beta_{TV} = \beta_{TV}(h, n), \quad (2.80)$$

$$\beta_{QV} = \beta_{QV}(h, n). \quad (2.81)$$

### Tunnel thrusters

No results for a tunnel thruster have been obtained in this work. From the results in Karlsen *et al.* (1986) and Minsaas *et al.* (1986), the behavior of a tunnel thruster is expected to be similar to that of a ducted propeller. A ventilation loss model similar to Figure 2.19 is therefore assumed to be applicable, with  $m = 0.575$  for calculation of  $\beta_{QV}$ . However, further research is needed in order to confirm this.

#### 2.4.5 Ventilation simulation model verification

Figure 2.20 shows  $\beta_{TV}$  from the simulation model as a function of  $h/R$ . The model parameters are the same as in Figure 2.19, the hysteresis rate limit is set to  $\dot{\beta}_{VH} = 0.7\text{s}^{-1}$ , and the shaft speed is set to  $n/n_{bp} = 0.7$ . The submergence is varied as a sinusoidal with mean value  $h/R = 1.6$  and amplitude 0.9. When comparing with Figure 2.16, the simulation model is found to capture the main behavior of the ventilation incident.

Figure 2.21 shows time series from a simulation where it has been attempted to reproduce the experiment shown in Figure 2.14. The ventilation model is used with the parameters for the ducted propeller as in Figure 2.19, and  $n_{bp} = 20\text{rps}$ . The propeller characteristics is simulated with a linear 1-quadrant model (2.25, 2.26), with parameters  $K_{T0} = 0.513$ ,  $\alpha_{T1} = -0.499$ ,  $K_{Q0} = 0.0444$ , and  $\alpha_{Q1} = -0.0696$ . The propeller diameter is  $D = 0.25\text{m}$ , and the mean submergence is  $h_0 = 0.3\text{m}$  ( $h_0/R = 1.2$ ). The waves are generated from 30 harmonic components extracted from the ITTC modified PM wave spectrum (C.19), with  $H_s = 8\text{cm}$  and  $T_p = 1.2\text{s}$ . The wave-induced  $V_a$  is calculated according to (C.33), and the propeller submergence is found from (C.35). The shaft speed is calculated from the thrust reference  $T_r$  according to (3.1). The

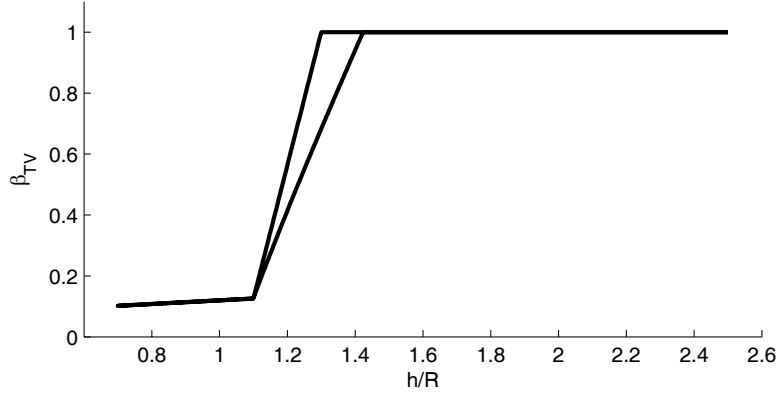


Figure 2.20: Ventilation thrust loss factor  $\beta_{TV}$  from the simulation model in Figure 2.19 as function of  $h/R$  for  $n/n_{bp} = 0.7$ , including the hysteresis effect.

simulation is found to reproduce the experiment with satisfactory accuracy, with the thrust mainly affected by wave-induced velocities for low  $T_r$ , and the effect of ventilation dominating the thrust production for  $T_r > 140\text{N}$ . It is important to note that the simulation model cannot capture the true chaotic behavior of ventilation. For example, the hysteresis effect shown in Figure 2.15 is difficult to model. When the propeller is in the ventilated regime as shown at the end of the time series in Figure 2.14, it is in reality hard to get rid of the ventilation by reducing the shaft speed. This is not reproduced by the ventilation model in Figure 2.21, which removes the ventilation as soon as  $T_r$  is reduced below 140N.

Figure 2.22 shows time series from three simulations attempting to reproduce the experiments shown in Figure 2.17. The ventilation model for the ducted propeller was used as shown in Figure 2.19, and the submergence varied sinusoidally with mean value 15cm, amplitude 15cm, and period 5s. When compared to Figure 2.17, the simulation model gives too little thrust loss for  $T_r = 100\text{N}$  when compared to  $T_r = 200\text{N}$  and  $T_r = 300\text{N}$ . It may also seem that the hysteresis rate limit is chosen slightly too small when comparing with the experimental time series. However, the inception and duration of the loss incident, and the general shape of the time series, are reasonably good. The discrepancies again show that the random nature of these loss effects is difficult to capture in a simulation model at the current complexity level.

In conclusion, the proposed loss models are coarse approximations of the real world, but captures the main characteristics of the phenomenon. They are also easy to implement, and are considered adequate for control system design and testing. Note that the loss models will be propeller specific, and that the parameters defining the loss models will vary.

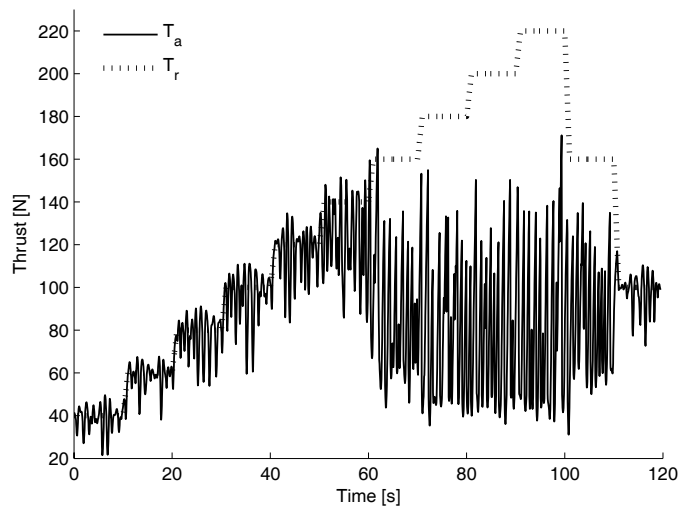


Figure 2.21: Simulated time series of thrust  $T_a$  for increasing thrust reference  $T_r$  in irregular waves.

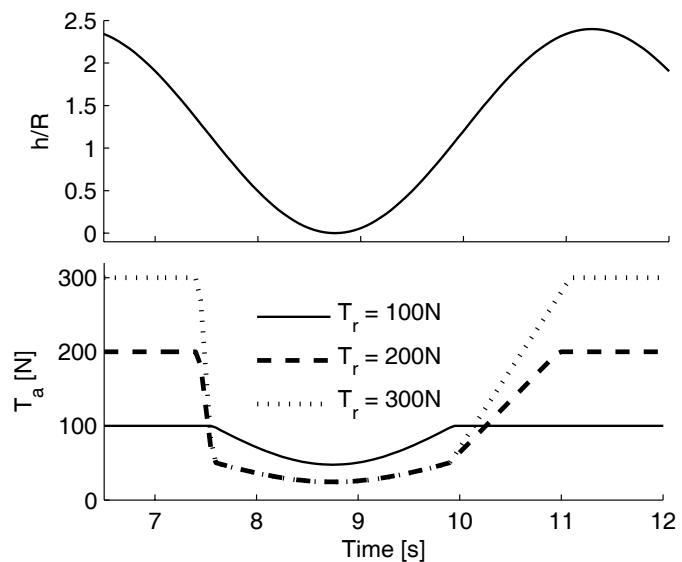


Figure 2.22: Simulated time series of thrust during ventilation at three different thrust references for a ducted propeller.

**Remark 2.10** Although the proposed ventilation simulation models show reasonably good performance when compared to the experiments, it is difficult to generalize the model, e.g. to other propeller types or to full scale propellers. This is due to the many scaling laws that must be satisfied in order to make such a generalization. However, the general structure of the ventilation loss functions, as shown in Figures 2.18 and 2.19, are expected to be applicable also to other propellers and in full scale. The models are therefore used for full-scale simulations in Chapter 6. Scaling is further discussed in Appendix D. A more sophisticated ventilation loss model, which is valid also for varying pitch ratios, is presented in Ruth and Smogeli (2006).

#### 2.4.6 Blade-frequency loading

The cavitation tunnel results and the ventilation simulation model only consider the mean load of the propeller during ventilation. The dynamic loading of the propeller at higher frequencies during ventilation is also an important topic, especially when considering mechanical wear and tear. There are few available references considering such high-frequency dynamic loads, but a summary of previous findings and a thorough investigation can be found in Olofsson (1996). The following summarizes the facts that are most relevant for this work:

- During ventilation, the loads on each propeller blade fluctuate in time as the blade goes through four phases: in-air, blade-entry, in-water, and blade-exit. These fluctuating forces introduce structural loads on the propeller blades.
- The sum of the blade loads for the whole propeller gives an oscillating propeller thrust and torque, as well as oscillating vertical and transverse forces. The main loads are found at the blade frequency, i.e. the shaft speed in rps times the number of propeller blades. The loads are highly dependent on the operating condition.
- It is especially in the transition to-and-from ventilation, i.e. the unstable, partially ventilated regime, that large high-frequency dynamic loads occur.
- In addition to the above mentioned loads, resonant blade vibration may cause large transient loads. This is especially evident at low advance velocities, since there is little hydrodynamic damping when the propeller is fully ventilated. This problem increases with increasing propeller speed, when the magnitude and frequency content of the encountered load increases danger of resonance. During resonance, the vibrations are amplified, and the resulting dynamic load is a combination of hydrodynamic and inertial loads due to fluid-structure interaction. Resonance typically occurs close to the blade's natural frequency in air and water. These loads can cause serious problems, since large stress transients may develop, resulting in peak stresses exceeding the yield strength of the blade material and hence causing structural fatigue.

In Hashimoto *et al.* (1984), it was also found that significant transverse and vertical force oscillations at the propeller frequency and twice the propeller frequency could be observed during ventilation. It should be noted that Olofsson (1996) and Hashimoto *et al.* (1984) mainly considered propellers at higher advance velocities. However, the effect of dynamic loading on the propeller should from a mechanical point of view be independent of the advance velocity. The results in Olofsson (1996) actually indicated that the loads on the propeller increased for decreasing  $V_a$ , due to decreased damping and resonance problems.

Recent results for the blade loading of a ventilated thruster at low advance velocity can be found in Koushan (2004, 2006). These results confirm that the high-frequency dynamic loading can be significant. The standard deviation of the shaft frequency propeller blade force fluctuations was found to be almost 100% of the average force when the propeller was partially submerged. Large fluctuations were found also for the fully submerged, ventilated condition. The dynamic loads on a propeller in high sea states can hence be divided in two:

- Wave frequency (or encounter frequency) fluctuations due to the mean propeller load during ventilation, caused by relative motion of the thruster with respect to the free surface. This corresponds to the loss of thrust e.g. shown in Figure 2.17.
- High frequency fluctuations due to individual propeller blade loads during ventilation.

In the experimental setup used in this work, the measurements of propeller thrust and torque were not of sufficient quality for studying the blade-frequency loading. For such a detailed analysis, more sophisticated equipment like the experimental setup used in Olofsson (1996) or Koushan (2004, 2006) must be used. Hence, no specific results on the high-frequency loading are presented in this thesis.

## 2.5 Propeller simulation model

From (2.50), (2.52), (2.13, 2.14), (2.71, 2.72), and (2.80, 2.81), the resulting simulation model of a propeller subject to time-varying inflow and submergence, including shaft and motor dynamics, becomes:

$$I_s \dot{\omega} = k_g Q_m - Q_a - Q_f(\omega), \quad (2.82)$$

$$\dot{Q}_m = \frac{1}{T_m}(Q_c - Q_m), \quad (2.83)$$

$$\begin{aligned} T_a &= f_T(\cdot) = T_n \beta_{TJ}(V_a, n) \beta_{TV}(h, n) \\ &= \rho D^4 n^2 K_{TJ}(V_a, n) \beta_{TV}(h, n), \end{aligned} \quad (2.84)$$

$$\begin{aligned} Q_a &= f_Q(\cdot) = Q_n \beta_{QJ}(V_a, n) \beta_{QV}(h, n) \\ &= \rho D^5 n^2 K_{QJ}(V_a, n) \beta_{QV}(h, n). \end{aligned} \quad (2.85)$$

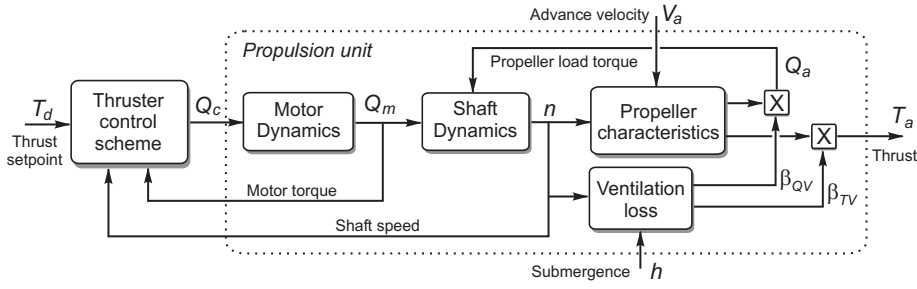


Figure 2.23: Block diagram of the propeller simulation model.

It has here been assumed that the loss effects due to ventilation and axial flow may be superposed. When present, however, the ventilation losses will dominate the axial flow losses. Models for transverse losses, thruster-thruster interaction and the Coanda effect could be included as modifications of the resulting thrust and torque.

The combination of the shaft and motor dynamics with the quasi-static propeller characteristics and loss models may seem inconsistent, but has been found to give good agreement with experimental results. For full-scale propellers on surface vessels, it can also be argued that the dynamics involved in the propeller loading is so fast that it will be dominated by the shaft dynamics. For small thrusters on underwater vehicles, the dynamics in the thrust production may have larger importance, as discussed in Section 2.2.5. A block diagram of the simulation model – including a thruster control scheme with desired thrust  $T_d$  as input and commanded torque  $Q_c$  as output – is shown in Figure 2.23.

A 4MW propulsion unit with a Wageningen B4-70 propeller will be used for the simulations presented throughout this thesis. The main characteristics of the B4-70 propeller are given in Table 2.2, and the remaining simulation data is presented in Appendix A.

## Chapter 3

# Propulsion control in normal conditions

The purpose of the low-level thruster controller is to relate the desired thrust  $T_d$  to the commanded torque  $Q_c$ . As discussed in Section 1.1,  $T_d$  may be given by the thrust allocation in DP or joystick mode, or manually in MTC mode. The thruster controllers may be divided in two control regimes, depending on the operating conditions:

- a) Thruster control in normal conditions, when experiencing low to moderate thrust losses.
- b) Thruster control in extreme conditions, when experiencing large and abrupt thrust losses due to ventilation and in-and-out-of-water effects.

This chapter first considers control aspects common to both control regimes, and then focuses on control regime a). Control regime b) is treated in Chapter 6.

### 3.1 Constraints

In most of this work, it is assumed that only the shaft speed  $n$  and the motor torque  $Q_m$  are available as measurements. Additional instrumentation on the propulsion unit is not common in industrial installations. For electric motors,  $Q_m$  is easily inferred from the motor current, and for diesel engines it is related to the fuel index. Some of the control options that become available with additional instrumentation are discussed in Appendix E.2. The presented controllers are mainly aimed at low-speed applications with FPP driven by electric motors, but may also be applicable to mechanical direct-drive FPP. The current concepts are also extendable to CPP with consolidated control (i.e. control of both pitch and speed) and transit operations. This will be shortly treated in Chapter 8.

The parameters needed for the various control schemes will be introduced consecutively. The basic control parameters are the propeller diameter  $D$ , the nominal thrust coefficient  $K_{T0}$  from (2.8), and the nominal torque coefficient  $K_{Q0}$  from (2.9). These three parameters are usually well known –  $K_{T0}$  and  $K_{Q0}$  can be found e.g. from the bollard pull thrust (2.63) and power (2.65), or from the open-water characteristics of the propeller. For asymmetric propellers, the reverse nominal thrust and torque coefficients  $K_{T0r}$  and  $K_{Q0r}$  are also needed for good performance.

Depending on the application and the chosen low-level thruster controller, knowledge of the friction parameters  $Q_s$  and  $K_\omega$  in (2.51), and the rotational inertia  $I_s$  in (2.50) may be desirable.  $Q_s$  and  $K_\omega$  may be found from system identification of the drive system.  $I_s$  is an important parameter for choice of electric motor, and should in most cases therefore be known. In Appendix B.3, it is discussed how estimates of these parameters can be identified during manual tuning of the controllers.

## 3.2 Control objectives

The ultimate goal of any thruster controller is to make the actual thrust  $T_a$  track the thrust reference  $T_r$ . In dynamic operating conditions, however, other goals may be as important as tracking  $T_r$ , e.g. reducing mechanical wear and tear and limiting power oscillations and peak values. This is especially true in thruster control regime *b*), where severe dynamic loads may persist over long periods of time. In this work, the following performance criteria are considered:

1. Thrust production in the presence of disturbances, i.e. ability to locally counteract thrust losses.
2. Mechanical wear and tear caused by transients and oscillations in motor and propeller torque.
3. Predictable power consumption.
4. Robust performance.

### 3.2.1 Thrust production

The structure of a DP system – including high-level controller, thrust allocation, and low-level thruster control – was introduced in Section 1.1. In order for the propulsion system to produce the desired thrust forces, the low-level thruster controllers must have reasonable accuracy with respect to thrust production. If this is not the case, the thrust allocation will have a difficult task in distributing thrust to the various propulsion units, since there is no feedback available from the actually produced thrust. An offset between the desired thrust and the actually produced thrust will eventually be captured by the integral action in the DP control system, and the setpoints to the thrusters increased or decreased

accordingly. However, this is a slow process, and inaccurate low-level thruster control will therefore lead to reduced bandwidth of the positioning system as a whole. Hence, significantly better positioning and tracking performance is expected with improved low-level thruster controllers (Sørensen *et al.*, 1997; Strand, 1999). Note that for the DP control system, it is the mean and slowly-varying values of thrust that are important: the oscillations in thrust induced by waves and wave-frequency vessel motion do not normally affect the vessel motion significantly.

### 3.2.2 Mechanical wear and tear

#### Normal conditions

There are few references discussing mechanical wear and tear of propulsion units in normal operating conditions. In older references, the torque loads on the propeller shaft from the firing of individual diesel engine cylinders have been an important topic. Apparently, the frequent failures of propeller shaft-lines were a main driving force for research on vibrations, vibration induced loads, and structural fatigue in general. This is extensively dealt with in e.g. Ker Wilson (1963). Another topic that has been researched is the dynamic shaft loading due to the non-uniform inflow to a propeller installed behind a hull, and its implications for structural fatigue, see e.g. Wereldsma (1965), Lewis (1989), and Carlton (1994).

From Section 2.3.1, it is clear that a time-varying inflow to the propeller, as induced by waves, will result in a time-varying propeller loading. Depending on the chosen low-level thruster control strategy, this will lead to oscillations in propeller torque and thrust, shaft speed, and motor torque and power. Especially in heavy seas, the time-varying loads can be significant, even if the propeller is deeply submerged. The oscillations in propeller and motor torque are transmitted through the shafts and gears, resulting in increased dynamic loads. This was investigated by Domachowski *et al.* (1997), who concluded that the dynamic loading because of waves gave rise to significant oscillations of torsional torques in shaft elements and flexible couplings, and that this over time would cause reduced fatigue strength and increased wear and tear.

To reduce mechanical wear and tear, it is assumed to be advantageous to reduce the torque oscillations to a minimum.

#### Extreme conditions

As discussed in Section 2.4.6, a propeller on a vessel in high to extreme seas may be subject to severe dynamic loading, both at the wave frequency due to the large changes in mean load during ventilation, and at the blade frequency and above due to the individual blade loads. As well as posing danger for structural damage to the propeller, dynamic loading of the propeller may lead to mechanical wear and tear of the propulsion system. In all propulsion units, the propulsive power is transmitted from the motor to the propeller through a

shaft held by bearings, and with a seal to protect against water ingress. Many thruster units in addition contain a transmission system consisting of gears, shafts, and bearings. Hence, the gears will be subject to the dynamic propeller and motor torque, the thrust gear or thrust block will be subject to the dynamic propeller thrust, and the bearings holding the propeller shaft and the shaft seal will be subject to transverse and vertical loads. The whole thruster unit will also be subject to any high-frequency vibration of the propeller. Although not well documented in the literature, mechanical wear and tear of thrusters is a well-known industrial problem that has received increased attention in recent years, especially for azimuthing thrusters and tunnel thrusters (Koushan, 2004, 2006). It is believed that the widespread mechanical failures in gears and bearings of such thrusters are mainly due to the combination of low-frequency ventilation loads and blade frequency load oscillations.

Various failure modes of propellers are extensively treated in IMCA M-129 (1995) and IMCA M-162 (2001). Although the topic of dynamic propeller loading is only briefly mentioned in these references, it seems apparent that the failures of shafts, gears, bearings, and seals may be partly contributed to dynamic loads and vibrations. This is also reflected in the recent efforts made to improve the understanding of these loads and their effects on the mechanical parts of the propulsion unit. As an example, Rolls-Royce in 2005 appointed NTNU in cooperation with MARINTEK as one of 25 world-wide University Technology Centres (UTC). The programme, which is to run for 10 years with extensive financing, is entitled “Performance in a Seaway”, and has specific focus on propulsion issues like dynamic propeller loading and improved controllers (Rolls-Royce Press Release, 2005; NTNU Press Release, 2005).

### 3.2.3 Power consumption

For DP vessels, the propulsion system is usually one of the main power consumers. It is also regarded as a critical system with respect to safety. For safe operation and minimization of fuel consumption, optimal control of the power generation and distribution system is essential. This task is usually performed by a Power Management System (PMS), or a more sophisticated Energy Management System (EMS). The PMS stops, starts, and synchronizes the main generator sets in response to the system loading, with the objective of preventing blackouts while minimizing the number of on-line generator sets. If the power load is increased too fast for the generators to respond, or the load is higher than the available power, the result is under-frequency on the power network. If the network frequency becomes too low, the generators will be disconnected, with a blackout as result. This is one of the worst scenarios onboard a DP vessel. In severe weather conditions, the dynamic loading of the thrusters may result in unpredictable power variations. In order to meet the power peaks, the operator may then be forced to have more power available than necessary. This increases fuel consumption, as well as wear, tear, and maintenance of the generator sets, since they get more running hours at lower loads. Hence, predictable power

consumption is of major concern to the power management system in order to avoid blackouts, improve the performance and stability of the power generation and distribution network, and minimize fuel consumption and wear and tear (Lauvdal and Ådnanes, 2000; May, 2003; Sørensen and Ådnanes, 2005; Radan *et al.*, 2005).

### 3.2.4 Robustness

As with all control systems, robustness is an important issue. The thruster controller should be robust with respect to modelling uncertainties, since one cannot assume perfect knowledge of the necessary parameters. In addition, some of the physical properties of the system, like the shaft friction, may change over the life-time of the propeller. The controller must also be able to handle a wide range of operating conditions, from calm seas with low thrust demands, to extreme seas with high thrust demands.

### 3.2.5 Surface vessels vs. underwater vehicles

For low-level thruster control, the main difference between surface vessels and small underwater vehicles like ROVs and AUVs is the dynamic response of the vessel. Because the time constants of the underwater vehicles are small, their closed-loop behavior may be strongly affected by the thruster dynamics (Yoerger *et al.*, 1991; Healey *et al.*, 1995). For a surface vessel, the dynamic response of the thruster will be of less importance for e.g. the station-keeping ability, since the time constant of the vessel itself is dominating. However, the thrust production is still of high importance.

There are also differences in the expected operating conditions for the propellers. The operating condition of a propeller on a surface vessel is influenced by the vessel load condition, vessel motions, waves, and current. An underwater vehicle is usually operated below the wave zone, and hence only affected by vehicle motions and current. Furthermore, the vessel motions due to the waves are much more violent for a surface vessel than for an underwater vehicle. This means that the requirements to the thruster controllers on a surface vessel may differ significantly from the corresponding requirements for an underwater vehicle. In this thesis, the main focus is on surface vessels.

## 3.3 Thruster controller structure

A block diagram of a propulsion unit with a reference generator, a thruster controller, and a torque limiting function is shown in Figure 3.1. The desired thrust  $T_d$  from the thrust allocation or manual thruster control is passed through a reference generator to avoid entering transients into the thruster controller. The output of the reference generator is the thrust reference  $T_r$ . The thruster controller calculates the commanded torque  $Q_{c0}$ , which in turn is passed through a torque limiting function in order to avoid commanding excessive torque or

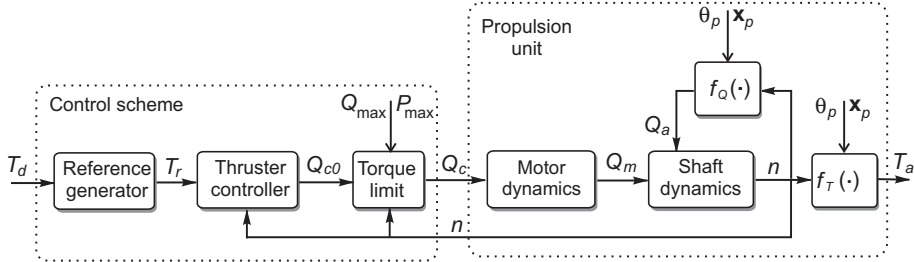


Figure 3.1: Block diagram of a propulsion unit with control scheme, including a reference generator, a thruster controller, and a torque/power limiting function.

power from the thruster motor. The torque and power limited commanded torque,  $Q_c$ , is used to control the motor. The output of the system is the thrust  $T_a$ . In the block diagram, the propeller thrust and torque are represented by the functions  $f_T(\cdot)$  and  $f_Q(\cdot)$  from (2.1) and (2.2).

**Remark 3.1** *In this work, the interface to the low-level thruster controller is chosen to be the desired thrust  $T_d$ . In industrial applications with shaft speed control, it is common that the interface is the desired shaft speed, which is calculated from  $T_d$  using the static mapping given in (3.1). This is only applicable if shaft speed control is used.*

### 3.4 State of the art

Three types of propellers are common: speed controlled FPP, pitch controlled CPP, and consolidated controlled CPP (CCP). For CCP, both the shaft speed and pitch can be controlled. Since the desired thrust can be produced by a number of combinations of shaft speed and pitch, this can be formulated as an optimal control problem. Optimal control of CCP is mainly relevant for transit operation. This is treated in e.g. Schanz (1967), Winterbone (1980), Beek and Mulder (1983), Parsons and Wu (1985), Bakountouzis (1992), Chachulski *et al.* (1995), Fukuba *et al.* (1996), Morville (1996), Young-Bok *et al.* (1998), and Whalley and Ebrahimi (2002), and an overview given in Ruth *et al.* (2006). A CCP may also be controlled by fixed mappings from desired thrust to pitch and shaft speed. This will be further discussed in Section 8.1, where the control concepts developed for FPP are extended to CCP.

For surface vessels with FPP, shaft speed control is the industry standard, both for electrically driven and mechanical direct-drive propellers (often, however, mechanical direct-drive propellers are CPP). The origin of PID type controllers for propeller shaft speed control is uncertain, but they have probably been utilized for as long as propellers have been used. The early mechanical

governors for steam turbines were of the centrifugal type, which corresponds to a pure P-controller (the Watt centrifugal governor). This was in time replaced by more sophisticated mechanical, hydraulic, pneumatic, and analog electronic governors used on e.g. diesel engines. Since the 1970's, digital electronic governors have given new possibilities for diesel engine control. This was exploited by Blanke and Busk Nielsen (1987, 1990), who designed and implemented a governor with three control modes: constant speed, constant torque, and constant power. The governor was installed successfully on a large number of ships. The power control mode was found to have good properties during transit, with reduced power oscillations in a seaway. This appears to be the first reference on the explicit concepts of torque and power control for FPP. In control of diesel engines, shaft speed control has still been the most commonly used solution, as reflected in e.g. the reference manual from Woodward Governor Company (2004), where torque and power control are not even mentioned. For CCP, the good properties of torque and power control were discussed by Schanz (1967), who proposed a constant shaft speed/torque/power controller. This is further discussed in Section 8.1.5.

For electrically driven FPP on surface vessels, shaft speed control has been the dominating solution. Although not documented in literature, other control methods have also been used in industry. According to Skjellnes (2006), Siemens delivered the first DC installation with torque and power control in 1982, and another one in 1994. Because of their positive experience with these concepts, power control was chosen when they started delivering AC installations. This is reflected in their sales brochure (Siemens AG, 2005). In a parallel development, ABB and NTNU also started working on torque and power control, culminating in the publications of Sørensen *et al.* (1997) and Strand (1999). These appear to be the first available references on torque and power control for electrically driven propellers on surface vessels, and have been the starting point for the work presented in this thesis. The formulations of torque and power control as given in (3.29) and (3.32) are taken from there. It should be noted that both Siemens and ABB only use torque and/or power control for transit operations, where these concepts have proven to be superior at rejecting load disturbances and limiting power oscillations. Subsequently, a combined torque and power controller was introduced in Smogeli *et al.* (2004a), and further developed in Smogeli *et al.* (2005a) and Sørensen and Smogeli (2006). The concept of anti-spin thruster control for electrically driven propellers in extreme operating conditions has been treated in Smogeli *et al.* (2003, 2004b, 2006) and Smogeli and Sørensen (2006b).

For underwater vehicles, both shaft speed control (Healey and Lienard, 1993; Egeskov *et al.*, 1995; Caccia and Veruggio, 2000; Refsnes and Sørensen, 2004; Omerdic and Roberts, 2004), and torque control (Yang *et al.*, 1999; Antonelli *et al.*, 2001; Smallwood and Whitcomb, 2004), have been used. Commercially available electric thrusters for underwater vehicles, as offered by e.g. Tecnadyne (2006) and Seaeye Marine Limited (2006), mainly appear to be speed controlled.

According to Yoerger *et al.* (1991), the predominating solution for under-

water vehicles at that time was torque control. They found that the thruster dynamics had a strong influence on the closed-loop underwater vehicle behavior. To compensate for this, they proposed several controllers, all based on torque control of the thruster motor. An adaptive sliding mode controller containing a compensation for propeller-induced flow effects was shown to improve the closed-loop vehicle performance significantly.

The investigation of model-based thruster control for underwater vehicles was continued by Whitcomb and Yoerger (1999b). They compared a pure torque controller with a high-gain proportional shaft speed controller, and a corresponding shaft speed controller with axial flow compensation. The latter was implemented with an ad hoc stable open-loop estimator for the axial flow velocity. They concluded that the torque controller was unsatisfactory for low thrust commands, probably due to unmodelled friction effects, but with improved performance for higher thrust commands. The high-gain shaft speed controller was shown to have poor performance, but gave good results with the addition of the axial flow compensation. It should be noted that all these experiments were performed at zero advance velocity.

Continuing the concept of axial flow compensation, Fossen and Blanke (2000) proposed a nonlinear output feedback shaft speed controller for propellers on underwater vehicles, with feedback from an estimate of the advance velocity. The advance velocity observer was designed based on the vehicle surge dynamics and a model of the flow dynamics. The closed-loop controller was shown to be globally asymptotically stable. The results were mainly applicable to a an underwater vehicle with one propeller operating in the first quadrant (i.e. positive shaft speed and positive advance velocity).

Tsukamoto *et al.* (1997) presented an experimental comparison study of five thruster control systems for underwater robots: on-line neural network control, off-line neural network control, fuzzy control, adaptive-learning control, and PID control. However, the controllers were based on direct control of the vehicle surge position using one thruster, evading the decoupling in thrust allocation and low-level thruster control that is considered here. Neural networks, fuzzy control, and adaptive-learning control will not be treated any further in this thesis.

Bachmayer and Whitcomb (2001) presented two model based thrust tracking controllers. The controllers were based on detailed knowledge of the propeller lift and drag curves for all 4 quadrants of operation, in addition to the shaft friction coefficients (2.51), the rotational inertia (2.50), and the parameters needed to describe an axial flow model, see Section 2.2.5. They were also based on the assumption that the advance velocity  $V_a \approx 0$ . Under these assumptions, experimental evidence of an asymptotically stable open-loop thrust tracking controller was presented, although no theoretical proof was given. A shaft speed feedback thrust tracking controller was shown to influence the rate of convergence of the tracking error. The proposed controllers appear to be mainly suited for underwater applications with high bandwidth positioning requirements, and strong coupling between the vessel and thruster dynamics. For industrial applications

on surface ships, the detailed model knowledge needed for such a controller cannot be expected to be available. Particularly, the complete hydrodynamic model of the propeller is practically never obtainable. The assumption of  $V_a \approx 0$  is also difficult to justify in practice.

Guibert *et al.* (2005) presented an output feedback thrust controller. The controller was based on a stationary extended Kalman filter for estimation of the hydrodynamic load torque  $Q_a$ , estimation of the thrust  $T_a$  from a numerical inversion of the propeller lift and drag curves and the flow dynamics model (2.70), and a PI controller operating on the thrust error. The controller required extensive model knowledge – both the lift and drag curves of the propeller and the parameters for the flow dynamics. The controller was tested by simulations, and found to be highly sensitive to modelling errors, both in the mechanical and the hydrodynamic model. Moreover, the flow dynamics model (2.70) is only valid in the first quadrant of operation, and requires knowledge of  $V_a$ . This approach is therefore not considered applicable to surface vessels. A different output feedback thrust controller, which circumvents most of these problems, is presented in Appendix E.3.

## 3.5 Control coefficients

The thruster control schemes are based on the thrust/torque/speed/power relationships given in (2.8), (2.9), and (2.10). Since the propeller diameter  $D$  and density of water  $\rho$  are known and constant, the only remaining parameters are the thrust and torque coefficients  $K_T$  and  $K_Q$ . The thrust and torque coefficients used in the controllers are termed  $K_{TC}$  and  $K_{QC}$ , and denoted *control coefficients*.

### 3.5.1 Shaft speed, torque, and power reference

The shaft speed reference  $n_r$ , torque reference  $Q_r$ , and power reference  $P_r$  will be needed in the following sections.  $n_r$  is calculated from the thrust reference  $T_r$  by the static mapping  $g_n(T_r)$ :

$$n_r = g_n(T_r) = \text{sign}(T_r) \sqrt{\frac{|T_r|}{\rho D^4 K_{TC}}}, \quad (3.1)$$

which is the inverse function of the nominal characteristics given in (2.8), with  $K_{T0}$  replaced by  $K_{TC}$ . The mapping  $g_q(T_r)$  from  $T_r$  to  $Q_r$  can be found from (2.8) and (2.9) with  $K_{T0}$  and  $K_{Q0}$  replaced by  $K_{TC}$  and  $K_{QC}$ :

$$Q_r = g_q(T_r) = \frac{K_{QC}}{K_{TC}} D T_r. \quad (3.2)$$

The mapping  $g_{p0}(T_r)$  from  $T_r$  to  $P_r$  is found by inserting  $Q_r$  from (3.2) and  $n_r$  from (3.1) in (2.10) such that:

$$P_r = g_{p0}(T_r) = Q_r 2\pi n_r = |T_r|^{3/2} \frac{2\pi K_{QC}}{\sqrt{\rho} D K_{TC}^{3/2}}. \quad (3.3)$$

The mapping  $g_p(T_r)$  from  $T_r$  to the signed power  $P_{rs}$  is defined as:

$$P_{rs} = g_p(T_r) = \text{sign}(T_r) P_r = \text{sign}(T_r) |T_r|^{3/2} \frac{2\pi K_{QC}}{\sqrt{\rho} D K_{TC}^{3/2}}. \quad (3.4)$$

The inverse mappings from  $n_r$ ,  $Q_r$ , and  $P_{rs}$  to  $T_r$  are termed  $g_n^{-1}(n_r)$ ,  $g_q^{-1}(n_r)$ , and  $g_p^{-1}(n_r)$ , respectively, and given by:

$$T_r = g_n^{-1}(n_r) = K_{TC} \rho D^4 n_r |n_r|, \quad (3.5)$$

$$T_r = g_q^{-1}(Q_r) = \frac{K_{TC}}{K_{QC} D} Q_r, \quad (3.6)$$

$$T_r = g_p^{-1}(P_{rs}) = \text{sign}(P_{rs}) |P_{rs}|^{2/3} \frac{\rho^{1/3} D^{2/3} K_{TC}}{(2\pi)^{2/3} K_{QC}^{2/3}}. \quad (3.7)$$

### 3.5.2 Choosing $K_{TC}$ and $K_{QC}$

In thruster control for station-keeping operations, estimates of the nominal thrust and torque coefficients  $K_{T0}$  and  $K_{Q0}$  are usually chosen as control coefficients, because the actual advance velocity is unknown to the controller. Doppler logs, GPS, etc. may be used to give estimates of the advance velocity, but these measurements are usually not of sufficient accuracy for inclusion in the low-level thruster control laws.

For thruster control in transit, only the main propellers of the vessel are used. If the propeller characteristics are known, improved controller performance may be achieved by estimating the propeller advance velocity  $V_a$  using the known vessel surge speed  $U$  and an estimated hull wake factor  $w_h$  as in (2.42), or a low-pass filtered measurement from a Doppler log or GPS.  $K_{TC}$  and  $K_{QC}$  could then be estimated from the propeller characteristics. This is further discussed in Section 8.2. Similar reasoning may be applied to an underwater vehicle, where the propeller normally is deeply submerged and not subject to wave effects, ventilation, or water exits. In the following, station-keeping and low-speed manoeuvring operations of surface vessels are of main concern, such that the control coefficients are taken as  $K_{T0}$  and  $K_{Q0}$ .

### 3.5.3 Reverse thrust

With the exception of tunnel thrusters, most propellers are asymmetric. To achieve good performance for both positive and negative thrust references, it may therefore be necessary to use two sets of control parameters. For low-speed

operations, this means that  $K_{T0}$  and  $K_{Q0}$  should be used for positive  $T_r$ , and the reverse thrust and torque coefficients  $K_{T0r}$  and  $K_{Q0r}$  for negative  $T_r$ , see Section 2.1. The following control coefficients are therefore proposed:

$$K_{TC} = K_{T0}\lambda_c + (1 - \lambda_c)K_{T0r}, \quad (3.8)$$

$$K_{QC} = K_{Q0}\lambda_c + (1 - \lambda_c)K_{Q0r}, \quad (3.9)$$

where  $\lambda_c$  is a smooth switching function given by:

$$\lambda_c = \lambda_c(n_r) = \frac{1}{2} + \frac{1}{2} \tanh(\varepsilon_c \frac{n_r}{n_c}). \quad (3.10)$$

The shaft speed reference  $n_r$  is given from  $T_r$  by (3.1), and  $n_c > 0$  and  $\varepsilon_c > 0$  are constants. With a properly chosen  $\varepsilon_c$ , the switching between the coefficients occurs smoothly in the interval  $n_r \in [-n_c, n_c]$ , such that  $\lambda_c \approx 0$  for  $n_r < -n_c$  and  $\lambda_c \approx 1$  for  $n_r > n_c$ . The switch “width”  $n_c$  may be chosen freely. (3.8, 3.9) does not affect the stability properties of the controllers when compared to using constant control coefficients, since  $K_{T0}$ ,  $K_{Q0}$ ,  $K_{T0r}$ , and  $K_{Q0r}$  all are strictly positive, and the values of  $K_{TC}$  and  $K_{QC}$  only affect the mappings from  $T_r$  to  $n_r$ ,  $Q_r$ , and  $P_{rs}$ . Using  $n_r$  as the switching variable instead of e.g. the measured shaft speed  $n$  means that no measurement noise is entered into the control law through (3.8, 3.9).

As an example, Figure 3.2 shows  $\lambda_c$  from (3.10) and  $K_{TC}$  from (3.8) for the 4MW Wageningen B4-70 example propeller with parameters given in Table 2.2, and the parameters for  $\lambda_c$  chosen as  $\varepsilon_c = 3$  and  $n_c = 0.2\text{rps}$ .

## 3.6 Reference generator

The desired thrust from the high-level controller should be filtered through a reference generator. There are several important reasons for doing this:

- It is in general undesirable to enter transients into a control loop. Especially in the case of a shaft speed thruster controller, the transients in motor torque may be large if no rate limits on the reference are imposed: if e.g. a large step in thrust is commanded, and the speed controller is tightly tuned, the motor will inevitably reach its maximum rating in a split second. Such torque transients may damage the mechanical components in the thruster unit, as discussed in Section 3.2.2.
- The power distribution network should be protected from large disturbances. If the loading of the network suddenly increases, the result may be a large frequency drop. If the frequency drop is too large, the generators may trip and a blackout occur, see Section 3.2.3. In order to avoid this, rapid increases of the power load of the thrusters should be avoided.

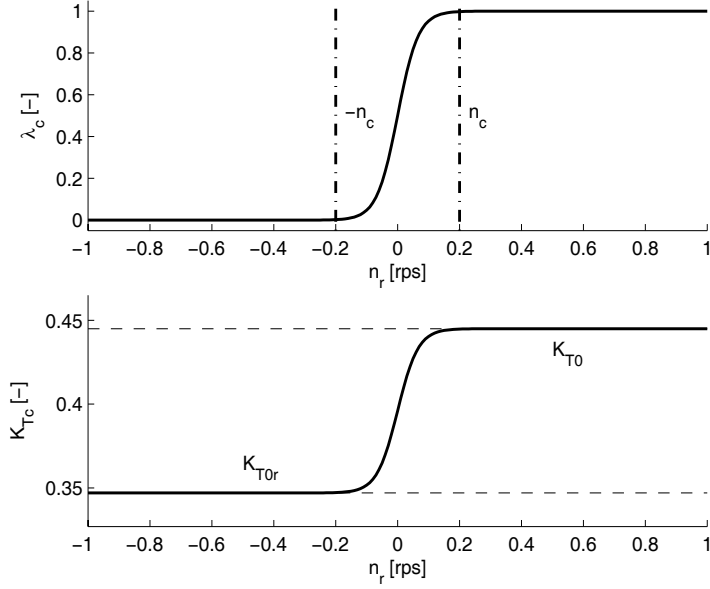


Figure 3.2: Control coefficient  $K_{TC}$  and switching function  $\lambda_c$  as functions of  $n_r$  for the 4MW Wageningen B4-70 example propeller.

### 3.6.1 Rate limiting function

In the following, a rate limiting function with certain properties will be needed. The rate limiting function  $f_{slew}(z, \dot{z}_{slew}^+, \dot{z}_{slew}^-)$  should enforce slew rate limits  $\dot{z}_{slew}^+ > 0$  for increasing magnitude of  $z$ , and  $\dot{z}_{slew}^- < 0$  for decreasing magnitude of  $z$ . This can be implemented by two simple rate limiting elements in series:

$$\begin{aligned} f_{slew}(z, \dot{z}_{slew}^+, \dot{z}_{slew}^-) &= z_1, \\ z_1 &= \min(\max(\dot{z}_0, -\dot{z}_{slew}^{\max}), \dot{z}_{slew}^{\max}), \\ \dot{z}_0 &= \text{sign}(z) \min(\max(|\dot{z}|, \dot{z}_{slew}^-), \dot{z}_{slew}^+), \\ \dot{z}_{slew}^{\max} &= \max(\dot{z}_{slew}^+, |\dot{z}_{slew}^-|), \end{aligned} \quad (3.11)$$

where  $\dot{z}_{slew}^{\max}$  is a parameter, and  $z_0$  and  $z_1$  are internal states. The second rate limiting element (with output  $z_1$ ) is only needed to avoid transients when  $z$  changes sign.

If the positive and negative slew rate limits have the same magnitude, i.e.  $\dot{z}_{slew}^+ = -\dot{z}_{slew}^- = \dot{z}_{slew}$ , the rate limiting function can be simplified to:

$$f_{slew}^0(z, \dot{z}_{slew}) = z_0 |_{z_0=\min(\max(\dot{z}, -\dot{z}_{slew}), \dot{z}_{slew})}. \quad (3.12)$$

Note that the rate limiting functions in (3.11) and (3.12) are easily implemented without the need for differentiation.

### 3.6.2 Shaft speed reference with rate limit

In the marine industry, the commonly used reference generator appears to be a rate limiting function on the shaft speed reference  $n_r$  (Ådnanes, 2006). The recommended magnitude of the slew rate will depend on the size and type of the propulsion unit. A typical 1-2 MW unit with shaft speed control would have a slew rate equivalent to ramping  $n_r$  from zero to max in about 7-8 seconds, and a typical 3-4 MW unit a slew rate equivalent to 10-15 seconds. The slew rate must be chosen in connection with the tuning of the speed controller, such that the total closed loop – including reference generator, speed control loop, and inner torque control loop – has the desired performance. It is also possible to implement a speed dependent reference generator. As a trade-off between thruster response and undesired disturbances on the power network, a solution sometimes seen in the industry is to use a fast reference generator for low shaft speeds, and a slower reference generator for high shaft speeds.

Since the chosen interface to the thruster unit is  $T_d$ , the reference generator for  $T_r$  can be implemented by using the shaft speed mapping  $g_n(T_r)$  in (3.1), its inverse  $g_n^{-1}(n_r)$  in (3.5), and the rate limiting function in (3.11) with slew rate limits  $\dot{n}_{slew}^+$  and  $\dot{n}_{slew}^-$ :

$$\begin{aligned} n_d &= g_n(T_d), \\ n_r &= f_{slew}(n_d, \dot{n}_{slew}^+, \dot{n}_{slew}^-), \\ T_r &= g_n^{-1}(n_r). \end{aligned} \quad (3.13)$$

### 3.6.3 Shaft speed reference with low-pass filter and rate limit

In order to reduce the transients in the commanded torque, it may be beneficial to add a low-pass filter to the reference generator in (3.13). For this system, a second-order filter with damping ratio  $\zeta_r$  and natural frequency  $\omega_{r0}$  is appropriate. The reference generator then becomes:

$$\begin{aligned} n_d &= g_n(T_d), \\ n_{d2} &= f_{slew}(n_d, \dot{n}_{slew}^+, \dot{n}_{slew}^-), \\ n_r(s) &= n_{d2}(s) \frac{\omega_{r0}^2}{s^2 + 2\zeta_r\omega_{r0}s + \omega_{r0}^2}, \\ T_r &= g_n^{-1}(n_r). \end{aligned} \quad (3.14)$$

The resulting reference generator is shown in Figure 3.3. Notice that the reference generator gives a continuous acceleration reference  $\dot{n}_r$ . This will be utilized in Section 3.7.2, where an inertia compensation scheme based on  $\dot{n}_r$  is designed. An alternative formulation, where the speed rate limit is implemented by an acceleration saturation element inside the filter, is proposed in Fossen (2002). A simple tuning rule for the filter parameters is to choose  $\zeta_r = 1$  (critically damped) and  $\omega_{r0} = 1.5/\tau_r$ , where  $\tau_r$  is the approximate “time constant” of the filter.

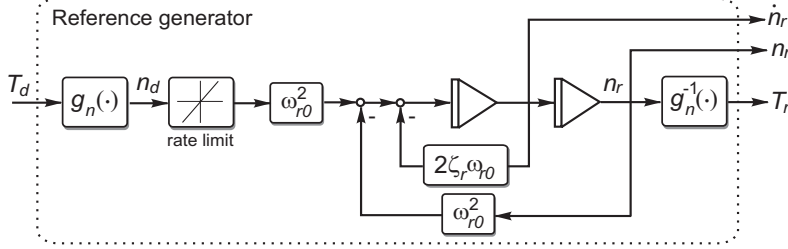


Figure 3.3: Reference generator based on a second order filter with shaft speed rate limit.

### 3.6.4 Power reference generator

For the power generation and distribution system, it is the rate of change of the consumed power that is critical for safe performance. Hence, it may be beneficial to design the reference generator to give a maximum rate of change of power (as opposed to a maximum rate of change of shaft speed). The reference generator is realized by the thrust-power mapping  $g_p(T_r)$  in (3.4), its inverse  $g_p^{-1}(P_r)$  in (3.7), the rate limiting function in (3.11) with slew rate limits  $\dot{P}_{slew}^+$  and  $\dot{P}_{slew}^-$ , and a low-pass filter as in (3.14):

$$\begin{aligned} P_{ds} &= g_p(T_d), \\ P_{d2} &= f_{slew}(P_{ds}, \dot{P}_{slew}^+, \dot{P}_{slew}^-), \\ P_{rs}(s) &= P_{d2}(s) \frac{\omega_{r0}^2}{s^2 + 2\zeta_r \omega_{r0} s + \omega_{r0}^2}, \\ T_r &= g_p^{-1}(P_{rs}). \end{aligned} \quad (3.15)$$

Note that the acceleration reference  $\dot{n}_r$  is not directly available from this reference generator. However, from (3.1) and (3.4), the following relationship may be established:

$$\begin{aligned} P_{rs} &= 2\pi K_{QC} \rho D^5 n_r^3, \\ &\Downarrow \\ \dot{P}_{rs} &= \frac{\partial P_{rs}}{\partial n_r} \dot{n}_r = 6\pi K_{QC} \rho D^5 n_r^2 \dot{n}_r, \\ &\Downarrow \\ \dot{n}_r &= \frac{\dot{P}_{rs}}{6\pi K_{QC} \rho D^5 n_r^2} = \frac{K_{TC}}{6\pi D K_{QC}} \frac{\dot{P}_{rs}}{|T_r|}. \end{aligned} \quad (3.16)$$

where (3.5) has been inserted. Since  $\dot{P}_{rs}$  is available from the implementation of the low-pass filter in (3.15),  $\dot{n}_r$  can be calculated without differentiation. An alternative formulation, where also the singularity for  $T_r = 0$  is avoided, is given

by:

$$\dot{n}_r = \frac{1}{6\pi} \frac{\dot{P}_{rs}}{\max(\varepsilon_r, |Q_r|)}, \quad (3.17)$$

where  $Q_r$  is calculated from (3.2), and  $\varepsilon_r$  is a small number.

### 3.6.5 Reference generator comparison

Figure 3.4 shows a comparison of the power reference generator in (3.15) and the speed reference generator in (3.14) for the Wageningen B4-70 example propeller; see Table A.1 for the propeller simulation data. The slew rates have been chosen as  $\dot{n}_{slew} = n_{bp}/10s$  and  $\dot{P}_{slew} = P_{bp}/10s$ , with  $K_{TC}$  and  $K_{QC}$  taken from Table 3.2. The filter parameters were chosen as  $\zeta_r = 1.0$  and  $\omega_0 = 1.5/\tau_r$ , with time constant  $\tau_r = 0.5s$ . Both  $T_r$ ,  $n_r$ ,  $Q_r$ ,  $P_{rs}$ , and  $\dot{n}_r$  are shown for two steps in the desired thrust: from  $-490kN$  to  $490kN$ , and from  $0kN$  to  $490kN$ . The results show that the two reference generators obtain their objectives. The speed reference generator rate limits  $n_r$ , resulting in slower changing  $P_r$  and  $T_r$  for low references, and faster changing for high references. The power reference generator rate limits  $P_r$ , resulting in faster changing  $n_r$  and  $T_r$  for low references, and slower changing for high references. However, the commanded shaft speed acceleration is high about the zero-crossing of  $T_r$  due to the singularity in (3.16). This must be kept in mind if  $\dot{n}_r$  is to be used in an inertia compensation scheme, as will be proposed in Section 3.7.2.

**Remark 3.2** *The shaft speed reference generator gives undesirable behavior of the power reference for large  $T_r$ , whereas the power reference generator gives undesirable behavior of the shaft speed reference for small  $T_r$ . This is inherent in the two approaches.*

**Remark 3.3** *The speed and power reference generators may be combined in order to enforce both a shaft speed rate limit and a power rate limit. This can be implemented by using the speed reference generator without low-pass filter in (3.13) and the power reference generator in (3.15) in series, i.e. use the output  $T_r$  from (3.13) as input to (3.15). In practice, this means that the shaft speed reference generator is active for small  $T_r$ , whereas the power reference generator is active for large  $T_r$ . This will also alleviate the problems with the power reference generator for low  $n$ .*

## 3.7 Friction and inertia compensation

In the design of the torque and power controllers, the friction term  $Q_f(\omega)$  will be assumed compensated by a feedforward controller. If this is not the case, and the friction is significant, the controllers will be inaccurate, since at steady state  $Q_{mp} \approx Q_a$  no longer holds, see (2.50). The result is less thrust than expected, since a portion of the motor power is spent on overcoming the shaft friction.

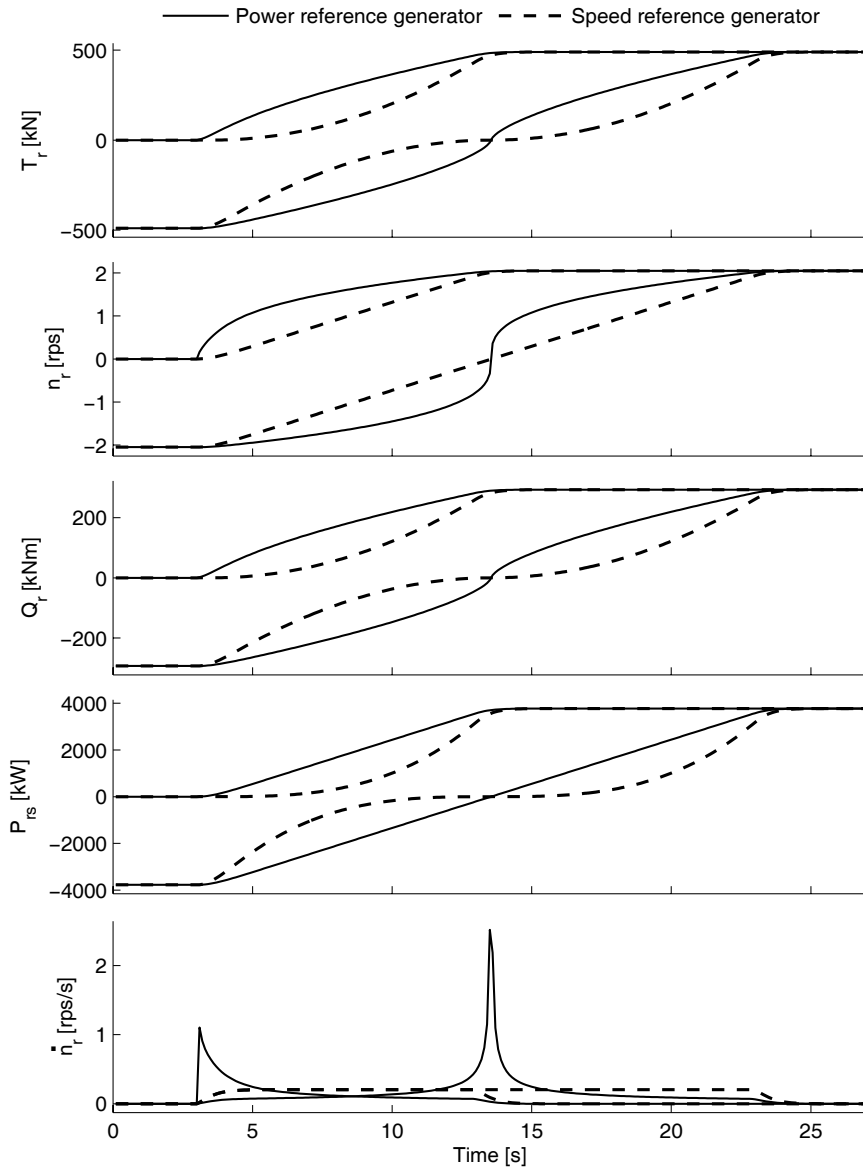


Figure 3.4: Comparison of the power and speed reference generators for two steps in desired thrust.

For a large thruster, the rotational inertia may be a dominating dynamic term. In order to achieve the desired closed loop properties with respect to response and tracking, it may therefore be beneficial to include an inertia compensation term.

In general, feedforward terms to account for friction and inertia should therefore be included in the control law, such that the total controller output  $Q_{c0}$  is given by:

$$Q_{c0} = Q_{ci} + Q_{ff} + Q_{if}, \quad (3.18)$$

where  $Q_{if}$  is the inertia compensation,  $Q_{ff}$  is the friction compensation, and the  $i$  in  $Q_{ci}$  is an index specific to the controller in use. For example,  $i = n$  for shaft speed control,  $i = q$  for torque control, and  $i = p$  for power control.

### 3.7.1 Friction compensation

For a full-scale thruster on a surface vessel, the shaft friction will in most cases be relatively small compared to the propeller torque. For smaller vehicles like ROV's and AUV's, the friction may be significant and lead to severely degraded performance if not accounted for in the controllers. This has been investigated in e.g. Whitcomb and Yoerger (1999b) and Bachmayer *et al.* (2000), where a friction model similar to (2.51) was proposed. In the experimental setup utilized in the current work, the friction was also found to be significant.

$Q_{ff}$  should be designed to compensate for the friction term  $Q_f(\omega)$ , i.e.  $Q_{ff} \approx Q_f(\omega)$ , without destabilizing the system. Therefore, a feedforward compensation based on the *reference* shaft speed  $n_r$  from (3.1) is chosen instead of a destabilizing feedback compensation based on  $n$ . Motivated by (2.51) the friction is assumed to consist of a static and a linear term, and the friction compensation scheme is proposed as:

$$Q_{ff}(n_r) = Q_{ff0}(n_r) + Q_{ff1}(n_r), \quad (3.19)$$

where the static term  $Q_{ff0}(n_r)$  and the linear term  $Q_{ff1}(n_r)$  are defined below. If considered necessary, higher-order friction compensation terms may be included in a similar manner.

#### Static friction

The contribution from the static term  $Q_s$  in (2.51) is discontinuous for  $\omega = 0$ . To avoid discontinuities in the control law, the signum function is replaced with a smooth switching function, such that the static friction compensation  $Q_{ff0}(n_r)$  is proposed as:

$$Q_{ff0}(n_r) = Q_{f0} \tanh\left(\varepsilon_f \frac{n_r}{n_f}\right), \quad (3.20)$$

where  $Q_{f0}$ ,  $\varepsilon_f$ , and  $n_f$  are constants. With a properly chosen  $\varepsilon_f$ , the switching between  $-Q_{f0}$  and  $Q_{f0}$  occurs smoothly in the interval  $n_r \in [-n_f, n_f]$ , such that  $|n_r| > n_f \Rightarrow Q_{ff0}(n_r) = \text{sign}(n_r)Q_{f0}$ , and  $n_r = 0 \Rightarrow Q_{ff0}(n_r) = 0$ . Note

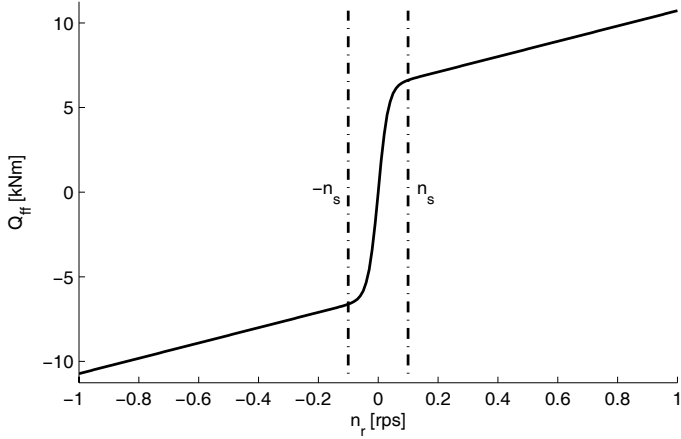


Figure 3.5: Friction compensation scheme for the 4MW Wageningen B4-70 example propeller.

that the switching function is of similar form as the one used in (3.10).  $n_f$  should be chosen such that  $|n_r| < n_f$  is not a relevant setpoint, and  $Q_{f0}$  should be chosen such that  $Q_{f0} \approx Q_s$ .

### Linear friction

The linear friction compensation  $Q_{ff1}$  is proposed as:

$$Q_{ff1}(n_r) = 2\pi Q_{f1} n_r, \quad (3.21)$$

where the linear friction coefficient  $Q_{f1}$  should be chosen such that  $Q_{f1} \approx K_\omega$ . In nominal conditions,  $n = n_r \Rightarrow Q_{ff1}(n_r) \approx K_\omega \omega$ . For  $n \neq n_r$ ,  $Q_{ff1}(n_r) \neq K_\omega \omega$ , but this only affects the performance about the equilibrium point.

### Example friction compensation model

An example friction compensation scheme for the 4MW Wageningen B4-70 propeller is shown as a function of  $n_r$  in Figure 3.5. The parameters have been taken as  $Q_{f0} = 6.2 \text{ kNm}$ ,  $Q_{f1} = 720 \text{ Nms}$ ,  $\varepsilon_f = 3$ , and  $n_f = 0.1 \text{ rps}$ .

### 3.7.2 Inertia compensation

The inertial term in the rotational dynamics (2.50) is  $\dot{\omega} I_s$ . Since differentiation of the measured shaft speed is undesirable, and the inertia compensation is wanted only when the thrust reference is changed, the following feedforward compensation is proposed:

$$Q_{if}(n_r) = I_c 2\pi \dot{n}_r, \quad (3.22)$$

where  $I_c$  is an estimate of the rotational inertia  $I_s$ , and  $\dot{n}_r$  is given by the reference generator, as shown e.g. in Figure 3.3. The inertia compensation scheme is expected to be important mainly for large propellers. In an industrial installation, the rotational inertia should be relatively accurately known, since it is an important parameter for the choice of electric motor and tuning of the motor drive, see Appendix B.1.

**Remark 3.4**  $Q_{if}$  is written as a function of  $n_r$  instead of  $\dot{n}_r$  in order to have consistent notation with other parts of the control schemes. In block diagrams etc.  $Q_{if}$  may take  $n_r$  or  $T_r$  as input, even though  $\dot{n}_r$  from the reference generator is used in practice.

### 3.7.3 Feedforward compensation properties

The friction and inertia feedforward compensation schemes in (3.19) and (3.22) may be related to the concept of *feedback linearization*, where the basic idea is to transform a nonlinear system to a linear one. This is treated in detail in e.g. Slotine and Li (1991), Isidori (1995), and Khalil (2002). In robotics, a similar concept is called *computed torque control*, see e.g. Sciavicco and Siciliano (2000). This is also utilized to develop control laws for marine systems in Fossen (2002).

For the propeller, the effect of the feedforward compensation schemes can be seen from the rotational dynamics (2.50). By neglecting the motor torque dynamics in (2.52), such that  $Q_{mp} = Q_{c0}$ , and inserting (3.18), the rotational dynamics become:

$$I_s \ddot{\omega} = Q_{ci} + Q_{ff}(n_r) + Q_{if}(n_r) - Q_a - Q_f(\omega). \quad (3.23)$$

By assuming perfect model knowledge such that  $Q_{f0} = Q_s$ ,  $Q_{f1} = K_\omega$ , and  $I_c = I_s$ , that  $|n_r| > n_f \Rightarrow Q_{ff0}(n_r) = \text{sign}(n_r)Q_{f0}$ , that  $\text{sign}(\omega) = \text{sign}(n_r)$ , and inserting (2.51), (3.19), and (3.22), (3.23) reduces to:

$$2\pi I_s (\dot{n} - \dot{n}_r) = Q_{ci} - Q_a - 2\pi K_\omega (n - n_r). \quad (3.24)$$

Hence, it remains to design  $Q_{ci}$  to compensate for the propeller torque  $Q_a$ . This is done by the various control laws presented in Sections 3.10 to 3.15.

## 3.8 Torque and power limiting

In order to avoid commanding excessive torque or power from the thruster motor, a torque limiting function – as shown in Figure 3.1 – should be included in the control scheme. The maximum admissible torque  $Q_{\max}$  and power  $P_{\max}$  for the motor are related to the rated torque and power (for continuous operation) by (2.55). The controller output should therefore be limited by a torque limiting function given by:

$$Q_c = \max\{Q_{c0}, k_g Q_{\max}, \frac{P_{\max}}{2\pi n}\}, \quad (3.25)$$

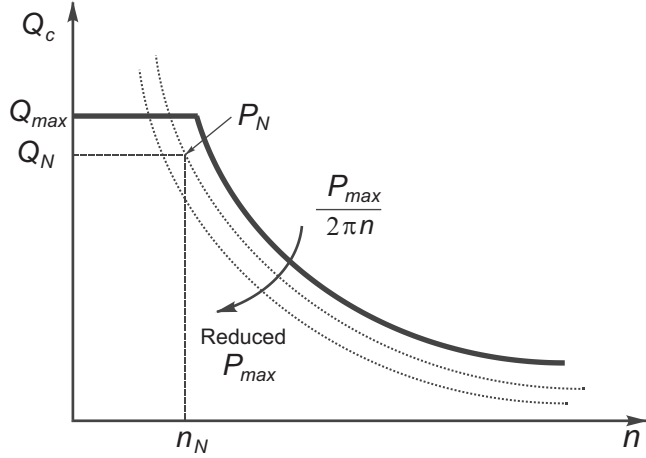


Figure 3.6: Torque limiting function parameterized by the maximum torque  $Q_{\max}$  and maximum power  $P_{\max}$ , adopted from Sørensen *et al.* (1997).

where  $Q_{c0}$  is the commanded torque from the controller, friction compensation, and inertia compensation (3.18), and  $k_g$  is the gear ratio, see Section 2.2.3. The commanded motor torque  $Q_{cm}$  to the motor is finally given as

$$Q_{cm} = Q_c/k_g. \quad (3.26)$$

The maximum power limit yields hyperbolic limit curves for the torque as a function of motor speed. This is shown in Figure 3.6, where  $n_N$  is the rated motor shaft speed. Since the maximum power is not limited by the converter and motor ratings only, but also by the available power on the network, this limit should be varied accordingly. By this method the power limitation will become fast and accurate, allowing to utilize the power system power capability with a built-in blackout prevention (Sørensen *et al.*, 1997).

### 3.9 Feedback signal filtering

The feedback signals  $n$  and  $Q_m$  should be filtered before they are entered into the control loop. This is proposed done by first order filters with appropriately chosen time constants  $T_f$  and  $T_{fq}$ , respectively. In a discrete-time implementation, the usual requirements to the filter bandwidth with respect to sampling period applies, see e.g. Åström and Wittenmark (1997).

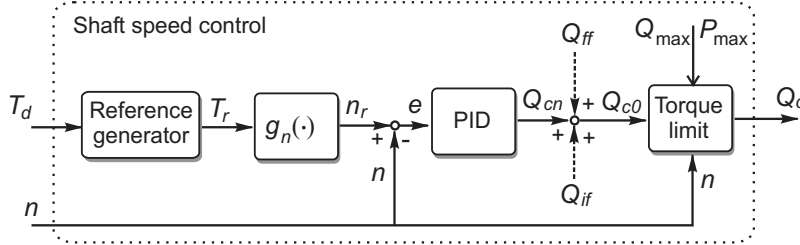


Figure 3.7: Shaft speed control scheme.

### 3.10 Shaft speed feedback control

The shaft speed controller is designed to keep the shaft speed  $n$  equal to the reference speed  $n_r$  (3.1). The typical solution is to use a PID controller operating on the shaft speed error  $e = n_r - n$ , which sets the commanded torque  $Q_{cn}$  according to

$$Q_{cn} = K_p e + K_i \int_0^t e(\tau) d\tau + K_d \dot{e}, \quad (3.27)$$

where  $K_p > 0$ ,  $K_i > 0$ , and  $K_d \geq 0$  are the PID gains. The motor torque is controlled by its inner torque control loop, as discussed in Section 2.2.2.  $K_i$  is often given as  $K_i = K_p/T_i$ , where  $T_i$  is the integral time constant. The integral term in the PID controller should be limited according to some maximum  $Q_{i,\max}$  to avoid integral windup, i.e.

$$\begin{aligned} \left| K_i \int_0^t e(\tau) d\tau \right| &\leq Q_{i,\max}, \\ Q_{i,\max} &= \kappa_s k_g Q_{\max}, \end{aligned} \quad (3.28)$$

where  $0 < \kappa_s \leq 1$  is a constant, usually chosen as  $\kappa_s \approx 0.8 - 0.9$ . In control of electric motors, a PI controller is considered to be the most appropriate solution (Leonhard, 1996). In this thesis, only PI controllers have been applied, such that  $K_d = 0$ . In the shaft speed control scheme, the friction compensation  $Q_{ff}$  and the inertial compensation  $Q_{if}$  may be omitted, since the controller automatically compensates for these terms when the shaft speed is kept at its reference. Hence,  $Q_{c0} = Q_{cn}$  in this case. Figure 3.7 shows a block diagram of the shaft speed control scheme, including a reference generator and a torque limiting block. It is also indicated how  $Q_{ff}$  and  $Q_{if}$  could be included if wanted. Tuning of the PI parameters is discussed in Appendix B.1.

### 3.11 Torque feedforward control

In the torque control strategy the outer speed control loop is removed, and the thruster is controlled by its inner torque control loop with a commanded torque

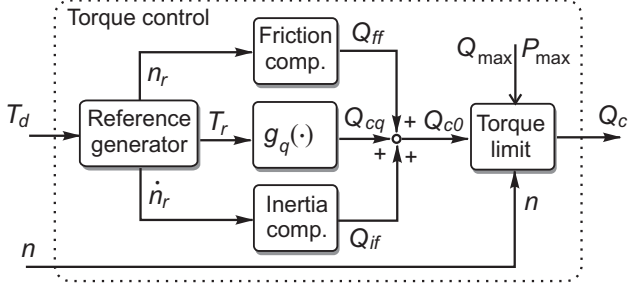


Figure 3.8: Torque control scheme.

$Q_{cq}$  as set-point (Sørensen *et al.*, 1997; Strand, 1999).  $Q_{cq}$  is set equal to the torque reference from (3.2):

$$Q_{cq} = Q_r = g_q(T_r) = \frac{K_{QC}}{K_{TC}} DT_r. \quad (3.29)$$

If the rotational inertia is large, the torque controller in its pure form (3.29) will respond slowly to a changing thrust reference, especially for low shaft speeds. In the work by Sørensen *et al.* (1997) and Strand (1999), it was suggested to add an “inner torque algorithm” with a reference generator and reference feedforward based on  $Q_{cq}$  to speed up the transient response. However, no explicit solution was given. In Section 3.18.1, it will be demonstrated that the transient response problem is solved by using the inertia compensation proposed in Section 3.7.2. Hence, the inner torque algorithm from Sørensen *et al.* (1997) is no longer necessary. Figure 3.8 shows a block diagram of the torque control scheme, including reference generator, torque limiting, friction compensation, and inertia compensation.

**Remark 3.5** The control law in (3.29) can also be written as:

$$Q_{cq} = K_{QC}\rho D^5 n_r^2, \quad (3.30)$$

where  $n_r$  is defined in (3.1). Using the nominal load torque model from (2.9), and assuming that  $K_{QC} = K_{Q0}$ , the rotational dynamics in (3.24) reduces to:

$$2\pi I_s(\dot{n} - \dot{n}_r) = -K_{Q0}\rho D^5(n^2 - n_r^2) - 2\pi K_\omega(n - n_r). \quad (3.31)$$

Hence, the torque controller combined with the friction and inertia compensation is equivalent to a complete feedback linearization or computed torque scheme, with no additional control law.

### 3.12 Power feedback control

Power control is based on controlling the power consumption of the thruster motor. The inner torque control loop is maintained, and the commanded torque

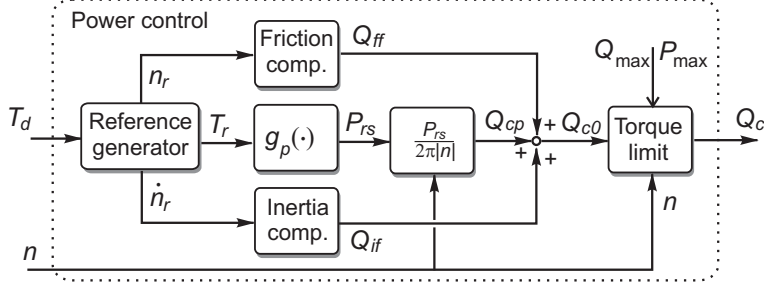


Figure 3.9: Power control scheme.

$Q_{cp}$  is calculated from  $P_{rs}$  in (3.4) using feedback from the measured shaft speed  $n$  according to (Sørensen *et al.*, 1997; Strand, 1999):

$$Q_{cp} = \frac{P_{rs}}{2\pi|n|} = \frac{K_{QC}}{\sqrt{\rho D} K_{TC}^{3/2}} \frac{\text{sign}(T_r)|T_r|^{3/2}}{|n|}, \quad n \neq 0. \quad (3.32)$$

Note that this controller is singular for zero shaft speed. Also the power controller will have a slow response to changes in  $T_r$  if  $I_s$  is large. As in torque control, the inertia compensation scheme (3.22) solves this problem, and replaces the “inner power algorithm” that was proposed in Sørensen *et al.* (1997). Figure 3.9 shows a block diagram of the power control scheme, including reference generator, torque limiting, friction compensation, and inertia compensation.

### 3.13 Combined torque/power control

A significant shortcoming of the power control scheme in (3.32) is the singularity for zero shaft speed. This means that power control should not be used close to the singular point, for example when commanding low thrust or changing the thrust direction. For low thrust commands, torque control shows better performance in terms of constant thrust production, since the mapping from thrust to torque is more directly related to the propeller loading than the mapping from thrust to power. In total, therefore, torque control is a better choice for low thrust commands. For high thrust commands, it is essential to avoid power transients, as these lead to higher fuel consumption, increased danger of blackouts, and harmonic distortion of the power plant network. Power control is hence a natural choice for high thrust commands. This motivates the construction of a combined torque/power control scheme, utilizing the best properties of both controllers.

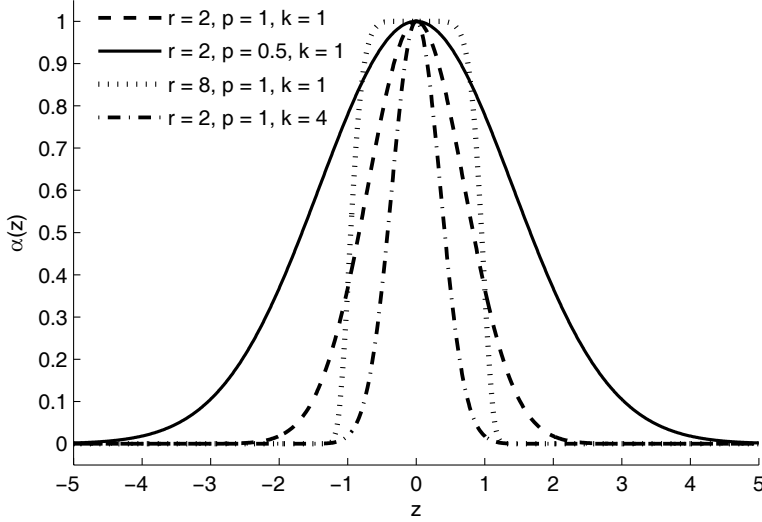


Figure 3.10: Weighting function  $\alpha(z)$  for varying  $r$ ,  $p$ , and  $k$ .

### 3.13.1 Weighting function

The weighting function  $\alpha(z) : \mathbb{R} \rightarrow \mathbb{R}$  will be needed in the following:

$$\alpha(z) = e^{-k|pz|^r}, \text{ for } z \in \mathbb{R}, \quad (3.33)$$

where  $k$ ,  $p$  and  $r$  are positive constants.  $\alpha(z)$  satisfies:

$$\lim_{z \rightarrow 0} \alpha(z) = 1, \quad \lim_{z \rightarrow \pm\infty} \alpha(z) = 0. \quad (3.34)$$

The derivative of  $\alpha$  with respect to  $z$  is

$$\begin{aligned} \partial\alpha(z)/\partial z &= -k|pz|^r e^{-k|pz|^r} (-kpr|pz|^{r-1}) \\ &= k^2 pr |pz|^{2r-1} e^{-k|pz|^r} = k^2 p^{2r} r |z|^{2r-1} \alpha(z), \end{aligned} \quad (3.35)$$

which is smooth in  $z$  for  $r \geq 0.5$ . Particularly,  $\partial\alpha/\partial z = 0$  for  $z = 0$  and  $z \rightarrow \pm\infty$ .

The parameter  $p$  will act as a scaling factor for  $z$ , such that a small  $p$  will widen the weighting function, giving a wider transition between 0 and 1. Increasing the parameter  $k$  sharpens the peak about  $z = 0$ , whereas increasing  $r$  widens the peak and makes the transition from 0 to 1 steeper. Figure 3.10 shows  $\alpha(z)$  for varying  $r$ ,  $p$ , and  $k$ .

### 3.13.2 Controller formulation

With the commanded torque  $Q_{cq}$  from the torque controller in (3.29) and the commanded torque  $Q_{cp}$  from the power controller in (3.32), the combined con-

troller commanded torque  $Q_{cc}$  is defined as:

$$Q_{cc} = \alpha_c(n)Q_{cq} + (1 - \alpha_c(n))Q_{cp}, \quad (3.36)$$

where  $\alpha_c(n)$  is a weighting function of the type (3.33). The shape of  $\alpha_c(n)$  defines the dominant regimes of the two control schemes, and can be used to tune the controller according to user specifications.

The control law (3.36) must show smooth behavior for all  $n$ . The derivative of the commanded torque with respect to  $n$  becomes:

$$\begin{aligned} \frac{\partial Q_{cc}}{\partial n} &= \frac{\partial \alpha_c(n)}{\partial n} Q_{cq} + \alpha_c(n) \frac{\partial Q_{cq}}{\partial n} + \frac{\partial (1 - \alpha_c(n))}{\partial n} Q_{cp} + (1 - \alpha_c(n)) \frac{\partial Q_{cp}}{\partial n} \\ &= k^2 p^{2r} r |n|^{2r-1} \alpha_c(n) \frac{K_{QC}}{K_{TC}} DT_r \\ &\quad - k^2 p^{2r} r |n|^{2r-2} \alpha_c(n) \frac{K_{QC} \operatorname{sign}(T_r) |T_r|^{3/2}}{\sqrt{\rho} D K_{TC}^{3/2}} \\ &\quad - \frac{1 - \alpha_c(n)}{|n|n} \frac{K_{QC} \operatorname{sign}(T_r) |T_r|^{3/2}}{\sqrt{\rho} D K_{TC}^{3/2}}. \end{aligned} \quad (3.37)$$

The first two terms contain no singularities for  $r \geq 1$ , and it remains to investigate the term:

$$\frac{1 - \alpha_c(n)}{|n|n} = \frac{1 - e^{-k|pn|^r}}{|n|n} \triangleq h_n(n). \quad (3.38)$$

The limit of  $h_n(n)$  in (3.38) as  $n$  tends to zero is:

$$\begin{aligned} \lim_{n \rightarrow 0} h_n(n) &= \lim_{n \rightarrow 0} \frac{1 - e^{-k|pn|^r}}{|n|n} = \lim_{n \rightarrow 0} \frac{\partial / \partial n (1 - e^{-k|pn|^r})}{\partial / \partial n (|n|n)} \\ &= \lim_{n \rightarrow 0} -k^2 p^{2r} r |n|^{2r-2} e^{-k|pn|^r} = 0, \text{ for } r \geq 1. \end{aligned}$$

The control law is hence smooth with respect to  $n$  as long as  $r \geq 1$  in the function  $\alpha_c(n)$ . The power control singularity for  $n = 0$  is thereby removed in the combined torque/power controller. Figure 3.9 shows a block diagram of the combined control scheme, including reference generator, torque limiting function, friction compensation, and inertia compensation.

## 3.14 Modified combined torque/power control

In some applications it may be desirable to abandon the combined controller for low thrust references (i.e. low shaft speed), and use shaft speed control instead. This requires an additional switch between the different controllers, which should be handled with care. Here, two approaches are suggested for a modification of the combined torque/power controller: *additive integral action*, and *vanishing integral action*. A third solution, with a slightly different approach, is given in the next section.

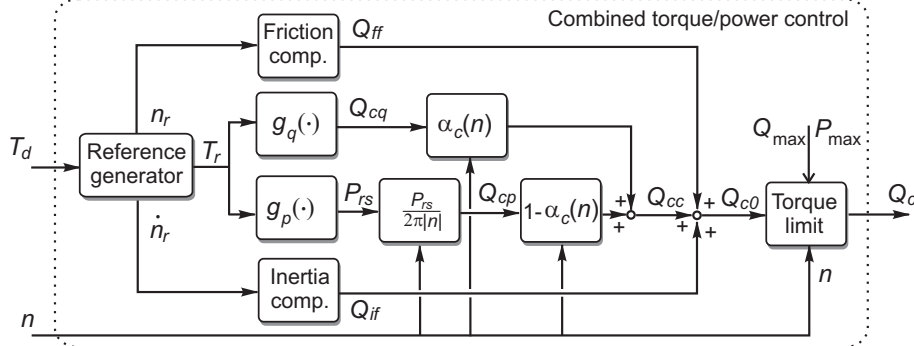


Figure 3.11: Combined torque/power control scheme.

### 3.14.1 Additive integral action

If the starting torque  $Q_s$  is significant but unknown, the static term  $Q_{ff0}$  in the friction compensation scheme (3.19) cannot be implemented. This means that the combined torque/power controller will give poor performance for low thrust references, since  $Q_s$  then will be of significant magnitude compared to the commanded torque  $Q_{ci}$  from the controller. For higher thrust references,  $Q_s$  will be small compared to  $Q_{ci}$ , and the performance will probably be satisfactory. A solution to this is to add an integral term operating on the shaft speed error as in (3.27) to the combined controller in (3.36) for low thrust references, and disable the integral update for high thrust references.

As in the friction compensation scheme, the shaft speed reference  $n_r$  from (3.1) is used as the switching variable. The threshold shaft speed for the switch is termed  $n_s > 0$ , such that  $|n_r| \leq n_s \Rightarrow$  shaft speed control, and  $|n_r| > n_s \Rightarrow$  combined control. The reason for using  $n_r$  instead of the measured shaft speed  $n$  to define the operating regimes is to avoid switching due to measurement noise and shaft speed oscillations. The controller output  $Q_{ccm}$  is formulated as the sum of the commanded torque  $Q_{cc}$  from the combined controller in (3.36) and an integral term  $Q_i$ :

$$Q_{ccm} = Q_{cc} + Q_i. \quad (3.39)$$

$Q_i$  is defined as:

$$Q_i = \begin{cases} \int_0^t K_i(n_r(\tau) - n(\tau))d\tau & \text{for } |n_r| \leq n_s, \\ \bar{Q}_i & \text{for } |n_r| > n_s, \end{cases} \quad (3.40)$$

where  $K_i$  is the integral gain, and  $\bar{Q}_i$  is the value of  $Q_i$  when  $|n_r| = n_s$ . This is easily implemented by freezing or disabling the integrator update when  $|n_r| > n_s$ . This can also be written as

$$Q_i = \int_0^t K_i e_i(\tau) d\tau, \quad e_i = \begin{cases} n_r - n & \text{for } |n_r| \leq n_s, \\ 0 & \text{for } |n_r| > n_s. \end{cases} \quad (3.41)$$

Assuming perfect shaft speed control (i.e.  $n = n_r$ ) for  $|n_r| \leq n_s$ , the torque balance when  $n = n_r = n_s$  from (2.50) becomes:

$$Q_{cc} + \bar{Q}_i + Q_{f1}2\pi n_r = \text{sign}(n)Q_s + K_\omega 2\pi n + Q_a. \quad (3.42)$$

The combined controller has been designed to cancel the propeller torque, such that  $Q_{cc} \approx Q_a$ . If the linear friction compensation is accurate, such that  $Q_{f1}2\pi n_r \approx K_\omega 2\pi n$ , it is clear that the frozen integral term is given by:

$$\bar{Q}_i \approx \text{sign}(n)Q_s. \quad (3.43)$$

Hence, by keeping  $\bar{Q}_i$  as a term in the controller also for  $|n_r| > n_s$ , the static friction is cancelled for the entire range of controller operation. For this to work properly, the limit  $n_s$  should be chosen relatively low, such that it can be assumed that the static friction is a significant term for  $|n_r| \leq n_s$ . If  $n_s$  is chosen too high, the static friction may be dominated by dynamics in the propeller loading, such that the assumption  $Q_{cc} \approx Q_a$ , and hence also (3.43), no longer holds. If no linear friction compensation is included, the frozen integral term will be given by  $\bar{Q}_i \approx \text{sign}(n)Q_s + K_\omega 2\pi n_s$ .

**Remark 3.6** *Perfect matching of  $\bar{Q}_i$  with the static friction can only be obtained in the ideal case, when  $K_\omega$  is known, the control coefficients  $K_{TC}$  and  $K_{QC}$  in the combined controller match the true thrust and torque coefficients, and there is no dynamic loading of the propeller (nominal conditions). If the conditions deviate from the nominal, perfect compensation can no longer be achieved, and the frozen integral term  $\bar{Q}_i \neq \text{sign}(n)Q_s$ . However, if  $Q_{f0}$  is unknown, the total controller performance will still probably be superior to the one without the added integral action.*

### 3.14.2 Vanishing integral action

If  $Q_s$  is known and can be included in the friction compensation (by  $Q_{f0} = Q_s$ ), but it still is desirable to use the shaft speed controller for low  $T_r$ , the approach described in the previous section is not appropriate. In this case it is possible to use a similar formulation, where the integral term used for shaft speed control when  $|n_r| \leq n_s$  is removed for high  $n_r$ . This is facilitated by adding a weighting function  $\alpha_i(n_r)$  of the type (3.33) to the integral term  $Q_i$  in (3.39):

$$Q_{ccm} = Q_{cc} + Q_i \alpha_i(n_{rel}), \quad (3.44)$$

$$n_{rel} = \max(0, |n_r| - n_s). \quad (3.45)$$

Hence,  $\alpha_i(n_{rel}) = 1$  for  $|n_r| \leq n_s$ , such that the controller here is identical to (3.39). For  $|n_r| > n_s$ ,  $\bar{Q}_i$  is scaled with  $\alpha_i(n_{rel})$  such that  $\bar{Q}_i \alpha_i(n_{rel})$  tends to zero for increasing  $n_r$ . The shaft speed reference for which  $\bar{Q}_i \alpha_i(n_{rel}) \approx 0$  is implicitly given by the parameters  $r$ ,  $p$ , and  $k$  in  $\alpha_i(n_{rel})$ .

### 3.15 Combined speed/torque/power control

As an alternative to the modified combined torque/power controller formulations presented in Section 3.14, it is possible to specify three control regimes explicitly: speed control for low shaft speed, torque control for medium shaft speed, and power control for high shaft speed. The regimes are defined as follows:

$$\begin{aligned} |n_r| \leq n_{s1} &\Rightarrow \text{shaft speed control}, \\ n_{s1} < |n_r| \leq n_{s2} &\Rightarrow \text{transition speed} \leftrightarrow \text{torque}, \\ n_{s2} < |n_r| \leq n_{s3} &\Rightarrow \text{torque control}, \\ n_{s3} < |n_r| \leq n_{s4} &\Rightarrow \text{transition torque} \leftrightarrow \text{power}, \\ |n_r| > n_{s4} &\Rightarrow \text{power control}, \end{aligned}$$

with switching shaft speeds  $n_{s1} < n_{s2} < n_{s3} < n_{s4}$ . The two transitions are done by the weighting functions  $\alpha_1(n_r)$  and  $\alpha_2(n_r)$ :

$$\alpha_1(n_r) = \alpha_s(\max(0, |n_r| - n_{s1})), \quad (3.46)$$

$$\alpha_2(n_r) = \alpha_s(\max(0, |n_r| - n_{s3})), \quad (3.47)$$

where  $\alpha_s$  is a weighting function of the type (3.33).  $n_{s1}$  and  $n_{s3}$  are chosen explicitly by the designer, whereas  $n_{s2}$  and  $n_{s4}$  are given implicitly by the functions  $\alpha_1$  and  $\alpha_2$ . Figure 3.12 shows the three control regimes with transition areas and weighting functions. With a modification of the shaft speed controller from (3.27), the torque controller from (3.29), a modification of the power controller from (3.32), and the two weighting functions  $\alpha_1$  and  $\alpha_2$ , the controller output  $Q_{cs}$  of the combined speed/torque/power controller is given from:

$$\begin{aligned} n_r &= sgn(T_r) \sqrt{\frac{|T_r|}{\rho D^4 K_{TC}}}, \quad e = n_r - n, \\ Q_{cn} &= K_p e + \int_0^t K_i e_i(\tau) d\tau, \quad e_i = \begin{cases} e & \text{for } |n_r| \leq n_{s1}, \\ 0 & \text{for } |n_r| > n_{s1}, \end{cases} \\ Q_{cq} &= \frac{K_{QC}}{K_{TC}} D T_r, \\ Q_{cp} &= \frac{K_{QC}}{\sqrt{\rho} D K_{TC}^{3/2}} \frac{sgn(T_r) |T_r|^{3/2}}{\max(|n|, \varepsilon_p)}, \\ \alpha_1(n_r) &= \exp(-k(p \max(0, |n_r| - n_{s1}))^r), \\ \alpha_2(n_r) &= \exp(-k(p \max(0, |n_r| - n_{s3}))^r), \\ Q_{cs} &= \alpha_1 \alpha_2 Q_{cn} + (1 - \alpha_1) \alpha_2 Q_{cq} + (1 - \alpha_1)(1 - \alpha_2) Q_{cp}. \end{aligned} \quad (3.48)$$

**Remark 3.7** In the combined power/torque controller it was necessary to use the shaft speed  $n$  in the weighting function in order to avoid the singularity for zero shaft speed. In (3.48), the singularity is easily avoided by using  $\max(|n|, \varepsilon_p)$  instead of  $|n|$  in the power equation, where  $\varepsilon_p$  is a small positive number. Since  $\alpha_2(n_r) \equiv 1$  for  $|n_r| < n_{s3}$  (and hence the contribution from the power controller is zero), this does not affect the controller output.

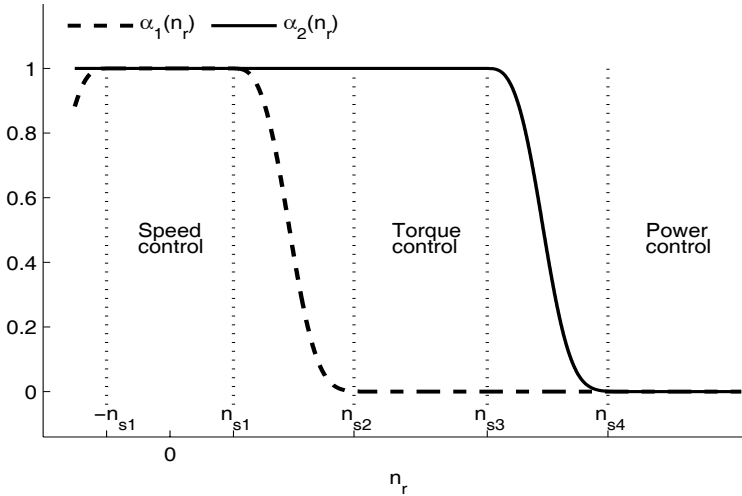


Figure 3.12: Example weighting functions  $\alpha_1(n_r)$  and  $\alpha_2(n_r)$  used in the combined speed/torque/power controller, with controller regimes and transition areas. The weighting functions are symmetric about  $n_r = 0$ .

**Remark 3.8** *The modification of the shaft speed controller term  $Q_{cn}$  is similar to the vanishing integral term in Section 3.14.2, with a disabled integrator for  $|n_r| > n_s$ .*

**Remark 3.9** *The control scheme in (3.48) is easily combined with the friction and inertia compensation schemes as in (3.18) if desired. However, by using shaft speed control for the lowest thrust references, the most important reason for using the friction compensation scheme, i.e. tracking properties for low thrust references, will in most cases be diminished. In some applications, like e.g. the experimental setup presented in Section 7.1, the friction is of significance also for the higher thrust references.*

### 3.16 Thrust control and additional instrumentation

If the propulsion unit could be equipped with additional instrumentation, new control options would appear. With a measurement of the actual thrust, *thrust control* becomes an option. This could be implemented e.g. by a PI controller operating on the thrust error. Without additional instrumentation, it is in some cases possible to construct an output feedback thrust controller, as pro-

Controller	Abbreviation	Section
Shaft speed control	S control	3.10
Torque control	Q control	3.11
Power control	P control	3.12
Combined torque/power control	QP control	3.13
Modified QP control w/ additive integral	MQP1 control	3.14.1
Modified QP control w/ vanishing integral	MQP2 control	3.14.2
Combined speed/torque/power control	SQP control	3.15
Friction compensation scheme	w/Q <sub>ff</sub>	3.7.1
Inertia compensation scheme	w/Q <sub>if</sub>	3.7.2

Table 3.1: Controllers for normal conditions.

posed in Guibert *et al.* (2005). These topics, as well as other control options that become available with additional instrumentation, are further treated in Appendices E.2 and E.3. Due to the increased complexity and necessary model knowledge, thrust control is not considered to be a desirable solution for industrial implementation on surface vessels.

### 3.17 Controller summary

For ease of notation, the controllers presented above will be given abbreviations as defined in Table 3.1. Shaft speed, torque, and power control are considered to be the *fundamental controllers*, since the other controllers are combinations of these. The abbreviations will be used as e.g. “QP w/Q<sub>ff</sub>”, meaning combined torque/power control with friction compensation.

### 3.18 Simulation results

This section presents simulations with the 4MW Wageningen B4-70 example propeller, with specifications given in Appendix A.

The control coefficients are taken according to (3.8, 3.9), with parameters given in Table 3.2. The resulting control coefficient  $K_{TC}$  is shown as a function of  $n_r$  in Figure 3.2. Note that the thrust and torque coefficients in Table 3.2 are identical to the true nominal model parameters as given in Table A.1. With the chosen  $\varepsilon_c$ ,  $\lambda_c(n_c) = 0.9975$ , and  $\lambda_c(-n_c) = 0.0025$ . Hence, the control coefficients are accurate for  $|n_r| > 0.2\text{rps}$ .

The shaft speed reference generator in (3.14) is utilized, with parameters given in Table 3.3. Unless otherwise specified, the friction and inertia compensation schemes are taken according to (3.19) and (3.22), with the parameters given in Table 3.4. The resulting friction compensation scheme is shown as a function of  $n_r$  in Figure 3.5. Perfect model knowledge has been assumed, such that the parameters  $I_c$ ,  $Q_{f0}$ , and  $Q_{f1}$  in Table 3.4 are identical to the true model

$K_{T0}$	$K_{T0r}$	$K_{Q0}$	$K_{Q0r}$	$\varepsilon_c$	$n_c$
0.445	0.347	0.0666	0.0628	3	0.2rps

Table 3.2: Control coefficient parameters for the 4MW Wageningen B4-70 example propeller.

$\dot{n}_{slew}^+$	$\dot{n}_{slew}^-$	$\zeta_r$	$\tau_r$
$0.2\text{s}^{-2}$	$-0.2\text{s}^{-2}$	1.0	2s

Table 3.3: Shaft speed reference generator parameters for the 4MW Wageningen B4-70 example propeller.

parameters  $I_s$ ,  $Q_s$ , and  $K_\omega$  as given in Table A.1. For the inertia compensation scheme,  $\dot{n}_r$  is calculated from the reference generator, as proposed in Section 3.6.

For the shaft speed PI controller in (3.27), the PI gains are taken as proposed in Appendix B.1, and given in Table 3.5. A torque limiting function as defined in (3.25) is used, with the parameters  $Q_{\max}$  and  $P_{\max}$  given in Table A.1. The remaining simulation parameters will be given case by case.

### 3.18.1 Controller response

This section investigates the controller response to a rapid change of thrust reference, and demonstrates the importance of the friction and inertia compensation schemes. The advance velocity is kept constant at  $V_a = 1\text{m/s}$ , simulating e.g. current. The measurement noise on  $n$  is turned off. Four controllers are tested: S control, Q control w/ $Q_{ff}$ , Q control w/ $Q_{if}$ , and Q control w/ $Q_{ff} + Q_{if}$ . The resulting shaft speed and thrust for a step in  $T_d$  from 0 to 117kN (corresponding to  $n_r = 1\text{rps}$ ) are found in Figure 3.13. The shaft speed reference is covered by the S controller, which tracks the shaft speed perfectly. However, there is a steady-state offset in the thrust due to  $V_a$ . The Q controller w/ $Q_{ff}$  has a slow response, but a smaller steady-state offset in thrust. The Q controller w/ $Q_{if}$  has a fast response, but a larger steady-state offset in thrust. The Q controller w/ $Q_{ff} + Q_{if}$  has the best performance, with fast response and little offset in thrust. Figure 3.14 shows the corresponding results for a step from 117 to 263kN (corresponding to  $n_r = 1.5\text{rps}$ ). Again, the shaft speed reference is covered by the S controller. The variations in response are smaller here, demonstrating that the friction and inertia compensation schemes are most important

$I_c$	$Q_{f0}$	$Q_{f1}$	$\varepsilon_f$	$n_f$
$25E3\text{kgm}^2$	6.2kNm	720Nms	3	0.1rps

Table 3.4: Friction and inertia compensation parameters for the 4MW Wageningen B4-70 example propeller.

$K_p$	$T_i$	$Q_{i,\max}$	$T_f$
7.6E5	0.10s	$0.9k_g Q_N$	0.01s

Table 3.5: Shaft speed PI controller parameters for the 4MW Wageningen B4-70 example propeller.

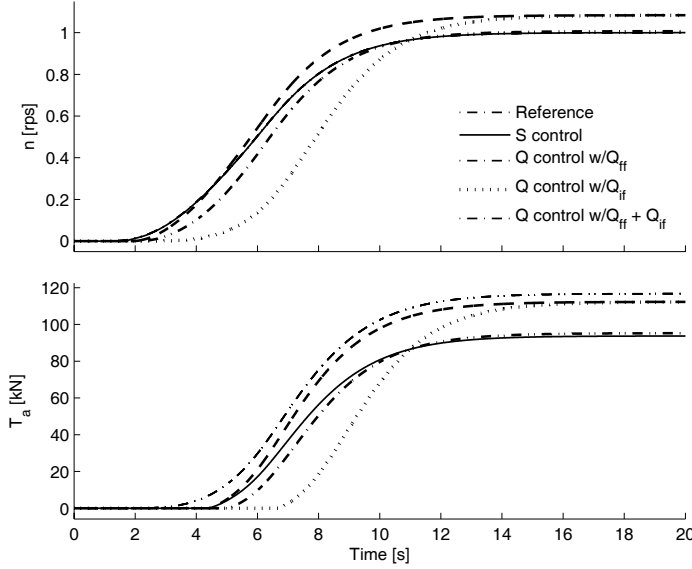


Figure 3.13: Comparison of the shaft speed and thrust response to a step in  $T_d$  from 0 to 117kN at  $V_a = 1.0\text{m/s}$  for four controllers.

for small  $T_r$ . Still, however, the inertia compensation speeds up the response, and the friction compensation reduces the steady-state thrust offset. In total, the Q controller w/ $Q_{ff} + Q_{if}$  has the best performance also here.

For  $V_a = 0$ , which is not shown here, the S controller and Q controller w/ $Q_{ff} + Q_{if}$  both track  $n_r$  and  $T_r$  perfectly, and only the Q controller w/ $Q_{if}$  has a steady-state offset. The response of the Q controller w/ $Q_{ff}$  is still slow. In conclusion, the friction compensation scheme is needed to avoid steady-state offset, and the inertia compensation needed get satisfactory response of the Q controller. However, as was seen in Figures 3.13 and 3.14, the resulting thrust without friction compensation may still be better than for the shaft speed controller when operating away from the nominal design point  $V_a = 0$ .

Without the inertia compensation scheme, the response of the P controller is slightly better than for the Q controller. Without the friction compensation scheme, the steady-state thrust offset of the P controller is slightly larger than for the Q controller.

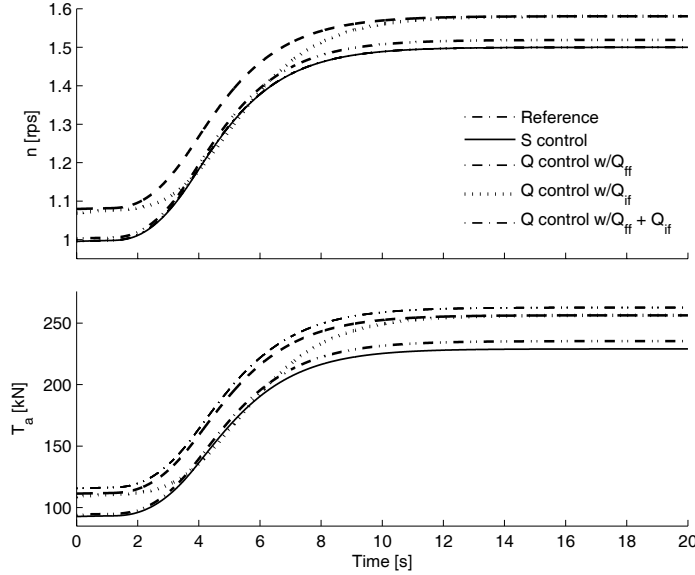


Figure 3.14: Comparison of the shaft speed and thrust response to a step in  $T_d$  from 117 to 263kN at  $V_a = 1.0\text{m/s}$  for four controllers.

### 3.18.2 Fundamental controllers in waves and current

Figure 3.15 shows a comparison of the three fundamental controllers subject to a sinusoidal wave with amplitude 2m and period 10s, with thrust reference  $T_r = 300\text{kN}$ . The mean submergence is  $h_0 = 6\text{m}$ , i.e.  $h_0/R = 1.5$ , and  $V_a$  is calculated from (C.33) with  $N = 1$ ,  $\zeta_1 = 2\text{m}$ ,  $\omega_1 = 2\pi/10\text{s}^{-1}$ , and  $\phi_1 = 0$ . The friction and inertia compensation schemes are used. The simulations show that the three controllers obtain their objectives: the shaft speed controller keeps the shaft speed constant, the torque controller keeps the motor torque constant, and the power controller keeps the motor power constant. The shaft speed controller has the largest oscillations in thrust, propeller torque, motor torque, and motor power. The torque controller has the smallest oscillations in thrust and propeller torque, and much smaller oscillations in motor power than the shaft speed controller, but has the largest oscillations in shaft speed. The power controller has slightly larger oscillations in thrust and propeller torque, and slightly smaller oscillations in shaft speed than the torque controller. It also has much smaller oscillations in motor torque than the shaft speed controller. Similar results could be obtained for any sea-state, propeller, and thrust reference, as these properties are inherent in the controllers. This will be further analyzed in Chapter 4. A small noise content can be seen in the motor torque and power for the shaft speed controller, and also for the power controller, due to the noise

on the shaft speed feedback signal.

Figure 3.16 shows the same three controllers, sea state, and thrust reference, but with the addition of a current that linearly increases the mean value of  $V_a$  from 0m/s at  $t = 5s$  to 3m/s at  $t = 105s$ . The results further demonstrate the good properties of the torque and power controllers. When the loading decreases due to the increased advance velocity, the controllers increase the shaft speed to keep the torque or power constant. The result is superior thrust production, in addition to reduced oscillations in torque and power.

### 3.18.3 Fundamental controllers with time-varying thrust reference

Figure 3.17 shows a comparison of the three fundamental controllers with a sinusoidal  $T_d$  of amplitude 50kN and period 50s. The mean submergence is  $h_0 = 6m$ . The propeller is subject to a current velocity of 0.5m/s (giving a positive  $V_a$ ) and irregular waves with  $H_s = 1m$ ,  $T_p = 7.6s$ , defined by 30 harmonic components extracted from the modified PM spectrum in (C.19). The wave-induced velocities are calculated from (C.33). The friction and inertia compensation schemes are used, but with a 20% error in both  $Q_{f0}$ ,  $Q_{f1}$ , and  $I_c$  when compared to the true parameters, i.e.  $Q_{f0} = 0.8Q_s$ ,  $Q_{f1} = 0.8K_\omega$ , and  $I_c = 0.8I_s$ . In addition, the torque controller is simulated without friction and inertia compensation. Figure 3.18 shows corresponding results with  $T_d$  of amplitude 200kN and period 70s. All the controllers track the thrust references satisfactory, except the pure torque controller. This shows the importance of the compensation schemes, and also that the compensation schemes work well in the presence of modelling errors. The singularity of the power controller for  $n = 0$  is clearly seen in the  $Q_m$  plots. The shaft speed controller has an overshoot in  $Q_m$  about the zero-crossing of  $n$ . This is mainly due to the static friction. However, inclusion of the friction compensation scheme does not remedy this problem. A small transient exists also for the torque controller, although much less apparent.

**Remark 3.10** *The reference generator gives a slight loss of amplitude in  $T_r$ , and also enforces a smoother zero-crossing of  $n$  when compared to the sinusoidal  $T_d$ .*

### 3.18.4 Combined controllers with time-varying thrust reference

As stated in Sections 3.13 and 3.15, the idea behind the combined QP and SQP controllers is to utilize the best properties of the various fundamental controllers.

Figure 3.19 shows time series where the QP controller  $w/Q_{ff} + Q_{if}$  is tested in regular waves with amplitude 2m and period 5s for a time-varying  $T_d$ , including two zero-crossings of  $n$ . The chosen weighting function parameters for

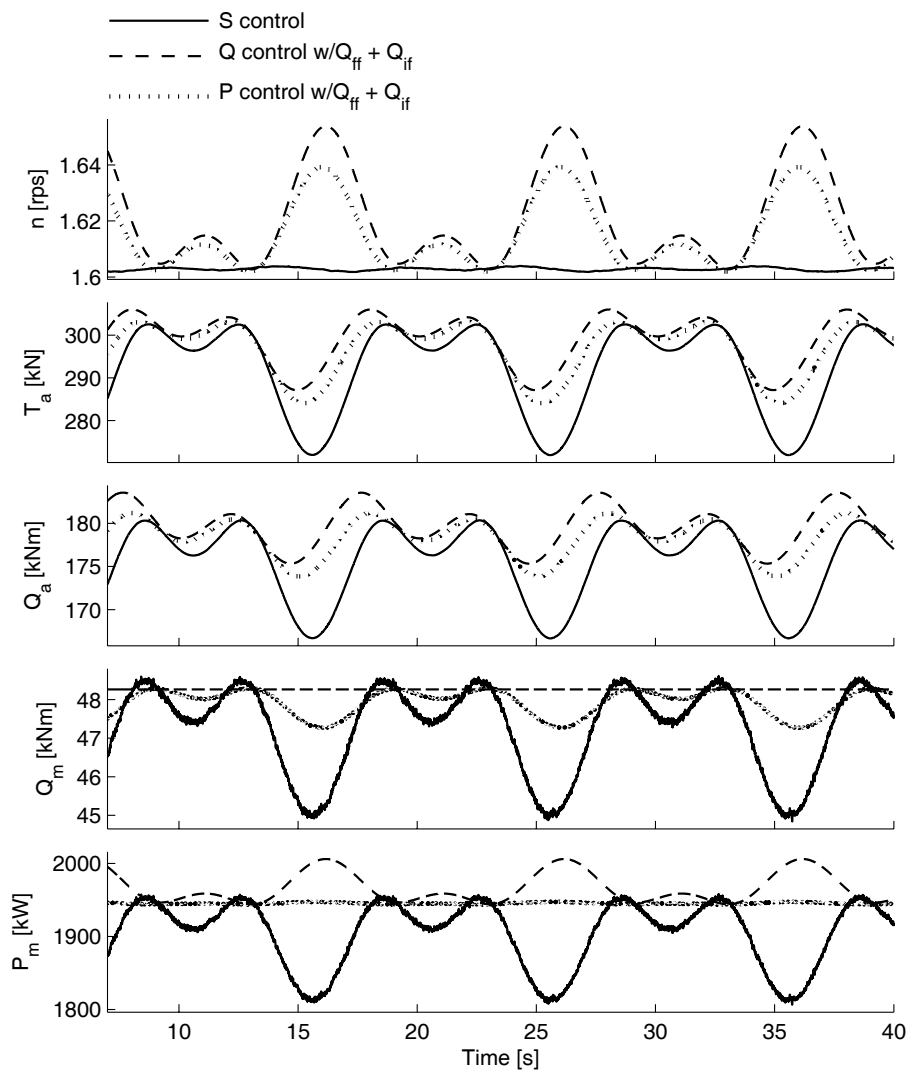


Figure 3.15: Comparison of shaft speed, torque, and power control for  $T_r = 300\text{kN}$  in harmonic waves.

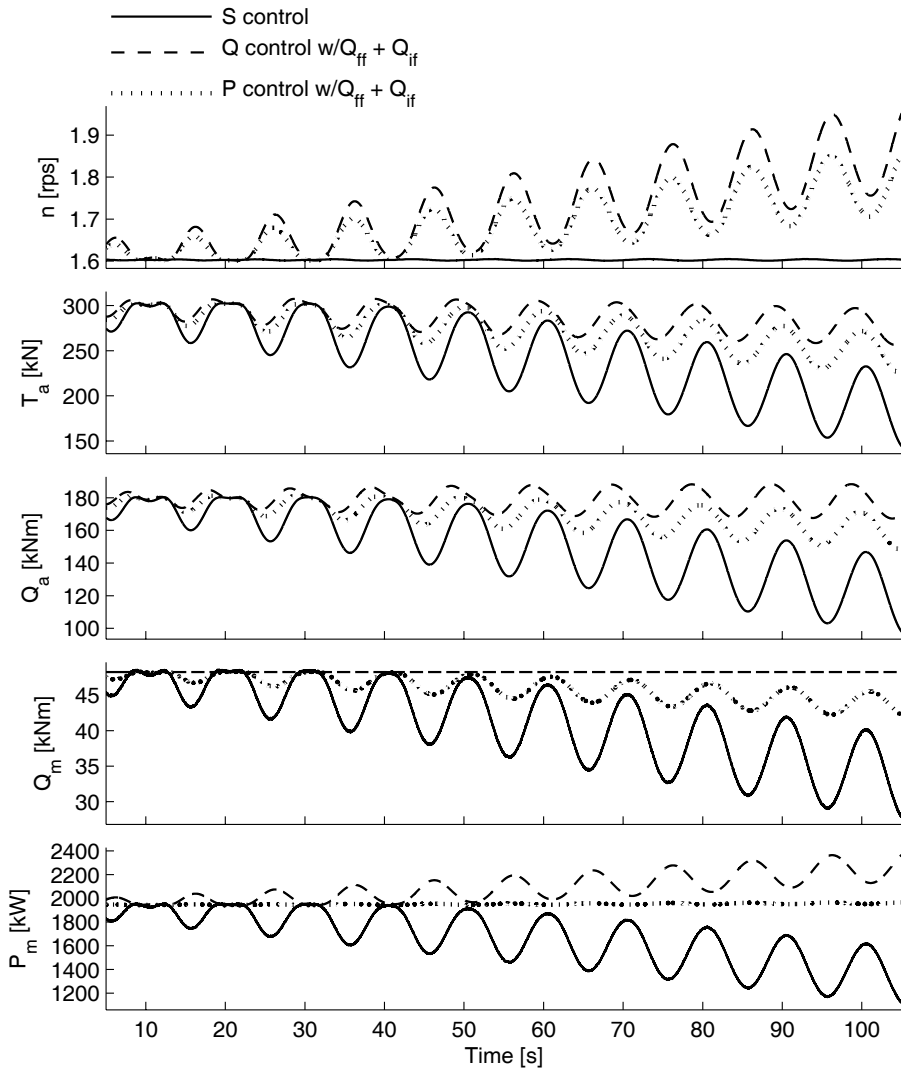


Figure 3.16: Comparison of shaft speed, torque, and power control for  $T_r = 300\text{kN}$  in harmonic waves and linearly increasing current.

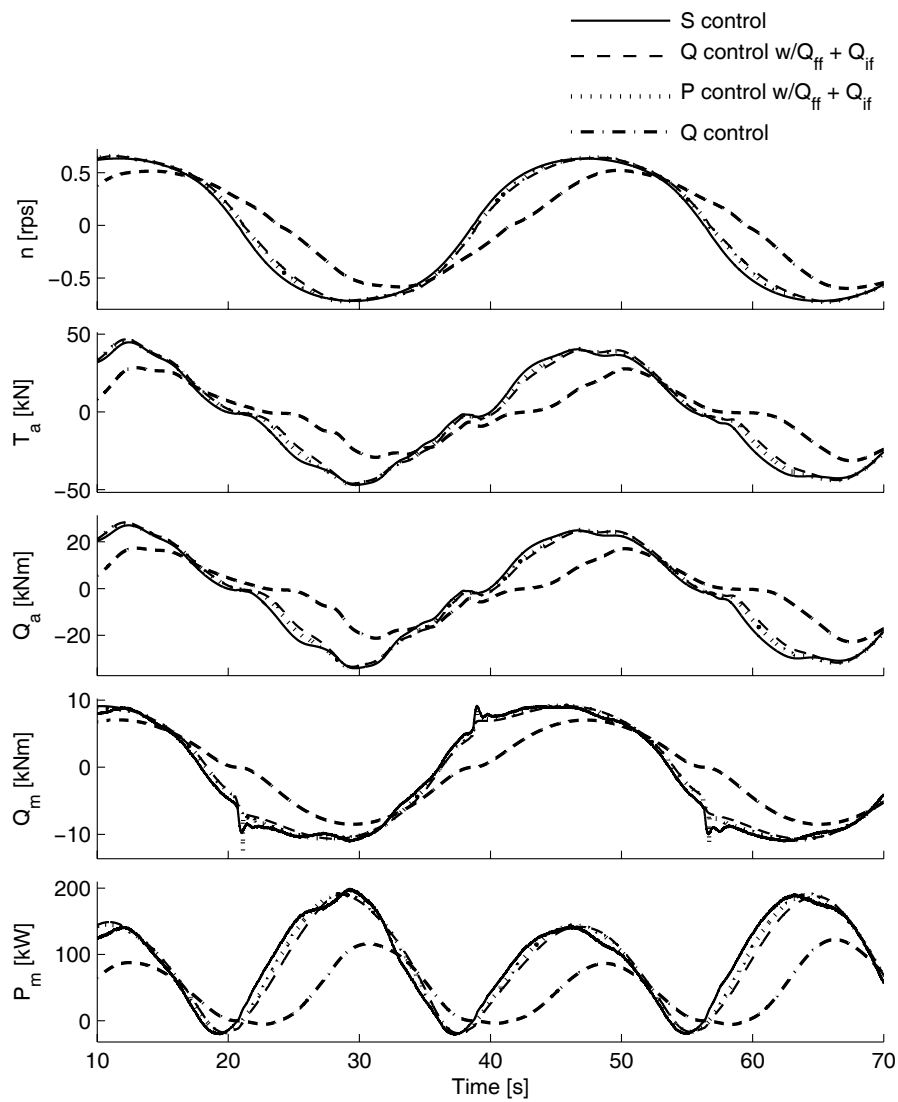


Figure 3.17: Comparison of shaft speed, torque, and power control for a simulated  $T_d$  with amplitude 50kN in irregular waves and 0.5m/s current, with 20% error in  $Q_{ff}$  and  $Q_{if}$ .

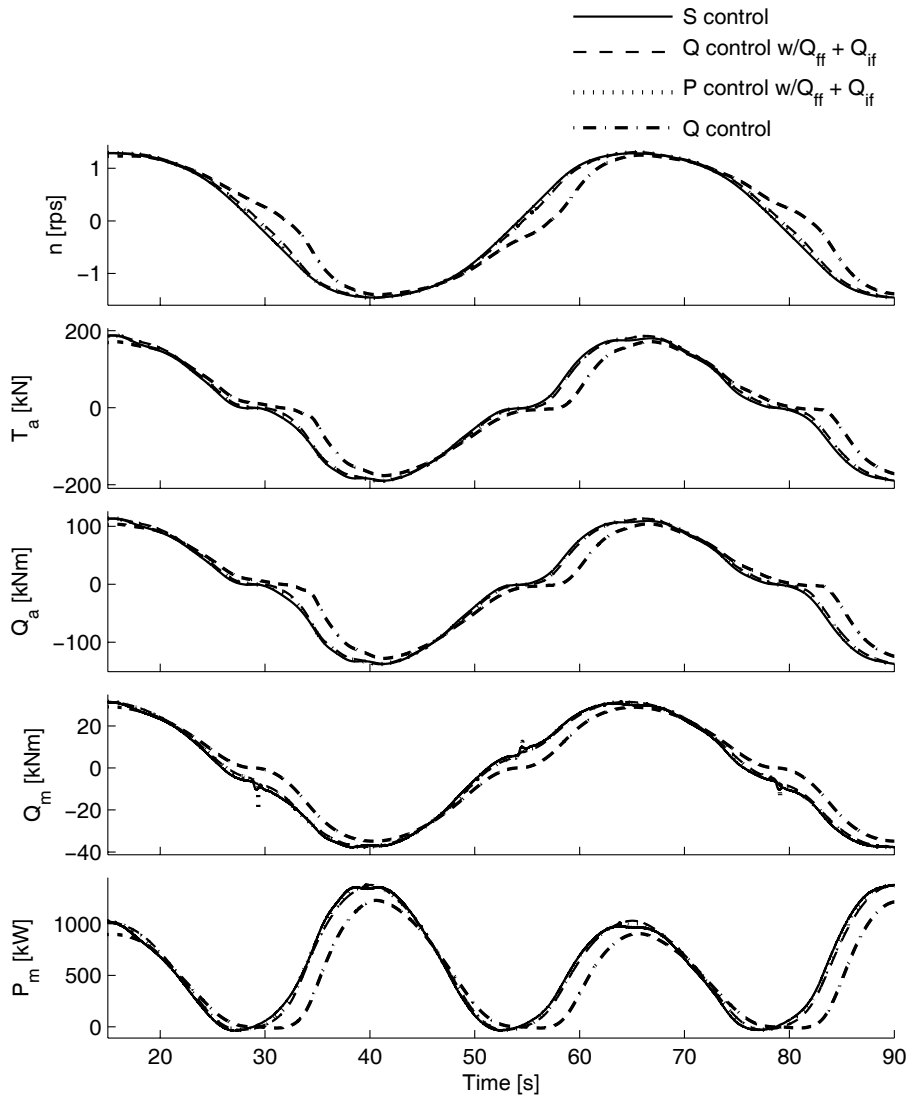


Figure 3.18: Comparison of shaft speed, torque, and power control for a sinusoidal  $T_d$  with amplitude 200kN in irregular waves and 0.5m/s current, with 20% error in  $Q_{ff}$  and  $Q_{if}$ .

$r$	$p$	$k$	Q ctr	P ctr
6	0.9	1	$ n  < 0.5$	$ n  > 1.5$

Table 3.6: Combined QP controller weighting function parameters for the 4MW Wageningen B4-70 example propeller.

Time interval	$T_d$	Corresp. $n_d$	Regime
$t < 20\text{s}$	50kN	$\approx 0.65\text{rps}$	Q ctr.
$20\text{s} < t < 35\text{s}$	300kN	$\approx 1.6\text{rps}$	P ctr.
$35\text{s} < t < 55\text{s}$	-30kN	$\approx -0.57\text{rps}$	Q ctr.
$55\text{s} < t < 100\text{s}$	300kN	$\approx 1.6\text{rps}$	P ctr.

Table 3.7: Desired thrust  $T_d$ , corresponding shaft speed  $n_d$ , and controller regimes for the combined QP controller simulation in Figure 3.19.

the QP controller in (3.36), as well as the implied range for pure Q and pure P control, are given in Table 3.6. The same 20% errors in the friction and inertia compensation schemes as in the previous section have been applied. The input  $T_d$  is given as specified in Table 3.7, where also the corresponding control regimes are given, and drawn by a dashed line in the thrust plot. When in Q control mode ( $t < 20\text{s}$ ), the expected oscillations in power are present, but cannot be seen in the figure due to the axis scaling. When in P control mode ( $t > 75\text{s}$ ), the oscillations in motor torque are barely visible, also here due to the axis scaling. The QP controller handles the two zero-crossings of  $n$  without any transients, and shifts from pure Q control to pure P control and back smoothly. The results also show that the reference generator works as intended, providing a smooth shaft speed reference with rate saturation.

Figure 3.20 shows time series where the SQP controller  $w/Q_{ff} + Q_{if}$  is tested in the same environmental conditions as the QP controller. The chosen weighting function parameters for the SQP controller in (3.48), as well as the implied range for pure S, pure Q, and pure P control are given in Table 3.8.  $T_d$  is given as specified in Table 3.9, where also the corresponding control regimes are given, and drawn by a dashed line in the thrust plot. The control regimes are also given in Table 3.9. Although it is difficult to make out the details in the figure, the simulations show that the SQP controller works as intended, and that the three controllers operate properly in the three control regimes. Some transients can be seen about the zero-crossings, apparently due to the static friction and high gains in the PI controller. The results also show that the control coefficient switch works seamlessly. Notice that a larger magnitude shaft speed is needed to produce negative thrust, since the propeller is asymmetric.

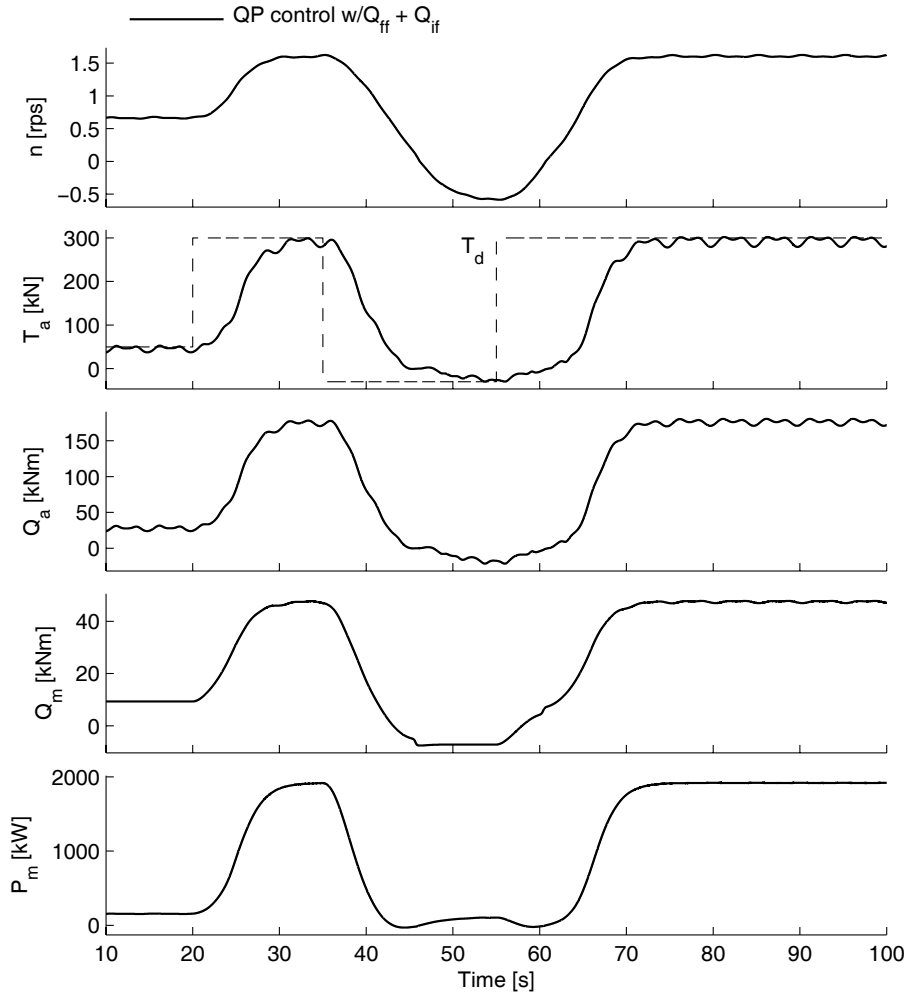


Figure 3.19: Time series of the combined QP controller in regular waves for a time-varying  $T_d$ .

$r$	$p$	$k$	$n_{s1}$	$n_{s3}$	S ctr	Q ctr	P ctr
4	4	2	0.3	1.1	$ n  < 0.3$	$0.64 <  n  < 1.1$	$ n  > 1.44$

Table 3.8: Combined SQP controller weighting function parameters for the 4MW Wageningen B4-70 example propeller.

Time interval	$T_d$	Corresp. $n_d$	Regime
$t < 20\text{s}$	10kN	$\approx 0.3\text{rps}$	S ctr.
$20\text{s} < t < 40\text{s}$	75kN	$\approx 0.8\text{rps}$	Q ctr.
$40\text{s} < t < 70\text{s}$	-75kN	$\approx -0.9\text{rps}$	Q ctr.
$70\text{s} < t < 100\text{s}$	350kN	$\approx 1.7\text{rps}$	P ctr.

Table 3.9: Desired thrust  $T_d$ , corresponding shaft speed  $n_d$ , and controller regimes for the combined SQP controller simulation in Figure 3.20.

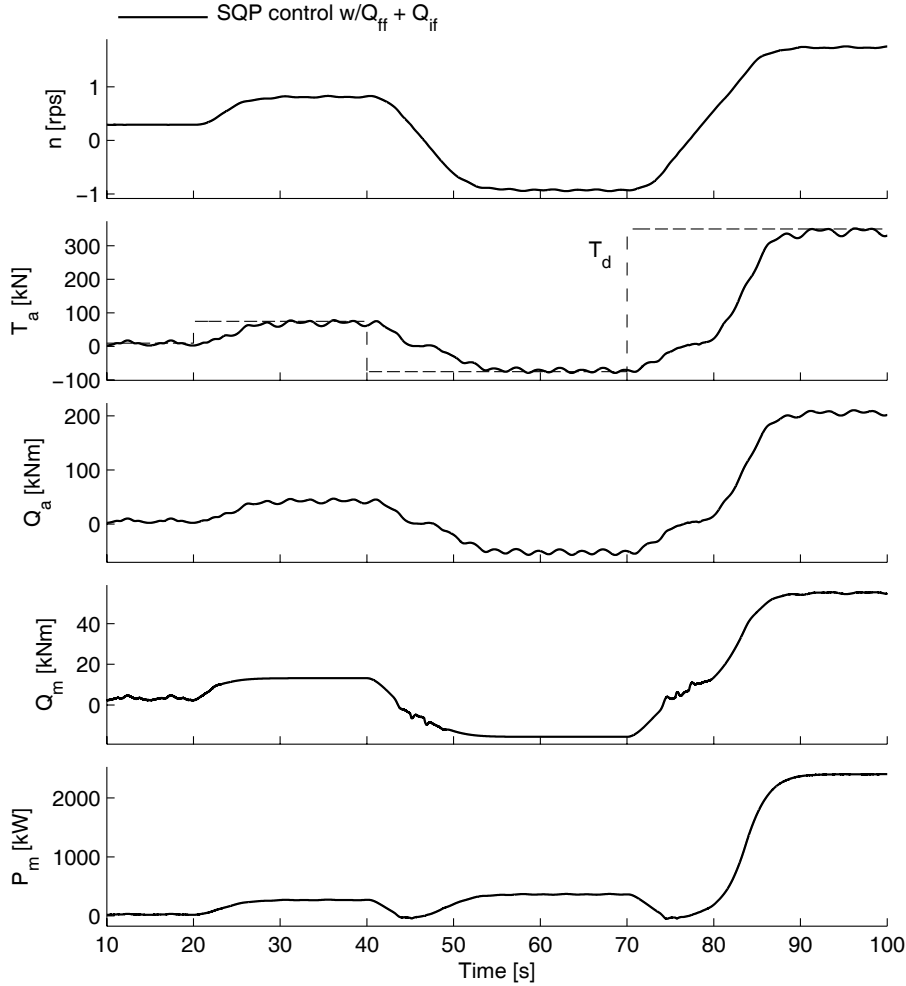


Figure 3.20: Time series of the combined SQP controller in regular waves for a time-varying  $T_d$ .

	Speed ctr.	Torque ctr.	Power ctr.
Thrust fluctuations	<i>Large</i>	<i>Small</i>	<i>Medium</i>
Torque fluctuations	<i>Large</i>	<i>Small</i>	<i>Medium</i>
Power fluctuations	<i>Large</i>	<i>Medium</i>	<i>Small</i>
Other issues	<i>Tuning</i>	<i>Power peaks</i>	<i>Singularity</i>
		<i>Friction</i>	<i>Friction</i>
		<i>Inertia</i>	<i>Inertia</i>

Table 3.10: Comparison of the main properties of the fundamental thruster controllers.

	Light load	Medium load	Heavy load
Thrust production	<i>High</i>	<i>High</i>	<i>High</i>
Mech. wear & tear	<i>Low</i>	<i>Medium</i>	<i>High</i>
Power fluctuations	<i>Low</i>	<i>Medium</i>	<i>High</i>
Friction/Inertia	<i>High</i>	<i>Low/Medium</i>	<i>Low</i>
Preferred ctr.	<i>Speed or Torque</i>	<i>Torque</i>	<i>Power</i>

Table 3.11: Summary of the relevance (low, medium, high) of the main performance criteria for light, medium, and heavy propeller loading.

### 3.19 Discussion

This chapter has presented several thruster controllers for normal operating conditions, including various additions like friction and inertia compensation, reference generators, and torque/power limiting. The controllers are summarized in Table 3.1. A summary of the main properties of the three fundamental controllers – shaft speed, torque, and power control – is given in Table 3.10. A summary of the relevance (low, medium, or high) of the main performance criteria for varying propeller loading is given in Table 3.11.

From these two tables, it is easy to motivate the construction of the combined controllers, i.e. QP, MQP1, MQP2, and SQP control:

- For medium propeller loading, the torque controller is preferable, and for high propeller loading the power controller is preferable. In these operating regimes, the knowledge of the friction and inertia parameters is of reduced importance. However, improved transient response and tracking properties is expected if the friction and inertia compensation schemes are used.
- For low propeller loading, torque or shaft speed control is preferable. If sufficient system knowledge to implement the friction and inertia compensation schemes is at hand, torque control will probably be sufficient. Then, the QP controller is a good choice. If the friction and inertia compensation schemes are implemented, but expected to be less accurate due to limited

	Small propellers	Large propellers
Friction	<i>Important</i>	<i>Less important</i>
Inertia	<i>Less important</i>	<i>Important</i>

Table 3.12: Importance of the friction and inertia compensation schemes for varying propeller sizes.

system knowledge, some kind of shaft speed control for low shaft speeds will be preferable. Then, the MQP1 or MQP2 controller is a good choice.

- If no inertia or friction compensation scheme is implemented, it is probably necessary to use shaft speed control for low to medium propeller loading, depending on the significance of the friction and inertia terms. In this case, the SQP controller may be the best option.

For small propellers, like thrusters on small underwater vehicles and propellers used in experimental setups, it is expected that the friction is of larger significance than the inertia. For large thrusters, the opposite is expected. Hence, it may not be necessary with both compensation schemes in all applications. The importance of the friction and inertia compensation schemes is summarized in Table 3.12.

The recommendations above should only serve as guidelines for the choice of controller. For some applications, other controllers than the ones presented here may be preferable. It is e.g. simple to construct a combined speed/power controller based on the SQP controller. In other applications, one of the fundamental controllers, i.e. S, Q, or P control, may be the better choice. In the literature, also other controllers – that may be more appropriate for the applications studied there – have been proposed, see the references listed in Section 3.4. Some additional control options, based on output feedback, are presented in Appendices E.3 and E.4.



## Chapter 4

# Sensitivity to thrust losses

The steady-state performance of the various control schemes introduced in Chapter 3 can be theoretically analyzed by establishing their sensitivity to thrust losses. Depending on the control scheme, a loss of propeller loading may, in addition to changes in propeller thrust and torque, lead to changes in shaft speed and power. The relationship between the *actual* and *reference* thrust, torque, shaft speed, and power are termed *sensitivity functions*:

$$\text{Thrust sensitivity: } st_i(n, \mathbf{x}_p, \boldsymbol{\theta}_p, T_r) \triangleq \frac{T_a}{T_r}. \quad (4.1)$$

$$\text{Speed sensitivity: } sn_i(n, \mathbf{x}_p, \boldsymbol{\theta}_p, T_r) \triangleq \frac{n}{n_r}. \quad (4.2)$$

$$\text{Torque sensitivity: } sq_i(n, \mathbf{x}_p, \boldsymbol{\theta}_p, T_r) \triangleq \frac{Q_a}{Q_r}. \quad (4.3)$$

$$\text{Power sensitivity: } sp_i(n, \mathbf{x}_p, \boldsymbol{\theta}_p, T_r) \triangleq \frac{P_a}{P_r}. \quad (4.4)$$

The index  $i$  indicates the type of controller:  $i = n$  for shaft speed control (Section 3.10),  $i = q$  for torque control (Section 3.11),  $i = p$  for power control (Section 3.12), and  $i = t$  for thrust control (Section 3.16). For notational simplicity, the arguments of the sensitivity functions will be omitted.  $n_r$ ,  $Q_r$ , and  $P_r$  are given from  $T_r$  by (3.1), (3.2), and (3.3), respectively.

When developing the sensitivity functions, it is assumed that all controllers obtain their objectives perfectly, i.e.  $n = n_r$  for shaft speed control,  $Q_a = Q_r$  for torque control,  $P_a = P_r$  for power control, and  $T_a = T_r$  for thrust control. It has hence been assumed that the friction is perfectly compensated for in torque and power control, i.e.  $Q_{ff} = Q_f$ . In Appendix F it is shown how this assumption may be relaxed. The sensitivity function concept was introduced in Sørensen *et al.* (1997) and Strand (1999), where the thrust sensitivity function  $st_i(\cdot)$  was used to analyze the properties of shaft speed, torque, and power control. The current presentation of the thrust sensitivity functions differs slightly from the original formulations. The sensitivity analysis is mainly of interest for the

fundamental thruster controllers, i.e. shaft speed, torque, and power control, as well as thrust control. The sensitivities of the other controllers in Table 3.1 may be directly inferred from the sensitivity of the fundamental controllers, depending on the chosen weighting functions.

The sensitivity analysis can only be used to evaluate the quasi-static performance of the various control schemes. To gain insight into the transient performance of the controllers, Section 4.10 presents a stability analysis based on Lyapunov theory.

**Remark 4.1** As mentioned in Section 3.16, the thrust controller requires additional instrumentation or a complex output feedback formulation, and is hence of limited industrial relevance. This is further discussed in Appendix E.2.1 and Appendix E.3.1. The sensitivity functions for thrust control are still derived, since it is interesting to analyze its properties alongside the fundamental controllers.

## 4.1 Thrust, torque, power, and shaft speed relations

In the following, the relationships between thrust, torque, power, and shaft speed will be needed. The shaft speed  $n$  can be expressed in terms of the thrust  $T_a$  or the torque  $Q_a$  by inverting (2.3) and (2.4):

$$n = \text{sign}(T_a) \sqrt{\frac{|T_a|}{\rho D^4 K_T}}, \quad (4.5)$$

$$n = \text{sign}(Q_a) \sqrt{\frac{|Q_a|}{\rho D^5 K_Q}}. \quad (4.6)$$

From (2.5), the magnitude of the shaft speed is expressed in terms of  $P_a$  by:

$$|n| = \frac{P_a^{1/3}}{(2\pi K_Q \rho)^{1/3} D^{5/3}}. \quad (4.7)$$

The thrust  $T_a$  can be expressed in terms of the torque  $Q_a$  by eliminating  $\text{sign}(n)\rho n^2 D^4$  between (2.3) and (2.4):

$$T_a = \frac{K_T}{K_Q D} Q_a. \quad (4.8)$$

Similarly,  $T_a$  can be expressed in terms of  $P_a$  by eliminating  $\text{sign}(n)\rho n^2 D^4$  between (2.3) and (2.5) and inserting (4.5):

$$|T_a| = \frac{\rho^{1/3} D^{2/3} K_T}{(2\pi)^{2/3} K_Q^{2/3}} P_a^{2/3}. \quad (4.9)$$

Finally,  $Q_a$  can be expressed in terms of  $P_a$  by inserting (4.6) in (2.5):

$$|Q_a| = \frac{\rho^{1/3} D^{5/3} K_Q^{1/3}}{(2\pi)^{2/3}} P_a^{2/3}. \quad (4.10)$$

The shaft speed, torque, and power mappings in (3.1), (3.2), and (3.3) can be used to establish the following relationships between the references  $T_r$ ,  $P_r$ ,  $Q_r$ , and  $n_r$ :

$$T_r = K_{TC} \rho D^4 n_r |n_r|, \quad (4.11)$$

$$Q_r = K_{QC} \rho D^5 n_r |n_r|, \quad (4.12)$$

$$P_r = 2\pi K_{QC} \rho D^5 |n_r|^3. \quad (4.13)$$

## 4.2 Thrust sensitivity

### 4.2.1 Shaft speed control thrust sensitivity

Assuming perfect control at steady state, i.e.  $n = n_r$ , the shaft speed is given in terms of  $T_r$  from (3.27):

$$n = n_r = \text{sign}(T_r) \sqrt{\frac{|T_r|}{\rho D^4 K_{TC}}}. \quad (4.14)$$

The actual thrust for shaft speed control is then given from (2.3) and (4.14):

$$T_a = \text{sign}(T_r) K_{TC} \rho D^4 \frac{|T_r|}{\rho D^4 K_{TC}} = \frac{K_T}{K_{TC}} T_r, \quad (4.15)$$

and the sensitivity function for shaft speed control  $st_n(\cdot)$  is:

$$st_n(\cdot) = \frac{T_a}{T_r} = \frac{K_T}{K_{TC}}. \quad (4.16)$$

### 4.2.2 Torque control thrust sensitivity

Assuming perfect control at steady state, i.e.  $Q_a = Q_r$ , the propeller torque is given in terms of  $T_r$  from (3.2):

$$Q_a = Q_r = \frac{K_{QC}}{K_{TC}} D T_r. \quad (4.17)$$

The actual thrust for torque control is expressed in terms of  $T_r$  by inserting (4.17) in (4.8):

$$T_a = \frac{K_T}{K_Q D} Q_a = \frac{K_{QC}}{K_Q} \frac{K_T}{K_{TC}} T_r, \quad (4.18)$$

and the sensitivity function for torque control  $st_q(\cdot)$  is:

$$st_q(\cdot) = \frac{T_a}{T_r} = \frac{K_T}{K_{TC}} \frac{K_{QC}}{K_Q}. \quad (4.19)$$

### 4.2.3 Power control thrust sensitivity

Assuming perfect control at steady state, i.e.  $P_a = P_r$ , the propeller power is given in terms of  $T_r$  from (3.32):

$$P_a = P_r = Q_r 2\pi n_r = |T_r|^{3/2} \frac{2\pi K_{QC}}{\sqrt{\rho} D K_{TC}^{3/2}}. \quad (4.20)$$

The actual thrust for power control is expressed in terms of  $T_r$  by inserting (4.20) in (4.9):

$$|T_a| = \left( \frac{\sqrt{\rho} D K_T^{3/2}}{K_Q 2\pi} P_a \right)^{2/3} = \frac{K_T}{K_{TC}} \frac{K_{QC}^{2/3}}{K_Q^{2/3}} |T_r|. \quad (4.21)$$

Assuming that the signs of the reference and produced thrust are equal, i.e.  $\text{sign}(T_a) = \text{sign}(T_r)$ , the sensitivity function for power control  $st_p(\cdot)$  is:

$$st_p(\cdot) = \frac{T_a}{T_r} = \frac{K_T}{K_{TC}} \left( \frac{K_{QC}}{K_Q} \right)^{2/3}. \quad (4.22)$$

### 4.2.4 Thrust control thrust sensitivity

If a thrust feedback or thrust output feedback controller is used, the thrust sensitivity function  $st_t(\cdot)$  by definition becomes unity:

$$st_t(\cdot) = 1, \quad (4.23)$$

since  $T_a \equiv T_r$  when perfect control is assumed.

### 4.2.5 Combined torque/power control thrust sensitivity

The analysis of the sensitivity of the combined torque/power controller is not as straightforward as in the preceding cases. However, since the combined controller is a linear combination of the torque and power controllers, it is a reasonable assumption that its sensitivity function  $st_c(\cdot)$  may be expressed as:

$$st_c(\cdot) = \frac{K_T}{K_{TC}} \left( \frac{K_{QC}}{K_Q} \right)^\kappa, \quad \text{for } \kappa \in [\frac{2}{3}, 1], \quad (4.24)$$

such that for high  $n$ ,  $st_c(\cdot) \approx st_p(\cdot)$  and for low  $n$ ,  $st_c(\cdot) \approx st_q(\cdot)$ . In Appendix F.1, it is shown that a good approximation of  $\kappa$  is given by

$$\kappa \approx 2/3 + 1/3\alpha_c(n), \quad (4.25)$$

where  $\alpha_c(n)$  is the combined controller weighting function, as used in (3.36). For analysis purposes, the following approximation to the combined controller thrust sensitivity function can therefore be used:

$$st_c(\cdot) \approx \frac{\beta_{TC}}{\beta_{QC}^{2/3+1/3\alpha_c(n)}}. \quad (4.26)$$

Through  $\alpha_c(n)$ ,  $st_c(\cdot)$  depends on the shaft speed  $n$ , which makes it less convenient for analysis. However, it is clear that  $st_c(\cdot)$  will lie in-between  $st_q(\cdot)$  and  $st_p(\cdot)$  for all  $n$ .

### 4.3 Shaft speed sensitivity

The shaft speed sensitivity function for shaft speed control  $sn_n(\cdot)$  is:

$$sn_n(\cdot) = \frac{n}{n_r} = \frac{n_r}{n_r} = 1, \quad (4.27)$$

since in this case  $n = n_r$ . Using (4.6) and (3.2), the shaft speed for torque control is expressed in terms of  $T_r$  by:

$$n = \text{sign}(Q_a) \sqrt{\frac{|Q_a|}{\rho D^5 K_Q}} = \text{sign}(T_r) \frac{K_{QC}^{1/2} |T_r|^{1/2}}{\rho^{1/2} D^2 K_Q^{1/2} K_{TC}^{1/2}}, \quad (4.28)$$

and the shaft speed sensitivity function for torque control  $sn_q(\cdot)$  is:

$$sn_q(\cdot) = \frac{n}{n_r} = \frac{\text{sign}(T_r) \sqrt{\frac{K_{QC} |T_r|}{K_{TC} \rho D^4 K_Q}}}{\text{sign}(T_r) \sqrt{\frac{|T_r|}{\rho D^4 K_{TC}}}} = \sqrt{\frac{K_{QC}}{K_Q}}. \quad (4.29)$$

Using (4.7) and (3.4) the shaft speed for power control is expressed in terms of  $T_r$  by:

$$|n| = \frac{P_a^{1/3}}{(2\pi K_Q \rho)^{1/3} D^{5/3}} = \frac{K_{QC}^{1/3}}{\rho^{1/2} D^2 K_{TC}^{1/2} K_Q^{1/3}} |T_r|^{1/2}. \quad (4.30)$$

Assuming  $\text{sign}(n) = \text{sign}(n_r)$ , the shaft speed sensitivity function for power control  $sn_p(\cdot)$  is:

$$sn_p(\cdot) = \frac{|n|}{|n_r|} = \frac{\frac{K_{QC}^{1/3}}{\rho^{1/2} D^2 K_{TC}^{1/2} K_Q^{1/3}} |T_r|^{1/2}}{\left| \text{sign}(T_r) \sqrt{\frac{|T_r|}{\rho D^4 K_{TC}}} \right|} = \frac{K_{QC}^{1/3}}{K_Q^{1/3}}. \quad (4.31)$$

From (4.5), the shaft speed for thrust control is:

$$n = \text{sign}(T_a) \sqrt{\frac{|T_a|}{\rho D^4 K_T}} = \text{sign}(T_r) \sqrt{\frac{|T_r|}{\rho D^4 K_T}}, \quad (4.32)$$

and the shaft speed sensitivity function for thrust control  $sn_t(\cdot)$  becomes:

$$sn_t(\cdot) = \frac{n}{n_r} = \frac{\text{sign}(T_r) \sqrt{\frac{|T_r|}{\rho D^4 K_T}}}{\text{sign}(T_r) \sqrt{\frac{|T_r|}{\rho D^4 K_{TC}}}} = \sqrt{\frac{K_{TC}}{K_T}}. \quad (4.33)$$

## 4.4 Torque sensitivity

Using (2.4) and (3.1), the torque for shaft speed control is expressed in terms of  $T_r$  by:

$$Q_a = \text{sign}(n)K_Q\rho D^5 n^2 = \frac{K_Q\rho D^5 T_r}{\rho D^4 K_{TC}} = \frac{K_Q D}{K_{TC}} T_r, \quad (4.34)$$

and the torque sensitivity function for shaft speed control  $sq_n(\cdot)$  is:

$$sq_n(\cdot) = \frac{Q_a}{Q_r} = \frac{\frac{K_Q D}{K_{TC}} T_r}{\frac{K_{QC} D}{K_{TC}} T_r} = \frac{K_Q}{K_{QC}}. \quad (4.35)$$

In torque control,  $Q_a = Q_r$ , and hence the torque sensitivity function for torque control  $sq_q(\cdot)$  is:

$$sq_q(\cdot) = \frac{Q_a}{Q_r} = \frac{Q_r}{Q_r} = 1. \quad (4.36)$$

Using (4.10) and (3.4), the torque for power control is expressed in terms of  $T_r$  by:

$$|Q_a| = \frac{\rho^{1/3} D^{5/3} K_Q^{1/3}}{(2\pi)^{2/3}} P_a^{2/3} = \frac{D K_Q^{1/3} K_{QC}^{2/3}}{K_{TC}} |T_r|. \quad (4.37)$$

Assuming  $\text{sign}(Q_a) = \text{sign}(Q_r)$ , the torque sensitivity function for power control  $sq_p(\cdot)$  is:

$$sq_p(\cdot) = \frac{|Q_a|}{|Q_r|} = \frac{\frac{D K_Q^{1/3} K_{QC}^{2/3}}{K_{TC}} |T_r|}{\left| \frac{K_{QC} D}{K_{TC}} T_r \right|} = \frac{K_Q^{1/3}}{K_{QC}^{1/3}}. \quad (4.38)$$

From (4.8) and (3.2), the torque sensitivity for thrust control  $sq_t(\cdot)$  becomes:

$$sq_t(\cdot) = \frac{Q_a}{Q_r} = \frac{\frac{K_Q D}{K_{TC}} T_a}{\frac{K_{QC} D}{K_{TC}} T_r} = \frac{\frac{K_Q D}{K_{TC}} T_r}{\frac{K_{QC} D}{K_{TC}} T_r} = \frac{K_Q}{K_{QC}} \frac{K_{TC}}{K_T}. \quad (4.39)$$

## 4.5 Power sensitivity

Using (2.5) and (3.1), the power for shaft speed control is expressed in terms of  $T_r$  by:

$$P_a = \text{sign}(n)2\pi K_Q \rho D^5 n^3 = \frac{2\pi K_Q}{\rho^{1/2} D K_{TC}^{3/2}} |T_r|^{3/2}, \quad (4.40)$$

and the power sensitivity function for shaft speed control  $sp_n(\cdot)$  is:

$$sp_n(\cdot) = \frac{P_a}{P_r} = \frac{K_Q}{K_{QC}}. \quad (4.41)$$

Using (4.10) and (3.2), the power for torque control is expressed in terms of  $T_r$  by:

$$P_a = \frac{2\pi}{\rho^{1/2} D^{5/2} K_Q^{1/2}} |Q_a|^{3/2} = \frac{2\pi K_{QC}^{3/2}}{\rho^{1/2} D K_Q^{1/2} K_{TC}^{3/2}} |T_r|^{3/2}, \quad (4.42)$$

and the power sensitivity function for torque control  $sp_q(\cdot)$  is:

$$sp_q(\cdot) = \frac{P_a}{P_r} = \frac{K_{QC}^{1/2}}{K_Q^{1/2}}. \quad (4.43)$$

In power control  $P_a = P_r$ , and hence the power sensitivity function for power control  $sp_p(\cdot)$  is:

$$sp_p(\cdot) = \frac{P_a}{P_r} = \frac{P_r}{P_r} = 1. \quad (4.44)$$

From (4.9) and (3.4), the power sensitivity function for thrust control  $sp_t(\cdot)$  becomes:

$$sp_t(\cdot) = \frac{P_a}{P_r} = \frac{\frac{2\pi K_Q}{\rho^{1/2} D K_T^{3/2}} |T_a|^{3/2}}{\frac{2\pi K_{QC}}{\rho^{1/2} D K_{TC}^{3/2}} |T_r|^{3/2}} = \frac{\frac{K_Q}{K_T^{3/2}} |T_r|^{3/2}}{\frac{K_{QC}}{K_{TC}^{3/2}} |T_r|^{3/2}} = \frac{K_Q}{K_{QC}} \frac{K_{TC}^{3/2}}{K_T^{3/2}}. \quad (4.45)$$

## 4.6 Sensitivity function summary

The various sensitivity functions are summarized in Table 4.1. If the control parameters  $K_{TC}$  and  $K_{QC}$  are replaced with the nominal parameters  $K_{T0}$  and  $K_{Q0}$ , as is proposed for thruster control in low-speed applications, the sensitivity functions may be expressed in terms of the thrust and torque loss factors  $\beta_T$  and  $\beta_Q$  from (2.11) and (2.12). This is summarized in Table 4.2.

**Remark 4.2** It is interesting to note that if the controllers have knowledge of the instantaneous values of  $K_T$  and  $K_Q$ , such that  $K_{TC} = K_T$  and  $K_{QC} = K_Q$  at all times, all the sensitivity functions in Table 4.1 reduce to unity. This means that all controllers perform identically.

Intuitively, the various sensitivity functions should be interrelated, regardless of the chosen controller. This is also the case, as can be found by inserting (2.3), (2.4), (2.5), (4.11), (4.12), and (4.13) in (4.1), (4.3), and (4.4), and inserting for (4.2):

$$st_i(\cdot) = \frac{\rho D^4 K_T n^2}{\rho D^4 K_{TC} n_r^2} = \beta_T sn_i(\cdot)^2, \quad (4.46)$$

$$sq_i(\cdot) = \frac{\rho D^5 K_Q n^2}{\rho D^5 K_{QC} n_r^2} = \beta_Q sn_i(\cdot)^2, \quad (4.47)$$

$$sp_i(\cdot) = \frac{2\pi \rho D^5 K_Q n^3}{2\pi \rho D^5 K_{QC} n_r^3} = \beta_Q sn_i(\cdot)^3. \quad (4.48)$$

Sensitivity	Speed control	Torque control
Thrust	$st_n(\cdot) = \frac{K_T}{K_{TC}}$	$st_q(\cdot) = \frac{K_T}{K_{TC}} \frac{K_{QC}}{K_Q}$
Speed	$sn_n(\cdot) = 1$	$sn_q(\cdot) = (\frac{K_{QC}}{K_Q})^{1/2}$
Torque	$sq_n(\cdot) = \frac{K_Q}{K_{QC}}$	$sq_q(\cdot) = 1$
Power	$sp_n(\cdot) = \frac{K_Q}{K_{QC}}$	$sp_q(\cdot) = (\frac{K_{QC}}{K_Q})^{1/2}$

Sensitivity	Power control	Thrust control
Thrust	$st_p(\cdot) = \frac{K_T}{K_{TC}} (\frac{K_{QC}}{K_Q})^{2/3}$	$st_t(\cdot) = 1$
Speed	$sn_p(\cdot) = (\frac{K_{QC}}{K_Q})^{1/3}$	$sn_t(\cdot) = (\frac{K_{TC}}{K_T})^{1/2}$
Torque	$sq_p(\cdot) = (\frac{K_Q}{K_{QC}})^{1/3}$	$sq_t(\cdot) = \frac{K_Q}{K_{QC}} \frac{K_{TC}}{K_T}$
Power	$sp_p(\cdot) = 1$	$sp_t(\cdot) = \frac{K_Q}{K_{QC}} (\frac{K_{TC}}{K_T})^{3/2}$

Table 4.1: Thrust, torque, power, and shaft speed sensitivity functions defined in terms of  $K_{TC}$ ,  $K_{QC}$ ,  $K_T$ , and  $K_Q$ .

Sensitivity	Speed ctr.	Torque ctr.	Power ctr.	Thrust ctr.
Thrust	$st_n(\cdot) = \beta_T$	$st_q(\cdot) = \frac{\beta_T}{\beta_Q}$	$st_p(\cdot) = \frac{\beta_T}{\beta_Q^{2/3}}$	$st_t(\cdot) = 1$
Speed	$sn_n(\cdot) = 1$	$sn_q(\cdot) = \frac{1}{\beta_Q^{1/2}}$	$sn_p(\cdot) = \frac{1}{\beta_Q^{1/3}}$	$sn_t(\cdot) = \frac{1}{\beta_T^{1/2}}$
Torque	$sq_n(\cdot) = \beta_Q$	$sq_q(\cdot) = 1$	$sq_p(\cdot) = \beta_Q^{1/3}$	$sq_t(\cdot) = \frac{\beta_Q}{\beta_T}$
Power	$sp_n(\cdot) = \beta_Q$	$sp_q(\cdot) = \frac{1}{\beta_Q^{1/2}}$	$sp_p(\cdot) = 1$	$sp_t(\cdot) = \frac{\beta_Q}{\beta_T^{3/2}}$

Table 4.2: Sensitivity functions defined in terms of the thrust and torque loss factors  $\beta_T$  and  $\beta_Q$ , under the assumption that  $K_{TC} = K_{T0}$  and  $K_{QC} = K_{Q0}$ .

From (4.47) and (4.48), it is also clear that:

$$sp_i(\cdot) = sq_i(\cdot)sn_i(\cdot), \quad (4.49)$$

as could have been expected. These relationships can also be verified for the individual controllers in Tables 4.1 and 4.2.

## 4.7 Steady-state performance

The steady-state performance of the various control schemes during a loss incident is conveniently analyzed with the sensitivity functions. However, the validity of the sensitivity functions rely on the steady-state values of  $\beta_T$  and  $\beta_Q$  being correct. This is not necessarily trivial, since  $\beta_T$  and  $\beta_Q$  in general depend on  $n$ , and for the same operating conditions therefore will change between the different controllers.

For the shaft speed controller (assuming that  $n = n_r$ ),  $\beta_T$  and  $\beta_Q$  are given directly. For the torque controller (assuming that  $Q_a = Q_r$ ), the analysis

becomes more complicated, because the resulting shaft speed is unknown. The loss factor  $\beta_Q = \beta_Q(\cdot, n)$  and the shaft speed must satisfy:

$$Q_r = Q_a = K_Q \rho n^2 D^5 = K_{Q0} \rho n^2 D^5 \beta_Q(\cdot, n), \quad (4.50)$$

where  $n$  is unknown. If  $\beta_Q(\cdot, n)$  can be expressed in terms of  $n$ , an analytical solution might be found. In the general case however, this is not possible, and  $n$  must be found by iteration. For the power controller (assuming  $P_a = P_r$ ), the analysis becomes similar as for torque control, but now the equation that must be satisfied is:

$$P_r = P_a = K_Q \rho n^2 D^5 2\pi n = 2\pi K_{Q0} \rho n^3 D^5 \beta_Q(\cdot, n). \quad (4.51)$$

If an iterative analysis is performed for the combined controller, the equation that has to be satisfied is (assuming  $Q_{cc} = Q_a$ ):

$$\alpha_c(n) Q_r + (1 - \alpha_c(n)) \frac{P_{rs}}{2\pi|n|} = K_{Q0} \rho n^2 D^5 \beta_Q(\cdot, n).$$

In thrust control, the equation to be satisfied is (assuming  $T_r = T_a$ ):

$$T_r = K_{T0} \rho n^2 D^4 \beta_T(\cdot, n). \quad (4.52)$$

**Remark 4.3** *The iterative solution procedure used to arrive at the correct steady-state sensitivity values can be viewed as an extension of the original presentation in Sørensen et al. (1997) and Strand (1999), where the influence of  $n$  on  $\beta_T$  and  $\beta_Q$  was not considered.*

## 4.8 Sensitivity to changes in advance velocity

Using the iterative solution procedure described above, the sensitivity to changes in advance velocity may be analyzed by expressing the various sensitivity functions as functions of  $V_a$  for given  $T_r$ . This is done in Figures 4.1 to 4.4 for the Wageningen B4-70 example propeller (see Figure 2.1 and Appendix A). The thrust references  $T_r = 50$ , 200, and 400kN have been chosen. The curves for  $T_r = 50$ kN stop at  $V_a \approx 2.7$ m/s, since the propeller here starts windmilling for shaft speed control, i.e. the thrust becomes negative. Figure 4.1 shows the thrust sensitivity functions  $st_n(\cdot)$  for shaft speed control,  $st_q(\cdot)$  for torque control, and  $st_p(\cdot)$  for power control. Clearly, the torque controller is the least sensitive to changes in  $V_a$ , the shaft speed controller the most sensitive, and the power controller in-between. This shows that the torque and power controllers will give significantly better thrust production than the shaft speed controller when subject to disturbances in  $V_a$ . Figure 4.2 shows the shaft speed sensitivity functions  $sn_n(\cdot)$  for shaft speed control,  $sn_q(\cdot)$  for torque control, and  $sn_p(\cdot)$  for power control. From this, it is clear that the torque and power controller achieve the increased thrust by increasing the shaft speed as  $V_a$  increases. Figure 4.3

shows the torque sensitivity functions  $sq_n(\cdot)$  for shaft speed control,  $sq_q(\cdot)$  for torque control, and  $sq_p(\cdot)$  for power control. This confirms that the loading of the propeller decreases with  $V_a$  for shaft speed and power control, whereas it is kept constant in torque control – explaining why the thrust production is superior. Figure 4.4 shows the power sensitivity functions  $sp_n(\cdot)$  for shaft speed control,  $sp_q(\cdot)$  for torque control, and  $sp_p(\cdot)$  for power control. This shows that the power controller keeps the power consumption constant regardless of  $V_a$ , whereas the torque controller power consumption increases and the shaft speed controller power consumption decreases with  $V_a$ . If control of the power consumption is of major concern, the power controller will therefore be superior to the torque controller.

**Remark 4.4** *Figure 4.1 is conveniently used to illustrate how the integral action in the DP controller must be used to counteract the thrust losses with a given low-level controller. If e.g.  $T_r = 200\text{kN}$  and  $V_a = 2\text{m/s}$ , and shaft speed control is used, the thrust sensitivity becomes  $st_n \approx 0.7$ . Hence, there is a lack of 30% of the thrust. Since the shaft speed controller is unable to counteract this loss, the DP controller must increase the setpoint until  $T_a = T_r st_n(\cdot) = 200\text{kN}$ . From iteration, the resulting thrust setpoint can be found to be  $T_r \approx 270\text{kN}$ . In torque control, the thrust sensitivity is  $st_q \approx 0.94$ , and there is hence only a 6% lack of thrust. From iteration, the resulting thrust setpoint needed to achieve  $T_a = T_r st_q(\cdot) = 200\text{kN}$  is  $T_r \approx 212\text{kN}$ . In power control,  $st_p \approx 0.86$ , and the resulting thrust setpoint needed to achieve  $T_a = T_r st_p(\cdot) = 200\text{kN}$  is  $T_r \approx 230\text{kN}$ .*

**Remark 4.5** *The figures show that higher thrust references give less sensitivity to  $V_a$ . This is natural, since the loading of the propeller is less affected by a given  $V_a$  when the shaft speed increases.*

**Remark 4.6** *The power sensitivity function slope is for most  $V_a$  larger for shaft speed control than for torque control. This means that in a time-varying inflow, the oscillations in power will be larger for the shaft speed controller than for the torque controller.*

Figure 4.5 shows the thrust sensitivity function  $st_c(\cdot)$  for the combined controller as a function of  $T_r$ , together with  $st_n(\cdot)$ ,  $st_q(\cdot)$ , and  $st_p(\cdot)$ . The parameters for the weighting function  $\alpha_c(n_r)$  in the combined controller were chosen as  $r = 10$ ,  $p = 0.8$ , and  $k = 0.3$ , which gives pure torque control for  $n < 0.8$  rps and pure power control for  $n > 1.6$  rps. This is mirrored in  $st_c(\cdot)$ , which equals  $st_q(\cdot)$  for low  $T_r$  and  $st_p(\cdot)$  for high  $T_r$ .

#### 4.8.1 Non-dimensional parametrization for $V_a$ and $T_r$

In order to plot unique sensitivity functions for any combination of  $T_r$  and  $V_a$ , valid for any propeller diameter, an alternative approach using the *reference advance number*  $J_r$  exists. This approach will also remove the necessity of an

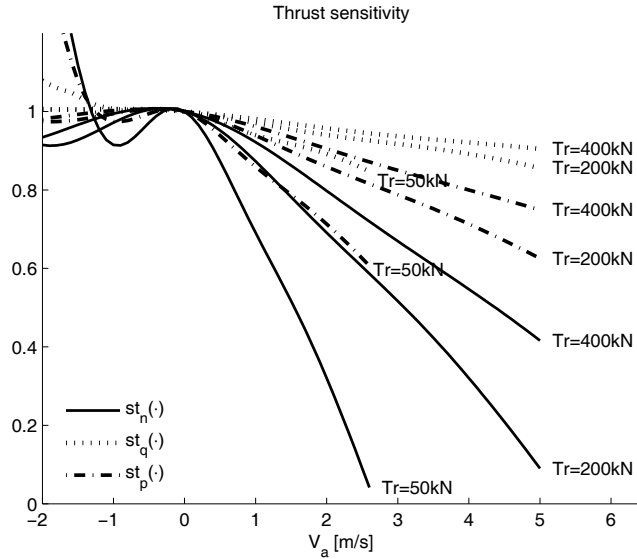


Figure 4.1: Thrust sensitivity  $st_n(\cdot)$  for shaft speed control,  $st_q(\cdot)$  for torque control, and  $st_p(\cdot)$  for power control as functions of advance velocity  $V_a$ .

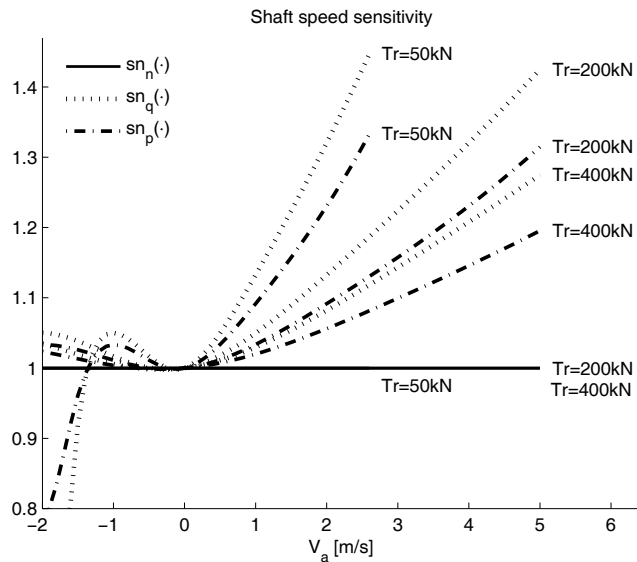


Figure 4.2: Shaft speed sensitivity  $sn_n(\cdot)$  for shaft speed control,  $sn_q(\cdot)$  for torque control, and  $sn_p(\cdot)$  for power control as functions of advance velocity  $V_a$ .

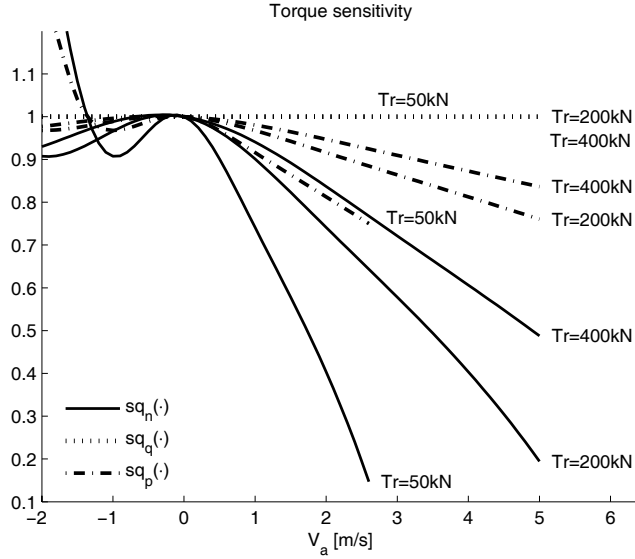


Figure 4.3: Torque sensitivity  $sq_n(\cdot)$  for shaft speed control,  $sq_q(\cdot)$  for torque control, and  $sq_p(\cdot)$  for power control as functions of advance velocity  $V_a$ .

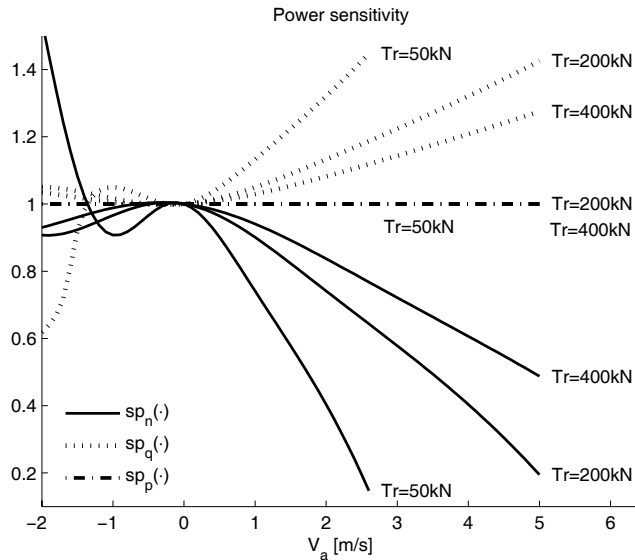


Figure 4.4: Power sensitivity  $sp_n(\cdot)$  for shaft speed control,  $sp_q(\cdot)$  for torque control, and  $sp_p(\cdot)$  for power control as functions of advance velocity  $V_a$ .

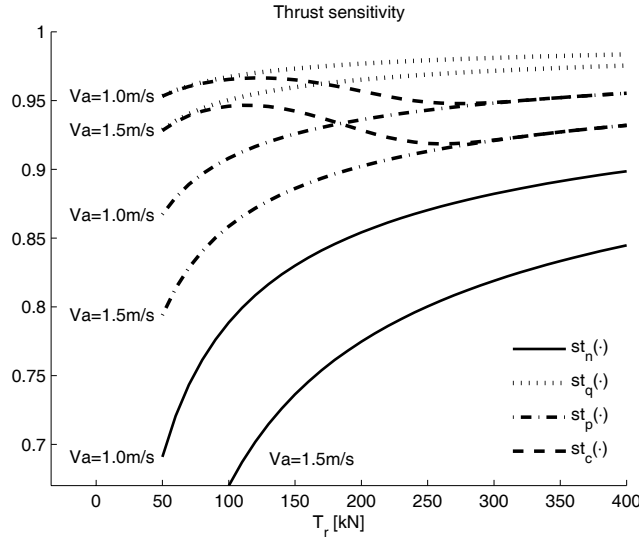


Figure 4.5: Thrust sensitivity  $sp_n(\cdot)$  for shaft speed control,  $sp_q(\cdot)$  for torque control,  $sp_p(\cdot)$  for power control, and  $sp_c(\cdot)$  for combined control as functions of thrust reference  $T_r$ .

iterative solution procedure.  $J_r$  is defined as:

$$J_r = \frac{V_a}{n_r D}, \quad (4.53)$$

where  $n_r$  is the reference shaft speed calculated from  $T_r$  using (3.1). The relationship between  $J_a$  in (2.16) and  $J_r$  is:

$$\frac{J_r}{J_a} = \frac{V_a n D}{n_r D V_a} = \frac{n}{n_r} \equiv sn_i(\cdot), \quad (4.54)$$

where  $sn_i(\cdot)$  is the shaft speed sensitivity function. Hence, for shaft speed control where  $n = n_r$  and  $sn_n(\cdot) = 1$ , the reference advance number  $J_{rn}$  is given by:

$$J_{rn} = J_a. \quad (4.55)$$

For torque and power control, however,  $n \neq n_r$  and  $J_a \neq J_r$ . In torque control the shaft speed sensitivity is given by (4.29), and the reference advance number for torque control,  $J_{rq}$ , is defined by

$$J_{rq} = J_a \sqrt{\frac{K_{QC}}{K_Q}}. \quad (4.56)$$

For a deeply submerged propeller, there is a particular value of  $K_Q$  for a given  $J_a$ , which again implies that there is a particular  $J_{rq}(J_a)$ :

$$J_{rq}(J_a) = J_a \sqrt{\frac{K_{QC}}{K_Q(J_a)}}. \quad (4.57)$$

Hence, it is possible to re-parameterize  $K_T$  and  $K_Q$  as functions of  $J_{rq}$  instead of  $J_a$  (i.e. given  $J_{rq}$ , there exists particular values of  $K_T$  and  $K_Q$ ). Furthermore, since  $J_{rq}$  is determined uniquely by  $V_a$  and  $T_r$ , the sensitivity functions for torque control are parameterized by  $J_{rq}$  using (4.57).

Using the shaft speed sensitivity function for power control in (4.31) and the same reasoning as for torque control,  $K_T$  and  $K_Q$  can be re-parameterized in the power control reference advance ratio  $J_{rp}(J_a)$ :

$$J_{rp}(J_a) = J_a \frac{K_{QC}^{1/3}}{K_Q(J_a)^{1/3}}. \quad (4.58)$$

For thrust control,  $K_T$  and  $K_Q$  can be re-parameterized in the thrust control reference advance ratio  $J_{rt}(J_a)$  by using (4.33):

$$J_{rt}(J_a) = J_a \sqrt{\frac{K_{TC}}{K_T(J_a)}}. \quad (4.59)$$

In order to establish the sensitivity functions without resorting to iteration, the following procedure can now be followed:

1. Choose the range of  $J_a$  for which to calculate the sensitivity function values.
2. For the chosen range of  $J_a$ , calculate the corresponding  $J_{rn}$  (speed control),  $J_{rq}$  (torque control),  $J_{rp}$  (power control), and  $J_{rt}$  (thrust control) from  $J_a$ ,  $K_T$ ,  $K_Q$ ,  $K_{TC}$ , and  $K_{QC}$  using the relationships defined in (4.55), (4.57), (4.58), and (4.59).
3. For each  $J_{ri}$ , calculate the sensitivity functions from  $K_T$  and  $K_Q$ .

What actually happens is that the advance ratio axis is scaled individually for each controller. Notice that neither  $T_r$ ,  $V_a$ , nor  $D$  appear explicitly in the calculations. Figures 4.6 to 4.9 show the thrust, shaft speed, torque, and power sensitivity functions for shaft speed, torque, power, and thrust control as functions of  $J_r$  for the Wageningen B4-70 propeller. These curves are hence generalizations of the curves shown in Figures 4.1 to 4.4, with the addition of the sensitivity functions for thrust control. If thrust control is a feasible solution, these curves show that the increased performance in thrust production is achieved by increasing the shaft speed, torque, and power additionally with respect to the torque controller.

**Remark 4.7** Since  $st_t(\cdot) = 1$  by definition, the sensitivity curves for thrust control are conveniently used to investigate how much the thrust setpoint must be increased to achieve a certain thrust for the various controllers, as discussed in Remark 4.4. Applying the same example, with  $T_r = 200\text{kN}$  and  $V_a = 2\text{m/s}$ , the shaft speed reference  $n_r \approx 1.31\text{rps}$  from (3.1), and the reference advance ratio from (4.53) becomes  $J_r \approx 0.38$ . For shaft speed control, Figure 4.7 shows that  $J_r \approx 0.38 \Rightarrow sn_t \approx 1.16$ . This means that in order to get  $T_a = 200\text{kN}$ ,  $n$  must be increased to  $n = n_r sn_t \approx 1.52$ . Mapping  $n$  back to  $T_r$  using (3.5), the resulting thrust reference is  $T_r \approx 270\text{kN}$ . Similarly, for torque control,  $Q_r \approx 120\text{kNm}$  from (3.2), and Figure 4.8 shows that  $J_r \approx 0.38 \Rightarrow sq_t \approx 1.06$ . This means that in order to get  $T_a = 200\text{kN}$ ,  $Q_a$  must be increased to  $Q_a = Q_r sq_t \approx 127\text{kN}$ . Mapping  $Q_a$  back to  $T_r$  using (3.6), the resulting thrust reference is  $T_r \approx 212\text{kN}$ . Finally, for power control,  $P_{rs} \approx 985\text{kW}$  from (3.4), and Figure 4.9 shows that  $J_r \approx 0.38 \Rightarrow spt \approx 1.23$ . This means that in order to get  $T_a = 200\text{kN}$ ,  $P_a$  must be increased to  $P_a = P_{rs} spt \approx 1212\text{kW}$ . Mapping  $P_a$  back to  $T_r$  using (3.7), the resulting thrust reference is  $T_r \approx 230\text{kN}$ .

**Remark 4.8** If some external integral action on  $T_r$  exists (e.g. a DP controller), such that  $T_r$  is increased until the desired  $T_a$  is produced, the mean values of  $T_a$ ,  $Q_a$ ,  $P_a$ , and  $n$  will be the same for all the controllers. Hence, also the sensitivity functions will have the same values. The differences between the controllers then lie in the responses to dynamic load changes due to e.g. waves and wave-frequency vessel motion, as well as the speed of convergence to the desired  $T_a$ .

#### 4.8.2 Friction compensation errors

In the derivation of the sensitivity functions, perfect friction compensation was assumed. However, since  $Q_{ff}$  is a function of  $n_r$  only, the linear compensation term is not adjusted when the shaft speed differs from  $n_r$ , as is the case in torque, power, and thrust control. This will give a small offset from the ideal sensitivity functions defined above, even with perfect model knowledge. In addition, if the static friction compensation term is wrong, such that  $Q_{f0} \approx Q_s$ , additional offsets from the ideal solutions are introduced. In either case, the sensitivity functions in terms of  $J_r$  will no longer be uniform for any  $V_a$ ,  $T_r$ , and  $D$ . Hence, the non-dimensional representation presented in Section 4.8.1 cannot be used. Appendix F.2 shows how the iterative solution procedure from Section 4.7 can be modified to account for the friction compensation errors, and how the errors affect the resulting sensitivity functions.

### 4.9 Sensitivity to large thrust losses

The sensitivity to the large thrust losses experienced during ventilation and water exits may also be analyzed with the sensitivity functions. This can be

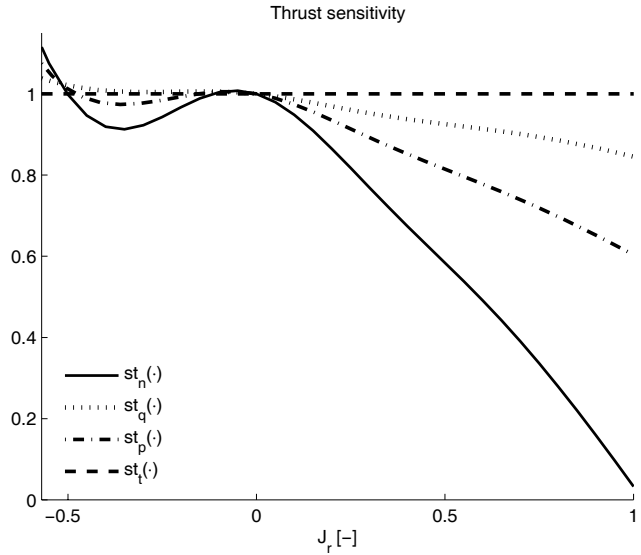


Figure 4.6: Thrust sensitivity for shaft speed, torque, power, and thrust control as functions of the reference advance number  $J_r$ .

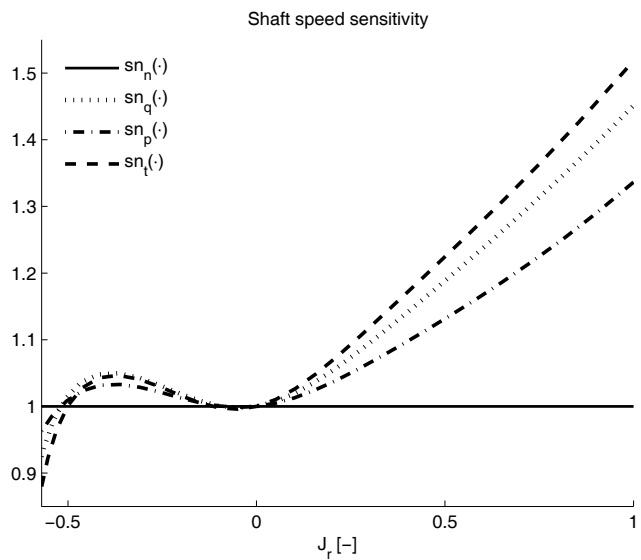


Figure 4.7: Shaft speed sensitivity for shaft speed, torque, power, and thrust control as functions of the reference advance number  $J_r$ .

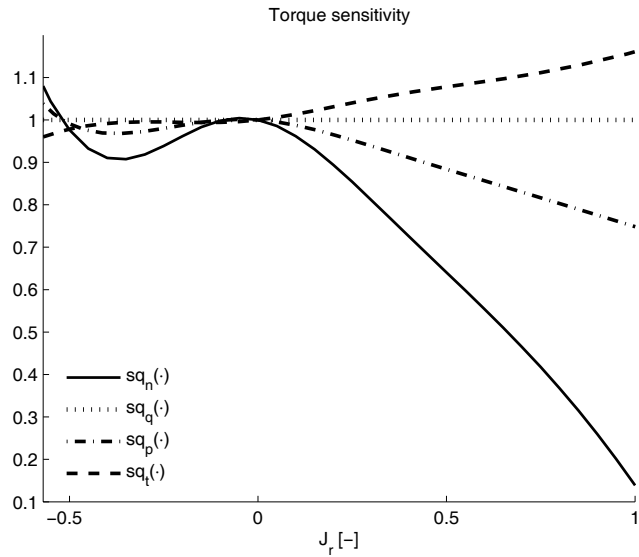


Figure 4.8: Torque sensitivity for shaft speed, torque, power, and thrust control as functions of the reference advance number  $J_r$ .

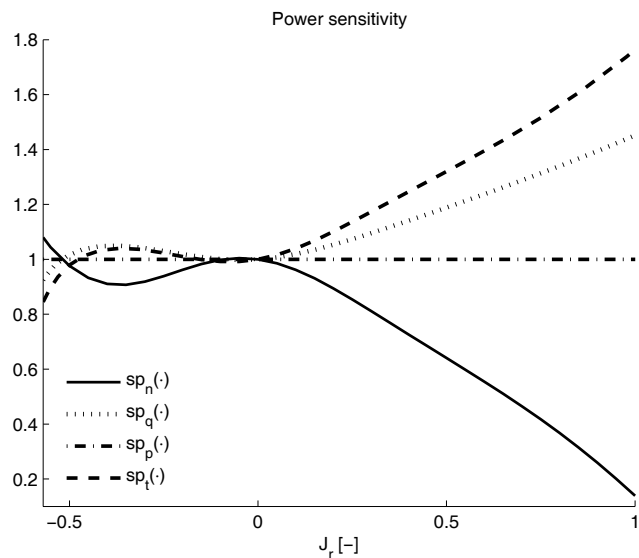


Figure 4.9: Power sensitivity for shaft speed, torque, power, and thrust control as functions of the reference advance number  $J_r$ .

done by using the steady-state iterative solution procedure described in Section 4.7, with  $\beta_Q$  and  $\beta_T$  defined by the ventilation loss models from Section 2.4.4. The analysis must be performed at a fixed  $h/R$ , such that  $\beta_Q = \beta_Q(n/n_{bp})$  and  $\beta_T = \beta_T(n/n_{bp})$ , where  $n_{bp}$  is the bollard pull shaft speed. Since ventilation and water exits in reality are dynamic processes, the sensitivity functions will only indicate the response of the propeller with different controllers – the resulting sensitivities will be steady-state values as could be found in e.g. a cavitation tunnel with fixed propeller submergence. Since the ventilation loss model is a function of  $n/n_{bp}$ , the shaft speed sensitivity  $sn_i(\cdot)$  may be utilized to perform the analysis independently of  $D$ ,  $K_{Q0}$  and  $K_{T0}$ .

The iteration procedure starts at the reference shaft speed, defined as  $n_r/n_{bp}$ . With  $\beta_Q = \beta_Q(n_r/n_{bp})$  and  $\beta_T = \beta_T(n_r/n_{bp})$ , the shaft speed sensitivities  $sn_n(\cdot)$ ,  $sn_q(\cdot)$ ,  $sn_p(\cdot)$ , and  $sn_t(\cdot)$  are found from Table 4.2. From this, the shaft speeds for the next iteration step are found from  $n_i/n_{bp} = sn_i(\cdot)n_r/n_{bp}$ , with  $i \in \{n, q, p, t\}$ . Note that  $sn_n(\cdot) = 1$  by definition, such that no iteration is needed for the shaft speed controller. With  $\beta_Q = \beta_Q(n_i/n_{bp})$  and  $\beta_T = \beta_T(n_i/n_{bp})$ , new shaft speed sensitivities  $sn_i(\cdot)$  can be calculated, and the procedure can be continued until the iteration converges. By performing a series of these analyses, the sensitivity functions can be expressed as functions of  $h/R$ .

For increased realism, it may be desirable to enforce torque and power limits according to the maximum rated torque  $Q_{\max}$  and rated power  $P_{\max}$  of the motor, as defined in (2.55). Because of the quadratic and cubed relationships between propeller shaft speed, torque and power, as defined in (2.4) and (2.5), the maximum allowable values of  $sq_i(\cdot)$  and  $sp_i(\cdot)$  can be directly inferred from  $n_r/n_{bp}$ . From (2.55), (2.63), and (2.66), and neglecting the power lost in friction (i.e. assuming mechanical efficiency  $\eta_m = 1$ ),  $Q_{\max}$  and  $P_{\max}$  are defined in terms of  $n_{bp}$  by:

$$Q_{\max} = k_m Q_N = \frac{k_m}{k_g} Q_{bp} = \frac{k_m}{k_g} \rho D^5 K_{Q0} n_{bp}^2, \quad (4.60)$$

$$\begin{aligned} P_{\max} &= k_m P_N = k_m P_{bp} = k_m Q_{bp} 2\pi n_{bp} \\ &= k_m 2\pi \rho D^5 K_{Q0} n_{bp}^3. \end{aligned} \quad (4.61)$$

From (4.12) and (4.13), ignoring signs, and using  $K_{QC} = K_{Q0}$ , the relationships between  $P_r$ ,  $Q_r$ , and  $n_r$  are:

$$Q_r = K_{Q0} \rho D^5 n_r^2, \quad (4.62)$$

$$P_r = 2\pi K_{Q0} \rho D^5 n_r^3. \quad (4.63)$$

The following relationships may then be established for torque:

$$\begin{aligned} \frac{k_g Q_{\max}}{k_m \rho D^5 K_{Q0} n_{bp}^2} &= \frac{Q_r}{K_{Q0} \rho D^5 n_r^2}, \\ \Downarrow \\ \frac{Q_r}{k_g Q_{\max}} &= \frac{1}{k_m} \left( \frac{n_r}{n_{bp}} \right)^2, \end{aligned} \quad (4.64)$$

and power:

$$\begin{aligned} \frac{P_{\max}}{k_m 2\pi\rho D^5 K_{Q0} n_{bp}^3} &= \frac{P_r}{2\pi K_{Q0} \rho D^5 n_r^3}, \\ &\Downarrow \\ \frac{P_r}{P_{\max}} &= \frac{1}{k_m} \left( \frac{n_r}{n_{bp}} \right)^3. \end{aligned} \quad (4.65)$$

The saturation limits  $sq_{\max}$  for  $sq_i(\cdot)$  and  $sp_{\max}$  for  $sp_i(\cdot)$  should correspond to  $Q_a = k_g Q_{\max}$  and  $P_a = P_{\max}$  respectively, such that:

$$sq_{\max} = \frac{k_g Q_{\max}}{Q_r} = k_m \left( \frac{n_r}{n_{bp}} \right)^{-2}, \quad (4.66)$$

$$sp_{\max} = \frac{P_{\max}}{P_r} = k_m \left( \frac{n_r}{n_{bp}} \right)^{-3}, \quad (4.67)$$

where (4.64) and (4.65) have been inserted. This shows that if e.g.  $n_r/n_{bp} = 0.5$  is chosen as a starting point for the sensitivity analysis, the saturation limits for torque and power become  $sq_{\max} = 4k_m$  and  $sp_{\max} = 8k_m$ , where  $k_m = 1.1 - 1.2$ . Implementation of the torque and power limits requires an additional iteration procedure to satisfy (4.66) or (4.67), which is activated if either limit is reached.

Figure 4.10 shows the ventilation thrust loss sensitivity analysis for an open propeller, i.e. with the ventilation loss function defined in Figure 2.18. The thrust reference  $T_r$  corresponds to  $n_r/n_{bp} = 0.5$ . Curves for the shaft speed, torque, power, and thrust controllers are shown. Notice that the shaft speed sensitivity for some controllers exceeds 2, which corresponds to  $n/n_{bp} = 1$ , since the shaft speed during ventilation can be higher than  $n_{bp}$  without exceeding  $sq_{\max}$  or  $sp_{\max}$ . In this analysis, the torque and power saturation limits were not reached. With respect to the performance criteria defined in Section 3.2, these results show that the thrust production is least sensitive to the ventilation loss incident using the thrust controller, followed by the torque controller, power controller, and shaft speed controller. However, the increased thrust production from the thrust and torque controllers will lead to excessive power consumption and propeller racing. This will probably lead to severe dynamic loading of the propeller, and hence increased mechanical wear and tear. The power controller will also lead to propeller racing, but keeps the power consumption constant.

Figure 4.11 shows the same analysis for a ducted propeller, i.e. with the ventilation loss function defined in Figure 2.19, with  $n_r/n_{bp} = 0.5$  and  $k_m = 1.2$  such that  $sq_{\max} = 4.8$  and  $sp_{\max} = 9.6$ . In this analysis the power limit is reached both for the torque and the thrust controller. The other main difference that can be noticed, is that all controllers give the same thrust when the propeller is fully ventilated, as is inherent in the ventilation loss function for ducted propellers. Hence, when compared to the shaft speed controller, the performance of the thrust, torque, and power controllers is in this case even worse than for the open propeller. In the extreme case of a water exit, when

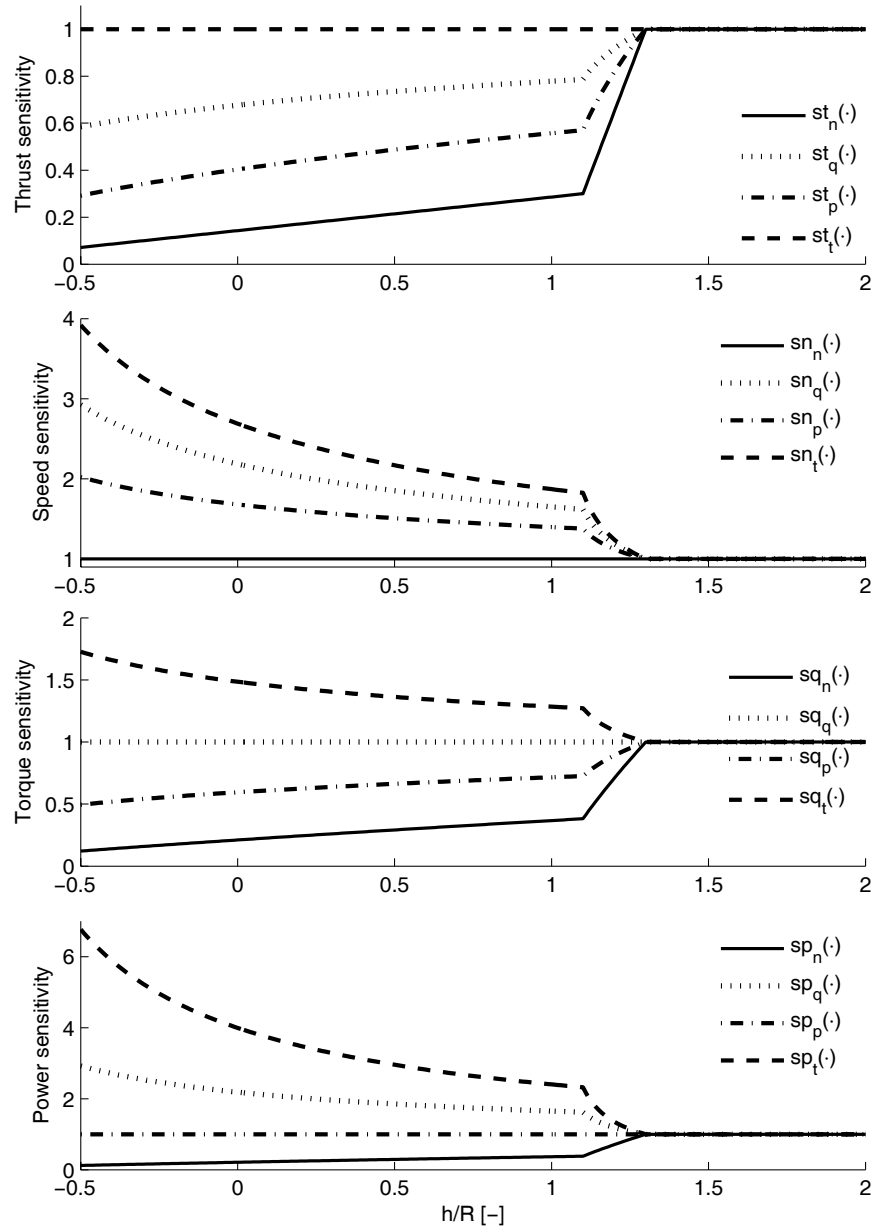


Figure 4.10: Sensitivity functions during ventilation for an open propeller, with thrust reference corresponding to  $n_r/n_{bp} = 0.5$ .

$\beta_Q \approx \beta_T \approx 0$ , the shaft speed of the thrust and torque controllers will only be limited by  $sq_{\max}$  and  $sp_{\max}$ .

The results show that the good properties of torque and power control turn to the opposite when the propeller is subject to large thrust losses, and that thrust control leads to even worse performance.

## 4.10 Stability properties

The sensitivity functions introduced in the previous sections are convenient for analyzing the quasi-static behavior of the controllers during a loss incident, but give no information on the transient behavior. This section investigates the stability properties of the shaft speed equilibrium when the propeller is subject to dynamic load disturbances. The analysis is generic, and applies to all of the low-level thruster controllers. The main goal is to investigate what happens when the propeller is operating at steady state, and then suddenly is subject to a load disturbance.

### 4.10.1 System definition

Inserting (2.4) for  $Q_a$ , the rotational dynamics of the propeller can from (2.50) and (2.51) be expressed as:

$$\begin{aligned} I_s \dot{\omega} &= Q_{mp} - Q_a - Q_f(\omega) \\ &= Q_{mp} - \text{sign}(\omega)Q_s - K_\omega \omega - \frac{K_Q \rho D^5}{4\pi^2} \omega |\omega|. \end{aligned} \quad (4.68)$$

For the stability analysis,  $K_Q$  will for notational simplicity be written as a function of the shaft speed  $\omega$  and time  $t$ , with time representing the exogenous thrust losses:  $K_Q(\cdot) = K_Q(t, \omega)$ . In extreme operating conditions,  $K_Q(t, \omega)$  will show highly nonlinear behavior, especially depending on the thruster loading and the relative submergence  $h/R$ , as described in Section 2.4.4. From (2.12),  $K_Q(t, \omega)$  can also be written in terms of the nominal torque coefficient and the torque loss factor:  $K_Q(t, \omega) = K_{Q0}\beta_Q(t, \omega)$ . The following property, lemma, and assumption are used in the stability analysis.

**Property 4.1** *The torque loss factor  $\beta_Q(t, \omega)$ , and hence the torque coefficient  $K_Q(t, \omega)$ , are strictly non-negative.*

**Remark 4.9** *This is easily justified from the physics of the system. In the extreme case of the propeller exiting the water completely,  $\beta_Q(t, \omega) = K_Q(t, \omega) = 0$ , but  $\beta_Q(t, \omega)$  and  $K_Q(t, \omega)$  cannot become negative.*

**Lemma 4.1** *Suppose the function  $\varphi : \mathbb{R} \rightarrow \mathbb{R}$  is continuously differentiable and satisfies:*

$$\frac{\partial \varphi}{\partial y} \geq 0, \quad \forall y \in \mathbb{R}, \quad (4.69)$$

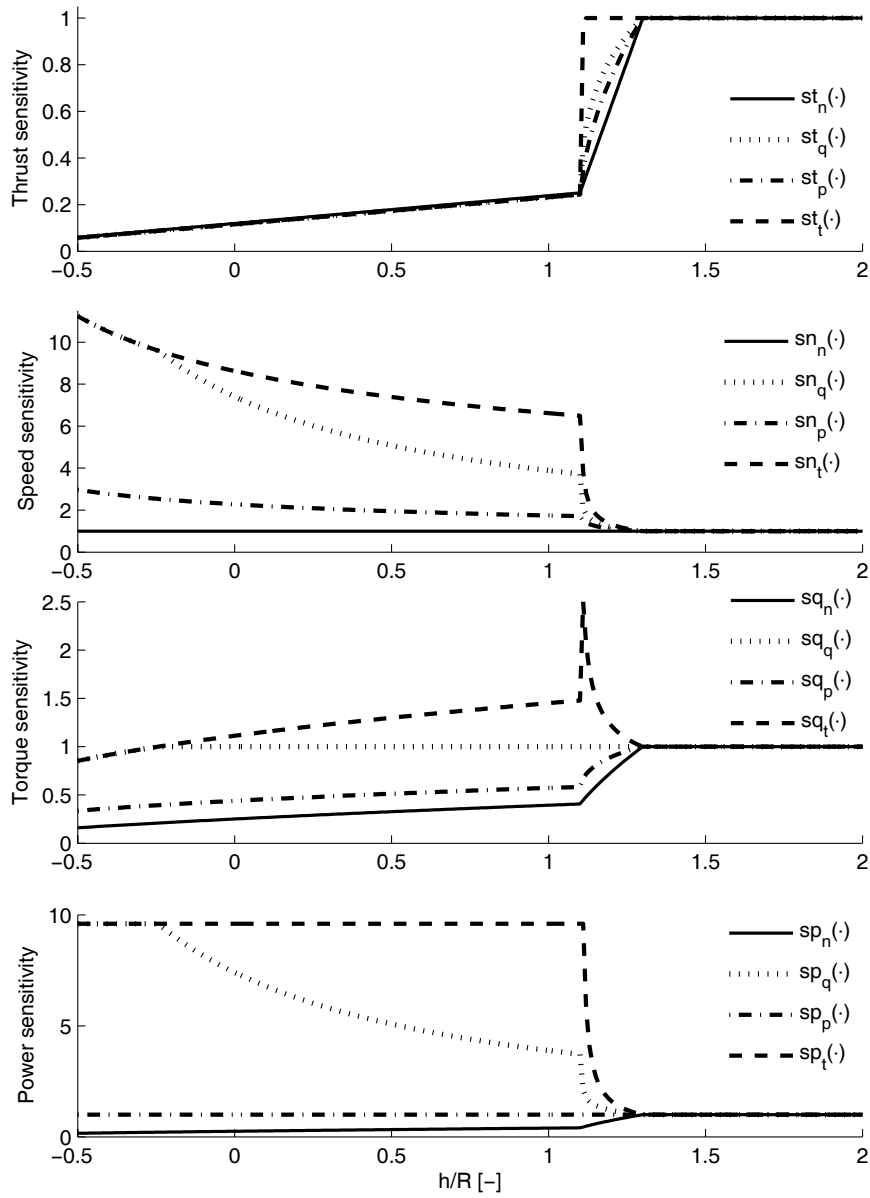


Figure 4.11: Sensitivity functions during ventilation for a ducted propeller, with thrust reference corresponding to  $n_r/n_{bp} = 0.5$ .

then it follows that:

$$(y - y_0)(\varphi(y) - \varphi(y_0)) \geq 0, \quad \forall \{y, y_0\} \in \mathbb{R}. \quad (4.70)$$

**Proof.** From the mean value theorem, see e.g. Khalil (2002), the following relationship holds:

$$\varphi(y) - \varphi(y_0) = \frac{\partial \varphi}{\partial y} \Big|_{y=z} (y - y_0),$$

where  $z$  is a point on the line segment connecting  $y$  and  $y_0$ . It follows that:

$$(y - y_0)(\varphi(y) - \varphi(y_0)) = \frac{\partial \varphi}{\partial y} \Big|_{y=z} (y - y_0)^2 \geq 0, \quad \forall \{y, y_0\} \in \mathbb{R}. \quad (4.71)$$

■

**Assumption 4.1** *The motor time constant  $T_m$  in (2.52) is negligible compared to the mechanical time constant, such that  $Q_m \approx Q_{cm}$  and  $Q_{mp} \approx Q_c$ .*

**Remark 4.10** *This is a common assumption – the motor dynamics are usually dominated by the rotational dynamics, and may in practice be neglected, at least for full-scale thrusters.*

The analysis proceeds by writing out the commanded torque, which from (3.18), (3.19), (3.20), (3.21), and (3.22) is expressed by:

$$Q_{c0} = Q_{ci} + Q_{if} + Q_{ff} = Q_{ci} + I_c \dot{\omega}_r + \tanh(\omega_r/\varepsilon) Q_{f0} + Q_{f1} \omega_r. \quad (4.72)$$

Here,  $\omega_r = 2\pi n_r$ ,  $n_r$  is defined in (3.1), and  $\varepsilon$  is given from (3.20) as:

$$\varepsilon = 2\pi n_f / \varepsilon_f. \quad (4.73)$$

Using Assumption 4.1, assuming that the torque limiting function is inactive such that  $Q_c = Q_{c0}$ , and inserting (4.72), the rotational dynamics in (4.68) becomes:

$$\begin{aligned} I_s \dot{\omega} &= Q_{ci} + I_c \dot{\omega}_r + \tanh(\omega_r/\varepsilon) Q_{f0} + Q_{f1} \omega_r \\ &\quad - \text{sign}(\omega) Q_s - K_\omega \omega - \frac{K_Q(t, \omega) \rho D^5}{4\pi^2} \omega |\omega| \\ &= Q_{ci} + I_s \dot{\omega}_r - Q_s (\tanh(\omega/\varepsilon) - \tanh(\omega_r/\varepsilon)) - K_\omega (\omega - \omega_r) \\ &\quad - \frac{K_Q(t, \omega) \rho D^5}{4\pi^2} \omega |\omega| + \dot{\omega}_r (I_c - I_s) + \delta Q_{f1}(\omega_r) + \delta Q_{f2}(\omega), \end{aligned} \quad (4.74)$$

where the friction modelling error terms  $\delta Q_{f1}(\omega_r)$  and  $\delta Q_{f2}(\omega)$  are:

$$\delta Q_{f1}(\omega_r) = \tanh(\omega_r/\varepsilon) (Q_{f0} - Q_s) + \omega_r (Q_{f1} - K_\omega), \quad (4.75)$$

$$\delta Q_{f2}(\omega) = (\tanh(\omega/\varepsilon) - \text{sign}(\omega)) Q_s. \quad (4.76)$$

**Assumption 4.2** The friction modelling error term  $\delta Q_{f2}(\omega)$  in (4.76) is negligible.

**Remark 4.11** As shown in Section 3.7.1,  $|\omega| > 2\pi n_f \Rightarrow \tanh(\omega/\varepsilon) \approx \text{sign}(\omega)$  with a properly chosen  $\varepsilon_f$ . Hence,  $\delta Q_{f2}(\omega)$  is for all practical purposes negligible. For  $|\omega| < 2\pi n_f$ ,  $\delta Q_{f2}(\omega)$  will be an additional damping term.

**Remark 4.12** With perfect friction knowledge, i.e.  $Q_{f0} = Q_s$  and  $Q_{f1} = K_\omega$ ,  $\delta Q_{f1}(\omega_r)$  in (4.75) disappears.

**Remark 4.13** With perfect inertia knowledge or a constant thrust reference ( $\dot{\omega}_r = 0$ ), the term  $\dot{\omega}_r(I_c - I_s)$  in (4.74) disappears.

Under Assumption 4.2, (4.74) is rewritten as a nonlinear mass-damper system given by:

$$\dot{\omega} - \dot{\omega}_r = u - b_0\theta(\omega_r, \omega) - b_1(\omega - \omega_r) - b_2(t, \omega)\omega |\omega| + \delta I\dot{\omega}_r + \delta b_f(\omega_r), \quad (4.77)$$

where  $u$  is the controller output,  $b_0$  is a static friction term,  $b_1$  is a linear friction term,  $b_2(t, \omega)$  is a time-varying quadratic damping term,  $\delta I$  is an inertia error term,  $\delta b_f(\omega_r)$  is a friction compensation error term, and  $\theta(\omega_r, \omega)$  is a function according to:

$$u = Q_{ci}/I_s, \quad (4.78)$$

$$b_0 = \frac{Q_s}{I_s}, \quad b_1 = \frac{K_\omega}{I_s}, \quad b_2(t, \omega) = \frac{K_Q(t, \omega)\rho D^5}{4\pi^2 I_s}, \quad (4.79)$$

$$\delta I = \frac{(I_c - I_s)}{I_s}, \quad \delta b_f(\omega_r) = \frac{\delta Q_{f1}(\omega_r)}{I_s}, \quad (4.80)$$

$$\theta(\omega_r, \omega) = \tanh(\omega/\varepsilon) - \tanh(\omega_r/\varepsilon). \quad (4.81)$$

Note that  $b_0 \geq 0$  and  $b_2(t, \omega) \geq 0$ , since the static friction  $Q_s$  and the torque coefficient  $K_Q(t, \omega)$  (from Property 4.1) are strictly non-negative, and the rotational inertia  $I_s > 0$ .  $b_1 > 0$  is assumed to be positive, which implies that the linear friction coefficient  $K_\omega > 0$ . The quadratic damping term is now rewritten as the sum of a steady-state value  $\bar{b}_2$ , which is known, and an unknown time-varying term  $b_{2\delta}(t, \omega)$ :

$$b_2(t, \omega) = \bar{b}_2 + b_{2\delta}(t, \omega). \quad (4.82)$$

In terms of the model parameters in (4.79) and (2.12),  $\bar{b}_2$  and  $b_{2\delta}(t, \omega)$  are defined as:

$$\bar{b}_2 = \frac{K_{Q0}\rho D^5}{4\pi^2 I_s}, \quad (4.83)$$

$$b_{2\delta}(t, \omega) = (\beta_Q(t, \omega) - 1) \frac{K_{Q0}\rho D^5}{4\pi^2 I_s}. \quad (4.84)$$

The primary task for the controller is to cancel the mean value of the quadratic term, since the time-varying part is unknown. This can be interpreted as a feedforward term. In addition the controller may have dynamic terms. The input  $u$  in (4.77) is therefore written as:

$$u = \bar{u} + u_\delta, \quad (4.85)$$

where  $\bar{u}$  is the steady-state controller output, and  $u_\delta$  is the dynamic controller output. In order to cancel  $\bar{b}_2$  at steady state with  $\delta b_f(\omega_r) = 0$  and  $\omega = \omega_r$ ,  $\bar{u}$  is given by:

$$\bar{u} = \bar{b}_2 \omega_r |\omega_r|. \quad (4.86)$$

**Remark 4.14** *The control law in (4.85) is a generalization of all the control laws considered earlier, where  $\bar{u}$  in (4.86) is the steady-state controller output in ideal conditions.*

With the new definitions of  $b_2(t, \omega)$  in (4.82) and  $u$  in (4.85), the mass-damper system in (4.77) becomes:

$$\begin{aligned} \dot{\omega} - \dot{\omega}_r &= -b_0\theta(\omega_r, \omega) - b_1(\omega - \omega_r) - \bar{b}_2(\omega|\omega| - \omega_r|\omega_r|) \\ &\quad - b_{2\delta}(t, \omega)\omega|\omega| + u_\delta + \delta I\dot{\omega}_r + \delta b_f(\omega_r). \end{aligned} \quad (4.87)$$

The system in (4.87) is now transformed to the desired equilibrium  $\omega_r$  by introducing the error state  $x = \omega - \omega_r$ :

$$\begin{aligned} \dot{x} &= -b_1x - \bar{b}_2((x + \omega_r)|x + \omega_r| - \omega_r|\omega_r|) \\ &\quad - b_{2\delta}(t, \omega)(x + \omega_r)|x + \omega_r| \\ &\quad - b_0\theta(\omega_r, \omega) + u_\delta + \delta I\dot{\omega}_r + \delta b_f(\omega_r). \end{aligned} \quad (4.88)$$

In the following sections, the system in (4.88) will be divided in a *nominal system* and a *perturbation term*.

#### 4.10.2 Nominal system stability

Assuming perfect friction and inertia knowledge, i.e.  $Q_{f0} = Q_s$ ,  $Q_{f1} = K_\omega$ , and  $I_c = I_s$ , such that  $\delta b_f(\omega_r) = 0$  and  $\delta I = 0$  in (4.80), and to be at the nominal load condition with  $b_{2\delta}(t, \omega) = 0$  and  $u_\delta = 0$ , (4.88) reduces to the *nominal system* defined as:

$$\dot{x} = -b_0\theta(\omega_r, \omega) - b_1x - \bar{b}_2((x + \omega_r)|x + \omega_r| - \omega_r|\omega_r|) \triangleq f(x). \quad (4.89)$$

**Proposition 4.1** *The equilibrium point  $x = 0$  of the nominal system  $\dot{x} = f(x)$  in (4.89) is globally exponentially stable (GES).*

**Proof.** The positive definite Lyapunov function candidate  $V(x)$ :

$$V(x) = \frac{1}{2}x^2, \quad (4.90)$$

satisfies:

$$k_1 \|x\|^a \leq V(x) \leq k_2 \|x\|^a, \quad (4.91)$$

with  $a = 2$  (Euclidian norm),  $k_1 \leq 1/2$ , and  $k_2 \geq 1/2$  for all  $x \in \mathbb{R}$ . The derivative of  $V(x)$  along the trajectories of  $f(x)$  in (4.89) is:

$$\begin{aligned} \dot{V}(x) &= -b_0\theta(\omega_r, \omega)x - b_1x^2 \\ &\quad - \bar{b}_2((x + \omega_r) - \omega_r)((x + \omega_r)|x + \omega_r| - \omega_r|\omega_r|). \end{aligned} \quad (4.92)$$

From Lemma 4.1, with  $\varphi(y) = y|y|$ ,  $y = x + \omega_r$ , and  $y_0 = \omega_r$ , it is clear that:

$$((x + \omega_r) - \omega_r)((x + \omega_r)|x + \omega_r| - \omega_r|\omega_r|) \geq 0. \quad (4.93)$$

Also from Lemma 4.1, with  $\varphi(y) = \tanh(y/\varepsilon)$ ,  $y = \omega$ , and  $y_0 = \omega_r$ :

$$\theta(\omega_r, \omega)x = (\tanh(\omega/\varepsilon) - \tanh(\omega_r/\varepsilon))(\omega - \omega_r) \geq 0. \quad (4.94)$$

With  $\bar{b}_2 > 0$  and  $b_0 \geq 0$  it follows that:

$$\dot{V}(x) \leq -b_1x^2 \leq -k_3\|x\|^a, \quad (4.95)$$

with  $a = 2$  and  $0 < k_3 \leq b_1$  for all  $x \in \mathbb{R}$ . The equilibrium point  $x = 0$  is therefore GES. ■

**Remark 4.15** In practice, the linear damping term  $b_1x$  in (4.89) will be dominated by the quadratic damping term proportional to  $\bar{b}_2$ . This is further discussed in Appendix F.3, where it is shown that for  $|x| < |\omega_r|$ ,  $\dot{V}(x)$  complies to:

$$\dot{V}(x) \leq -(b_1 + \bar{b}_2|\omega_r|)x^2. \quad (4.96)$$

Hence, the result in (4.95) is conservative.

#### 4.10.3 Perturbed system stability

In dynamic operating conditions,  $b_{2\delta}(t, \omega) = 0$  and  $u_\delta = 0$  no longer holds. In general, also the friction error term  $\delta b_f(\omega_r) \neq 0$  and  $\delta I \neq 0$ . The system (4.88) can then be viewed as the sum of the nominal system in (4.89) and a perturbation term  $g(t, x)$ :

$$\dot{x} = f(x) + g(t, x), \quad (4.97)$$

where  $f(x)$  is given in (4.89) and  $g(t, x)$  is defined as:

$$g(t, x) \triangleq u_\delta - b_{2\delta}(t, \omega)(x + \omega_r)|x + \omega_r| + \delta I\dot{\omega}_r + \delta b_f(\omega_r). \quad (4.98)$$

The perturbation term does not necessarily vanish at the origin  $x = 0$ , since  $g(t, 0) = b_{2\delta}(t, \omega)\omega_r|\omega_r| + \delta I\dot{\omega}_r + \delta b_f(\omega_r) \neq 0$ .  $g(t, x)$  is, therefore, a *nonvanishing perturbation*, which means that the origin will not be an equilibrium point of the perturbed system.

**Proposition 4.2** For any uniformly bounded disturbance  $g(t, x)$ , the solutions  $x(t)$  of the perturbed system in (4.97) are uniformly ultimately bounded (UUB).

**Proof.**  $V(x)$  given in (4.90) satisfies:

$$\left\| \frac{\partial V}{\partial x} \right\| \leq k_4 \|x\|, \quad (4.99)$$

for all  $x \in \mathbb{R}$  and  $k_4 \geq 1$ , since  $\|\partial V/\partial x\| = \|x\|$ . With the origin of the nominal system (4.89) exponentially stable, Lemma 9.2 in Khalil (2002) can be applied. Since (4.91), (4.95), and (4.99) are satisfied for all  $x \in \mathbb{R}$ , they also hold for  $x \in D_r$ , where  $D_r$  is a ball of radius  $r$ :

$$D_r = \{x \in \mathbb{R} \mid \|x\| < r\}. \quad (4.100)$$

Assume that the perturbation term  $g(t, x)$  in (4.98) satisfies:

$$\|g(t, x)\| \leq \delta < \frac{k_3}{k_4} \sqrt{\frac{k_1}{k_2}} \theta r, \quad (4.101)$$

$\forall t \geq 0$ ,  $\forall x \in D_r$ , and some positive constant  $\theta < 1$ . The solution of the perturbed system then satisfies the bound:

$$\|x(t)\| \leq k e^{-\xi(t-t_0)} \|x(t_0)\|, \quad \forall t_0 \leq t < t_0 + T, \quad (4.102)$$

for all  $\|x(t_0)\| < \sqrt{k_1/k_2}r$ , and the ultimate bound:

$$\|x(t)\| \leq b, \quad \forall t \geq t_0 + T, \quad (4.103)$$

for some finite  $T$ , where

$$k = \sqrt{\frac{k_2}{k_1}}, \quad \xi = \frac{(1-\theta)k_3}{2k_2}, \quad b = \frac{k_4}{k_3} \sqrt{\frac{k_2}{k_1}} \frac{\delta}{\theta}. \quad (4.104)$$

Hence, the solutions  $x(t)$  of (4.97) are UUB, and the ultimate bound  $b$  is proportional to the upper bound  $\delta$  on the perturbation. Since the origin of the nominal system (4.89) is GES and  $\delta \rightarrow \infty$  as  $r \rightarrow \infty$  in (4.101),  $x(t)$  will be UUB for all uniformly bounded perturbations. ■

**Remark 4.16** The friction model error  $\delta b_f(\omega_r)$  in (4.80) is expected to be small. The effect of  $\delta b_f(\omega_r) \neq 0$  is from Proposition 4.2 that the equilibrium of (4.97) will be shifted.

**Remark 4.17** For  $|\omega| > 2\pi n_f$ , Assumption 4.2 can be relaxed without implications. For  $|\omega| < 2\pi n_f$ , relaxation of Assumption 4.2 will give a slightly shifted equilibrium.

#### 4.10.4 Implications for shaft speed, torque, and power control

The analysis in the previous sections considers a generic control law given in (4.85). This section investigates the implications of the stability analysis for shaft speed, torque, and power control. For the sake of simplicity, it is here assumed that  $\delta I\dot{\omega}_r + \delta b_f(\omega_r) = 0$  in (4.98).

In terms of the original system parameters, (4.85) translates to:

$$Q_{ci} = \bar{Q}_{ci} + \delta Q_{ci} = \frac{K_{QC}\rho D^5}{4\pi^2} \omega_r |\omega_r| + \delta Q_{ci}, \quad (4.105)$$

where (4.83) and (4.78) have been inserted,  $\bar{Q}_{ci}$  is the steady-state controller output, and  $\delta Q_{ci}$  is the dynamic controller output.  $K_{QC}$  has been used instead of  $K_{Q0}$  in (4.83) since  $K_{QC}$  is the torque coefficient used in the controller. This means that  $\bar{Q}_{ci} \equiv Q_r$  from (4.12).

The shaft speed controller in (3.27) attempts to keep the shaft speed constant regardless of the disturbance. In an ideal speed controller, this means that the perturbation term  $g(t, x) = 0$  in (4.98), and hence that  $u_\delta = b_{2\delta}(t, \omega)\omega |\omega|$ . In the system parameters, this translates to:

$$\delta Q_{ci} = (\beta_Q(t, \omega) - 1) \frac{K_{Q0}\rho D^5}{4\pi^2} \omega |\omega|, \quad (4.106)$$

where (4.84) and (4.78) have been used. This essentially means that the change in propeller loading (parameterized by  $\beta_Q(t, \omega)$ ) is instantly compensated for by the controller.

The torque controller in (3.29) is a pure feedforward controller. Hence,  $u_\delta = \delta Q_{ci} = 0$ , such that  $u = \bar{u}$  in (4.85) and  $Q_{ci} = \bar{Q}_{ci} = Q_r$  in (4.105). This means that  $g(t, x)$  in (4.98) consists only of the load perturbation. The disturbance bound  $\delta$  in (4.101), and hence also the ultimate bound  $b$  in (4.104), will then depend only on the size of the perturbation, since the torque controller takes no action to reduce the perturbation (and thereby control the shaft speed).

The dynamic controller term of the power controller in (3.32) can be found by equating  $P_r$  from (4.13) with the power implied by (4.105):

$$\begin{aligned} 2\pi K_{QC}\rho D^5 |n_r|^3 &= 2\pi n(K_{QC}\rho D^5 n_r |n_r| + \delta Q_{ci}) \\ &\Downarrow \\ \delta Q_{ci} &= K_{QC}\rho D^5 n_r |n_r| \frac{n_r - n}{n} = Q_r \frac{n_r - n}{n}, \end{aligned} \quad (4.107)$$

where  $Q_r$  from (4.12) has been inserted. Hence,  $n = n_r \Rightarrow \delta Q_{ci} = 0$ . This shows that the feedback from  $n$  will reduce the controller output when the shaft speed increases, and increase the controller output when the shaft speed decreases with respect to  $n_r$ . Hence, the power controller will reduce  $g(t, x)$  when compared to the torque controller, and hence also  $\delta$  and  $b$ .

**Remark 4.18** During ventilation the load may drop suddenly by 70-80%, as shown in Section 2.4. For the torque and power controllers, this means that the bound  $b$  will be large, such that the shaft speed will increase significantly. These considerations are consistent with the sensitivity analysis for high thrust losses presented in Section 4.9: if no action is taken during ventilation, the performance of the torque and power controllers will be unsatisfactory. This motivates the need for an anti-spin controller that can detect the ventilation incidents and take control of the shaft speed to reduce the propeller racing.



# Chapter 5

## Propeller observers

Most of the work presented in this thesis is based on the assumption that the only available measurements are the shaft speed  $n$  and the motor torque  $Q_m$ . However, in some applications it will be convenient to have estimates of other system states. Based on the available measurements, this chapter introduces estimation schemes that can be used for e.g. performance monitoring, thrust loss estimation, ventilation detection, anti-spin thruster control, thrust allocation, and output feedback thrust control.

A physical limitation is that only thrust loss effects that are observable from the propeller can be estimated. In Section 2.3, the loss effects were divided in two groups: losses that affect the propeller loading, and losses that affect the propeller race. It is only the first group, which consists of variations in the in-line inflow to the propeller, ventilation, and in-and-out-of-water effects, that can be estimated in the low-level thruster control scheme.

Section 5.1 presents a propeller load torque observer. This is a modification of the observer first introduced in Smogeli *et al.* (2004a). Section 5.2 presents an alternative load torque estimation scheme based on nonlinear parameter estimation. Both schemes yield estimates of the load torque  $Q_a$ , the torque coefficient  $K_Q$ , and the torque loss factor  $\beta_Q$ . Section 5.3 shows how estimates of the propeller thrust  $T_a$  and thrust loss factor  $\beta_T$  in some cases may be deduced from the torque coefficient estimate. Performance monitoring for use in e.g. thrust allocation is treated in Section 5.4. Section 5.5 demonstrates the performance of the various schemes by simulations. Extensions of the estimation schemes to transit and CPP is treated in Chapter 8. An adaptive load torque observer for the case of an unknown linear friction coefficient can be found in Appendix G.

## 5.1 Propeller load torque observer

From (2.50), the following control plant model of the propeller rotational dynamics is proposed:

$$\begin{aligned} I_s \dot{\omega} &= Q_{mp} - Q_a - Q_{ff0}(n_r) - Q_{f1}\omega + \delta_f, \\ \dot{Q}_a &= w_{Q_a}. \end{aligned} \quad (5.1)$$

Since  $f_Q(n, \mathbf{x}_p, \boldsymbol{\theta}_p)$  in (2.2) is unknown and may exhibit highly nonlinear behavior,  $Q_a$  is modelled as a bias term driven by an exogenous, bounded disturbance  $w_{Q_a}$ . The static friction compensation term  $Q_{ff0}(n_r)$  from (3.20) is used instead of a static friction model based on  $\omega$ , in order to avoid oscillations in this term about  $\omega = 0$ . Errors in the friction model when compared to  $Q_f(\omega)$  in (2.51) are accounted for by  $\delta_f$ :

$$\delta_f = Q_{ff0}(n_r) - Q_{f1}\omega - Q_s \operatorname{sign}(\omega) - K_\omega \omega. \quad (5.2)$$

With the measurement  $y = \omega + v$  contaminated with a bounded disturbance  $v$  and the input  $u$  given by:

$$u = Q_{mp} - Q_{ff0}(n_r) = k_g Q_m - Q_{ff0}(n_r), \quad (5.3)$$

the shaft dynamics (5.1) can be written on matrix form as:

$$\begin{aligned} \dot{x} &= Ax + Bu + w, \\ y &= Cx + v, \end{aligned} \quad (5.4)$$

where:

$$\begin{aligned} x &= \begin{bmatrix} \omega \\ Q_a \end{bmatrix}, \quad A = \begin{bmatrix} -Q_{f1}/I_s & -1/I_s \\ 0 & 0 \end{bmatrix}, \\ B &= \begin{bmatrix} 1/I_s \\ 0 \end{bmatrix}, \quad w = \begin{bmatrix} \delta_f/I_s \\ w_{Q_a} \end{bmatrix}, \quad C = [1 \ 0]. \end{aligned} \quad (5.5)$$

The system is observable from  $y$ , since the observability matrix:

$$O = \begin{bmatrix} C \\ CA \end{bmatrix} = \begin{bmatrix} 1 & 0 \\ -Q_{f1}/I_s & -1/I_s \end{bmatrix}, \quad (5.6)$$

has full rank. Copying the control plant model (5.1), the proposed propeller load torque observer is:

$$\begin{aligned} \dot{\hat{\omega}} &= \frac{1}{I_s} (u - \hat{Q}_a - Q_{f1}\hat{\omega}) + k_a(y - \hat{y}), \\ \dot{\hat{Q}}_a &= k_b(y - \hat{y}), \end{aligned} \quad (5.7)$$

where  $k_a$  and  $k_b$  are the observer gains. On matrix form, with  $K = [k_a, k_b]^\top$ , (5.7) becomes:

$$\begin{aligned}\dot{\hat{x}} &= A\hat{x} + Bu + K\tilde{y}, \\ \hat{y} &= C\hat{x}.\end{aligned}\quad (5.8)$$

The observer error dynamics obtained by subtracting (5.8) from (5.4) are:

$$\begin{aligned}\dot{\tilde{x}} &= Ax + Bu + w - (A\hat{x} + Bu + K\tilde{y} + Kv) \\ &= A\tilde{x} - KC\tilde{x} + w - Kv = F\tilde{x} + \Delta,\end{aligned}\quad (5.9)$$

where the system matrix  $F$  and the vector  $\Delta$  containing modelling errors and noise are:

$$\begin{aligned}F &= A - KC = - \begin{bmatrix} Q_{f1}/I_s + k_a & 1/I_s \\ k_b & 0 \end{bmatrix}, \\ \Delta &= w + Kv = \begin{bmatrix} \delta_f/I_s - k_a v \\ w_{Q_a} - k_b v \end{bmatrix}, \quad \|\Delta\| < \Delta_{\max}.\end{aligned}\quad (5.10)$$

**Proposition 5.1** *With a constant load torque  $Q_a$  implied by  $w_{Q_a} = 0$ , zero measurement disturbance  $v = 0$ , and perfect friction knowledge such that  $\delta_f = 0$  in (5.2), the equilibrium point  $\tilde{x} = 0$  of the observer estimation error in (5.9) is GES if the observer gains are chosen as  $k_a > -Q_{f1}/I_s$  and  $k_b < 0$ .*

**Proof.**  $w_{Q_a} = v = \delta_f = 0$  implies that the input vector  $\Delta = 0$ , and hence that the error dynamics (5.9) is reduced to the unforced linear system  $\dot{\tilde{x}} = F\tilde{x}$ . With  $k_a$  and  $k_b$  chosen as specified,  $F$  is Hurwitz, and the origin  $\tilde{x} = 0$  is GES. ■

**Proposition 5.2** *With a time-varying load torque  $Q_a$  implied by a nonzero but bounded  $w_{Q_a}$ , a bounded friction model error  $\delta_f$ , and a bounded measurement error  $v$ , the observer error dynamics in (5.9) is input-to-state stable (ISS), and the observer error  $\tilde{x}$  is UUB.*

**Proof.** With  $w_{Q_a}$ ,  $\delta_f$ , and  $v$  assumed to be bounded, the input vector  $\|\Delta\| < \Delta_{\max}$ . With the unforced linear system GES and the input bounded, ISS and boundedness of the observer error  $\tilde{x}$  is inherent (Khalil, 2002). ■

**Remark 5.1** *In the observer in (5.7), the actual rotational inertia  $I_s$  from (2.50) has been used instead of the inertia compensation parameter  $I_c$  from (3.22). This is to account for the fact that  $I_c$  may be tuned manually in order to get the desired transient response of the system, see Appendix B.3. In the observer, it is desired to have an estimate of  $I_s$  that is as close as possible to the true value. If  $I_s$  is unknown, it may be found with reasonable accuracy from the tuning scheme presented in Appendix B.3 – even if  $I_c$  is chosen differently.*

**Remark 5.2** *If a higher-order friction model than (2.51) is considered appropriate, the observer should be modified accordingly. Such an observer, with the same stability properties as (5.7), is presented in Pivano et al. (2006b).*

### 5.1.1 Observer tuning

The observer gains  $k_a$  and  $k_b$  can be tuned based on the error dynamics (5.9) using e.g. pole placement. The poles  $s_i$  are found from:

$$s_i = \frac{-(Q_{f1}/I_s + k_a) \pm \sqrt{(Q_{f1}/I_s + k_a)^2 + 4k_b/I_s}}{2},$$

and the undamped natural frequency  $\omega_n$  and damping ratio  $\zeta$  are:

$$\omega_n = \sqrt{\frac{-k_b}{I_s}}, \quad \zeta = \frac{Q_{f1} + k_a I_s}{2\sqrt{-k_b I_s}}. \quad (5.11)$$

The gains may hence be chosen by specifying desired values for  $\omega_n$  and  $\zeta$ :

$$k_a = 2\zeta\omega_n - Q_{f1}/I_s, \quad k_b = -I_s\omega_n^2. \quad (5.12)$$

Typically, the damping ratio could be chosen in the range  $0.7 < \zeta < 1.1$ . The natural frequency should be chosen according to the specific thruster. A suggestion is choose it to be as fast as the bollard pull shaft speed  $n_{bp}$  of the propeller, i.e.  $\omega_n = 2\pi n_{bp}$ . Using these rules for the 4MW Wageningen B4-70 example propeller (see Appendix A), with  $\zeta = 0.7$  and  $\omega_n = 2\pi \cdot 2 \approx 12.6$ , the gains become:

$$k_a \approx 17.6, \quad k_b \approx -4E6. \quad (5.13)$$

### 5.1.2 Torque loss estimation

The estimated load torque  $\hat{Q}_a$  can be used to calculate an estimate  $\hat{\beta}_Q$  of the torque loss factor  $\beta_Q$ . For DP operation the *expected* nominal propeller load torque  $\hat{Q}_n$  may be calculated from (2.9) by feedback from the propeller shaft speed  $n$  as:

$$\hat{Q}_n = K_{QC}\rho D^5 n |n|, \quad (5.14)$$

where the control coefficient  $K_{QC}$  (usually equal to  $K_{Q0}$ ) is used. Based on (2.12),  $\hat{\beta}_Q$  is calculated from  $\hat{Q}_a$  in (5.7) and  $\hat{Q}_n$  in (5.14) as:

$$\hat{\beta}_Q = \frac{\hat{Q}_a}{\hat{Q}_n} = \frac{\hat{Q}_a}{K_{QC}\rho D^5 n |n|}, \quad n \neq 0. \quad (5.15)$$

$\hat{\beta}_Q$  should be saturated by an upper limit  $\beta_{Q,\max}$  and a lower limit  $\beta_{Q,\min}$  in order to avoid out-of-bounds values for low  $n$ , and the singularity for  $n = 0$  should be avoided. Since there are no thrust losses for  $n = 0$ , the singularity can be avoided by redefining (5.15) as:

$$\hat{\beta}_Q = \max(\min([\alpha_b(n) + (1 - \alpha_b(n))\hat{Q}_a/\hat{Q}_n], \beta_{Q,\max}), \beta_{Q,\min}), \quad (5.16)$$

where  $\alpha_b(n)$  is a weighting function of the type (3.33), and the saturation limits  $\beta_{Q,\max}$  and  $\beta_{Q,\min}$  have been implemented. Applying similar reasoning as in

Section 3.13, it can be shown that the singularity is removed by choosing  $r \geq 1.5$  in  $\alpha_b(n)$ . In this work, the limits will be taken as  $\beta_{Q,\max} = 2$  and  $\beta_{Q,\min} = 0$ . If desired, an estimate  $\hat{K}_Q$  of the torque coefficient is easily inferred from  $\hat{\beta}_Q$  in (5.16) by:

$$\hat{K}_Q = K_{QC}\hat{\beta}_Q. \quad (5.17)$$

## 5.2 $K_Q$ estimation

As an alternative to the load torque observer presented in Section 5.1, it is possible to use a nonlinear online parameter estimation scheme to find an estimate  $\hat{K}_Q$  of the propeller torque coefficient. Estimates of the load torque  $Q_a$  and torque loss factor  $\beta_Q$  can then be calculated directly from  $\hat{K}_Q$ , motivated by (2.4) and (2.12) respectively:

$$\hat{Q}_a = \hat{K}_Q \rho D^5 n |\omega|, \quad (5.18)$$

$$\hat{\beta}_Q = \hat{K}_Q / K_{QC}. \quad (5.19)$$

An advantage of this approach is that the singularity in the calculation of  $\hat{\beta}_Q$  is removed.

As in (5.1), the parameter estimation scheme is based on the shaft dynamics in (2.50) and the friction model from (3.19), with the addition of the torque model from (2.4). The control plant model then becomes:

$$I_s \dot{\omega} = Q_{mp} - \frac{K_Q \rho D^5}{4\pi^2} \omega |\omega| - Q_{f0}(n_r) - Q_{f1}\omega. \quad (5.20)$$

It is here assumed that the friction parameters are known, such that  $\delta_f \approx 0$  in (5.2). Defining the input  $u$  as in (5.3) and the unknown parameter  $\theta$  as:

$$\theta = \frac{K_Q \rho D^5}{4\pi^2}, \quad (5.21)$$

the system in (5.20), which is affine in  $\theta$ , can be rewritten as:

$$\dot{\omega} = f(\omega, u, \theta) = F(\omega)\theta + g(\omega, u), \quad (5.22)$$

where:

$$f(\omega, u, \theta) = \frac{1}{I_s}(u - \theta\omega|\omega| - Q_{f1}\omega), \quad (5.23)$$

$$F(\omega) = \frac{\partial f(\omega, u, \theta)}{\partial \theta} = -\frac{\omega|\omega|}{I_s}, \quad (5.24)$$

$$g(\omega, u) = \frac{1}{I_s}(u - Q_{f1}\omega). \quad (5.25)$$

**Proposition 5.3** *The nonlinear parameter estimation scheme:*

$$\hat{K}_Q = \frac{4\pi^2}{\rho D^5} \hat{\theta}, \quad (5.26)$$

$$\dot{\hat{\theta}} = -k_0 \frac{|\omega|^3}{3I_s} + z, \quad (5.27)$$

$$\dot{z} = k_0 \frac{\omega |\omega|}{I_s^2} (u - \hat{\theta} \omega |\omega| - Q_{f1} \omega), \quad (5.28)$$

will yield the error dynamics  $\dot{\tilde{\theta}} = \dot{\hat{\theta}} - \dot{\hat{\theta}}$  uniformly globally stable (UGS) for all  $\omega$ , and uniformly globally exponentially stable (UGES) for  $\omega \neq 0$ .

**Proof.** From Friedland (1997), an estimate  $\hat{\theta}$  of  $\theta$  can be obtained from the following parameter update law:

$$\hat{\theta} = \phi(\omega) + z, \quad (5.29)$$

$$\dot{z} = -\Phi(\omega) f(\omega, u, \hat{\theta}), \quad (5.30)$$

where  $\phi(\omega)$  is a nonlinear function to be defined, and  $\Phi(\omega)$  its Jacobian:

$$\Phi(\omega) = \partial \phi(\omega) / \partial \omega. \quad (5.31)$$

Assuming  $\theta$  to be slowly-changing, the estimation error  $\tilde{\theta}$  and its dynamics are:

$$\begin{aligned} \tilde{\theta} &= \theta - \hat{\theta}, \\ \dot{\tilde{\theta}} &= -\dot{\hat{\theta}} = -\dot{\phi}(\omega) - \dot{z} = -\partial \phi(\omega) / \partial \omega \dot{\omega} - \dot{z} \\ &= -\Phi(\omega) \dot{\omega} + \Phi(\omega) f(\omega, u, \hat{\theta}) \\ &= -\Phi(\omega) [f(\omega, u, \theta) - f(\omega, u, \hat{\theta})] \\ &= -\Phi(\omega) F(\omega)(\theta - \hat{\theta}) = -L(t)\tilde{\theta}, \end{aligned} \quad (5.32)$$

where  $L(t) = \Phi(\omega(t))F(\omega(t))$  is time-varying. Stability properties are investigated by the positive definite Lyapunov function  $V(\tilde{\theta})$ :

$$V(\tilde{\theta}) = \frac{1}{2} \tilde{\theta}^2. \quad (5.33)$$

The derivative of  $V$  along the trajectories of (5.32) is given by:

$$\dot{V} = \tilde{\theta} \dot{\tilde{\theta}} = -L(t)\tilde{\theta}^2. \quad (5.34)$$

It remains to choose  $\phi(\omega)$  to yield  $L(t)$  positive semidefinite. One option is to choose  $\phi(\omega)$  to satisfy (Friedland, 1997):

$$\Phi(\omega) = k_0 F(\omega) = -\frac{k_0 \omega |\omega|}{I_s}, \quad (5.35)$$

where  $k_0$  is a positive constant, such that:

$$L(t) = \Phi(\omega)F(\omega) = k_0F(\omega)^2 = \frac{k_0\omega^4}{I_s^2}. \quad (5.36)$$

A candidate  $\phi(\omega)$  satisfying this is:

$$\phi(\omega) = -\frac{k_0}{3I_s} |\omega|^3. \quad (5.37)$$

This yields the following error dynamics:

$$\dot{\tilde{\theta}} = -\frac{k_0\omega(t)^4}{I_s^2} \tilde{\theta}, \quad (5.38)$$

where the time-dependence of  $\omega$  has been emphasized. Clearly,  $\dot{V}_1 = 0$  for  $\tilde{\theta} \neq 0$  iff  $\omega(t) \equiv 0$ . This is the case of zero shaft speed, for which one cannot expect to extract any information. However, the error dynamics are still UGS:  $\omega(t) = 0 \Rightarrow \phi(\omega) = \Phi(\omega) = \dot{z} = 0$ , which means that parameter adaption stops, but does not diverge. The condition that  $\omega(t) \neq 0$  can be seen as a persistency of excitation (PE) requirement, leading to UGES of the error dynamics, since:

$$\frac{1}{2} \|\tilde{\theta}\|^2 \leq V(\tilde{\theta}) \leq \frac{1}{2} \|\tilde{\theta}\|^2, \quad (5.39)$$

$$\dot{V} \leq -\frac{k_0\omega_{\min}^4}{I_s^2} \|\tilde{\theta}\|^2 < 0, \quad \forall |\omega| \geq \omega_{\min}. \quad (5.40)$$

where  $\omega_{\min} > 0$ . ■

Appropriate choice of the gain  $k_0$  in the  $K_Q$  estimation scheme (5.26) is highly dependent on the application. If the gain is chosen high, the scheme will estimate the instantaneous loading of the propeller, such that  $\hat{Q}_a$  from (5.18) and  $\hat{\beta}_Q$  from (5.19) will be comparable to (5.7) and (5.15) from Section 5.1. If  $k_0$  is chosen low, the high-frequency disturbances in the load torque will not be captured. Instead, an *average torque coefficient* and an *average torque loss factor* will be estimated. With appropriate tuning, the slow changes in the mean loading due to e.g. current and vessel low-frequency motion will be captured, while wave-frequency loads and noise are filtered out. This will be utilized in Appendix G.2, where approximations of the prevailing thrust and torque coefficients are calculated.

From  $\hat{K}_Q$  in (5.26), the estimates  $\hat{Q}_a$ , and  $\hat{\beta}_Q$  are calculated from (5.18) and (5.19), respectively. When compared to the  $Q_a$  observer presented in Section 5.1, the two approaches have the same inputs and outputs, and also require the same model knowledge. The most notable difference is that tuning of the single gain  $k_0$  in the  $K_Q$  estimation scheme may be simpler than tuning of the two gains  $k_a$  and  $k_b$  in the  $Q_a$  observer. The performance of the two schemes will be compared by simulations in Section 5.5.

### 5.3 Thrust estimation

In some applications it is feasible to use the estimated propeller torque to estimate also the propeller thrust. For open propellers, it was in Section 2.1.8 shown that a linear relationship between  $K_T$  and  $K_Q$  holds across a wide range of operating conditions. Motivated by (2.48), an estimate  $\hat{K}_T$  can be calculated from  $\hat{K}_Q$  in (5.17) or (5.26) by:

$$\hat{K}_T = a_t \hat{K}_Q + b_t, \quad (5.41)$$

where  $a_t$  and  $b_t$  are propeller constants inferred from the open-water characteristics. From (2.3) and (2.11), estimates  $\hat{T}_a$  of the propeller thrust and  $\hat{\beta}_T$  of the thrust loss factor are then found from:

$$\hat{T}_a = \hat{K}_T \rho D^4 n |n|, \quad (5.42)$$

$$\hat{\beta}_T = \hat{K}_T / K_{TC}. \quad (5.43)$$

A similar thrust estimation scheme is presented in more detail in Pivano *et al.* (2006b), and experimentally validated in Pivano *et al.* (2006a). The thrust estimate will be utilized in Appendix E.3.1, where an output feedback thrust controller is proposed.

### 5.4 Performance monitoring

Whereas  $\hat{\beta}_Q$  gives important information on the local operating conditions of the propeller, no information of its performance with respect to the thrust setpoint  $T_d$  can be directly inferred. This is due to the fact that  $\hat{\beta}_Q$  is calculated from the measured shaft speed. Depending on the low-level thruster controller and the instantaneous propeller operating conditions, the shaft speed, thrust, and torque may deviate significantly from the reference values. This was further analyzed in Chapter 4. For performance monitoring of the thruster, the main idea is to compare the actual thrust production with the thrust reference. Since the estimated thrust  $\hat{T}_a$  only can be estimated with reasonable accuracy for an open propeller, it is in general necessary to use  $\hat{Q}_a$  from (5.7) or (5.18) for the performance monitoring. The proposed torque performance factor estimate  $\hat{\chi}_Q$  is defined as the ratio of  $\hat{Q}_a$  to the reference load torque  $Q_r$  from (3.2):

$$\hat{\chi}_Q = \frac{\hat{Q}_a}{Q_r} = \frac{\hat{Q}_a}{\frac{K_{QC}}{K_{TC}} DT_r}, \quad T_r \neq 0. \quad (5.44)$$

$\hat{\chi}_Q$  is singular for  $T_r = 0$ , so a similar precaution as for  $\hat{\beta}_Q$  in (5.16) should be taken for the zero-crossing of  $T_r$ :

$$\hat{\chi}_Q = \alpha_\chi(T_r) + (1 - \alpha_\chi(T_r)) \frac{\hat{Q}_a}{Q_r}, \quad (5.45)$$

$I_s$	$Q_{f0}$	$Q_{f1}$	$k_a$	$k_b$	$\beta_{Q,\max}$	$\beta_{Q,\min}$
$25E3\text{kgm}^2$	$6.2\text{kNm}$	$720\text{Nms}$	$17.6$	$-4E6$	$2$	$0$
$r$	$p$	$k$	$k_0$	$a_t$	$b_t$	
$4$	$8$	$2$	$5E5$	$7.52$	$-0.054$	

Table 5.1: Estimation parameters for the 4MW Wageningen B4-70 example propeller.

where  $\alpha_\chi(T_r)$  is a weighting function of the type (3.33) such that  $\hat{\chi}_Q(0) = 1$ .

For open propellers, the thrust performance factor estimate  $\hat{\chi}_T$  can be calculated from  $\hat{T}_a$  in (5.42). With a similar precaution for the zero-crossing of  $T_r$  as in (5.45),  $\hat{\chi}_T$  is given by:

$$\hat{\chi}_T = \alpha_\chi(T_r) + (1 - \alpha_\chi(T_r)) \frac{\hat{T}_a}{T_r}. \quad (5.46)$$

**Remark 5.3** From (4.3),  $\hat{\chi}_Q$  in (5.45) can be regarded an estimate of the torque sensitivity function  $sq_i(\cdot)$ .

**Remark 5.4** From (4.1),  $\hat{\chi}_T$  in (5.46) can be regarded as an estimate of the thrust sensitivity function  $st_i(\cdot)$ .

**Remark 5.5**  $Q_r$  can be expressed in terms of the reference shaft speed  $n_r$  by (4.12). Hence, for shaft speed control, where  $n \approx n_r$  such that  $\hat{Q}_n \approx Q_r$ ,  $\hat{\chi}_Q$  and  $\hat{\beta}_Q$  are nearly identical. For the controllers in Table 3.1 based on torque and power control,  $n \neq n_r$  in non-ideal conditions, and therefore also  $\hat{\chi}_Q \neq \hat{\beta}_Q$ .

## 5.5 Simulation results

The simulations are performed with the 4MW Wageningen B4-70 example propeller, with model parameters given in Tables A.1 and A.2. The shaft speed controller is used with the parameters given in Table 3.5, and the shaft speed reference generator is used with parameters given in Table 3.3. The parameters for the estimation schemes are given in Table 5.1. Note that perfect model knowledge is assumed, such that  $I_s$ ,  $Q_{f0}$ , and  $Q_{f1}$  are equal to the true parameters given in Table A.1.  $k_a$  and  $k_b$  are taken from the tuning rules in (5.13),  $a_t$  and  $b_t$  are taken from Section 2.1.8, and  $r$ ,  $p$ , and  $k$  are the parameters for  $\alpha_b(n)$  in (5.16). For calculation of  $\hat{\beta}_Q$  in (5.16) or (5.19),  $K_{QC}$  is used as specified in (3.9), with parameters given in Table 3.2.

### 5.5.1 Simulations in waves

Figure 5.1 shows time series from simulations with the  $Q_a$  observer from Section 5.1 and the  $K_Q$  estimation scheme from Section 5.2.  $T_d$  is given in Table 5.2.

Time interval	$T_d$	Corresp. $n_d$
$t < 30\text{s}$	50kN	$\approx 0.65\text{rps}$
$30\text{s} < t < 65\text{s}$	-100kN	$\approx -1.05\text{rps}$
$65\text{s} < t < 100\text{s}$	200kN	$\approx 1.31\text{rps}$

Table 5.2: Desired thrust  $T_d$  and corresponding shaft speed  $n_d$  for the simulation in Figure 5.1.

The mean submergence is  $h_0 = 6\text{m}$ , and the propeller is subject to irregular waves with  $H_s = 3\text{m}$ ,  $T_p = 9.7\text{s}$ , defined by 30 harmonic components extracted from the modified PM spectrum in (C.19). The wave-induced velocities are calculated from (C.33).

The upper two plots show the advance velocity  $V_a$  and the shaft speed  $n$ . Plots 3, 4, and 5 from above show results for the  $Q_a$  observer: the actual vs. estimated load torque, the actual vs. estimated torque loss factor, and the actual vs. estimated thrust. The lower two plots show results for the  $K_Q$  estimation scheme: the actual vs. estimated load torque, and the actual vs. estimated torque loss factor. The actual  $\beta_Q$  is calculated from  $Q_a$  and  $Q_n$  using (2.12), which results in singularities for the zero-crossing of  $n$ .

The results show that the  $Q_a$  observer tracks the actual propeller torque closely. The torque loss calculation works well except for very low  $n$ , where the singularity avoidance in (5.16) works as intended. The thrust estimation is based on (5.17), (5.41), and (5.42). For this propeller, the thrust is estimated with good accuracy. The estimate is better for positive  $n$  than for negative  $n$ , since the  $K_T - K_Q$  relationship in (5.41) is more accurate for  $n > 0$ ; see Figure 2.5. The  $K_Q$  estimation scheme is shown to work satisfactory for high  $n$ , but has trouble tracking  $Q_a$  for low  $n$ . The torque loss calculation from (5.19) has no singularities, but the estimate is not useful for low  $n$ . The level of noise in all the estimates is satisfactory.

### 5.5.2 Simulations with ventilation

Figure 5.2 shows time series from simulations with the propeller subject to ventilation. The simulation setup is as in the previous section, but the irregular waves are given by  $H_s = 8\text{m}$  and  $T_p = 13.1\text{s}$ . The ventilation simulation model from Figure 2.18 is used with the parameters given in Table A.2, and the propeller submergence calculated from (C.35). The thrust reference is 300kN.

The upper two plots show the advance velocity  $V_a$ , the submergence  $h$ , and the shaft speed  $n$ , plots 3, 4, and 5 from above show results for the  $Q_a$  observer, and the lower two plots show results for  $K_Q$  estimation scheme. The time series show that both estimation schemes track the actual load torque accurately, even with the abrupt losses due to ventilation, and that the torque loss calculations and thrust estimation schemes work satisfactory.

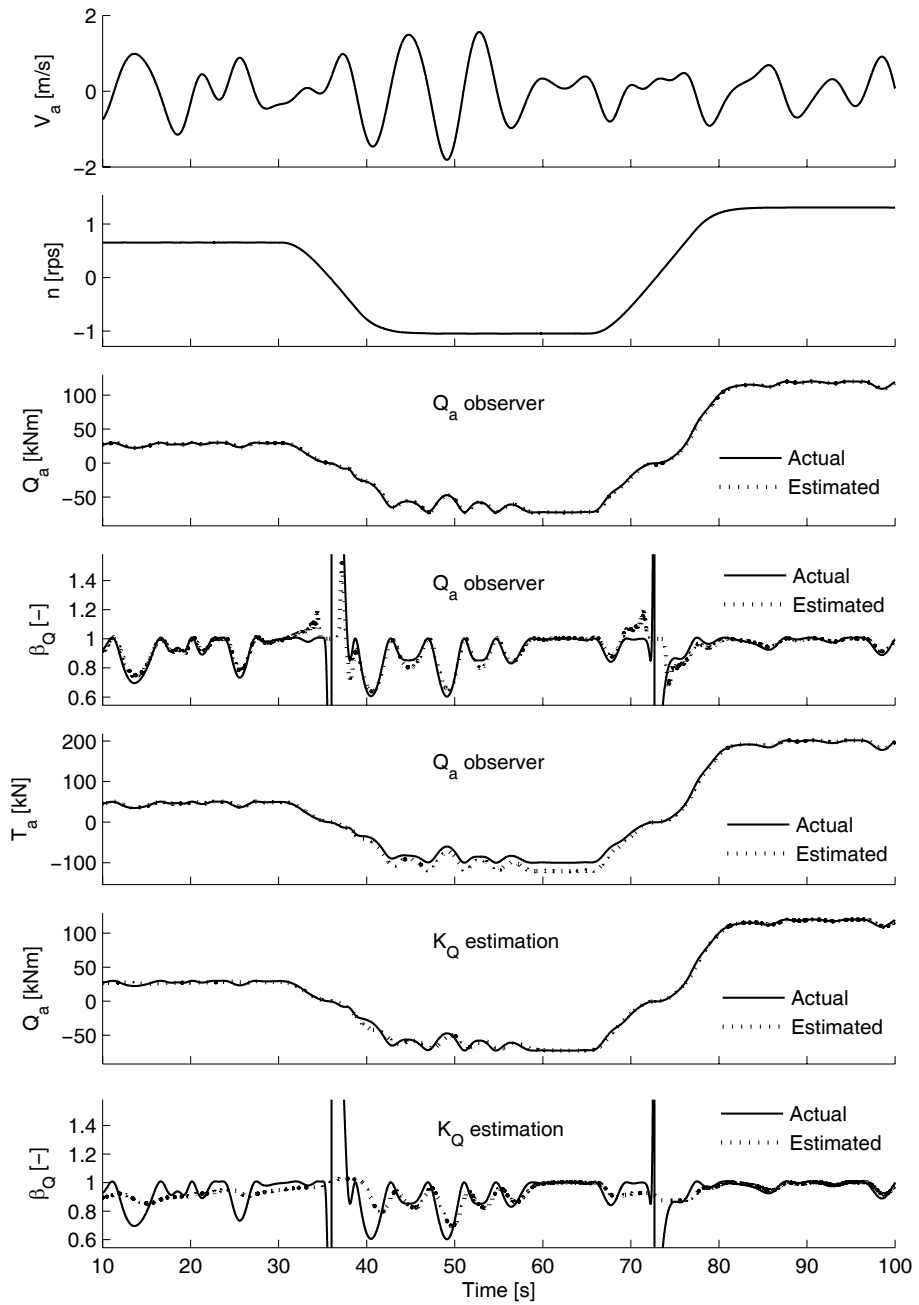


Figure 5.1: Time series of the  $Q_a$  observer (plots 3,4, and 5 from above) and  $K_Q$  estimation scheme (plots 6 and 7 from above), for varying  $T_r$  in waves.

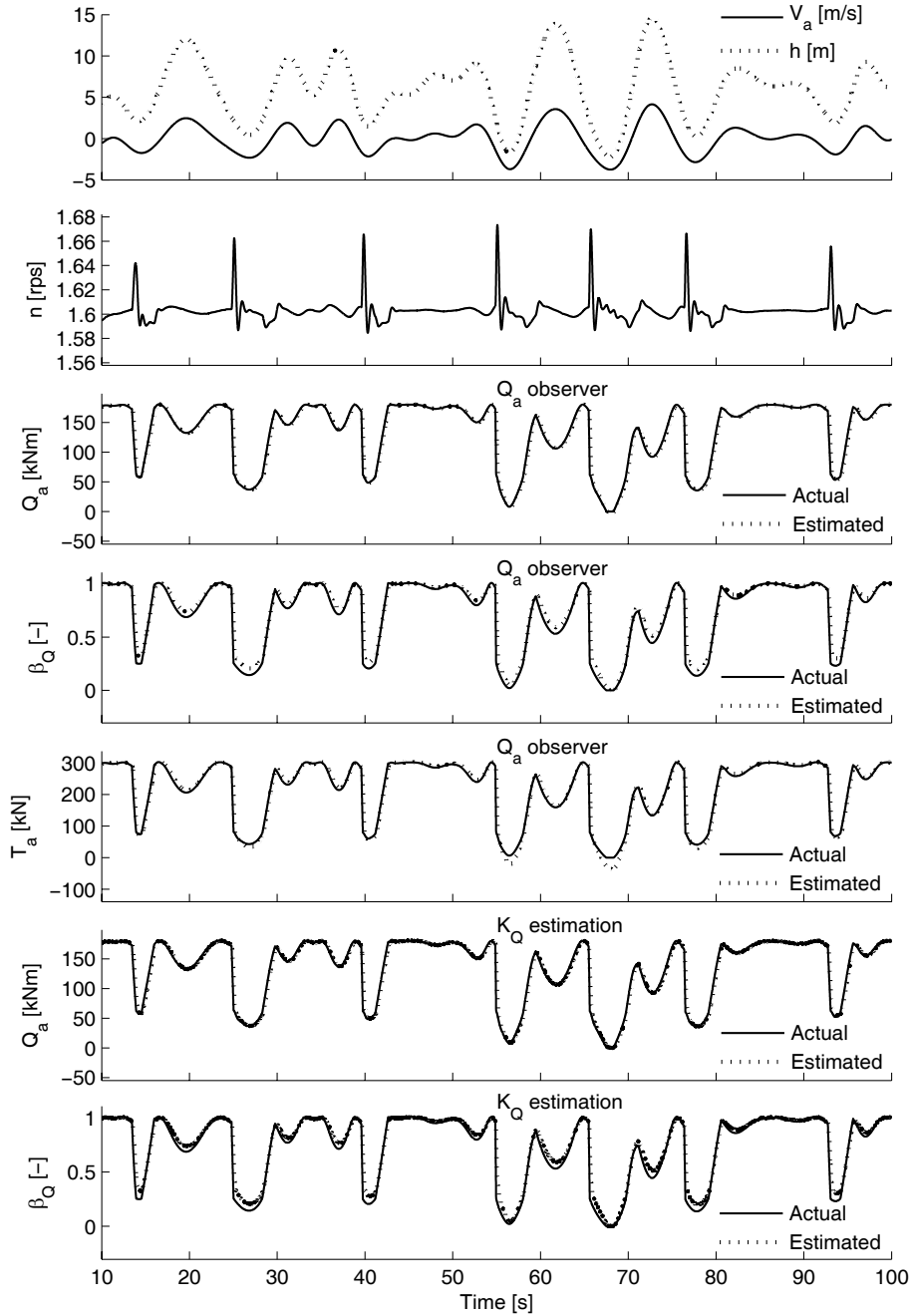


Figure 5.2: Time series of the  $Q_a$  observer (plots 3,4, and 5 from above) and  $K_Q$  estimation scheme (plots 6 and 7 from above), for  $T_r = 300\text{kN}$  in large waves, with the propeller subject to ventilation.

## Chapter 6

# Propulsion control in extreme conditions

The various controllers designed in Chapter 3 have so far mainly been evaluated for normal operating conditions, i.e. subject to moderate thrust losses. From the simulations in Section 3.18 and the sensitivity analysis in Section 4.8, it was found that controllers based on torque and power control have many desirable properties. However, as shown in Section 2.4, a propeller subject to *extreme conditions* may experience large load transients due to ventilation and in-and-out-of water effects. The controllers designed for normal conditions may then no longer give satisfactory performance. This was briefly treated in Section 4.9, where the controller performance when subject to large thrust losses was investigated with the quasi-static sensitivity functions, and in Section 4.10, where the stability properties of the shaft speed equilibrium was investigated. The results showed that the torque and power controllers have very poor performance in such conditions: since the objectives of torque and power control are to keep the motor torque or power constant, a loss of propeller load torque will lead to severe motor racing. As discussed in Sections 2.4.6 and 3.2.2, this leads to mechanical wear and tear because of the unsteady loading of the propeller. The torque controller will also give excessive power consumption. The shaft speed controller is partly able to handle the high thrust losses, since the objective of the controller is to keep the shaft speed constant. However, problems could arise because a well-tuned PID controller for normal conditions may give bad performance when subject to the rapid variations in load torque experienced during ventilation.

To assure satisfactory performance for all conditions, it is therefore necessary to introduce a new control strategy for use also in extreme conditions. This strategy has been denoted *anti-spin thruster control*. The nature of the control task is in many ways similar to that of controlling a car wheel with loss of traction on a slippery surface during acceleration or braking. The work on anti-

spin thruster control has therefore been motivated by similar control strategies in car anti-spin and ABS braking systems, see for example Haskara *et al.* (2000) or Johansen *et al.* (2001) and the references therein. This is also further discussed in Smogeli *et al.* (2006).

The concept of anti-spin thruster control was first introduced in Smogeli *et al.* (2003), followed by the introduction of combined torque/power control and a load torque observer with loss estimation in Smogeli *et al.* (2004a). Based on the two previous publications, the first complete anti-spin thruster control solution was presented in Smogeli *et al.* (2004b). The concept was further analyzed in Smogeli *et al.* (2006), where also two new, simplified anti-spin solutions were presented. Experimental results and a stability analysis of the proposed concept is presented in Smogeli and Sørensen (2006b).

## 6.1 Anti-spin control objectives

The general objectives of a thruster controller, as discussed in Section 3.2, are independent of the operating condition. However, because of the special nature of the ventilation losses, some additional considerations on the control objectives in extreme conditions are appropriate. The main objectives of anti-spin thruster control are to:

- Reduce the mechanical wear and tear of the propulsion unit.
- Limit power peaks.
- Assure robust and predictable performance.

From the experimental results with ventilated propellers, as presented in Sections 2.4.1 and 2.4.2 and Appendix D – and also from the discussions on mechanical wear and tear in Sections 2.4.6 and 3.2.2 – the following observations relevant to low-level thruster control can be made:

- Ventilation may occur abruptly when the propeller is operated at high loading and close to the free surface. It is a stochastic process that cannot easily be predicted.
- A ventilated propeller experiences large high-frequency loads and vibrations due to blade-frequency loading. The severity of these dynamic loads increase with the shaft speed.
- For a highly loaded propeller, the thrust during ventilation is almost independent of the shaft speed, especially for ducted propellers. For open propellers, a small increase in thrust is achievable by increasing the shaft speed.
- From a quasi-static point of view, there appears to be an optimal shaft speed that gives the highest thrust (“optimal thrust”) during ventilation,

especially for ducted propellers. Once ventilation has occurred, however, even a significant reduction of shaft speed may be insufficient for terminating the air suction (see Figure 2.15 and Remark 2.9). Hence, the optimal thrust can only be achieved by avoiding ventilation inception. This is not considered a realistic option, since it is assumed that ventilation cannot be predicted.

To summarize, the shaft speed of a highly loaded propeller during ventilation should be lowered in order to reduce the mechanical wear and tear. This can be done without significantly affecting the thrust production. From a total evaluation of the control objectives and the known behavior of a ventilating propeller, it is hence found that the following actions are the most appropriate during ventilation:

1. Primary anti-spin action: take control of the shaft speed.
2. Secondary anti-spin action: reduce the shaft speed.

The first action mainly applies to the torque and power controllers, which suffer from severe propeller racing during ventilation. The second action applies equally to all controllers. Its main objective is to reduce mechanical wear and tear, and ease the transition back to the fully loaded condition.

## 6.2 The anti-spin control concept

The proposed anti-spin concept is a hybrid control scheme, where the condition of the thruster is monitored, and anti-spin control actions are invoked when a ventilation incident is detected. The complete thruster control scheme is composed of four main functions:

1. The *core thruster controller*, which normally is left to work undisturbed. This could be any of the controllers in Table 3.1.
2. A *performance monitoring* scheme. This would typically be one of the observers presented in Chapter 5.
3. A *ventilation detection* scheme, based on the output of the performance monitoring scheme.
4. An *anti-spin controller*, which is invoked by the ventilation detection scheme.

A block diagram of the proposed anti-spin control concept is shown in Figure 6.1, where the performance monitoring and ventilation detection schemes have been assembled in one block. When comparing this figure with the structure of the control scheme for normal conditions in Figure 3.1, the proposed concept can

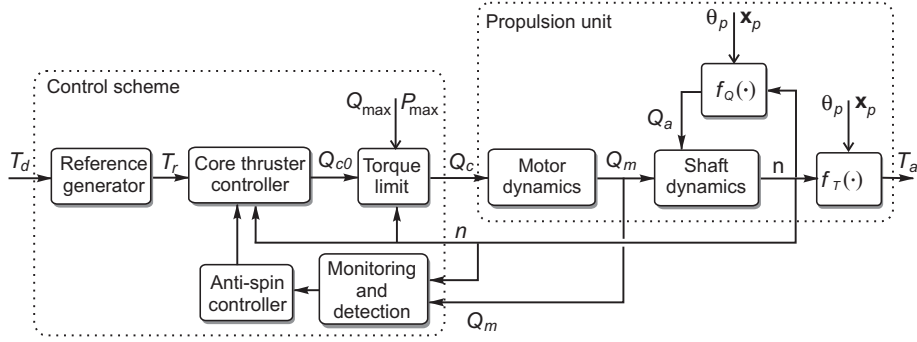


Figure 6.1: Block diagram of the proposed anti-spin control concept, including the core thruster controller, detection scheme, and anti-spin controller.

be seen as an add-on of the two functional blocks “Monitoring and detection” and “Anti-spin controller”.

In this work, anti-spin thruster control is primarily treated as a necessary addition to the controllers based on torque and/or power control, since these have been found preferable in normal operating conditions. However, it may also be possible to improve the performance of a shaft speed controller during ventilation by introducing anti-spin control: a primary anti-spin action can be added in order to improve the transient performance at ventilation inception and termination, and a secondary anti-spin action can be used to reduce the shaft speed during ventilation. This is shortly treated in Section 6.6.3.

### 6.3 Ventilation detection

The detection of high thrust losses may be done in several ways. A simplistic approach is to set the detection criteria by rate of change of shaft speed and/or motor torque – if the shaft speed increases quickly or the torque drops quickly, this indicates a high loss situation. A similar approach for car wheel anti-spin was presented in Haskara *et al.* (2000). A more sophisticated detection algorithm can be designed based on the performance monitoring tools presented in Chapter 5. Since the anti-spin control scheme is highly dependent on fast and accurate detection of the ventilation incidents, the latter approach has been preferred.

Estimates of the propeller load torque, torque coefficient, and torque loss factor can be found from the propeller load torque observer in (5.7), or the  $K_Q$  estimation scheme in (5.26). From experience with the various formulations, the load torque torque observer in (5.7) has been found to give the best over-all performance. The torque loss estimate  $\hat{\beta}_Q$  is then calculated from (5.16), and the ventilation detection is done by monitoring  $\hat{\beta}_Q$  and the motor torque  $Q_m$ . The detection algorithm is implemented by defining limits for the onset and termi-

nation of ventilation,  $\beta_{v,on}$  and  $\beta_{v,off}$ . An additional criterion for detection is that the magnitude of the motor torque is non-increasing, i.e.  $\text{sign}(Q_m)\dot{Q}_m \leq 0$ . Finally, the detection scheme should only be active for  $|n_r| > n_{\min}$ , where  $n_{\min}$  is a chosen threshold, and  $n_r$  given from (3.1). This is to avoid false detection and chattering for low propeller loading, where anti-spin control is not needed – the simulation results in Section 5.5 clearly showed that the loss estimation was unreliable for low  $n$ .

The detection signal is termed  $\zeta$ . It is set to 1 when ventilation is detected, and 0 otherwise. A typical ventilation incident will then give the following evolution of  $\zeta$ , with time instants  $t_1 < t_2 < t_3$ :

$$\begin{aligned} t_1 : \quad & \hat{\beta}_Q > \beta_{v,on} & \Rightarrow \zeta = 0, \\ t_2 : \quad & \hat{\beta}_Q \leq \beta_{v,on} \cap \text{sign}(Q_m)\dot{Q}_m \leq 0 \cap |n_r| > n_{\min} & \Rightarrow \zeta = 1, \\ t_3 : \quad & \hat{\beta}_Q \geq \beta_{v,off} & \Rightarrow \zeta = 0. \end{aligned} \quad (6.1)$$

To avoid switching and chattering of  $\zeta$  due to measurement noise and transients, an algorithm implementing a detection delay is added, such that once  $\zeta$  has changed value, it cannot be reset until after a given time interval  $T_{vent}$ . The detection delay can be seen as an implementation of the switching dwell-time proposed in Hespanha and Morse (2002) and Hespanha *et al.* (2003). The motor torque should be low-pass filtered before numerical differentiation. This ventilation detection scheme has shown good performance in both simulations and experiments.

**Remark 6.1** *To allow natural oscillations about the nominal propeller loading due to time-varying inflow to the propeller, and noise in the estimate  $\hat{\beta}_Q$ ,  $\beta_{v,on}$  must be chosen significantly lower than 1.*

## 6.4 Anti-spin control actions

During operation in normal conditions, one of the core thruster controllers proposed in Table 3.1 is used. When extreme conditions are encountered, the anti-spin control actions are triggered by the ventilation detection algorithm. Different approaches to the anti-spin actions are possible, with the two most general being:

1. Switch to a completely new control strategy.
2. Modify the existing control strategy.

If an approach with switching is chosen, two options exist:

- 1a. Switch anti-spin on and off every time ventilation is detected and terminated.

- 1b.** Switch to an anti-spin control mode when ventilation is first detected, and stay in this mode until no ventilation incidents have been detected for a given time interval.

Alternative 1a may introduce problems with ensuring performance and stability during switching, although new results have improved the ability to analyze stability of such switching control schemes (Hespanha and Morse, 2002; Hespanha *et al.*, 2003). Bumpless transfer and switching problems are also discussed in for example Åström and Wittenmark (1997). This approach will not be further treated here. Alternative 1b is a more practical approach for this problem – one could e.g. use a controller based on torque and power control for normal conditions, and once a ventilation incident is detected switch to shaft speed control. This scheme is of course based on the presumption that the shaft speed controller has acceptable performance during ventilation. An implementation like this was apparently used for the diesel engine governor presented in Blanke and Busk Nielsen (1987, 1990); when the governor was run in power mode, and an excessive shaft speed was detected, the governor was automatically switched to shaft speed control.

The switching problem of strategy 1a is alleviated by choosing the second anti-spin approach. In this case, the existing control strategy must be compatible with the desired anti-spin control actions. Two natural modifications of the core thruster control strategies when ventilation is detected are:

- 2a.** Reduce the controller output  $Q_{ci}$  (3.18) in order to reduce the motor torque and lower the shaft speed.
- 2b.** Lower the thrust reference  $T_r$  in order to reduce the motor torque indirectly.

The torque and thrust modification factors are termed  $\gamma_Q$  and  $\gamma_T$ , respectively, and used such that the anti-spin commanded torque  $Q_{cas}$  and anti-spin thrust reference  $T_{ras}$  are defined as:

$$Q_{cas} = \gamma_Q Q_{ci}, \quad (6.2)$$

$$T_{ras} = \gamma_T T_r. \quad (6.3)$$

In the next section, it will be shown that alternative 2a, i.e. (6.2), is convenient for implementing the *primary anti-spin action*, which is to take control of the shaft speed, while alternative 2b, i.e. (6.3), is convenient for implementing the *secondary anti-spin action*, which is to reduce the shaft speed to an appropriate value.

## 6.5 Main anti-spin control result: torque scaling

The proposed anti-spin controller is based on the ventilation detection scheme from Section 6.3, which gives a detection signal  $\zeta \in \{0, 1\}$ , and the estimated torque loss factor  $\hat{\beta}_Q$  from Section 5.1.

### 6.5.1 Primary anti-spin action

The primary anti-spin control action will be motivated from a Lyapunov stability analysis, with the analysis from Section 4.10 as a starting point. The following assumption is made for the anti-spin analysis:

**Assumption 6.1** *The friction and inertia coefficients are known, such that  $\delta b_f(\omega_r) = 0$  and  $\delta I = 0$  in (4.80).*

Under Assumption 6.1, the rotational dynamics in (4.88) is written as:

$$\begin{aligned}\dot{x} &= -b_1 x - \bar{b}_2((x + \omega_r)|x + \omega_r| - \omega_r|\omega_r|) \\ &\quad - b_{2\delta}(t, \omega)(x + \omega_r)|x + \omega_r| - b_0\theta(\omega_r, \omega) + u_\delta \\ &= f(x) + g(t, x),\end{aligned}\tag{6.4}$$

where  $f(x)$  is defined in (4.89).  $g(t, x)$  from (4.98) (under Assumption 6.1) is rewritten as:

$$g(t, x) = u_\delta + (1 - \beta_Q(t, x + \omega_r))\bar{b}_2(x + \omega_r)|x + \omega_r|. \tag{6.5}$$

Note that (4.84) has been used to insert  $b_{2\delta}(t, \omega) = -(1 - \beta_Q(t, \omega))\bar{b}_2$ .

Assume that the propeller is initially operating at steady state with input  $\bar{u}$  and quadratic damping coefficient  $\bar{b}_2$ . The loading of the propeller then changes due to a ventilation incident, described by the torque loss factor  $\beta_Q(t, \omega)$ . Motivated by (6.2), the primary anti-spin action is to modify the controller output  $Q_{ci}$  with a torque scaling factor  $\gamma_Q$ :

$$Q_{cas} = \gamma_Q Q_{ci} \Leftrightarrow u = \gamma_Q \bar{u}, \tag{6.6}$$

where  $Q_{cas}$  is the anti-spin commanded torque. During ventilation,  $\gamma_Q$  is proposed to be given by  $\gamma_Q = \hat{\beta}_Q$ . In normal operation,  $\gamma_Q = 1$  such that  $Q_{cas} = Q_{ci}$ . In order to reduce transients, the transitions of  $\gamma_Q$  between 1 and  $\hat{\beta}_Q$  at ventilation detection and termination should not be done abruptly. It is therefore proposed to add a rate limiting function as given in (3.11) with slew rate limits  $\dot{\gamma}_{rise} > 0$  and  $\dot{\gamma}_{fall} < 0$ , and a first order low-pass filter with time constant  $\tau_\gamma$ . The filter will also remove noise in the estimate  $\hat{\beta}_Q$  that otherwise would have been inserted into the control law. The implementation of  $\gamma_Q$  becomes:

$$\begin{aligned}\gamma_1 &= \begin{cases} 1 & \text{for } \zeta = 0 \text{ (not ventilated),} \\ \hat{\beta}_Q & \text{for } \zeta = 1 \text{ (ventilated),} \end{cases} \\ \gamma_2 &= f_{slew}(\gamma_1, \dot{\gamma}_{rise}, \dot{\gamma}_{fall}), \\ \gamma_Q(s) &= \gamma_2(s) \frac{1}{\tau_\gamma s + 1},\end{aligned}\tag{6.7}$$

where  $\gamma_1$  and  $\gamma_2$  are internal states. Tuning of  $\dot{\gamma}_{rise}$ ,  $\dot{\gamma}_{fall}$ , and  $\tau_\gamma$  is discussed in Section 6.8.1.

**Theorem 6.1** In the presence of an unknown disturbance  $\beta_Q(t, \omega)$ , the primary anti-spin control law from (6.6) and (6.7):

$$u = \gamma_Q \bar{u}, \quad (6.8)$$

will yield the solutions  $x(t)$  of (6.4) UUB.

**Proof.** With  $u$  given by (6.8),  $u_\delta = (\gamma_Q - 1)\bar{u}$ . Inserting  $\bar{u}$  from (4.86), the perturbation term  $g(t, x)$  in (6.5) becomes:

$$\begin{aligned} g(t, x) &= (\gamma_Q - 1)\bar{b}_2\omega_r |\omega_r| + (1 - \beta_Q(t, \omega))\bar{b}_2(x + \omega_r) |x + \omega_r| \\ &= h(t, x) + g_2(t, x), \end{aligned} \quad (6.9)$$

where  $h(t, x)$  and  $g_2(t, x)$  are given by:

$$h(t, x) = \bar{b}_2(1 - \beta_Q(t, \omega))((x + \omega_r) |x + \omega_r| - \omega_r |\omega_r|), \quad (6.10)$$

$$g_2(t, x) = (\gamma_Q - \beta_Q(t, \omega))\bar{b}_2\omega_r |\omega_r| = (\gamma_Q - \beta_Q(t, \omega))\bar{u}. \quad (6.11)$$

The perturbed system (6.4) can now be rewritten in terms of a new nominal system  $f_2(t, x)$  and a new perturbation term  $g_2(t, x)$ :

$$\dot{x} = f_2(t, x) + g_2(t, x), \quad (6.12)$$

where  $f_2(t, x)$  from (4.89) and (6.10) is:

$$\begin{aligned} f_2(t, x) &= f(t, x) + h(t, x) \\ &= -b_0\theta(\omega_r, \omega) - b_1x - \bar{b}_2\beta_Q(t, \omega)((x + \omega_r) |x + \omega_r| - \omega_r |\omega_r|). \end{aligned} \quad (6.13)$$

The stability of the unperturbed system (6.12) with  $g_2(t, x) = 0$  is analyzed with  $V(x)$  given by (4.90). The derivative of  $V(x)$  along the trajectories of  $f_2(t, x)$  in (6.12) becomes:

$$\dot{V}(x) = -b_0\theta(\omega_r, \omega)x - b_1x^2 - \bar{b}_2\beta_Q(t, \omega)x((x + \omega_r) |x + \omega_r| - \omega_r |\omega_r|). \quad (6.14)$$

Using Lemma 4.1, (4.93), and (4.94) as in the proof of Proposition 4.1, and Property 4.1, it follows that:

$$b_0\theta(\omega_r, \omega)x + \bar{b}_2\beta_Q(\cdot)x((x + \omega_r) |x + \omega_r| - \omega_r |\omega_r|) \geq 0, \quad (6.15)$$

for all  $x \in \mathbb{R}$ . Hence, (4.95) holds also in this case:

$$\dot{V}(x) \leq -b_1x^2 \leq -k_3 \|x\|^2. \quad (6.16)$$

The equilibrium point  $x = 0$  of the unperturbed system (6.12) and hence (6.4) is therefore GES.

The perturbed system (6.12) with  $g_2(t, x) \neq 0$  is subject to a non-vanishing perturbation. By using Lemma 9.2 in Khalil (2002) as in Proposition 4.2, the solutions  $x(t)$  of (6.12) and hence (6.4) are shown to be UUB. ■

**Corollary 6.1** *In the presence of a known disturbance  $\beta_Q(t, \omega)$ , the anti-spin control law:*

$$u = \beta_Q(t, \omega)\bar{u}, \quad (6.17)$$

*will yield the equilibrium  $x = 0$  of (6.4) GES.*

**Proof.** With  $u$  given by (6.17), this is equivalent to using  $\gamma_Q = \beta_Q(t, \omega)$  in (6.8). Hence, the perturbation term  $g_2(t, x) = 0$  in (6.11), and (6.12) reduces to the unperturbed system  $\dot{x} = f_2(t, x)$ , which was shown to be GES. ■

For a further investigation of the *transient* behavior of the perturbed system in (6.4), the Lyapunov analysis can be extended to give estimates of the trajectory bounds by using the comparison method, as shown in Lemma 9.4 and 9.6 in Khalil (2002). This is further treated in Appendix F.3.

**Remark 6.2** *The proposed primary anti-spin action in (6.6) is independent of the chosen core thruster controller, and is hence compatible with any of the controllers in Table 3.1. However, a well-tuned shaft speed PI controller will not benefit from the primary anti-spin action, since there is no need for additional measures to control the shaft speed in this case. For the controllers based on torque and/or power control (i.e. the Q, P, QP, MQP1, MQP2, and SQP controllers), the primary anti-spin action will alleviate the problem of propeller racing during ventilation.*

**Remark 6.3** *Corollary 6.1 states that perfect shaft speed control during ventilation would be possible if the ventilation incident could be foreseen, and  $\beta_Q(t, \omega)$  was known. However, since the propeller torque is not available as a measurement, and the ventilation incidents are random processes caused by wave elevation and vessel motion, this is not possible. An implementable solution is therefore to use the torque loss estimation and ventilation detection schemes as proposed in Theorem 6.1. The deviation of the shaft speed from the steady-state solution will depend on the time series of the deviation of the torque modification factor  $\gamma_Q$  from the actual torque loss factor  $\beta_Q(t, \omega)$ , as shown in (6.11). The deviation will be affected by the ventilation detection scheme, the accuracy of the estimated torque loss factor  $\hat{\beta}_Q$ , and the chosen rate limits and low-pass filter for  $\gamma_Q$ .*

### 6.5.2 Secondary anti-spin action

For reduction of wear and tear due to dynamic propeller loading during ventilation, it may be desirable to lower the propeller shaft speed, as discussed in Section 6.1. As indicated in (6.3), this can be done by modifying the thrust reference during ventilation, since the primary anti-spin control action assures that the shaft speed is kept close to its reference. The desired shaft speed during ventilation,  $n_{as}$ , will be a thruster specific parameter, and must be chosen as a trade-off between thrust production, wear and tear, and response time.  $n_r$

should not be changed to  $n_{as}$  instantaneously, as this will lead to undesired transients. It is therefore proposed to add a low-pass filter with time constant  $\tau_n$  and a rate limiting algorithm with rate limits  $\dot{n}_{vent}^+ > 0$  and  $\dot{n}_{vent}^- < 0$  to the switch between  $n_r$  and  $n_{as}$  at ventilation detection and termination. The filtered and rate limited shaft speed reference is termed  $n_{ras}$ , and the corresponding thrust reference termed  $T_{ras}$ .

The implementation is similar to the shaft speed reference generator in (3.14), with the mappings  $g_n(T_r)$  and  $g_n^{-1}(n_r)$  defined in (3.1) and (3.5), a rate limiting function  $f_{slew}(\cdot)$  as defined in (3.11), and a first order filter:

$$\begin{aligned} n_r &= g_n(T_r), \\ n_{r2} &= \begin{cases} n_r & \text{for } \zeta = 0 \text{ (not ventilated),} \\ \text{sign}(n_r)n_{as} & \text{for } \zeta = 1 \text{ (ventilated),} \end{cases} \\ n_{r3} &= f_{slew}(n_{r2}, \dot{n}_{vent}^+, \dot{n}_{vent}^-), \\ n_{ras}(s) &= n_{r3}(s) \frac{1}{\tau_n s + 1}, \\ T_{ras} &= g_n^{-1}(n_{ras}), \end{aligned} \quad (6.18)$$

where  $n_{r2}$  and  $n_{r3}$  are internal states. The mapping from  $T_r$  to  $T_{ras}$  in (6.18) will also be referred to as a *setpoint mapping*.

### Including inertia compensation

If the rotational inertia is significant, it was shown in Section 3.18.1 that the response of the thruster to a change of torque setpoint may be slow, and that an inertia compensation scheme was needed to speed up the response of the controllers based on torque and power control. Hence, if a fast response to the secondary anti-spin action is wanted, it may be necessary to include an additional inertia compensation term. This can be done by extracting  $\dot{n}_{ras}$  from the low-pass filter in (6.18) and  $\dot{n}_r$  from the reference generator, and use the difference between  $\dot{n}_r$  and  $\dot{n}_{ras}$  in an additional inertia compensation scheme:

$$Q_{if,as} = \text{sign}(T_r) \min(0, \text{sign}(T_r) I_c 2\pi (\dot{n}_{ras} - \dot{n}_r)). \quad (6.19)$$

Here,  $I_c$  is the rotational inertia as in (3.22), and  $Q_{if,as}$  is the additional inertia compensation torque. With a time-varying  $T_r$  and no ventilation,  $\dot{n}_{ras} = \dot{n}_r$ , and  $Q_{if,as} = 0$ . During ventilation, with  $\dot{n}_{ras} \neq \dot{n}_r$ , (6.19) will speed up the convergence to  $n_{ras}$  at ventilation detection.

**Remark 6.4** *With the formulation of  $Q_{if,as}$  in (3.22), no additional inertia compensation is used to speed up the transition to  $n_r$  at ventilation termination. This is to avoid a too rapid increase in motor torque and shaft speed.*

To reduce mechanical wear and tear, the additional inertia compensation from (6.19), should not be allowed to change the commanded torque direction.

A saturation of the total commanded torque can be implemented by redefining  $Q_{cas}$  in (6.6) as:

$$Q_{cas} = \text{sign}(\gamma_Q Q_{ci}) \max(0, [\text{sign}(\gamma_Q Q_{ci})(\gamma_Q Q_{ci} + Q_{if,as})]). \quad (6.20)$$

### 6.5.3 Resulting anti-spin controller

Figure 6.2 shows a block diagram of the resulting thruster controller with anti-spin. The additional inertia compensation for the secondary anti-spin action has been omitted in the figure.

### 6.5.4 Steady-state analysis

A similar result as the one given in Corollary 6.1 may be obtained by analyzing the steady-state properties of the proposed ideal anti-spin control law (6.17) during a ventilation incident with a constant torque loss factor  $\beta_Q$ . At a steady state ventilation condition with perfect friction compensation, i.e.  $Q_{ff}(n_r) = Q_f(\omega)$ , the propeller load torque  $Q_a$  and the commanded torque  $Q_c$  are equal. With  $Q_a = Q_c$ ,  $Q_c = \beta_Q Q_{ci}$  from (6.17), and  $\beta_Q$  from (2.12) and (2.9), the following relationship can be established:

$$Q_a = Q_c = \beta_Q Q_{ci} = \frac{Q_a}{\text{sign}(n) K_{Q0} \rho D^5 n^2} Q_{ci}, \quad n \neq 0. \quad (6.21)$$

Under the assumption that  $\text{sign}(n) = \text{sign}(Q_{ci})$  and  $K_{Q0} = K_{QC}$ , the resulting shaft speed is:

$$n = \text{sign}(Q_{ci}) \sqrt{\frac{|Q_{ci}|}{K_{QC} \rho D^5}}. \quad (6.22)$$

Inserting for the torque controller in (3.29), the steady-state shaft speed becomes:

$$\begin{aligned} n &= \text{sign}(Q_{eq}) \sqrt{\frac{|Q_{eq}|}{K_{QC} \rho D^5}} = \text{sign}(T_r) \sqrt{\frac{\frac{K_{QC}}{K_{TC}} D |T_r|}{K_{QC} \rho D^5}} \\ &= \text{sign}(T_r) \sqrt{\frac{|T_r|}{\rho D^4 K_{TC}}} = n_r, \end{aligned} \quad (6.23)$$

where  $n_r$  is the shaft speed reference given by (3.1). Inserting for the power controller (3.32) in (6.22) and solving with respect to  $n$ , the same result is obtained. This is also true for the combined controller, since it is a linear combination of the torque and power controllers. Actually, from Corollary 6.1,  $n = n_r$  regardless of the choice of core thruster controller, as long as (6.17) is applied.

It is interesting to note that this also could be inferred from the shaft speed sensitivity functions presented in Chapter 4. Using (6.17) with the torque or

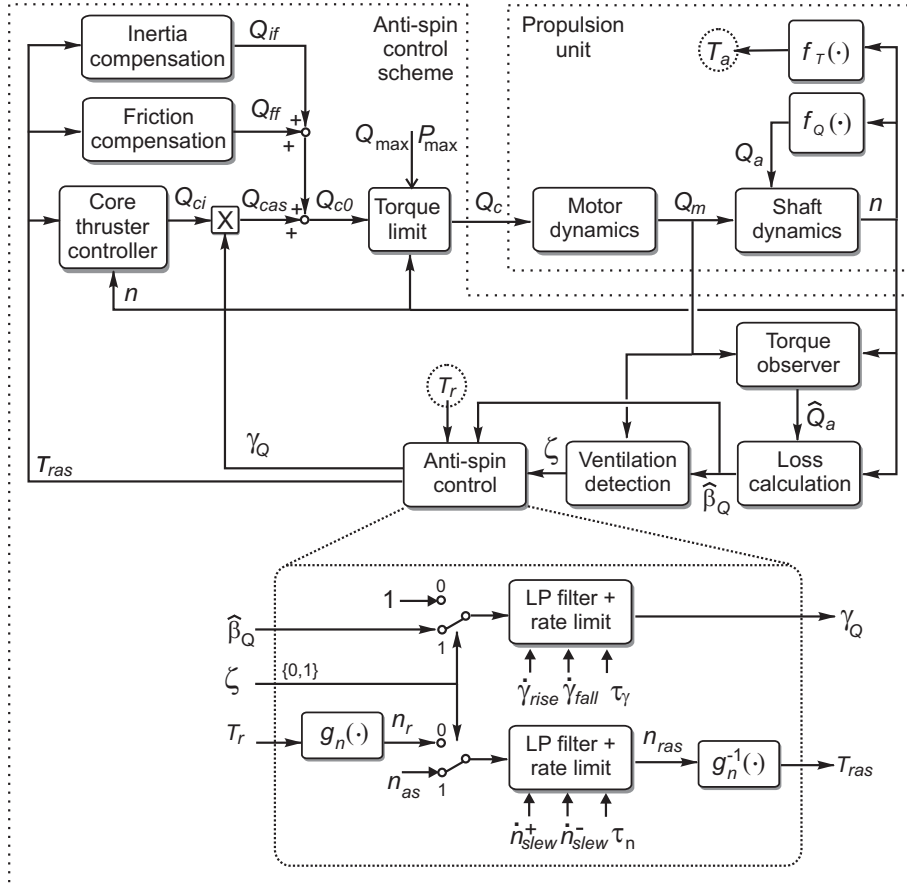


Figure 6.2: The proposed torque scaling anti-spin control scheme, including core thruster controller, inertia and friction compensation, torque limiting function, torque observer, loss calculation, ventilation detection, and anti-spin control actions. The input  $T_r$  and output  $T_a$  of the propulsion unit with thruster controller are marked with dotted circles.

power controller involves multiplying the controller formulations in (3.29) and (3.32) with  $\beta_Q = K_Q/K_{QC}$ , see (2.12). This is the same as using the two controllers with  $K_{QC} \equiv K_Q$ . From the definitions of the shaft speed sensitivity functions  $sn_q(\cdot)$  and  $sn_p(\cdot)$  in Table 4.1, this implies that  $sn_q(\cdot) \equiv 1$  and  $sn_p(\cdot) \equiv 1$ , which means that  $n \equiv n_r$ .

## 6.6 Alternative anti-spin controllers

The anti-spin controller presented in Section 6.5 was shown to be compatible with all the core thruster controllers in Table 3.1, and has been chosen as the preferred solution. This section presents some alternative anti-spin solutions, with varying degrees of complexity.

### 6.6.1 Speed bound anti-spin control

This is the simplest of the anti-spin control formulations presented in this work. A dynamic shaft speed bound is added to the core thruster controller, which can be any of the controllers in Table 3.1 based on torque and/or power control. This limits the propeller racing, since the shaft speed is kept within the desired bounds. Using the shaft speed reference  $n_r$  from (3.1), the dynamic speed bound  $n_b$  is defined as:

$$n_b = (1 + r_b)n_r, \quad (6.24)$$

where  $r_b$  is the speed bound factor, typically in the range  $r_b \in [0.2, 0.3]$ . This means that the shaft speed is allowed to deviate by 20 – 30% from its nominal value. The shaft speed can then vary freely as long as  $|n| < |n_b|$ , such that the core thruster controller mostly is allowed to work undisturbed. In a high loss situation, when torque or power control normally would lead to severe propeller racing, the shaft speed is bounded by  $n \approx n_b$ .

The shaft speed bound is implemented by an additive shaft speed PI controller, which is only activated when  $|n| \geq |n_b|$ :

$$Q_{cas} = Q_{ci} + Q_b, \quad (6.25)$$

where  $Q_{ci}$  is the core thruster controller output, and the additive PI term  $Q_b$  is defined as:

$$\begin{aligned} Q_b &= \text{sign}(T_r) \min \left( 0, K_p e_b + K_i \int_0^t e_b(\tau) d\tau \right), \\ e_b &= |n_b| - |n|. \end{aligned} \quad (6.26)$$

As in (3.27),  $K_p > 0$  and  $K_i > 0$  are the proportional and integral gains, which should be tuned to give rapid response, and  $e_b$  is the bound error. The minimum operator in (6.26) means that  $Q_b$  is only allowed to reduce the magnitude of the commanded torque. To avoid integral windup, the integral term in (6.26) may only assume negative values (upper windup limit at zero). With respect to the

anti-spin control actions defined in Section 6.4, only the torque modification  $\gamma_Q$  is used, with  $\gamma_Q$  in this case implicitly given by:

$$\gamma_Q = \frac{Q_{cas}}{Q_{ci}} = \frac{Q_{ci} + Q_b}{Q_{ci}}. \quad (6.27)$$

This formulation does not utilize a dedicated ventilation detection scheme as proposed in Section 6.3, but “detects” ventilation simply by an excessive shaft speed. The number of control parameters is therefore kept low, such that the controller is relatively easy to tune.

**Remark 6.5** When the propeller is subject to increasing advance velocities, the torque and power controllers will increase the shaft speed in order to compensate for the reduced loading. This increase should not be detected as a ventilation incident. A weakness of the speed bound anti-spin controller is therefore that in order to allow the core thruster controller to work undisturbed,  $r_b$  should be chosen relatively high. This means that the propeller is allowed to spin more out during ventilation.

### 6.6.2 Additive PI anti-spin control

This anti-spin control scheme is similar to the solution presented in Section 6.5, but applies an additive shaft speed PI controller as primary anti-spin action instead of the torque scaling used in (6.6). Using the detection scheme from Section 6.3, the primary anti-spin control action is formulated as follows:

$$Q_{cas} = \begin{cases} Q_{ci} & \text{for } \zeta = 0, \\ \text{sign}(T_r) \max(0, \text{sign}(T_r)(Q_{ci} + Q_{PI})) & \text{for } \zeta = 1, \end{cases} \quad (6.28)$$

where  $Q_{ci}$  is the core thruster controller output, and the additive PI term  $Q_{PI}$  is defined similarly as in (3.27):

$$\begin{aligned} Q_{PI} &= K_p e + K_i \int_0^t e(\tau) d\tau, \\ e &= n_r - n. \end{aligned} \quad (6.29)$$

As before,  $K_p > 0$  and  $K_i > 0$  are the proportional and integral tuning gains, and  $e$  is the shaft speed error. The integral term in (6.29) is continuously reset for  $\zeta = 0$  to avoid integral windup. To reduce mechanical wear and tear, the total commanded torque  $Q_{cas}$  in (6.28) is saturated as in (6.20), such that the torque direction cannot be reversed by the additive PI controller.

As a secondary antispin action, the thrust reference  $T_r$  may be lowered when  $\zeta = 1$  as in (6.18).

### 6.6.3 Shaft speed anti-spin control

If a well-tuned shaft speed controller is chosen for operation in normal condition, the need for anti-spin control is reduced. Since the shaft speed controller aims at

keeping the shaft speed constant regardless of the propeller loading, no primary anti-spin action to regain control of the shaft speed during ventilation may be necessary. Actually, the primary anti-spin control action presented in (6.6) is compatible with the shaft speed PI controller. Simulations show, however, that the performance of the shaft speed controller is not improved by adding (6.6). This could be expected, since (6.6) does not modify the PI controller directly, but only scales its output; in order to improve the performance, it is necessary to address the PI terms directly.

### PI controller with setpoint mapping

If the secondary anti-spin action is deemed appropriate, the setpoint mapping in (6.18) may be applied directly to a conventional shaft speed PI controller. This requires a ventilation detection scheme, as proposed in Section 6.3. In addition to the torque observer and the ventilation detection scheme, the equations for implementation are taken directly from (3.1), (3.27), and (6.18). With a well-tuned PI controller, the performance of this scheme during ventilation is expected to be similar to the scheme presented in Section 6.5.

**Remark 6.6** *This scheme relies on the PI gains to be tuned to give good performance during ventilation. As will be shown in Section 6.8, a PI controller that is tightly tuned for good performance in normal conditions, may give unsatisfactory results when subject to the large load transients experienced during ventilation. If such a scheme is chosen, the PI gains should therefore be tuned with care.*

### PI controller with integrator reset and setpoint mapping

One of the potential problems with a shaft speed PI controller during ventilation is integrator discharge. When most of the propeller load suddenly disappears, the integral term must wind down quickly. If the PI gains are not tuned to cope with this situation, the consequence may be large oscillations in the controller output. This is certainly not desirable, and may inflict damage to the mechanical components of the thruster.

A possible solution to this problem is to use an *integrator reset* mechanism, see e.g. Zheng *et al.* (2000) and the references therein. The idea is to monitor the control system performance, and reset the integral term when large process discrepancies are detected. A simple approach is to use the ventilation detection scheme from Section 6.3, and reset the integral term to zero when ventilation is detected. Combined with the secondary anti-spin action in (6.18), this approach gives a very rapid reduction in shaft speed. However, it gives no performance improvements when ventilation terminates. From simulations and experiments, this approach seems to be too coarse to get good results. The rapid change in controller output may also add to the mechanical wear and tear instead of reducing it.

Controller	Abbreviation	Section
Torque scaling anti-spin control	TS AS control	6.5
Speed bound anti-spin	SB AS control	6.6.1
Additive PI anti-spin control	API AS control	6.6.2
Primary anti-spin action	p	6.5.1
Secondary anti-spin action	s	6.5.2

Table 6.1: Anti-spin controllers for extreme conditions.

A more sophisticated Lyapunov-based integrator reset approach is presented in Bakkeheim *et al.* (2006). In this work, a load torque observer as presented in Section 5.1 is utilized for online calculation of a Lyapunov function origin (equilibrium point). The Lyapunov function value will jump to a higher value when the propeller starts or stops ventilating. A multiple model Lyapunov algorithm then decides when to take integrator reset actions, and selects the integrator value that gives the greatest drop in the Lyapunov function value. This enables tuning of the PI gains to be done with focus on normal operating conditions, since the reset mechanism handles the transients during extreme conditions. The setpoint mapping in (6.18) may also be applied. The concept was tested experimentally with the setup described in Section 7.1, and proven successful.

**Remark 6.7** *The complexity of the shaft speed PI controller with Lyapunov-based integrator reset is comparable to that of the proposed anti-spin scheme in Section 6.5. The two approaches share the load torque observer, ventilation detection scheme, and secondary anti-spin action. The properties of the PI controller, including the integrator reset mechanism, can therefore be directly compared with the torque/power controller, including the primary anti-spin action. Since the controllers based on torque and power control have been shown to be superior in normal operating conditions, and their performance during ventilation rendered acceptable by the anti-spin controller in Section 6.5, this has been chosen as the preferred solution. The shaft speed anti-spin controllers introduced in this section will therefore not be further treated here.*

## 6.7 Controller summary

For ease of notation, the anti-spin controllers presented above will be given abbreviations as defined in Table 6.1. The abbreviations will be used as e.g. “QP TS AS p+s”, meaning “combined torque/power control with torque scaling anti-spin, using both primary and secondary anti-spin action”.

$\beta_{v,on}$	$\beta_{v,off}$	$n_{\min}$	$T_{vent}$
0.6	0.9	0.5rps	2s

Table 6.2: Ventilation detection scheme parameters for the 4MW Wageningen B4-70 example propeller.

$\tau_\gamma$	$\dot{\gamma}_{rise}$	$\dot{\gamma}_{fall}$	$\tau_n$	$\dot{n}_{vent}^+$	$\dot{n}_{vent}^-$	$n_{as}$
0.1s	$0.5\text{s}^{-1}$	$-1\text{s}^{-1}$	0.5s	$1\text{s}^{-2}$	$-1\text{s}^{-2}$	1.1rps

Table 6.3: TS anti-spin controller parameters for the 4MW Wageningen B4-70 example propeller.

## 6.8 Simulation results

The simulations are performed with the 4MW Wageningen B4-70 example propeller, with model parameters given in Tables A.1 and A.2. For the ventilation detection scheme, the  $Q_a$  observer from Section 5.1 is used with the parameters given in Table 5.1. The motor torque is filtered by a second order Butterworth filter with cutoff at 10Hz before numerical differentiation. The remaining detection scheme parameters are given in Table 6.2. The basic control parameters are given in Table 3.2, the parameters for the friction and inertia compensation schemes in Table 3.4, the parameters for the S controller in Table 3.5, and the parameters for the combined QP controller in Table 3.6. The Q, P, and QP controllers are in this section always used with the friction and inertia compensation schemes, which are not explicitly mentioned in the controller abbreviations. The combined SQP controller from Section 3.15 is not tested here, since it is assumed that the speed control regime will be chosen such that  $n_{s2} \leq n_{\min}$ . That is, the anti-spin controller is de-activated in the speed control regime. For higher shaft speeds, the SQP controller becomes a QP controller. Hence, the anti-spin simulations with the QP controller are valid also for the SQP controller. The same reasoning applies to the MQP1 and MQP2 controllers.

The chosen parameters for the TS anti-spin controller from Section 6.5 are given in Table 6.3. However, Section 6.8.1 will discuss tuning of the various parameters, as well as the shaft speed PI control parameters. The additional inertia compensation scheme for the secondary anti-spin action is implemented as proposed in (6.19) and (6.20). The parameters for the SB and API anti-spin schemes are given in Table 6.4. Notice that the same PI parameters as for the S controller in Table 3.5 have been chosen. For the API anti-spin controller, the secondary anti-spin parameters from Table 6.3 are used.

### 6.8.1 Controller tuning

Figure 6.3 shows the shaft speed and motor torque for four different shaft speed PI controllers during a ventilation incident. The ventilation incident is generated by a sinusoidal heave (vertical) motion of the propeller with mean submergence

$K_p$	$T_i$	$r_b$
7.9E5	0.1s	0.3

Table 6.4: SB and API anti-spin parameters for the 4MW Wageningen B4-70 example propeller.

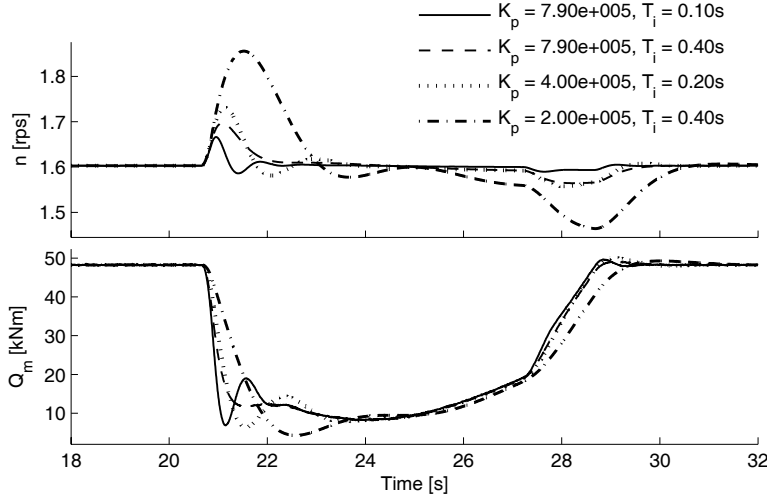


Figure 6.3: Comparison of the shaft speed PI controller with varying tuning gains  $K_p$  and  $T_i$  during a ventilation incident.

6m, amplitude 7m, and period 20s. No waves are simulated, such that the loss effects only are due to ventilation and in-and-out-of water effects as given by the ventilation loss model. The thrust reference is  $T_r = 300\text{kN}$ . The ventilation incident starts at  $t \approx 20.5\text{s}$ , and terminates at  $t \approx 28.5\text{s}$ . The results indicate that the PI gains found in Appendix B.1 and given in Table 3.5 may be too tight, and that e.g. the use of  $K_p = 7.9E3$  and  $T_i = 0.4\text{s}$  would be preferable in this situation. Since the parameters in Table 3.5 are tuned using common industrial methods, these will still be used for the comparisons in the following sections. However, it appears that it may be beneficial to account for such high thrust loss situations in the PI tuning guidelines. The results also show that a loosely tuned controller suffer both from a period of increased shaft speed during ventilation, and slow convergence back to the reference after the ventilation incident. A too tightly tuned controller, on the other hand, may give oscillations due to integrator discharge.

Figure 6.4 shows comparisons of the QP TS AS p controller with varying time constants  $\tau_\gamma$  during the same ventilation incident at  $T_r = 300\text{kN}$ . The rate limits are set to  $\dot{\gamma}_{rise} = 0.5\text{s}^{-1}$  and  $\dot{\gamma}_{fall} = -1\text{s}^{-1}$ . The results show that

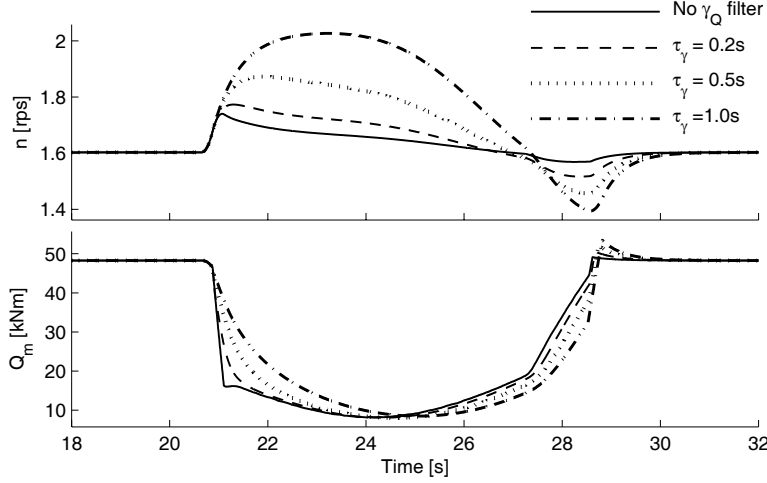


Figure 6.4: Comparison of the QP TS AS p controller with varying filter time constants  $\tau_\gamma$  during a ventilation incident.

increasing  $\tau_\gamma$  gives a smoother motor torque, but also increased shaft speed during ventilation. With the current noise content in  $\hat{\beta}_Q$ , there is limited need for the filter, and  $\tau_\gamma = 0.1\text{s}$  will be used in the remainder of the simulations.

Figure 6.5 shows comparisons of the QP TS AS p controller with varying torque scaling slew rates  $\dot{\gamma}_{rise}$  and  $\dot{\gamma}_{fall}$  during the same ventilation incident at  $T_r = 300\text{kN}$ . The filter time constant is set to  $\tau_\gamma = 0.1\text{s}$ . The results show that the main importance for avoiding shaft speed racing is not to choose the slew rates too small. In the remainder of the simulations, the parameters are chosen as  $\dot{\gamma}_{rise} = 0.5\text{s}^{-1}$  and  $\dot{\gamma}_{fall} = -1\text{s}^{-1}$ .

Tuning of the secondary anti-spin parameters is less critical for the controller performance; the three parameters  $\dot{n}_{vent}^+$ ,  $\dot{n}_{vent}^-$ , and  $n_{as}$  must be chosen as a trade-off between desired speed reduction during ventilation, and possible wear and tear as a result of the setpoint mapping.

### 6.8.2 TS AS control vs. API AS control

The TS AS and API AS controllers are relatively similar in principle; the difference is the manner in which the anti-spin controller takes control of the shaft speed during ventilation. The two primary anti-spin schemes are therefore compared in Figures 6.6 and 6.7, with the QP and the Q controller as core thruster controllers, respectively. All the controllers are tested both with primary and primary + secondary anti-spin action. The simulation scenario from the previous section is used, with  $T_r = 300\text{kN}$  in Figure 6.6, and  $T_r = 200\text{kN}$  in Figure 6.7. With  $|n| > 1.5$  for the QP controller, it acts as a pure P controller. The re-

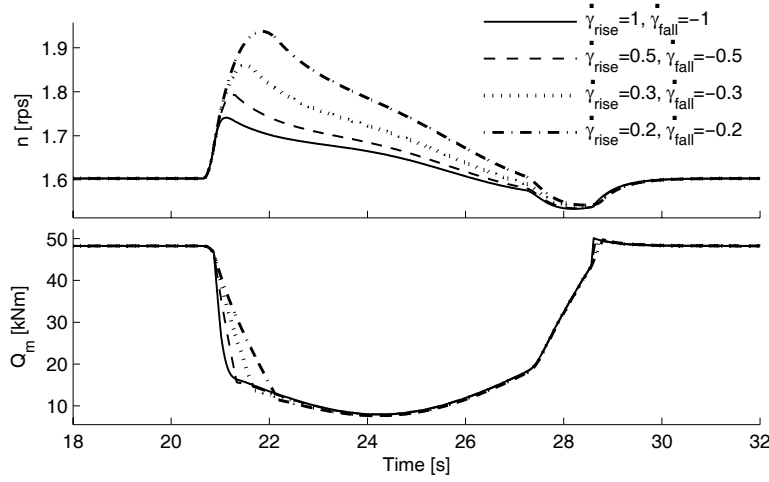


Figure 6.5: Comparison of the QP TS AS p controller with varying slew rates  $\dot{\gamma}_{rise}$  and  $\dot{\gamma}_{fall}$  during a ventilation incident.

sults show that both the TS AS and API AS controllers have good performance, that they work well for both P and Q control, and with both primary and secondary anti-spin action. The API AS controller gives tighter shaft speed control, but at the expense of more motor torque transients. The TS AS controller gives a smooth torque, but less tight speed control. However, the overshoot in shaft speed is still only in the order of 10%, which is not considered a problem. The convergence to  $n_{as}$  during ventilation with the TS AS p+s controller is also slower than for the API AS p+s controller. However, the TS AS controller is still preferred due to better control of the motor torque. In the following, only results for the TS AS controller will be presented.

### 6.8.3 Single ventilation incidents

This section presents comparisons of six controllers during a ventilation incident, divided in two groups:

- 1a)** Shaft speed PI controller (S).
- 1b)** Combined torque/power controller (QP) – acts as a P controller for  $n > 1.5\text{rps}$ .
- 1c)** Torque controller (Q).
- 2a)** Combined torque/power controller with torque scaling primary anti-spin action (QP TS AS p).

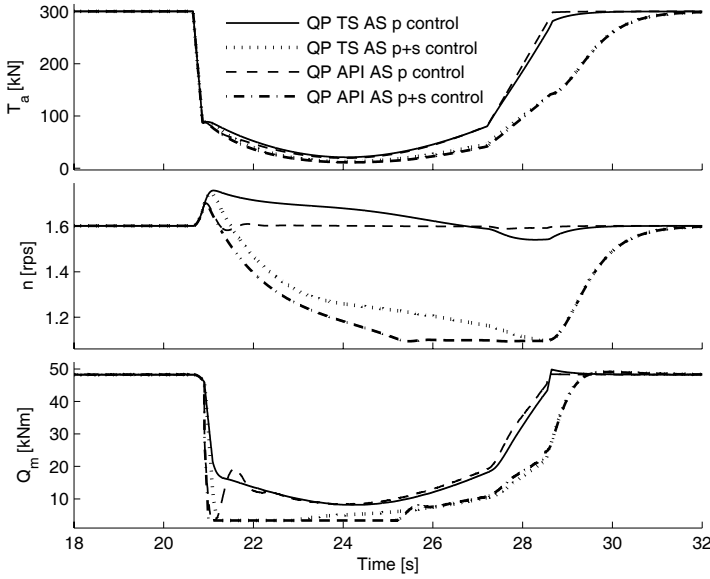


Figure 6.6: Comparison of TS and API anti-spin control during a ventilation incident at  $T_r = 300\text{kN}$ , using the QP core thruster controller.

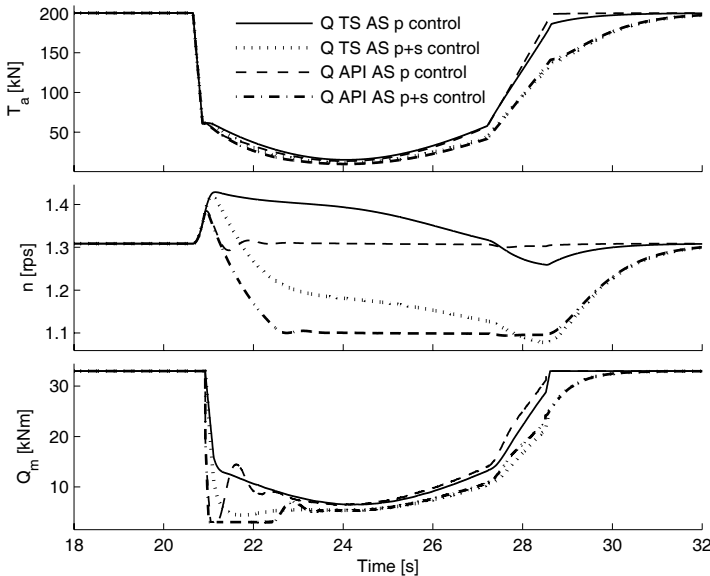


Figure 6.7: Comparison of TS and API anti-spin control during a ventilation incident at  $T_r = 200\text{kN}$ , using the Q core thruster controller.

- 2b) Combined torque/power controller with torque scaling primary and secondary anti-spin action (QP TS AS p+s).
- 2c) Combined torque/power controller with speed bound anti-spin (QP SB AS).

Figure 6.8 shows the six controllers at  $T_r = 300\text{kN}$  for a single ventilation incident, generated as in the previous sections. As already seen in Figure 6.3, the S controller keeps the shaft speed within small bounds, also during ventilation. The Q controller leads to shaft speed racing and excessive power consumption. The torque limiting function in (3.25) is active for a short while, limiting the power consumption at  $P_{\max} = 4800\text{kW}$ . The QP controller also leads to shaft speed racing, but keeps the power limited. The three anti-spin controllers all obtain their objectives; the QP TS AS p controller keeps the shaft speed within small bounds, the QP TS AS p+s controller lowers the shaft speed towards  $n_{as}$  during ventilation, and the QP SB AS controller bounds the shaft speed at the designated level. Figure 6.9 shows the corresponding results for  $T_r = 450\text{kN}$ . The main differences to notice are the increased activation of the torque limiting function for the Q controller, and the larger drop in motor torque needed to bound the shaft speed. Figure 6.10 shows details from the QP TS AS p+s controller, demonstrating that the load torque estimation, ventilation detection, and primary and secondary anti-spin actions work as intended.

#### 6.8.4 Time-varying $T_r$

Figure 6.11 shows the main simulation results for the QP TS AS p+s controller in waves and with a time-varying  $T_r$ . Figure 6.12 shows the details from the controller. The mean submergence is  $h_0 = 6\text{m}$ , and the propeller is subject to irregular waves with  $H_s = 7\text{m}$ ,  $T_p = 12.6\text{s}$ , defined by 30 harmonic components extracted from the modified PM spectrum in (C.19). The wave-induced velocities are calculated from (C.33), and the propeller submergence calculated from (C.35). The thrust reference is varied as a sinusoidal with period 100s and amplitude 450kN. No reference generator is used. The results show that the controller performs satisfactory also in these conditions. The anti-spin controller is only activated during large thrust losses, and the QP controller is otherwise left to work undisturbed. The secondary anti-spin action is only activated for high  $n$ . There is one apparently false detection as  $n$  crosses zero at  $t \approx 58\text{s}$ . However, this does not affect the performance significantly, and gives no large transients in the motor torque.

## 6.9 Discussion

This chapter has introduced the concept of anti-spin thruster control for extreme operating conditions. Several anti-spin controllers at varying complexity levels have been presented, including a ventilation detection scheme and a secondary

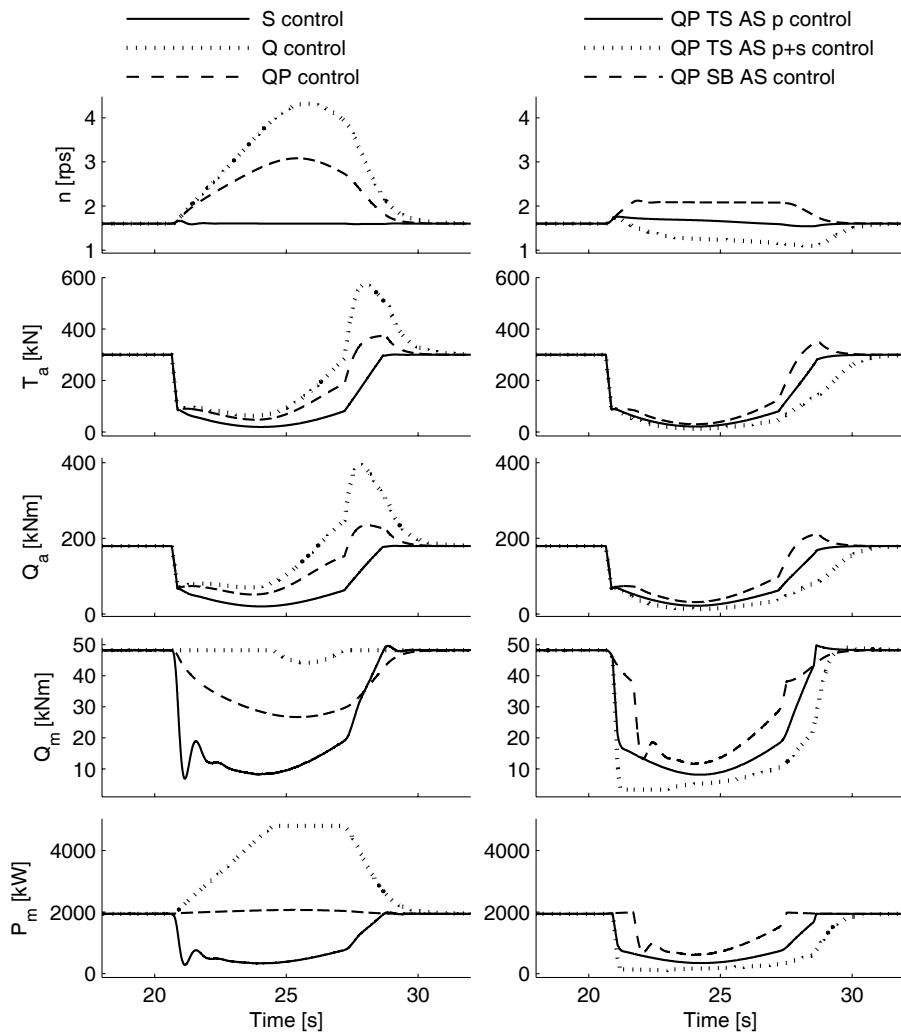


Figure 6.8: Comparison of six controllers during a ventilation incident at  $T_r = 300\text{kN}$ .

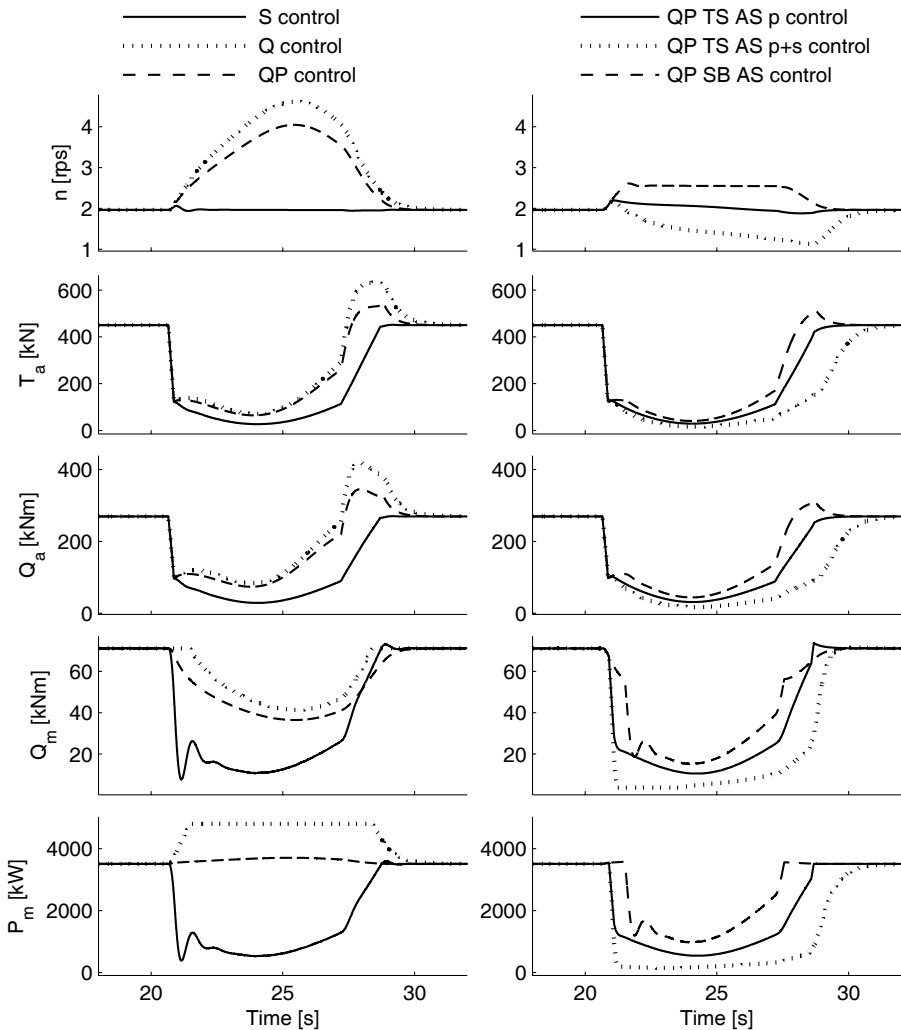


Figure 6.9: Comparison of six controllers during a ventilation incident at  $T_r = 450\text{kN}$ .

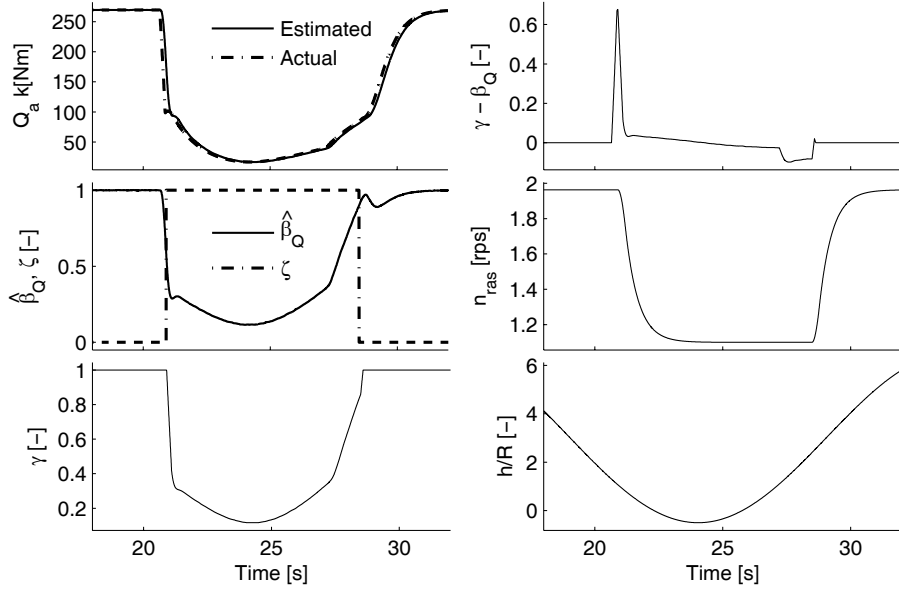


Figure 6.10: Details from the QP TS AS p+s controller during a ventilation incident at  $T_r = 450\text{kN}$ .

anti-spin action that reduces the shaft speed during ventilation. The results indicate that:

- If a shaft speed controller is found acceptable for normal operating conditions, the anti-spin controllers are of limited applicability. However, the performance during ventilation may be improved by accounting for such situations during tuning of the PI control parameters, and possibly also by modifications of the integral term. The secondary anti-spin action may be applied to reduce the dynamic loading during ventilation.
- If a controller based on torque and/or power control is chosen for normal operating conditions, ventilation will lead to excessive power consumption (mainly for the torque controller) and increased mechanical wear and tear due to unsteady propeller loading. Both analyses and simulations show that the unacceptable performance of torque and power control when subject to large thrust losses can be rendered acceptable by an anti-spin controller.
- The main purpose of the anti-spin controller is to limit the shaft speed during ventilation. All the proposed anti-spin schemes in Table 6.1 contains such functionality.

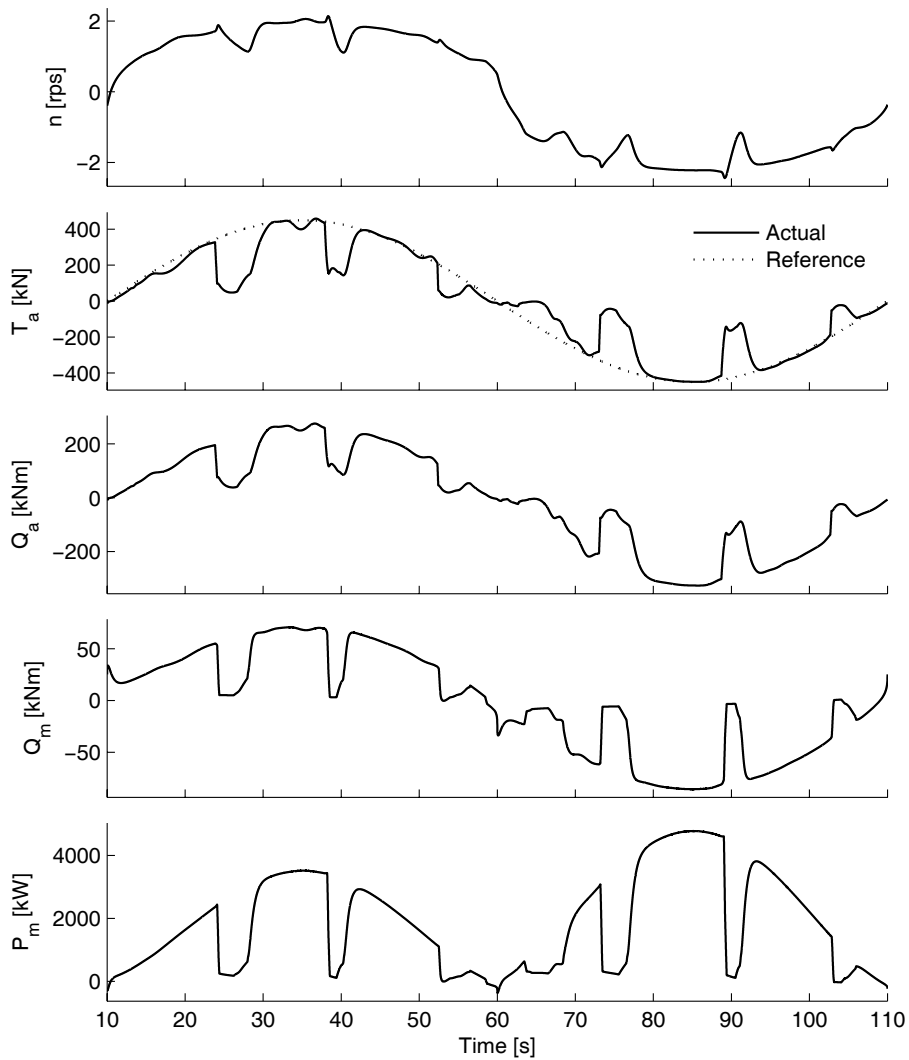


Figure 6.11: Simulation results for the QP TS AS p+s controller in waves for a time-varying  $T_r$ .

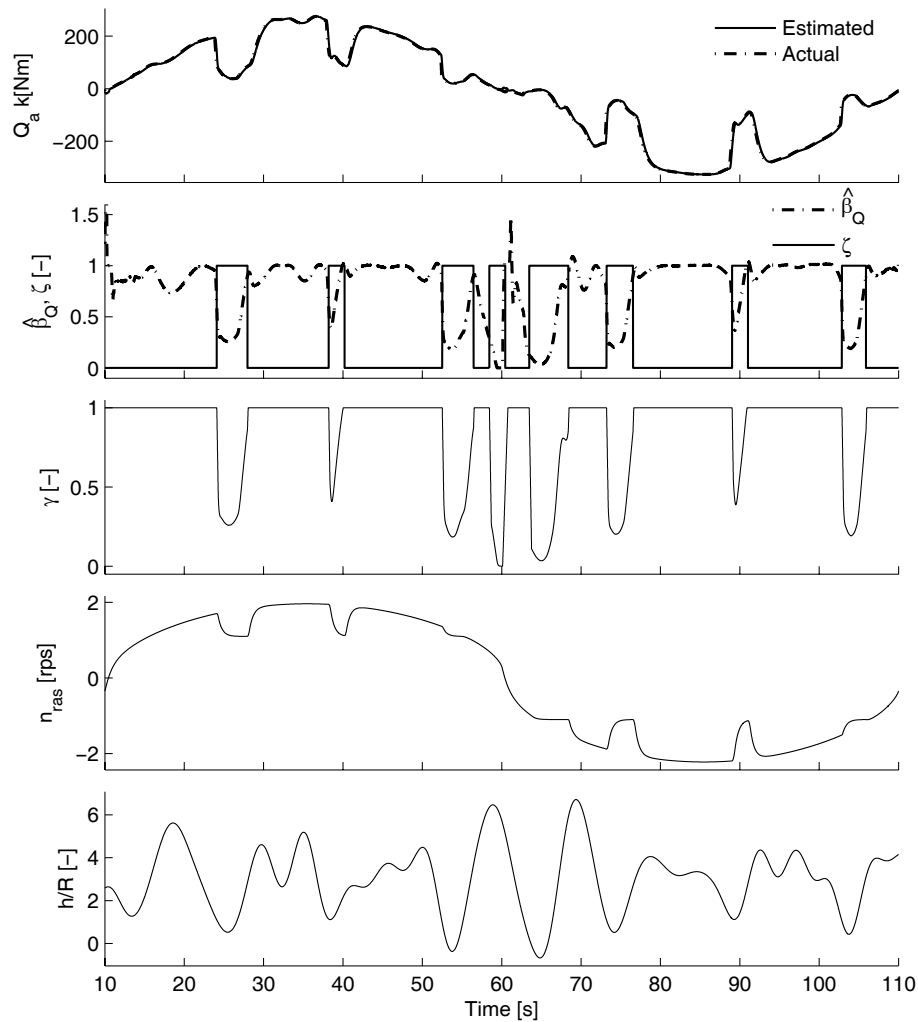


Figure 6.12: Details from the QP TS AS p+s controller in waves for a time-varying  $T_r$ .

- The SB anti-spin controller, which is the simplest formulation presented here, gives the least control over the shaft speed, and is not compatible with the secondary anti-spin action. Its simplicity may, however, be an advantage for industrial applications.
- The TS and API anti-spin controllers give increased control over the shaft speed during ventilation, and can be combined with the secondary anti-spin action. These controllers give the best over-all performance, but at the expense of increased complexity.

# Chapter 7

## Experimental results

In order to test and validate the proposed control concepts, experiments with a model scale propeller have been carried out in the Marine Cybernetics Laboratory (MCLab) at NTNU. The experimental setup is described in Section 7.1, followed by experiments in normal conditions in Section 7.2, and experiments in extreme conditions in Section 7.3.

### 7.1 Experimental setup

The MCLab basin is 40m long, 6.45m wide, and 1.5m deep, and is equipped with a towing carriage and a wave-maker system. The tested propeller was of conventional design, and used both with and without duct. The main dimensions of the propeller and duct are given in Tables 7.1 and 7.2. The propeller was attached to a shaft equipped with thrust and torque sensors inside an underwater housing, and driven by an electric motor via shafts and gears with gear ratio 1:1. The rig with motor, gears, underwater housing, shaft and propeller was fixed to the towing carriage on a vertical slide, which was used to control the submergence of the propeller relative to the free surface. The submergence was measured with a wave probe. The advance velocity of the propeller was equal to the towing velocity of the carriage, in addition to components from current and/or waves. The motor torque was controlled from a PC onboard the carriage, using feedback from the propeller shaft speed and the motor torque. The control code was generated by rapid control prototyping using Opal RT-Lab and source code in Matlab/Simulink. This enabled use of the same Simulink code that was used for simulations. A sketch of the experimental setup is given in Figure 7.1, and a picture shown in Figure 7.2.

Propeller Number	P 1020
Diameter, $D$	250mm
Blade number, $Z$	4
Pitch ratio, $P/D$	1.0
Expanded blade area ratio, $A_e/A_0$	0.55

Table 7.1: Propeller specification.

Duct Number	D 143
Inner diameter	252.1mm
Max. outer diameter	302.4mm
Min. outer diameter	267.7mm
Duct length	118.8mm

Table 7.2: Duct specification.

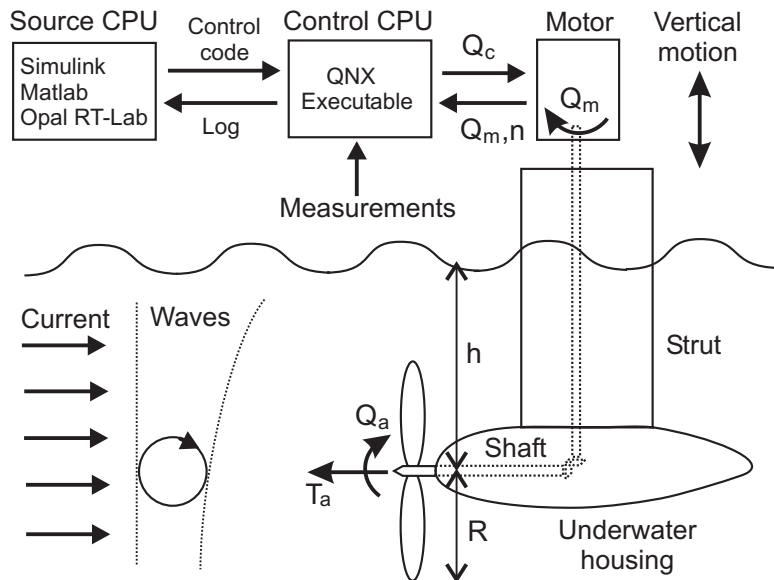


Figure 7.1: Sketch of the MCLab experimental setup.

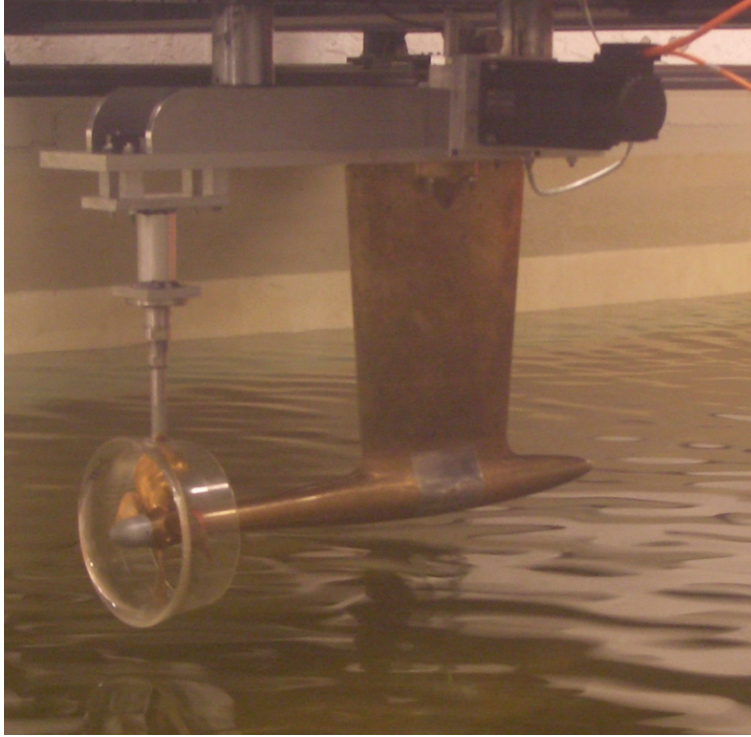


Figure 7.2: Picture of the MCLab experimental setup.

### 7.1.1 Measurements, data logging, and filtering

The measurements are summarized in Table 7.3. In addition, all relevant states and parameters in the control laws were logged. Some comments on the various measurements are given below.

- The *duct thrust* measurement contained a lot of high-frequency noise, but seemed reasonable after filtering.
- The *propeller thrust* measurement was the most noisy signal. Due to the nature of the thrust sensor, oscillations at the shaft frequency were induced, in addition to other high-frequency components.
- The *propeller torque* measurement was of better quality than the thrust measurement, but contained significant noise at twice the shaft frequency, probably due to the mounting of the shaft.
- The *shaft speed* measurement was of reasonable quality, with some high-frequency noise and wild-points, and some noise at twice the shaft frequency.

Parameter	Symbol	Unit	Sensor
Duct thrust	$T_{ad}$	N	Strain gauges
Propeller thrust	$T_{ap}$	N	Inductive transducer
Propeller torque	$Q_a$	Nm	Strain gauges
Shaft speed	$n$	1/s	Tachometer
Motor torque	$Q_m$	Nm	Motor drive
Submergence	$h$	m	Wave probe

Table 7.3: Measurements in the MCLab experimental setup.

- The *motor torque* measurement mainly suffered from quantization due to limited bit resolution in the output from the motor drive, and contained some high-frequency noise.
- The *submergence* measurement was of reasonable quality.

All measurements have been filtered for presentation in time-series. The thrust noise at the shaft frequency meant that the filter cutoff frequency had to be lower than the shaft speed. For most of the time series, the filter cutoff frequency was chosen as 4Hz. The filter was a finite impulse response filter (Matlab function *fir1*) of order 100, which gave a relatively sharp cutoff. In order not to leave out any significant dynamic effects, careful investigations of the raw data time series have been performed. Figure 7.3 compares some raw and filtered time series. In the control laws, where only the shaft speed  $n$  and motor torque  $Q_m$  were used as feedback, no filtering was applied except in the detection scheme, where  $Q_m$  was filtered by a second order Butterworth filter with cutoff at 10Hz.

**Remark 7.1** *The total thrust is given from:*

$$T_a = T_{ap} + T_{ad}, \quad (7.1)$$

where the duct thrust  $T_{ad} = 0$  for an open propeller.

**Remark 7.2** *The gear ratio in the experimental setup is 1:1. From Section 2.2.3, this means that  $Q_{cm} = Q_c$  and  $Q_{mp} = Q_m$ .*

### 7.1.2 Propeller characteristics and control coefficients

The propeller has previously been through extensive cavitation tunnel tests at NTNU, and the open-water characteristics are therefore well known, both for the ducted and the open case.

Figure 7.4 shows the open-water characteristics of the open propeller, based on data points from the quasi-static tests performed during this work, see Section 7.2.2.  $K_T$ ,  $K_Q$ , and  $\eta_0$  were calculated from (2.6), (2.7), and (2.17), using the mean values of  $T_a$ ,  $Q_a$ , and  $n$  from each run. Second order polynomial curves have been fitted to the  $K_T$  and  $K_Q$  values for positive advance velocities.

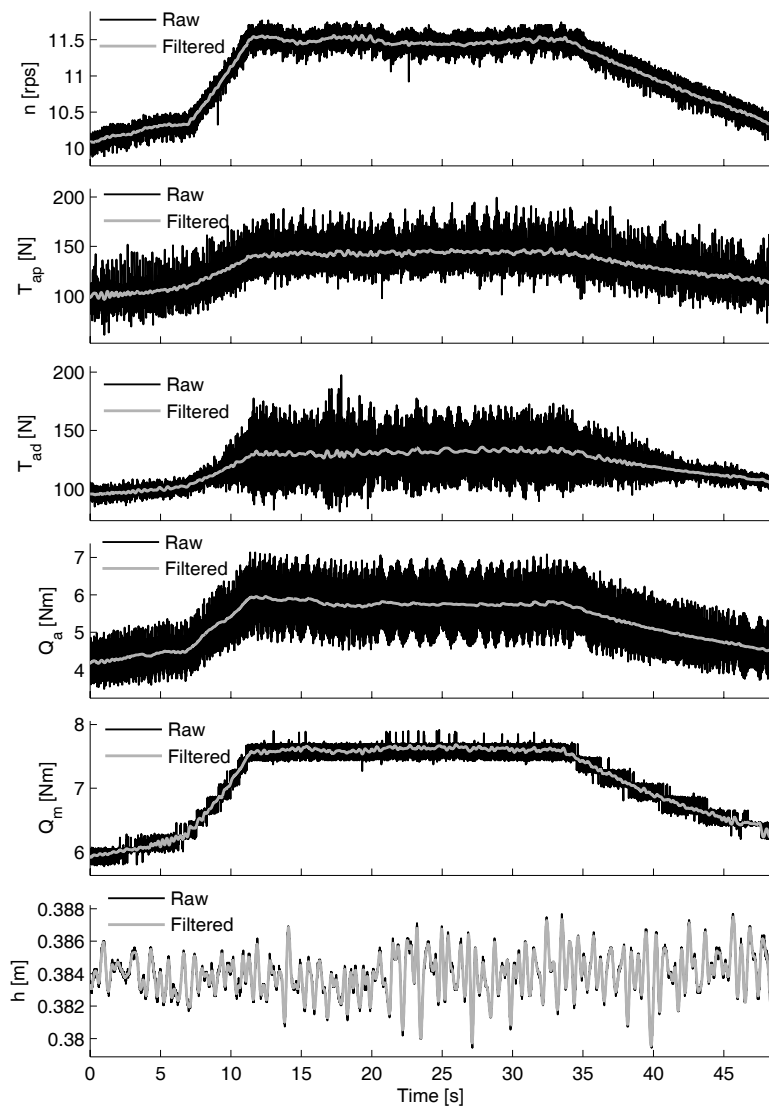


Figure 7.3: Examples of the raw and filtered measurements in the MCLab experimental setup.

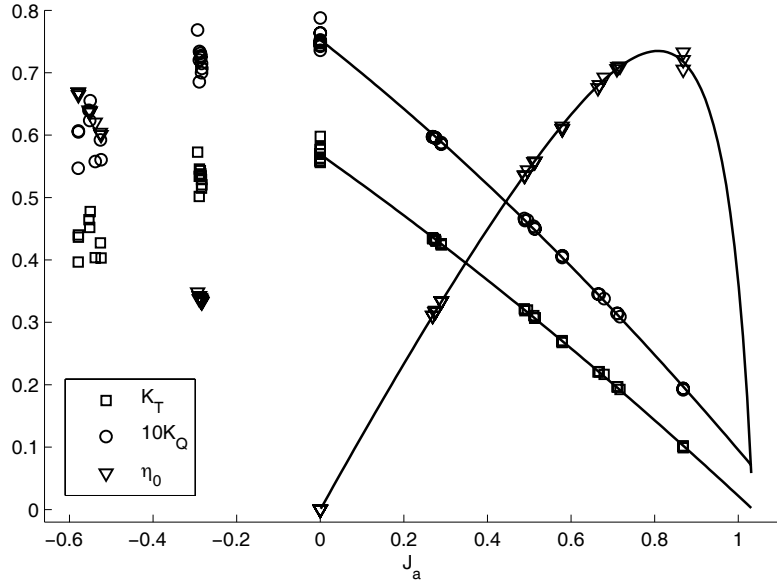


Figure 7.4: Open-water characteristics for the open propeller.

The curves correspond well with previously reported open-water characteristics. Note that the uncertainty of the tests increase with decreasing negative advance numbers, which give unsteady inflow to the propeller. The nominal thrust and torque coefficients were found to be  $K_{T0} = 0.570$  and  $K_{Q0} = 0.0750$ . The nominal thrust and torque coefficients for reverse thrust were found to be  $K_{T0r} = 0.393$  and  $K_{Q0r} = 0.0655$ . Figure 7.5 shows the  $K_T - K_Q$  relationship, and a linear fit as proposed in Section 2.1.8. The same data points that are shown in Figure 7.4 are used (i.e.  $-0.6 \leq J_a \leq 0.9$ ), and the parameters for the linear fit are  $a_t = 8.4$  and  $b_t = -0.068$ . Clearly, the linear relationship fits well.

The ducted propeller has mainly been used for testing of the anti-spin control schemes, i.e. at  $V_a \approx 0$ . The open-water characteristics were therefore not experimentally determined during the experiments. Figure 7.6 shows the open-water characteristics from previous tests (Ruth, 2005). The nominal thrust and torque coefficients were found to be  $K_{T0} = 0.513$  and  $K_{Q0} = 0.0444$ . The reverse coefficients were not determined.

**Remark 7.3** Comparing coefficients for the open and ducted propeller, it is clear that the addition of the duct gives a better bollard pull efficiency, as discussed in Section 2.1.6.

For the open propeller, the control coefficients  $K_{TC}$  and  $K_{QC}$  were chosen as in (3.8, 3.9) with  $\varepsilon_c = 4.5$ ,  $n_c = 3$ , and using the nominal thrust and torque

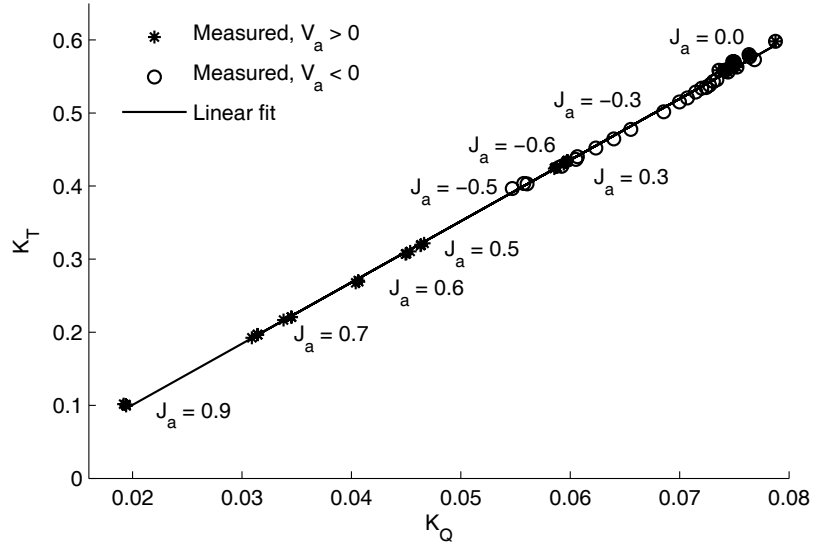


Figure 7.5: Relationship between  $K_T$  and  $K_Q$  for the open propeller, in the range  $-0.6 \leq J_a \leq 0.9$ .

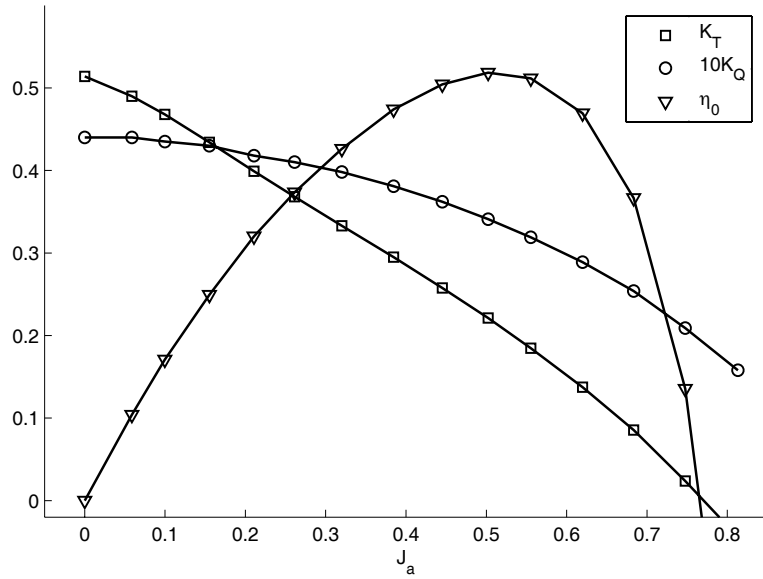


Figure 7.6: Open-water characteristics for the ducted propeller, with data taken from Ruth (2005).

coefficients specified above. The ducted propeller was not tested with  $n < 0$ , such that the coefficients could be set as constants, i.e.  $K_{TC} = K_{T0}$  and  $K_{QC} = K_{Q0}$ .

**Remark 7.4** *The smooth switch of the control coefficients for the open propeller was not implemented as in (3.10), but instead as:*

$$\lambda_c = \lambda_c(n_r) = \frac{1}{2} + \frac{1}{\pi} \arctan(7 \frac{n_r}{n_c} + 125 \frac{n_r^3}{n_c^3}). \quad (7.2)$$

*This is almost equivalent to using (3.10) with  $\varepsilon_c = 4.5$ .*

### 7.1.3 Friction and inertia compensation

In the experiments presented here, the shaft friction turned out to affect the performance of the torque and power controllers significantly. A feedforward friction compensation scheme as proposed in Section 3.7.1 was therefore implemented. The friction was found to be rather nonlinear. It was clearly affected by the temperature in the gears, bearings, and oil, with decreasing friction as the temperature increased. Additionally, the friction exhibited a hysteresis, with less friction for reducing shaft speed than for increasing shaft speed. This is described in more detail in Pivano *et al.* (2006c). However, for control purposes the static plus linear friction compensation in (3.19) was found to be satisfactory. Over the course of the experiments, the friction coefficients were found to be in the range  $Q_s \in [0.8, 1.0]$  and  $K_\omega \in [0.009, 0.011]$ . The switch “width” of the smooth switching function in (3.20) was chosen as  $n_f = 0.5$ , and the constant  $\varepsilon_f = 4.5$ . Figure 7.7 shows an example friction model where  $Q_{f0} = 1.0$  and  $Q_{f1} = 0.01$ , together with a time series for a sinusoidal thrust reference. This clearly illustrates the nonlinearities in the experienced friction.

The rotational inertia was approximated to  $I_s \approx 0.05 \text{kgm}^2$ , and did not appear to affect the response of the system significantly. An inertia compensation scheme as proposed in (3.22) was therefore not implemented.

**Remark 7.5** *The smooth switch in the static friction compensation was not implemented as in (3.20), but instead as:*

$$Q_{ff0}(n_r) = Q_{f0} \frac{2}{\pi} \arctan(7 \frac{n_r}{n_f} + 125 \frac{n_r^3}{n_f^3}). \quad (7.3)$$

*This is almost equivalent to using (3.20) with  $\varepsilon_f = 4.5$ .*

## 7.2 Experiments in normal conditions

This section presents experimental results with the controllers from Chapter 3, i.e. designed for normal operating conditions, including validation of the

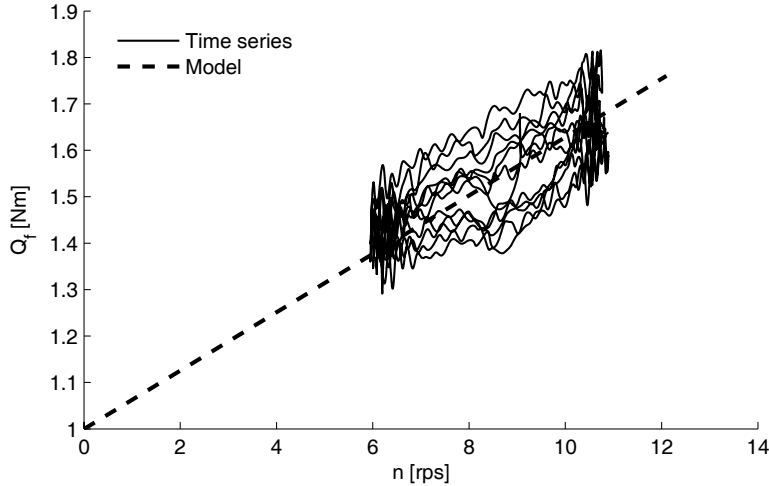


Figure 7.7: Linear friction compensation used in the experiments, together with experimental time series for a sinusoidal thrust reference.

sensitivity functions from Chapter 4. The importance of the friction compensation scheme is investigated, and the dynamic performance of the controllers in various operating conditions tested.

The majority of the experiments were conducted for shaft speed control, torque control, and power control, in order to test the properties of the fundamental thruster control schemes. Three main sets of tests are presented in the following:

1. Quasi-static tests with the open propeller: steady-state tests with constant  $V_a$  and  $T_r$ , used to validate the steady-state performance of the fundamental controllers and verify the sensitivity functions.
2. Test in waves with the open propeller: dynamic tests in waves with constant  $T_r$ , used to investigate the disturbance rejection properties of the fundamental controllers.
3. Tracking tests with the open propeller: dynamic tests in calm water with time-varying  $T_r$ , used to investigate the tracking properties of the fundamental controllers, as well as some of the other controllers from Table 3.1.

Finally, an additional test of the combined SQP controller is presented. The submergence ratio was kept constant at  $h/R = 4$  for the quasi-static and tracking tests, and at  $h/R = 3$  for the tests in waves. For all the tests, time series are shown for the shaft speed  $n$ , total thrust  $T_a$ , propeller torque  $Q_a$ , motor

$D$	$K_{T0}$	$K_{Q0}$	$K_{T0r}$	$K_{Q0r}$	$n_c$
0.25m	0.570	0.0750	0.393	0.0655	3rps
$Q_{f0}$	$Q_{f1}$	$n_f$	$I_c$		
1.0Nm	0.01Nms	0.5rps	0kgm <sup>2</sup>		

Table 7.4: Basic control parameters used in the experiments with the open propeller.

Ctr.	$K_p$	$T_i$ [s]	$r$	$p$	$k$	$n_s$ [rps]	$n_{s1}$ [rps]	$n_{s3}$ [rps]
S	0.2	0.05	-	-	-	-	-	-
QP	-	-	4	0.5	1	-	-	-
SQP	0.3	0.03	3	1	1	-	5	8
MQP1	0.3	0.03	4	0.5	1	5	-	-

Table 7.5: Parameters for the various controllers used in the experiments with the open propeller.

torque  $Q_m$ , and motor power  $P_m$ . The motor torque differs from the commanded torque only by a small time constant, and illustrates the output of the controllers.

### 7.2.1 Controller parameters

Due to the relatively noisy shaft speed measurement, the shaft speed PI controller in (3.27) could not be tuned too tightly. The parameters were chosen as  $K_p = 0.2$  and  $T_i = 0.05$ s, which gave adequate tracking properties in normal conditions. The choice of PI parameters will be further motivated in Section 7.3.2. For the combined QP controller in (3.36), the parameters for the weighting function  $\alpha_c(n)$  in (3.33) were chosen as  $[r, p, k] = [4, 0.5, 1]$ . This gave a pure torque controller for  $n < 0.5$ rps and a pure power controller for  $n > 3$ rps.

For the combined SQP controller in (3.48), the PI parameters were chosen as  $K_p = 0.3$  and  $T_i = 0.03$ , the parameters for the weighting function  $\alpha_s(n_r)$  were chosen as  $[r, p, k] = [3, 1, 1]$ , and the switching shaft speeds chosen as  $n_{s1} = 5$ rps and  $n_{s3} = 8$ rps. This gives pure shaft speed control for  $n_r < 5$ rps, pure torque control for  $6.8 \text{rps} < n_r < 8$ rps, and pure power control for  $n_r > 9.8$ rps.

For the combined MQP1 controller, the weighting function parameters were chosen as for the QP controller, i.e.  $[r, p, k] = [4, 0.5, 1]$ , the integral gain was chosen as  $K_i = 10$ , and the integral threshold shaft speed was chosen as  $n_s = 5$ rps. This means that the torque controller in practice was used only to facilitate the zero-crossings of  $n$ , since the additive integral action overlaps the torque control regime.

A summary of all the control parameters is given in Tables 7.4 and 7.5. Note that the MQP1 controller only has integral action, with parameter  $K_i = K_p/T_i$ .

### 7.2.2 Quasi-static tests

In the quasi-static tests the thrust reference was kept constant at  $T_r = 100\text{N}$ , the advance velocities were  $V_a = \{-1, -0.5, 0, 0.5, 1, 1.5\}\text{m/s}$ , and the speed, torque, and power controllers were used. Each combination was run three times, showing good repeatability. The length of the test series were limited by the length of the basin, but gave adequate statistical values.

The performance of the three controllers is summed up in Figure 7.8, where the mean values of  $T_a$ ,  $Q_a$ ,  $n$ ,  $Q_m$ , and  $P_m$  are shown for varying advance speeds. The friction compensation is not included in the plots of motor torque and power. The three controllers obtain their objectives: the shaft speed controller keeps the shaft speed most constant, the torque controller keeps the motor torque most constant, and the power controller keeps the motor power most constant. As the advance speed increases, the effective angle of attack of the propeller blades is decreased, and the propeller loading decreases for a constant shaft speed. This can be seen in terms of reduced propeller thrust and torque at increasing advance velocities for the shaft speed controller: at  $V_a = 1.5\text{m/s}$ , the propeller thrust is reduced from 100N to 18N. The torque and power controllers have much better performance, since they increase the shaft speed as the propeller loading decreases: at  $V_a = 1.5\text{m/s}$ , the propeller thrust is reduced from 100N to 65N and 50N, respectively.

The performance of the various controllers may also be studied in terms of the sensitivity functions described in Section 4. The thrust, shaft speed, torque, and power sensitivity functions for the quasi-static tests can be found in Figure 7.9. They compare well with the theoretically derived sensitivity functions in Table 4.1.

### 7.2.3 Dynamic tests in waves

To validate the dynamic performance of the fundamental controllers when the propeller is subject to a rapidly changing inflow, tests in regular and irregular waves were performed. The thrust reference was  $T_r = 90\text{N}$  and the carriage was kept stationary. A comparison of the controller performance in regular waves with wave height 8cm and period 1s is shown in Figure 7.10. The results are summarized in the following:

- The shaft speed controller keeps the shaft speed constant, and has to vary the motor torque and power in order to achieve this. The resulting propeller thrust and torque have the largest variance.
- The torque controller keeps the motor torque constant, and as a result the shaft speed varies with the loading. The resulting propeller thrust and torque have the smallest variance.
- The power controller keeps the motor power constant, and as a result both the shaft speed and motor torque varies with the loading. The re-

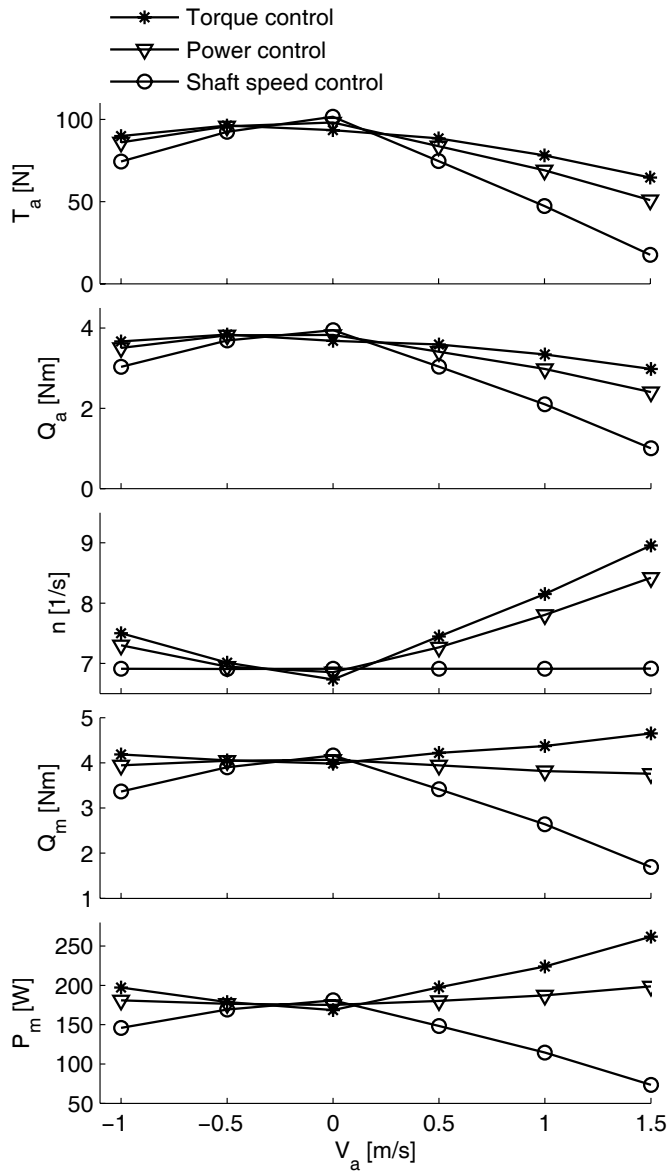


Figure 7.8: Comparison of propeller thrust  $T_a$ , torque  $Q_a$ , shaft speed  $n$ , motor torque  $Q_m$ , and power  $P_m$  for the shaft speed, torque, and power controllers for varying advance velocity  $V_a$ .

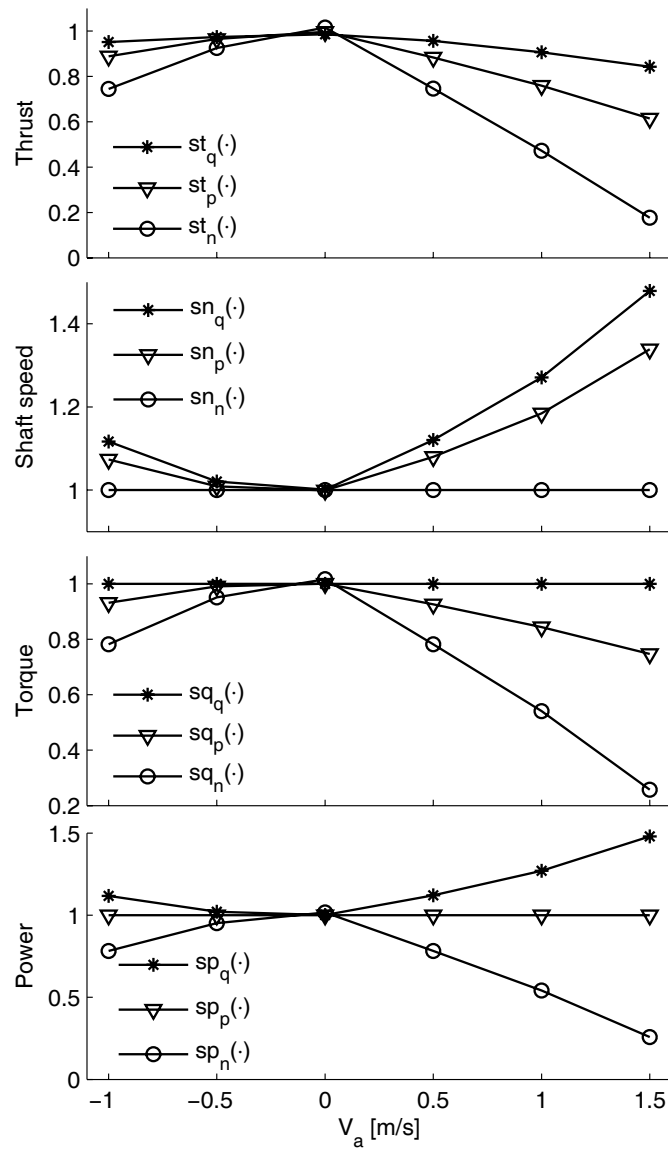


Figure 7.9: Experimental thrust, shaft speed, torque, and power sensitivity functions for torque control (star), power control (triangle), and speed control (circle).

sulting propeller thrust and torque lie between the shaft speed and torque controller values.

Similar results were obtained for other thrust references and waves. Results for the three fundamental controllers with a slowly-varying advance velocity are shown in Appendix E.4.

#### 7.2.4 Tracking tests

The tests presented in this section were performed in calm water with zero advance velocity and time-varying thrust reference  $T_r$ , in order to investigate the tracking properties of the various controllers. Results for seven controllers are presented, divided in two groups:

- 1a)** Shaft speed PI controller (S).
- 1b)** Torque controller with friction compensation ( $Q w/Q_{ff}$ ).
- 1c)** Combined torque/power controller with friction compensation ( $QP w/Q_{ff}$ ).
- 2a)** Torque controller without friction compensation ( $Q$ ).
- 2b)** Combined torque/power controller without friction compensation ( $QP$ ).
- 2c)** Combined speed/torque/power controller with friction compensation (SQP  $w/Q_{ff}$ ).
- 2d)** Combined torque/power controller with additive integral action and no friction compensation (MQP1).

The controllers were tested for three different cases, using sinusoidal thrust references with amplitude  $T_{rA}$ :

- 1.**  $T_{rA} = 50\text{N}$ , period 3s.
- 2.**  $T_{rA} = 100\text{N}$ , period 5s.
- 3.**  $T_{rA} = 200\text{N}$ , period 7s.

The power controller could not be tested due to the zero-crossing of  $T_r$  (and hence  $n$ ), but with the chosen weighting function parameters, the QP controller was a pure power controller for  $n > 3$ .

Figures 7.11 and 7.12 show the controllers in group 1 and 2 for  $T_{rA} = 50\text{N}$ . The thrust measurements suffer from the noise problems discussed in Section 7.1.1, since the shaft speed is too low to allow proper filtering. However, the trend is still clear. Figures 7.13 and 7.14 show the corresponding results for  $T_{rA} = 100\text{N}$ , and Figures 7.15 and 7.16 for  $T_{rA} = 200\text{N}$ .

From Figures 7.11, 7.13, and 7.15, the controllers in group 1 have acceptable performance for all the test cases. The S controller has a small overshoot

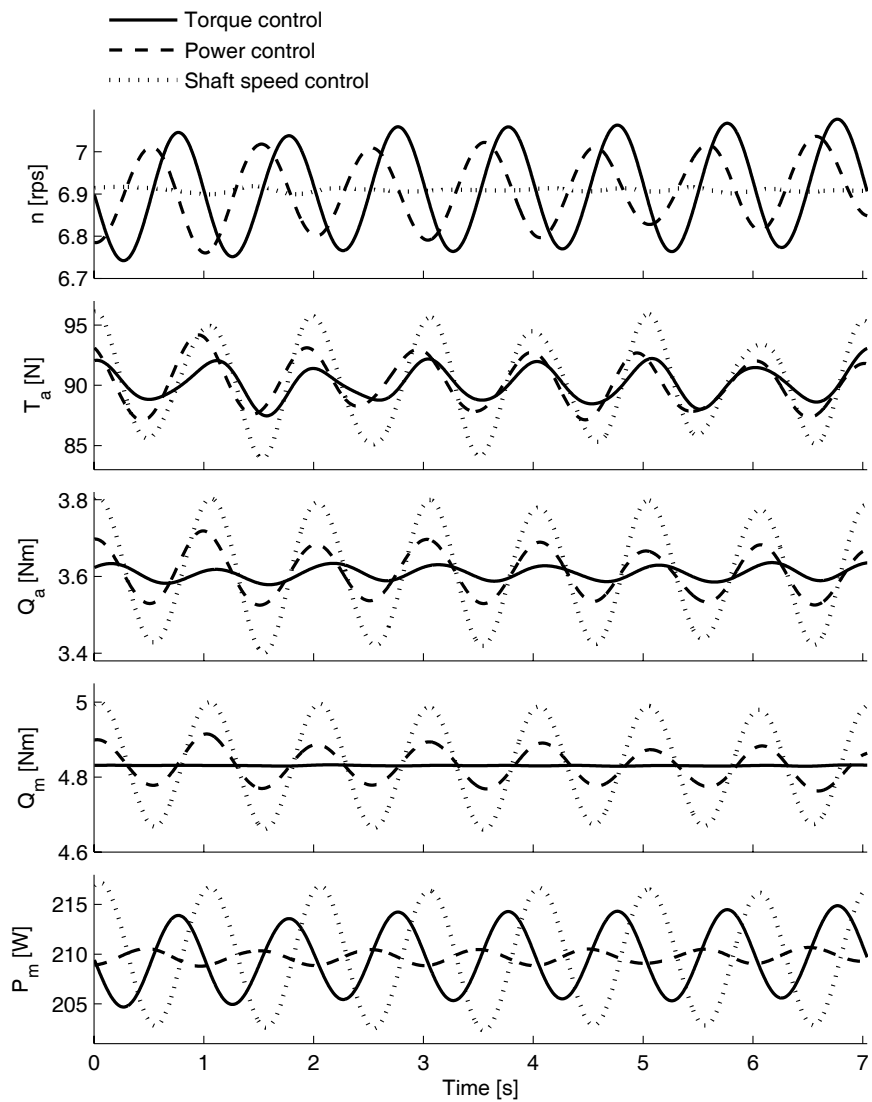


Figure 7.10: Comparison of shaft speed, torque, and power control in regular waves.

in the shaft speed after the zero-crossings. This is believed to be connected with the static friction. Apart from this, the three controllers have comparable performance in terms of all the measured parameters. For increasing  $T_{rA}$ , the Q w/ $Q_{ff}$  and QP w/ $Q_{ff}$  controllers track the thrust reference better than the S controller, which gives an overshoot in thrust for positive shaft speed and a loss of thrust for negative shaft speed. Such thrust overshoots during rapid command changes has earlier been described in Healey *et al.* (1995) and Whitcomb and Yoerger (1999a), and was explained by the dynamics of the inflow to the propeller. It is interesting to note that the Q w/ $Q_{ff}$  and QP w/ $Q_{ff}$  controllers avoid this overshoot, and therefore give better tracking properties without any explicit compensation for the advance velocity.

The importance of the friction compensation in the Q and QP controllers can be seen in Figures 7.12, 7.14, and 7.16. Without the friction compensation, the performance is not acceptable for  $T_{rA} = 50\text{N}$ , but improves with increasing  $T_{rA}$ , and is acceptable at  $T_{rA} = 200\text{N}$ . This is consistent with the results from Whitcomb and Yoerger (1999b), where a feedforward torque control scheme was compared with two shaft speed controllers. The poor performance of the torque controller was explained by unmodelled friction. It was found that the problems were most evident at low thrust references, where friction is more dominating.

Figures 7.12, 7.14, and 7.16 also show results for the SQP w/ $Q_{ff}$  and MQP1 controllers. For  $T_{rA} = 50\text{N}$ ,  $n_r < 5\text{rps}$ , and both controllers become shaft speed controllers. This is seen in the time series, which are similar to the S controller. The difference in performance is probably due to the lack of a proportional term in the MQP1 controller. For  $T_{rA} = 100\text{N}$  and  $200\text{N}$ , the SQP w/ $Q_{ff}$  controller gives acceptable performance, although the tracking properties (with respect to  $T_r$ ) are not as good as for the Q w/ $Q_{ff}$  and QP w/ $Q_{ff}$  controllers, with a small overshoot after the zero-crossings. This appears to be due to the shaft speed controller being engaged and disengaged for low  $T_r$ . A similar behavior is seen for the MQP1 controller. In addition, the MQP1 controller gives too high thrust for  $T_{rA} = 100\text{N}$  and  $200\text{N}$ , especially in reverse. This is due to the frozen integral term, which gives a too big contribution after the rapid transition past  $n_s$  (at 5rps). For a slower-changing thrust reference, this would probably not have been a problem.

### 7.2.5 Test of the combined SQP controller

To further test the properties of the SQP w/ $Q_{ff}$  controller, the carriage was moved in the propeller axial direction, with motion amplitude 0.5m and velocity amplitude 0.25m/s. The thrust reference was increased in steps from 50N to 120N and 220N. The three levels correspond to pure speed, torque, and power control. The results are shown in Figure 7.17, and corresponds well with the results with the fundamental controllers shown in Figure 7.10. This demonstrates that the three controllers work as intended, with seamless transitions between the control regimes. There were some problems with the thrust measurements, which can be seen as noise for  $T_r = 220\text{N}$ .

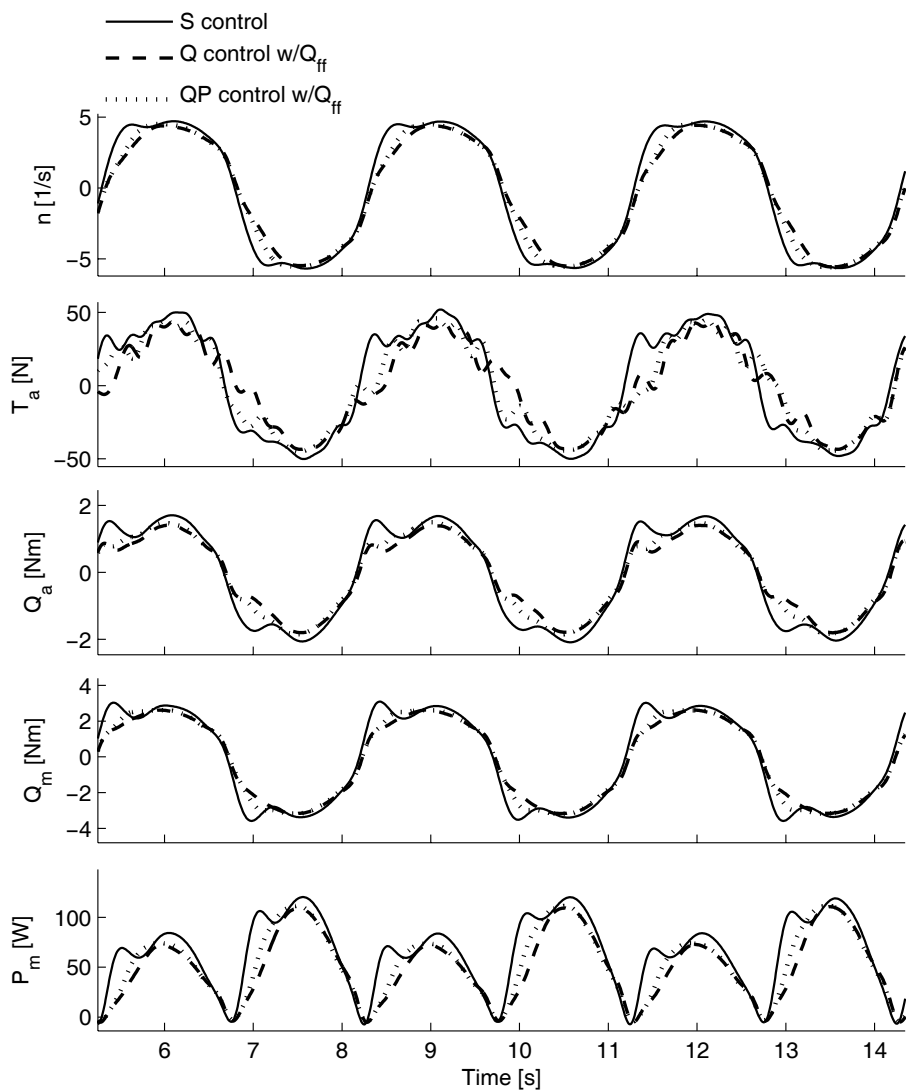


Figure 7.11: Comparison of three controllers tracking a sinusoidal thrust reference with amplitude 50N and period 3s.

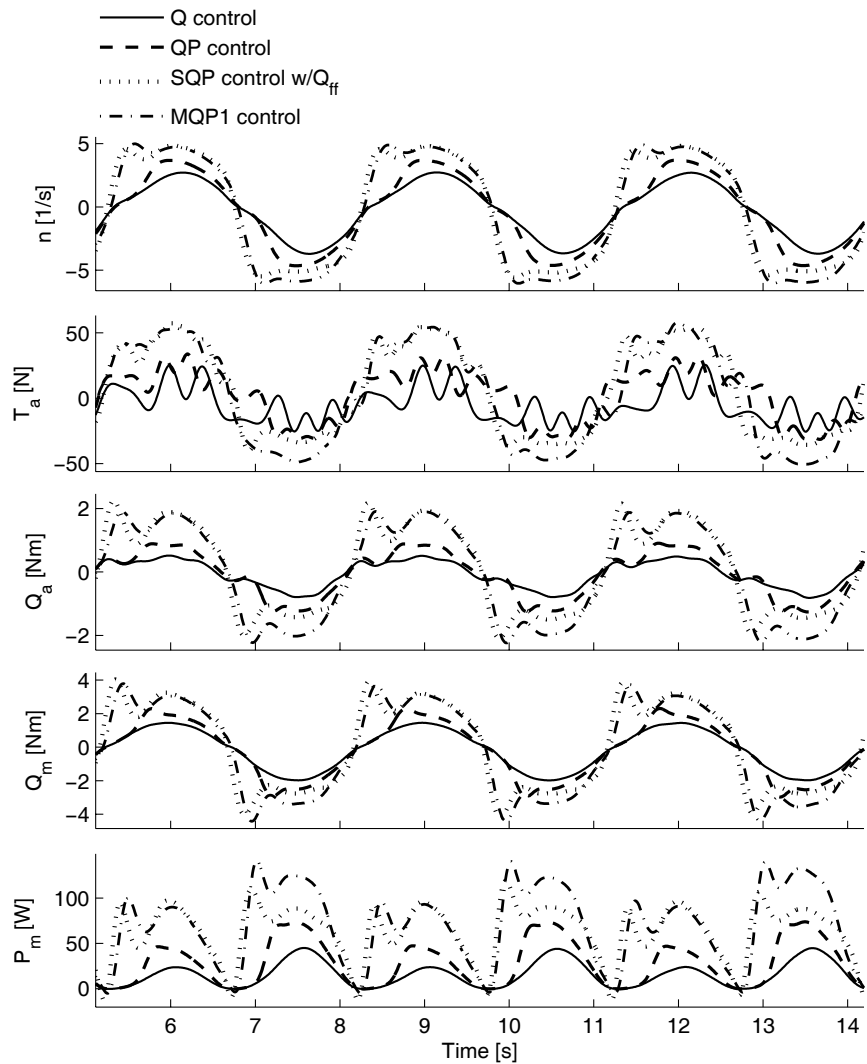


Figure 7.12: Comparison of four controllers tracking a sinusoidal thrust reference with amplitude 50N and period 3s.

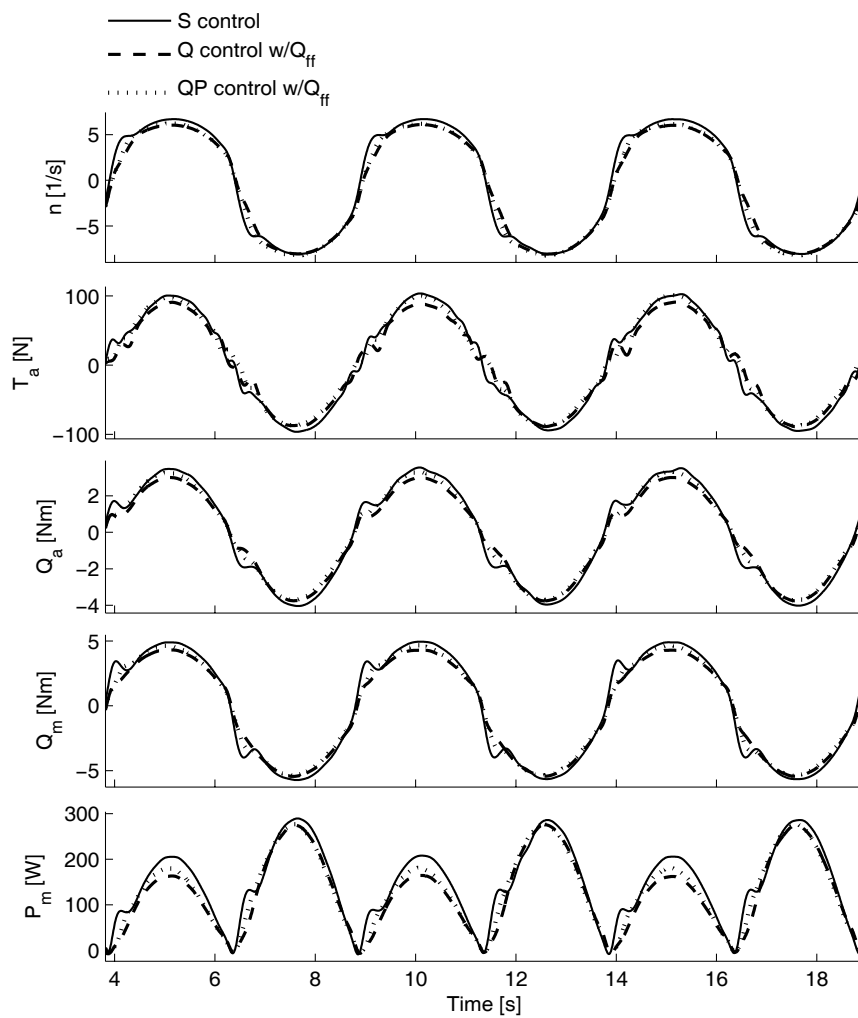


Figure 7.13: Comparison of three controllers tracking a sinusoidal thrust reference with amplitude 100N and period 5s.

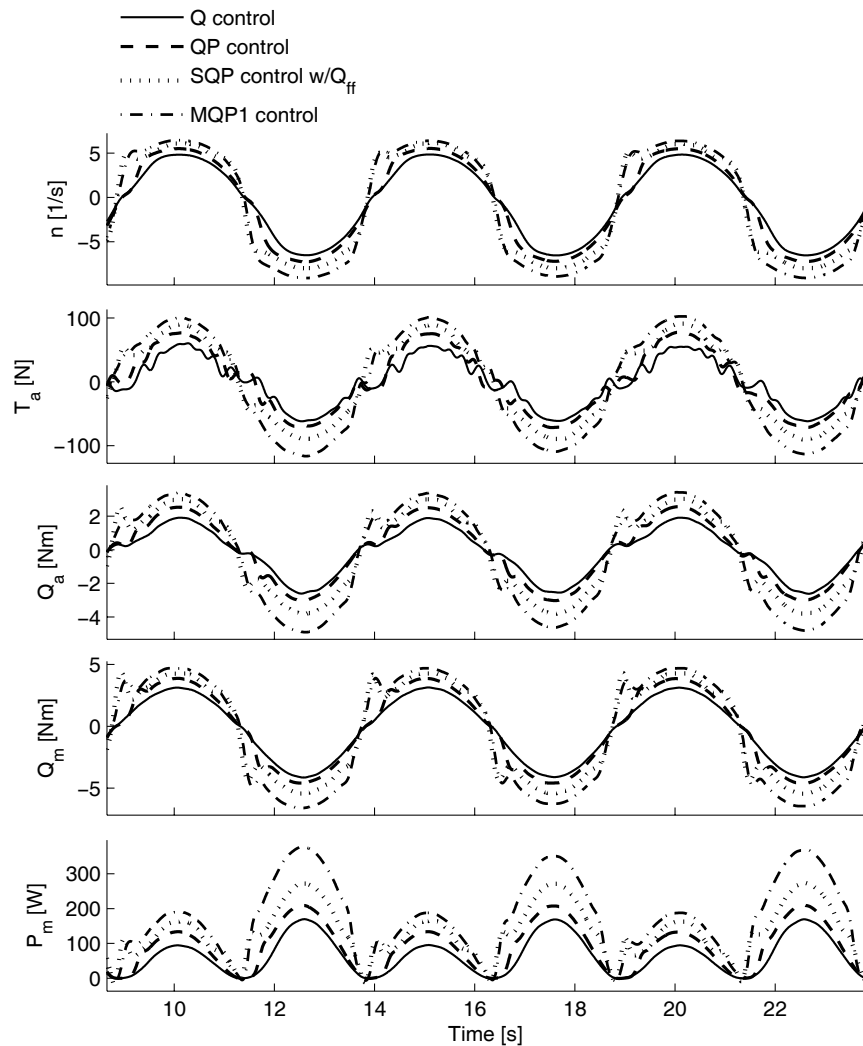


Figure 7.14: Comparison of four controllers tracking a sinusoidal thrust reference with amplitude 100N and period 5s.

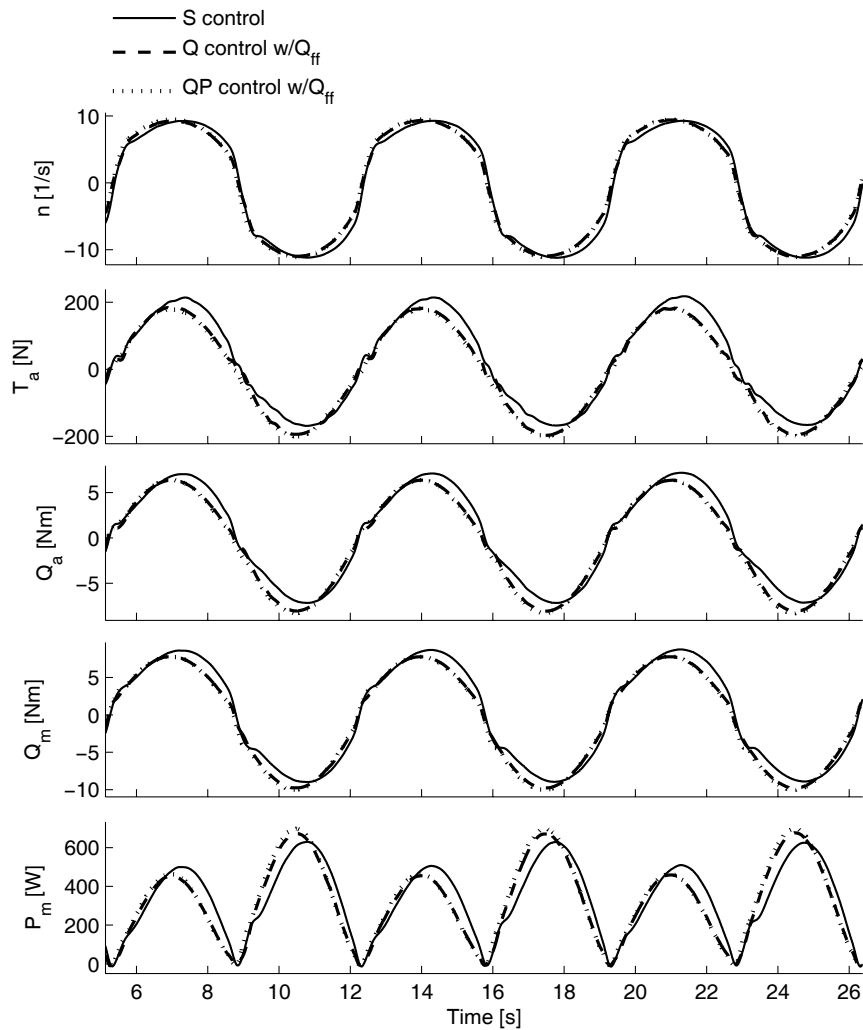


Figure 7.15: Comparison of three controllers tracking a sinusoidal thrust reference with amplitude 200N and period 7s.

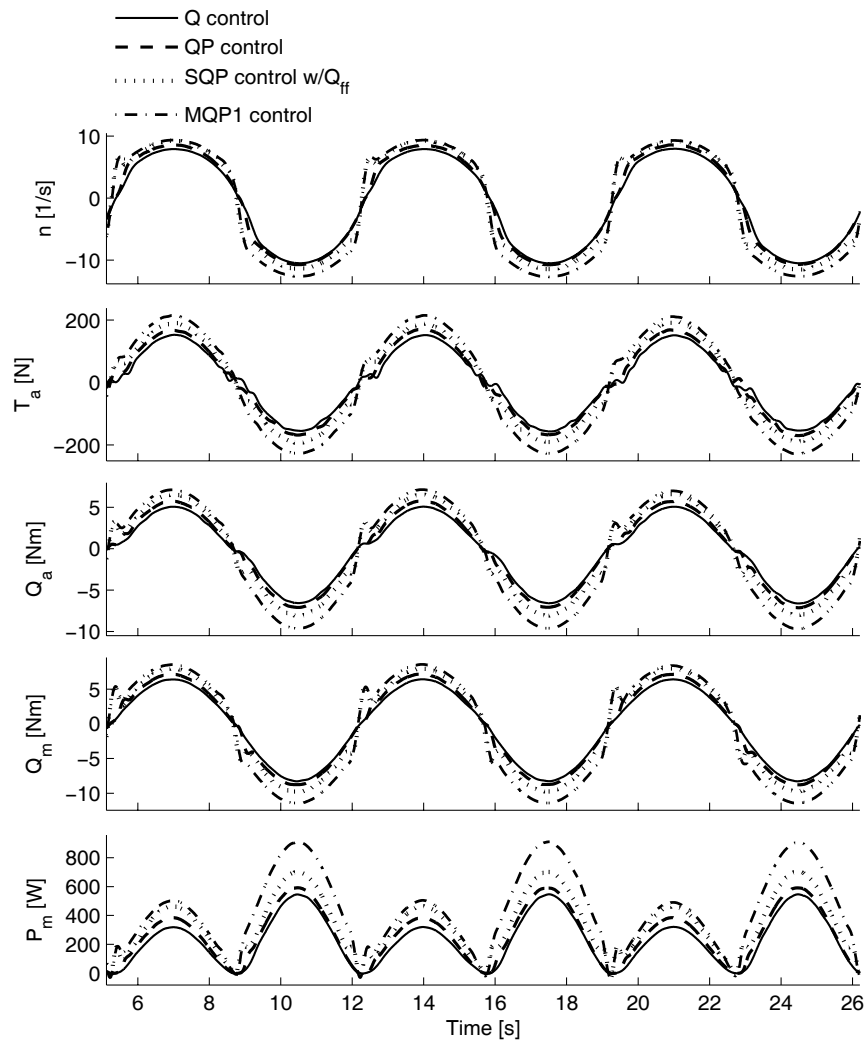


Figure 7.16: Comparison of four controllers tracking a sinusoidal thrust reference with amplitude 200N and period 7s.

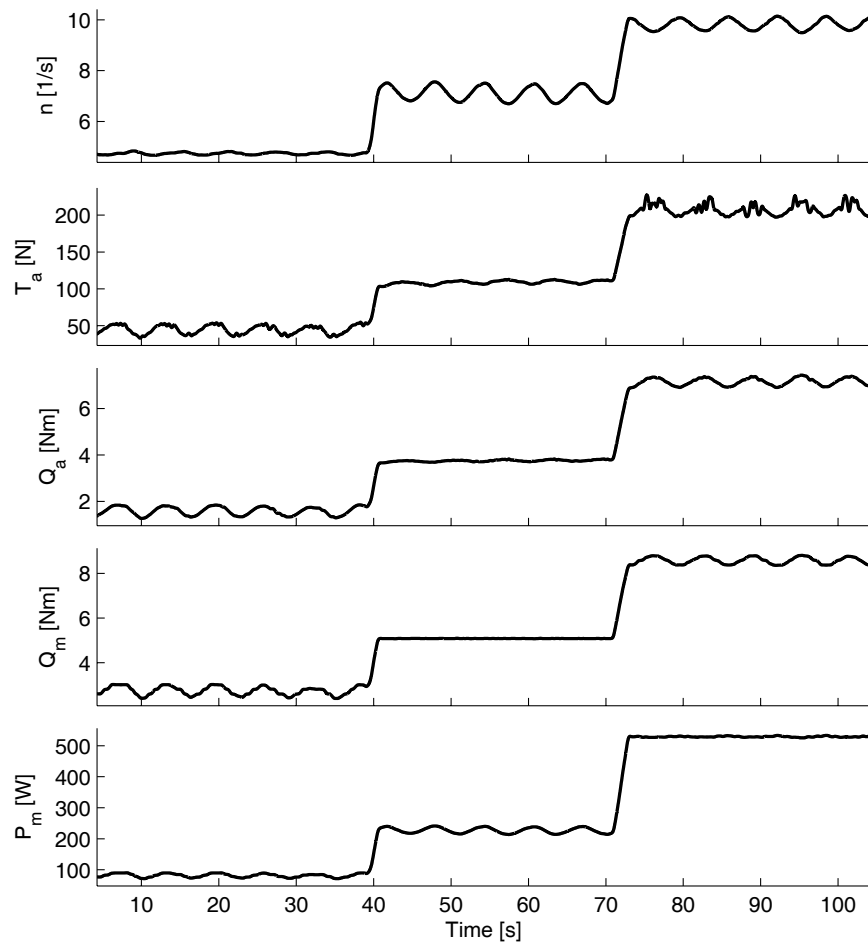


Figure 7.17: Combined SQP control for  $T_r = 50\text{N}$ ,  $120\text{N}$ , and  $220\text{N}$ , with a sinusoidally varying  $V_a$ .

## 7.3 Experiments in extreme conditions

This section presents experiments with the propeller subject to extreme conditions. Results are given for some of the controllers for normal conditions presented in Chapter 3, as well as for the controllers designed for extreme conditions presented in Chapter 6. The observer and loss estimation scheme from Section 5.1 are tested as parts of the anti-spin controllers. Results are given both for the ducted and open propeller.

The propellers have been tested in a variety of operating conditions: for constant and time-varying thrust references, in waves, with a calm free surface and forced vertical motion, and in combinations of waves and vertical motion. In the majority of the results presented here, the thrust reference was kept constant during forced vertical motion with a calm free surface. This improved the repeatability and enabled comparison of various controllers, since the time series could be synchronized by comparing the relative vertical motion of the propeller. Because of the chaotic nature of ventilation, the actual operating conditions for the propeller vary from one test run to another. The time series must therefore only be considered as examples of the performance of the various controllers. However, the repeatability is in general good. The forced vertical motion is parameterized in terms of the sinusoidal amplitude  $A_v$  and period  $T_v$ , as well as the mean submergence  $h_0$ . Two cases will mainly be used:

1.  $h_0 = 25$  cm,  $A_v = 15$  cm, and  $T_v = 10$  s. This means that the propeller blades just exit the surface at the highest point of the trajectory.
2.  $h_0 = 15$  cm,  $A_v = 15$  cm, and  $T_v = 5$  s. This means that the submergence ratio  $h/R = 0$  at the highest point of the trajectory, i.e. the propeller shaft is level with the free surface.

As for the tests in normal conditions, the results are shown in terms of  $n$ ,  $T_a$ ,  $Q_a$ ,  $Q_m$ , and  $P_m$ .

### 7.3.1 Controller parameters

For the open propeller, the basic control parameters were chosen as in Table 7.4. For the ducted propeller,  $K_{TC}$  and  $K_{QC}$  were taken as 0.513 and 0.0444, respectively. That is, (3.8) and (3.9) were implemented with  $K_{T0} = K_{T0r} = 0.513$  and  $K_{Q0} = K_{Q0r} = 0.0444$ . A summary of the ducted propeller control parameters is given in Table 7.6. Notice that all the basic control parameters except the thrust and torque coefficients are equal for both propellers. The parameters for the S and QP controller were chosen as in Table 7.5. However, the next section will discuss tuning of the S controller PI parameters.

For the load torque observer and loss calculation from Section 5.1,  $Q_{f0}$  and  $Q_{f1}$  were chosen as in Table 7.4,  $I_s$  was set to  $0.05\text{kgm}^2$ , the observer gains were chosen as  $k_a = 15$  and  $k_b = -25$ , and the parameters for the weighting function  $\alpha_b(n)$  were chosen as  $[r, p, k] = [8, 0.5, 1]$ . In the ventilation detection

$D$	$K_{T0}$	$K_{Q0}$	$K_{T0r}$	$K_{Q0r}$	$n_c$
0.25m	0.513	0.0444	0.513	0.0444	3rps
$Q_{f0}$	$Q_{f1}$	$n_f$	$I_c$		
1.0Nm	0.01Nms	0.5rps	0kgm <sup>2</sup>		

Table 7.6: Basic control parameters used in the experiments with the ducted propeller.

$Q_{f0}$	$Q_{f1}$	$I_s$	$k_a$	$k_b$
1.0Nm	0.01Nms	0.05kgm <sup>2</sup>	15	-25
$r$	$p$	$k$	$\beta_{v,on}$	$\beta_{v,off}$
8	0.5	1	0.6	0.9

Table 7.7: Parameters for the load torque observer, loss estimation, and ventilation detection, used for both propellers.

scheme from Section 6.3, the threshold parameters were chosen as  $\beta_{v,on} = 0.6$  and  $\beta_{v,off} = 0.9$ , and the detection delay was set to  $T_{vent} = 1\text{s}$ . A summary of the observer and loss calculation parameters is given in Table 7.7.

For the TS AS controller from Section 6.5, the settings for the primary anti-spin action were  $\dot{\gamma}_{rise} = 1\text{s}^{-1}$ ,  $\dot{\gamma}_{fall} = -1\text{s}^{-1}$ , and unless otherwise stated  $\tau_\gamma = 0.3\text{s}$ . Tuning of  $\tau_\gamma$  is discussed in the next section. For the secondary anti-spin action, the filter time constant was chosen as  $\tau_n = 0.05\text{s}$ , and the rate limits were chosen as  $\dot{n}_{vent}^+ = 3\text{s}^{-2}$  and  $\dot{n}_{vent}^- = -3\text{s}^{-2}$ . The desired shaft speed during ventilation was set to  $n_{as} = 9\text{rps}$ . This choice was motivated from observations during the tests, where it seemed that the most violent dynamic loading disappeared below 10rps. A summary of the TS AS controller parameters is given in Table 7.8.

For the SB AS controller from Section 6.6.1, the PI parameters were chosen as  $K_p = 0.5$  and  $T_i = 0.05\text{s}$ , and the speed bound factor was chosen as  $r_b = 0.2$ . The parameters are summed up in Table 7.9.

A maximum shaft speed of  $n_{max} = 25\text{rps}$  was enforced in all the experiments, in order to avoid damaging the setup by uncontrolled propeller racing.

### 7.3.2 Controller tuning

Figure 7.18 shows the shaft speed and the motor torque during a ventilation incident for the open propeller with three different shaft speed controllers. The

$\dot{\gamma}_{rise}$	$\dot{\gamma}_{fall}$	$\tau_\gamma$	$\dot{n}_{vent}^+$	$\dot{n}_{vent}^-$	$\tau_n$	$n_{as}$
$1\text{s}^{-1}$	$-1\text{s}^{-1}$	$0.3\text{s}$	$3\text{s}^{-2}$	$-3\text{s}^{-2}$	$0.05\text{s}$	$9\text{rps}$

Table 7.8: Parameters for the torque scaling anti-spin (TS AS) controller, used for both propellers.

$K_p$	$T_i$	$r_b$
0.5	0.05s	0.2

Table 7.9: Parameters for the speed bound anti-spin (SB AS) controller, used for both propellers.

ventilation incidents were generated by vertical motion of the propeller, with parameters  $h_0 = 15\text{cm}$ ,  $A_v = 15\text{cm}$ , and  $T_v = 5\text{s}$ . The thrust reference was  $T_r = 200\text{N}$ . The figure demonstrates the importance of the tuning of the PI parameters. Too low gains lead to significant propeller racing during ventilation, as well as long recovery time after the incident has terminated. On the other hand, too high gains may lead to oscillations in the controller output due to integrator discharge, or high sensitivity to measurement noise if a high proportional gain is chosen.  $K_p = 0.2$  and  $T_i = 0.05\text{s}$  were found to be good trade-offs, and are used in the following. Figure 7.19 shows similar time series for the QP TS AS p controller, with varying filter time constants  $\tau_\gamma$ . With primary action only, the goal of the anti-spin controller was to keep the shaft speed constant. The choice of  $\tau_\gamma$  can be seen to have a similar effect as the choice of PI parameters for the shaft speed controller. If no filter is used, the response of the controller is fast, but at the expense of a more noisy control signal. If the filter time constant is too high, the anti-spin controller becomes slow and allows the propeller to race out significantly before the ventilation incident is “caught”. This could have been expected from the analysis in Section 6.5.1, where it was shown that the bound on the shaft speed was determined by the deviation of  $\gamma$  from  $\beta_Q$  during the ventilation incident.  $\tau_\gamma = 0.3\text{s}$  was found to be a good trade-off between response time and noise in the control law, and used in the remainder of the tests. By comparing the shaft speeds in Figures 7.18 and 7.19 it is apparent that the QP TS AS p controller has similar performance as a reasonably well-tuned PI shaft speed controller during ventilation.

### 7.3.3 Single ventilation incidents with the ducted propeller

This section presents comparisons of six controllers during a ventilation incident with the ducted propeller, divided in two groups:

- 1a)** Torque controller (Q).
- 1b)** Combined torque/power controller (QP) – acts as a P controller for  $n > 3\text{rps}$ .
- 1c)** Shaft speed PI controller (S).
- 2a)** Combined torque/power controller with torque scaling primary anti-spin action (QP TS AS p).
- 2b)** Combined torque/power controller with torque scaling primary and secondary anti-spin action (QP TS AS p+s).

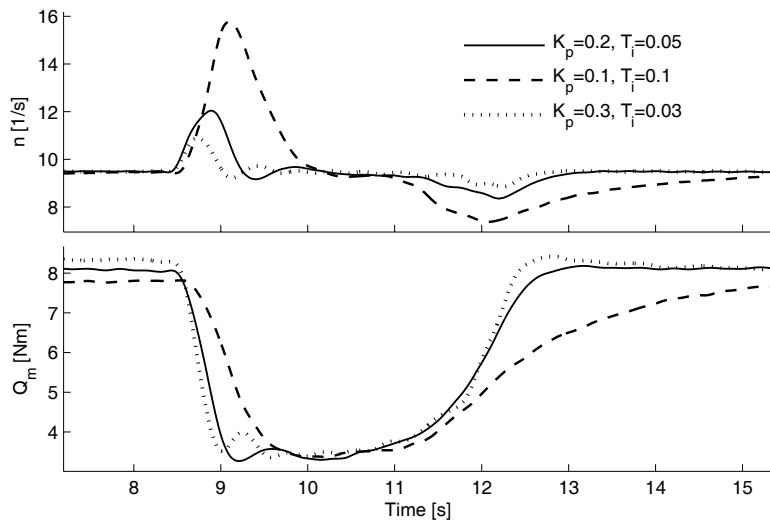


Figure 7.18: Comparison of shaft speed and motor torque during a ventilation incident for the shaft speed controller with varying PI parameters at  $T_r = 200\text{N}$ .

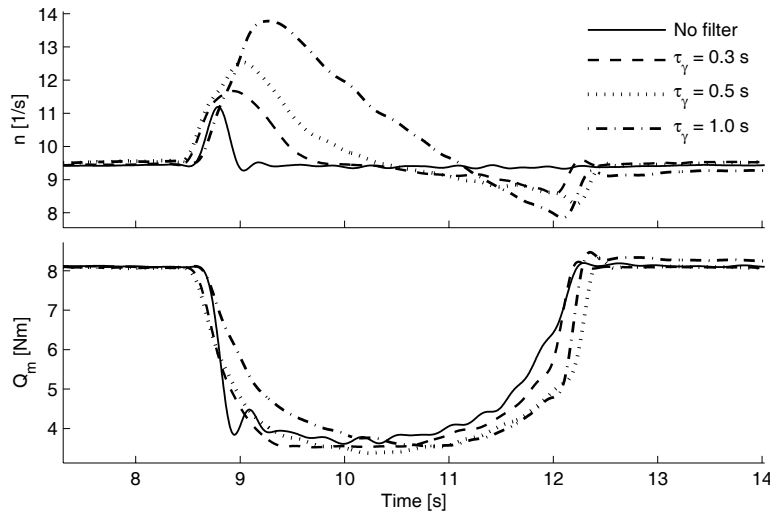


Figure 7.19: Comparison of shaft speed and motor torque during a ventilation incident for the QP TS AS p controller, using varying filter time constants at  $T_r = 200\text{N}$ .

**2c)** Combined torque/power controller with speed bound anti-spin (QP SB AS).

The friction compensation scheme was used for all the controllers.

The ventilation incidents were generated by vertical motion of the propeller, with parameters  $h_0 = 15\text{cm}$ ,  $A_v = 15\text{cm}$ , and  $T_v = 5\text{s}$ . Figures 7.20, 7.21, and 7.22 show results for  $T_r = 100\text{N}$ ,  $200\text{N}$ , and  $300\text{N}$ , respectively. The time series show that the Q controller and the QP controller both lead to propeller racing. The S controller and the anti-spin controllers limit the shaft speed as intended, with the secondary anti-spin action of the QP TS AS p+s controller giving a reduced shaft speed during ventilation. The Q controller could not be tested for  $T_r = 300\text{N}$ , since the propeller racing was too severe to give sensible results. At  $T_r = 100\text{N}$ ,  $n_r < n_{as}$ , such that the secondary action of the QP TS AS p+s controller never is activated. The time series is therefore nearly identical to the QP TS AS p controller. Note also that there is a transient in the motor torque at the end of the ventilation incident for these controllers. This is due to a “false” detection – the antispin controller is first switched off, and then on and off again. This is unfortunate with respect to mechanical wear and tear. For all thrust references, the resulting thrust during ventilation is about the same for all controllers – in Figure 7.21 the QP TS AS p+s controller, which reduces the shaft speed to 9rps during ventilation, produces the same thrust as the Q controller, which races to 25rps. The power consumption of the Q controller is unacceptably high, whereas the QP controller keeps the power consumption limited. The reason for the power not being constant is that the control coefficients  $K_{TC}$  and  $K_{QC}$  no longer match the true coefficients during ventilation. The S and anti-spin controllers give a significantly reduced power consumption during ventilation. This is inevitable, and may be a problem if the power system and PMS are not designed to cope with the sudden excess of power. It can be noted that the QP TS AS p controller has a similar performance as the S controller during ventilation, which also is the intention. Figure 7.23 shows details from the QP TS AS p+s controller during a ventilation incident at  $T_r = 300\text{N}$ , showing that the proposed anti-spin controller – including the load torque observer and ventilation detection scheme – performs as intended.

### 7.3.4 Single ventilation incidents with the open propeller

Figures 7.24, 7.25, and 7.26 present similar results as in the previous section, but for the open propeller. The same six controllers are tested, with the vertical motion given by  $h_0 = 25\text{cm}$ ,  $A_v = 15\text{cm}$ , and  $T_v = 10\text{s}$ . Since the average submergence is higher in these tests, the ventilation is less severe than in the previous section. The QP TS AS p+s controller was not tested for  $T_r = 100\text{N}$  in Figure 7.24, since it is identical to the QP TS AS p controller in this case. For  $T_r = 300\text{N}$  in Figure 7.26, the Q controller was not tested, since the propeller racing was considered too severe. The main difference to notice from the previous section, is that increased shaft speed gives increased thrust during ventilation. This is consistent with the findings in Section 2.4. The result

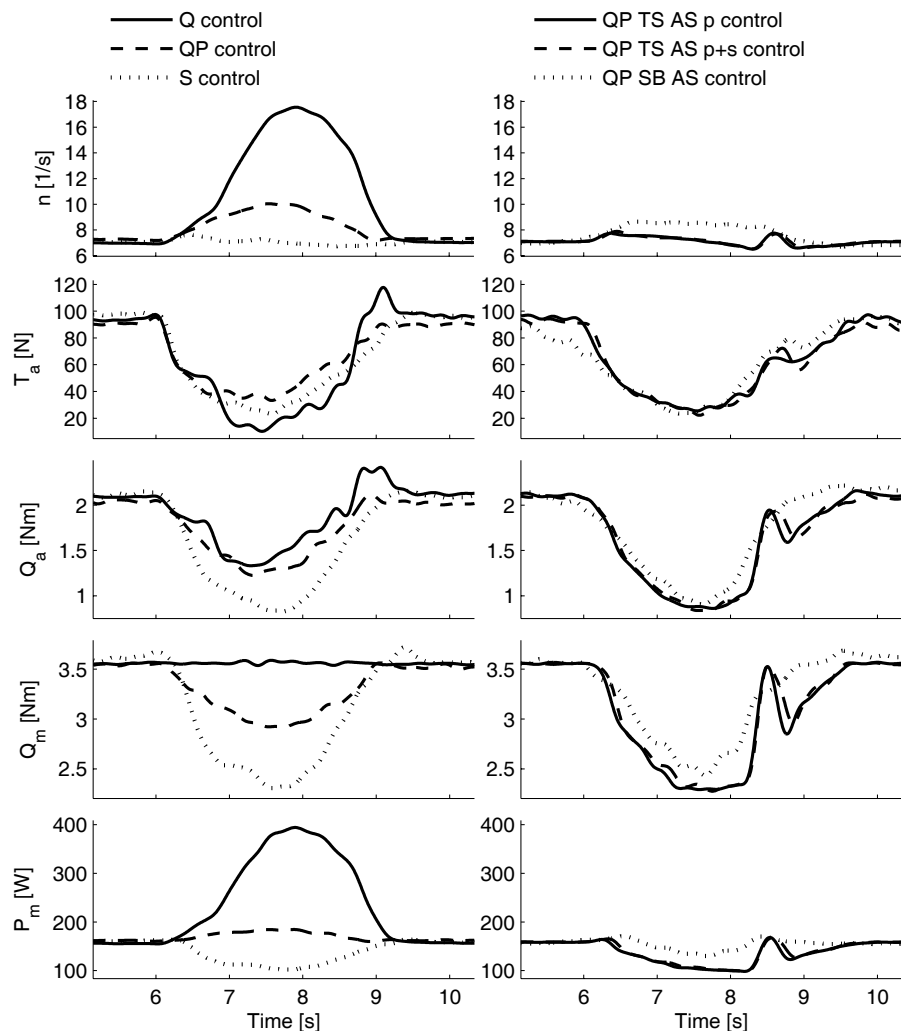


Figure 7.20: Comparison of six controllers during a ventilation incident at  $T_r = 100\text{N}$  for the ducted propeller.

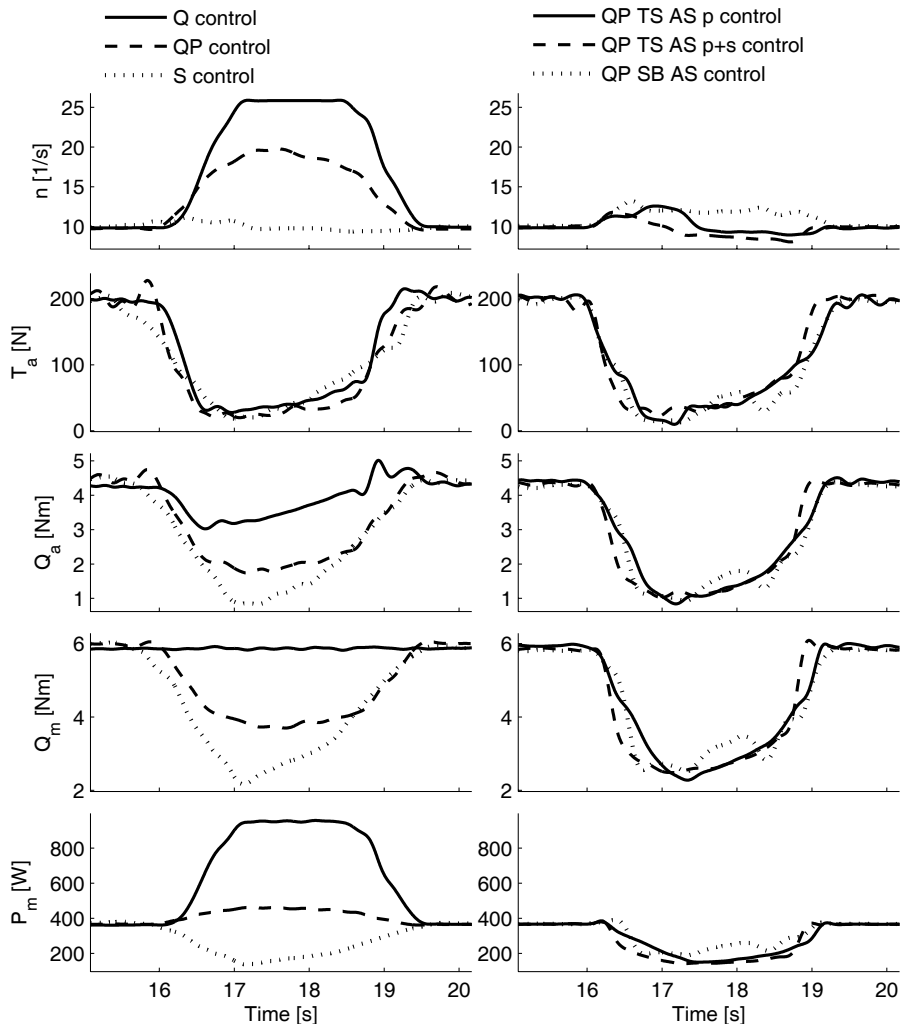


Figure 7.21: Comparison of six controllers during a ventilation incident at  $T_r = 200\text{N}$  for the ducted propeller.

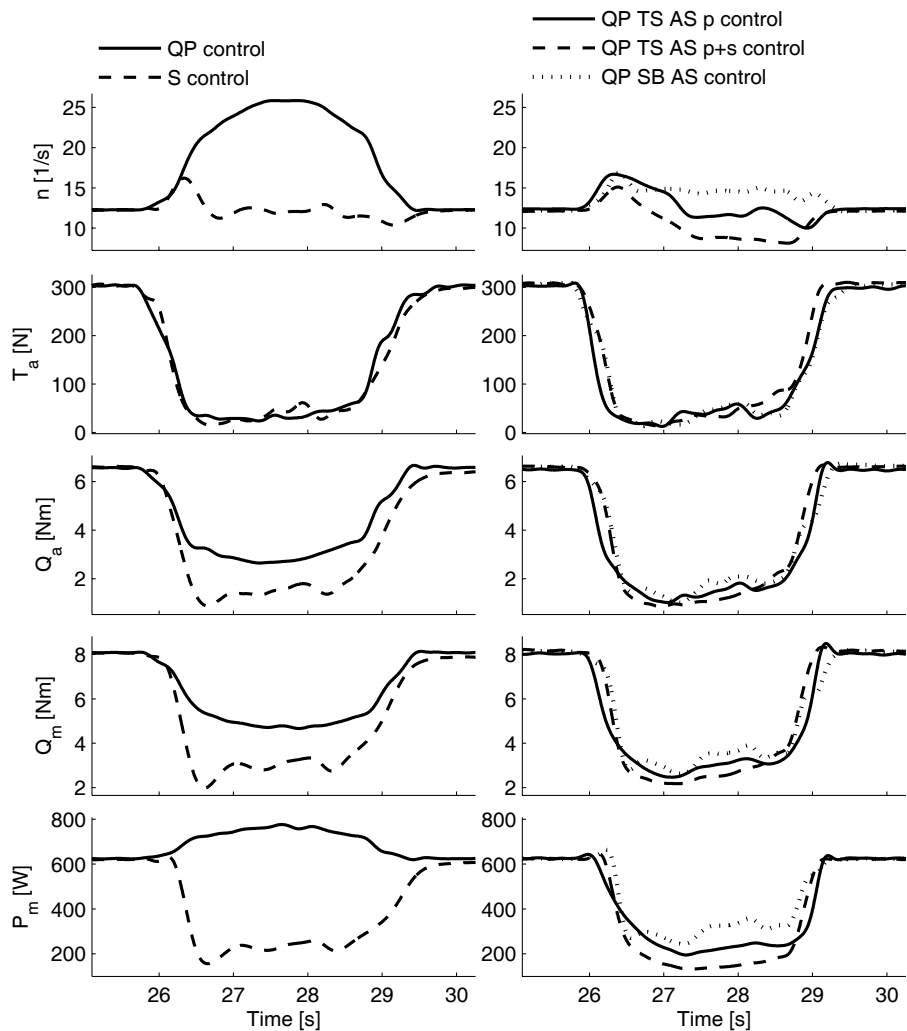


Figure 7.22: Comparison of five controllers during a ventilation incident at  $T_r = 300\text{N}$  for the ducted propeller.

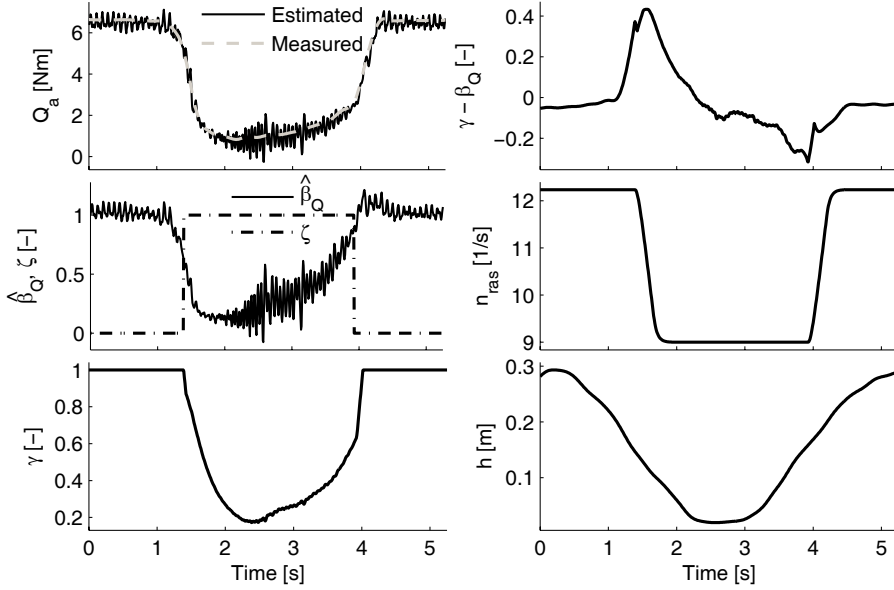


Figure 7.23: Time series of the main parameters in the QP TS AS p+s controller during a ventilation incident at  $T_r = 300\text{N}$  for the ducted propeller.

is that the Q and QP controllers give more thrust than the others. From the discussion in Section 3.2.2, the price to pay is increased mechanical wear and tear due to the unsteady propeller loading. This was also experienced during the experiments; when the propeller raced out, as e.g. with the Q controller at  $T_r = 200\text{N}$ , violent vibrations could be heard and felt in the whole MCLab carriage.

### 7.3.5 Additional tests

Figures 7.27 and 7.28 show results for the QP AS p+s controller for the open propeller with a sinusoidal  $T_r$  of amplitude 50N, period 7s, and offset 200N. The ventilation incidents were generated by vertical motion of the propeller with  $h_0 = 15\text{cm}$ ,  $A_v = 15\text{cm}$ , and  $T_v = 10\text{s}$ . Figure 7.27 shows the main results, with  $T_r$  plotted together with  $T_a$ , and Figure 7.28 shows details from the controller. The results demonstrate that the proposed anti-spin controller performs as intended also with a time-varying reference.

Figures 7.29 and 7.30 show results for the QP TS AS p+s controller for the open propeller at a fixed mean submergence of  $h_0 = 0.44\text{m}$  ( $h_0/R = 1.75$ ) in irregular waves. The waves were generated from the modified PM spectrum (C.19) with  $H_s = 0.06\text{m}$  and  $T_p = 1.2\text{s}$ , and the thrust reference set to  $T_r = 240\text{N}$ . Figure 7.29 shows that only random ventilation incidents were experienced. Figure

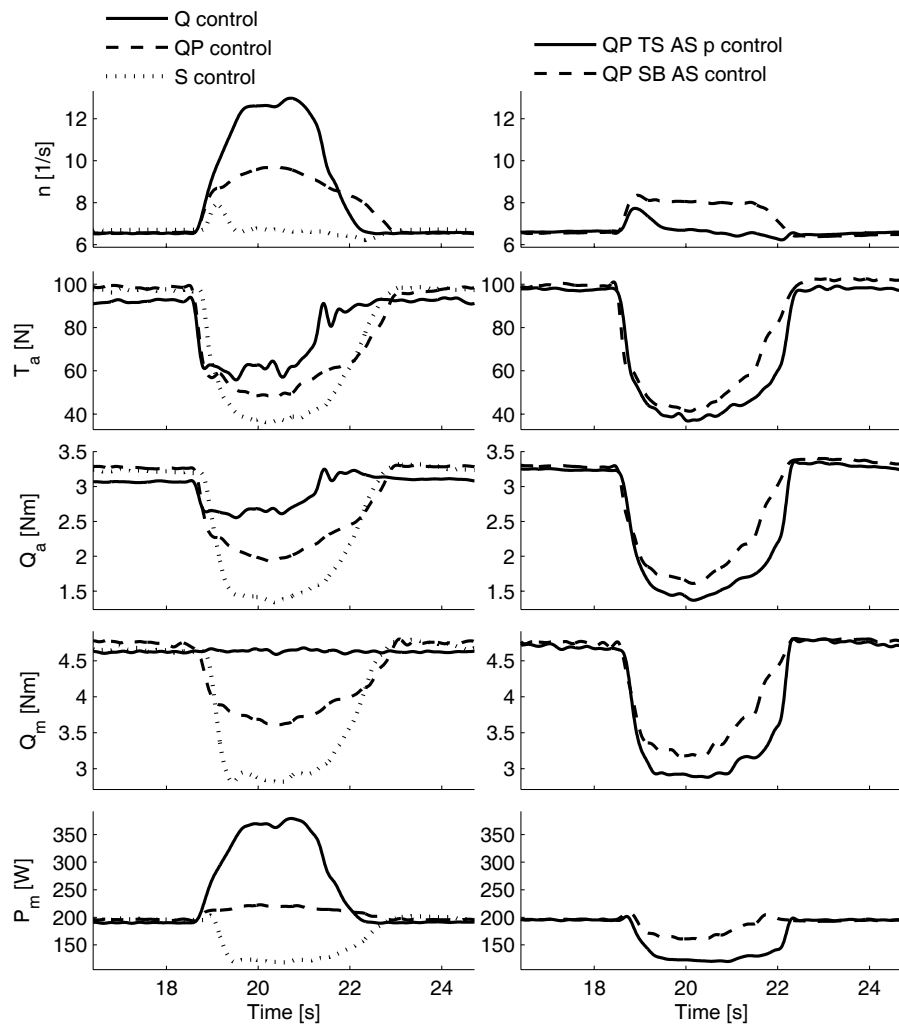


Figure 7.24: Comparison of five controllers during a ventilation incident at  $T_r = 100\text{N}$  for the open propeller.

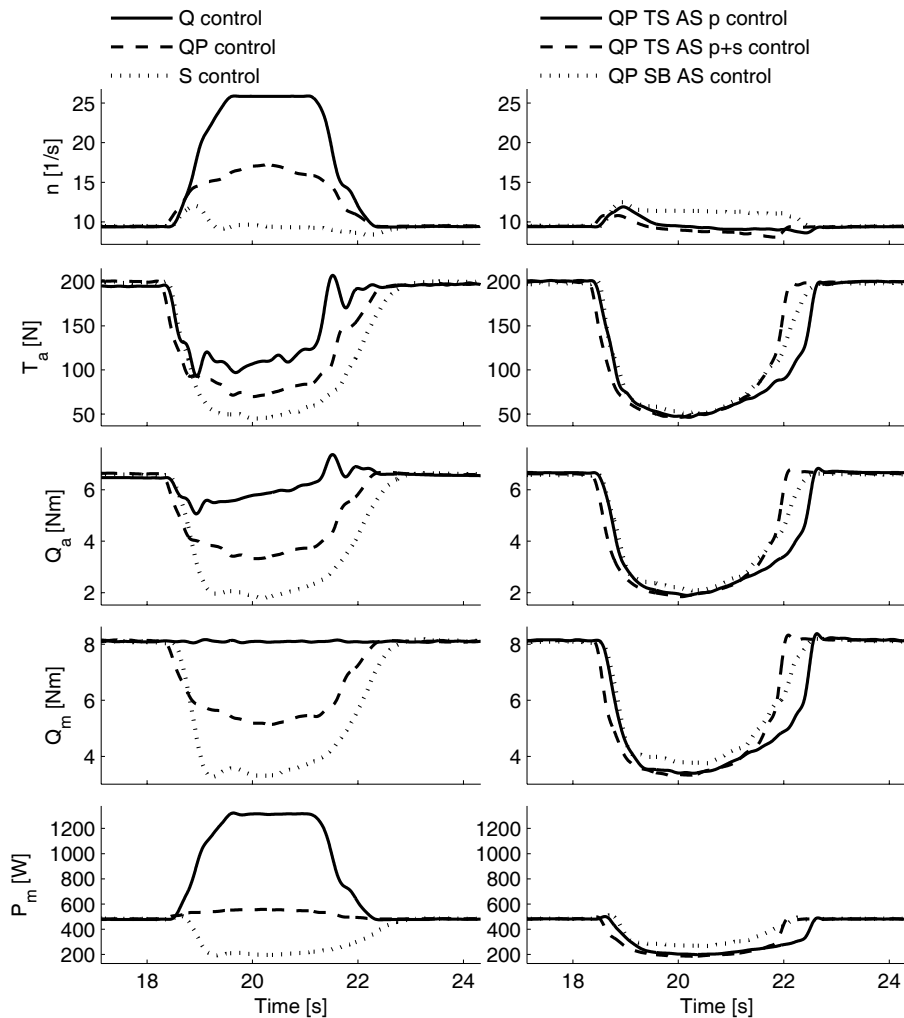


Figure 7.25: Comparison of six controllers during a ventilation incident at  $T_r = 200\text{N}$  for the open propeller.

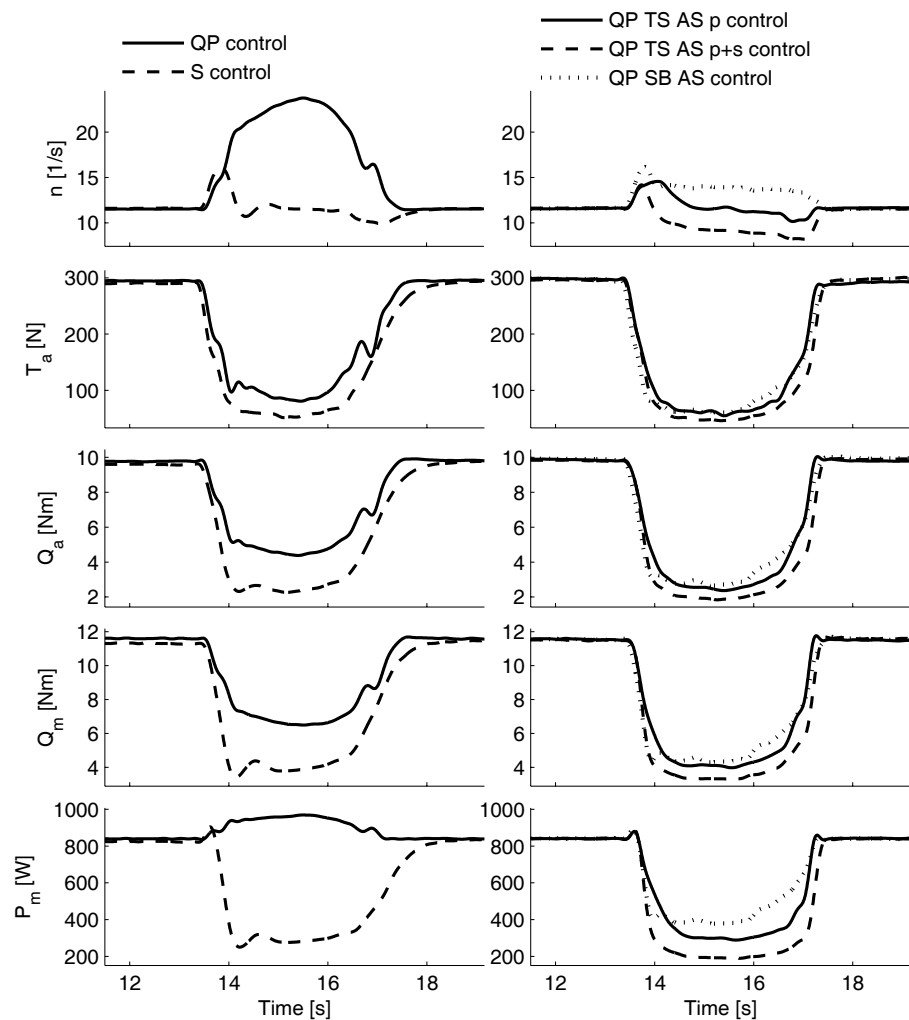


Figure 7.26: Comparison of five controllers during a ventilation incident at  $T_r = 300\text{N}$  for the open propeller.

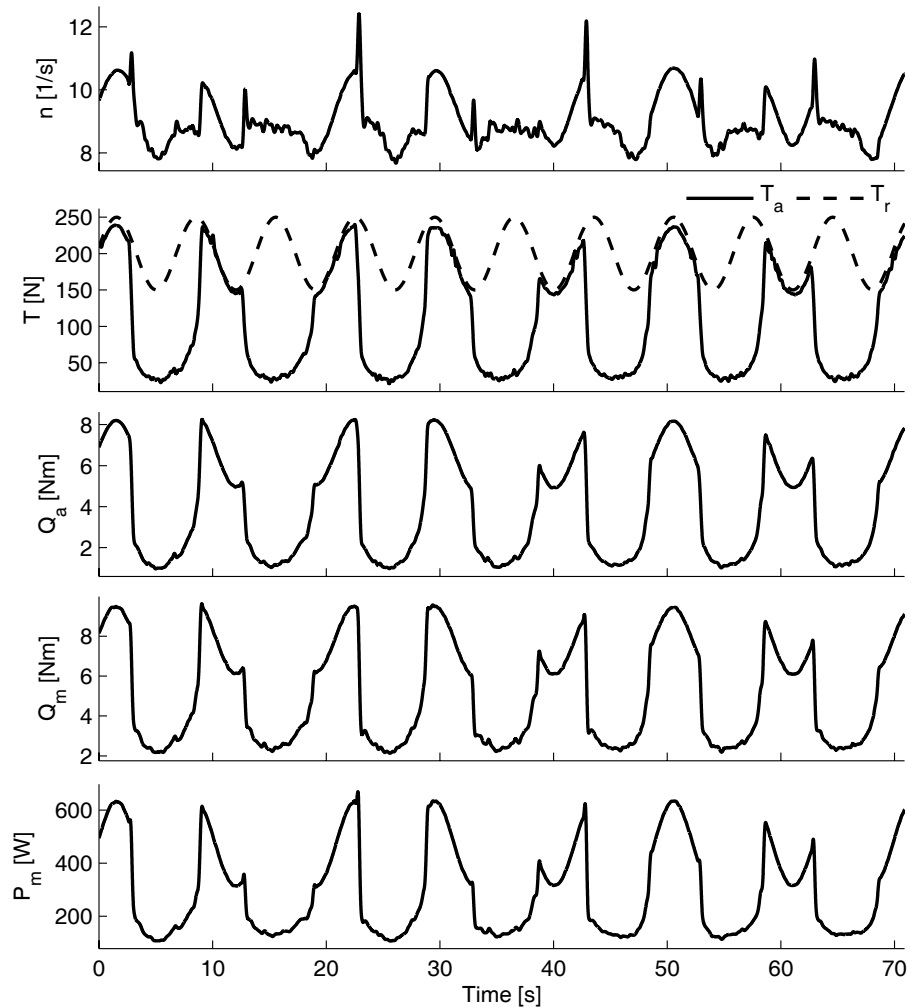


Figure 7.27: Time series of the open propeller with a sinusoidal thrust reference and ventilation incidents, with the QP TS AS p+s controller.

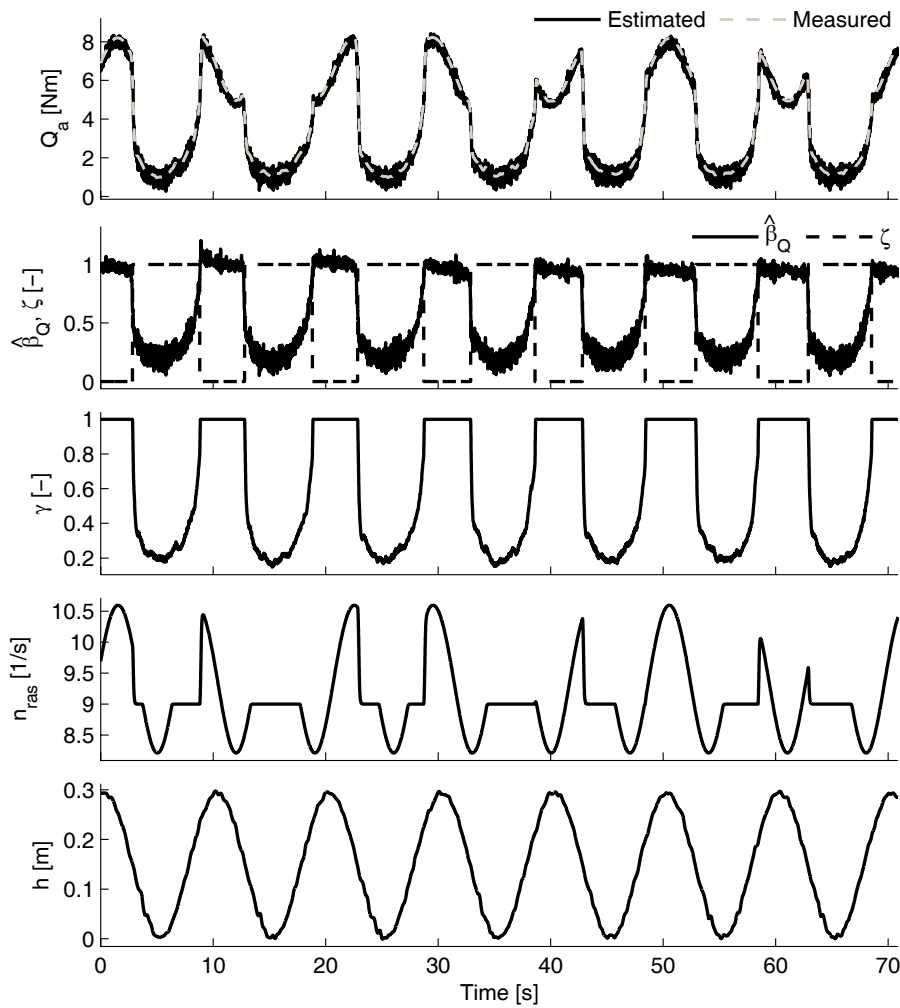


Figure 7.28: Details from the QP TS AS p+s controller for the open propeller with a sinusoidal thrust reference and ventilation incidents.

7.30 shows that the anti-spin controller works as intended: when there is no or little ventilation, the QP controller is left to work undisturbed, and when a ventilation incident suddenly appears, the anti-spin actions are activated to take control of and reduce the shaft speed.

## 7.4 Discussion

The experiments presented in this chapter have provided a fairly extensive validation of the various proposed control concepts. The results also act as a verification of the simulation results presented in Chapters 3, 5, and 6.

The quasi-static properties of the fundamental controllers when subject to varying advance velocity were theoretically analyzed in Chapter 4, and their performance in waves and current was tested by simulations in Chapter 3. The experimental results confirmed that the shaft speed controller is the most sensitive to changes in  $V_a$ , followed by the power and torque controllers, as summed up in Table 3.10. The experimentally derived sensitivity functions in Figure 7.9 also compared well with the theoretical functions derived in Chapter 4.

The tracking tests with the fundamental controllers confirmed the simulations in Chapter 3, and showed that the performance of the torque and power controllers with the appropriate friction and inertia compensation schemes were as good as or better than that of the shaft speed controller. The experiments also confirmed that, if the friction is significant, the lack of a friction compensation scheme in the torque and power controllers would lead to poor tracking performance for low thrust references. The combined QP controller – which with the weighting function parameters in Table 7.5 essentially was a power controller with torque control to facilitate zero-crossings – worked as intended, with a seamless transition between the two fundamental controllers. The combined SQP and MQP1 controllers also worked satisfactory, with the MQP1 controller facilitating reasonable tracking properties even without a friction compensation scheme.

In extreme conditions, the experiments confirmed the bad performance of torque and power control. This verified the analysis in Chapter 4 and the simulations in Chapter 6, which also showed severe propeller racing during ventilation incidents. However, it is apparent that the propeller rotational inertia has a significant influence on the amount of propeller racing; the simulations with a full-scale propeller from Chapter 6 gave less racing than the experiments with the model-scale propeller presented in this chapter.

The experiments further confirmed that the problems with propeller racing could be alleviated by introducing anti-spin control. The proposed torque scaling anti-spin scheme from Section 6.5 (TS AS p+s) was shown to work as intended, including the load torque observer, loss estimation, ventilation detection, and primary and secondary anti-spin action. The observer gave reasonable estimates of the propeller load torque, even with relatively noisy feedback signals, and the ventilation incidents were detected with acceptable accuracy. The

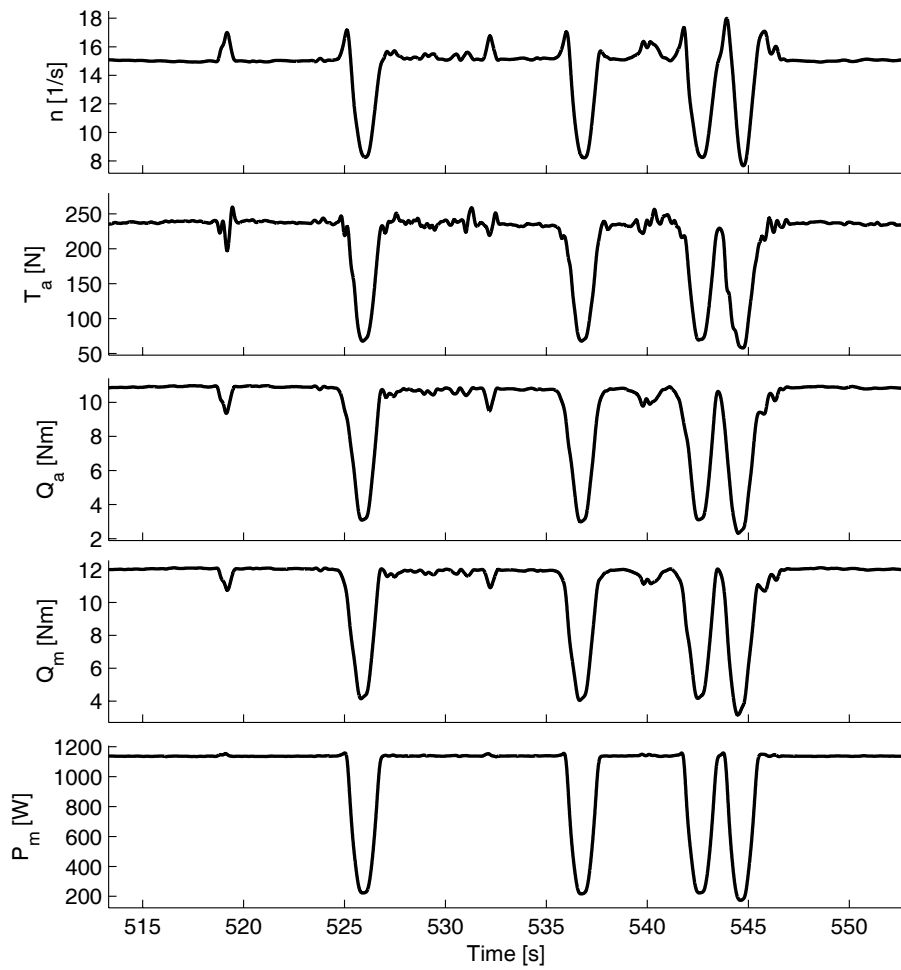


Figure 7.29: Time series of the open propeller at a fixed submergence in irregular waves, with the QP TS AS p+s controller.

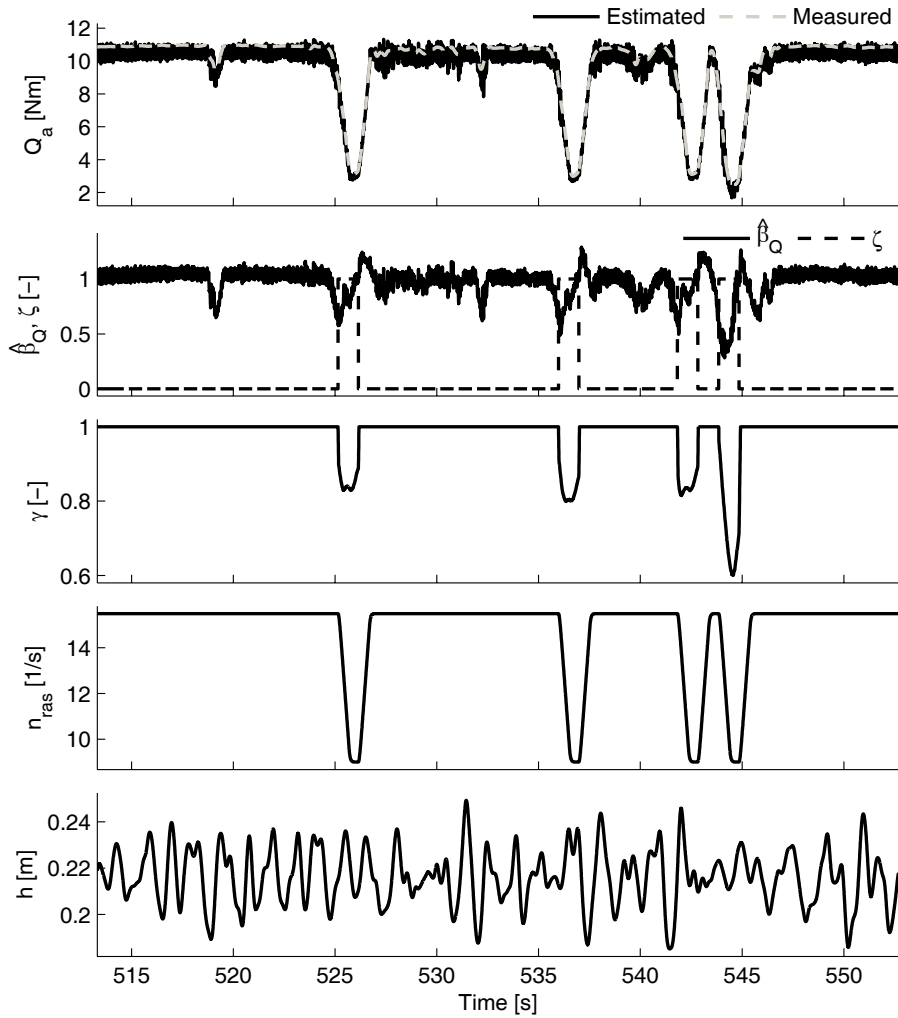


Figure 7.30: Details from the QP TS AS p+s controller for the open propeller at a fixed submergence in irregular waves.

results were hence consistent with the simulations from Chapter 6. The stability analysis in Section 6.5 was performed for a constant thrust reference. Both simulations and experiments, however, showed that the anti-spin scheme worked well also for a time-varying  $T_r$ .

The speed bound anti-spin controller (SB AS) was also shown to work as intended, with experimental results comparable to the simulations from Chapter 6.

The weighting function parameters for the QP controller were chosen to give pure power control for  $n > 3\text{rps}$ . Hence, the anti-spin controllers were in practice only presented as add-ons to P control. Anti-spin experiments with a Q controller have also been also performed (i.e. with anti-spin as an add-on to torque control, Q TS AS). The results were comparable to the QP TS AS controller, although with a slightly reduced performance during ventilation. This is consistent with the simulations presented in Figures 6.6 and 6.7.

From the discussions in Sections 2.4.6 and 3.2.2, ventilation of a propeller at low  $V_a$  will give large unsteady loads, which are suspected to cause significant mechanical wear and tear. The experimental setup was not capable of measuring these high-frequency loads, and the benefits of limiting the propeller racing could hence not be verified directly. The unsteady loads were, however, physically experienced during the experiments through vibrations and noise as the propeller raced out.

In conclusion, the introduction of anti-spin control meant that the performance of the torque and power controllers became acceptable also in extreme environmental conditions. From an over-all performance evaluation, the QP, SQP, or MQP controllers with anti-spin and the appropriate friction and inertia compensation schemes appear to be the best solution, combining the advantages of the QP controller in normal conditions with acceptable shaft speed control and limited transients in the motor torque during ventilation. However, the choice of core thruster controller and eventually an anti-spin controller will depend on the type of propeller, the type of vessel, and the expected operating conditions.

If an anti-spin controller is deemed appropriate, additional tuning is required. This will complicate commissioning of the thruster controller. The main challenge will probably be tuning of the load torque observer, since this is the core element of the anti-spin controller. However, with the tuning guidelines from Section 5.1.1, reasonable model knowledge, and increased experience, this should not be of major concern.



# Chapter 8

## Extensions to CPP and transit

The presented controllers and estimation schemes have all been aimed at FPP for DP operations. This chapter presents extensions of the presented concepts to CPP and transit.

### 8.1 Extensions to CPP

A CPP has two controllable parameters: the shaft speed  $n$  and the pitch ratio  $P/D$ . There are hence three possible ways of controlling the thrust from a CPP:

1. Speed control: the pitch is fixed at some preselected value, and the shaft speed is varied.
2. Pitch control: the shaft speed is fixed at some preselected value, and the pitch is varied.
3. Consolidated control: both shaft speed and pitch are varied dynamically.  
A consolidated controlled CPP is here termed a CCP.

*Speed control* corresponds to using the CPP as a FPP. This only makes sense if the pitch actuator is broken and the blades are fixed at a certain pitch. In this case, the control concepts in Table 3.1 can be used as is, preferably with  $K_{TC}$  and  $K_{QC}$  selected according the current pitch.

*Pitch control* is the classic use of a mechanical direct-drive CPP. If the installation is equipped with a shaft generator, the prime mover must keep the shaft speed within certain thresholds to keep the frequency on the power grid within acceptable limits. Hence, a CPP with pitch control is the only solution. This also enables the diesel to be run at its optimal RPM at all times. Pitch control

has also been widespread in diesel-electric installations, where fixed speed electromotors have been used in tunnel thrusters and azimuthing thrusters due to their low cost and simplicity.

*Consolidated control* combines many of the good properties of both variable speed FPP and fixed speed, variable pitch CPP, but also inherits some of the cons of the CPP propellers (Schanz, 1967; Morville, 1996; Andresen, 2000). The main advantages of a CCP are reduced noise and the ability to operate at high efficiency for a wide range of  $V_a$  and  $n$ . This is clearly seen in Figure 2.3, where the optimal open-water efficiency is found at higher  $J_a$  for increasing  $P/D$ . With two controllable parameters, optimal control also becomes a feasible solution, since the desired thrust often can be met by a number of combinations of speed and pitch. The task is then to find the combination of shaft speed and pitch that e.g. gives the lowest power demand, and hence fuel consumption. For DP, this combination can be found from the pitch dependent propeller characteristics. In transit, however, the optimization becomes a dynamic task. This is further treated in Schanz (1967), Winterbone (1980), Beek and Mulder (1983), Parsons and Wu (1985), Bakountouzis (1992), Chachulski *et al.* (1995), Fukuba *et al.* (1996), Morville (1996), Young-Bok *et al.* (1998), and Whalley and Ebrahimi (2002). More details on this can also be found in Ruth *et al.* (2006). In the following, extensions of the presented control and estimation concepts for FPP to CCP will be treated. Consolidated control based on optimal control will not be further treated.

### 8.1.1 Controller modifications for CCP

A consolidated control scheme must contain mappings from the thrust reference  $T_r$  to the pitch angle reference  $\phi_r$ , and one other parameter. In a conventional implementation based on pitch and shaft speed control, the other parameter would be the shaft speed reference  $n_r$ . Not considering optimal control schemes, which are more complex, there is then a unique relationship between  $T_r$  and  $\phi_r$ , expressed by the function  $g_\phi$ :

$$\phi_r = g_\phi(T_r). \quad (8.1)$$

The relationship between the pitch ratio  $P/D$  and the pitch angle  $\phi$  is given in (2.41). From Section 2.1.5, the open-water characteristics of a CPP can be parameterized by  $\phi$  (in addition to  $V_a$  and  $n$ ). Hence, the nominal thrust and torque coefficients may be expressed as functions of  $\phi$ :

$$K_{T0} = K_{T0}(\phi), \quad K_{Q0} = K_{Q0}(\phi). \quad (8.2)$$

The relationships in (8.2) should be known from the propeller characteristics. It is therefore possible to parameterize the control coefficients from (3.8, 3.9) in the same manner, based on  $\phi_r$ :

$$K_{TC} = K_{TC}(n_r, \phi_r), \quad K_{QC} = K_{QC}(n_r, \phi_r). \quad (8.3)$$

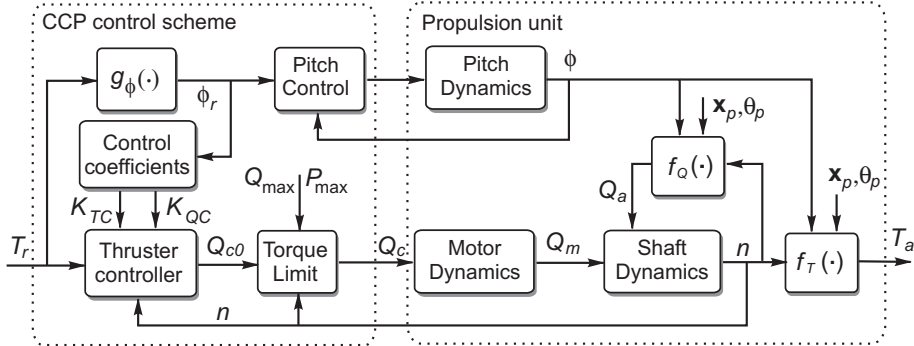


Figure 8.1: Block diagram of a consolidated control scheme for CPP, including the feedback loop for pitch control.

If the CPP motor is unidirectional,  $K_{TC}$  and  $K_{QC}$  no longer depend on  $n_r$ , and are given explicitly in terms of  $\phi_r$ . With  $\phi_r$  given by (8.1), and  $K_{TC}$  and  $K_{QC}$  given by (8.3), any of the controllers in Table 3.1 can be used without further modifications. Figure 8.1 shows a block diagram of a consolidated control scheme for CPP. The figure can be seen as an extension of Figure 3.1 to be valid also for CCP, with the inertia and friction compensation schemes embedded in the ‘Thruster controller’ block. The feedback loop of the pitch controller has also been included in the figure. Implementation of the pitch controller will not be further treated here. It is instead assumed that a pitch controller exists, and is capable of acceptable performance.

### 8.1.2 Consolidated controller example

Design of the pitch mapping (8.1) requires detailed knowledge of the hydrodynamics of the propeller, which would typically be provided by the propeller manufacturer. However, once this is given, the extension to consolidated control as shown in Figure 8.1 is trivial. To illustrate the proposed approach, a pitch mapping will be assumed.

Using the Wageningen B4-70 data from Oosterveld and van Oossanen (1975) – as given in Figure 2.3 –  $K_{T0}$  and  $K_{Q0}$  can be found for the pitch range  $0.6 \leq P/D \leq 1.4$ . Data points for this interval are shown in Figure 8.2, together with second order polynomial fits. The data points for  $P/D = 0$  have been added to get consistent curves for the whole operating range of the propeller. It has been assumed that  $P/D = 0$  gives a slightly positive thrust ( $K_{T0} = 0.05$ ), and a propeller power consumption of 10% of the value at about  $P/D = 1.2$

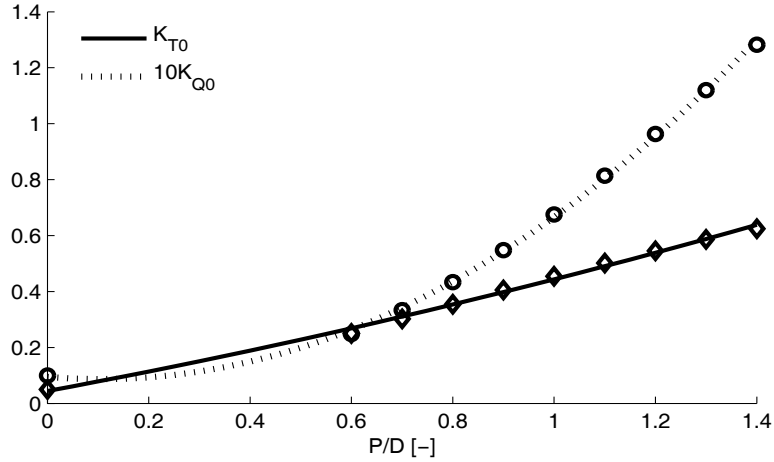


Figure 8.2: Nominal thrust and torque coefficients as functions of the pitch ratio  $P/D$  for the Wageningen B4-70 propeller.

$(K_{Q0} = 0.01)$ . The polynomials are used as control coefficients, which become:

$$K_{TC}(\phi_r) = 0.05 + 0.974\phi_r + 1.044\phi_r |\phi_r|, \quad (8.4)$$

$$K_{QC}(\phi_r) = 0.01 - 0.0843\phi_r + 0.878\phi_r |\phi_r|. \quad (8.5)$$

It has been assumed that a unidirectional motor is used, such that the control coefficients in (8.4, 8.5) are independent of  $n_r$ . For negative  $\phi_r$ , the polynomials should be adjusted, since the propeller is less efficient with negative pitch. This will not be further treated here.

From Figure 8.2, it is clear that a certain pitch ratio is needed in order to produce any significant thrust. Hence, the pitch mapping in (8.1) should have a steep slope about  $T_r = 0$ . For high  $T_r$ , the pitch may e.g. be chosen to be at the max value for DP operation, called  $\phi_{DP}$ . For this example, the following mapping is chosen:

$$\phi_r = g_\phi(T_r) = \tanh(\varepsilon_\phi \frac{T_r}{T_{bp}}) \phi_{DP}, \quad (8.6)$$

where  $\varepsilon_\phi$  is a small constant determining the shape of the mapping, and  $T_{bp}$  is the bollard pull thrust. The maximum pitch for DP is chosen as  $P/D = 1.0$ , which gives  $\phi_{DP} = 0.308$ , and  $\varepsilon_\phi$  is chosen as  $\varepsilon_\phi = 0.3$ . The resulting mapping from (8.6) is shown in Figure 8.3, together with the control coefficients found from (8.4, 8.5), as well as the shaft speed reference  $n_r$ , torque reference  $Q_r$ , and power reference  $P_r$  found from (3.1), (3.2), and (3.3) respectively. The dip in  $K_{QC}$  for low  $T_r$  is due to the polynomial fit used in establishing (8.5), and is easily avoided by better model knowledge for low pitch ratios.

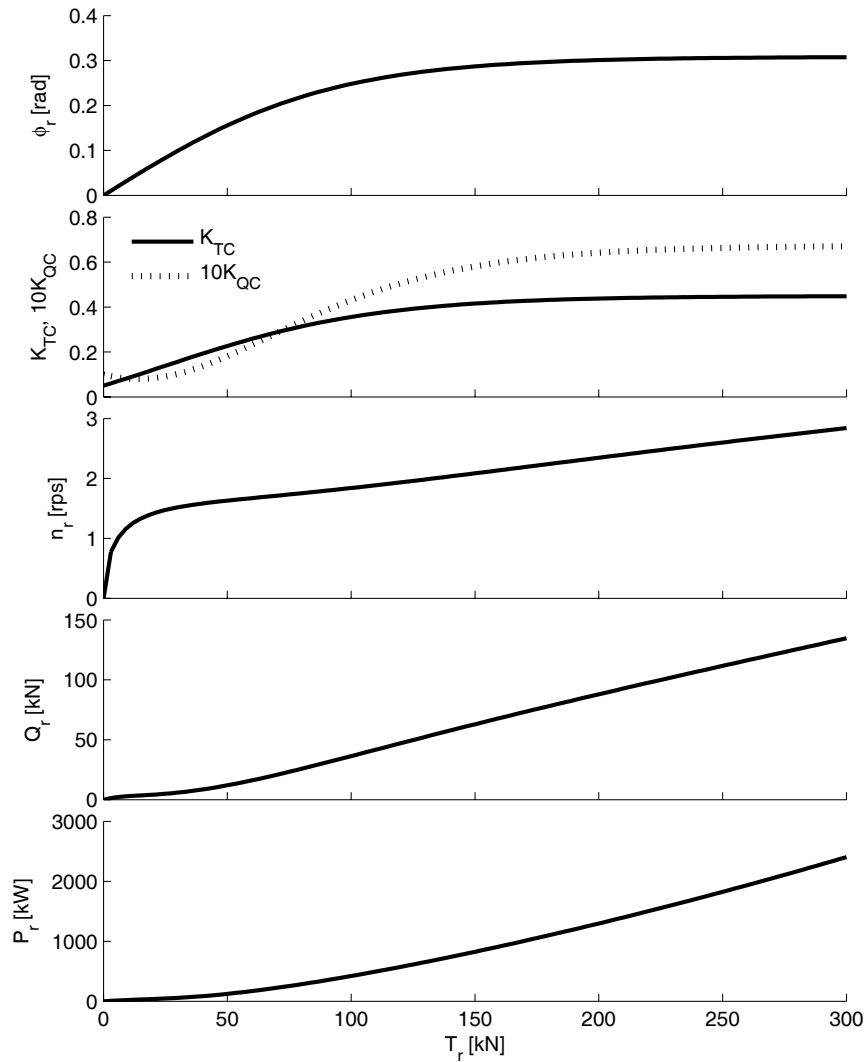


Figure 8.3: Consolidated controller example, with a chosen mapping from  $T_r$  to  $\phi_r$ , the corresponding  $K_{TC}$  and  $K_{QC}$  from the propeller characteristics, and  $n_r$ ,  $Q_r$  and  $P_r$  to be used in shaft speed, torque, or power control, respectively.

**Remark 8.1** The whole pitch range is not necessarily used in DP, since it may be advantageous with higher pitch ratios in transit than in DP. The chosen maximum pitch for DP will depend on the rating and speed range of the thruster motor.

### 8.1.3 Observer and estimation extensions to CCP

The estimated load torque  $\hat{Q}_a$  and torque coefficient  $\hat{K}_Q$  from (5.7) and (5.17), or (5.18) and (5.26), are completely independent of the propeller hydrodynamics and the operating conditions – they are calculated solely from the rotational dynamics of the propeller shaft. Hence, these schemes are valid also for CCP and transit without modifications. However, the estimated torque loss factor  $\hat{\beta}_Q$  from (5.16) or (5.19) is based on the control coefficient  $K_{QC}$ , and the torque performance factor  $\hat{\chi}_Q$  from (5.45) is based on both  $K_{QC}$  and  $K_{TC}$ . This must be accounted for if the loss estimation and performance monitoring schemes are to be used for CCP or transit.

Section 8.1.1 showed how the control schemes for FPP could be extended to CCP by letting  $K_{TC}$  and  $K_{QC}$  be functions of the the pitch angle reference  $\phi_r$ . Since  $K_{TC}$  and  $K_{QC}$  are used to represent the nominal performance of the propeller, the same approach can be used for  $\hat{\beta}_Q$  and  $\hat{\chi}_Q$ . Hence, the loss estimation and performance monitoring schemes are valid also for CCP when  $K_{TC}(\phi_r)$  and  $K_{QC}(\phi_r)$  are chosen as for the thruster controllers, i.e. as in (8.3).

### 8.1.4 Anti-spin controller extensions to CCP

The ventilation detection scheme in (6.1) and the primary anti-spin action in (6.6) are both based on  $\hat{\beta}_Q$ , and are hence valid as long as the calculation of  $\hat{\beta}_Q$  is valid. The secondary anti-spin action in (6.18) is based on the shaft speed mapping in (3.1), which again is based on  $K_{TC}$ , and therefore holds as long as (8.3) is applied.

This means that the proposed anti-spin thruster control scheme in Section 6.5 is valid also for CCP simply by applying (8.3), since the four main components in the scheme:

- Core thruster controller,
- Load torque observer,
- Ventilation detection,
- Anti-spin control actions,

all have been shown to be valid.

As for FPP, the main purpose of the proposed anti-spin control scheme for CCP is to take control of the shaft speed during severe thrust loss incidents. This is performed by the primary anti-spin action, which does not affect the

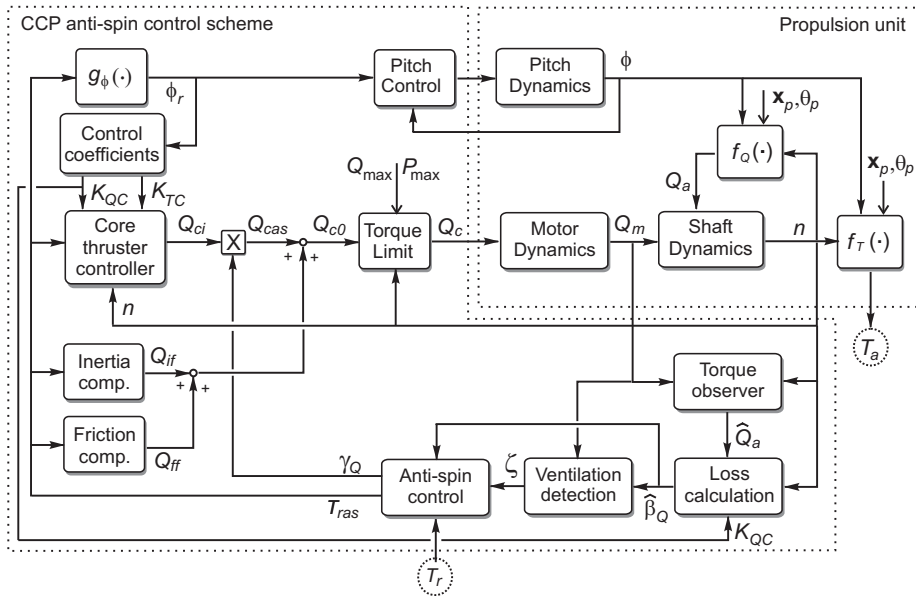


Figure 8.4: Block diagram of the proposed anti-spin control scheme for CCP.

propeller pitch. Avoiding propeller racing by pitch control is not considered feasible, due to the limited bandwidth of the pitch actuator.

For the secondary anti-spin action, two options exist:

1. Reduce the thrust reference only to the core thruster controller.
2. Reduce the thrust reference to both the core thruster controller *and* the pitch controller.

Option 2 should only be considered if the pitch actuator has the sufficient bandwidth. Figure 8.4 shows a block diagram of the proposed anti-spin control scheme for CCP, where option 2 has been chosen. If option 1 is to be used,  $T_r$  should be routed directly to the pitch mapping  $g_\phi(\cdot)$ .

In Ruth and Smogeli (2006), experimental results for a ventilating CPP was presented. The results showed that the propeller was less sensitive to ventilation with a lower pitch angle. That is, the inception of ventilation was postponed when  $\phi$  was reduced, such that a higher thrust could be produced. A CCP can, within a large thrust range, meet the desired thrust for a range of combinations of pitch and shaft speed. If there is a high probability for ventilation, the results in Ruth and Smogeli (2006) indicate that it is beneficial to run the CCP with a low pitch angle and high shaft speed. This again suggests that it may be useful to have at least two pitch mappings  $g_\phi(\cdot)$ : one for normal operating conditions, and one for extreme operating conditions. The latter mapping should then, for a given  $T_r$ , give a lower  $\phi_r$  than the mapping for normal conditions.

This result also indicates that, if the pitch actuator bandwidth is sufficiently high, option 2 for the secondary anti-spin action should be chosen; a reduced pitch angle during ventilation would probably hasten termination of the ventilation incident and reduce the load transients. This must, however, only be considered as speculation, since the experimental setup did not allow for testing of a CPP with dynamic pitch control.

### 8.1.5 A near optimal controller

A basic problem with on-line optimal control of CCP is the need to know the propeller advance speed. If the advance speed is not known, an off-line optimization scheme must be utilized. This is discussed in more detail in Ruth *et al.* (2006). A simple, yet smart, consolidated controller that avoids this problem was presented by Schanz (1967). In this control scheme, the motor torque is kept constant, while the shaft speed is kept constant by adjusting the propeller pitch (called a “propeller governor”). The pitch can be controlled by e.g. a PID controller operating on the shaft speed error, exactly as for the PID shaft speed controller in (3.27). With constant motor torque and shaft speed, also the power is constant. Hence, the propeller governor gives a constant speed/torque/power controller, which can be shown to be very near optimal.

The performance of the controller will depend on the PID tuning and bandwidth of the pitch actuator. If a relatively low bandwidth is chosen, such that wave-frequency disturbances are not counteracted, the controller will be very similar to the torque controller in (3.29) with control coefficient curves from (8.3). This will give wave-frequency oscillations in power. If the pitch actuator bandwidth is sufficiently high, and the PID is tuned tightly, the constant speed/torque/power relationships will be maintained also in waves. This may, however, give unnecessary wear and tear of the pitch actuator.

## 8.2 Extensions to transit

During DP operation, the advance velocities of the propellers are assumed to be of moderate magnitude. The controllers in Table 3.1 are then expected to give adequate performance with control coefficients based on the nominal thrust and torque coefficients, as proposed in Section 3.5.

During transit, the propellers are subject to higher advance velocities, and the actual thrust and torque coefficients will deviate significantly from the nominal coefficients proposed as control coefficients in (3.8, 3.9). This is easily seen from e.g. (2.25, 2.26) or (2.20, 2.21). Depending on the chosen controller, the mapping from reference to actual thrust will become inaccurate, and one may ask if the controllers in Table 3.1 then are appropriate. In order to investigate this, the differences in control objectives for DP and transit operations must be clarified, before possible extensions of the controllers are introduced.

### 8.2.1 DP vs. transit

In DP mode, the vessel is usually *fully actuated* or *over-actuated*. As described in Section 3.2.1, accurate thrust production is then important for the bandwidth of the vessel control system as a whole. In transit, normally only the main propellers are used. This means that the vessel becomes *underactuated*, i.e. it is unable to command accelerations in all 3 horizontal-plane DOF simultaneously. The control task therefore inherently becomes a 2DOF problem, where the main objectives usually are to keep a certain vessel speed and heading. It is important to note that vessels that are fully actuated for low-speed applications, from a practical point of view still may become underactuated at higher speeds. Such vessels may e.g. be equipped with main propellers in the stern and a number of tunnel thrusters in the bow and stern. At higher vessel speeds, the tunnel thrusters lose most of their efficiency due to the water speed at the tunnel outlets (Chislett and Björheden, 1966; Brix, 1978; Karlsen *et al.*, 1986). It is also becoming increasingly common to have one or two azimuthing thrusters in the bow or mid-ship to assist in DP operations. These are often of the retractable or swing-up type, and are stowed inside the hull for transit operations.

In classic autopilot schemes, see e.g. Fossen (2002) and references therein, the control task is usually divided in two: a dedicated speed controller, and a course auto-pilot. Typically, the speed controller, which also could be manual speed control from the bridge, controls the setpoint of the main propellers, whereas the course autopilot controls the rudder or azimuth angles. The two control objectives (speed and course) are hence *decoupled*. The control allocation therefore becomes much simpler than in the DP case, especially for the propeller setpoints, which are set by the speed controller. Control allocation for the rudders or azimuth angles may become more involved, especially if including other control objectives such as rudder-roll damping. This is treated in detail in Perez (2005). In this thesis, only control of the propellers is considered. With the speed/course decoupling, the mapping from the thrust reference to the actually produced thrust is of less importance. Since the bandwidth requirements for the speed controller are less strict than for DP, the setpoints of the main propellers can simply be increased until the desired vessel speed is reached. Hence, the mean values of thrust, torque, shaft speed, and power will be the same, regardless of the chosen low-level thruster controller. With respect to the performance criteria defined in Section 3.2, the dynamic properties of the various controllers in Table 3.1 will remain the same, even if there is a steady-state offset between thrust reference and the actually produced thrust.

A third vessel control regime that must be considered is trajectory tracking and manoeuvring control (Fossen, 2002; Skjetne, 2004; Skjetne *et al.*, 2004). In trajectory tracking, the objective is to force the vessel to track a desired path in time. In manoeuvring control the objective is to converge to and follow a parameterized path, and satisfy a desired dynamic behavior along the path. Such controllers are appropriate where high performance with respect to path following is required, e.g. for manoeuvring in restricted waters, replenishment

operations, and formation control. These concepts will therefore probably benefit from a higher system bandwidth than what is necessary for the speed/course decoupled autopilot; the latter is usually used for long distance journeys like ocean crossings, where accurate path following is of less importance. Hence, modifications of the low-level thruster controllers to meet these requirements should be considered.

For a vessel that operates across a large speed regime, the traditional approach has been to design dedicated controllers for each regime, and switch between these controllers according to given criteria. However, recent results have demonstrated that a unified control concept valid for a larger speed envelope is feasible (Brevik and Fossen, 2005). Such a controller may also benefit from the increased system bandwidth provided by improved low-level thruster control across all operating regimes.

### 8.2.2 Controller modifications for transit

Having clarified the requirements to the low-level thruster controllers for the various vessel control regimes, the following conclusions may be drawn:

- For a decoupled speed controller/course autopilot, the low-level thruster controllers in Table 3.1 based on the nominal thrust and torque coefficients will probably be adequate.
- For a trajectory tracking/manoeuvring or unified controller, it may be desirable to modify the controllers to increase the system bandwidth.

As for CCP, a modification of the thruster controllers for transit should be realized by changing the control coefficients  $K_{TC}$  and  $K_{QC}$ . In transit, the propellers will be in the first quadrant of operation, for which the open-water characteristics normally is available. Using the measured ship speed  $U$  and an estimate of the hull wake factor  $w_h$ , the advance velocity  $V_a$  and advance number  $J_a$  of the propeller may be calculated from (2.42) and (2.16). Then, the estimated  $K_{TJ}$  and  $K_{QJ}$  from the open-water characteristics can be used as control coefficients, i.e.

$$K_{TC} = K_{TJ}(V_a, n), \quad K_{QC} = K_{QJ}(V_a, n). \quad (8.7)$$

It may be preferable to use gain scheduling with discrete updates of  $K_{TC}$  and  $K_{QC}$ , in order to avoid dynamically changing control coefficients. Note that this approach requires that the ship speed measurement is made available to the low-level thruster controllers, which may be a practical limitation. If gain-scheduled control coefficients are used, the properties of the various low-level thruster controllers from Table 3.1 will remain the same with respect to disturbance rejection, as well as oscillations in torque and power.

### 8.2.3 Performance evaluation for transit

The performance evaluations undertaken in Section 3.18 and Chapter 4 are applicable also to transit. For example, it is a known problem that a vessel in heavy head seas will experience large load variations on the propellers. This is because of oscillations in inflow to the propeller, due to both waves and oscillations in the ship forward speed. If shaft speed control is used, the resulting motor torque and power will have large oscillations. This increases the danger of exceeding the motor torque or power limit, and increases the mechanical wear and tear. In torque or power control, the propeller shaft speed will adapt itself to the propeller loading, giving lower oscillations in torque and power. Power control for transit has been successfully used in industrial installations by Siemens (Siemens AG, 2005) and ABB (Ådnanes, 2006), and possibly also by other vendors.

In Blanke (1994), various control schemes for diesel engines on vessels in transit were evaluated based on an economical cost criterion. In particular, it was investigated how the ship speed control loop should react to changes in local weather and actual ship resistance characteristics. It was concluded that torque control of the diesel engine would reduce the economical loss when compared to shaft speed control if the ship experiences added resistance due to waves and wind. In Blanke and Busk Nielsen (1990), it is stated that power control of the diesel engine has a similar beneficial effect on fuel consumption.

### 8.2.4 Observer and estimation extensions to transit

As stated in Section 8.1.3, the load torque observer in (5.7) and  $K_Q$  estimation scheme in (5.26) are valid for transit without modifications. However, extensions of the loss and performance estimation schemes to transit depends on the application for which they are intended. For the performance monitoring scheme,  $K_{TC}$  and  $K_{QC}$  should be used without modifications, i.e. equal to the coefficients used in the controllers.  $\hat{\chi}_Q$  will then resemble the torque sensitivity function  $sq_i$  from (4.3). If the controllers are used with the nominal coefficients ( $K_{TC} = K_{Q0}$  and  $K_{QC} = K_{Q0}$ ), the performance of the shaft speed and power controllers will deteriorate with increasing advance velocity, as shown in Figure 4.3. If  $K_{TC}$  and  $K_{QC}$  are updated according to the vessel speed, as suggested in Section 8.2.2, the performance of the various controllers will be more similar.

For the loss estimation scheme, things get more tricky. This is mainly a problem for anti-spin control in transit, which is further discussed in the next section.

### 8.2.5 Anti-spin controller extensions to transit

Whether the core thruster controller should be modified for transit or not, was discussed in Section 8.2.2. This choice can be made separately from the anti-spin controller, since both the primary and the secondary anti-spin actions are compatible with any core thruster controller.

Section 8.2.4 clarified that the load torque estimation schemes in (5.7) and (5.26) were valid for transit without modifications. For the calculation of  $\hat{\beta}_Q$ , however, precautions must be taken.  $\hat{\beta}_Q$  is calculated from (5.16) or (5.19), and reflects the loss of torque when compared to the operating condition described by  $K_{QC}$ . If  $K_{QC}$  is chosen as suggested in Section 3.5, i.e.  $K_{QC} = K_{Q0}$ ,  $\hat{\beta}_Q$  is an estimate of the total loss of torque when compared to the nominal situation with  $V_a = 0$  and no other losses. When  $V_a > 0$ ,  $K_Q$  decreases, and so does  $\hat{\beta}_Q$ , see e.g. Figure 2.1. This behavior of  $\hat{\beta}_Q$  means that it is difficult to choose values for the ventilation detection parameters  $\beta_{v,on}$  and  $\beta_{v,off}$  in (6.1). The scheme should not detect a high  $V_a$  as a ventilation incident, and hence  $\beta_{v,on}$  and  $\beta_{v,off}$  should be chosen small. On the other hand, for the detection scheme to work at a low  $V_a$ ,  $\beta_{v,on}$  and  $\beta_{v,off}$  should not be chosen too low. In conclusion, the detection scheme must be modified for transit.

The solution to this problem is to let  $K_{QC}$  in (5.15) or (5.19) be updated according to the vessel speed, i.e.  $K_{QC} = K_{QJ}(V_a, n)$ , such that it reflects the prevailing operating conditions, in a similar manner as proposed in (8.7). Then,  $\hat{\beta}_Q$  will stay close to unity when there is no ventilation, and the ventilation detection scheme can be used with the same parameters as for DP. Note that the update of  $K_{QJ}(V_a, n)$  for calculation of  $\hat{\beta}_Q$  may be done *independently* of an eventual update of control parameters for the core thruster controllers.

If external updates of  $K_{QC}$  according to the vessel speed are not available, it may be possible to incorporate the update of  $K_{QC}$  in the low-level thruster controller without the use of additional instrumentation. This is discussed in Appendix G.2.

# Chapter 9

## Thrust allocation in extreme conditions

The bulk of this thesis has been focused on low-level thruster control. In this context, the thrust setpoint  $T_d$  has been considered as an exogenous input. As discussed in Section 1.1,  $T_d$  is for DP and joystick operations calculated by the thrust allocation algorithm, which distributes the high-level thrust demands to the various propulsion units. This chapter investigates how the thruster performance monitoring tools presented in Chapter 5 can be utilized also to improve thrust allocation. The goals are closely related to the control objectives presented in Section 3.2, and can be summarized as:

- Reduce mechanical wear and tear.
- Reduce power transients.
- Improve the overall propulsion efficiency.

The concept of *anti-spin thrust allocation* has been motivated by the working principles of advanced four-wheel drive systems on cars. In essence, these systems aim at transferring the maximum achievable torque to each wheel; if one wheel starts spinning, the torque is instead transferred to the other wheels. In a similar manner, it should be possible to detect that a propeller has lost its “traction”, and transfer the desired thrust to other propellers with better working conditions. This, of course, necessitates that the vessel is over-actuated, such that there exists propellers to which the desired thrust can be transferred. This will be a presumption in the remainder of the chapter.

### 9.1 Basic principles

As a background for the following sections, the basic principles of thrust allocation will be shortly summarized.

### 9.1.1 Actuator configuration

Considering only 3 degrees of freedom, a thruster located at the horizontal-plane position  $[x_{pj}, y_{pj}]$  producing a thrust  $T_{aj}$  in the direction  $\alpha_j$  will give the thrust vector  $\tau_j$ :

$$\tau_j = \begin{bmatrix} \tau_{xj} \\ \tau_{yj} \\ \tau_{mj} \end{bmatrix} = \begin{bmatrix} \cos \alpha_j \\ \sin \alpha_j \\ x_{pj} \sin \alpha_j - y_{pj} \cos \alpha_j \end{bmatrix} T_{aj} = \mathbf{t}_j T_{aj}, \quad (9.1)$$

where  $\mathbf{t}_j$  is the thrust configuration vector for thruster  $j$ . With  $N$  thrusters, the total thrust vector becomes:

$$\tau = \tau_1 + \tau_2 + \dots + \tau_N = [\mathbf{t}_1 \quad \mathbf{t}_2 \quad \dots \quad \mathbf{t}_N] \begin{bmatrix} T_{a1} \\ T_{a2} \\ \dots \\ T_{aN} \end{bmatrix} = \mathbf{T}\mathbf{F}, \quad (9.2)$$

where  $\mathbf{T}$  is the *thrust configuration matrix*, and  $\mathbf{F}$  is the vector of thrust forces.

### 9.1.2 Unconstrained allocation for non-rotatable thrusters

The simplest thrust allocation scheme considers only thrusters with fixed directions, and do not account for thruster saturation limits. While simple, the method is illustrative for the general task of thrust allocation. The optimal thrust allocation for non-rotatable thrusters is given by the generalized inverse  $\mathbf{T}_w^\dagger$  of  $\mathbf{T}$ , see e.g. Fossen (2002):

$$\mathbf{T}_w^\dagger = \mathbf{W}^{-1} \mathbf{T}^\dagger (\mathbf{T} \mathbf{W}^{-1} \mathbf{T}^\dagger)^{-1}, \quad (9.3)$$

where  $\mathbf{W}$  is a positive definite cost matrix (usually diagonal) weighting the contributions from each thruster. A high cost factor means that a thruster is “expensive” to use, and gets less thrust allocated. The vector of generalized desired forces from the high-level control system is denoted  $\tau_d$ , and the thrust setpoint vector  $\mathbf{u}$  is calculated from  $\tau_d$  using  $\mathbf{T}_w^\dagger$  by:

$$\mathbf{u} = \begin{bmatrix} T_{d1} \\ T_{d2} \\ \dots \\ T_{dN} \end{bmatrix} = \mathbf{T}_w^\dagger \begin{bmatrix} F_x \\ F_y \\ M_z \end{bmatrix} = \mathbf{T}_w^\dagger \tau_d, \quad (9.4)$$

where  $T_{dj}$  is the thrust setpoint of thruster  $j$ , and  $F_x$ ,  $F_y$ , and  $M_z$  are the desired forces in surge and sway and moment in yaw. For  $\mathbf{W} = \mathbf{I}_{N \times N}$ ,  $\mathbf{T}_w^\dagger$  reduces to the Moore-Penrose pseudo-inverse  $\mathbf{T}^\dagger = \mathbf{T}^\dagger (\mathbf{T} \mathbf{T}^\dagger)^{-1}$ . Note that the magnitude of the cost factors in  $\mathbf{W}$  are irrelevant; only the ratio of the individual entries affects  $\mathbf{T}_w^\dagger$ .  $\mathbf{W}$  can be used to cancel the allocation to one thruster by setting its cost to a high value. This may, however, result in a close to singular matrix. Instead, the allocation should be performed without that thruster, i.e. by removing the corresponding column from  $\mathbf{T}$ .

## 9.2 Current thrust allocation solutions

Various thrust allocation schemes exist. For non-rotatable thrusters with constraints, Johansen *et al.* (2004a) presented a solution using multi-parametric quadratic programming. For azimuthing thrusters with constraints, an explicit solution using singular value decomposition and filtering techniques was presented in Sørdalen (1997a) and Sørdalen (1997b), iterative solutions using linear programming were presented in Lindfors (1993) and Webster and Sousa (1999), and solutions using quadratic programming were presented in Johansen *et al.* (2004b) and Liang and Cheng (2004). Thrust allocation for surface vessels with rudders was treated in Lindegaard and Fossen (2003) and Johansen *et al.* (2003). A general Lyapunov-based nonlinear control allocation scheme was presented in Johansen (2004), and an adaptive extension presented in Tjønnås and Johansen (2005). The common point of all these solutions is that they attempt to fulfill the high-level thrust command, i.e.  $\tau = \tau_d$ , while meeting a given set of constraints and optimizing a certain criterion.

## 9.3 Motivation

What happens when the performance of the individual thrusters is not accounted for in the thrust allocation algorithm? In calm to moderate seas this is no problem, since the thrusters will have decent operating conditions, and the thrust losses will be limited. In high to extreme seas, however, when the thrusters may be subject to ventilation and water exits, and the thrust losses increase, problems may arise. Assume that thruster  $j$  is subject to heavy ventilation, and not producing its demanded thrust, i.e.  $T_{aj} \neq T_{dj}$ . The vessel will then eventually start to drift off position, since  $T_{aj} \neq T_{dj}$  from (9.2) and (9.4) implies that  $\tau \neq \tau_d$ . The response from the high-level control system is then to increase  $\tau_d$  to stay on position. Through  $\mathbf{T}_w^\dagger$  in (9.4), this is transformed to new setpoints  $\mathbf{u}$  to the thrusters. Since the loss of thrust on thruster  $j$  is reflected in the motion of the vessel, and the new  $\tau_d$  is calculated to compensate for this motion, the setpoint of thruster  $j$  will be increased (along with other co-allocated thrusters) in order to produce the “missing” thrust. Hence, the response of the complete vessel control system to the loss of thrust on a given propulsion unit, is to increase its setpoint. As discussed in Sections 2.4.6 and 3.2.2, increasing the shaft speed when a thruster is subject to ventilation may lead to increased dynamic loading, and correspondingly increased mechanical wear and tear. At the same time, the actual thrust is not increased significantly. Hence, this response is rather unfortunate. Not only does it increase wear and tear, it also means that the overall closed-loop performance of the vessel deteriorates, since the thrust commands from the high-level control system are not properly met. Instead, the thrust allocation system should have attempted to re-allocate thrust to other propulsion units that were less subject to thrust losses.

## 9.4 Performance monitoring

The tools presented in Chapter 5 may be utilized to monitor the performance of the individual propulsion units. There is, however, a multitude of possible performance criteria. In the following, a thruster performance measure that is believed to be appropriate for thrust allocation will be proposed.

### 9.4.1 Sensitivity estimation

For monitoring of the instantaneous working conditions of the propeller, the torque loss factor  $\hat{\beta}_Q$  is the most relevant parameter. This was utilized e.g. in the anti-spin controllers presented in Chapter 6. For thrust allocation, the main interest is in the propeller thrust production with respect to its reference, i.e.  $T_a$  vs.  $T_r$ . As shown in Section 5.4, an estimate  $\hat{T}_a$  of  $T_a$  is in general not available, since the  $\hat{K}_T - \hat{K}_Q$  relationship in (5.41) used to calculate  $\hat{T}_a$  in (5.42) only holds for open propellers. The thrust performance factor estimate  $\hat{\chi}_T$  in (5.46) is therefore not always available. Instead, the performance monitoring will be based on the torque performance factor defined in (5.44):

$$\hat{\chi}_Q = \frac{\hat{Q}_a}{Q_r}, \quad Q_r \neq 0, \quad (9.5)$$

and the non-singular representation in (5.45).  $\hat{Q}_a$  is calculated e.g. by the observer in (5.7) or from the  $K_Q$  estimation scheme in (5.26) using (5.18), and  $Q_r$  is calculated from  $T_r$  using (3.2). As stated in Section 5.4,  $\hat{\chi}_Q$  can be seen as an estimate of the torque sensitivity function  $sq_i(\cdot)$  in (4.3).  $\hat{\chi}_Q$  therefore contains specific information on the performance of the propulsion unit with respect to its *torque* reference. However, since the propeller thrust and torque are closely related,  $\hat{\chi}_Q$  is considered also to be a good measure of the performance with respect to the thrust reference.

If  $\hat{\chi}_Q$  in (9.5) is based on the load torque observer in (5.7), or the  $K_Q$  estimation scheme in (5.26) with a high estimation gain  $k_0$ , it will be an instantaneous estimate. For use in thrust allocation, an average performance factor may be more appropriate. The average torque performance factor  $\bar{\chi}_Q$  is defined as:

$$\bar{\chi}_Q = \frac{1}{T} \int_{t-T}^t \hat{\chi}_Q(\tau) d\tau, \quad (9.6)$$

where  $T$  is the averaging period. A larger  $T$  will give less fluctuation in  $\bar{\chi}_Q$ , but also a slower response to changes in the operating conditions. A similar estimate could be obtained with the  $K_Q$  estimation scheme in (5.26) using a low estimation gain  $k_0$ .

**Remark 9.1**  $\hat{\chi}_Q$  will be affected by both current, wave- and vessel-induced inflow velocities, and ventilation. For  $\bar{\chi}_Q$ , the wave-frequency disturbances will be more or less filtered out, leaving only current, vessel low-frequency motion, and ventilation.

**Remark 9.2** From a statistical consideration, the minimum theoretical value of  $\bar{\chi}_Q$  is approximately 0.5. This corresponds to the thruster being above water half the time, and otherwise fully submerged. In practice, the minimum value will probably be larger.

### 9.4.2 Ventilation monitoring

Another criterion that may be used to evaluate the thruster performance, is the count of the number of ventilation incidents over a given time interval. This gives explicit information about the level of mechanical wear and tear and power transients, and is easily implemented by monitoring the ventilation detection signal  $\zeta$  from (6.1). Since ventilation detection is a discrete event, some choices must be made with respect to continuous-time performance evaluation. A suggestion is as follows, with the performance factor denoted  $\chi_V$ :

- Select a time interval  $T_V$  for performance evaluation.
- Select a lower limit  $\chi_{V,\min}$  for  $\chi_V$ .
- Denote the count of ventilation incidents during the last  $T_V$  seconds  $m_V$ .
- Select the number of ventilation incidents  $m_{V,\max}$  during  $T_V$  that should give  $\chi_V = \chi_{V,\min}$ .

Choosing  $\chi_V$  to be linear in  $m_V$ , it can then be calculated from:

$$\chi_V = 1 - \frac{\min(m_V, m_{V,\max})}{m_{V,\max}}(1 - \chi_{V,\min}). \quad (9.7)$$

A scheme for counting of  $m_V$  based on  $\zeta$  and  $T_V$  is easily implemented.

### 9.4.3 A thruster performance measure

To arrive at a total thruster performance measure, it seems sensible to combine the two performance factors  $\bar{\chi}_Q$  in (9.6) and  $\chi_V$  in (9.7). The proposed performance measure  $\chi_j$  is therefore chosen as:

$$\chi_j = \bar{\chi}_Q \chi_V. \quad (9.8)$$

In calm seas with no current and little vessel motion,  $\chi_j \approx 1$  since  $\bar{\chi}_Q \approx 1$  and  $\chi_V = 1$ . In normal operating conditions, with moderate waves and some current,  $\chi_j = \bar{\chi}_Q \approx sq_i(\cdot)$ , since  $\chi_V = 1$  as long as there are no ventilation incidents. This means that  $\chi_j$  will depend on the ability of the low-level thruster controller to counteract disturbances from current and low-frequency vessel motion, as can be seen e.g. in Figure 4.3. In extreme operating conditions, when the thruster is subject to ventilation,  $\chi_j = \bar{\chi}_Q \chi_V$ , since both  $\bar{\chi}_Q$  and  $\chi_V$  will decrease with the number of ventilation incidents. However, depending on the choice of  $\chi_{V,\min}$ ,  $\chi_j$  will probably be dominated by  $\chi_V$ .

**Remark 9.3** In nominal conditions with ideal performance,  $\chi_j = 1$ . With the theoretical minimum value of  $\bar{\chi}_Q \approx 0.5$ , and the chosen minimum value  $\chi_{V,\min}$  for  $\chi_V$ , the minimum value of  $\chi_j$  becomes  $\chi_{\min} \approx \chi_{V,\min}/2$ . The range of  $\chi_j$  hence is:

$$\chi_j \in \left[ \frac{\chi_{V,\min}}{2}, 1 \right]. \quad (9.9)$$

## 9.5 Implications for thrust allocation

Having arrived at the performance measure  $\chi_j$ , the next challenge is to incorporate this into the thrust allocation scheme. As summarized in Section 9.2, a variety of allocation schemes exist, with varying degree of complexity and application areas. To arrive at a general answer to how the performance measure can be integrated into the allocation schemes is therefore considered neither feasible nor practical, since the various schemes may benefit from different approaches. In the following, some considerations regarding use of  $\chi_j$  will still be made.

It is assumed that the performance monitoring scheme is implemented for all the thrusters on the vessel, such that the performance measure vector  $\boldsymbol{\chi}$  can be defined as:

$$\boldsymbol{\chi} = [\chi_1, \chi_2, \dots, \chi_N]^\top, \quad (9.10)$$

where  $\chi_j$  is the performance measure for propulsion unit number  $j$ , and  $N$  is the total number of thrusters.

**Remark 9.4** If  $\chi_j$  for some reason is not available for some of the propulsion units, their values can simply be set to 1. These propulsion units will then be treated as if they were working perfectly at all times. This could be the case e.g. for a mechanical direct-drive main propeller with a shaft generator, for which a load torque observer may be difficult to implement.

As shown in Section 9.2, the various thrust allocation schemes all have an optimization criterion and a set of constraints that must be met. How to integrate  $\boldsymbol{\chi}$  from (9.10) into the allocation scheme, if at all possible, largely depends on the implementation. At least two options seem apparent:

1. Use  $\boldsymbol{\chi}$  to adjust the entries in the cost matrix  $\mathbf{W}$ . By increasing the cost of an ill-performing thruster, it will be less utilized as long as there are other thrusters available that can take its load.
2. Include  $\boldsymbol{\chi}$  in the optimization criterion, e.g. as maximization of  $\|\boldsymbol{\chi}\|$ . This criterion must then be weighted against the other criteria in the optimization routine.

Venturing further into the details of implementation would require a thorough analysis of a given thrust allocation scheme. This is not further considered here.

# Chapter 10

## Conclusions and recommendations

### 10.1 Conclusions

This thesis has focused on modelling, simulation, and control of marine propellers. More specifically, the problem statement formulated in Section 1.2 has been thoroughly explored, and various thruster controllers have been designed, analyzed, and tested.

Chapter 2 gave an overview of propeller modelling for simulation and control design. Based on systematic model tests from a cavitation tunnel and time-series from open water tests, the behavior of a propeller subject to ventilation and water exits at low advance velocities was analyzed, and a simplified simulation model of the corresponding thrust loss effects was developed.

Chapter 3 introduced the main control objectives considered in this work: thrust production, mechanical wear and tear, predictable power consumption, and robust performance. The use of reference generators, friction compensation, inertia compensation, and torque/power limiting was motivated, and the applicability of these concepts to various control options was discussed. The fundamental thruster controllers – shaft speed, torque, and power control – were introduced, followed by various combined controllers. The performance of the controllers was compared by simulations, and the importance of the reference generator and friction and inertia compensation schemes was demonstrated.

Chapter 4 introduced thrust, torque, shaft speed, and power sensitivity functions, which were used to analyze the steady-state performance of the fundamental control concepts in the presence of thrust losses. For thrust losses due to changes in advance velocity, the results showed that the torque and power controllers were much less sensitive than the shaft speed controller. This agreed with the simulation results from Chapter 3, and confirmed that torque and power control have superior properties in normal operating conditions. The

sensitivity functions were also utilized to investigate the controller response to large thrust losses due to ventilation and water exits. The results showed that the performance of the torque and power controllers was highly unacceptable, since the loss of loading led to severe propeller racing for both controllers, and also to excessive power consumption for the torque controller.

Chapter 5 presented several tools for monitoring of the propeller performance. The main result was a propeller load torque observer, which based on the available measurements estimated the hydrodynamic load torque of the propeller. The estimated load torque was utilized to estimate the torque loss factor, which gave explicit information on the operating condition of the propeller. The proposed estimation scheme was validated by simulations in various operating conditions, and shown to be able to capture even the rapid changes in load torque during ventilation and water exits.

Thruster control in extreme conditions was treated in detail in Chapter 6, where the concept of anti-spin thruster control was introduced. The proposed anti-spin thruster controller was designed to let the core thruster controller work undisturbed in normal conditions, and take action only when a ventilation incident was detected. It then took control of and reduced the shaft speed until the ventilation incident was terminated. The purpose of this was to reduce the dynamic loads on the propeller, and ease the transition back to the non-ventilated condition. The stability of the proposed anti-spin control scheme was investigated by a Lyapunov analysis, and its performance tested by simulations.

In Chapter 7 results from open-water experiments with a model scale propeller were presented. The results confirmed the performance characteristics previously inferred from simulations and sensitivity functions, and showed that it is feasible to use torque and power control with anti-spin in all operating regimes. The anti-spin controller was shown to work well also in the presence of unmodelled dynamics, model uncertainty, and noisy measurements.

Chapter 8 showed how the presented control concepts could be extended to CPP and transit simply by letting the control coefficients be functions of the propeller pitch and vessel speed, respectively.

Chapter 9 introduced the concept of anti-spin thrust allocation. Based on the performance monitoring tools presented in Chapter 5, the idea was to redistribute the thrust setpoints in order to utilize the various propulsion units in the most sensible way. In this manner, the total thrust production could be improved, and the need for anti-spin thruster control reduced, since the most exposed propulsion units would be less utilized.

The main purpose of this thesis has been to demonstrate the importance of low-level thruster control and the many aspects of the total vessel performance that it affects. Based on a total evaluation of the performance across all operating regimes, the results indicate that the combined torque/power controller from Section 3.13 or the combined speed/torque/power controller from Section 3.15 are the most favorable solutions. If the propeller may be subject to high thrust losses, this solution requires the addition of an anti-spin controller, as proposed

in Section 6.5. Also, if the rotational inertia and/or friction is significant, the corresponding compensation schemes from Section 3.7 may be necessary. However, the choice of control solution for a specific installation should probably be made from an independent evaluation of the performance criteria on a case by case basis.

## 10.2 Recommendations for future work

- The theoretical work and testing of the proposed thruster control schemes – both for normal and extreme conditions – have reached a point where preliminary full-scale testing in DP is the natural next step. With the experience gained from this, full-scale industrial implementation could be close at hand.
- As discussed in Section 8.2.5, some modifications of the ventilation detection scheme and anti-spin control laws are necessary for use in transit. Although a solution is suggested, this problem requires further attention.
- The fundamental controllers should be tested for oblique inflow to the propeller. Based on the results on “thrust vectoring” in Stettler *et al.* (2005), it would be interesting to see how the torque and power controllers handle this situation. If the performance differs significantly from that of a shaft speed controller, this will also have an impact on thrust allocation, both in DP and transit.
- Some of the results presented in the appendices are incomplete, and require further work on analysis and testing.
- This work has only briefly touched upon the topic of thrust allocation, and attempted to illustrate how the overall performance of the propulsion system on a vessel may be improved by accounting for the performance of the individual thruster units. In this connection, a thruster performance criterion was proposed, based on available measurements and system knowledge. How to incorporate this information into existing thrust allocation schemes has not been further considered. This is a challenge for future research: with increasingly complex installations, the need for improved thrust allocation schemes accounting for thruster performance, as well as e.g. power consumption on individual power buses, will be an important contribution in the quest for increased performance.



# Bibliography

- Aarseth, L. (2003). Anti-spin control system for marine thrusters. Master's thesis. Department of Marine Technology, Norwegian University of Science and Technology – NTNU.
- Ådnanes, A. K. (2006). Private conversations with Dr. A. K. Ådnanes, now IPP Consulting, previously ABB.
- Ådnanes, A. K., A. J. Sørensen and T. Hackmann (1997). Essential Characteristics of Electrical Propulsion and Thruster Drives in DP Vessels. In: *Proc. DP Conference*. Houston, Texas.
- Andresen, K. (2000). Thrusters for Auxiliary Propulsion and Manoeuvrability. In: *Proc. Int. Conf. Ship Propulsion Systems - SPS 2000*. Manchester, UK. Organized by Lloyds List.
- Antonelli, G., S. Chiaverini, N. Sarkar and M. West (2001). Adaptive Control of an Autonomous Underwater Vehicle: Experimental Results on ODIN. *IEEE Transactions on Control Systems Technology* **9**(5), 756–765.
- Åström, K. J. and B. Wittenmark (1997). *Computer-Controlled Systems*. Prentice Hall, New Jersey.
- ATTC (1974). Surface Ventilated Flows. In: *17th American Towing Tank Conference*. Vol. 1. pp. 185–187.
- Bachmayer, R. and L. L. Whitcomb (2001). A Nonlinear Model Based Thrust Controller for Marine Thrusters. In: *Proc. 2001 IEEE/RSJ International Conference on Intelligent Robots and Systems*. Hawaii. pp. 1817–1823.
- Bachmayer, R., L. L. Whitcomb and M. A. Grosenbaugh (2000). An Accurate Four-Quadrant Nonlinear Dynamical Model for Marine Thrusters: Theory and Experimental Validation. *IEEE Journal of Oceanic Engineering* **25**(1), 146–159.
- Bakkeheim, J., Ø. N. Smogeli, T. A. Johansen and A. J. Sørensen (2006). Improved Transient Performance by Lyapunov-based Integrator Reset of PI Thruster Control in Extreme Seas. In: *Proc. 45<sup>th</sup> IEEE Conference on Decision and Control (CDC'2006)*. San Diego, California.

- Bakountouzis, L. (1992). CPP Systems Optimization Requirements of Automatic Control. In: *Maritime Technology 21st Century Conference*. Melbourne, Australia.
- Balchen, J. G., N. A. Jenssen and S. Sælid (1976). Dynamic Positioning Using Kalman Filtering and Optimal Control Theory. In: *Proc. of the IFAC/IFIP Symp. On Automation in Offshore Oil Field Operation*. Bergen, Norway. pp. 183–186.
- Balchen, J. G., N. A. Jenssen and S. Sælid (1980a). Dynamic Positioning of Floating Vessels Based on Kalman Filtering and Optimal Control.. In: *Proceedings of the 19th IEEE Conference on Decision and Control*. New York, NY. pp. 852–864.
- Balchen, J. G., N. A. Jenssen, E. Mathisen and S. Sælid (1980b). Dynamic Positioning System Based on Kalman Filtering and Optimal Control. *Modeling, Identification and Control MIC-1(3)*, 135–163.
- Beek, O. and E. Mulder (1983). A New Generation of Controllable Pitch Propellers. *International Shipbuilding Progress* **30**(351), 258–266.
- Blanke, M. (1981). Ship Propulsion Losses Related to Automated Steering and Prime Mover Control. PhD thesis. The Technical University of Denmark. Lyngby, Denmark.
- Blanke, M. (1994). Optimal Speed Control for Cruising. In: *Proc. 3rd IFAC Conference on Manoeuvring and Control of Marine Craft (MCMC'94)*. Southampton, UK. pp. 125–134.
- Blanke, M. and P. Busk Nielsen (1987). Electronic Governor Control for two stroke Engines. In: *Nordisk Sjøfartsteknisk Årsbok – Svensk Sjöfarts Tidning*. Vol. 40. pp. 82–84.
- Blanke, M. and P. Busk Nielsen (1990). The Marine Engine Governor. In: *Proc. 2nd Int. Conf. on Maritime Communications and Control*. London, UK. pp. 11–20.
- Blanke, M., K. P. Lindegaard and T. I. Fossen (2000). Dynamic Model for Thrust Generation of Marine Propellers. In: *Proc. 5th IFAC Conference of Manoeuvring and Control of Marine Craft (MCMC'00)*. Aalborg, Denmark.
- Blanke, M., M. Kinnaert, J. Lunze and M. Staroswiecki (2003). *Diagnosis and Fault-Tolerant Control*. Springer-Verlag.
- Blanke, M., R. Izadi-Zamanabadi and T. F. Lootsma (1998). Fault Monitoring and Re-configurable Control for a Ship Propulsion Plant. *Journal of Adaptive Control and Signal Processing* **12**, 671–688.

- Brandt, H. (1973). Modellversuche mit Schiffsspropellern an der Wasseroberfläche. *Schiff und Hafen* **26**(5,6), 243–256 + 493–504. In German. “Model Tests with Ship Propellers at the Water Surface”.
- Bray, D. (2003). *Dynamic Positioning*. Vol. 9 of *Oilfield Seamanship*. Oilfield Publications Limited.
- Brevik, M. and T. I. Fossen (2005). A Unified Concept for Controlling a Marine Surface Vessel Through the Entire Speed Envelope. In: *Proc. Mediterranean Conference on Control and Automation (MED'05)*. Limassol, Cyprus.
- Brix, J. (1978). *Querstrahlsteuer*. Forschungszentrum des Deutschen Schiffbaus, Bericht Nr. 80. In German. “Steering with Lateral Thrusters”.
- Brown, D. T. and L. Ekstrom (2005). Vessel Thruster-Thruster Interactions During Azimuthing Operations. In: *Proc. 24<sup>th</sup> Int. Conf. on Offshore Mechanics and Arctic Engineering (OMAE'05)*. Halkidiki, Greece.
- Caccia, M. and G. Veruggio (2000). Guidance and Control of a Reconfigurable Unmanned Underwater Vehicle. *Control Engineering Practice* **8**, 21–37.
- Carlton, J. S. (1994). *Marine Propellers & Propulsion*. Butterworth-Heinemann Ltd.
- Chachulski, K., W. Kozera and J. Szcześniak (1995). Optimal Control System for Propulsion Unit with Controllable Pitch Propeller. In: *Proc. 3<sup>rd</sup> IFAC Workshop on Control Applications in Marine Systems (CAMS'95)*. pp. 332–337.
- Chislett, M. S. and O. Björheden (1966). *Influence of Ship Speed on the Effectiveness of a Lateral-Thrust Unit*. Hydro- og Aerodynamisk Laboratorium Report No Hy-8. Lyngby, Denmark.
- Chu, C., Z. L. Chan, Y. S. She and V. Z. Yuan (1979). The 3-Bladed JD-CPP Series. In: *Proc. 4<sup>th</sup> LIPS Propeller Symposium*. Drunen, Holland. pp. 53–79.
- Deniellou, L., P. Gallou, P. Gourmelen and N. Seube (1998). Force Control of Underwater Thrusters with Application to AUV Motion Control. In: *Proc. IEEE/OES OCEANS'98*. Nice, France. pp. 1054–1058.
- Deter, D. (1997). Principal Aspects of Thruster Selection. In: *Proc. DP Conference*. Houston, Texas.
- Domachowski, Z., W. Próchnicki and Z. Puhaczewski (1997). The investigation of the influence of the disturbances caused by the ship propeller on the dynamic processes of the ship propulsion system. In: *Marine Technology II* (T. Graczyk, T. Jastrzebski and C. A. Brebbia, Eds.). pp. 237–246. WIT Press, Southampton, UK.

- Dong, Nguyen Trong (2005). Design of Hybrid Marine Control Systems for Dynamic Positioning. PhD thesis. National University of Singapore.
- Drzewiecki, S. (1920). *Théorie Générale de l'Hélice Propulsive*. Paris. In French. “General Theory of the Propulsive Helix”.
- Durand, W. F. (Ed.) (1963). *Aerodynamics Theory*. Vol. IV. Dover Publications, Inc., New York.
- Egeskov, P., A. Bjerrum, A. Pascoal, C. Silvestre, C. Aage and L. Wagner Smitt (1995). Design, Construction, and Hydrodynamic Testing of the MARIUS AUV. In: *Proc. IEEE Symp. Autonomous Underwater Vehicle Technology*. Cambridge, Massachusetts. pp. 199–207.
- Ekstrom, L. and D. T. Brown (2002). Interactions Between Thrusters Attached to a Vessel Hull. In: *Proc. 21<sup>st</sup> Int. Conf. on Offshore Mechanics and Arctic Engineering (OMAE'02)*. Oslo, Norway.
- Faltinsen, O. M., K. J. Minsaas, N. Liapis and S. O. Skjørdal (1980). Prediction of Resistance and Propulsion of a Ship in a Seaway. In: *Proceedings of the Thirteenth Symposium on Naval Hydrodynamics, Tokyo*.
- Fleischer, K. P (1973). Untersuchungen über Das Zusammenwirken Von Schiff und Propeller Bei Teilgetauchten Propellern. *Bericht Nr. 35 Forschungszentrum des Deutschen Schiffbaus*. In German. “Investigations of the Interaction Between Ship and Propeller for Partly Submerged Propellers”.
- Fossen, T. I. (2002). *Marine Control Systems: Guidance, Navigation and Control of Ships, Rigs and Underwater Vehicles*. Marine Cybernetics. Trondheim, Norway.
- Fossen, T. I. and J. P. Strand (1999). Passive Nonlinear Observer Design for Ships Using Lyapunov Methods: Experimental Results with a Supply Vessel. *Automatica* **35**(1), 3–16.
- Fossen, T. I. and J. P. Strand (2001). Nonlinear Passive Weather Optimal Positioning Control (WOPC) System for Ships and Rigs: Experimental Results. *Automatica* **37**(5), 701–715.
- Fossen, T. I. and M. Blanke (2000). Nonlinear Output Feedback Control of Underwater Vehicle Propellers Using Feedback From Estimated Axial Flow Velocity. *IEEE Journal of Oceanic Engineering* **25**(2), 241–255.
- Fossen, T. I. and Ø. N. Smogeli (2004). Nonlinear Time-Domain Strip Theory Formulation for Low-Speed Maneuvering and Station-Keeping. *Modelling Identification and Control (MIC)* **25**(4), 201–221.
- Friedland, B. (1997). A Nonlinear Observer for Estimating Parameters in Dynamic Systems. *Automatica* **33**(8), 1525–1530.

- Fukuba, H., S. Morita and T. Maeda (1996). Simulation of NOx Reduction by Consolidated Control of Main Engine and CPP. *Bulletin of Marine Engineering Society in Japan* **24**(1), 21–27.
- Grøvlen, Å., A. J. Sørensen and M. F. Aarset (1998). Impacts of Signal Processing and Local Thrust Control in an Integrated Power, Automation and Positioning System. In: *Proc. IMCA 98- Station Keeping Seminar & Workshops*. Rio de Janeiro, Brazil.
- Guibert, C., E. Foulon, N. Aït-Ahmed and L. Loron (2005). Thrust control of electric marine thrusters. In: *Proc. 32<sup>nd</sup> Annual Conf. IEEE Industrial Electronics Society (IECON2005)*. Raleigh, North Carolina, USA.
- Guoqiang, W., J. Dashan, C. Meiliang and S. Zhenbang (1989). Propeller Air Ventilation and Performance of Ventilated Propeller. In: *Proc. 4<sup>th</sup> Int. Symp. Practical Design of Ships and Mobile Units (PRADS'89)*. Vol. 1. Varna, Bulgaria. pp. 6–1–6–8.
- Gutsche, F. A. (1967). Einfluss der Tauchung auf Schub und Wirkungsgrad von Schiffpropellern. *Schiffbauforchung* **6**(5/6), 256–277. In German. “Influence of Submergence on Thrust and Efficiency of Ship Propellers”.
- Gutsche, F. A. and G. Schroeder (1963). Freifahruntersuche an Propellern mit Festen und Verstellbaren Flügeln ‘Voraus’ und ‘Zurück’. *Schiffbauforchung*. In German. “Free-running Tests of Propellers with Fixed and Adjustable Blades ‘Ahead’ and ‘Astern’ ”.
- Haessig, D. and B. Friedland (1997). A Method for Simultaneous State and Parameter Estimation in Nonlinear Systems. In: *Proceedings of the American Control Conference (ACC'97)*. Albuquerque, New Mexico, USA. pp. 947–951.
- Hashimoto, J., E. Nishikawa and Z. Li (1984). An Experimental Study on Propeller Air Ventilation and Its Induced Vibratory Forces. *Bulletin of Marine Engineering Society of Japan* **11**(1), 11–21.
- Haskara, İ., Ü. Özgüner and J. Winkelman (2000). Wheel Slip Control for Anti-spin Acceleration via Dynamic Spark Advance. *Control Engineering Practice* **8**, 1135–1148.
- Healey, A. J. and D. Lienard (1993). Multivariable Sliding-Mode Control for Autonomous Diving and Steering of Unmanned Underwater Vehicles. *IEEE Journal of Oceanic Engineering* **18**(3), 327–339.
- Healey, A. J., S. M. Rock, S. Cody., D. Miles and J. P. Brown (1995). Toward an improved understanding of thruster dynamics for underwater vehicles. *IEEE Journal of Oceanic Engineering* **29**(4), 354–361.
- Hermann, R. and A. J. Krener (1977). Nonlinear controllability and observability. *IEEE Trans. on Automatic Control* **22**(5), 728–740.

- Hespanha, J. P. and A. S. Morse (2002). Switching between stabilizing controllers. *Automatica* **38**(11), 1905–1917.
- Hespanha, J. P., D. Liberzon and A. S. Morse (2003). Hysteresis-based switching algorithms for supervisory control of uncertain systems. *Automatica* **39**(2), 263–272.
- IMCA M-129 (1995). Failure Modes of CPP Thrusters. Technical Report M 129. IMCA Marine Division.
- IMCA M-162 (2001). Failure Modes of Variable Speed Thrusters. Technical Report M 162. IMCA Marine Division.
- Ioannou, P. A. and J. Sun (1995). *Robust Adaptive Control*. 1<sup>st</sup> ed.. Prentice Hall PTR.
- Isidori, A. (1995). *Nonlinear Control Systems*. 3<sup>rd</sup> ed.. Springer-Verlag.
- ITTC (1999a). ITTC–Recommended Procedures, 7.5-02-03-01.4. Technical report. ITTC.
- ITTC (1999b). The Special Committee on Unconventional Propulsors, Surface Piercing Propellers. In: *22th International Towing Tank Conference*. Vol. 2. pp. 316–317.
- Johansen, T. A. (2004). Optimizing Nonlinear Control Allocation. In: *Proc. 43rd IEEE Conference on Decision and Control (CDC'04)*. Paradise Island, Bahamas. pp. 3435–3440.
- Johansen, T. A., J. Kalkkuhl and I. Petersen (2001). Hybrid Control Strategies in ABS. In: *Proc. American Control Conference (ACC'01)*. Arlington, VA, USA. pp. 1704–1705.
- Johansen, T. A., T. I. Fossen and P. Tøndel (2004a). Efficient Optimal Constrained Control Allocation via Multi-Parametric Programming. *AIAA Journal of Guidance, Control and Dynamics* **28**, 506–515.
- Johansen, T. A., T. I. Fossen and S. P. Berge (2004b). Constrained Nonlinear Control Allocation with Singularity Avoidance using Sequential Quadratic Programming. *IEEE Transactions on Control Systems Technology* **12**(1), 211–216.
- Johansen, T. A., T. P. Fugleseth, P. Tøndel and T. I. Fossen (2003). Optimal Constrained Control Allocation in Marine Surface Vessels with Rudders. In: *Proc. 6<sup>th</sup> IFAC Conference on Manoeuvring and Control of Marine Craft (MCMC'03)*. Girona, Spain. pp. 215–220.
- Kallah, A. (1997). A Comparison of Thruster Propellers and Variable Speed Drives for DP Vessels. In: *Proc. DP Conference*. Houston, Texas.

- Karlsen, S., K. Martinussen and K. J. MinsaaS (1986). Towing Performance and Effectiveness of Bow Thrusters in Waves and Current. In: *The International Tug Convention*.
- Ker Wilson, W. (1963). *Practical Solution of Torsional Vibration Problems*. Vol. 2: Amplitude Calculations. 3<sup>rd</sup> ed.. Chapman & Hall, London.
- Khalil, H. K. (2002). *Nonlinear Systems*. Prentice-Hall, New Jersey.
- Kim, J. and W. K. Chung (2006). Accurate and Practical Thruster Modeling for Underwater Vehicles. *Ocean Engineering* **33**, 566–586.
- Kort, L. (1934). Der neue Düsenschrauben-Antrieb. *Werft, Reederei und Hafen* **15**(4), 41–43. In German. “The New Ducted Thruster”.
- Koushan, K. (2004). Environmental and Interaction Effects on Propulsion Systems used in Dynamic Positioning, an Overview. In: *Proc. 9<sup>th</sup> Int. Symp. Practical Design of Ships and Other Floating Structures (PRADS'04)*. Lübeck-Travemünde, Germany. pp. 1013–1020.
- Koushan, K. (2006). Dynamics of Ventilated Propeller Blade Loading on Thrusters. In: *World Maritime Technology Conference (WMTC'06)*. London, U.K.
- Kruppa, C. (1972). Testing of Partially Submerged Propellers. In: *13<sup>th</sup> International Towing Tank Conference (ITTC)*. pp. 761–775. Report of Cavitation Committee, Appendix V.
- Lauvdal, T. and A. K. Ådnanes (2000). Power Management System with Fast Acting Load Reduction for DP Vessels. In: *Proc. DP Conference*. Houston, Texas.
- Lehn, E. (1992). FPS-2000 Mooring and Positioning, Part 1.6 Dynamic Positioning - Thruster Efficiency: Practical Methods for Estimation of Thrust Losses. Technical Report 513003.00.06. Marintek, SINTEF, Trondheim, Norway.
- Lemarquand, V. (1997). Differential Inductive Torque Sensor for Autonomous Underwater Vehicles. In: *Proc. 10<sup>th</sup> International Symposium on Unmanned Untethered Submersible Technology (UUST'97)*. Durham, New Hampshire. pp. 170–176.
- Leonhard, W. (1996). *Control of Electrical Drives*. 2<sup>nd</sup> ed.. Springer-Verlag, Berlin.
- Lerbs, H. W. (1952). On the Effects of Scale and Roughness on Free Running Propellers. *Naval Engineers Journal*.
- Lewis, E. V. (Ed.) (1989). *Principles of Naval Architecture*. 2<sup>nd</sup> ed.. Society of Naval Architects and Marine Engineers (SNAME).

- Liang, C. C. and W. H. Cheng (2004). The Optimum Control of Thruster System for Dynamically Positioned Vessels. *Control Engineering Practice* **31**, 97–110.
- Lindgaard, K.-P. (2003). Acceleration Feedback in Dynamic Positioning Systems. PhD thesis. Dept. of Engineering Cybernetics, Norwegian University of Science and Technology. Trondheim.
- Lindgaard, K.-P. and T. I. Fossen (2001). A Model Based Wave Filter for Surface Vessels using Position, Velocity and Partial Acceleration Feedback. In: *Proc. of the IEEE Conf. on Decision and Control (CDC'2001)*. IEEE. Orlando, FL. pp. 946–951.
- Lindgaard, K.-P. and T. I. Fossen (2003). Fuel Efficient Rudder and Propeller Control Allocation for Marine Craft: Experiments with a Model Ship. *IEEE Transactions on Control Systems Technology* **11**(6), 850–862.
- Lindfors, I. (1993). Thrust Allocation Method for the Dynamic Positioning System. In: *10th International Ship Control Systems Symposium (SCSS'93)*. Ottawa, Canada. pp. 3.93–3.106.
- Lloyd, A. R. J. M. (1998). *Seakeeping; Ship Behavior in Rough Weather*. RPM Reprographics, Sussex, UK.
- May, J. J. (2003). Improving Engine Utilization on DP Drilling Vessels. In: *Proc. DP Conference*. Houston, Texas.
- Miniovich, I. Y. (1960). *Investigation of Hydrodynamic Characteristics of Screw Propellers under Conditions of Reversing and Calculation Methods for Backing of Ships*. Buships Translation 697.
- Minsaas, K. J., H. J. Thon and W. Kauczynski (1986). Influence of Ocean Environment on Thruster Performance. In: *Proc. Int. Symp. Propeller and Cavitation, supplementary volume*. Shanghai, China. pp. 124–142.
- Minsaas, K. J., H. J. Thon and W. Kauczynski (1987). Estimation of Required Thruster Capacity for Operation of Offshore Vessels under Severe Weather Conditions. In: *Proc. 3rd Int. Symp. Practical Design of Ship and Mobile Units (PRADS'87)*. Trondheim, Norway. pp. 411–427.
- Minsaas, K. J., O. Faltinsen and B. Persson (1983). On the Importance of Added Resistance, Propeller Immersion and Propeller Ventilation for Large Ships in a Seaway. In: *Proc. 2nd Int. Symp. Practical Design in Shipbuilding (PRADS'83)*. Tokyo & Seoul. pp. 149–159.
- Morvillo, R. A. (1996). Application of Modern Digital Controls to Improve the Operational Efficiency of Controllable Pitch Propellers. In: *SNAME Annual Meeting Technical Sessions*. pp. 6–1–6–15.
- Newman, J. N. (1977). *Marine Hydrodynamics*. MIT Press. Cambridge, MA.

- Nilsen, R. (2001). *SIE1025 Elektriske Motordrifter*. NTNU. Trondheim, Norway.  
Lecture notes in Norwegian. “Electric Motor Drives”.
- Nilsen, R. (2006). Private conversations with Prof. Roy Nilsen, Dept. of Electric  
Power Engineering NTNU.
- NTNU Press Release (2005). 09.05.05 Rolls-Royce establishes University Tech-  
nology Centre (UTC) at the Norwegian University of Science and Technology.  
<<http://www.ntnu.no/pm>>.
- Ochi, M. K. (1998). *Ocean Waves, The Stochastic Approach*. Cambridge Ocean  
Technology Series, Vol. 6. Cambridge University Press.
- Olofsson, N. (1996). Force and Flow Characteristics of a Partially Submerged  
Propeller. PhD thesis. Chalmers University of Technology. Göteborg, Sweden.
- Omerdic, E. and G. Roberts (2004). Thruster Fault Diagnosis and Accommo-  
dation for Open-frame Underwater Vehicles. *Control Engineering Practice*  
**12**, 1575–1598.
- Oosterveld, M. W. C. (1970). Wake Adapted Ducted Propellers. Technical Re-  
port 345. NSMB Wageningen Publ.
- Oosterveld, M. W. C. and P. van Oossanen (1975). Further Computer Analyzed  
Data of the Wageningen B-Screw Series. *International Shipbuilding Progress*  
**22**(251), 251–262.
- Overå, E. S. (2003). A theoretical and experimental study of a ventilating ducted  
propeller. Master’s thesis. Department of Marine Technology, Norwegian Uni-  
versity of Science and Technology – NTNU.
- Panteley, E., A. Loria and A. Sokolov (1999). Global Uniform Asymptotic Sta-  
bility of Nonlinear Nonautonomous Systems: Application to a Turbo-Diesel  
Engine. *European Journal of Control* **5**, 107–115.
- Parsons, M. G. and J. Y.-C. Wu (1985). Limit Cycles in Diesel/Controllable  
Pitch Propeller Propulsion Systems using Load Control. *International Ship-  
building Progress* **32**(375), 246–263.
- Parsons, M. G. and W. S. Vorus (1981). Added Mass and Damping Estimates for  
Vibrating Propellers. In: *Proc. SNAME Propellers '81 Symposium*. Virginia  
Beach, Virginia. pp. 273–301.
- Perez, T. (2005). *Ship Motion Control: Course Keeping and Roll Reduction  
using Rudders and Fins*. Advances in Industrial Control. Springer-Verlag,  
London.
- Perez, T. and T. I. Fossen (2006). Time-domain Models of Marine Surface Ves-  
sels Based on Seakeeping Computations. In: *Proc. 7th IFAC Conference on  
Manoeuvring and Control of Marine Craft (MCMC'06)*. Lisbon, Portugal.

- Pivano, L., Ø. N. Smogeli, T. A. Johansen and T. I. Fossen (2006a). Experimental Validation of a Marine Propeller Thrust Estimation Scheme for a Wide Range of Operations. In: *Proc. 7<sup>th</sup> IFAC Conference on Manoeuvring and Control of Marine Craft (MCMC'06)*. Lisbon, Portugal.
- Pivano, L., Ø. N. Smogeli, T. A. Johansen and T. I. Fossen (2006b). Marine Propeller Thrust Estimation in Four-Quadrant Operations. In: *Proc. 45<sup>th</sup> IEEE Conference on Decision and Control (CDC'2006)*. San Diego, California.
- Pivano, L., T. I. Fossen and T. A. Johansen (2006c). Nonlinear model identification of a marine propeller over four-quadrant operations. In: *Proc. 14<sup>th</sup> IFAC Symposium on System Identification (SYSID'06)*. Newcastle, Australia.
- Radan, D., T. A. Johansen, A. J. Sørensen and A. K. Ådnanes (2005). Optimization of Load Dependent Start Tables in Marine Power Management Systems with Blackout Prevention. *WSEAS Transactions on Circuits and Systems* **4**(12), 1861–1866.
- Refsnes, J. E. and A. J. Sørensen (2004). Design of Control System of Torpedo Shaped ROV with Experimental Results. In: *Proc. MTS/IEEE OCEANS'04*. Kobe, Japan. pp. 262–270.
- Rolls-Royce Press Release (2005). 09.05.05 Rolls-Royce opens first technology centre in Norway to conduct marine research. <<http://www.rolls-royce.com/media>>.
- Ruth, E. (2005). Modelling and control of controllable pitch thrusters subject to large losses. Master's thesis. Department of Marine Technology, Norwegian University of Science and Technology – NTNU.
- Ruth, E. and Ø. N. Smogeli (2006). Ventilation of Controllable Pitch Thrusters. *SNAME Marine Technology* **43**(4), 170–179.
- Ruth, E., Ø. N. Smogeli and A. J. Sørensen (2006). Overview of Propulsion Control for Surface Vessels. In: *Proc. 7<sup>th</sup> IFAC Conference on Manoeuvring and Control of Marine Craft (MCMC'06)*. Lisbon, Portugal.
- Schanz, F. (1967). The Controllable Pitch Propeller as an Integral Part of the Ship's Propulsion System. In: *Transactions of SNAME*. Vol. 75. pp. 1–24.
- Scherer, J. O. (1977). Partially Submerged and Supercavitating Propeller Systems. In: *18th general meeting of the American Towing Tank Conference (ATTC)*. Vol. 1. pp. 161–166.
- Sciavicco, L. and B. Siciliano (2000). *Modeling and Control of Robot Manipulators*. 2<sup>nd</sup> ed.. Sprenger-Verlag. London, UK.
- Seaeye Marine Limited (2006). Seaeye Brushless DC Thrusters. <<http://www.seaeye.com/thrusters.html>>.

- Shiba, H. (1953). Air-Drawing of Marine Propellers. In: *Report of Transportation Technical Research Institute*. The Unyu-Gijutsu Kenkyujo, Japan.
- Siemens AG (2005). Improved Dynamic Behavior and Protection for Propulsion Systems with SISHIP<sup>CIS</sup> Drive LV. <[http://www.industry.siemens.com/broschueren/pdf/marine/siship/en/SISHIP\\_propulsion\\_drives.pdf](http://www.industry.siemens.com/broschueren/pdf/marine/siship/en/SISHIP_propulsion_drives.pdf)>.
- Skjellnes, A. (2006). Private e-mail correspondence with A. Skjellnes, Technical Manager, Energy and Automation Division, Siemens AG.
- Skjetne, R. (2004). The Maneuvering Problem. PhD thesis. Dept. of Engineering Cybernetics, Norwegian University of Science and Technology.
- Skjetne, R., T. I. Fossen and P. V. Kokotović (2004). Robust Output Maneuvering for a Class of Nonlinear Systems. *Automatica* **40**(3), 373–383.
- Slotine, J. J. E. and W. Li (1991). *Applied Nonlinear Control*. Prentice-Hall Inc.. Englewood Cliffs, New Jersey.
- Smallwood, D. A. and L. L. Whitcomb (2004). Model-based dynamic positioning of underwater robotic vehicles: Theory and experiment. *IEEE Journal of Oceanic Engineering* **29**(1), 169–185.
- Smogeli, Ø. N., A. J. Sørensen and K. J. Minsaas (2006). The Concept of Anti-Spin Thruster Control. *Control Engineering Practice*. To appear.
- Smogeli, Ø. N., A. J. Sørensen and T. I. Fossen (2004a). Design of a Hybrid Power/Torque Thruster Controller with Thrust Loss Estimation. In: *Proc. IFAC Conference on Control Applications in Marine Systems (CAMS'04)*. Ancona, Italy.
- Smogeli, Ø. N. and A. J. Sørensen (2006a). Adaptive Observer Design for a Marine Propeller. In: *Proc. 14<sup>th</sup> IFAC Symposium on System Identification (SYSID'06)*. Newcastle, Australia.
- Smogeli, Ø. N. and A. J. Sørensen (2006b). Anti-Spin Thruster Control for Ships. *Automatica*. Submitted.
- Smogeli, Ø. N., E. Ruth and A. J. Sørensen (2005a). Experimental Validation of Power and Torque Thruster Control. In: *Proc. Mediterranean Conference on Control and Automation (MED'05)*. Limassol, Cyprus.
- Smogeli, Ø. N., J. Hansen, A. J. Sørensen and T. A. Johansen (2004b). Anti-Spin Control for Marine Propulsion Systems. In: *Proc. 43<sup>rd</sup> IEEE Conference on Decision and Control (CDC'04)*. Paradise Island, Bahamas.
- Smogeli, Ø. N., L. Aarseth, E. S. Overå, A. J. Sørensen and K. J. Minsaas (2003). Anti-spin Thruster Control in Extreme Seas. In: *Proc. 6<sup>th</sup> IFAC Conference on Manoeuvring and Control of Marine Craft (MCMC'03)*. Girona, Spain. pp. 221–226.

- Smogeli, Ø. N., T. Perez, T. I. Fossen and A. J. Sørensen (2005b). The Marine Systems Simulator State-Space Model Representation for Dynamically Positioned Surface Vessels. In: *Proc. 11<sup>th</sup> Cong. International Maritime Association of the Mediterranean (IMAM'05)*. Lisbon, Portugal.
- Sørdalen, O. J. (1997a). Full Scale Sea Trials with Optimal Thrust Allocation. In: *Proceedings of the 4<sup>th</sup> IFAC Conference on Manoeuvring and Control of Marine Craft (MCMC'97)*. Brijuni, Croatia. pp. 150–155.
- Sørdalen, O. J. (1997b). Optimal Thrust Allocation for Marine Vessels. *Control Engineering Practice* **5**(9), 1223–1231.
- Sørensen, A. J. (2005). Structural Issues in the Design and Operation of Marine Control Systems. *IFAC Journal of Annual Reviews in Control* **29**(1), 125–149.
- Sørensen, A. J., A. K. Ådnanes, T. I. Fossen and J. P. Strand (1997). A New Method of Thruster Control in Positioning of Ships based on Power Control. In: *Proc. 4<sup>th</sup> IFAC Conference on Manoeuvring and Control of Marine Craft (MCMC'97)*. Brijuni, Croatia.
- Sørensen, A. J. and A. K. Ådnanes (2005). Reconfigurable Marine Control Systems and Electrical Propulsion Systems for Ships. In: *Proc. ASNE Reconfiguration and Survivability Symposium*. Florida.
- Sørensen, A. J. and Ø. N. Smogeli (2006). Torque and Power Control of Electrically Driven Propellers on Ships. *IEEE Journal of Oceanic Engineering*. Accepted for publication.
- Sørensen, A. J., S. I. Sagatun and T. I. Fossen (1996). The Design of a Dynamic Positioning System Using Model-Based Control. *Control Engineering Practice* **4**(3), 359–368.
- Stettler, J. W., F. S. Hover and M. S. Triantafyllou (2005). Investigating the steady and unsteady maneuvering dynamics of an azimuthing podded propulsor. *Transactions of SNAME*.
- Strand, J. P. (1999). Nonlinear Position Control Systems Design for Marine Vessels. PhD thesis. Department of Engineering Cybernetics, Norwegian University of Science and Technology, Trondheim, Norway.
- Strand, J. P. and A. J. Sørensen (2000). Marine Positioning Systems. In: *Ocean Engineering Handbook* (F. El-Hawary, Ed.). Chap. 3, pp. 163–176. CRC Press, USA.
- Strand, J. P. and T. I. Fossen (1999). Nonlinear Passive Observer for Ships with Adaptive Wave Filtering. In: *New Directions in Nonlinear Observer Design* (H. Nijmeijer and T. I. Fossen, Eds.). Chap. I-7, pp. 113–134. Springer-Verlag, London.

- Strom-Tejsen, J. and R. R. Porter (1972). Prediction of Controllable-pitch Propeller Performance in Off-design Conditions. In: *Third Ship Control Systems Symposium, Paper VII B-1*. Bath, UK.
- Tecnadyne (2006). Tecnadyne DC Brushless Thrusters. <<http://www.tecnadyne.com/thrusters.htm>>.
- Tjønnås, J. and T. A. Johansen (2005). Optimizing Nonlinear Adaptive Control Allocation. In: *Proc. IFAC World Congress*. Prague, Czech Republic.
- Tsukamoto, C. L., W. Lee, S. K. Choi and J. Lorentz (1997). Comparison Study on Advanced Thruster Control of Underwater Robots. In: *Proc. IEEE Int. Conf. on Robotics and Automation*. Albuquerque, New Mexico. pp. 1845–1850.
- van Lammeren, W. P. A., J. D. van Manen and M. W. C. Oosterveld (1969). The Wageningen B-Screw Series. *Transactions of SNAME*.
- Wagner, H. (1925). Über die Entstehung des dynamischen Auftriebes vom Tragflügeln. *Zeitschrift für angew. Math. und Mech.* **5**(1), 17–35. In German. “On the Origin of dynamic Lift on a Lifting Surface”.
- Webster, W. C. and J. Sousa (1999). Optimum Allocation for Multiple Thrusters. In: *Proc. of the Int. Society of Offshore and Polar Engineers Conference (ISOPE'99)*. Brest, France.
- Wereldsma, R. (1965). *Dynamic Behavior of Ship Propellers*. Internationale Periodieke Pers, Rotterdam.
- Whalley, R. and M. Ebrahimi (2002). Gas Turbine Propulsion Plant Control. *Naval Engineers Journal* **114**(4), 79–94.
- Whitcomb, L. L. and D. R. Yoerger (1999a). Development, Comparison, and Preliminary Experimental Validation of Nonlinear Dynamic Thruster Models. *IEEE Journal of Oceanic Engineering* **24**(4), 481–494.
- Whitcomb, L. L. and D. R. Yoerger (1999b). Preliminary Experiments in Model-Based Thruster Control for Underwater Vehicle Positioning. *IEEE Journal of Oceanic Engineering* **24**(4), 495–506.
- Winterbone, D. E. (1980). Adaptive Multi-Variable Control of Ship Propulsion Plant. In: *3rd IFAC Symposium on Ship Operation Automation*. pp. 305–312.
- Woodward Governor Company (2004). Reference Manual 26260: Governor Fundamentals and Power Management. <<http://www.woodward.com/pubs/pubpage.cfm>>.
- Yang, K. C. H., J. Yuh and S. K. Choi (1999). Fault-tolerant System Design of an Autonomous Underwater Vehicle – ODIN: an Experimental Study. *Int. Journ. Systems Science* **30**(9), 1011–1019.

- Yoerger, D. R., J. G. Cooke and J. J. E. Slotine (1991). The Influence of Thruster Dynamics on Underwater Vehicle Behavior and Their Incorporation Into Control System Design. *IEEE Journal of Oceanic Engineering* **15**(3), 167–179.
- Young-Bok, K., J. Byun, B. Jung and J. Yang (1998). Optimization Control for Fuel Consumption of a Ship Propulsion System with CPP using Decoupling and LMI Approach. In: *Proc. IFAC Conf. Control Applications in Marine Systems (CAMS'98)*. pp. 315–320.
- Zheng, Y., Y. Chait, C. V. Hollot, M. Steinbuch and M. Norg (2000). Experimental Demonstration of Reset Control Design. *Control Engineering Practice* **8**(2), 113–120.
- Zhinkin, V. B. (1989). Determination of the Screw Propeller Thrust when the Torque or Shaft Power is Known. In: *Fourth Int. Symp. on Practical Design of Ships and Mobile Units (PRADS'89)*. pp. 121–1–121–4.

# Appendix A

## Propeller simulation data

This appendix presents simulation data for a 4MW propulsion unit equipped with a Wageningen B4-70 propeller of diameter 4m. The simulation parameters are assumed to be representative for a typical azimuth or podded propeller used for main propulsion on e.g. an offshore service vessel<sup>1</sup>. Note that a modern propeller will have better hydrodynamic properties than the Wageningen B-series propeller, which means that less power would be required to produce the same thrust. However, for the simulation studies performed here, this is of no major importance.

### A.1 Main propeller parameters

The main parameters of the B4-70 propeller are given in Table 2.2, and the open-water characteristics in Figure 2.1. The remaining simulation parameters for the propeller dynamics are given in Table A.1. The measurements  $n$  and  $Q_m$  are contaminated by white noise with power  $w_n$  and  $w_{Qm}$ , respectively, and filtered with first order filters with time constants  $T_f$  and  $T_{fq}$ . Simulation parameters for the ventilation loss function are given in Table A.2. Many of the simulation parameters in Table A.1 are interrelated. The maximum motor torque and power,  $Q_{\max}$  and  $P_{\max}$ , are related to the rated torque and power for continuous operation,  $Q_N$  and  $P_N$ , by (2.55) with  $k_m = 1.2$ . In addition, the various parameter relationships from Section 2.2.3 are satisfied.

### A.2 4-quadrant model parameters

Table A.3 shows the Fourier coefficients used in the 4-quadrant model of the Wageningen B4-70 propeller, taken from van Lammeren *et al.* (1969). The

---

<sup>1</sup>Thanks to Leif Aarseth at Rolls-Royce Ulsteinvik, Norway, for providing realistic example data for various thruster types.

Parameter	Symbol	Value
Diameter	$D$	4m
Nominal thrust coefficient	$K_{T0}$	0.445
Nominal torque coefficient	$K_{Q0}$	0.0666
Reverse thrust coefficient	$K_{T0r}$	0.347
Reverse torque coefficient	$K_{Q0r}$	0.0628
Rotational inertia	$I_s$	$25E3\text{kgm}^2$
Linear friction coefficient	$K_\omega$	720Nms
Static friction	$Q_s$	6.2kNm
Gear ratio motor:propeller	$k_g$	4
Rated motor torque	$Q_N$	78kNm
Rated motor power	$P_N$	4000kW
Rated motor speed	$n_N$	8.2rps
Max motor torque	$Q_{\max}$	93kNm
Max motor power	$P_{\max}$	4800kW
Motor time constant	$T_m$	0.001s
Shaft speed filter time constant	$T_f$	0.01s
Motor torque filter time constant	$T_{fq}$	0.01s
Bollard pull thrust	$T_{bp}$	490kN
Bollard pull torque	$Q_{bp}$	295kNm
Bollard pull prop. power	$P_{bp}$	3800kW
Bollard pull shaft speed	$n_{bp}$	2.05rps
Mech. efficiency	$\eta_m$	0.95
Density of water	$\rho$	$1025\text{kg/m}^3$
Shaft speed noise power	$w_n$	$1E - 9$
Motor torque noise power	$w_{Qm}$	1.0
Sampling frequency	$f$	250Hz

Table A.1: Parameters for the 4MW Wageningen B4-70 example propeller model.

Parameter	Symbol	Value
Minimum ventilation loss	$b_1$	0.3
Maximum ventilation loss	$b_2$	0.25
Submergence ratio 1	$h_1$	1.1
Submergence ratio 2	$h_2$	1.3
Shaft speed ratio 1	$n_1$	0.2
Shaft speed ratio 2	$n_2$	0.5
Torque loss exponent	$m$	0.8
Bollard pull shaft speed	$n_{bp}$	2.05rps
Hysteresis rate limit	$\dot{\beta}_{VH}$	$0.5\text{s}^{-1}$

Table A.2: Parameters for the 4MW Wageningen B4-70 propeller ventilation loss model, see Section 2.4.4 for details.

k	$A_T$	$B_T$	$A_Q$	$B_Q$
0	2.5350E-02	0.0000E-00	2.4645E-03	0.0000E-00
1	1.7820E-01	-7.4777E-01	2.6718E-02	-1.1081E-01
2	1.4674E-02	-1.3822E-02	1.6056E-03	1.5909E-04
3	2.8054E-02	1.0077E-01	6.5822E-03	1.6455E-02
4	-1.6328E-02	-1.1318E-02	-2.2497E-03	-2.0601E-03
5	-5.3041E-02	4.7186E-02	-7.8062E-03	8.5343E-03
6	6.0605E-04	1.0666E-02	2.4126E-04	8.7856E-04
7	3.6823E-02	-9.0239E-03	6.1475E-03	-3.1327E-03
8	-2.5429E-03	-7.8452E-03	-1.6065E-03	-9.6650E-04
9	-1.7680E-02	2.3941E-02	-3.3291E-03	4.3190E-03
10	2.7331E-03	8.0787E-03	1.2311E-03	1.2453E-03
11	2.1436E-02	-1.4942E-04	3.1123E-03	9.5986E-05
12	-2.4782E-03	-3.1925E-03	-1.2559E-03	-7.9986E-04
13	1.2317E-03	9.2620E-03	1.3948E-03	1.5073E-03
14	5.0980E-03	1.5527E-03	8.8397E-04	2.4595E-04
15	7.8076E-03	-6.5683E-03	5.0358E-05	-1.6918E-03
16	-3.7816E-03	-6.1655E-04	-7.9990E-04	5.1603E-04
17	3.5353E-03	5.1033E-03	1.3345E-03	1.1504E-03
18	5.3014E-03	-6.0263E-04	1.1928E-03	-4.7976E-04
19	2.1940E-03	-8.2244E-03	-1.3556E-04	-1.4566E-03
20	-2.8306E-03	-6.3789E-04	-7.0825E-04	2.3280E-04

Table A.3: Wageningen B4-70 propeller 4-quadrant model Fourier coefficients.

equations for implementation of the model are given in Section 2.1.2, and the resulting 4-quadrant  $C_T$  and  $C_Q$  curves given in Figure 2.2.

Note that the propeller characteristics obtained from van Lammeren *et al.* (1969) differ slightly from the characteristics given in Oosterveld and van Oossanen (1975). For example, the nominal thrust and torque coefficients  $K_{T0}$  and  $K_{Q0}$ , which are important characteristic parameters, are not exactly the same. From the parametrization given in Oosterveld and van Oossanen (1975) – see (2.18, 2.19) – the coefficients are directly calculated with  $J_a = 0$  to become  $K_{T0} = 0.455$  and  $K_{Q0} = 0.0675$ . From the parametrization given in van Lammeren *et al.* (1969), the coefficients are calculated according to (2.37, 2.38), and become  $K_{T0} = 0.445$  and  $K_{Q0} = 0.0666$ . The discrepancy is not of significant magnitude, and may probably be explained by the different data fitting used in the two references. In this work, the representation from van Lammeren *et al.* (1969) has been used.



## Appendix B

# Thruster controller tuning issues

An inevitable challenge when attempting to make a fair comparison of various controllers is tuning. This appendix presents some rules-of-thumb for tuning of the controllers presented in Chapter 3.

### B.1 Shaft speed controller PI tuning

The PI controller tuning parameters  $K_p$  and  $T_i$  should be chosen according to the rating of the motor, the motor time constant  $T_m$ , the shaft speed filter time constant  $T_f$ , the rotational inertia  $I_s$ , and the desired closed loop properties. Various guides to the tuning of PI controllers exist.

From Leonhard (1996), a commonly used model-based PI tuning rule for variable speed drives is the so-called “symmetrical optimum”. Using the first-order representation of motor and inner current loop from (2.52), the transfer function  $h_0(s)$  of the open speed control loop is approximated by:

$$h_0(s) = K_p \frac{T_i s + 1}{T_i s} \frac{1}{T_m s + 1} \frac{1}{T_f s + 1} \frac{1}{T_{Is} s}, \quad (\text{B.1})$$

where  $T_m$  is the time constant of the motor and current loop,  $T_f$  is the shaft speed filter time constant, and  $T_{Is}$  is the mechanical time constant, which is equal to the rotational inertia, i.e.  $T_{Is} = I_s$ . Since  $T_m \ll T_{Is}$  and  $T_f \ll T_{Is}$ , (B.1) can be approximated by (Nilsen, 2001):

$$h_0(s) \approx K_p \frac{T_i s + 1}{T_i s} \frac{1}{T_{sum} s + 1} \frac{1}{T_{Is} s}, \quad (\text{B.2})$$

$$T_{sum} = T_m + T_f. \quad (\text{B.3})$$

The symmetric optimum tuning guideline is:

$$\begin{aligned} T_i &= a^2 T_{sum}, \\ K_p &= \frac{1}{a} \frac{T_{Is}}{T_{sum}} = \frac{1}{a} \frac{I_s}{T_{sum}}, \end{aligned} \quad (\text{B.4})$$

where  $a > 1$  is a constant related to the damping ratio  $\zeta$  by:

$$\zeta = \frac{a - 1}{2}. \quad (\text{B.5})$$

Nilsen (2001, 2006) recommends  $a = 2 - 3$ , which gives an underdamped to critically damped system, i.e.  $\zeta = 0.5 - 1.0$ . The resulting step response exhibits a large overshoot. It is therefore recommended to use a reference generator for the speed command (Leonhard, 1996). In this method, the hydrodynamic load torque – which effectively represents a large quadratic damping term – has not been accounted for. Hence, a submerged propeller will have a significantly more damped response than what is indicated by  $\zeta$ . For a propeller subject to large thrust losses, e.g. due to a water exit, the hydrodynamic damping is much smaller.

A rule-of-thumb used for initial tuning, also in marine industrial installations, is to choose  $K_p$  such that 10 – 20% error in the shaft speed gives 100% torque, and  $T_i$  at least four times larger than  $T_{sum}$  (Ådnanes, 2006; Nilsen, 2006). This corresponds to a proportional gain of 5 – 10 in a “per unit” sense, as is commonly used in electrical engineering. With the parameter  $k_p$  representing the per unit gain, i.e.  $k_p \in [5, 10]$ , and  $k_t$  the integral time constant ratio, i.e.  $k_t \geq 4$ , the tuning rule becomes:

$$K_p = k_p \frac{k_g Q_N}{n_{bp}}, \quad T_i = k_t T_{sum}, \quad (\text{B.6})$$

where  $n_{bp}$  is the bollard pull shaft speed. After application of (B.6) for initial tuning, the motor drives are usually tuned manually to give satisfactory performance (Ådnanes, 2006).

Using the example propeller from Table A.1, the tuning rules in (B.6) with  $k_p = 5$  and  $k_t = 5$  gives:

$$\begin{aligned} K_p &= k_p \frac{k_g Q_N}{n_{bp}} = 5 \frac{4 \cdot 78E3}{2.05} \approx 7.6E5, \\ T_i &= 0.05. \end{aligned} \quad (\text{B.7})$$

Using the tuning rules in (B.4) with  $a = 3$ , the result is:

$$\begin{aligned} K_p &= \frac{1}{a} \frac{I_s}{T_{sum}} = \frac{1}{3} \frac{25E3}{(0.01 + 0.001)} \approx 7.6E5, \\ T_i &= 9(0.01 + 0.001) \approx 0.1. \end{aligned} \quad (\text{B.8})$$

The values in (B.8) have been used in the simulation studies in this thesis.

## B.2 Torque and power control tuning

In their pure form, as given in (3.29) and (3.32), the only parameters needed in the torque and power controllers are the control coefficients  $K_{TC}$  and  $K_{QC}$ , which leaves no tunable parameters. However, for good performance, these controllers rely on the inertia and friction feedforward compensation schemes in (3.22) and (3.19), which require tuning.

## B.3 Inertia and friction compensation tuning

Tuning of the friction compensation scheme  $Q_{ff}(n_r)$  in (3.19) and inertia compensation scheme  $Q_{if}(n_r)$  in (3.22) is mainly done by choosing the friction parameters  $Q_{f0}$  and  $Q_{f1}$ , and the rotational inertia  $I_c$ . If  $Q_s$  and  $K_\omega$  in (2.51), and  $I_s$  in (2.50) are known, no further tuning should be necessary with the following choices:  $Q_{f0} = Q_s$ ,  $Q_{f1} = K_\omega$ , and  $I_c = I_s$ .  $I_s$  is usually known with reasonable accuracy, since it is an important parameter for the choice of electric motor and PI controller tuning, as shown in Section B.1. It is less likely to have decent a priori knowledge of  $Q_s$  and  $K_\omega$ . The main purpose of the compensation schemes are:

- $Q_{ff}(n_r)$ : Improve the steady-state performance of the system.
- $Q_{if}(n_r)$ : Improve the transient response of the system.

If  $Q_s$  and/or  $K_\omega$  are unknown,  $Q_{f0}$  and  $Q_{f1}$  must be tuned manually. Since  $Q_{ff}(n_r)$  only is intended to improve the steady-state performance, tuning should be performed at steady state. One possible approach is as follows:

1. Run the motor until its oil, bearings, etc. reaches working temperature.
2. Initially, let  $Q_{f0} = 0$  and  $Q_{f1} = 0$ .
3. Set  $T_d$  to a low value, such that the friction at steady state is dominated by the static term  $Q_s$ . A suggestion is to choose  $T_d$  such that  $n_r = n_f$  from (3.20), i.e.  $T_d = K_{TC}\rho D^4 n_f^2$ .
4. Increase  $Q_{f0}$  slowly until the motor turns with  $n = n_f$ . This should correspond to  $Q_{f0} \approx Q_s$ , and  $Q_{f0}$  can be fixed at this value.
5. Set  $T_d$  to a high value, preferably to the bollard pull thrust  $T_{bp}$ . The corresponding shaft speed  $n_{bp}$  should be known from the propeller characteristics.
6. Increase  $Q_{f1}$  until  $n \approx n_{bp}$ . This should correspond to  $Q_{f1} \approx K_\omega$  and  $Q_{f1}$  can be fixed at this value.

If  $I_s$  is unknown or uncertain,  $I_c$  may be tuned manually. Since the sole purpose of  $Q_{if}(n_r)$  is to improve the tracking properties of the controllers,  $I_c$  can be adjusted to give the desired step response of the system. With a reference generator as in (3.14),  $\dot{n}_r$  is available to  $Q_{if}(n_r)$ . Tuning can then be done by commanding a step in  $T_d$ , and comparing  $n_r$  with  $n$ . If  $Q_{ff}(n_r)$  is already tuned,  $I_c$  should be adjusted until  $n \approx n_r$ . If  $Q_{ff}(n_r)$  is not tuned,  $I_c$  should be adjusted such that  $\dot{n} \approx \dot{n}_r$  during the step. This implies that, if desired,  $I_c$  can be chosen different from  $I_s$  to get the desired transient response of the system.

## B.4 Choice of parameters for the combined controllers

The QP, MQP1, MQP2, and SQP controllers – see Table 3.1 – all rely on the weighting function  $\alpha(z)$  in 3.33 for transitions between the fundamental controllers. How  $k$ ,  $p$ , and  $r$  affect the shape of  $\alpha(z)$  is discussed in Section 3.13.1. It will probably be beneficial to choose the parameters to give a limited steepness of the weighting function, in order to make the transition between the fundamental controllers smoother.

## Appendix C

# Simulation of relative propeller motion

In order to perform realistic simulations of a propulsion system, including loss effects, it is necessary to have reasonable approximations of the motion of each thruster unit relative to the surrounding water. This appendix provides the transformation tools needed to couple the thruster and vessel motion and forces.

### C.1 Vessel motion

Vessel motion is typically described by the motion of a body-fixed frame ( $b$ -frame) with respect to an earth-fixed frame ( $n$ -frame), see Fossen (2002) for details. The  $n$ -frame position  $\mathbf{p}^n = [n, e, d]^\top$  (north, east, down) and Euler angles  $\Theta = [\phi, \theta, \psi]^\top$  (roll, pitch, yaw) are defined in terms of the generalized coordinate vector  $\boldsymbol{\eta}$ :

$$\boldsymbol{\eta} = [(\mathbf{p}^n)^\top, \Theta^\top]^\top = [n, e, d, \phi, \theta, \psi]^\top. \quad (\text{C.1})$$

The  $b$ -frame translational velocities  $\mathbf{v}_o^b = [u, v, w]^\top$  (surge, sway, heave) and angular velocities  $\boldsymbol{\omega}_{nb}^b = [p, q, r]^\top$  (roll, pitch, yaw) of the  $b$ -frame with respect to the  $n$ -frame, expressed in the  $b$ -frame, are defined in terms of the generalized velocity vector  $\boldsymbol{\nu}$ :

$$\boldsymbol{\nu} = [(\mathbf{v}_o^b)^\top, (\boldsymbol{\omega}_{nb}^b)^\top]^\top = [u, v, w, p, q, r]^\top. \quad (\text{C.2})$$

$O$  is the origin of the  $b$ -frame. The translational velocity transformation between the  $b$ - and  $n$ -frame is:

$$\mathbf{v}_o^n = \mathbf{R}_b^n(\Theta)\mathbf{v}_o^b, \quad (\text{C.3})$$

where  $\mathbf{v}_o^n = \dot{\mathbf{p}}^n$ , and the Euler angle rotation matrix (*zyx*-convention) from the *b*-frame to the *n*-frame  $\mathbf{R}_b^n(\Theta) \in \mathbb{R}^{3 \times 3}$  is defined as:

$$\mathbf{R}_b^n(\Theta) = \begin{bmatrix} c\psi c\theta & -s\psi c\phi + c\psi s\theta s\phi & s\psi s\phi + c\psi c\phi s\theta \\ s\psi c\theta & c\psi c\phi + s\psi s\theta s\phi & -c\psi s\phi + s\theta s\psi c\phi \\ -s\theta & c\theta s\phi & c\theta c\phi \end{bmatrix}. \quad (\text{C.4})$$

Here,  $s\cdot = \sin(\cdot)$  and  $c\cdot = \cos(\cdot)$ . Note that the rotation matrix  $\mathbf{R}_a^b$  between any two frames *a* and *b* (from *a* to *b*) has the special properties that  $(\mathbf{R}_a^b)^{-1} = (\mathbf{R}_a^b)^\top = \mathbf{R}_b^a$ . The Euler angle rates satisfy:

$$\dot{\Theta} = \mathbf{T}_\Theta(\Theta)\boldsymbol{\omega}_{bn}^b, \quad (\text{C.5})$$

where  $\mathbf{T}_\Theta(\Theta) \in \mathbb{R}^{3 \times 3}$  is the Euler angle attitude transformation matrix:

$$\mathbf{T}_\Theta(\Theta) = \begin{bmatrix} 1 & s\phi t\theta & c\phi t\theta \\ 0 & c\phi & -s\phi \\ 0 & s\phi/c\theta & c\phi/c\theta \end{bmatrix}, \quad \theta \neq \pm\frac{\pi}{2}, \quad (\text{C.6})$$

and  $t\cdot = \tan(\cdot)$ . Consequently:

$$\dot{\boldsymbol{\eta}} = \mathbf{J}(\Theta)\boldsymbol{\nu}, \quad (\text{C.7})$$

where  $\mathbf{J}(\Theta) \in \mathbb{R}^{6 \times 6}$  is the generalized velocity transformation matrix:

$$\mathbf{J}(\Theta) = \begin{bmatrix} \mathbf{R}_b^n(\Theta) & \mathbf{0}_{3 \times 3} \\ \mathbf{0}_{3 \times 3} & \mathbf{T}_\Theta(\Theta) \end{bmatrix}, \quad \theta \neq \pm\frac{\pi}{2}. \quad (\text{C.8})$$

To sum up, the rigid-body vessel motion is uniquely expressed by the two vectors  $\boldsymbol{\eta}$  in (C.1) and  $\boldsymbol{\nu}$  in (C.2), which are related through (C.7).

There are two conventional ways of calculating the total vessel motion. In the control literature, the vessel motion has usually been decoupled into a low-frequency part and a wave-frequency part. The low-frequency motion is then calculated from the vessel rigid-body dynamics and the low-frequency loads from current, wind, waveldrift, and the propulsion system, and the wave-frequency motion is calculated from motion transfer functions (or response amplitude operators – RAOs). The two contributions are then superposed to yield the total vessel motion.

In an alternative approach, force transfer functions are used to represent the first-order wave excitation forces, and the fluid memory effects associated with the radiation forces are expressed in a state-space form. In this way, the wave-frequency model is integrated with the low-frequency model through force superposition instead of motion superposition. Other effects like viscous forces, multi-body interactions, and ship motion control systems can then be incorporated into the model by means of force superposition; see Fossen and Smogeli (2004), Smogeli *et al.* (2005b), Perez and Fossen (2006), and the references therein.

## C.2 Transformation tools

Calculation of the motion of an arbitrary point  $P$  fixed to the vessel and inclusion of the forces acting on this point in the  $b$ -frame equations of motion requires transformations of positions, velocities, accelerations, and forces between the  $b$ -frame origin  $O$  and  $P$ . The translational velocity  $\mathbf{v}_p^b$  of the point  $P$  decomposed in the  $b$ -frame is given by:

$$\mathbf{v}_p^b = \mathbf{v}_o^b + \boldsymbol{\omega}_{nb}^b \times \mathbf{r}_p^b, \quad (\text{C.9})$$

where  $\mathbf{r}_p^b = [x_p, y_p, z_p]^\top$  is the vector from  $O$  to  $P$ . The vector cross product  $\times$  is defined in terms of the matrix  $\mathbf{S}(\mathbf{r}_p^b) \in \mathbb{R}^{3 \times 3}$  such that:

$$\boldsymbol{\omega}_{nb}^b \times \mathbf{r}_p^b \triangleq -\mathbf{S}(\mathbf{r}_p^b) \boldsymbol{\omega}_{nb}^b = \mathbf{S}(\mathbf{r}_p^b)^\top \boldsymbol{\omega}_{nb}^b, \quad (\text{C.10})$$

where:

$$\mathbf{S}(\mathbf{r}_p^b) = -\mathbf{S}^\top(\mathbf{r}_p^b) = \begin{bmatrix} 0 & -z_p & y_p \\ z_p & 0 & -x_p \\ -y_p & x_p & 0 \end{bmatrix}. \quad (\text{C.11})$$

Since the angular velocities in  $P$  and  $O$  are the same, the translational and angular velocity transformation from  $O$  to  $P$  can be expressed by the screw transformation matrix  $\mathbf{H}(\mathbf{r}_p^b) \in \mathbb{R}^{6 \times 6}$ :

$$\begin{bmatrix} \mathbf{v}_p^b \\ \boldsymbol{\omega}_{nb}^b \end{bmatrix} = \mathbf{H}(\mathbf{r}_p^b) \begin{bmatrix} \mathbf{v}_o^b \\ \boldsymbol{\omega}_{nb}^b \end{bmatrix}, \quad (\text{C.12})$$

$$\mathbf{H}(\mathbf{r}_p^b) \triangleq \begin{bmatrix} \mathbf{I}_{3 \times 3} & \mathbf{S}(\mathbf{r}_p^b)^\top \\ \mathbf{0}_{3 \times 3} & \mathbf{I}_{3 \times 3} \end{bmatrix}. \quad (\text{C.13})$$

From this, the position  $\mathbf{x}_p^n$ , generalized velocity  $\boldsymbol{\nu}_p = [\mathbf{v}_p^b, \boldsymbol{\omega}_{nb}^b]^\top$ , and generalized acceleration  $\dot{\boldsymbol{\nu}}_p$  of  $P$  are given by:

$$\mathbf{x}_p^n = \mathbf{p}^n + \mathbf{R}_b^n(\boldsymbol{\Theta}) \mathbf{r}_p^b, \quad (\text{C.14})$$

$$\boldsymbol{\nu}_p = \mathbf{H}(\mathbf{r}_p^b) \boldsymbol{\nu}, \quad (\text{C.15})$$

$$\dot{\boldsymbol{\nu}}_p = \mathbf{H}(\mathbf{r}_p^b) \dot{\boldsymbol{\nu}}, \quad (\text{C.16})$$

where  $\mathbf{R}_b^n(\boldsymbol{\Theta})$  and  $\mathbf{H}(\mathbf{r}_p^b)$  are defined by (C.4) and (C.13), respectively. Correspondingly, the generalized force vector  $\boldsymbol{\tau}_p$  with point of attack  $P$  is transformed to the generalized force  $\boldsymbol{\tau}$  in the origin  $O$  by:

$$\boldsymbol{\tau} = \begin{bmatrix} \mathbf{I}_{3 \times 3} & \mathbf{0}_{3 \times 3} \\ \mathbf{S}(\mathbf{r}_p^b) & \mathbf{I}_{3 \times 3} \end{bmatrix} \boldsymbol{\tau}_p = \mathbf{H}^\top(\mathbf{r}_p^b) \boldsymbol{\tau}_p. \quad (\text{C.17})$$

Hence, given the vessel motion in terms of  $\boldsymbol{\eta}$  and  $\boldsymbol{\nu}$ , the motion of a propeller located at  $P$  is given by (C.14)-(C.16). The thrust  $T_a$  is transformed to the  $b$ -frame equations of motion by (C.17) and:

$$\boldsymbol{\tau}_p = \begin{bmatrix} \cos \alpha_p \\ \sin \alpha_p \\ \mathbf{0}_{4 \times 1} \end{bmatrix} T_a, \quad (\text{C.18})$$

where  $\alpha_p$  is the propeller azimuth (i.e. angle between the propeller shaft and the  $b$ -frame x-axis).

**Remark C.1** The first, second, and sixth entry in  $\boldsymbol{\tau}$  given from (C.17) and (C.18) corresponds to the 3DOF thrust vector  $\boldsymbol{\tau}_j$  in (9.1).

### C.3 Wave- and current-induced velocities

Irregular waves are commonly described by a wave spectrum  $S_w(\omega_w, \psi_w) = S(\omega_w)D(\psi_w)$ , where the frequency spectrum  $S(\omega_w)$  describes the distribution of wave energy in the sea state over different frequencies  $\omega_w$ , and the spreading function  $D(\psi_w)$  describes the distribution of wave energy over directions  $\psi_w$  in the  $n$ -frame. Common frequency spectra and spreading functions may be found in e.g. Ochi (1998). In this work, the two-parameter ITTC/ISSC modified Pierson-Moskowitz (PM) spectrum is used (Lloyd, 1998):

$$S(\omega_w) = \frac{A}{\omega_w^5} \exp\left(-\frac{B}{\omega_w^4}\right), \quad A = 487 \frac{H_s^2}{T_p^4}, \quad B = \frac{1949}{T_p^4}, \quad (\text{C.19})$$

where  $H_s$  is the significant wave height, and  $T_p$  is the peak (modal) wave period.

For simulation, the sea state is realized as a superposition of harmonic components extracted from the wave spectrum, where harmonic component  $j$  is defined in terms of wave amplitude  $\zeta_j$ , frequency  $\omega_j$ , direction  $\psi_j$ , and random phase  $\phi_j$ . The wave particle velocities in the  $n$ -frame due to harmonic component  $j$  at the point  $P$  are termed  $u_{wj}$ ,  $v_{wj}$ , and  $w_{wj}$  in the x-, y-, and z-direction, and are written as:

$$u_{wj}(x_p, y_p, z_p, t) = \zeta_j \omega_j \exp(-k_j z_p) \cos \psi_j \sin \theta_j, \quad (\text{C.20})$$

$$v_{wj}(x_p, y_p, z_p, t) = \zeta_j \omega_j \exp(-k_j z_p) \sin \psi_j \sin \theta_j, \quad (\text{C.21})$$

$$w_{wj}(x_p, y_p, z_p, t) = \zeta_j \omega_j \exp(-k_j z_p) \sin(\theta_j - \frac{\pi}{2}), \quad (\text{C.22})$$

$$\theta_j = \omega_j t + \phi_j - k_j(x_p \cos \psi_j + y_p \sin \psi_j). \quad (\text{C.23})$$

Here, the wave number  $k_j$  is given by the deep-water dispersion relation  $k_j = \omega_j^2/g$ , where  $g$  is the acceleration of gravity. Letting  $P$  move about with the ship in the  $n$ -frame, it can be shown that the frequency of encounter is captured in the change of  $x_p$  and  $y_p$  in (C.23). Using linear theory, the harmonic components are superposed to give the total wave-induced velocity vector  $\mathbf{V}_w = [u_w, v_w, w_w]^\top$ , i.e.:

$$\mathbf{V}_w(x_p, y_p, z_p, t) = \sum_{j=1}^N [u_{wj}(\cdot), v_{wj}(\cdot), w_{wj}(\cdot)]^\top, \quad (\text{C.24})$$

where  $N$  is the number of harmonic components. The corresponding surface

elevation  $\zeta_w(x_p, y_p, t)$  and shaft submergence  $h(x_p, y_p, t)$  are calculated from:

$$\zeta_w(x_p, y_p, t) = \sum_{j=1}^N \zeta_j \sin[\omega_j t + \phi_j - k_j(x_p \cos \psi_j + y_p \sin \psi_j)], \quad (\text{C.25})$$

$$h(x_p, y_p, t) = h_0 + \zeta_w(x_p, y_p, t), \quad (\text{C.26})$$

where  $h_0$  is the submergence of the shaft with respect to the mean free surface.

For freely-floating surface vessels, only the surface current is of any importance. If the current is given by magnitude  $U_c$  and direction  $\beta_c$  in the  $n$ -frame, the current velocity vector  $\mathbf{V}_c$  in the  $n$ -frame is written as:

$$\mathbf{V}_c = U_c [\cos \beta_c, \sin \beta_c, 0]^\top. \quad (\text{C.27})$$

## C.4 Calculation of relative motion

The propeller rigid-body velocity  $\mathbf{V}_v$  in the  $n$ -frame is calculated from  $\mathbf{v}_p^b$  in (C.12) by:

$$\mathbf{V}_v = \mathbf{R}_b^n(\Theta) \mathbf{v}_p^b. \quad (\text{C.28})$$

Accounting for the wave-induced velocities  $\mathbf{V}_w$  from (C.24), the current-induced velocity  $\mathbf{V}_c$  from (C.27), and the motion of the propeller due to the vessel motion  $\mathbf{V}_v$  from (C.28), the total relative velocity  $\mathbf{V}_p^n$  of the water with respect to the propeller in the  $n$ -frame is given by:

$$\mathbf{V}_p^n = \mathbf{V}_w + \mathbf{V}_c - \mathbf{V}_v. \quad (\text{C.29})$$

The relative velocities are decomposed in an in-line component, which corresponds to  $V_a$ , and a transverse component  $V_t$  by transforming  $\mathbf{V}_p^n$  into the  $b$ -frame velocity vector  $\mathbf{V}_p^b$ :

$$\mathbf{V}_p^b = \mathbf{R}_b^n(\Theta)^\top \mathbf{V}_p^n, \quad (\text{C.30})$$

where  $\mathbf{R}_b^n(\Theta)$  is given in (C.4). Then,  $V_a$  and  $V_t$  are found from:

$$V_a = -[\cos \alpha_p, \sin \alpha_p, 0] \mathbf{V}_p^b, \quad (\text{C.31})$$

$$V_t = \|[-\sin \alpha_p, \cos \alpha_p, 0] \mathbf{V}_p^b + [0, 0, 1] \mathbf{V}_p^b\|_2, \quad (\text{C.32})$$

where  $\alpha_p$  is the propeller azimuth.

**Remark C.2** The sign of  $V_a$  in (C.31) is needed since a positive  $V_a$  is defined as water flow into the propeller, whereas the propeller frame of reference has positive  $x$ -axis in the thrust direction.

**Remark C.3** The approach described here should only serve as a rough estimate, since it is assumed that the waves are unaffected by the presence of the vessel hull, and the velocity contributions from waves, current, and vessel motion have been superposed.

## C.5 Simplified calculations

In the simulations presented in this thesis, only long-crested waves are considered, and no vessel motion is included. It has therefore been chosen to set  $x_p = y_p = 0$ ,  $z_p = h_0$ ,  $\psi_j = 0$ ,  $\mathbf{R}_b^n(\Theta) = \mathbf{I}_{3 \times 3}$ ,  $\alpha_p = 0$ ,  $\beta_c = 0$ , and  $\mathbf{V}_v = \mathbf{0}_{1 \times 3}$ , such that (C.31), (C.25), and (C.26) can be simplified to:

$$V_a(t) = -\sum_{j=1}^N \zeta_j \omega_j \exp(-k_j h_0) \sin[\omega_j t + \phi_j], \quad (\text{C.33})$$

$$\zeta_w(t) = \sum_{j=1}^N \zeta_j \sin[\omega_j t + \phi_j], \quad (\text{C.34})$$

$$h(t) = h_0 + \zeta_w(t). \quad (\text{C.35})$$

## Appendix D

# Additional ventilation results

As an extension of Section 2.4, this appendix presents the experimental set-up used in the cavitation tunnel, gives a discussion on scaling laws for ventilated propellers, shows additional experimental results for ducted and open propellers subject to ventilation and in-and-out-of water effects, and provides further comparisons of the simulation model and the experimental results.

### D.1 Experimental set-up

The tests in the cavitation tunnel at NTNU were conducted on two occasions: the first time by Aarseth (2003) and Overå (2003), and the second time by Ruth (2005). The description of the experimental setup has been adopted from Ruth (2005). The equipment was arranged according to Figures D.1 and D.2. Most of the test runs were performed with a ducted propeller, but some were performed without the duct present. The main dimensions of the duct and propeller are given in Section 7.1.

A list of the measurements is given in Table D.1. The accuracy is high for all the measurements, except for the advance speed  $V_a$  when it is lower than 1m/s. The measured duct thrust  $T_{ad}$  includes the drag on the pole holding the duct. This error source is of little importance because of the low advance speeds during the tests. The total thrust is given from  $T_a = T_{ad} + T_{ap}$ .

The measurements were sampled at 1000Hz. The mean values were obtained by averaging the time series over a period of approximately 5s. This corresponds to at least 10 propeller revolutions per averaging period for  $n > 2$ rps, which is sufficient to obtain representative mean values. The averaged segments of the time series were chosen manually.

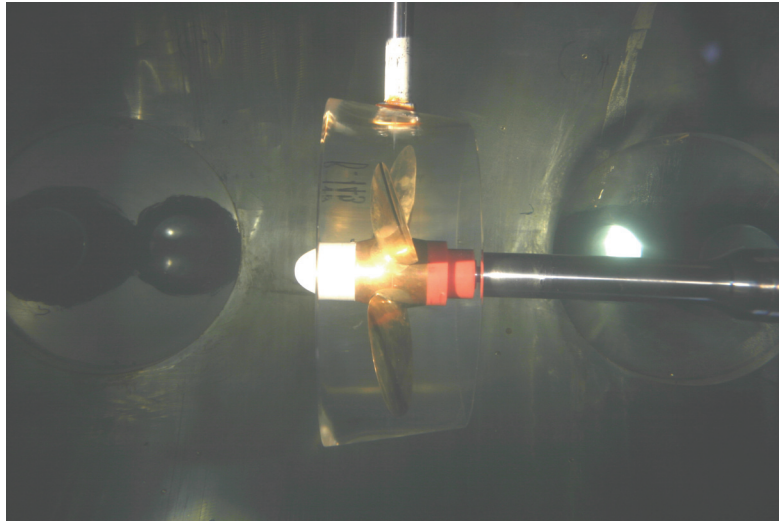


Figure D.1: Photo of the cavitation tunnel experimental set-up.

Parameter	Symbol	Unit	Accuracy	Sensor
Advance speed	$V_a$	m/s	1% ( $V_a > 1$ )	Pitot tube
Duct trust	$T_{ad}$	N	0.5%	Strain gauges
Propeller thrust	$T_{ap}$	N	0.5%	Inductive transducer
Propeller torque	$Q_a$	Nm	0.5%	Strain gauges
Shaft speed	$n$	1/s	0.5%	Pulse counter
Submergence	$h$	m	0.5%	Ultra sonic

Table D.1: Measurements in the cavitation tunnel experimental setup.

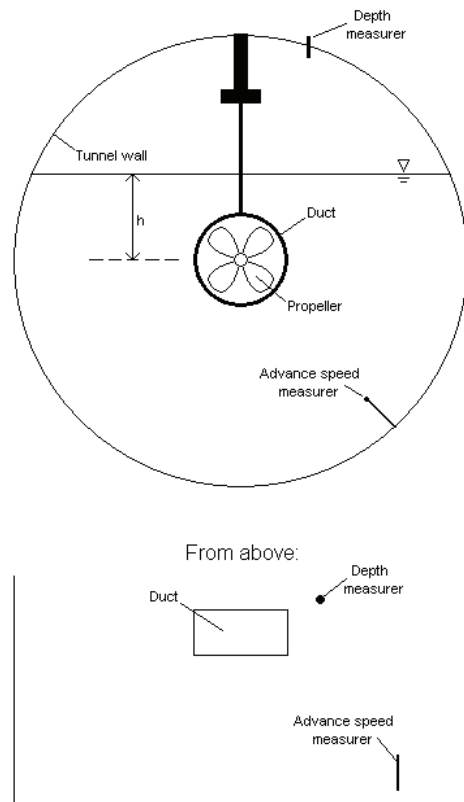


Figure D.2: Sketch of the cavitation tunnel experimental set-up, taken from Ruth (2005).

## D.2 Scaling laws

This section is taken entirely from Ruth and Smogeli (2006). According to Shiba (1953) the two most important parameters when scaling propeller performance from model scale to full scale are:

1. Geometrical similarity:

$$\frac{L_s}{L_m} = \lambda. \quad (\text{D.1})$$

2. Kinematic similarity:

$$J_{a,m} = \frac{V_{a,m}}{n_m D_m} = \frac{V_{a,s}}{n_s D_s} = J_{a,s}. \quad (\text{D.2})$$

Here,  $\lambda$  is the scale,  $L$  is any characteristic length,  $J_a$  is the advance number,  $V_a$  is the advance speed,  $n$  is the shaft speed,  $D$  the propeller diameter, suffix  $s$  means full scale, and suffix  $m$  means model scale. Further, depending on the operational condition, the following dimensionless parameters have influence on the propeller performance (Shiba, 1953; Gutsche, 1967; Kruppa, 1972; Brandt, 1973; ATTC, 1974; Scherer, 1977; Guoqiang *et al.*, 1989; Olofsson, 1996; ITTC, 1999b):

3. Submergence ratio:

$$\frac{h}{R}. \quad (\text{D.3})$$

4. Reynolds' number:

$$R_n = \frac{V_\infty c}{\nu}. \quad (\text{D.4})$$

Reynolds' number similarity is not required if  $R_n > 5 \cdot 10^5$ , or if corrections for  $R_n$  are done according to ITTC (1999a), which requires  $R_n > 2 \cdot 10^5$ .

5. Froude number:

$$F_{nD} = n \sqrt{\frac{D}{g}}. \quad (\text{D.5})$$

Froude number similarity is not required if  $F_{nD} > 3 - 4$ . In full scale,  $F_{nD}$  will typically be between 0 and 1.4 (Shiba, 1953).

6. Cavitation number:

$$\sigma_c = \frac{p_{static} - p_{cav}}{\frac{1}{2} \rho V_\infty^2}. \quad (\text{D.6})$$

7. Weber's number:

$$W = nD \sqrt{\frac{\rho}{s} D}. \quad (\text{D.7})$$

Scaling requirement:	1	2	3	4	5	6	7
Non-ventilated	x	x	x	x			
Fully ventilated	x	x	x	x	x	(x)	
Partially ventilated	x	x	x	x	x	x	

Table D.2: Scaling requirements in the different regimes at low advance speeds.  
Scaling requirement 1-7 refers to (D.1)-(D.7).

Here,  $h$  is the submergence of the propeller shaft,  $R$  is the propeller radius,  $V_\infty$  is the velocity seen by the propeller blade at  $0.7R$ ,  $c$  is the chord length of the propeller blade at radius  $0.7R$ ,  $\nu$  is the kinematic viscosity of the water,  $g$  is the gravity,  $\rho$  is the density of the water,  $s$  is the surface tension of the water, which equals 0.072 in fresh water,  $p_{static}$  is the static water pressure at a given submergence, and  $p_{cav}$  is the pressure in the cavity.

The total thrust  $T_a$  and the propeller torque  $Q_a$  are scaled by the total thrust coefficient  $K_T$  and the torque coefficient  $K_Q$ , as in (2.6, 2.7):

$$K_T (J_a, P/D) = \frac{T_a}{\rho D^4 n^2}, \quad (\text{D.8})$$

$$K_Q (J_a, P/D) = \frac{Q_a}{\rho D^5 n^2}, \quad (\text{D.9})$$

where  $P/D$  is the pitch ratio. As stated in Section 2.3.2, the operating condition of the propeller may be divided into three regions; non-ventilated, partially ventilated, and fully ventilated (Gutsche, 1967; Brandt, 1973; Fleischer, 1973; Hashimoto *et al.*, 1984; Guoqiang *et al.*, 1989). All these regimes are found in the experimental results from the cavitation tunnel. The scaling laws described here are based on experiments with non-ducted propellers, but are assumed to be valid also for ducted propellers, since non-ducted propellers and ducted propellers are scaled in the same way in the non-ventilated regime. The scaling laws in the different regimes are summarized in Table D.2 and further commented below.

### D.2.1 The non-ventilated regime

In this regime, no significant ventilation occurs. This means that the propeller is deeply submerged, or that the ventilation is light and not affecting the total thrust or the torque significantly. When both the model scale and the full scale propeller are in the non-ventilated regime, it is possible to scale the results by satisfying the requirements given in Table D.2. According to Scherer (1977) it is believed that the full scale propeller does not ventilate as easily as the model scale propeller. It is therefore assumed that if the model scale propeller is non-ventilating, then also the full-scale propeller will be non-ventilating. Reynolds' number of  $2 \cdot 10^5$  corresponds to a shaft speed of  $n = 4$  in the model tests. The conclusion is that the non-ventilated model scale results can be scaled to full scale when the shaft speed  $n > 4$  in model scale.

### D.2.2 The fully ventilated regime

This is when a single ventilated cavity is covering the propeller blade, meaning that the pressure on the suction side of the propeller blade is almost atmospheric. If the conditions given in Table D.2 are satisfied, and both the model scale propeller and the full-scale propeller are fully ventilated, it is possible to scale the results in this regime. It is, however, uncertain how to confirm whether or not the full scale propeller is going to be fully ventilated. Requirement 6, cavitation number similarity, is actually obtained through kinematic similarity, submergence ratio similarity, and Froude number similarity. With  $p_{static} = p_{atm} + \rho gh$ , where  $p_{atm}$  is the atmospheric pressure, the cavitation number becomes:

$$\sigma_c = \frac{p_{atm} + \rho gh - p_{cav}}{\frac{1}{2}\rho V_\infty^2}. \quad (\text{D.10})$$

Since  $p_{cav} \approx p_{atm}$  when the propeller is fully ventilated, (D.10) can be simplified to:

$$\sigma_c = \frac{2gh}{V_\infty^2} = \frac{1}{((0.35\pi)^2 + J_a^2)} \frac{h}{R} \frac{g}{Dn^2}. \quad (\text{D.11})$$

If  $J_{a,m} = J_{a,s}$ ,  $h_m/R_m = h_s/R_s$  and  $F_{nD,m} = F_{nD,s}$ , the result is that  $\sigma_{c,m} = \sigma_{c,s}$ . The Reynolds' number criterion restricts the scaling to shaft speeds equal to 4 and larger in model scale. The realistic Froude numbers in full scale corresponds to shaft speeds from 0 to 9 in model scale.

### D.2.3 The partially ventilated regime

This is when only part of the propeller is ventilated. The ventilation is said to be unstable when the propeller's degree of ventilation is not stationary, but is a function of time. The required scaling parameters are summarized in Table D.2. Although the pressure in the ventilated cavity is nearly atmospheric, there may exist other non-ventilated cavities (Kruppa, 1972). These non-ventilated cavities require cavitation number similarity. It would then require a free surface depressurized cavitation tunnel to do the experiments. The model tests presented here were all performed at atmospheric pressure.

In conclusion, it is not possible to scale the results in the partially ventilated regime to full scale for the experimental results presented here. There is, however, no reason to believe that the qualitative behavior of a full scale propeller will differ much from the results obtained for a model scale propeller.

### D.2.4 Effect of Weber's number

The Weber's number  $W$  describes the relationship between surface tension forces and inertial forces. Shiba (1953) and ITTC (1999b) state that  $W$  is important when determining the critical advance number, which is the advance number at which ventilation occurs for a given submergence ratio and shaft speed. In this

work, only low advance numbers are considered, and the results are extrapolated to be valid for  $J_a = 0$ . This means that the critical advance number in this case is of small interest.  $W$  will no longer influence the critical advance number when it is larger than 180. In the model tests performed in the cavitation tunnel,  $W$  is between 15 and 368, and  $W > 180$  for  $n > 12$ .

## D.3 Additional experimental results

### D.3.1 Ducted propeller

Figure D.3 shows the ventilation thrust loss factor  $\beta_{TV}$  and the relative thrust  $T_a/T_{\max}$  from the experiments with a ducted propeller in the cavitation tunnel (Aarseth, 2003), and the corresponding  $\beta_{TV}$  and  $T_a/T_{\max}$  from the simulation model for ducted propellers, as shown in Figure 2.19. The experimental results are the same as the ones given in Figures 2.12 and 2.13, where  $n_{bp}$  has been set to 20 for the scaling of  $n$ . The propeller torque loss factor  $\beta_{QV}$  and relative torque  $Q_a/Q_{\max}$  – from both experiments and the simulation model – are shown in Figure D.4.  $\beta_{QV}$  is calculated from (2.77) with  $m = 0.65$ . By comparing the experimental results with the simulation model, it is clear that the main characteristics of both the thrust and torque loss is captured in the model. From the curves alone, it seems that the parameters of the loss function could have been chosen to give better correspondence. However, these parameters were used in the simulation model time-series verification in Section 2.4.5, and found to give good correspondence there.

A new set of experiments with the same experimental set-up was performed by Ruth (2005), and partly presented in Ruth and Smogeli (2006). An example of the results is given in Figure D.5, which shows the thrust as a function of  $h/R$  and  $n$  for the ducted propeller with  $P/D = 1$ . More results for varying  $P/D$ , and a simulation model for a ducted CPP can be found in Ruth and Smogeli (2006). The figure should be comparable to the lower left plot in Figure D.3. The results largely agree, but it is clearly seen that the transition between the ventilated and the non-ventilated regime for high  $n$  is less steep in Figure D.5. This deserves some further attention. First of all, it should be noted that the transition between the ventilated and the non-ventilated regime is done through the partially ventilated regime, corresponding approximately to  $0.9 \leq h/R \leq 1.2$  for the higher propeller shaft speeds. As discussed in Section 2.3.2 and illustrated in Figure 2.11, this regime mainly exists as an unstable transition between the non-ventilated and ventilated regime for low  $J_a$ . Interpretation of the experimental results in the unstable, partially ventilated regime is difficult. If a long time series is recorded, where the propeller shifts between ventilated and non-ventilated condition, and the mean values from the whole run are used, the slope of the thrust loss factor will become less steep. A simulation model based on this may give a wrong evolution of a single ventilation incident, since the actual ventilation develops faster than the average values would indicate. Hence,

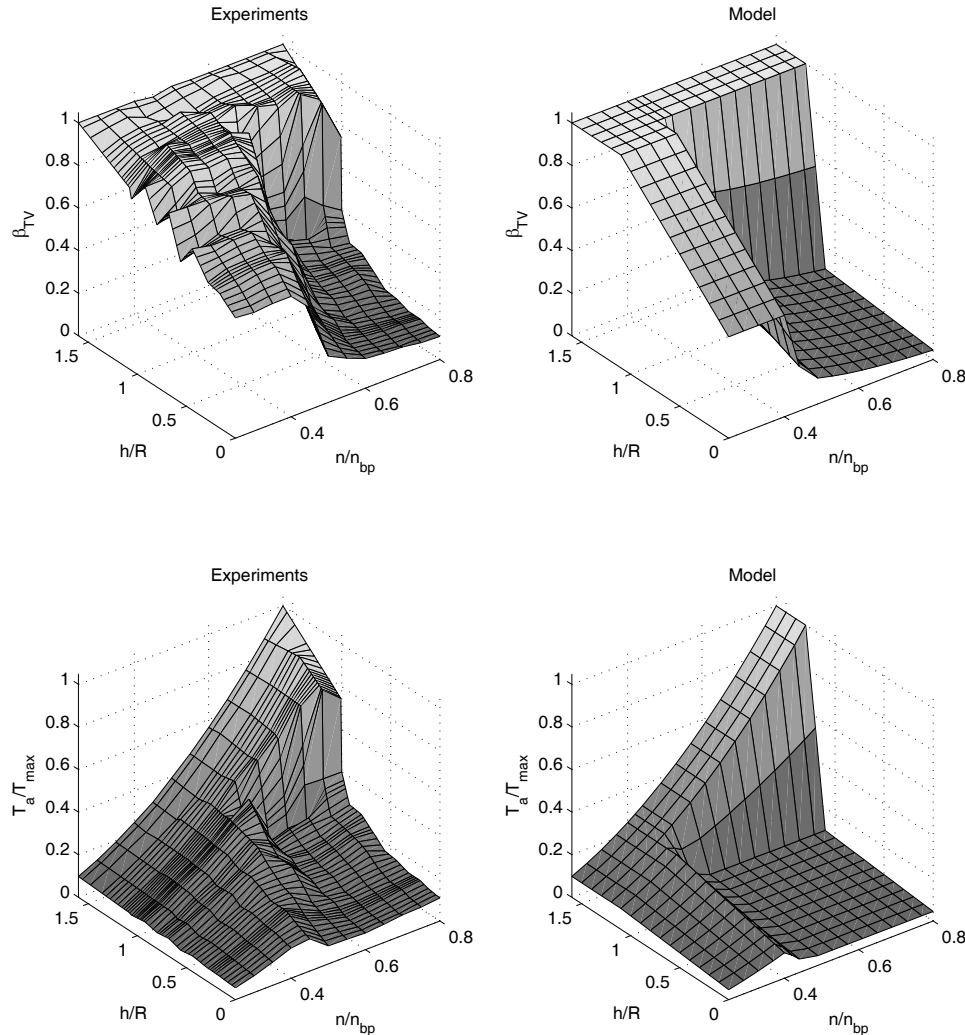


Figure D.3: Comparison of the thrust of a ducted propeller during ventilation, from experimental results (left) and the simulation model (right).

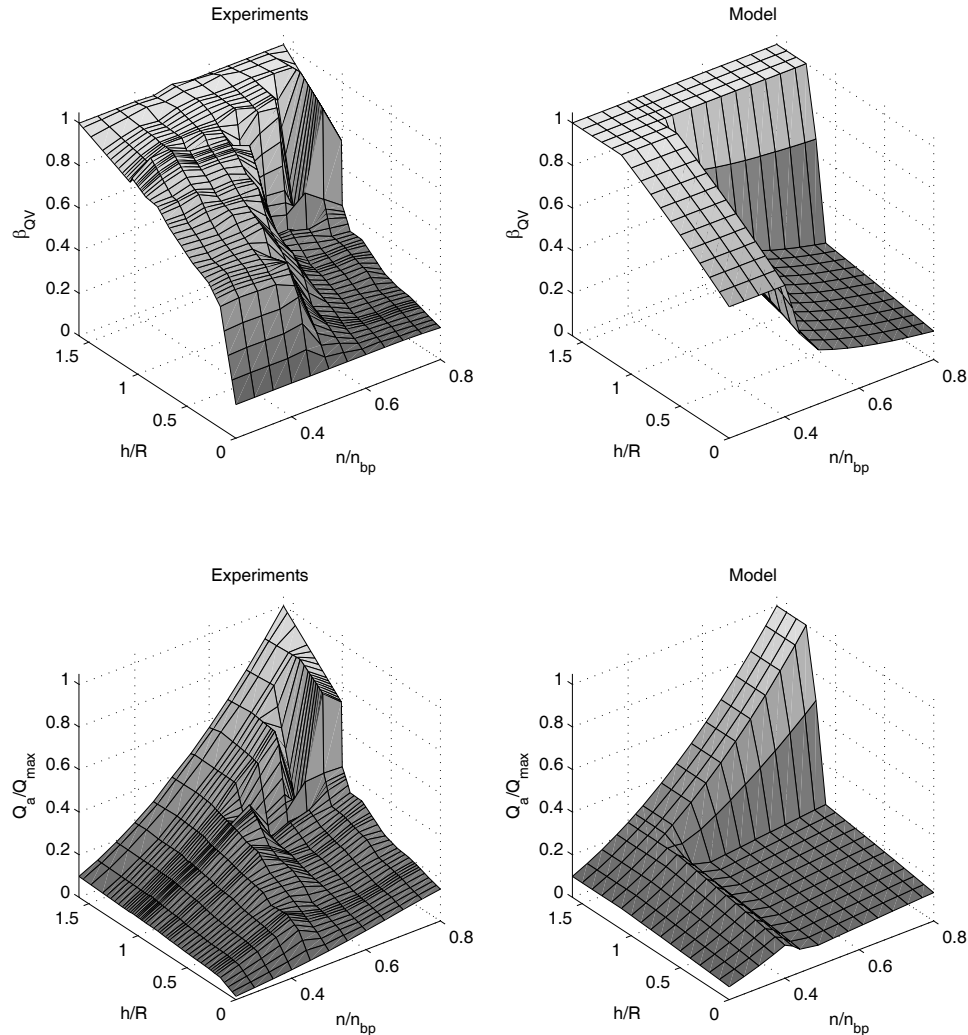


Figure D.4: Comparison of the torque of a ducted propeller during ventilation, from experimental results (left) and the simulation model (right).

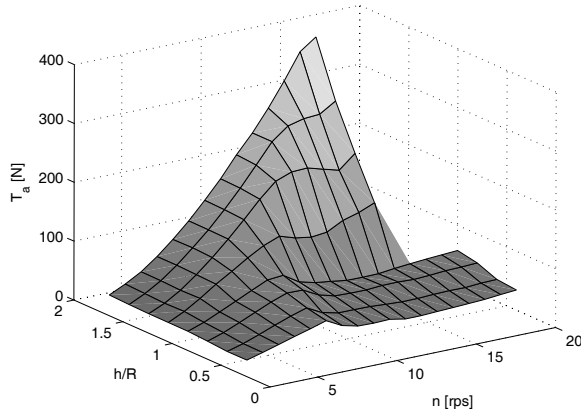


Figure D.5: Thrust  $T_a$  as a function of  $h/R$  and  $n$  for a ducted propeller.

the simulation model should have sharper transitions between non-ventilated and ventilated regime in order to improve the time-domain simulations.

In the experimental results from Aarseth (2003) shown in Figures D.3 and D.4, the time series on which the curves are based have been chosen with this in mind; manual inspection revealed if the propeller operating condition seemed to be dominated by ventilation or not, and the time series picked accordingly. The simulation model could then be based directly on these curves.

In the results in Ruth (2005), the mean values from the runs in the unstable ventilated regime were used, giving lower steepness of the thrust loss factor slope. However, a simulation model for controllable pitch propellers developed from these results was in Ruth and Smogeli (2006) still shown to give good agreement with experimental time series.

Another possible explanation of the deviation between the two sets of results, is that the experiments in Aarseth (2003) were performed at  $J_a = 0.2$ , whereas the experiments in Ruth (2005) were performed at the lowest achievable advance ratio, and then extrapolated to  $J_a = 0$ . It is plausible that the operating condition may have been more stable at  $J_a = 0.2$ , and that the results therefore were easier to interpret. Anyhow, both the simulation model presented in Section 2.4.4 and the simulation model from Ruth and Smogeli (2006) have shown good agreement with experimental time series.

### D.3.2 Open propeller

Figure D.6 shows the relative thrust  $T_a/T_{\max}$  and torque  $Q_a/Q_{\max}$  for an open propeller from Ruth (2005), and the corresponding values from the simulation model in Figure 2.18.  $n_{bp}$  has been set to 20 for the scaling of  $n$  in the experimental results. The parameters for the simulation model were chosen as

in Figure 2.18, and  $\beta_{QV}$  calculated from (2.77) with  $m = 0.8$ . As discussed above, it has been chosen to model a sharper transition between the ventilated and non-ventilated condition than what is indicated by the experimental results. Apart from this, the simulation model can be seen to capture the main characteristics of the ventilation loss effects. It is interesting to notice the difference in behavior during ventilation for the ducted propeller in Figure D.5 and the open propeller in Figure D.6. For low  $h/R$ , the ducted propeller has a distinct “ridge” of higher thrust for low shaft speed ( $n \approx 9\text{rps}$  is Figure D.5, and  $n/n_{bp} \approx 0.35$  in Figure D.3), and the thrust is not increasing for increasing shaft speed during ventilation. For the open propeller, the “ridge” of higher thrust seems not to be present, and the thrust during ventilation is slightly increasing for increasing shaft speeds. This difference in characteristics is also present in the experimental results presented in Chapter 7.

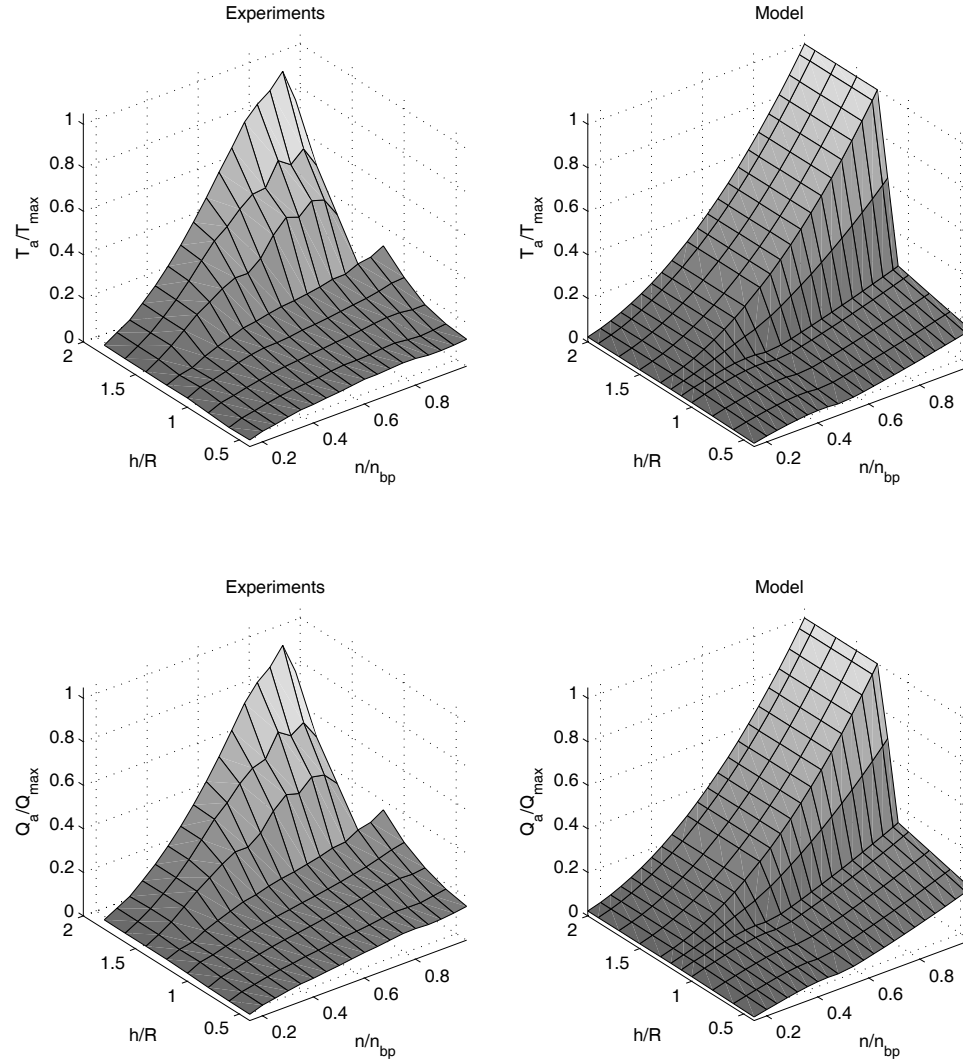


Figure D.6: Comparison of the thrust and torque of an open propeller during ventilation, from experimental results (left) and the simulation model (right).

## Appendix E

# Additional thruster control results

This appendix contains additional control laws and discussions. Section E.1 shows how torque control can be used in fault-tolerant thruster control, Section E.2 demonstrates some of the control options that become available with additional instrumentation, and Section E.3 presents some related output feedback controllers. Section E.4 presents an output feedback shaft speed controller with implicit advance velocity compensation, including experimental results.

### E.1 Fault-tolerant control

Fault-tolerant control is in general considered to be outside the scope of this thesis. However, it is interesting to note that the torque controller as formulated in (3.29) with the friction compensation scheme from (3.19) and the inertia compensation scheme from (3.22) is a pure feedforward controller, and hence independent of any feedback signal. If one of the controllers in Table 3.1 is in use, and the shaft speed feedback fails, it is then possible to switch to the torque controller. It is assumed that the inner torque control loop of the motor still is working; this is a prerequisite for any thruster controller to work. If a torque limiting algorithm as in (3.25) is implemented in the controller, it will also be necessary to replace  $n$  with  $n_r$  from (3.1) in (3.25). The operation can then be continued without significant performance deterioration.

This fault-tolerant control scheme requires that the shaft speed feedback signal failure is detected. This may be done by common signal quality checking, considering e.g. signal range, wild-points, and signal variance (Grøvlen *et al.*, 1998), or by statistical methods like the CUSUM algorithm (Blanke *et al.*, 2003).

Since the performance of the active controller already may be unacceptable by the time the sensor failure is detected, it is desirable to carry out a rapid switch to torque control. Additionally, it is not considered pertinent to have an

automatic switch back to the old controller – when a sensor failure is detected, the failure should be corrected before a manual restart of the system is performed. Hence, concepts like dwell-time and hysteresis-based switching, which can be utilized to ensure stability when switching between a set of controllers (Hespanha and Morse, 2002; Hespanha *et al.*, 2003), will probably not be necessary. It is instead considered sufficient to switch from the current controller output  $Q_{ci}$  to the output  $Q_{cq}$  of the torque controller immediately after the failure has been detected. It may also be appropriate to include a rate limit on the switched output in order to reduce transients in the motor input. Details of implementation will not be further considered here.

The scenario outlined above is reminiscent of the case study of a ship propulsion system presented in Blanke *et al.* (1998, 2003), where fault-tolerant control of a diesel engine with a mechanical direct-drive CPP is considered. The ship propulsion system is in these references treated in a much broader perspective, with various fault scenarios, diagnosis, and fault handling. However, one specific case study, which also is the focus of Blanke *et al.* (1998), is a fault in the shaft speed feedback measurement. This is considered to be a high risk fault. It is detected by a nonlinear adaptive observer, which also enables distinguishing between a fault in the shaft speed feedback and a fault in the engine governor. When a shaft speed feedback fault is detected, the proposed remedial action is to apply sensor fusion using the relationships between propeller torque, vessel speed, and shaft speed. For a given pitch, the propeller torque characteristics is taken to be linear as in (2.26), i.e.:

$$Q_a \approx Q_{nn}(P/D)n|n| + Q_{nv}(P/D)|n|V_a, \quad (\text{E.1})$$

where  $Q_{nn}$  and  $Q_{nv}$  are functions of the pitch ratio  $P/D$ . The advance velocity  $V_a$  is estimated from the vessel speed  $U$  and a hull wake factor  $w_h$  using (2.42). The motor torque  $Q_m$  is assumed measurable from the governor setting, i.e.  $Q_m = K_y Y$ , where  $Y$  is the governor input from a shaft speed PI controller as in (3.27), and  $K_y$  the motor torque constant, see (2.56). Neglecting friction and using the steady-state torque balance from the rotational dynamics (2.50), an estimate  $\hat{n}$  of the shaft speed, which is assumed to be positive for a CPP, is found from:

$$\begin{aligned} Q_m &= Q_a \\ K_y Y &= Q_{nn}(P/D)\hat{n}|n| + Q_{nv}(P/D)|n|U(1-w_h) \\ \downarrow \\ \hat{n} &= \frac{-Q_{nv}(P/D)U(1-w_h)}{2Q_{nn}(P/D)} \\ &\quad + \frac{\sqrt{Q_{nv}(P/D)^2U^2(1-w_h)^2 + 4Q_{nn}(P/D)K_y Y}}{2Q_{nn}(P/D)}. \end{aligned} \quad (\text{E.2})$$

The faulty signal  $n$  is then replaced by  $\hat{n}$  in the shaft speed controller, and the operation can continue with reduced performance.

There are, however, a few limitations that should be addressed. The linear torque characteristics is mainly applicable to open propellers in the first quadrant of operation. It is also assumed that the ship speed  $U$  is available as a measurement to the low-level thruster controller. Additionally, for propellers other than the main propeller, there is normally no good estimate of the advance velocity available. Hence, for DP operations with multiple propellers operating in dynamic flow, this approach may be of limited applicability. The simpler approach outlined in the beginning of this section may then be more appropriate. It is also expected that the thrust production will be superior with the torque controller when compared to the re-configured shaft speed controller based on  $\hat{n}$ .

## E.2 Additional instrumentation

In most of this work, it has been assumed that only the shaft speed and the motor torque are available as measurements, see Section 3.1. However, if the propulsion unit could be equipped with additional instrumentation, new control options would appear. The two most desirable measurements for low-level thruster controller design would be the propeller thrust and torque, with the feedback signals termed  $T_{fb}$  and  $Q_{fb}$ , respectively. This section explores some of the new options that become available with propeller thrust and/or torque measurements.

### E.2.1 Thrust feedback control

If a thrust feedback signal of high quality is available, it is possible to close the loop directly with the thrust measurement in e.g. a PID controller. With the thrust error  $e_t$ , the thrust controller output  $Q_{ct}$  becomes :

$$\begin{aligned} e_t &= T_r - T_{fb}, \\ Q_{ct} &= K_{tp}e_t + K_{ti} \int_0^t e_t(\tau) d\tau + K_{td}\dot{e}_t, \end{aligned} \quad (\text{E.3})$$

where  $K_{tp}$ ,  $K_{ti}$ , and  $K_{td}$  are the nonnegative PID gains. As before, the motor torque is controlled by its inner torque loop. In order to give good performance, such a formulation requires a relatively low level of noise on  $T_{fb}$ . Additionally, the thrust sensor must have a high level of reliability. As of today, thrust control seems not to be a realistic solution in industrial implementations for surface vessels. This may be explained by a lack of suitable sensors, and industrial reluctance to install such sensors even if available.

In Beek and Mulder (1983) a system for fuel optimization of CCP is presented, based on measurements of propeller speed, pitch, and thrust. The proposed thrust measurement was realized by sensitive semi-conductor strain gauges attached to the propeller shaft, achieving repeatability better than 0.5% over several successful trials. A similar approach is taken in Bakountouzis

(1992). However, long-term reliability of the feedback signal is not discussed. Deniellou *et al.* (1998) proposed a thrust control scheme as in (E.3) for AUV's. The thrust was measured by a displacement gauge and a displacement sensor, with a measurement uncertainty of less than 0.1% of the effective measurement range. Also the dynamic response was investigated, and found to be satisfactory. Experimental results with a PI controller were provided to show the step response and tracking properties of the controller.

With a controller such as (E.3), the torque feedback  $Q_{fb}$  becomes superfluous. However, if available, it could be used for diagnostics and fault-tolerant control. This will not be further treated here. A thrust controller will be valid for any vessel speed, since the mapping from reference to actual thrust is accurate regardless of the inflow to the propeller. Hence, controller modifications for transit, as discussed in Section 8.2, are not needed.

### E.2.2 Thrust control from torque feedback

In Section 2.1.8, it was shown that there for open propellers is a nearly linear relationship between the thrust and torque coefficients, and that this relationship is valid across a large range of operating conditions. Hence, if a thrust feedback signal is unavailable, but a propeller torque feedback signal is available, the  $K_T - K_Q$  relationship in (2.48) can be used to calculate an estimate  $\hat{T}_{fb}$  of  $T_a$  from  $Q_{fb}$ :

$$\begin{aligned} K_T &= a_t K_Q + b_t, \\ \Downarrow \\ \hat{T}_{fb} &= \frac{a_t}{D} Q_{fb} + b_t \rho n^2 D^4, \end{aligned} \quad (\text{E.4})$$

where  $a_t$  and  $b_t$  are propeller constants found from the open-water characteristics.  $\hat{T}_{fb}$  from (E.4) can then replace  $T_{fb}$  in (E.3). This control formulation requires a high quality torque feedback signal. The performance of the thrust controller with torque feedback is then expected to be similar to the one with thrust feedback. A torque sensor for this purpose was presented in Lemarquand (1997), and reported to give satisfactory signal quality. The torque feedback thrust controller is in principle only feasible for open propellers. For ducted propellers, no simple relationship between thrust and torque has been shown, and (E.4) cannot be expected to hold.

### E.2.3 Propeller torque feedback control

With a propeller torque feedback signal, it is possible to close the thruster control loop directly with this, instead of using the torque-thrust relationship as proposed in the previous section. This can be done in a similar manner as in

Section E.2.1, with a PID controller operating on the torque error  $e_q$ :

$$\begin{aligned} e_q &= Q_r - Q_{fb}, \\ Q_{cqp} &= K_{qp}e_q + K_{qi}\int_0^t e_q(\tau)d\tau + K_{qd}\dot{e}_q, \end{aligned} \quad (\text{E.5})$$

where  $Q_r$  is the torque reference calculated from (3.2),  $Q_{cqp}$  is the propeller torque controller output, and  $K_{qp}$ ,  $K_{qi}$ , and  $K_{qd}$  are the nonnegative PID gains. As before, the motor torque is controlled by its inner torque loop. The same requirements to signal quality and reliability as for the thrust controller presented in Section E.2.1 apply. The friction and inertia compensation schemes from Section 3.7 become unnecessary with the propeller torque feedback controller, since the propeller torque is controlled directly.

#### E.2.4 Propeller power feedback control

Another control option that becomes available with a propeller torque measurement, is propeller power control. With the measurements  $Q_{fb}$  and  $n$ , the signed measured propeller power  $P_{fb}$  becomes:

$$P_{fb} = Q_{fb}2\pi|n|, \quad (\text{E.6})$$

and the control loop may be closed with a PID controller operating on the power error  $e_p$ :

$$\begin{aligned} e_p &= P_{rs} - P_{fb}, \\ Q_{cpp} &= K_{pp}e_p + K_{pi}\int_0^t e_p(\tau)d\tau + K_{pd}\dot{e}_p, \end{aligned} \quad (\text{E.7})$$

where  $P_{rs}$  is the signed power reference calculated from (3.4),  $Q_{cpp}$  is the propeller power controller output, and  $K_{pp}$ ,  $K_{pi}$ , and  $K_{pd}$  are the nonnegative PID gains. The motor torque is controlled by its inner torque loop, and the same requirements to signal quality and reliability as for the thrust controller presented in Section E.2.1 apply. The friction and inertia compensation schemes from Section 3.7 become unnecessary with the propeller power controller, since the propeller power is controlled directly.

#### E.2.5 Dynamic control coefficients

If both propeller thrust and torque measurements are available, but the quality of the signals is not of sufficient quality for closing the loop directly (due to noise, update rate, reliability, etc.), an alternative approach exists. From (2.6, 2.7), the feedback signals  $T_{fb}$  and  $Q_{fb}$  may, together with the measured  $n$ , be used in an on-line parameter estimation scheme for the prevailing thrust and torque coefficients, termed  $\hat{K}_T$  and  $\hat{K}_Q$ . The adaption should be slow enough to avoid e.g. wave-induced disturbances and noise, but fast enough to capture

the change in operating conditions due to steady-state current or vessel speed. The estimates can then be used as control coefficients, i.e.  $K_{TC} = \hat{K}_T$  and  $K_{QC} = \hat{K}_Q$ , with any one of the control schemes defined in Table 3.1. This means that  $\hat{K}_T$  and  $\hat{K}_Q$  are used instead of the nominal coefficients  $K_{T0}$  and  $K_{Q0}$  in the controllers. Assuming that the estimates  $\hat{K}_T$  and  $\hat{K}_Q$  will be close to the true mean values of  $K_T$  and  $K_Q$ , the main advantages of this approach are:

- The control schemes will give good performance for all vessel speeds, since estimates of the actual thrust and torque coefficients are used. This removes most of the difficulties discussed in Section 8.2, since less model knowledge is needed.
- The quality of the feedback signals is less critical for performance, which means that the control schemes are feasible with low-cost sensors.
- If a sensor fails, the parameter adaption can be switched off, and either 1) the current values of the estimates can be used in continued operation, or 2) the control coefficients can be ramped back to the nominal values  $K_{T0}$  and  $K_{Q0}$ . The control scheme is therefore robust with respect to sensor failure.
- For e.g. the combined torque/power controller, the good properties with respect to wear and tear and predictable power consumption may be utilized, with increased performance during transit.

The on-line parameter estimation schemes for  $\hat{K}_T$  and  $\hat{K}_Q$  can be found from e.g. Ioannou and Sun (1995). Defining the output  $y_T = T_{fb}$  and the input  $u_T = \rho D^4 n |n|$ , (2.3) can be written as:

$$y_T = K_T u_T. \quad (\text{E.8})$$

Using the estimate  $\hat{K}_T$  of  $K_T$ , the predicted output  $\hat{y}_T$  and the prediction error  $\varepsilon_T$  become:

$$\hat{y}_T = \hat{K}_T u_T, \quad (\text{E.9})$$

$$\varepsilon_T = y_T - \hat{y}_T = K_T u_T - \hat{K}_T u_T = -\hat{K}_T u_T, \quad (\text{E.10})$$

where the parameter estimation error  $\tilde{K}_T = \hat{K}_T - K_T$ . Using the gradient method, the recursive parameter estimation scheme becomes:

$$\dot{\hat{K}}_T = -\gamma_T \varepsilon_T u_T, \quad \hat{K}_T(0) = \bar{K}_T, \quad (\text{E.11})$$

where  $\gamma_T > 0$  is the adaptive gain and  $\bar{K}_T$  the initial value of  $\hat{K}_T$ . For any bounded  $u(t)$  and  $\dot{u}(t)$ , the prediction error converges to zero (Ioannou and Sun, 1995). Additionally, it can be shown that a necessary and sufficient condition for  $\tilde{K}_T(t)$  to converge to zero exponentially fast is that  $u(t)$  is PE.  $u(t)$  is PE

if it is sufficiently rich of order 1, i.e. at least a nonzero constant signal. This corresponds to nonzero shaft speed, which is an intuitively sensible requirement. Correspondingly, the estimate  $\hat{K}_Q$  of  $K_Q$  can be calculated from:

$$\dot{\hat{K}}_Q = -\gamma_Q \varepsilon_Q u_Q, \quad \hat{K}_Q(0) = \bar{K}_Q, \quad (\text{E.12})$$

with adaption gain  $\gamma_Q > 0$ , output  $y_Q = Q_{fb}$ , input  $u_Q = \rho D^5 n |n|$ , prediction error  $\varepsilon_Q = y_Q - \hat{K}_Q u_T$ , and initial value  $\bar{K}_Q$ . As stated above, the gains  $\gamma_T$  and  $\gamma_Q$  should be chosen such that noise and wave-frequency disturbances are rejected, while a change in operating condition due to vessel speed or current is captured. From a practical point of view, it may also be desirable to disable adaption below a certain shaft speed threshold  $n_a$ , i.e.

$$\varepsilon_T = \begin{cases} y_T - \hat{y}_T, & |n| \geq n_a, \\ 0, & |n| < n_a, \end{cases} \quad (\text{E.13})$$

and similarly for  $\varepsilon_Q$ .

In extreme operating conditions, with ventilation and water exits, the adaption should be switched off, since the thrust and torque models (2.6, 2.7) then will lead to rapidly changing  $K_T$  and  $K_Q$ . With low adaption gains,  $\hat{K}_T$  and  $\hat{K}_Q$  will not converge to any sensible values, and probably exhibit a drifting behavior. These uncertain parameters are not wanted in the control laws, and it would hence be preferable to use the values found from steady-state operation. How to detect such high loss incidents was treated in Section 6.3.

The torque measurement could, together with the motor torque  $Q_m$ , also be used to estimate the coefficients  $Q_{f0}$  and  $Q_{f1}$  used in the friction compensation scheme (3.19).

### E.3 Thrust, torque, and power output feedback control

In Section E.2, several new control options that become available with additional instrumentation were presented. All these controllers were of the PID type, closing the control loop with the error between desired and measured propeller thrust, torque, or power. Usually, however, additional instrumentation is not available. As additional control options, the controllers from Section E.2 may instead be implemented by output feedback, using one of the propeller torque estimation schemes presented in Chapter 5. These controllers then become significantly more complex than the other controllers for normal operating conditions, which are summarized in Table 3.1. As briefly discussed in Section E.2, the thrust, propeller torque, and propeller power feedback controllers circumvent the need for friction and inertia compensation, and hence reduce the necessary model knowledge. However, when implemented as output feedback controllers, this model knowledge is needed in order to implement the load

torque observer. For extreme conditions, the output feedback controllers are not believed to be appropriate, due to the problems with assuring robust performance during ventilation. The stability properties of the output feedback controllers will not be further considered.

### E.3.1 Thrust output feedback

The thrust output feedback scheme is similar to the thrust control scheme from Section E.2.2, except that the propeller load torque feedback  $Q_{fb}$  in (E.4) is replaced with the estimated load torque  $\hat{Q}_a$  from one of the observers. This scheme is therefore mainly applicable to open propellers, where the linear  $K_T - K_Q$  relationship in (2.48) holds. As discussed in Section 4.9, a thrust controller is not suited for applications where the propeller may be subject to large thrust losses – its performance during ventilation is significantly worse than that of the torque and power controllers. Hence, the thrust output feedback scheme is mostly relevant for underwater applications like AUV's or ROV's, or for deeply submerged propellers like azimuthing thrusters on a semi-submersibles. The latter are, however, usually of the ducted type, where (2.48) may not hold.

Using the linear observer from (5.7), the thrust-torque mapping from (E.4), and the controller from (E.3), the thrust output feedback scheme may be summarized as:

$$\begin{aligned} u &= k_g Q_m - Q_{ff0}(n_r), \\ \dot{\omega} &= \frac{1}{I_s} (u - \hat{Q}_a - Q_{f1}\dot{\omega}) + k_a(\omega - \dot{\omega}), \\ \dot{\hat{Q}}_a &= k_b(\omega - \dot{\omega}), \\ \hat{T}_a &= \frac{a_t}{D} \hat{Q}_a + b_t \rho n^2 D^4, \\ e_t &= T_r - \hat{T}_a, \\ Q_{ct} &= K_{tp} e_t + K_{ti} \int_0^t e_t(\tau) d\tau + K_{td} \dot{e}_t. \end{aligned} \quad (\text{E.14})$$

Here,  $Q_{ct}$  is the controller output,  $n_r$  is given from  $T_r$  by (3.1),  $\omega = 2\pi n$ ,  $Q_{ff0}(n_r)$  is given by (3.20),  $I_s$ ,  $Q_{f1}$ ,  $D$ ,  $a_t$ , and  $b_t$  are propeller constants,  $k_a$  and  $k_b$  are the observer gains, and  $K_{tp}$ ,  $K_{ti}$ , and  $K_{td}$  are the PID gains.

### E.3.2 Torque output feedback

The torque output feedback controller is similar to (E.5), with  $Q_{fb}$  replaced by  $\hat{Q}_a$ . The  $Q_a$  observer is formulated as in (E.14), and the remaining controller given from:

$$\begin{aligned} e_q &= Q_r - \hat{Q}_a, \\ Q_{cqp} &= K_{qp} e_q + K_{qi} \int_0^t e_q(\tau) d\tau + K_{qd} \dot{e}_q, \end{aligned} \quad (\text{E.15})$$

with  $Q_{cqp}$  the controller output,  $Q_r$  given from  $T_r$  by (3.2), and  $K_{qp}$ ,  $K_{qi}$ , and  $K_{qd}$  the PID gains.

### E.3.3 Power output feedback

The power output feedback controller is similar to (E.7), with  $P_{fb}$  replaced by  $\hat{P}_a$ , and  $\hat{P}_a$  calculated from  $\hat{Q}_a$ . The  $Q_a$  observer is formulated as in (E.14), and the remaining controller given from:

$$\begin{aligned}\hat{P}_a &= \hat{Q}_a |\dot{\omega}|, \\ e_p &= P_{rs} - \hat{P}_a, \\ Q_{cpp} &= K_{pp}e_p + K_{pi} \int_0^t e_p(\tau) d\tau + K_{pd}\dot{e}_p,\end{aligned}\quad (\text{E.16})$$

with  $Q_{cpp}$  the controller output,  $P_{rs}$  given from  $T_r$  by (3.4), and  $K_{pp}$ ,  $K_{pi}$ , and  $K_{pd}$  the PID gains.

## E.4 Shaft speed control with implicit $V_a$ compensation

In Fossen and Blanke (2000), a nonlinear output feedback propeller shaft speed controller for underwater vehicles, with feedback from estimated advance velocity, was presented. The advance velocity observer was designed based on the vehicle surge dynamics and a model of the flow dynamics. The flow dynamics model was as proposed in Blanke *et al.* (2000), based on the results by Yoerger *et al.* (1991), Healey *et al.* (1995), and Whitcomb and Yoerger (1999a). As discussed in Section 2, increasing advance velocity leads to decreasing thrust if the shaft speed is kept constant. The idea behind the controller in Fossen and Blanke (2000) was to compensate for the advance velocity, in order to improve the mapping from desired to actually produced thrust. The output feedback controller was shown to be uniformly globally asymptotically and uniformly locally exponentially stable. There are, however, three main limitations to the result: the propeller model was based on a linear open-water characteristics as in (2.25, 2.26), the advance velocity observer was only valid for  $V_a \geq 0$ , and the observer relied on the coupling between the propeller thrust and the vehicle surge dynamics. The two first limitations indicate that the result only is valid for open propellers in the first quadrant of operation, where the linear open-water characteristics approximation is relatively accurate, and  $V_a \geq 0$ . The third limitation indicates that the observer only will work for a vehicle equipped with a single propeller for each degree of freedom (or alternatively with several coordinated propellers), since it otherwise may be difficult to separate the contributions from several propellers to the surge dynamics. For an AUV or UUV, the limitations are not of major importance, since these vehicles usually operate at cruising speed in the first quadrant of operation, and are

equipped with a simple propulsion system for surge motion. For other vehicles, e.g. ROVs and surface vessels in DP, that may experience changing inflow due to current, waves, and low-speed manoeuvring, these limitations may become a problem.

#### E.4.1 Controller formulation

Instead of calculating an *explicit* estimate of  $V_a$  and using this in a model of the propeller characteristics, it is possible to formulate a shaft speed controller that *implicitly* compensates for changes in the advance velocity. The starting point is the shaft speed thrust sensitivity function from (4.16):

$$st_n(\cdot) \triangleq \frac{T_a}{T_r} = \frac{K_T}{K_{TC}}. \quad (\text{E.17})$$

In Figures 4.2 and 4.6, it is shown how  $st_n(\cdot)$  decreases with increasing  $V_a$ . This is also easily seen from an open-water diagram, e.g. Figure 2.1, since  $K_T$  for a fixed  $n$  decreases with increasing  $V_a$ . This is the behavior that the controller from Fossen and Blanke (2000) attempts to compensate for by increasing the shaft speed when the advance velocity increases. From (E.17), this could also be achieved by adjusting the control coefficient  $K_{TC}$ : with  $K_{TC} = K_T$ , the thrust sensitivity  $st_n(\cdot) = 1$ , and the desired thrust is produced. It is therefore proposed to use one of the observers from Section 5 to calculate an estimate  $\hat{K}_Q$  of  $K_Q$ , use the  $K_T - K_Q$  relationship in (2.48) to calculate an estimate  $\hat{K}_T$  of  $K_T$ , and use  $K_{TC} = \hat{K}_T$  in the normal shaft speed PI controller from (3.27). Using the  $K_Q$  estimation scheme in (5.26), the shaft speed controller with implicit advance speed compensation becomes:

$$\begin{aligned} u &= k_g Q_m - Q_{ff0}(n_r), \\ \hat{K}_Q &= \frac{4\pi^2}{\rho D^5} \hat{\theta}, \\ \hat{\theta} &= -\frac{k_0 |\omega|^3}{3I_s} + z, \\ \dot{z} &= k_0 \frac{\omega |\omega|}{I_s^2} (u - \hat{\theta} \omega |\omega| - Q_{f1}\omega), \\ K_{TC} &= a_t \hat{K}_Q + b_t, \\ n_r &= \text{sign}(T_r) \sqrt{\frac{|T_r|}{\rho D^4 K_{TC}}}, \\ Q_{cn} &= K_p e + K_i \int_0^t e(\tau) d\tau, \quad e = n_r - n. \end{aligned} \quad (\text{E.18})$$

Here,  $Q_{cn}$  is the controller output,  $k_0$  is the estimation gain, and  $K_p$  and  $K_i$  are the PI gains. A block diagram of the resulting control scheme is given in Figure

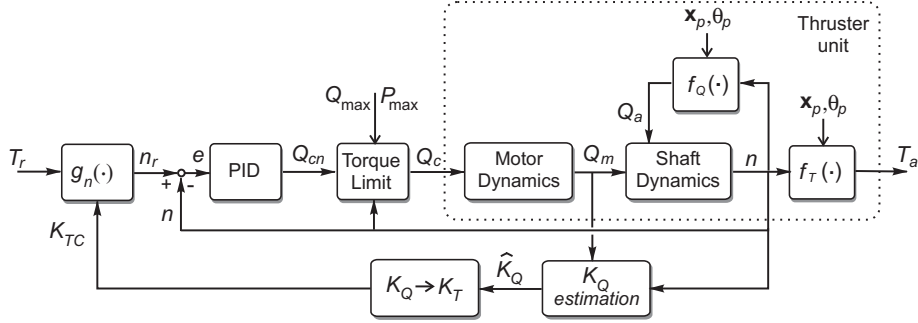


Figure E.1: Block diagram of the shaft speed controller with implicit  $V_a$  compensation.

E.1. Notice that the sole purpose of the observer is to aid in calculating the shaft speed setpoint  $n_r$ . Hence, the PI controller and  $K_Q$  estimation scheme can be tuned separately. The choice of  $k_0$  should be motivated from the desired properties of the closed-loop controller. If it is desired to compensate for all changes in inflow, also due waves and wave-frequency vessel motion,  $k_0$  must be chosen sufficiently high to capture these effects. If the motivation is to compensate only for the *mean* changes in inflow due to current and vessel low-frequency motion,  $k_0$  should be chosen lower, such that the wave-frequency disturbances are filtered out. If desired, the load torque observer in (5.7) with  $\hat{K}_Q$  calculation from (5.17) and (5.16) may be used instead of the  $K_Q$  estimation scheme from (5.26).

Since no assumption about the advance velocity or shape of the open-water characteristics has been made, except for the linear  $K_T - K_Q$  relationship in (2.48), this controller is valid for all 4 quadrants of operation – or as long as (2.48) holds. In addition, since no vessel dynamics are involved in the observer, the controller is valid for any open propeller on any vessel. The restriction to open propellers is due to the limitation in applicability of (2.48) for ducted propellers.

**Remark E.1** *If the main purpose of the controller is to counteract the loss of thrust due to varying advance velocity, the pure torque controller in (3.29) should also be considered. As can be seen in Figures 4.2 and 4.6, the torque controller is significantly less sensitive to changes in  $V_a$  than the other controllers. The level of complexity of the torque controller with friction and inertia compensation is also lower than that of the implicit  $V_a$  compensation controller in (E.18).*

**Remark E.2** *The stability of the proposed control scheme has not yet been addressed, and is considered a topic for further research.*

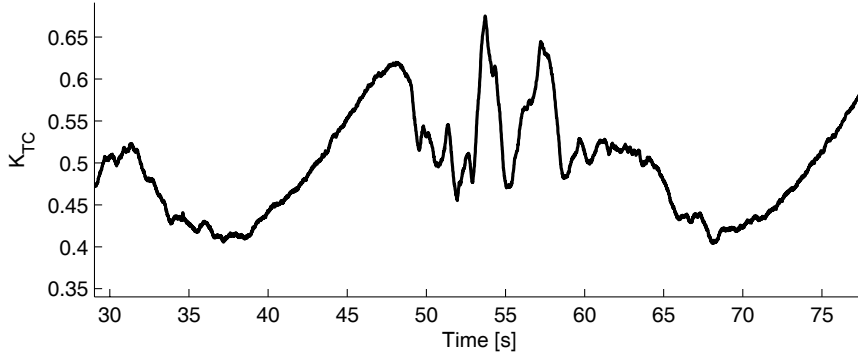


Figure E.2: Control coefficient  $K_{TC}$  used in the implicit  $V_a$  compensation scheme, calculated from the nonlinear observer. From experiments.

#### E.4.2 Experimental results

The implicit  $V_a$  compensation scheme was tested with the experimental facility described in Chapter 7.1, using the open propeller. As seen in Figure 7.5, the linear  $K_T - K_Q$  relationship in (2.48) holds well in this case. The propeller was kept deeply submerged, with no waves, and the carriage moved in a sinusoidal motion in the axial direction of the propeller to create inflow oscillations with velocity amplitude 1m/s and period 31.4s. The thrust reference was  $T_r = 200\text{N}$ . Four controllers were compared: shaft speed control, torque control, power control, and shaft speed control with implicit  $V_a$  compensation. The three fundamental controllers were used with the friction compensation scheme and other settings as described in Tables 7.4 and 7.5.

For the implicit  $V_a$  compensation scheme in (E.4), the PI gains were chosen as for the pure shaft speed controller, i.e.  $K_p = 0.2$  and  $T_i = 0.05$ . In the  $K_Q$  estimation scheme,  $Q_{f0}$ ,  $Q_{f1}$ , and  $I_s$  were chosen as in Table 7.7, and the estimation gain was chosen as  $k_0 = 1E - 10$ . In addition, it was chosen to filter  $\hat{K}_Q$  using a first order filter with time constant 0.1s.

The estimated thrust coefficient used in the implicit  $V_a$  compensation scheme is shown in Figure E.2, and the resulting time series of  $n$ ,  $T_a$ ,  $Q_a$ ,  $Q_m$ , and  $P_m$  are shown in Figure E.3. The propeller has positive inflow approximately for  $30s < t < 45s$  and  $62s < t < 77s$ , and negative inflow approximately for  $45s < t < 62s$ . Because of the uncontrollable nature of the flow in the basin, the time series should not be compared directly, but only serve as an indication of the performance of the various controllers. Especially for reverse flow, the loading is highly unstable. The three fundamental controllers can be seen to obtain their objectives: the shaft speed controller keeps the shaft speed nearly constant, the torque controller keeps the motor power constant, and the power

controller keeps the motor power nearly constant. It is interesting to note that the behavior of the implicit  $V_a$  compensation scheme is quite similar to the torque controller; the thrust and torque are kept nearly constant, even in the reverse flow regime, and the oscillations in shaft speed and power follow closely.

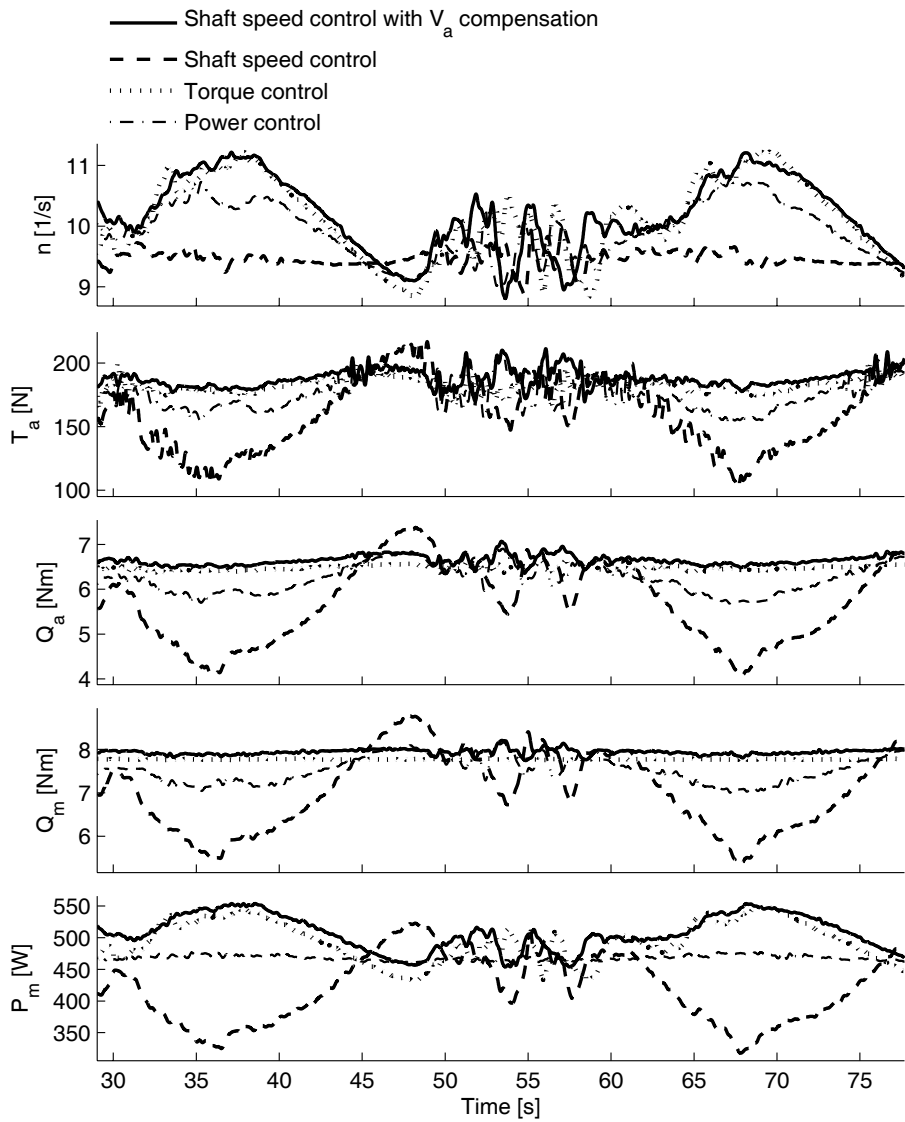


Figure E.3: Comparison of the implicit  $V_a$  compensation scheme with shaft speed, torque, and power control. From experiments.

## Appendix F

# Additional sensitivity function results

This appendix presents additional results for the sensitivity functions that were introduced in Chapter 4. Section F.1 presents the derivation of the combined QP controller thrust sensitivity function presented in Section 4.2.5, Section F.2 presents an extension of the sensitivity functions to account for friction compensation errors, and Section F.3 extends the Lyapunov analysis from Section 6.5.1 to get explicit bounds on the trajectories of the perturbed system.

### F.1 Combined controller thrust sensitivity

In Section 4.2.5, it was assumed that the combined controller thrust sensitivity function could be expressed as:

$$st_c(\cdot) = \frac{K_T}{K_{TC}} \left( \frac{K_{QC}}{K_Q} \right)^\kappa, \quad \text{for } \kappa \in [\frac{2}{3}, 1]. \quad (\text{F.1})$$

An approximation to  $\kappa$  will be derived in the following. Assume as before that at steady state  $Q_a = Q_{cc}$ , with  $\alpha_c = \alpha_c(n)$  from (3.36):

$$Q_a = Q_{cc} = \alpha_c Q_{cq} + (1 - \alpha_c) Q_{cp}. \quad (\text{F.2})$$

Inserting (3.29) for  $Q_{cq}$ , (3.32) for  $Q_{cp}$ , and (4.5) for  $n$  in (F.2):

$$\begin{aligned} Q_a &= \alpha_c \frac{K_{QC}}{K_{TC}} DT_r + (1 - \alpha_c) \frac{P_{rs}}{2\pi|n|} \\ &= \alpha_c \frac{K_{QC}}{K_{TC}} DT_r + (1 - \alpha_c) \frac{K_{QC}}{\sqrt{\rho} D K_{TC}^{3/2}} \frac{sgn(T_r) |T_r|^{3/2}}{|sgn(T_a)| \sqrt{\frac{|T_a|}{\rho D^4 K_T}}} \\ &= \frac{K_{QC}}{K_{TC}} D [\alpha_c T_r + (1 - \alpha_c) \frac{K_T^{1/2}}{K_{TC}^{1/2}} \frac{sgn(T_r) |T_r|^{3/2}}{|T_a|^{1/2}}]. \end{aligned} \quad (\text{F.3})$$

Using (4.8) and solving for  $T_a/T_r$ :

$$\begin{aligned} T_a &= \frac{K_T}{K_Q D} Q_a \\ &= \frac{K_T}{K_{TC}} \frac{K_{QC}}{K_Q} [\alpha_c T_r + (1 - \alpha_c) \frac{K_T^{1/2}}{K_{TC}^{1/2}} \frac{\operatorname{sgn}(T_r) |T_r|^{3/2}}{|T_a|^{1/2}}], \end{aligned} \quad (\text{F.4})$$

↓

$$\begin{aligned} \frac{T_a}{T_r} &= \frac{K_T}{K_{TC}} \frac{K_{QC}}{K_Q} [\alpha_c + (1 - \alpha_c) \frac{K_T^{1/2}}{K_{TC}^{1/2}} \frac{|T_r|^{1/2}}{|T_a|^{1/2}}] \\ &= \alpha_c \frac{K_T}{K_{TC}} \frac{K_{QC}}{K_Q} + (1 - \alpha_c) \frac{K_T^{3/2}}{K_{TC}^{3/2}} \frac{K_{QC}}{K_Q} \left( \frac{T_r}{T_a} \right)^{1/2}. \end{aligned} \quad (\text{F.5})$$

Inserting the definition of  $st_c(\cdot)$  from (4.1) in (F.5), and defining the ratios of control to actual thrust and torque parameters  $\beta_{TC} = \frac{K_T}{K_{TC}}$  and  $\beta_{QC} = \frac{K_Q}{K_{QC}}$ :

$$\begin{aligned} st_c &= \alpha_c \beta_{TC} \beta_{QC}^{-1} + (1 - \alpha_c) \beta_{TC}^{3/2} \beta_{QC}^{-1} st_c^{-1/2} \\ &= \alpha_c \frac{\beta_{TC}}{\beta_{QC}} + (1 - \alpha_c) \frac{\beta_{TC}^{3/2}}{\beta_{QC}} \frac{1}{st_c^{1/2}}. \end{aligned} \quad (\text{F.6})$$

Assuming the solution of (F.6) to be given by (F.1):

$$\begin{aligned} st_c &= \frac{\beta_{TC}}{\beta_{QC}^\kappa}, \\ &\Downarrow \\ \frac{\beta_{TC}}{\beta_{QC}^\kappa} &= \alpha_c \frac{\beta_{TC}}{\beta_{QC}} + (1 - \alpha_c) \frac{\beta_{TC}^{3/2}}{\beta_{QC}} \frac{1}{(\frac{\beta_{TC}}{\beta_{QC}^\kappa})^{1/2}}, \\ \frac{\beta_{TC}}{\beta_{QC}^\kappa} &= \alpha_c \frac{\beta_{TC}}{\beta_{QC}} + (1 - \alpha_c) \frac{\beta_{TC} \beta_{QC}^{\kappa/2}}{\beta_{QC}}, \\ \frac{1}{\beta_{QC}^\kappa} &= \frac{\alpha_c}{\beta_{QC}} + (1 - \alpha_c) \frac{\beta_{QC}^{\kappa/2}}{\beta_{QC}} \cdot \beta_{QC}^\kappa \beta_{QC}, \\ 0 &= (1 - \alpha_c) \beta_{QC}^{3\kappa/2} - \beta_{QC} + \alpha_c \beta_{QC}^\kappa, \end{aligned} \quad (\text{F.7})$$

which implicitly gives  $\kappa$  under the assumption in (F.1). The limiting values are  $\alpha_c = 1 \Rightarrow \kappa = 1$  (as in pure torque control), and  $\alpha_c = 0 \Rightarrow \kappa = 2/3$  (as in pure power control). Clearly, for  $\beta_{QC} = 1$  and  $\beta_{QC} = 0$ , any values for  $\kappa$  are valid, independently of  $\alpha_c$ . It remains to find a solution for  $\kappa$  in the interval  $\beta_{QC} \in \langle 0, 1 \rangle$ ,  $\alpha_c \in \langle 0, 1 \rangle$ . The result from solving (F.7) numerically (i.e.  $\kappa$  as function of  $\alpha_c$  and  $\beta_{QC}$ ) is shown in Figure F.1. A good approximation to this surface is the following intuitive linear function in  $\alpha_c$ :

$$\kappa \approx 2/3 + 1/3\alpha_c, \quad (\text{F.8})$$

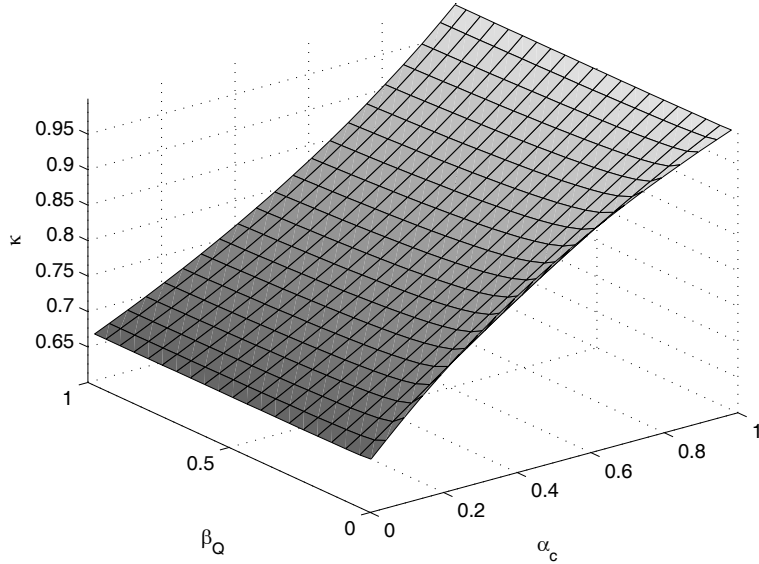


Figure F.1:  $\kappa$  as function of  $\alpha_c$  and  $\beta_Q$ .

which for  $\beta_{QC} > 0.02$  gives an error of less than 5%, and has the correct limiting values for  $\alpha_c = 0$  and  $\alpha_c = 1$ . Hence,  $st_c(\cdot)$  can be approximated by:

$$st_c(\cdot) = \frac{K_T}{K_{TC}} \left( \frac{K_{QC}}{K_Q} \right)^{2/3 + 1/3\alpha_c(n)}. \quad (\text{F.9})$$

## F.2 Friction compensation sensitivity function errors

In the derivation of the sensitivity functions, perfect friction compensation was assumed. As discussed in Section 4.8.2 the linear friction compensation will give a small deviation from the ideal sensitivity functions, even with perfect model knowledge, and an error in the static friction compensation will give an additional offset. In the following, modifications of the iterative solution procedure from Section 4.7 to account for the friction compensation errors will be presented.

### F.2.1 Linear friction compensation

Since  $Q_{ff}$  in (3.19) is a function of  $n_r$  only, the linear compensation term is not adjusted when the shaft speed differs from  $n_r$ , as is the case in torque and

power control. Instead of (4.50) or (4.51), the actual steady-state equation to be solved is:

$$Q_{mp} - Q_a - \text{sign}(\omega)Q_s + K_\omega\omega = 0. \quad (\text{F.10})$$

With  $Q_{mp} = Q_{ci} + Q_{ff}(n_r)$ , and assuming perfect model knowledge such that  $Q_{f0} = Q_s$  and  $Q_{f1} = K_\omega$ , (F.10) becomes:

$$\begin{aligned} Q_{ci} + Q_{ff}(n_r) - Q_a - \text{sign}(\omega)Q_s - K_\omega\omega &= 0, \\ Q_{ci} + \text{sign}(\omega)Q_{f0} + 2\pi Q_{f1}n_r - Q_a - \text{sign}(\omega)Q_s - K_\omega\omega &= 0, \\ Q_{ci} - Q_a + 2\pi K_\omega(n_r - n) &= 0. \end{aligned} \quad (\text{F.11})$$

Here the friction compensation term  $2\pi K_\omega(n_r - n)$  is new when compared to the analysis in Section 4.7. The steady-state equations that must be solved iteratively are derived in the following.

### Torque control

For torque control, with  $Q_{ci} = Q_{cq} = Q_r$  from (3.29), (F.11) becomes:

$$\begin{aligned} Q_r &= Q_a - 2\pi K_\omega(n_r - n) \\ &= K_{Q0}\rho n^2 D^5 \beta_Q \left( \frac{V_a}{nD} \right) - 2\pi K_\omega(n_r - n). \end{aligned} \quad (\text{F.12})$$

Solving with respect to  $n$ , the resulting equation for the iterative solution is:

$$n = \frac{-\pi K_\omega + \sqrt{\pi^2 K_\omega^2 + K_{Q0}\rho D^5 \beta_Q \left( \frac{V_a}{nD} \right) (2\pi K_\omega n_r + Q_r)}}{K_{Q0}\rho D^5 \beta_Q \left( \frac{V_a}{nD} \right)}. \quad (\text{F.13})$$

If  $K_\omega = 0$ , the result is as in (4.50).

### Power control

For power control, with  $Q_{ci} = Q_{cp} = P_{rs}/(2\pi|n|)$  from (3.32), and assuming that  $P_{rs}/(2\pi|n|) = P_r/(2\pi n)$  with  $P_r$  given in (3.3), (F.11) becomes:

$$\begin{aligned} \frac{P_r}{2\pi n} - Q_a + 2\pi K_\omega(n_r - n) &= 0, \\ P_r - 2\pi n K_{Q0}\rho n^2 D^5 \beta_Q \left( \frac{V_a}{nD} \right) + 2\pi n 2\pi K_\omega(n_r - n) &= 0, \\ 2\pi K_{Q0}\rho D^5 \beta_Q \left( \frac{V_a}{nD} \right) n^3 + 4\pi^2 K_\omega n^2 - 4\pi^2 K_\omega n_r n - P_r &= 0. \end{aligned} \quad (\text{F.14})$$

On standard cubic form, (F.14) is written as:

$$n^3 + a_2 n^2 + a_1 n + a_0 = 0, \quad (\text{F.15})$$

where the coefficients  $a_i$  are defined as:

$$a_2 = \frac{4\pi^2 K_\omega}{2\pi K_{Q0} \rho D^5 \beta_Q(\frac{V_a}{nD})}, \quad (\text{F.16})$$

$$a_1 = -\frac{4\pi^2 K_\omega n_r}{2\pi K_{Q0} \rho D^5 \beta_Q(\frac{V_a}{nD})}, \quad (\text{F.17})$$

$$a_0 = -\frac{P_r}{2\pi K_{Q0} \rho D^5 \beta_Q(\frac{V_a}{nD})}. \quad (\text{F.18})$$

The polynomial has the real solution:

$$n = -\frac{1}{3}a_2 + (S + T), \quad (\text{F.19})$$

where  $S$  and  $T$  are given by:

$$S = \sqrt[3]{R + \sqrt{U}}, \quad T = \sqrt[3]{R - \sqrt{U}}, \quad (\text{F.20})$$

$$U = Q^3 + R^2, \quad Q = \frac{3a_1 - a_2^2}{9}, \quad (\text{F.21})$$

$$R = \frac{9a_2 a_1 - 27a_0 - 2a_2^3}{54}. \quad (\text{F.22})$$

The solution for  $n$ , which constitutes the equation for the iterative solution procedure, can hence be found directly, but is not suited for being written out explicitly. In the case where  $K_\omega = 0$ , (F.19) reduces to (4.51).

## F.2.2 Static friction compensation error

If the static friction compensation term is wrong such that  $Q_{f0} \neq Q_s$ , the sensitivity analysis as presented in Chapter 4 also becomes wrong. Assuming  $\omega > 0$ , the steady-state equation to be solved by the iterative solution procedure becomes:

$$\begin{aligned} Q_{ci} + Q_{ff}(n_r) - Q_a - Q_s - K_\omega \omega &= 0, \\ Q_{ci} + Q_{f0} + 2\pi Q_{f1} n_r - Q_a - Q_s - K_\omega \omega &= 0, \\ Q_{ci} + \Delta Q_f - Q_a + 2\pi K_\omega (n_r - n) &= 0, \end{aligned} \quad (\text{F.23})$$

which is identical to (F.11), except for the static friction compensation error  $\Delta Q_f = Q_{f0} - Q_s$ . The solution will then be the same, except that  $Q_{ci}$  must be adjusted with the term  $\Delta Q_f$ . In the solutions for torque and power control given in (F.13) and (F.19), respectively, this is easily done by adding  $\Delta Q_f$  to where  $2\pi K_\omega n_r$  appears in the expressions for  $n$ . Hence, for torque control, the expression for  $n$  from (F.13) becomes:

$$n = \frac{-\pi K_\omega + \sqrt{\pi^2 K_\omega^2 + K_{Q0} \rho D^5 \beta_Q(\frac{V_a}{nD}) (2\pi K_\omega n_r + Q_r + \Delta Q_f)}}{K_{Q0} \rho D^5 \beta_Q(\frac{V_a}{nD})}. \quad (\text{F.24})$$

In the case where  $K_\omega = 0$  the result is:

$$n = \sqrt{\frac{Q_r + \Delta Q_f}{K_{Q0}\rho D^5 \beta_Q(\frac{V_a}{nD})}}. \quad (\text{F.25})$$

Similarly, the result for power control in (F.19) is adjusted by redefining  $a_1$  in (F.17) as:

$$a_1 = -\frac{4\pi^2 K_\omega n_r + 2\pi \Delta Q_f}{2\pi K_{Q0}\rho D^5 \beta_Q(\frac{V_a}{nD})}. \quad (\text{F.26})$$

### F.2.3 Result of errors

The error due to the linear friction compensation will always be present, even with perfect model knowledge. The error due to the static friction compensation, however, disappears with perfect model knowledge. As an example, the Wageningen B4-70 simulation propeller is used. The linear friction term and friction compensation are taken as  $K_\omega = Q_{f1} = 720$  Nms, and the error in the static friction compensation is taken as  $\Delta Q_f = -2E3$  kNm. In Figures F.2 to F.5 the thrust, shaft speed, torque, and power sensitivities are shown for two thrust references:  $T_r = 50$  kN and  $T_r = 400$  kN. The effect of accounting for the linear friction compensation is best seen in slope of the torque sensitivity curves for torque control,  $sq_q(\cdot)$  in Figure F.4, and the slope of the power sensitivity curves for power control,  $sp_p(\cdot)$  in Figure F.5. If the friction had not been accounted for, these would have been flat. The effect of the static friction compensation error can be seen in all the figures, since the torque and power controllers no longer give unity sensitivity functions for  $V_a = 0$ . Obviously, the error has a larger impact for the lowest thrust reference.

## F.3 Robustness analysis using Lyapunov theory

Accurate estimates of the resulting (steady-state) shaft speed during a thrust loss incident with a given controller is most conveniently found by using the sensitivity functions presented in Section 4 and summarized in Table 4.1, or eventually by the extensions provided in Section F.2. For analysis of the *transient* behavior of the system, an analysis based on Lyapunov tools may prove useful.

### F.3.1 Using the comparison method

With the stability analysis in Section 6.5.1 as a starting point, the bound on the solutions of the perturbed system in (6.4) may be estimated by the comparison method for non-vanishing perturbations, as described in Lemma 9.4 and 9.6 in Khalil (2002). Assume that (4.91), (4.95), and (4.99) hold for  $x \in D_r$ , where  $D_r$  is a ball of radius  $r$ :

$$D_r = \{x \in \mathbb{R} \mid \|x\|_2 < r\}. \quad (\text{F.27})$$

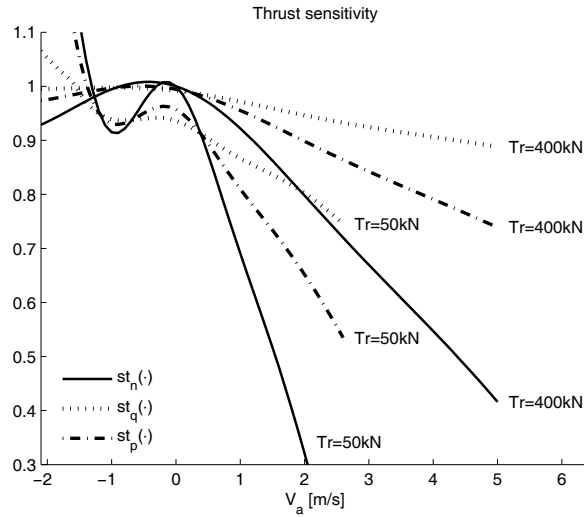


Figure F.2: Thrust sensitivity functions for shaft speed, torque, and power control when accounting for the linear friction compensation and including an error in the static friction compensation.

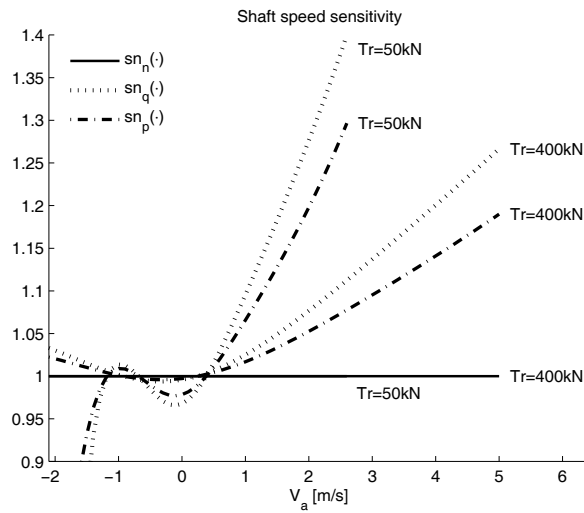


Figure F.3: Shaft speed sensitivity functions for shaft speed, torque, and power control when accounting for the linear friction compensation and including an error in the static friction compensation.

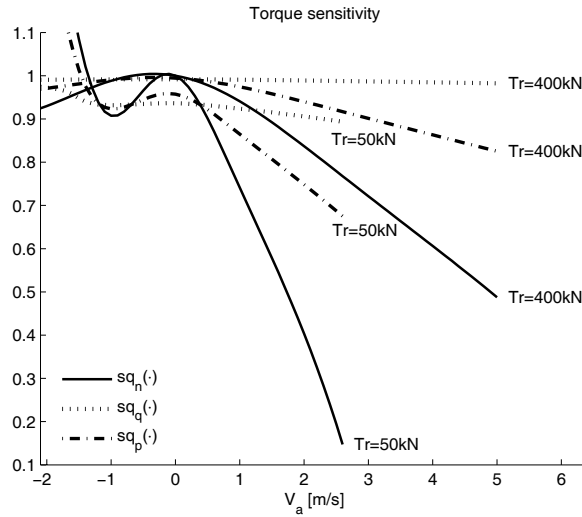


Figure F.4: Torque sensitivity functions for shaft speed, torque, and power control when accounting for the linear friction compensation and including an error in the static friction compensation.

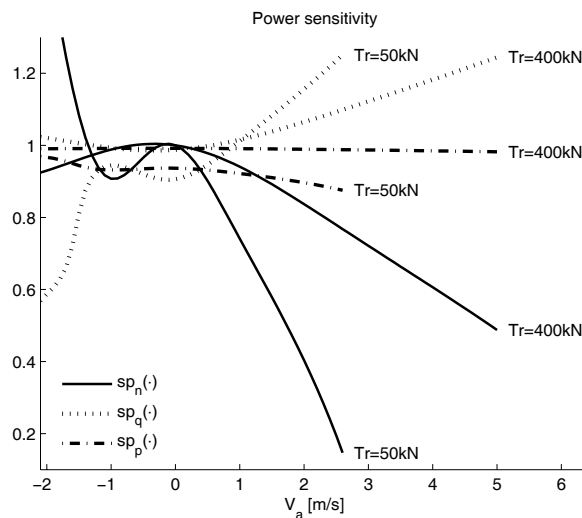


Figure F.5: Power sensitivity functions for shaft speed, torque, and power control when accounting for the linear friction compensation and including an error in the static friction compensation.

The numerical values  $k_1 = k_2 = 1/2$  and  $k_4 = 1$  can be chosen in (4.91) and (4.99). How to choose  $k_3$  in (4.95) is further discussed below. The perturbation term  $g_2(t, x)$  is defined in (6.11). Suppose that  $g_2(t, x)$  satisfies:

$$\|g_2(t, x)\| \leq \xi(t) \|x\| + \delta(t), \quad \forall t \geq 0, \forall x \in D, \quad (\text{F.28})$$

where  $\xi : \mathbb{R} \rightarrow \mathbb{R}$  is nonnegative, continuous for all  $t \geq 0$ , and satisfies the condition:

$$\int_{t_0}^t \xi(\tau) d\tau \leq \varepsilon(t - t_0) + \eta, \quad (\text{F.29})$$

for  $0 \leq \varepsilon < k_3$  and  $\eta \geq 0$ , and that  $\delta : \mathbb{R} \rightarrow \mathbb{R}$  is nonnegative, continuous, and bounded for all  $t \geq 0$ . For this system,  $\varepsilon$  and  $\eta$  can be chosen as  $\varepsilon = 0$  and  $\eta = 0$ , such that  $g_2(t, x)$  must satisfy:

$$\|g_2(t, x)\| \leq \delta(t), \quad \forall t \geq 0, \forall x \in D. \quad (\text{F.30})$$

From Lemma 9.4 in Khalil (2002), provided:

$$\|x(t_0)\| < \frac{r}{\rho} \sqrt{\frac{k_1}{k_2}} = r, \quad (\text{F.31})$$

$$\sup_{t \geq t_0} \delta(t) < \frac{2k_1 \alpha r}{k_4 \rho} = k_3 r, \quad (\text{F.32})$$

where it has been inserted that:

$$\begin{aligned} \rho &= \exp\left(\frac{k_4 \eta}{2k_1}\right) = \exp(\eta) = 1, \\ \alpha &= \frac{1}{2}\left(\frac{k_3}{k_2} - \varepsilon \frac{k_4}{k_1}\right) = k_3 - \varepsilon = k_3, \end{aligned} \quad (\text{F.33})$$

the solution of the perturbed system then satisfies:

$$\|x(t)\| \leq \|x(t_0)\| e^{-k_3(t-t_0)} + \int_{t_0}^t e^{-k_3(t-\tau)} \delta(\tau) d\tau. \quad (\text{F.34})$$

Additionally, from Lemma 9.6 in Khalil (2002), if:

$$\int_{t_0}^t e^{-k_3(t-\tau)} \delta(\tau) d\tau \leq \sigma, \quad \forall t \geq t_0, \quad (\text{F.35})$$

for some constant  $\sigma > 0$ , then  $x(t)$  is uniformly ultimately bounded with ultimate bound  $b$ :

$$b = \frac{\sigma}{\theta}, \quad (\text{F.36})$$

where  $\theta$  is an arbitrary constant  $0 < \theta < 1$ . This shows that the bound and ultimate bound on  $x(t)$  depend only on its initial condition and the time history of the bound  $\delta(t)$  on the perturbation term  $g(t, x)$ . The remaining difficulties in order to achieve realistic numerical bounds on the solutions is to find a sensible value for  $k_3$  in (4.95), and a reasonable model for the disturbance bound  $\delta(t)$  in (F.30). The ultimate bound will not be further considered here – for steady-state performance, the sensitivity functions give a more correct analysis.

### F.3.2 Determining the damping

In the proofs of Proposition 4.1 and Theorem 6.1, Lemma 4.1 was used to remove the nonlinear damping from the analysis, and hence it would seem natural to choose  $k_3 = b_1$ . In reality, the nonlinear terms may give a much larger contribution to the stability of the system than the linear terms. For the nominal system (4.89), assume e.g. to be operating about a positive equilibrium  $\omega_r$ , and that  $|x| < \omega_r$  such that  $x + \omega_r > 0$ .  $\dot{V}(x)$  in (4.92) then becomes:

$$\dot{V}(x) = -b_0\theta(\omega_r, \omega)x - b_1x^2 - \bar{b}_2x((x + \omega_r)^2 - \omega_r^2), \quad (\text{F.37})$$

and by applying (4.94):

$$\begin{aligned} \dot{V}(x) &\leq -b_1x^2 - \bar{b}_2x((x + \omega_r)^2 - \omega_r^2) \\ &= -b_1x^2 - \bar{b}_2x(x^2 + 2x\omega_r + \omega_r^2 - \omega_r^2) \\ &= -b_1x^2 - \bar{b}_2x^3 - 2\bar{b}_2x^2\omega_r \\ &= -(b_1 + 2\bar{b}_2\omega_r)x^2 - \bar{b}_2x^3. \end{aligned} \quad (\text{F.38})$$

The sign of the  $x^3$  term is indefinite, and must be dominated by the  $x^2$  term. Since it is assumed that  $|x| < \omega_r$  and  $\omega_r > 0$ , it follows that  $\omega_r x^2 > x^3$ . Hence:

$$\begin{aligned} \dot{V}(x) &\leq -(b_1 + \bar{b}_2\omega_r)x^2 - \bar{b}_2\omega_r x^2 - \bar{b}_2x^3 \\ &\leq -(b_1 + \bar{b}_2\omega_r)x^2. \end{aligned} \quad (\text{F.39})$$

Similarly, if  $\omega_r < 0$  and  $|x| < |\omega_r|$  such that  $x + \omega_r < 0$ ,  $\dot{V}(x)$  becomes:

$$\begin{aligned} \dot{V}(x) &= -b_0\theta(\omega_r, \omega)x - b_1x^2 - \bar{b}_2x(-(x + \omega_r)^2 + \omega_r^2) \\ &\leq -b_1x^2 - \bar{b}_2x(-x^2 - 2x\omega_r - \omega_r^2 + \omega_r^2) \\ &= -b_1x^2 + \bar{b}_2x^3 + 2\bar{b}_2x^2\omega_r \\ &= -b_1x^2 + \bar{b}_2x^3 - 2\bar{b}_2x^2|\omega_r| \\ &= -(b_1 + 2\bar{b}_2|\omega_r|)x^2 + \bar{b}_2x^3. \end{aligned} \quad (\text{F.40})$$

As above, it follows that  $\omega_r x^2 > x^3$  such that:

$$\begin{aligned} \dot{V}(x) &\leq -(b_1 + \bar{b}_2|\omega_r|)x^2 - \bar{b}_2|\omega_r|x^2 + \bar{b}_2x^3 \\ &\leq -(b_1 + \bar{b}_2|\omega_r|)x^2. \end{aligned} \quad (\text{F.41})$$

Combining the results for positive and negative  $\omega_r$ , i.e. (F.39) and (F.41), it follows that for all  $|x| < |\omega_r|$ ,  $\dot{V}(x)$  complies to:

$$\dot{V}(x) \leq -(b_1 + \bar{b}_2|\omega_r|)x^2. \quad (\text{F.42})$$

This demand on  $x$  is quite realistic, since it only excludes perturbations that cause the rotational direction of the propeller to change, or increase to more than the double of its nominal value  $\omega_r$ . For normal operation, the shaft speed will not change direction. With some kind of anti-spin functionality in the

controller, the shaft speed should not be allowed to exceed  $2\omega_r$ , even during large thrust losses. Without an anti-spin controller, however, this may well be the case with torque and power control. These considerations show, as should be expected, that the damping introduced by the fluid also contributes to the stability properties of the system. Comparing realistic values of  $b_1$  and  $\bar{b}_2 |\omega_r|$ , it is apparent that the nonlinear damping by far is the dominating. Hence, for the following Lyapunov analysis,  $k_3$  is chosen as:

$$k_3 = b_1 + \bar{b}_2 |\omega_r|. \quad (\text{F.43})$$

For the system during ventilation, as analyzed in Theorem 6.1, such a consideration becomes more difficult, since the nonlinear damping depends on the torque loss factor  $\beta_Q(t, \omega)$ . The Lyapunov analysis of the nominal system (6.4) during the loss incident resulted in (6.14):

$$\dot{V}(x) = -b_0 \theta(\omega_r, \omega) x - b_1 x^2 - \bar{b}_2 \beta_Q(t, \omega) x((x + \omega_r) |x + \omega_r| - \omega_r |\omega_r|). \quad (\text{F.44})$$

Similar reasoning as for the nominal system without losses may be applied, such that for all  $|x| < |\omega_r|$ ,  $\dot{V}(x)$  complies to:

$$\dot{V}(x) \leq -(b_1 + \beta_Q(t, \omega) \bar{b}_2 |\omega_r|) x^2. \quad (\text{F.45})$$

The presence of  $\beta_Q(t, \omega)$  means that a more conservative estimate of  $k_3$  is needed. During pure *ventilation*, when the propeller still is submerged, the minimum value of  $\beta_Q(t, \omega)$  is approximately 0.2, see Section 2.4. In the case of a complete *water exit*, the propeller loses all load torque, such that  $\beta_Q(t, \omega) \approx 0$ . The bound on the shaft speed then only depends on the friction term. This is clearly seen in the analysis, since  $k_3$  then must be taken as  $k_3 = b_1$ . This demonstrates the importance of designing a fast anti-spin controller: if the ventilation incident is not caught quickly, the shaft speed may increase rapidly, since most of the damping in the system is removed. For the ventilated propeller,  $k_3$  must hence be taken as:

$$k_3 = b_1 + \bar{\beta}_Q \bar{b}_2 |\omega_r|, \quad (\text{F.46})$$

where  $\bar{\beta}_Q$  is the lowest expected value of  $\beta_Q(t, \omega)$  during the loss incident.

### F.3.3 Quantifying the trajectory bound

In order to quantify the trajectory bound in (F.34) further, some simplifications are needed. As an example, take a ventilation incident where the propeller initially is at its equilibrium, such that  $x(t_0) = 0$ , and  $\beta_Q(t, \omega)$  drops from 1 to  $\bar{\beta}_Q$  instantaneously. The anti-spin controller needs some time to catch the ventilation incident before  $\gamma_Q$  converges to  $\bar{\beta}_Q$ , and the error  $\gamma_Q - \beta_Q(t, \omega)$  is modelled as a square wave with amplitude  $\gamma_e$  and duration  $T$  seconds. The perturbation bound  $\delta(t)$  from (F.30) then becomes a square wave with amplitude  $\gamma_e \bar{u}$  and duration  $T$ , i.e.:

$$\delta(t) = \begin{cases} \gamma_e \bar{u} & \text{for } t \leq t_0 + T, \\ 0 & \text{for } t > t_0 + T. \end{cases} \quad (\text{F.47})$$

With  $\beta_Q(t, \omega) = \bar{\beta}_Q$ ,  $k_3$  can be taken as in (F.46). According to (F.34), the trajectories of the system then satisfy:

$$\begin{aligned}\|x(t)\| &\leq x(t_0) + \int_{t_0}^t e^{-k_3(t-\tau)} \delta(\tau) d\tau \\ &= 0 + \gamma_e \bar{u} \int_{t_0}^{t_0+T} e^{-k_3(t-\tau)} d\tau = \frac{\gamma_e \bar{u}}{k_3} (e^{k_3 T} - 1) e^{k_3(t_0-t)} \\ &= \frac{\gamma_e \bar{u}}{b_1 + \bar{\beta}_Q \bar{b}_2 |\omega_r|} (e^{(b_1 + \bar{\beta}_Q \bar{b}_2 |\omega_r|)T} - 1) e^{(b_1 + \bar{\beta}_Q \bar{b}_2 |\omega_r|)(t_0-t)}. \quad (\text{F.48})\end{aligned}$$

In the conservative case of zero linear damping, i.e.  $b_1 = 0$ , this reduces to:

$$\begin{aligned}\|x(t)\| &\leq \frac{\gamma_e \bar{u}}{\bar{\beta}_Q \bar{b}_2 |\omega_r|} (e^{(\bar{\beta}_Q \bar{b}_2 |\omega_r|)T} - 1) e^{(\bar{\beta}_Q \bar{b}_2 |\omega_r|)(t_0-t)} \\ &= \omega_r \frac{\gamma_e}{\bar{\beta}_Q} (e^{(\bar{\beta}_Q \bar{b}_2 |\omega_r|)T} - 1) e^{(\bar{\beta}_Q \bar{b}_2 |\omega_r|)(t_0-t)},\end{aligned}$$

where  $\bar{u} = \bar{b}_2 \omega_r |\omega_r|$  from (4.86) has been inserted. Clearly, the bound on the trajectories is proportional to the magnitude of the perturbation  $\gamma_e$ , and increasing with the duration  $T$ .

**Remark F.1** For zero duration  $T = 0$ , or zero magnitude  $\gamma_e = 0$ ,  $\|x(t)\| \equiv 0$  as should be expected. This corresponds to the case of a known disturbance, as shown in Corollary 6.1.

# Appendix G

## Additional observer results

This appendix contains additional observer results. Section G.1 presents an adaptive extension of the load torque observer from Section 5.1, including experimental results, and section G.2 shows how the prevailing control coefficients can be estimated from the available measurements.

### G.1 Adaptive load torque observer

The load torque observer presented in Section 5.1 is based on knowledge of the shaft friction parameters  $Q_s$  and  $K_\omega$ . In the case were these are uncertain, or expected to change significantly over the life-time of the thruster, the observer may be extended to include a parameter adaption scheme for  $K_\omega$ . It is still assumed that the static friction term  $Q_s$  is known with reasonable accuracy. The estimate  $\hat{K}_\omega$  can then also be used to replace the parameter  $Q_{f1}$  in the linear friction compensation (3.21). The adaptive observer was first published in Smogeli and Sørensen (2006a).

#### G.1.1 Observability

If  $K_\omega$  is modelled as a random process driven by a bounded disturbance  $w_{K_\omega}$ , and augmented to the observer state vector  $x$  in (5.4), this will give the new state vector  $x_a$ :

$$x_a = [\omega, Q_a, K_\omega]^\top, \quad (\text{G.1})$$

and process plant model:

$$\dot{x}_a = f_a(x_a) + B_a u + G_a w_a, \quad (\text{G.2})$$

$$y = h(x_a) = C_a x_a + v, \quad (\text{G.3})$$

where the following matrices and vectors have been used:

$$\begin{aligned} f_a(x_a) &= \begin{bmatrix} -\omega K_\omega / I_s - Q_a / I_s \\ 0 \\ 0 \end{bmatrix}, \quad G_a = I_{3 \times 3}, \\ B_a &= \begin{bmatrix} 1/I_s \\ 0 \\ 0 \end{bmatrix} \quad w_a = \begin{bmatrix} \delta_f / I_s \\ w_{Q_a} \\ w_{K_\omega} \end{bmatrix}, \quad C_a = \begin{bmatrix} 1 \\ 0 \\ 0 \end{bmatrix}^\top. \end{aligned} \quad (\text{G.4})$$

The bounded disturbances  $w_a$  and  $v$  are assumed uncorrelated. From Isidori (1995), the observability matrix of the nonlinear system becomes:

$$O = \begin{bmatrix} \frac{\partial}{\partial x_a} h(x_a) \\ \frac{\partial}{\partial x_a} L_{f_a} h(x_a) \\ \frac{\partial}{\partial x_a} L_{f_a}^2 h(x_a) \end{bmatrix} = \begin{bmatrix} 1 & 0 & 0 \\ -\frac{K_\omega}{I_s} & -\frac{1}{I_s} & -\frac{\omega}{I_s} \\ \frac{K_\omega^2}{I_s^2} & \frac{K_\omega}{I_s^2} & \frac{2\omega K_\omega + Q_a}{I_s^2} \end{bmatrix}, \quad (\text{G.5})$$

which has rank 3 for all  $x_a \in \mathbb{R}^3 - [0, 0, 0]^\top$ . The nonlinear system is hence weakly locally observable according to the definitions in Hermann and Krener (1977). Notice, however, that the linearization about the current estimate  $\hat{x}_a$  as used in e.g. an extended Kalman filter becomes:

$$A_a = \left. \frac{\partial f_a(x_a)}{\partial x_a} \right|_{x_a=\hat{x}_a} = \begin{bmatrix} -\hat{K}_\omega / I_s & -1/I_s & -\hat{\omega} / I_s \\ 0_{2 \times 3} & & \end{bmatrix}, \quad (\text{G.6})$$

and the Kalman observability matrix becomes:

$$O = \begin{bmatrix} C_a \\ C_a A_a, \\ C_a A_a^2 \end{bmatrix} = \begin{bmatrix} 1 & 0 & 0 \\ -\frac{\hat{K}_\omega}{I_s} & -\frac{1}{I_s} & -\frac{\hat{\omega}}{I_s} \\ \frac{\hat{K}_\omega^2}{I_s^2} & \frac{\hat{K}_\omega}{I_s^2} & \frac{\hat{K}_\omega \hat{\omega}}{I_s^2} \end{bmatrix}, \quad (\text{G.7})$$

which has rank 2. This means that linear estimation methods like extended Kalman filtering, SDRE Filtering (Haessig and Friedland, 1997), etc. are non-applicable, whereas a nonlinear estimation scheme should be possible to construct.

### G.1.2 $K_\omega$ estimation

The nonlinear system dynamics used in the estimation scheme is based on the shaft dynamics (2.50), with the static friction  $Q_s \text{sign}(\omega)$  replaced by the static friction compensation (3.20), and  $Q_a$  replaced by the *nominal* torque model  $\hat{Q}_n$  from (5.14):

$$I_s \dot{\omega} = k_g Q_m - Q_{ff0}(n_r) - K_\omega \omega - \hat{Q}_n. \quad (\text{G.8})$$

The error in the static friction compensation, i.e. the deviation of  $Q_{ff0}(n_r)$  from  $Q_s \text{sign}(\omega)$ , will partly be captured in the adaption of  $K_\omega$ .

**Remark G.1** Using the nominal torque model  $\hat{Q}_n$  in the parameter estimation can be justified, since the estimation of  $K_\omega$  is a slow process, and in DP the deviation of  $K_Q$  from  $K_{Q0}$  will be small. In waves, the deviation will average to zero over time, whereas in current there will be a small steady-state offset. The offset will depend on the size and type of propeller, and the magnitude and direction of the current. Note that an offset in  $K_Q$  will lead to an offset in the estimate of  $K_\omega$ , but in DP this deviation is expected to be small.

With the motor torque adjusted for the static friction as input as in (5.3), i.e.  $u = k_g Q_m - Q_{ff0}(n_r)$ , the shaft friction coefficient  $K_\omega$  as an unknown parameter, and inserting for  $\hat{Q}_n$ , the system in (G.8) becomes:

$$\dot{\omega} = \frac{1}{I_s}u - \frac{K_\omega}{I_s}\omega - \frac{K_{QC}\rho D^5}{4\pi^2 I_s}\omega |\omega| \triangleq f(\omega, u, K_\omega). \quad (\text{G.9})$$

The system is affine in  $K_\omega$ , and can be written as:

$$f(\omega, u, K_\omega) = F(\omega)K_\omega + g(\omega, u), \quad (\text{G.10})$$

where:

$$F(\omega) = \frac{\partial f(\omega, u, K_\omega)}{\partial K_\omega} = -\frac{\omega}{I_s}, \quad (\text{G.11})$$

$$g(\omega, u) = \frac{1}{I_s}u - \frac{K_{Q0}\rho D^5}{4\pi^2 I_s}\omega |\omega|. \quad (\text{G.12})$$

Following a similar approach as in Section 5.2, an estimate  $\hat{K}_\omega$  of  $K_\omega$  can be obtained from a parameter update law on the form (Friedland, 1997):

$$\begin{aligned} \hat{K}_\omega &= \phi(\omega) + z, \\ \dot{z} &= -\Phi(\omega)f(\omega, u, \hat{K}_\omega), \end{aligned} \quad (\text{G.13})$$

where  $\phi(\omega)$  is a nonlinear function to be defined, and  $\Phi(\omega)$  is its Jacobian,  $\Phi(\omega) = \partial\phi(\omega)/\partial\omega$ . As in Section 5.2, the estimation error  $\tilde{K}_\omega$  and its dynamics are:

$$\tilde{K}_\omega = K_\omega - \hat{K}_\omega, \quad (\text{G.14})$$

$$\begin{aligned} \dot{\tilde{K}}_\omega &= -\dot{\hat{K}}_\omega = -\dot{\phi}(\omega) - \dot{z} \\ &= -\Phi(\omega)F(\omega)(K_\omega - \hat{K}_\omega) = -L(t)\tilde{K}_\omega, \end{aligned} \quad (\text{G.15})$$

where  $L(t) = \Phi(\omega(t))F(\omega(t))$  is time-varying. It remains to choose  $\phi(\omega)$  to yield  $L(t)$  positive semidefinite. From Friedland (1997), one option is to choose  $\phi(\omega)$  to satisfy

$$\Phi(\omega) = k_c F(\omega) = -k_c \frac{\omega}{I_s}, \quad (\text{G.16})$$

where  $k_c$  is a positive constant, such that

$$L(t) = k_c F(\omega)^2 = k_c \frac{\omega^2}{I_s^2}. \quad (\text{G.17})$$

A candidate  $\phi(\omega)$  satisfying this is:

$$\phi(\omega) = -\frac{k_c \omega^2}{2I_s}. \quad (\text{G.18})$$

This yields the following error dynamics:

$$\dot{\tilde{K}}_\omega = -k_c \frac{\omega(t)^2}{I_s^2} \tilde{K}_\omega, \quad (\text{G.19})$$

where the time-dependence of  $\omega$  has been emphasized. Stability properties are investigated by the positive definite Lyapunov function  $V_1(\tilde{K}_\omega)$ :

$$V_1(\tilde{K}_\omega) = \frac{1}{2} \tilde{K}_\omega^2, \quad (\text{G.20})$$

such that the derivative of  $V_1$  along the trajectories of (G.9) are given by:

$$\dot{V}_1 = \tilde{K}_\omega \dot{\tilde{K}}_\omega = -k_c \frac{\omega(t)^2}{I_s^2} \tilde{K}_\omega^2 \leq 0. \quad (\text{G.21})$$

Clearly,  $\dot{V}_1 = 0$  for  $\tilde{K}_\omega \neq 0$  iff  $\omega(t) \equiv 0$ . This is the case of zero shaft speed, for which one cannot expect to extract any information. However, the error dynamics are still uniformly globally stable (UGS). Note that  $\omega(t) = 0 \Rightarrow \phi(\omega) = \Phi(\omega) = \dot{z} = 0$ , which means that parameter adaption stops, but does not diverge. The condition that  $\omega(t) \neq 0$  can be seen as a persistency of excitation (PE) requirement, leading to uniform global exponential stability (UGES) of the error dynamics, since:

$$r_1 \left\| \tilde{K}_\omega \right\|^2 \leq V_1(\tilde{K}_\omega) \leq r_2 \left\| \tilde{K}_\omega \right\|^2, \quad (\text{G.22})$$

$$\dot{V}_1 \leq -r_3 \left\| \tilde{K}_\omega \right\|^2, \quad (\text{G.23})$$

for  $r_1 = r_2 = 0.5$  and  $r_3 = k_c \omega_{\min}^2 / I_s^2$ , where  $\omega_{\min}$  is the lowest shaft speed magnitude to be considered.

### G.1.3 Adaptive observer design

With the chosen decoupling of parameter estimation and observer, the parameter estimation scheme in (G.13) may be combined with the observer in (5.7) to give an adaptive observer in the following form:

$$\begin{aligned} \dot{\hat{\omega}} &= \frac{1}{I_s}(u - \hat{Q}_a - \hat{K}_\omega \hat{\omega}) + k_a \tilde{\omega}, \\ \dot{\hat{Q}}_a &= k_b \tilde{\omega}, \\ \dot{z} &= k_c \frac{\omega}{I_s^2}(u - \hat{K}_\omega \omega - \frac{K_{QC}\rho D^5}{4\pi^2} \omega |\omega|), \\ \dot{\hat{K}}_\omega &= -\frac{k_c \omega^2}{2I_s} + z, \end{aligned} \quad (\text{G.24})$$

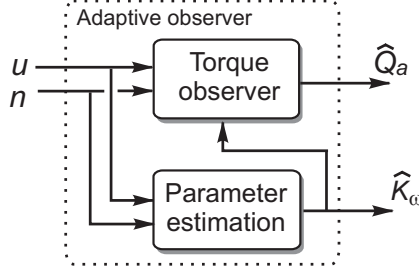


Figure G.1: Block diagram showing the cascaded structure of the adaptive observer.

where  $\tilde{\omega} = \omega - \hat{\omega} = \tilde{y}$  and  $u = k_g Q_m - Q_{ff0}(n_r)$  as in (5.3). The parameter estimation and load torque observer can then be viewed as two systems interconnected in a cascaded structure; see Figure G.1.

**Remark G.2** If the nominal torque model in (G.24) is replaced with the estimated load torque  $\hat{Q}_a$ , the parameter estimation is coupled with the observer, as discussed in Section G.1.1. The estimates then no longer converge to sensible values. No formulation with such a coupling of the observer and parameter estimation has yet been found.

**Remark G.3** Following the approach from Friedland (1997), it is possible to construct a nonlinear parameter estimation scheme for both  $K_Q$  and  $K_\omega$ . However, simulations show that the parameter estimates converge only when  $K_Q$  and  $K_\omega$  are constant. With a time-varying  $K_Q$ , as is inevitable in reality, the estimates do not converge. It should be noted that constant parameters is a basic assumption in Friedland (1997).

Neglecting the modelling error and noise, as represented by  $\Delta$  in the  $Q_a$  observer error dynamics in (5.9), the error dynamics of the shaft speed estimate from (5.1) and (G.24) becomes:

$$\begin{aligned}
 \dot{\tilde{\omega}} &= -\frac{1}{I_s}(Q_a - \hat{Q}_a) - \frac{1}{I_s}(K_\omega \omega - \hat{K}_\omega \hat{\omega}) - k_a \tilde{\omega} \\
 &= -\frac{1}{I_s}\hat{Q}_a - \frac{1}{I_s}(K_\omega \omega - K_\omega \hat{\omega} + K_\omega \hat{\omega} - \hat{K}_\omega \hat{\omega}) - k_a \tilde{\omega} \\
 &= -\frac{1}{I_s}\hat{Q}_a - \left(\frac{K_\omega}{I_s} + k_a\right)\tilde{\omega} - \frac{\hat{\omega}}{I_s}\hat{K}_\omega,
 \end{aligned} \tag{G.25}$$

and the error dynamics of the load torque estimate from (5.1) and (G.24) is as before:

$$\dot{\hat{Q}}_a = -k_b \tilde{\omega}. \tag{G.26}$$

The parameter estimation error dynamics is given in (G.19). On state-space form, the adaptive observer error dynamics can be written as two cascaded systems:

$$\begin{aligned}\Sigma_1 &: \dot{x}_1 = f_1(x_1) + g(t, x_1)x_2, \\ \Sigma_2 &: \dot{x}_2 = f_2(t, x_2),\end{aligned}\quad (\text{G.27})$$

where:

$$x_1 = \begin{bmatrix} \tilde{\omega} \\ \tilde{Q}_a \end{bmatrix}, \quad x_2 = \tilde{K}_\omega, \quad (\text{G.28})$$

$$f_1(x_1) = \begin{bmatrix} -\frac{1}{I_s}\tilde{Q}_a - \left(\frac{K_\omega}{I_s} + k_a\right)\tilde{\omega} \\ -k_b\tilde{\omega} \end{bmatrix} = Fx_1, \quad (\text{G.29})$$

$$g(t, x_1) = -\frac{\dot{\omega}(t)}{I_s} = -\frac{\omega(t) - \tilde{\omega}}{I_s}, \quad (\text{G.30})$$

$$f_2(t, x_2) = -\frac{k_c\omega(t)^2}{I_s^2}\tilde{K}_\omega. \quad (\text{G.31})$$

The parameter estimation error in  $\Sigma_2$  was in Section G.1.2 shown to be UGES under PE conditions, and the observer error dynamics without the coupling term  $g(t, x_1)$  in  $\Sigma_1$  was in Section 5.1 shown to be GES. That is, the positive definite Lyapunov function  $V_2(x_1)$ :

$$V_2(x_1) = \frac{1}{2}x_1^\top Px_1, \quad P = \begin{bmatrix} p_{11} & 0 \\ 0 & p_{22} \end{bmatrix}, \quad (\text{G.32})$$

has a derivative along the trajectories of  $f_1(x_1)$  given by:

$$\dot{V}_2 = x_1^\top P\dot{x}_1 < 0 \quad \forall x_1 \in \{\mathbb{R}^2 - (0, 0)\}, \quad (\text{G.33})$$

for any positive constants  $p_{11}$  and  $p_{22}$ , given that the observer gain requirements in Proposition 5.1 are met. To demonstrate stability of the cascaded system, it must be shown that the interconnection term  $g(t, x_1)$  satisfy certain growth rate requirements. With  $\Sigma_2$  UGES and the unperturbed  $\Sigma_1$  system GES, Theorem 2 in Panteley *et al.* (1999) states that the cascaded system in (G.27) is uniformly globally asymptotically stable (UGAS) if the following additional requirements are met:

1.  $V_2(x_1)$  must satisfy:

$$\left\| \frac{\partial V_2}{\partial x_1} \right\| \|x_1\| \leq c_1 V_2(x_1) \quad \text{for all } \|x_1\| \geq \eta. \quad (\text{G.34})$$

2. The function  $g(t, x)$  must satisfy:

$$\|g(t, x_1)\| \leq \theta_1(\|x_2\|) + \theta_2(\|x_2\|) \|x_1\|, \quad (\text{G.35})$$

where  $\theta_1, \theta_2 : \mathbb{R}_{\geq 0} \rightarrow \mathbb{R}_{\geq 0}$  are continuous.

Since:

$$\begin{aligned} \left| \frac{\partial V_2}{\partial x_1} \right| |x_1| &= \left| \frac{\partial}{\partial x_1} \left( \frac{1}{2} p_{11} x_1^2 + \frac{1}{2} p_{22} x_2^2 \right) \right| |x_1| \\ &= |p_{11} x_1| |x_1| = p_{11} x_1^2, \end{aligned} \quad (\text{G.36})$$

and:

$$c_1 V_2(x_1) = c_1 \frac{1}{2} (p_{11} x_1^2 + p_{22} x_2^2) \geq \frac{c_1}{2} p_{11} x_1^2, \quad (\text{G.37})$$

requirement 1 is met for  $c_1 = 2$  and  $\eta = 0$ . Furthermore, since  $g(t, x_1)$  satisfies:

$$\begin{aligned} |g(t, x_1)| &= \frac{|\omega(t) - \tilde{\omega}|}{I_s} \leq \frac{|\omega(t)| + |\tilde{\omega}|}{I_s} \\ &\leq \frac{\omega_{\max} + |\tilde{\omega}|}{I_s} = \frac{\omega_{\max}}{I_s} + \frac{1}{I_s} |\tilde{\omega}| \\ &\leq \frac{\omega_{\max}}{I_s} + \frac{1}{I_s} |x_1| = \theta_1 + \theta_2 |x_1|, \end{aligned} \quad (\text{G.38})$$

where  $\omega_{\max}$  is the maximum shaft speed of the propeller and:

$$\theta_1 = \frac{\omega_{\max}}{I_s}, \quad \theta_2 = \frac{1}{I_s}, \quad (\text{G.39})$$

also requirement 2 is met. The cascaded system (G.27) is thereby shown to be UGAS. Note that the PE condition on  $\omega$  (i.e.  $\omega(t) \neq 0$ ) still applies.

#### G.1.4 Experimental results

The experiments were conducted at the Marine Cybernetics Laboratory (MCLab) at NTNU with the experimental setup described in Section 7.1. The open propeller was used. The true friction coefficient was found to be  $K_\omega \approx 0.01 \text{ Nms}$ .

The adaptive observer (G.24) was implemented together with a torque controller (3.29) and friction feedforward scheme (3.19) with  $Q_{f1}$  replaced with the estimate  $\hat{K}_\omega$ . The observer and parameter adaption gains were chosen as  $k_a = 15$ ,  $k_b = -25$ , and  $k_c = 5E - 10$ . Experiments in calm water with the adaptive observer alone confirmed that the parameter estimate converged to its true value, and that the propeller torque was tracked by the observer. In the experiments presented here, the propeller shaft had a mean submergence of 30cm, and the propeller was subject to irregular waves from the modified PM spectrum (C.19), with  $H_s = 5 \text{ cm}$  and  $T_p = 1.2 \text{ s}$ . The initial friction coefficient estimate was  $\hat{K}_{\omega 0} = 0$ , and the thrust reference was kept constant at  $T_r = 200 \text{ N}$ . The resulting time series are given in Figure G.1, which shows the raw and filtered shaft speed  $n$ , the raw and filtered motor torque  $Q_m$ , the actual friction coefficient  $K_\omega$  versus the estimated friction coefficient  $\hat{K}_\omega$ , the commanded torque  $Q_c$  with and without friction compensation  $Q_{ff}$ , the thrust reference  $T_r$  versus

the actual thrust  $T_a$ , and the actual torque  $Q_a$  versus the estimated torque  $\hat{Q}_a$ . The raw shaft speed and motor torque signals – which are used by the adaptive observer – are contaminated with some noise, and the motor torque is also clearly subject to quantization due to limited bit resolution. The parameter adaption scheme is enabled at approximately  $t = 12\text{s}$ , and clearly tracks the actual friction coefficient. This leads to an increased commanded torque (due to  $Q_{ff}$ ), and hence also increased shaft speed and thrust. The adaption of  $K_\omega$  also leads to a more correctly estimated load torque, which before the adaption was estimated too high. Experiments with varying thrust references and other operating conditions show similar performance.

### G.1.5 Extensions

As discussed in Chapter 8 with respect to the thruster controllers and observers, the adaptive observer is extendable to CPP and transit by letting  $K_{QC}$  in (G.24) be a function of the propeller pitch and vessel speed respectively.

The adaptive observer can also be used in extreme operating conditions, i.e. when the propeller is subject to ventilation. In order to get convergence of  $\hat{K}_\omega$ , however, it is necessary to disable estimation during ventilation. From Section 6.3, a ventilation detection signal  $\zeta$  is available from the loss calculation in (5.16) and the ventilation detection scheme in (6.1). The following modification can then be made to the adaptive observer in (G.24):

$$k_c = \begin{cases} k_{cc}, & \text{for } \zeta = 0 \quad (\text{no ventilation}), \\ 0, & \text{for } \zeta = 1 \quad (\text{ventilation}), \end{cases} \quad (\text{G.40})$$

where  $k_{cc} > 0$  is the chosen estimation gain. Experiments show that the adaptive observer then gives convergence of  $\hat{K}_\omega$  and a good estimate of  $\hat{Q}_a$ , even if the propeller is subject to frequent ventilation.

## G.2 Online control parameter estimation

In some applications, it will be useful to have estimates of the prevailing thrust and torque coefficients, in order to substitute these for the nominal values in the control coefficients. The prevailing thrust and torque coefficients,  $\bar{K}_T$  and  $\bar{K}_Q$ , are here defined as the mean coefficients over a finite time horizon, *including* the effect of steady-state advance velocity changes (due to current and vessel low-frequency motion), but *excluding* the losses due to ventilation, water exits, wave-induced water velocities, and vessel wave-frequency motion. That is, they would ideally be equal to low-pass filtered versions of  $K_{TJ}$  and  $K_{QJ}$  defined in Section 2.1.1. The desired properties of  $\bar{K}_T$  and  $\bar{K}_Q$  are the same as for the coefficient estimates proposed in Section E.2.5.

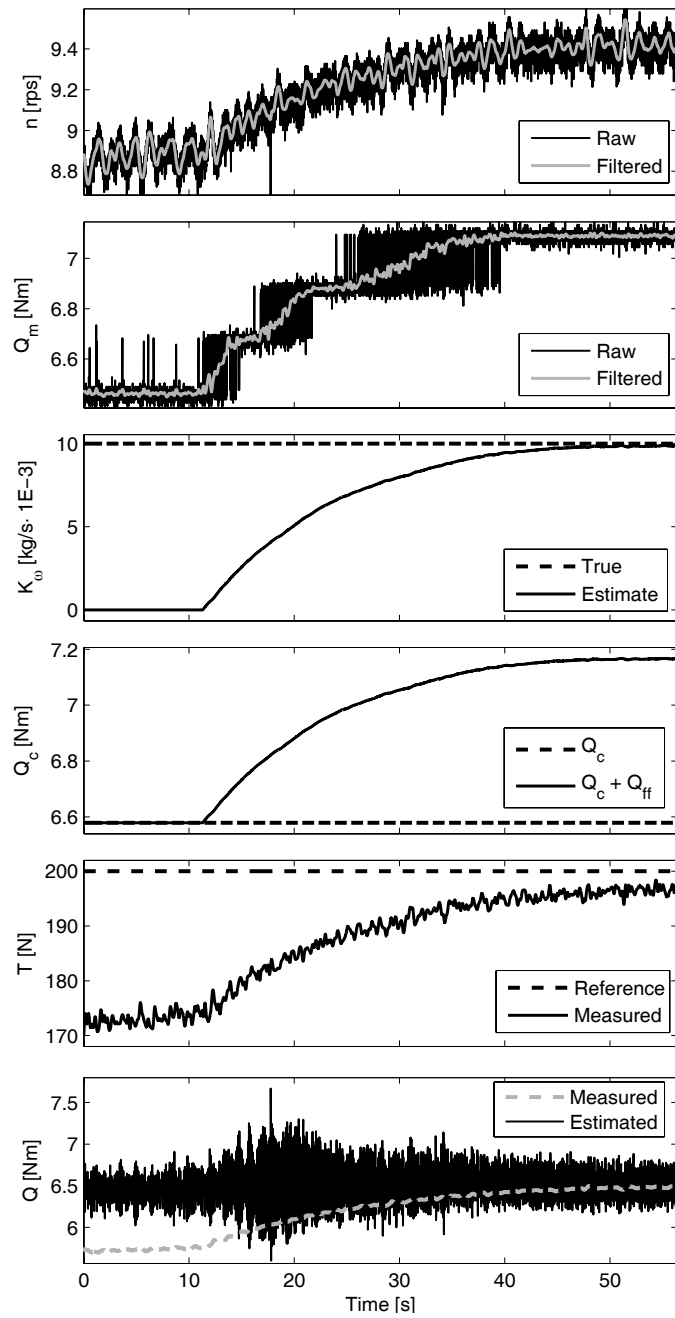


Figure G.2: Experimental results with the adaptive observer in irregular waves.

### G.2.1 Implementation for normal conditions

In normal operating conditions,  $\bar{K}_Q$  can be estimated directly from the  $K_Q$  estimation scheme in (5.26) using an appropriately low gain  $k_0$ . Alternatively, the load torque observer in (5.7) and  $\hat{K}_Q$  calculation in (5.17) can be used, and  $\bar{K}_Q$  taken as an average value of  $\hat{K}_Q$  over a time interval  $T$ :

$$\bar{K}_Q(t) = \frac{1}{T} \int_{t-T}^t \hat{K}_Q(\tau) d\tau. \quad (\text{G.41})$$

$\bar{K}_T$  can then be calculated from  $\bar{K}_Q$  using (2.48) by:

$$\bar{K}_T = a_t \bar{K}_Q + b_t. \quad (\text{G.42})$$

**Remark G.4** *The prevailing thrust coefficient  $\bar{K}_T$  can only be calculated with reasonable accuracy for an open propeller, due to the limitations of the  $K_T - K_Q$  relationship in (2.48).*

### G.2.2 Extension to extreme conditions

A possible useful application of  $\bar{K}_Q$  is ventilation detection during transit. This problem was discussed in Section 8.2.5. If  $\bar{K}_Q$  is used to replace  $K_{QC}$  in (5.16) and (5.19),  $\hat{\beta}_Q$  will stay close to unity regardless of the vessel forward speed and current, and be affected only by wave-frequency disturbances and ventilation.

For rejecting disturbances due to waves in  $\bar{K}_Q$ , it is sufficient to use a low estimation gain, or equivalently average the estimate over a time period  $T$ , as suggested in (G.41). If the propeller is subject to ventilation, however, additional measures are needed to remove the large thrust losses in the estimation of  $\bar{K}_Q$ . If not,  $\bar{K}_Q$  would be estimated too low. In Section 6.3, a ventilation detection scheme based on  $\hat{\beta}_Q$ , which outputs a detection signal  $\zeta \in \{0, 1\}$ , was developed. This can be utilized to disable estimation during ventilation:

$$\begin{aligned} \bar{K}_Q &= -k_0 c(\zeta) + z, \\ \dot{z} &= k_v(\zeta) \frac{\omega |\omega|}{I_s^2} (u - \hat{K}_Q \omega |\omega| - Q_f \omega), \\ k_v(\zeta) &= \begin{cases} k_0, & \text{for } \zeta = 0 \quad (\text{no ventilation}), \\ 0, & \text{for } \zeta = 1 \quad (\text{ventilation}), \end{cases} \\ c(\zeta) &= \begin{cases} \frac{|\omega|^3}{3I_s}, & \text{for } \zeta = 0 \quad (\text{no ventilation}), \\ \bar{c}, & \text{for } \zeta = 1 \quad (\text{ventilation}), \end{cases} \end{aligned} \quad (\text{G.43})$$

where the  $K_Q$  estimation scheme from (5.26) has been used as a starting point, and  $\bar{c}$  is the value of  $c(\zeta)$  at the instant of the switch  $\zeta : 0 \rightarrow 1$  (i.e. the “frozen” value of  $c(\zeta)$ ).

**Remark G.5** *The combination of  $\bar{K}_Q$  with  $\hat{K}_Q$  to calculate  $\hat{\beta}_Q$  depends on time scale separation: for the scheme to be valid, the update of  $\bar{K}_Q$  must be much slower than the update of  $\hat{K}_Q$ .*





**RAPPORTER  
UTGITT VED**  
**INSTITUTT FOR MARIN TEKNIKK**  
**(tidligere: FAKULTET FOR MARIN TEKNIKK)**  
**NORGES TEKNISK-NATURVITENSKAPELIGE UNIVERSITET**

- UR-79-01 Brigt Hatlestad, MK:  
The finite element method used in a fatigue evaluation of fixed offshore platforms.  
(Dr.Ing.Thesis)
- UR-79-02 Erik Pettersen, MK:  
Analysis and design of cellular structures.  
(Dr.Ing.Thesis)
- UR-79-03 Sverre Valsgård, MK:  
Finite difference and finite element methods applied to nonlinear analysis of plated structures.  
(Dr.Ing.Thesis)
- UR-79-04 Nils T. Nordsve, MK:  
Finite element collapse analysis of structural members considering imperfections and stresses due to fabrication. (Dr.Ing.Thesis)
- UR-79-05 Ivar J.Fylling, MK:  
Analysis of towline forces in ocean towing systems. (Dr.Ing.Thesis)
- UR-80-06 Nils Sandmark, MM:  
Analysis of Stationary and Transient Heat Conduction by the Use of the Finite Element Method. (Dr.Ing.Thesis)
- UR-80-09 Sverre Haver, MK:  
Analysis of uncertainties related to the stochastic modeling of Three-Dimensional Flow Past Lifting Surfaces and Blunt Bodies. (Dr.Ing.Thesis)
- UR-85-46 Alf G. Engseth, MK:  
Finite element collapse analysis of tubular steel offshore structures. (Dr.Ing.Thesis)
- UR-86-47 Dengody Sheshappa, MP:  
A Computer Design Model for Optimizing Fishing Vessel Designs Based on Techno-Economic Analysis. (Dr.Ing.Thesis)
- UR-86-48 Vidar Aanesland, MH:  
A Theoretical and Numerical Study of Ship Wave Resistance. (Dr.Ing.Thesis)
- UR-86-49 Heinz-Joachim Wessel, MK:  
Fracture Mechanics Analysis of Crack Growth in Plate Girders. (Dr.Ing.Thesis)
- UR-86-50 Jon Tabby, MK:  
Ultimate and Post-ultimate Strength of Dented Tubular Members. (Dr.Ing.Thesis)

- UR-86-51 Walter Lian, MH:  
A Numerical Study of Two-Dimensional Separated Flow Past Bluff Bodies at Moderate KC-Numbers. (Dr.Ing.Thesis)
- UR-86-52 Bjørn Sortland, MH:  
Force Measurements in Oscillating Flow on Ship Sections and Circular Cylinders in a U-Tube Water Tank. (Dr.Ing.Thesis)
- UR-86-53 Kurt Strand, MM:  
A System Dynamic Approach to One-dimensional Fluid Flow. (Dr.Ing.Thesis)
- UR-86-54 Arne Edvin Løken, MH:  
Three Dimensional Second Order Hydrodynamic Effects on Ocean Structures in Waves. (Dr.Ing.Thesis)
- UR-86-55 Sigurd Falch, MH:  
A Numerical Study of Slamming of Two-Dimensional Bodies. (Dr.Ing.Thesis)
- UR-87-56 Ame Braathen, MH:  
Application of a Vortex Tracking Method to the Prediction of Roll Damping of a Two-Dimension Floating Body. (Dr.Ing.Thesis)
- UR-87-57 Bernt Leira, MR:  
Caussian Vector Processes for Reliability Analysis involving Wave-Induced Load Effects. (Dr.Ing.Thesis)
- UR-87-58 Magnus Småvik, MM:  
Thermal Load and Process Characteristics in a Two-Stroke Diesel Engine with Thermal Barriers (in Norwegian) (Dr.Ing.Thesis)
- MTA-88-59 Bernt Arild Bremdal, MP:  
An Investigation of Marine Installation Processes - A Knowledge- Based Planning Approach. (Dr.Ing.Thesis)
- MTA-88-60 Xu Jun, MK:  
Non-linear Dynamic Analysis of Space-framed Offshore Structures. (Dr.Ing.Thesis)
- MTA-89-61 Gang Miao, MH:  
Hydrodynamic Forces and Dynamic Responses of Circular Cylinders in Wave Zones. (Dr.Ing.Thesis)
- MTA-89-62 Martin Greenhow, MH:  
Linear and Non-Linear Studies of Waves and Floating Bodies. Part I and Part II. (Dr.Techn.Thesis)
- MTA-89-63 Chang Li, MH:  
Force Coefficients of Spheres and Cubes in Oscillatory Flow with and without Current.(Dr.Ing.Thesis)

- MTA-89-64 Hu Ying, MP:  
A Study of Marketing and Design in Development  
of Marine Transport Systems. (Dr.Ing.Thesis)
- MTA-89-65 Arlid Jæger, MH:  
Seakeeping, Dynamic Stability and Performance  
of a Wedge Shaped Planing Hull. (Dr.Ing.Thesis)
- MTA-89-66 Chan Siu Hung, MM:  
The dynamic characteristics of tilting-pad  
bearings.
- MTA-89-67 Kim Wikstrøm, MP:  
Analysis av projekteringen for ett offshore projekt.  
(Licentiat-avhandl.)
- MTA-89-68 Jiao Guoyang, MR:  
Reliability Analysis of Crack Growth under  
Random Loading, considering Model Updating.  
(Dr.Ing.Thesis)
- MTA-89-69 Arnt Olufsen, MK:  
Uncertainty and Reliability Analysis of Fixed  
Offshore Structures. (Dr.Ing.Thesis)
- MTA-89-70 Wu Yu-Lin, MR:  
System Reliability Analyses of Offshore  
Structures using improved Truss and Beam  
Models. (Dr.Ing.Thesis)
- MTA-90-71 Jan Roger Hoff, MH:  
Three-dimensional Green function of a vessel with  
forward speed in waves. (Dr.Ing.Thesis)
- MTA-90-72 Rong Zhao, MH:  
Slow-Drift Motions of a Moored  
Two-Dimensional Body in Irregular Waves.  
(Dr.Ing.Thesis)
- MTA-90-73 Atle Minsaas, MP:  
Economical Risk Analysis. (Dr.Ing. Thesis)
- MTA-90-74 Knut-Arild Farnes, MK:  
Long-term Statistics of Response in Non-linear  
Marine Structures. (Dr.Ing. Thesis)
- MTA-90-75 Torbjørn Sotberg, MK:  
Application of Reliability Methods for Safety  
Assessment of Submarine Pipelines. (Dr.Ing.  
Thesis)
- MTA-90-76 Zeuthen, Steffen, MP:  
SEAMAID. A computational model of the design  
process in a constraint-based logic programming  
environment. An example from the offshore  
domain. (Dr.Ing. Thesis)
- MTA-91-77 Haagensen, Sven, MM:  
Fuel Dependant Cyclic Variability in a Spark  
Ignition Engine - An Optical Approach. (Dr.Ing.  
Thesis)
- MTA-91-78 Løland, Geir, MH:  
Current forces on and flow through fish farms.  
(Dr.Ing. Thesis)

- MTA-91-79 Hoen, Christopher, MK:  
System Identification of Structures Excited by Stochastic Load Processes. (Dr.Ing. Thesis)
- MTA-91-80 Haugen, Stein, MK:  
Probabilistic Evaluation of Frequency of Collision between Ships and Offshore Platforms. (Dr.Ing. Thesis)
- MTA-91-81 Sødahl, Nils, MK:  
Methods for Design and Analysis of Flexible Risers. (Dr.Ing. Thesis)
- MTA-91-82 Ormberg, Harald, MK:  
Non-linear Response Analysis of Floating Fish Farm Systems. (Dr.Ing. Thesis)
- MTA-91-83 Marley, Mark J., MK:  
Time Variant Reliability Under Fatigue
- MTA-91-79 Hoen, Christopher, MK:  
System Identification of Structures Excited by Stochastic Load Processes. (Dr.Ing. Thesis)
- MTA-91-80 Haugen, Stein, MR:  
Probabilistic Evaluation of Frequency of Collision between Ships and Offshore Platforms. (Dr.Ing. Thesis)
- MTA-91-81 Sødahl, Nils, MK:  
Methods for Design and Analysis of Flexible Risers. (Dr.Ing. Thesis)
- MTA-91-82 Ormberg, Harald, MK:  
Non-linear Response Analysis of Floating Fish Farm Systems. (Dr.Ing. Thesis)
- MTA-91-83 Marley, Mark J., MK:  
Time Variant Reliability Under Fatigue Degradation. (Dr.Ing. Thesis)
- MTA-91-84 Krokstad, Jørgen R., MH:  
Second-order Loads in Multidirectional Seas. (Dr.Ing. Thesis)
- MTA-91-85 Molteberg, Gunnar A., MM:  
The application of system identification techniques to Performance Monitoring of four stroke turbocharged Diesel Engines. (Dr.Ing. Thesis)
- MTA-92-86 Mørch, Hans Jørgen Bjelke, MH:  
Aspects of Hydrofoil Design; with Emphasis on Hydrofoil Interaction in Calm Water. (Dr.Ing. Thesis)
- MTA-92-87 Chan Siu Hung, MM:  
Nonlinear Analysis of Rotordynamic Instabilities in High-speed Turbomachinery. (Dr.Ing. Thesis)
- MTA-92-88 Bessason, Bjarni, MK:  
Assessment of Earthquake Loading and Response of Seismically Isolated Bridges. (Dr.Ing. Thesis)

MTA-92-89 <u>Langli, Geir</u> , MP:	Improving Operational Safety through exploitation of Design Knowledge - an investigation of offshore platform safety. (Dr.Ing. Thesis)
MTA-92-90 <u>Sævik, Svein</u> , MK:	On Stresses and Fatigue in Flexible Pipes. (Dr.Ing. Thesis)
MTA-92-91 <u>Ask, Tor Ø.</u> , MM:	Ignition and Flame Growth in Lean Gas-Air Mixtures. An Experimental Study with a Schlieren System. (Dr.Ing. Thesis)
MTA-86-92 <u>Hessen, Gunnar</u> , MK:	Fracture Mechanics Analysis of Stiffened Tubular Members. (Dr.Ing. Thesis)
MTA-93-93 <u>Steinebach, Christian</u> , MM:	Knowledge Based Systems for Diagnosis of Rotating Machinery. (Dr.Ing. Thesis)
MTA-93-94 <u>Dalane, Jan Inge</u> , MK:	System Reliability in Design and Maintenance of Fixed Offshore Structures. (Dr.Ing. Thesis)
MTA-93-95 <u>Steen, Sverre</u> , MH:	Cobblestone Effect on SES. (Dr.Ing. Thesis)
MTA-93-96 <u>Karunakaran, Daniel</u> , MK:	Nonlinear Dynamic Response and Reliability Analysis of Drag-dominated Offshore Platforms. (Dr.Ing. Thesis)
MTA-93-97 <u>Hagen, Arnulf</u> , MP:	The Framework of a Design Process Language. (Dr.Ing. Thesis)
MTA-93-98 <u>Nordrik, Rune</u> , MM:	Investigation of Spark Ignition and Autoignition in Methane and Air Using Computational Fluid Dynamics and Chemical Reaction Kinetics. A Numerical Study of Ignition Processes in Internal Combustion Engines. (Dr.Ing.Thesis)
MTA-94-99 <u>Passano, Elizabeth</u> , MK:	Efficient Analysis of Nonlinear Slender Marine Structures. (Dr.Ing.Thesis)
MTA-94-100 <u>Kvålsvold, Jan</u> , MH:	Hydroelastic Modelling of Wetdeck Slamming on Multihull Vessels. (Dr.Ing.Thesis)
MTA-94-101	(Dr.Ing.Thesis) <i>Ikke godkjent.</i>
MTA-94-102 <u>Bech, Sidsel M.</u> , MK:	Experimental and Numerical Determination of Stiffness and Strength of GRP/PVC Sandwich Structures. (Dr.Ing.Thesis)
MTA-95-103 <u>Paulsen, Hallvard</u> , MM:	A Study of Transient Jet and Spray using a Schlieren Method and Digital Image Processing. (Dr.Ing.Thesis)

- MTA-95-104 Hovde, Geir Olav, MK:  
Fatigue and Overload Reliability of Offshore Structural Systems, Considering the Effect of Inspection and Repair. (Dr.Ing.Thesis)
- MTA-95-105 Wang, Xiaozhi, MK:  
Reliability Analysis of Production Ships with Emphasis on Load Combination and Ultimate Strength. (Dr.Ing.Thesis)
- MTA-95-106 Ulstein, Tore, MH:  
Nonlinear Effects of a Flexible Stern Seal Bag on Cobblestone Oscillations of an SES. (Dr.Ing.Thesis)
- MTA-95-107 Solas, Frøydis, MH:  
Analytical and Numerical Studies of Sloshing in Tanks. (Dr.Ing.Thesis)
- MTA-95-108 Hellan, øyvind, MK:  
Nonlinear Pushover and Cyclic Analyses in Ultimate Limit State Design and Reassessment of Tubular Steel Offshore Structures. (Dr.Ing.Thesis)
- MTA-95-109 Hermundstad, Ole A., MK:  
Theoretical and Experimental Hydroelastic Analysis of High Speed Vessels. (Dr.Ing.Thesis)
- MTA-96-110 Bratland, Anne K., MH:  
Wave-Current Interaction Effects on Large-Volume Bodies in Water of Finite Depth. (Dr.Ing.Thesis)
- MTA-96-111 Herfjord, Kjell, MH:  
A Study of Two-dimensional Separated Flow by a Combination of the Finite Element Method and Navier-Stokes Equations. (Dr.Ing.Thesis)
- MTA-96-112 Æsøy, Vilmar, MM:  
Hot Surface Assisted Compression Ignition in a Direct Injection Natural Gas Engine. (Dr.Ing.Thesis)
- MTA-96-113 Eknes, Monika L., MK:  
Escalation Scenarios Initiated by Gas Explosions on Offshore Installations. (Dr.Ing.Thesis)
- MTA-96-114 Erikstad, Stein O., MP:  
A Decision Support Model for Preliminary Ship Design. (Dr.Ing.Thesis)
- MTA-96-115 Pedersen, Egil, MH:  
A Nautical Study of Towed Marine Seismic Streamer Cable Configurations. ( Dr.Ing.Thesis)
- MTA-97-116 Moksnes, Paul O., MM:  
Modeling Two-Phase Thermo-Fluid Systems Using Bond Graphs. (Dr.Ing. Thesis)
- MTA-97-117 Halse, Karl H., MK:  
On Vortex Shedding and Prediction of Vortex-Induced Vibrations of Circular Cylinders. (Dr.Ing. Thesis)

- MTA-97-118 Igland, Ragnar T., MK:  
A Thesis Submitted in Partial Fulfilment of the Requirements for the Degree of "Doktor Ingeniør". (Dr.Ing. Thesis)
- MTA-97-119 Pedersen, Hans-P., MP:  
Levendefiskteknologi for fiskefartøy. ( Dr.Ing. Thesis)
- MTA-98-120 Vikestad, Kyrre, MK:  
Multi-Frequency Response of a Cylinder Subjected to Vortex Shedding and Support Motions. (Dr.Ing. Thesis)
- MTA-98-121 Azadi, Mohammad R.E., MK:  
Analysis of Static and Dynamic Pile-Soil-Jacket Behaviour. (Dr.Ing. Thesis)
- MTA-98-122 Ulltang, Terje, MP:  
A Communication Model for Product Information. (Dr.Ing. Thesis)
- MTA-98-123 Torbergsen, Erik, MM:  
Impeller/Diffuser Interaction Forces in Centrifugal Pumps. (Dr.Ing. Thesis)
- MTA-98-124 Hansen, Edmond, MH:  
A Discrete Element Model to Study Marginal Ice Zone Dynamics and the Behaviour of Vessels Moored in Broken Ice. (Dr.Ing. Thesis)
- MTA-98-125 Videiro, Paulo M., MK:  
Reliability Based Design of Marine Structures. (Dr.Ing. Thesis)
- MTA-99-126 Mainçon, Philippe, MK:  
Fatigue Reliability of Long Welds Application to Titanium Risers. (Dr.Ing. Thesis)
- MTA-99-127 Haugen, Elin M., MH:  
Hydroelastic Analysis of Slamming on Stiffened Plates with Application to Catamaran Wetdecks. (Dr.Ing. Thesis)
- MTA-99-128 Langhelle, Nina K., MK:  
Experimental Validation and Calibration of Nonlinear Finite Element Models for Use in Design of Aluminium Structures Exposed to Fire. (Dr.Ing. Thesis)
- MTA-99-129 Berstad, Are J., MK:  
Calculation of Fatigue Damage in Ship Structures. (Dr.Ing. Thesis)
- MTA-99-130 Andersen, Trond M., MM:  
Short Term Maintenance Planning. (Dr.Ing.Thesis)
- MTA-99-131 Tveiten, Bård Wathne, MK:  
Fatigue Assessment of Welded Aluminum Ship Details. (Dr.Ing.Thesis)

- MTA-99-132 Søreide, Fredrik, MP:  
Applications of underwater technology in deep water archaeology. Principles and practice.  
(Dr.Ing.Thesis)
- MTA-99-133 Tønnesen, Rune, MH:  
A Finite Element Method Applied to Unsteady Viscous Flow Around 2D Blunt Bodies With Sharp Corners. (Dr.Ing.Thesis)
- MTA-99-134 Elvekrok, Dag R., MP:  
Engineering Integration in Field Development Projects in the Norwegian Oil and Gas Industry. The Supplier Management of Norne.  
(Dr.Ing.Thesis)
- MTA-99-135 Fagerholt, Kjetil, MP:  
Optimeringsbaserte Metoder for Ruteplanlegging innen skipsfart. (Dr.Ing.Thesis)
- MTA-99-136 Bysveen, Marie, MM:  
Visualization in Two Directions on a Dynamic Combustion Rig for Studies of Fuel Quality.  
(Dr.Ing.Thesis)
- MTA-2000-137 Storteig, Eskild, MM:  
Dynamic characteristics and leakage performance of liquid annular seals in centrifugal pumps.  
(Dr.Ing.Thesis)
- MTA-2000-138 Sagli, Gro, MK:  
Model uncertainty and simplified estimates of long term extremes of hull girder loads in ships.  
(Dr.Ing.Thesis)
- MTA-2000-139 Tronstad, Harald, MK:  
Nonlinear analysis and design of cable net structures like fishing gear based on the finite element method. (Dr.Ing.Thesis)
- MTA-2000-140 Kroneberg, André, MP:  
Innovation in shipping by using scenarios.  
(Dr.Ing.Thesis)
- MTA-2000-141 Haslum, Herbjørn Alf, MH:  
Simplified methods applied to nonlinear motion of spar platforms. (Dr.Ing.Thesis)
- MTA-2001-142 Samdal, Ole Johan, MM:  
Modelling of Degradation Mechanisms and Stressor Interaction on Static Mechanical Equipment Residual Lifetime. (Dr.Ing.Thesis)
- MTA-2001-143 Baarholm, Rolf Jarle, MH:  
Theoretical and experimental studies of wave impact underneath decks of offshore platforms.  
(Dr.Ing. Thesis)
- MTA-2001-144 Wang, Lihua, MK:  
Probabilistic Analysis of Nonlinear Wave-induced Loads on Ships. (Dr.Ing. Thesis)

MTA-2001-145 <u>Kristensen, Odd H.</u> , MK:	Ultimate Capacity of Aluminium Plates under Multiple Loads, Considering HAZ Properties. (Dr.Ing. Thesis)
MTA-2001-146 <u>Greco, Marilena</u> , MH:	A Two-Dimensional Study of Green-Water Loading. (Dr.Ing. Thesis)
MTA-2001-147 <u>Heggelund, Svein E.</u> , MK:	Calculation of Global Design Loads and Load Effects in Large High Speed Catamarans. (Dr.Ing. Thesis)
MTA-2001-148 <u>Babalola, Olusegun T.</u> , MK:	Fatigue Strength of Titanium Risers - Defect Sensitivity. (Dr.Ing. Thesis)
MTA-2001-149 <u>Mohammed, Abuu K.</u> , MK:	Nonlinear Shell Finite Elements for Ultimate Strength and Collapse Analysis of Ship Structures. (Dr.Ing. Thesis)
MTA-2002-150 <u>Holmedal, Lars E.</u> , MH:	Wave-current interactions in the vicinity of the sea bed. (Dr.Ing. Thesis)
MTA20-02-151 <u>Rognebakke, Olav F.</u> , MH:	Sloshing in rectangular tanks and interaction with ship motions (Dr.ing.thesis)
MTA-2002-152 <u>Lader, Pål Furset</u> , MH:	Geometry and Kinematics of Breaking Waves. (Dr.Ing. Thesis)
MTA-2002-153 <u>Yang, Qinzheng</u> , MH:	Wash and wave resistance of ships in finite water depth. (Dr.Ing. Thesis)
MTA-2002-154 <u>Melhus, Øyvin</u> , MM:	Utilization of VOC in Diesel Engines. Ignition and combustion of VOC released by crude oil tankers. (Dr.Ing. Thesis)
MTA-2002-155 <u>Ronæss, Marit</u> , MH:	Wave Induced Motions of Two Ships Advancing on Parallel Course. (Dr.Ing. Thesis)
MTA-2002-156 <u>Økland, Ole D.</u> , MK:	Numerical and experimental investigation of whipping in twin hull vessels exposed to severe wet deck slamming. (Dr.Ing. Thesis)
MTA-2002-157 <u>Ge, Chunhua</u> , MK:	Global Hydroelastic Response of Catamarans due to Wet Deck Slamming. (Dr.Ing. Thesis)
MTA-2002-158 <u>Byklum, Eirik</u> , MK:	Nonlinear Shell Finite Elements for Ultimate Strength and Collapse Analysis of Ship Structures. (Dr.Ing. Thesis).

IMT-2003-1 <u>Chen, Haibo</u> , MK:	Probabilistic Evaluation of FPSO-Tanker Collision in Tandem Offloading Operation. (Dr.Ing.Thesis)
IMT-2003-2 <u>Skaugset, Kjetil Bjørn</u> , MK	On the Suppression of Vortex Induced Vibrations of Circular Cylinders by Radial Water Jets. (Dr.ing.Thesis)
IMT-2003-3 Chezhian, Muthu	Three-Dimensional Analysis of Slamming (Dr.ing.Thesis)
IMT-2003-4 Buhaug, Øyvind	Deposit Formation on cylinder Liner Surfaces in Medium Speed Engines (Dr.ing.thesis)
IMT-2003-5 Tregde, Vidar	Aspects of Ship Design; Optimization of Aft Hull with Inverse Geometry Design (Dr.ing.thesis)
IMT-2003-6 Wist, Hanne Therese	Statistical Properties of Successive Ocean Wave Parameters (Dr.ing.thesis)
IMT-2004-7, Ransau, Samuel	Numerical Methods for Flows with Evolving Interfaces (Dr.ing.thesis)
IMT-2004-8, Soma, Torkel	Blue-Chip or Sub-Standard. A data interrogation approach of identity safety characteristics of shipping organization (Dr.ing.thesis)
IMT-2004-9 Ersdal, Svein	An experimental study of hydrodynamic forces on cylinders and cables in near axial flow (Dr.ing.thesis)
IMT-2005-10 Brodtkorb, Per Andreas	The Probability of Occurrence of Dangerous Wave Situations at Sea (Dr.ing.thesis)
IMT-2005-11 Yttervik, Rune	Ocean current variability in relation to offshore engineering (Dr.ing.thesis)
IMT-2005-12 Fredheim, Arne	Current Forces on Net-Structures (Dr.ing.thesis)
IMT-2005-13 Heggernes, Kjetil	Flow around marine structures (Dr.ing. thesis)
IMT-2005-14 Fouques, Sébastien	Lagrangian Modelling of Ocean Surface Waves and Synthetic Aperture Radar Wave Measurements (Dr.ing. thesis)
IMT-2006-15 Holm, Håvard	Numerical calculation of viscous free surface flow around Marine structures

IMT-2006-16 Bjørheim, Lars G.

Failure Assessment of Long Through Thickness  
Fatigue Cracks in Ship Hulls (Dr.ing.thesis)

IMT-2006-17 Hansson, Lisbeth

Safety Management for Prevention of  
Occupational Accidents (Dr.ing.thesis)

IMT-2006-18 Zhu, Xinying

Application of the CIP Method to Strongly  
Nonlinear Wave-Body Interaction Problems  
(Dr.ing.thesis)

IMT-2006-19 Reite, Karl Johan

Modeling and Control of Trawl Systems